

REPORT DOCUMENTATION PAGE			Form Approved OMB NO. 0704-0188		
<p>The public reporting burden for this collection of information is estimated to average 1 hour per response, including the time for reviewing instructions, searching existing data sources, gathering and maintaining the data needed, and completing and reviewing the collection of information. Send comments regarding this burden estimate or any other aspect of this collection of information, including suggestions for reducing this burden, to Washington Headquarters Services, Directorate for Information Operations and Reports, 1215 Jefferson Davis Highway, Suite 1204, Arlington VA, 22202-4302. Respondents should be aware that notwithstanding any other provision of law, no person shall be subject to any penalty for failing to comply with a collection of information if it does not display a currently valid OMB control number.</p> <p>PLEASE DO NOT RETURN YOUR FORM TO THE ABOVE ADDRESS.</p>					
1. REPORT DATE (DD-MM-YYYY) 09-02-2016		2. REPORT TYPE Final Report		3. DATES COVERED (From - To) 20-Sep-2009 - 19-Sep-2015	
4. TITLE AND SUBTITLE Final Report: Multiscale Design and Manufacturing of Hybrid DWCNT-Polymer Fibers			5a. CONTRACT NUMBER W911NF-09-1-0541		
			5b. GRANT NUMBER		
			5c. PROGRAM ELEMENT NUMBER 611103		
6. AUTHORS Horacio Espinosa, Markus Buehler			5d. PROJECT NUMBER		
			5e. TASK NUMBER		
			5f. WORK UNIT NUMBER		
7. PERFORMING ORGANIZATION NAMES AND ADDRESSES Northwestern University Evanston Campus 1801 Maple Avenue Evanston, IL 60201 -3149			8. PERFORMING ORGANIZATION REPORT NUMBER		
9. SPONSORING/MONITORING AGENCY NAME(S) AND ADDRESS (ES) U.S. Army Research Office P.O. Box 12211 Research Triangle Park, NC 27709-2211			10. SPONSOR/MONITOR'S ACRONYM(S) ARO		
			11. SPONSOR/MONITOR'S REPORT NUMBER(S) 56159-CH-MUR.72		
12. DISTRIBUTION AVAILABILITY STATEMENT Approved for Public Release; Distribution Unlimited					
13. SUPPLEMENTARY NOTES The views, opinions and/or findings contained in this report are those of the author(s) and should not be construed as an official Department of the Army position, policy or decision, unless so designated by other documentation.					
14. ABSTRACT This project was aimed to develop advanced fibers with high strength, stiffness, and toughness with low weight and cost for next-generation flexible armors. Toward this goal, this MURI team performed multiscale testing of hierarchical yarns; fabricated directly spun and mat-derived yarns for comparative studies of static mechanical properties and structural characterization; applied molecular mechanics and coarse-grained modeling of carbon nanotubes and bundles to predict shear interactions, interface properties, and load sharing; explored the effect of carbon nanotubes on the mechanical properties of graphene oxide paper as a macroscopic model to study the					
15. SUBJECT TERMS carbon nanotubes, hierarchical materials, DWNTpolymer fibers, bioinspired nanocomposites, lateral interactions, toughness, multiscale modeling, multiscale experiments, crosslinking					
16. SECURITY CLASSIFICATION OF:			17. LIMITATION OF ABSTRACT UU	15. NUMBER OF PAGES	19a. NAME OF RESPONSIBLE PERSON Horacio Espinosa
a. REPORT UU	b. ABSTRACT UU	c. THIS PAGE UU			19b. TELEPHONE NUMBER 847-/46-7598

Report Title

Final Report: Multiscale Design and Manufacturing of Hybrid DWCNT-Polymer Fibers

ABSTRACT

This project was aimed to develop advanced fibers with high strength, stiffness, and toughness with low weight and cost for next-generation flexible armors. Toward this goal, this MURI team performed multiscale testing of hierarchical yarns; fabricated directly spun and mat-derived yarns for comparative studies of static mechanical properties and structural characterization; applied molecular mechanics and coarse-grained modeling of carbon nanotubes and bundles to predict shear interactions, interface properties, and load sharing; explored the effect of carbon nanotubes on the mechanical properties of graphene oxide paper as a macroscopic model to study the interface between adjacent carbon-based nanofillers; and optimized polyacrylonitrile-nanofibers and nanofibers templated with graphene oxide nanoparticles.

Enter List of papers submitted or published that acknowledge ARO support from the start of the project to the date of this printing. List the papers, including journal references, in the following categories:

(a) Papers published in peer-reviewed journals (N/A for none)

<u>Received</u>	<u>Paper</u>
02/09/2016 67.00	Reza Mirzaeifar, Leon S. Dimas, Zhao Qin, Markus J. Buehler. Defect-Tolerant Bioinspired Hierarchical Composites: Simulation and Experiment, ACS Biomaterials Science & Engineering, (05 2015): 0. doi: 10.1021/ab500120f
02/09/2016 71.00	Tristan Giesa, Nicola M. Pugno, Joyce Y. Wong, David L. Kaplan, Markus J. Buehler. What's Inside the Box? - Length-Scales that Govern Fracture Processes of Polymer Fibers, Advanced Materials, (01 2014): 0. doi: 10.1002/adma.201303323
02/09/2016 70.00	Reza Mirzaeifar, Zhao Qin, Markus J Buehler. Tensile strength of carbyne chains in varied chemical environments and structural lengths, Nanotechnology, (09 2014): 0. doi: 10.1088/0957-4484/25/37/371001
02/09/2016 69.00	Arun K. Nair, Alfonso Gautieri, Markus J. Buehler. Role of Intrafibrillar Collagen Mineralization in Defining the Compressive Properties of Nascent Bone, Biomacromolecules, (07 2014): 0. doi: 10.1021/bm5003416
02/09/2016 68.00	Reza Mirzaeifar, Zhao Qin, Markus J. Buehler. Mesoscale mechanics of twisting carbon nanotube yarns, Nanoscale, (2015): 0. doi: 10.1039/C4NR06669C
08/30/2012 23.00	Graham Bratzel, Markus J. Buehler. Sequence-structure correlations in silk: Poly-Ala repeat of N. clavipes MaSp1 is naturally optimized at a critical length scale, Journal of the Mechanical Behavior of Biomedical Materials, (03 2012): 0. doi: 10.1016/j.jmbbm.2011.07.012
08/30/2012 25.00	Owen C. Compton, Zhi An, Karl W. Putz, Bong Jin Hong, Brad G. Hauser, L. Catherine Brinson, SonBinh T. Nguyen. Additive-free hydrogelation of graphene oxide by ultrasonication, Carbon, (08 2012): 0. doi: 10.1016/j.carbon.2012.01.061
08/30/2012 24.00	Owen C. Compton, Ali Abouimrane, Zhi An, Marc J. Palmeri, L. Catherine Brinson, Khalil Amine, SonBinh T. Nguyen. Exfoliation and Reassembly of Cobalt Oxide Nanosheets into a Reversible Lithium-Ion Battery Cathode, Small, (04 2012): 0. doi: 10.1002/sml.201101131
08/30/2013 43.00	T. Filleter, H.D. Espinosa. Multi-scale mechanical improvement produced in carbon nanotube fibers by irradiation cross-linking, Carbon, (12 2012): 1. doi: 10.1016/j.carbon.2012.12.016
08/30/2013 44.00	Allison M. Beese, Alexander Goponenko, Yan Zou, Dmitry Papkov, Mohammad Naraghi, Horacio D. Espinosa, Biswajit Saha, George C. Schatz, Alexander Moravsky, Raouf Loutfy, Sonbinh T. Nguyen, Yuris Dzenis. Extraordinary Improvement of the Graphitic Structure of Continuous Carbon Nanofibers Templated with Double Wall Carbon Nanotubes, ACS Nano, (12 2012): 126. doi: 10.1021/nn303423x
08/30/2013 47.00	Yin Zhang, Nicholas Valley, Alexandra H. Brozena, Yanmei Piao, Xiaoping Song, George C. Schatz, YuHuang Wang. Propagative Sidewall Alkylcarboxylation that Induces Red-Shifted Near-IR Photoluminescence in Single-Walled Carbon Nanotubes, The Journal of Physical Chemistry Letters, (03 2013): 826. doi: 10.1021/jz400167d

- 08/30/2013 48.00 Graham H. Bratzel, Tobin Filleter, Zhi An, Xiaoding Wei, SonBinh T. Nguyen, Markus J. Buehler, Horacio D. Espinosa, Mohammad Naraghi. Atomistic Investigation of Load Transfer Between DWNT Bundles "Crosslinked" by PMMA Oligomers, *Advanced Functional Materials*, (04 2013): 1883. doi: 10.1002/adfm.201201358
- 08/30/2013 49.00 Raouf O. Loutfy, Markus J. Buehler, SonBinh T. Nguyen, Horacio D. Espinosa, Allison M. Beese, Sourangsu Sarkar, Arun Nair, Mohammad Naraghi, Zhi An, Alexander Moravsky. Bio-Inspired Carbon Nanotube–Polymer Composite Yarns with Hydrogen Bond-Mediated Lateral Interactions, *ACS Nano*, (04 2013): 3434. doi: 10.1021/nn400346r
- 08/30/2013 50.00 Dmitry Papkov, Shuyou Li, Yuris Dzenis, Horacio D. Espinosa, Allison M. Beese. In situ transmission electron microscope tensile testing reveals structure–property relationships in carbon nanofibers, *Carbon*, (04 2013): 246. doi: 10.1016/j.carbon.2013.04.018
- 08/30/2013 51.00 Yanmei Piao, Brendan Meany, Lyndsey R. Powell, Nicholas Valley, Hyejin Kwon, George C. Schatz, YuHuang Wang. Brightening of carbon nanotube photoluminescence through the incorporation of sp³ defects, *Nature Chemistry*, (07 2013): 1. doi: 10.1038/nchem.1711
- 08/30/2013 52.00 Dmitry Papkov, Alexander Goponenko, Owen C. Compton, Zhi An, Xing-Zhong Li, Alexander Moravsky, SonBinh T. Nguyen, Yuris A. Dzenis. Improved Graphitic Structure of Continuous Carbon Nanofibers via Graphene Oxide Templating, *Advanced Functional Materials*, (06 2013): 1. doi: 10.1002/adfm.201300653
- 08/30/2013 54.00 Alfonso Gautieri, Shu-Wei Chang, Markus J. Buehler, Arun K. Nair. Molecular mechanics of mineralized collagen fibrils in bone, *Nature Communications*, (04 2013): 1. doi: 10.1038/ncomms2720
- 08/30/2013 55.00 Nicola M. Pugno, Steven W. Cranford, Markus J. Buehler. Synergetic Material and Structure Optimization Yields Robust Spider Web Anchorages, *Small*, (07 2013): 2747. doi: 10.1002/smll.201201343
- 08/30/2013 56.00 Yan Zou, Mohammad Nahid Andalib, Alexander Goponenko, Dmitry Papkov, Stephen Z. D. Cheng, Yuris A. Dzenis. Simultaneously Strong and Tough Ultrafine Continuous Nanofibers, *ACS Nano*, (04 2013): 3324. doi: 10.1021/nn400028p
- 08/31/2011 16.00 Zhao Qin, Markus Buehler. Cooperative deformation of hydrogen bonds in beta-strands and beta-sheet nanocrystals, *Physical Review E*, (12 2010): 0. doi: 10.1103/PhysRevE.82.061906
- 08/31/2011 22.00 Haoqing Hou, Yuris A. Dzenis, Alexander V. Goponenko. Avoiding fusion of electrospun 3,3',4,4'-biphenyltetracarboxylic dianhydride-4,4'-oxydianiline copolymer nanofibers during conversion to polyimide, *Polymer*, (8 2011): 0. doi: 10.1016/j.polymer.2011.06.023
- 08/31/2011 15.00 Markus J. Buehler. Tu(r)ning weakness to strength, *Nano Today*, (09 2010): 0. doi: 10.1016/j.nantod.2010.08.001
- 08/31/2011 12.00 Dipanjan Sen, Markus J. Buehler. Structural hierarchies define toughness and defect-tolerance despite simple and mechanically inferior brittle building blocks, *Scientific Reports*, (7 2011): 0. doi: 10.1038/srep00035
- 08/31/2011 9.00 Yanmei Piao, Chien-Fu Chen, Alexander A. Green, Hyejin Kwon, Mark C. Hersam, Cheng S. Lee, George C. Schatz, YuHuang Wang. Optical and Electrical Properties of Inner Tubes in Outer Wall-Selectively Functionalized Double-Wall Carbon Nanotubes, *The Journal of Physical Chemistry Letters*, (07 2011): 0. doi: 10.1021/jz200687u
- 08/31/2011 8.00 Shunliu Deng, Yin Zhang, Alexandra H. Brozena, Maricris Lodriguito Mayes, Parag Banerjee, Wen-An Chiou, Gary W. Rubloff, George C. Schatz, YuHuang Wang. Confined propagation of covalent chemical reactions on single-walled carbon nanotubes, *Nature Communications*, (7 2011): 0. doi: 10.1038/ncomms1384

- 08/31/2011 7.00 Graham H. Bratzel, Steven W. Cranford, Horacio Espinosa, Markus J. Buehler. Bioinspired noncovalently crosslinked "fuzzy" carbon nanotube bundles with superior toughness and strength, *Journal of Materials Chemistry*, (09 2010): 0. doi: 10.1039/c0jm01877e
- 08/31/2011 6.00 R. Bernal, S. Li, H.D. Espinosa, T. Filleter. Ultrahigh Strength and Stiffness in Cross-Linked Hierarchical Carbon Nanotube Bundles, *Advanced Materials*, (07 2011): 0. doi: 10.1002/adma.201100547
- 08/31/2011 5.00 Mohammad Naraghi, Tobin Filleter, Alexander Moravsky, Mark Locascio, Raouf O. Loutfy, Horacio D. Espinosa. A Multiscale Study of High Performance Double-Walled Nanotube?Polymer Fibers, *ACS Nano*, (11 2010): 0. doi: 10.1021/nn101404u
- 08/31/2011 20.00 Karl W. Putz, Owen C. Compton, Claire Segar, Zhi An, SonBinh T. Nguyen, L. Catherine Brinson. Evolution of Order During Vacuum-Assisted Self-Assembly of Graphene Oxide Paper and Associated Polymer Nanocomposites, *ACS Nano*, (08 2011): 0. doi: 10.1021/nn202040c
- 08/31/2011 19.00 Zhi An, Owen C. Compton, Karl W. Putz, L. Catherine Brinson, SonBinh T. Nguyen. Bio-Inspired Borate Cross-Linking in Ultra-Stiff Graphene Oxide Thin Films, *Advanced Materials*, (07 2011): 0. doi: 10.1002/adma.201101544
- 08/31/2011 18.00 Owen C. Compton, Bonny Jain, Dmitriy A. Dikin, Ali Abouimrane, Khalil Amine, SonBinh T. Nguyen. Chemically Active Reduced Graphene Oxide with Tunable C/O Ratios, *ACS Nano*, (06 2011): 0. doi: 10.1021/nn1030725
- 08/31/2011 17.00 Markus J. Buehler, Cranford. Materiomics: biological protein materials, from nano to macro, *Nanotechnology, Science and Applications*, (11 2010): 0. doi: 10.2147/NSA.S9037
- 08/31/2012 26.00 Owen C. Compton, Steven W. Cranford, Karl W. Putz, Zhi An, L. Catherine Brinson, Markus J. Buehler, SonBinh T. Nguyen. Tuning the Mechanical Properties of Graphene Oxide Paper and Its Associated Polymer Nanocomposites by Controlling Cooperative Intersheet Hydrogen Bonding, *ACS Nano*, (03 2012): 0. doi: 10.1021/nn202928w
- 08/31/2012 40.00 Tobin Filleter, Horacio D. Espinosa, Rodrigo A. Bernal. In Situ TEM Electromechanical Testing of Nanowires and Nanotubes, *Small*, (08 2012): 1. doi: 10.1002/sml.201200342
- 08/31/2012 39.00 Horacio D. Espinos, David Grégoire, Felix Latourte, Owen Loh. Identification of Deformation Mechanism in Abalone Shells Through AFM and Digital Image Correlation, *Procedia IUTAM*, (01 2012): 0. doi: 10.1016/j.piutam.2012.05.004
- 08/31/2012 37.00 Chien-Fu Chen, Alexander A. Green, Yanmei Piao, Hyejin Kwon, Mark C. Hersam, Cheng S. Lee, George C. Schatz, YuHuang Wang. Optical and Electrical Properties of Inner Tubes in OuterWall-Selectively Functionalized Double-Wall Carbon Nanotubes, *Journal of Physical Chemistry Letters*, (06 2011): 1577. doi:
- 08/31/2012 36.00 Mohammad Naraghi, Horacio D. Espinosa, Xiaoding Wei. Optimal Length Scales Emerging from Shear Load Transfer in Natural Materials: Application to Carbon-Based Nanocomposite Design, *ACS Nano*, (03 2012): 0. doi: 10.1021/nn204506d
- 08/31/2012 35.00 Tristan Giesa, David I. Spivak, Elizabeth Wood, Markus J. Buehler, Laurent Kreplak. Category Theoretic Analysis of Hierarchical Protein Materials and Social Networks, *PLoS ONE*, (9 2011): 0. doi: 10.1371/journal.pone.0023911
- 08/31/2012 34.00 Biswajit Saha, George C. Schatz. Carbonization in Polyacrylonitrile (PAN) Based Carbon Fibers Studied by ReaxFF Molecular Dynamics Simulations, *The Journal of Physical Chemistry B*, (04 2012): 0. doi: 10.1021/jp300581b
- 08/31/2012 33.00 Zhao Qin, Markus J. Buehler, Arun K. Nair. Cooperative deformation of carboxyl groups in functionalized carbon nanotubes, *International Journal of Solids and Structures*, (09 2012): 0. doi: 10.1016/j.ijsolstr.2012.05.002

- 08/31/2012 32.00 S. W. Cranford, M. J. Buehler, A. K. Nair. The minimal nanowire: Mechanical properties of carbyne, EPL (Europhysics Letters), (07 2011): 0. doi: 10.1209/0295-5075/95/16002
- 08/31/2012 31.00 Ajeet Kumar, Subrata Mukherjee, Jeffrey T. Paci, Karthick Chandraseker, George C. Schatz. A rod model for three dimensional deformations of single-walled carbon nanotubes, International Journal of Solids and Structures, (10 2011): 0. doi: 10.1016/j.ijsolstr.2011.06.004
- 08/31/2012 30.00 Tristan Giesa, Melis Arslan, Nicola M. Pugno, Markus J. Buehler. Nanoconfinement of Spider Silk Fibrils Begets Superior Strength, Extensibility, and Toughness, Nano Letters, (11 2011): 0. doi: 10.1021/nl203108t
- 08/31/2012 29.00 Tobin Filleter, Scott Yockel, Mohammad Naraghi, Jeffrey T. Paci, Owen C. Compton, Maricris L. Mayes, SonBinh T. Nguyen, George C. Schatz, Horacio D. Espinosa. Experimental-Computational Study of Shear Interactions within Double-Walled Carbon Nanotube Bundles, Nano Letters, (02 2012): 0. doi: 10.1021/nl203686d
- 08/31/2012 28.00 Steven W. Cranford, Anna Tarakanova, Nicola M. Pugno, Markus J. Buehler. Nonlinear material behaviour of spider silk yields robust webs, Nature, (02 2012): 0. doi: 10.1038/nature10739
- 08/31/2012 27.00 Markus Buehler, Steven Cranford. Packing efficiency and accessible surface area of crumpled graphene, Physical Review B, (11 2011): 0. doi: 10.1103/PhysRevB.84.205451
- 10/06/2014 57.00 Zhi An, Al'ona Furmanchuk, Rajaprakash Ramachandramoorthy, Tobin Filleter, Michael R. Roenbeck, Horacio D. Espinosa, George C. Schatz, SonBinh T. Nguyen. Inherent carbonaceous impurities on arc-discharge multiwalled carbon nanotubes and their implications for nanoscale interfaces, Carbon, (12 2014): 1. doi: 10.1016/j.carbon.2014.07.069
- 10/06/2014 58.00 Michael R. Roenbeck, Xiaoding Wei, Allison M. Beese, Mohammad Naraghi, Al'ona Furmanchuk, Jeffrey T. Paci, George C. Schatz, Horacio D. Espinosa. Scanning Electron Microscope Peeling To Quantify Surface Energy between Multiwalled Carbon Nanotubes and Graphene, ACS Nano, (01 2014): 124. doi: 10.1021/nn402485n
- 12/16/2015 66.00 Allison M. Beese, Zhi An, Sourangsu Sarkar, S. Shiva P. Nathamgari, Horacio D. Espinosa, SonBinh T. Nguyen. Defect-Tolerant Nanocomposites through Bio-Inspired Stiffness Modulation, Advanced Functional Materials, (05 2014): 0. doi: 10.1002/adfm.201303503
- 12/16/2015 65.00 Allison M. Beese, Xiaoding Wei, Sourangsu Sarkar, Rajaprakash Ramachandramoorthy, Michael R. Roenbeck, Alexander Moravsky, Matthew Ford, Fazel Yavari, Denis T. Keane, Raouf O. Loutfy, SonBinh T. Nguyen, Horacio D. Espinosa. Key Factors Limiting Carbon Nanotube Yarn Strength: Exploring Processing-Structure-Property Relationships, ACS Nano, (11 2014): 0. doi: 10.1021/nn5045504
- 12/16/2015 64.00 Xiaoding Wei, Tobin Filleter, Horacio D. Espinosa. Statistical shear lag model – Unraveling the size effect in hierarchical composites, Acta Biomaterialia, (05 2015): 0. doi: 10.1016/j.actbio.2015.01.040
- 12/16/2015 61.00 Xiaoding Wei, Matthew Ford, Rafael A. Soler-Crespo, Horacio D. Espinosa. A new Monte Carlo model for predicting the mechanical properties of fiber yarns, Journal of the Mechanics and Physics of Solids, (11 2015): 0. doi: 10.1016/j.jmps.2015.08.005
- 12/16/2015 62.00 Michael R. Roenbeck, Al'ona Furmanchuk, Zhi An, Jeffrey T. Paci, Xiaoding Wei, SonBinh T. Nguyen, George C. Schatz, Horacio D. Espinosa. Molecular-Level Engineering of Adhesion in Carbon Nanomaterial Interfaces, Nano Letters, (07 2015): 0. doi: 10.1021/acs.nanolett.5b01011
- 12/16/2015 60.00 Xiaoding Wei, Lily Mao, Rafael A. Soler-Crespo, Jeffrey T. Paci, Jiaying Huang, SonBinh T. Nguyen, Horacio D. Espinosa. Plasticity and ductility in graphene oxide through a mechanochemically induced damage tolerance mechanism, Nature Communications, (08 2015): 0. doi: 10.1038/ncomms9029

TOTAL: 54

Number of Papers published in peer-reviewed journals:

(b) Papers published in non-peer-reviewed journals (N/A for none)

<u>Received</u>	<u>Paper</u>
-----------------	--------------

TOTAL:

Number of Papers published in non peer-reviewed journals:

(c) Presentations

- H. D. Espinosa, “Peeling at the Nanoscale: Experiments and Simulations”, Gordon Research Conference: Nano-Mechanical Interfaces, Hong Kong, China, Jul. 19-24, 2015.
- H. D. Espinosa, M. R. Roenbeck, X. Wei, J. T. Paci, G. C. Schatz, “Role of Interfacial Chemistry Assessed Through In Situ SEM Peeling Experiments”, Society for Experimental Mechanics Annual Conference, Costa Mesa, CA, Jun. 8-11, 2015.
- M. R. Roenbeck, X. Wei, A. M. Beese, M. Naraghi, A. Furmanchuk, J. T. Paci, G. C. Schatz and H. D. Espinosa, “Investigating MWCNT-graphene surface energy through in situ SEM Peeling”, Society of Engineering Science Annual Technical Meeting, West Lafayette, IN, Oct. 1-3, 2014.
- M. Buehler, “Multiscale modelling of structuremechanics relationships of biological fibrous materials” 6th International Conference on Mechanics of Biomaterials and Tissues, Waikoloa, Hawaii, 2015, December 6–10
- M. Buehler, “Bioinspired materials achieved by design, optimization and manufacturing” 6th International Conference on Mechanics of Biomaterials and Tissues, Waikoloa, Hawaii, 2015, December 6–10
- M. Buehler, “Designs of Nanoporous Materials for High-Speed Water Filtration by Considering Nonlinear Viscosity of Water at Interfaces” Materials Research Society (MRS) Fall Meeting, Boston, MA, 2015, November 29–December 4
- M. Buehler, “Secondary Structure Transition and Critical Stress during the Assembly of Spider Silk Fibers” Materials Research Society (MRS) Fall Meeting, Boston, MA, 2015, November 29–December 4
- M. Buehler, “Optimization Algorithm Combined with 3D-Printing Technology to Create Tougher and Stronger Composites” Materials Research Society (MRS) Fall Meeting, Boston, MA, 2015, November 29–December 4
- M. Buehler, “Nano-Deformation Mechanisms in Bone Tissue in Tension and Compression” Materials Research Society (MRS) Fall Meeting, Boston, MA, 2015, November 29–December 4
- M. Buehler, “Multiscale computational modeling of collagen fibrils”, TERMIS World Congress, Boston, 2015, Sept. 9
- M. Buehler, “Bottom-up Design of the Structure and Mechanics of Interfacial Materials”, 7th World Congress of Biomechanics (WCB), Boston, 2014, July 6-11
- M. Buehler, “Bottom-up Design of the Structure and Mechanics of Interfacial Materials”, AmeriMech Symposium, Virginia Tech, Blacksburg, VA, 2014, May
- M. Buehler, “Bio-Inspired Graphene Oxide - Polydopamine Nanocomposite with Enhanced Mechanical Properties” Materials Research Society (MRS) Fall Meeting, Boston, MA, 2015, November 29–December 4
- M. Buehler, “Silk-Inspired Design, Optimization and Manufacturing of Synthetic Structural Materials for High Strength” Materials Research Society (MRS) Fall Meeting, Boston, MA, 2015, November 29–December 4
- M. Buehler, “Mechanics of Fragmentation of Crocodile Skin and Bio-Inspired Composites Designs” Materials Research Society (MRS) Fall Meeting, Boston, MA, 2015, November 29–December 4
- M. Buehler, “3D-Printed Bone-Inspired Composites” Materials Research Society (MRS) Fall Meeting, Boston, MA, 2015, November 29–December 4
- M. Buehler, “Behavior of a Silkworm Silk Fiber Web Structure under Wind Load” Materials Research Society (MRS) Fall Meeting, Boston, MA, 2015, November 29–December 4
- M. Buehler, “Multi-Scale Modelling of Wood Cell Wall Material” Materials Research Society (MRS) Fall Meeting, Boston, MA, 2015, November 29–December 4
- M. Buehler, “Molecular Mechanics of Polycrystalline Graphene with Enhanced Fracture Toughness” Materials Research Society (MRS) Fall Meeting, Boston, MA, 2015, November 29–December 4
- M. Buehler, “Morphology and Mechanics of 2D Nanomaterials on Substrates: From Wrinkle to Exfoliation and Fracture” Materials Research Society (MRS) Fall Meeting, Boston, MA, 2015, November 29–December 4

Number of Presentations: 20.00

Non Peer-Reviewed Conference Proceeding publications (other than abstracts):

Received Paper

TOTAL:

Number of Non Peer-Reviewed Conference Proceeding publications (other than abstracts):

Peer-Reviewed Conference Proceeding publications (other than abstracts):

Received Paper

TOTAL:

(d) Manuscripts

<u>Received</u>	<u>Paper</u>
02/22/2011	1.00 Mohammad Naraghi, Tobin Filleter, Alexander Moravsky, Mark Locascio, Raouf O. Loutfy, Horacio D. Espinosa†. A Multiscale Study of High Performance Double-Walled Nanotube rPolymer Fibers, ACS Nano (10 2010)
02/22/2011	3.00 T. Filleter, R. Bernal, S. Li, H.D. Espinosa. Ultrahigh Strength and Stiffness in Cross-Linked Hierarchical Carbon Nanotube Bundles, Advanced Materials (02 2011)
02/22/2011	2.00 Graham H. Bratzel, Steven W. Cranford, Horacio Espinosa, Markus J. Buehler. Bioinspired noncovalently crosslinked fuzzy carbon nanotube bundles with superior toughness and strength, Journal of Materials Chemistry (09 2010)
10/06/2014	59.00 Allison Beese, Xioding Wei, Sourangsu Sarkar, Rajaprakash Ramachandramoorthy, Michael Roenbeck, Alexander Moravsky, Matthew Ford, Fazel Yavari, Denis Keane, Raouf Loutfy, SonBinh Nguyen, Horacio Espinosa. What Limits the Strength of Carbon Nanotube Yarns? Exploring Processing-Structure-Property Relationships, ACS Nano (07 2014)
TOTAL:	4

Number of Manuscripts:

Books

<u>Received</u>	<u>Book</u>
08/30/2013	45.00 M.J. Buehler, S.W. Cranford. Biomateriomics, New York: Springer, (08 2012)
08/31/2012	38.00 Markus Buehler, Steven Cranford. Biomateriomics, New York, NY: Springer, (01 2012)
08/31/2012	41.00 Horacio Espinosa, Gang Bao. Nano and Cell Mechanics - Fundamentals and Frontiers, New York: Wiley, (01 2013)
TOTAL:	3

Received

Book Chapter

TOTAL:

Patents Submitted

Patents Awarded

Awards

M. Buehler - Elected Member, Society of Engineering Science Board of Directors, 2016

M. Buehler - McAfee Professor of Engineering, MIT-wide Endowed Chair Professorship, 2015

M. Buehler - Elected Fellow, AIMBE, 2015

M. Buehler - ASME Journal of Applied Mechanics Award 2014

Graduate Students

<u>NAME</u>	<u>PERCENT SUPPORTED</u>	Discipline
Siyan Dong	0.25	
Shiva Nathamgari	0.75	
Michael Roenbeck	0.00	
Rafael Soler-Crespo	0.00	
Dieter Brosnan Brommer	0.00	
Tristan Giesa	0.00	
Grace Gu	0.00	
GangSeob Jung	0.00	
Anna Tarakanova	0.00	
FTE Equivalent:	1.00	
Total Number:	9	

Names of Post Doctorates

<u>NAME</u>	<u>PERCENT SUPPORTED</u>
Wei Gao	0.63
Srikanth Ammu	0.13
Josh Broussard	0.25
Rebecca McNaughton	0.92
Fan Zhou	0.14
Changjin Huang	0.35
Shu-wei Chang	0.00
Baptiste Depalle	0.00
Francisco Martin-Martinez	0.00
FTE Equivalent:	2.42
Total Number:	9

Names of Faculty Supported

<u>NAME</u>	<u>PERCENT SUPPORTED</u>	National Academy Member
Horacio Espinosa	0.01	
Markus Buehler	0.00	
FTE Equivalent:	0.01	
Total Number:	2	

Names of Under Graduate students supported

<u>NAME</u>	<u>PERCENT SUPPORTED</u>
FTE Equivalent:	
Total Number:	

Student Metrics

This section only applies to graduating undergraduates supported by this agreement in this reporting period

The number of undergraduates funded by this agreement who graduated during this period: 0.00

The number of undergraduates funded by this agreement who graduated during this period with a degree in science, mathematics, engineering, or technology fields:..... 0.00

The number of undergraduates funded by your agreement who graduated during this period and will continue to pursue a graduate or Ph.D. degree in science, mathematics, engineering, or technology fields:..... 0.00

Number of graduating undergraduates who achieved a 3.5 GPA to 4.0 (4.0 max scale):..... 0.00

Number of graduating undergraduates funded by a DoD funded Center of Excellence grant for Education, Research and Engineering:..... 0.00

The number of undergraduates funded by your agreement who graduated during this period and intend to work for the Department of Defense 0.00

The number of undergraduates funded by your agreement who graduated during this period and will receive scholarships or fellowships for further studies in science, mathematics, engineering or technology fields: 0.00

Names of Personnel receiving masters degrees

<u>NAME</u>
Total Number:

Names of personnel receiving PhDs

<u>NAME</u> Tristan Giesa Shu-Wei Chang Total Number:	2
-----------------------------------------------------------------------	----------

Names of other research staff

<u>NAME</u>	<u>PERCENT SUPPORTED</u>
FTE Equivalent:	
Total Number:	

Sub Contractors (DD882)

Inventions (DD882)

Scientific Progress

See Attachment

Technology Transfer

**MURI Award No. W911NF-08-1-0541
FINAL REPORT
Scientific Progress and Accomplishments**

Table of Contents

Award year 2010	2
Award year 2011	23
Award year 2012	64
Award year 2013	122
Award year 2014	172
Award year 2015 (Extension)	216

MURI Award No. W911NF-08-1-0541
Scientific Progress and Accomplishments

The primary activities of the **Espinosa group** were to both develop the *ex-situ fabrication of and conduct multiscale testing of DWNT/Polymer yarns and their constituents*. Yarns are fabricated in collaboration with **A. Moravsky** using DWNT mats produced by MER Corp. The work on the development of an ex-situ fabrication system for DWNT/Polymer yarns directly relates to the development of polymer crosslinking elements in the **Nguyen** group. In-situ SEM/TEM multiscale mechanical testing methods are used to investigate the mechanical behavior at the individual CNT, CNT bundle, and macroscopic yarn hierarchical levels. Tensile and pullout experiments on individual CNTs and bundles are being directly compared to atomistic calculations in the **Schatz** group, which focus on tube-tube interactions of functionalized nanotubes, and larger scale coarse grained calculations in the **Buehler** group which model entire CNT bundles. The methodologies developed for testing DWNT materials are also being translated to study electrospun fibers by the **Dzenis** group.

As part of the aforementioned activities, we have performed initial characterization on the DWNT material from MER Corp. to identify the structure of the polymer coating formed during the CVD process. In addition, we have identified a heat treatment protocol which allows for the removal of the polymer coating without significantly affecting the structure of the DWNTs. A spinning system which incorporates polymer infiltration during the fabrication process has been developed. Figure 1 shows the hierarchical structure at different levels for DWNT/Polymer yarns spun from DWNT mats produced by MER Corp. Initial studies have demonstrated the effect of the polymer coating or “sizing” which forms on the tubes in the CVD reactor. Through multiscale experiments, we have identified that the polymer has a significant contribution to improve the ductility and energy to failure behavior of yarns. In addition, in-situ testing on isolated DWNT bundles has given us insights into the current utilization of DWNTs within the macroscopic yarns and suggested how we can improve performance in future work.

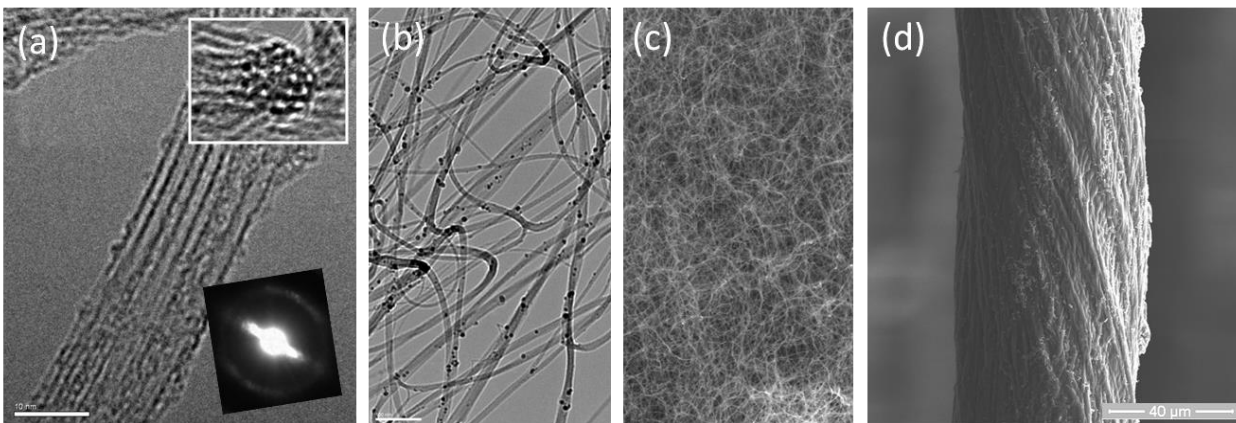


Figure 1: Hierarchy of DWNT mat materials. **(a)** TEM image of a individual DWNT bundle. Insets: **(top)** the cross-section of an individual bundle; **(bottom)** the nano-diffraction pattern of an individual bundle. **(b)** TEM image of interconnected DWNT bundles including imbedded Fe particles. **(c)** SEM image of a DWNT mat. **(d)** SEM image of a DWNT yarn.

The primary activity of the **Schatz group** was to *model the structural and mechanical properties of functionalized carbon nanotubes and nanotube bundles*, including DWNTs and sizing that are modeled on the MER Corporation (**A. Moravsky**) synthesis (Figure 2). Both electronic structure and empirical force field methods are used, with electronic structure theory providing validation for the empirical force fields. This work relates directly to experiments being done in the **Espinosa** group, and it provides calibration for the larger scale calculations that are being done by **Buehler**. In addition, related studies

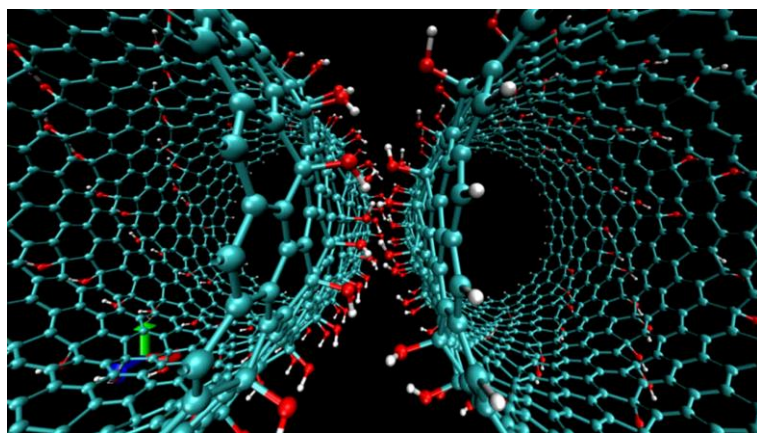


Figure 2: Model of two (27,0) single-walled nanotubes separated by 4.4 Angstroms with 15% sizing which is assumed to be OH groups

and films of carbon nanotubes, including so-called buckypaper (see Figure 3 for a visualization of the coarse-graining approach used here). Carbon nanotube sheets or films, also known as “buckypaper”, have been proposed for use in actuating, structural, and filtration systems, based in part on their unique and robust mechanical properties. Computational modeling of such a fibrous nanostructure was thus far hindered by both the random arrangement of the constituent elements, as well as the time and length scales accessible to atomistic-level molecular dynamics modeling. This new model is important to tie in with the efforts at MER corporation (**A. Moravsky**), the **Espinosa** and **Schatz** groups, and other MURI groups as it provides a powerful basis to capture the mesoscale structure and properties, believed to be a key scale in understanding carbon nanotube bundle and fiber mechanics by enabling a quantitative link between atomistic (chemical) scales and large micrometer and beyond scales.

The **Nguyen group** has worked on *understanding and enhancing the chemical rationale behind load transfer and mechanical properties in hierarchal materials with covalently linked organic nanostructures as load-bearing units*. We have studied graphene oxide films and polymer composite films as a well-characterized model system to determine the efficacy of both hydrogen bonding and covalent cross-linking between graphene oxide sheets in load transfer. In collaboration with **Buehler** and **Schatz**, these systems have been simulated to further elucidate the effect of cross-linking molecules. In collaboration with **Espinosa**, proven cross-linking techniques in the graphene oxide model system have been transferred to carbon nanotube-polymer yarns to enhance their mechanical properties.

The goal of the **Dzenis group**’s research is to *design, manufacture, and demonstrate high-performance disruptive fibers based on continuous nanofilaments*. The focus in the reporting period was on individual nanofilaments. Nanomanufacturing and characterization of both poly(acrylonitrile) (PAN) and Carbon Nanofilaments has been carried out. In particular, the mechanical behavior of these nanofilaments was found to be strongly dependant on fiber diameter. Carbon nanofiber precursors were modified in collaboration with the **Nguyen** group by incorporating graphene

(described below) are useful for characterizing graphene and polymer/CNT structures that are relevant to the **Nguyen** and **Dzenis** experiments.

The thrust in the **Buehler group**’s research program was geared towards the *development, validation and application of a carbon nanotube coarse-grain model*.

The objective of this model was to develop a description of carbon nanotubes that is computationally highly efficient, and that thereby allows us to simulate large assemblies, clusters (see Figure 3 for a visualization of the

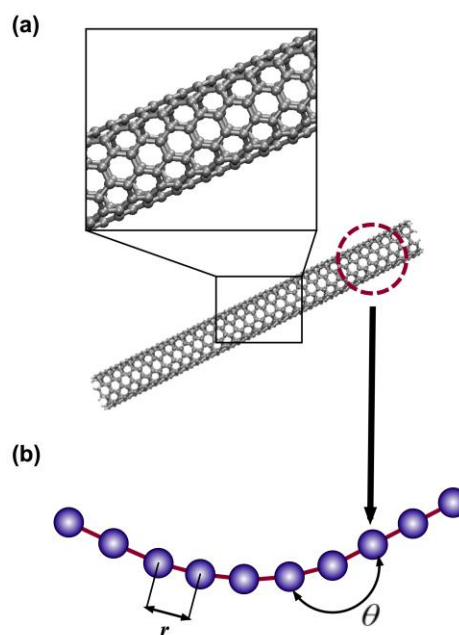


Figure 3: Coarse-grain representation of carbon nanotube through “fine-trains-coarse” approach: (a) Full atomistic and corresponding (b) mesoscopic bead-spring model of a carbon nanotube. Parameters for tensile, bending, and pair potentials are developed for both (5,5) SWCNT and (8,8)-(12,12) DWCNT.

nanoparticles into PAN nanofibers for the first time. Purified DWNTs fabricated by **A. Moravsky** at MER Corp. were also incorporated into continuous nanofibers. Ultrathin PAN and Carbon Nanofilaments have also been sent to the **Espinosa** group for future in-situ Raman and TEM mechanical testing to track deformation of embedded graphene nanoparticles in PAN filaments as well as structural changes in small diameter Carbon filaments.

The goal of the **Moravsky group** at MER Corp., in close collaboration with the **Espinosa** group, is to *develop the methodologies to fabricate DWNT-based yarns* using two approaches. In the first approach, the focus was on fabricating DWNT yarns by carrying out elaborate processing on DWNT mats which are grown inside their CVD reactor. Since the spinning of the yarns and processing yarns is performed outside the reactor, the method facilitates the application of different treatments on the yarns and optimization of the processing treatments which are then to be applied to yarns spun directly inside the CVD reactor. The processing include the application of bonding agents and crosslinks to enhance the interactions between CNT bundles, mechanical treatments such as twisting and stretching of the mats into yarns, and thermal treatments. The second approach into spinning DWNT yarns is to develop the capabilities to grow DWNT-based yarns in situ CVD reactor. The efforts in this direction have proven to be fruitful as will be explained in the following sections. These efforts are closely linked to the multiscale mechanical characterization done by the **Espinosa** group, in which further treatments are applied on the in situ CVD spun yarns to obtain flaw resistant yarns with relatively uniform diameters.

Scientific Accomplishments:

Fabrication of CNT/polymer and electrospun nanofilaments and yarns

*1. Ex-situ fabrication of high performance DWNT/Polymer yarns. (***)**Proprietary**(***)*

As-produced mats of DWNTs were provided by A. Moravsky at MER Corporation. They were highly porous (with a density of $\sim 0.04 \text{ gcm}^{-3}$), as shown in Figure 1b and c. Mats were spun into yarns by the Espinosa group using a set up located at MER Corporation. For the spinning process, the CNT mats were cut into 1/8"- 1/2" wide and several-inch-long ribbons. Subsequently, they were twisted to a few turns per millimeter of length of the ribbons. The twisting procedure was found to substantially reduce the fragility of the original mat, and turn them into fine yarns with the diameter of $\sim 40\text{-}100 \text{ }\mu\text{m}$, as measured in SEM, Figure 1 d. The twisting procedure was also accompanied by stretching the yarns. The load in the yarn during the process of spinning was monitored to avoid the rupture of the yarn and premature twist. During spinning, oleum was sprayed on the sample which promoted sample relaxation, by allowing for the mutual sliding of bundles and dissolving of the sizing. After spinning, the samples were left at room temperature for a few hours to dry and reform lateral bonds between DWNTs.

Recently a spinning setup was fabricated in Northwestern University by the Espinosa group. The set up, shown in Figure 4, includes an atomizer (for enhanced infiltration of solvents and polymers) as well as actuation and sensing for full automated processing with feedback control implemented in LabView. This set up is currently being used in collaboration with the Nguyen group to investigate borate crosslinks as well as other chemical crosslinking/modification strategies.

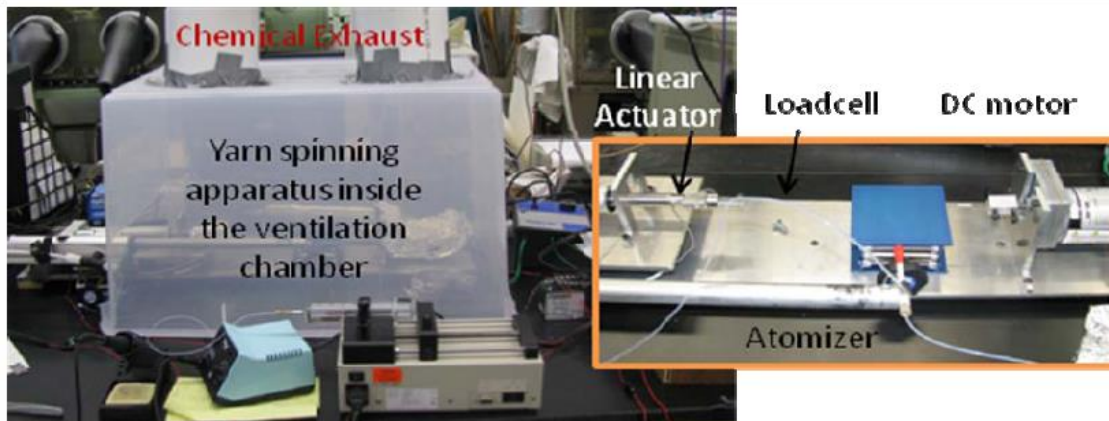


Figure 4: Fabrication yarn-spinning apparatus with cross-linking agent introduction system. The atomizer moves along the yarn during spinning, spraying various solvents, chemical modifiers, or polymers. For example, we have employed sodium borate in N,N-dimethyl formamide, which simultaneously dissolves the polymer coating and introduces the cross-linking agent into the structure.

2. In-situ CVD fabrication of DWNT/Polymer yarns (****Proprietary****)

Despite the high strength and toughness of the *ex-situ* CVD fabricated yarns, their mass production is not yet well-realized. In addition, it is not trivial through *ex-situ* fabrication to obtain high CNT bundle alignment, due to the presence of significant entanglement between bundles. An alternative approach toward the fabrication of CNT based yarns is to spin the CNT aerogel sock that is formed inside the hot zone of the CVD reactor. In this regard, the Moravsky group has developed the capability to fabricate CNT based yarns directly from the CNT aerogel inside a CVD reactor at MER Corp.

The directly spun yarns are produced as follows. A hollow cylindrical shape aerogel sock consisting of loosely connected long nanotubes and their bundles is formed in the hot zone of the vertical CVD reactor and is carried downstream by the flow of gas (Figure 5). At a moment, a spindle (cold finger) is moved through the vacuum port in the lower flange of the reactor tube to contact the sock, which is stretched and twisted into a yarn by driving downward and rotating the spindle (Figure 5). Twisted yarns of up to 10" length are produced, limited by the size of hermetic compartment, and released from the reactor through the bottom port.

A highly uniform cylindrical shape of twisted yarns of ~ 10-30 μm diameter can extend over a few inch lengths. As thin as 5 μm in diameter twisted yarns can be produced, which is the smallest size known for fibers made of nanotubes. Smaller diameter is generally conducive to higher strength of yarns, which tendency has been confirmed for directly spun DWNT yarns by tensile testing. Another distinctive feature of directly spun twisted yarns is a very large twist angle, up to 60° , that can be achieved (Figure 6) in more compact high twist yarns, the intertube load transfer becomes more effective and the mechanical properties improve. Further compaction can be achieved by additional post-synthesis stretching of the as-produced yarns, which is expedient to perform with yarns wetted by a solvent capable of dissolving or swelling sizing, thus providing re-distribution of sizing in the yarn, facilitating mutual displacement of bundles and increasing the strength of inter-bundle contacts. Diameter and twisting angle of wetted and additionally stretched yarns decrease by up to ~ 10-15 % and display an increase in the strength and the modulus by up to 50%.

Stretching is the major mechanism of aligning nanotubes in the directly spun yarns. Twisting can significantly add to the degree of alignment. A better alignment of nanotubes in the directly spun yarns, compared to *ex-situ* yarns made of random DWNT mats; is due to a lower amount of intertube contacts in the sock. Substantial alignment of bundles commonly persists in SEM images (Figure 7) and is the main reason for generally higher strength of directly spun yarns.

Despite being relatively well aligned, the density of bundles in the directly spun yarns is low. Analysis of SEM images provides a value of 10 to 25 % for the DWNT volume fraction (V_f), which can be used to preliminarily estimate the strength and the modulus of yarns from the tensile testing data that was obtained for a set of first samples at a gauge length ca. 1 cm. These estimates show that the directly spun DWNT yarns can exhibit very high mechanical properties. The tensile strength and the modulus can reach ~ 4 GPa and ~ 200 GPa for the best samples of very thin yarns. Elongation to break can reach 20-30% for the highly twisted thin yarns, however is commonly limited to 3-10% values by the presence of structural defects. The toughness of the best samples reaches outstanding values around 250 J/g, supposedly due to the low defect density and high twist, while the values of 40-100 J/g are characteristic of the main body of samples. A more accurate evaluation of mechanical properties can be performed by precisely measuring the linear density of a few micrograms by weight tensile test samples of very thin yarns. Despite being a real challenge, the task is surmountable the work is in fair progress.

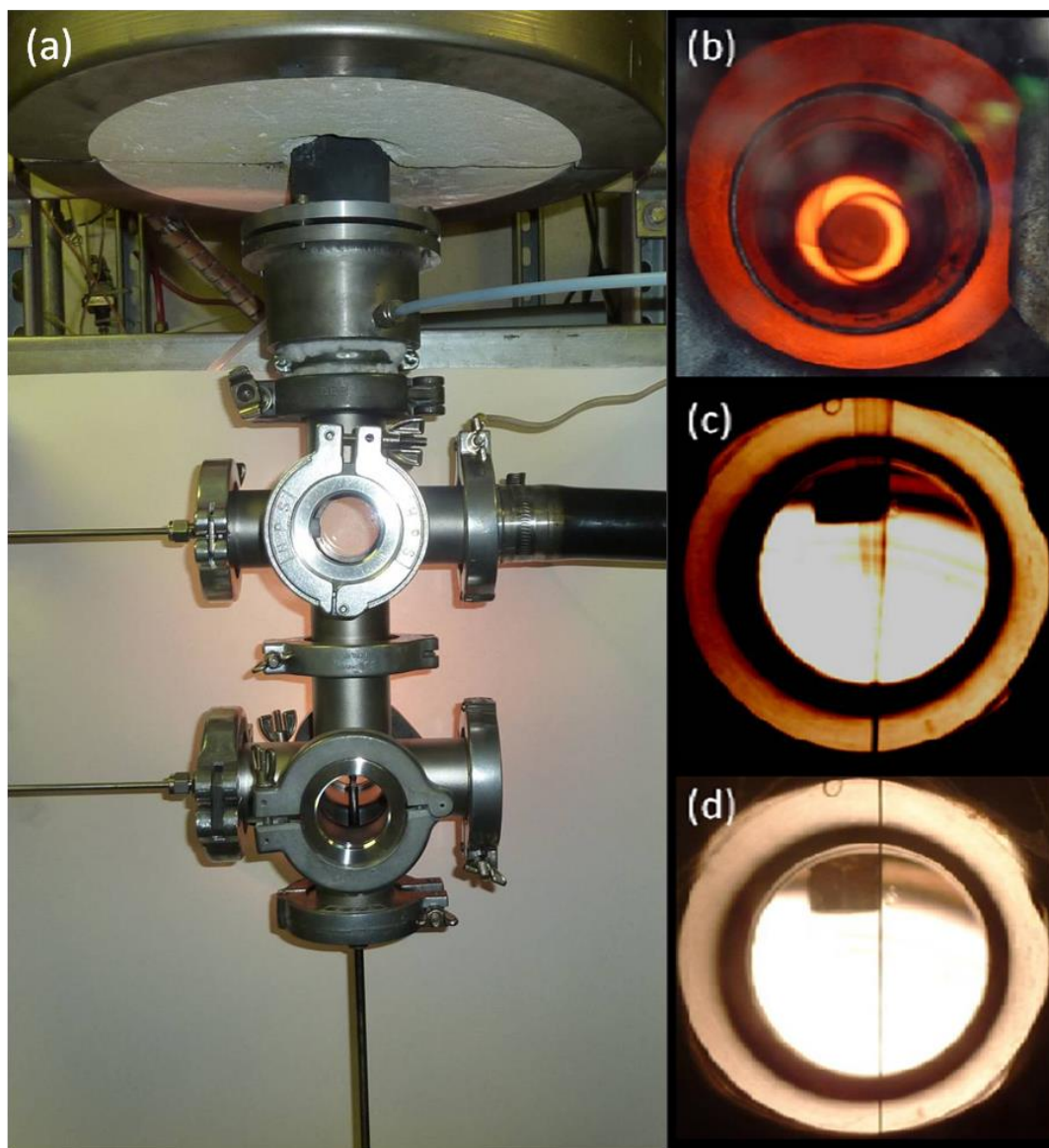


Figure 5: *In-situ* fabrication of DWNT/Polymer yarns. (a) The hermetic harvesting setup at MER Corp. used for in-situ spinning of DWNT yarns. (b) Bottom view looking up the CVD reactor showing the aerogel sock composed of DWNTs. (c) Side view looking inside the CVD reactor during the *in-situ* spinning process. (d) DWNT yarn being spun in-situ the CVD reactor.

The high scatter in mechanical properties also suggests a large concentration of defects, which dominate the mechanical performance of this initial batch of *in-situ* spun yarns. Continued development of the *in-situ* spinning process will improve their uniformity and enable taking full advantage of the improved alignment of CNTs within the yarns.

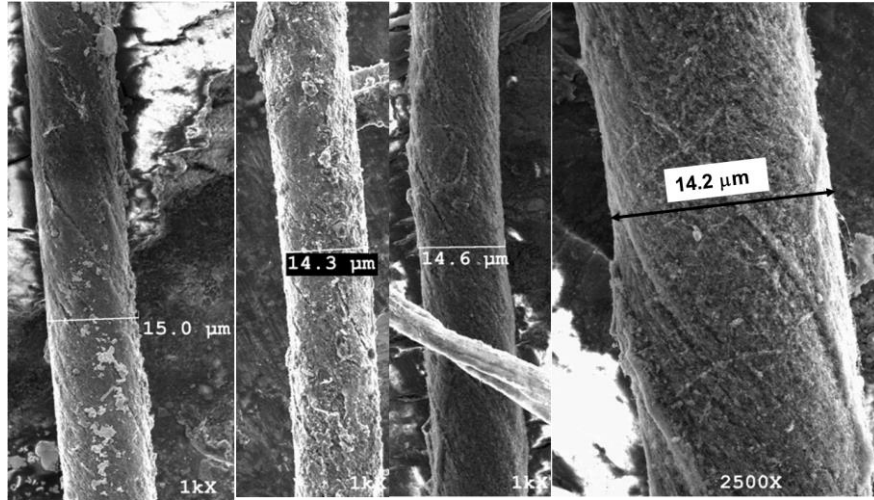


Figure 6: SEM images of the in-situ CVD grown yarns

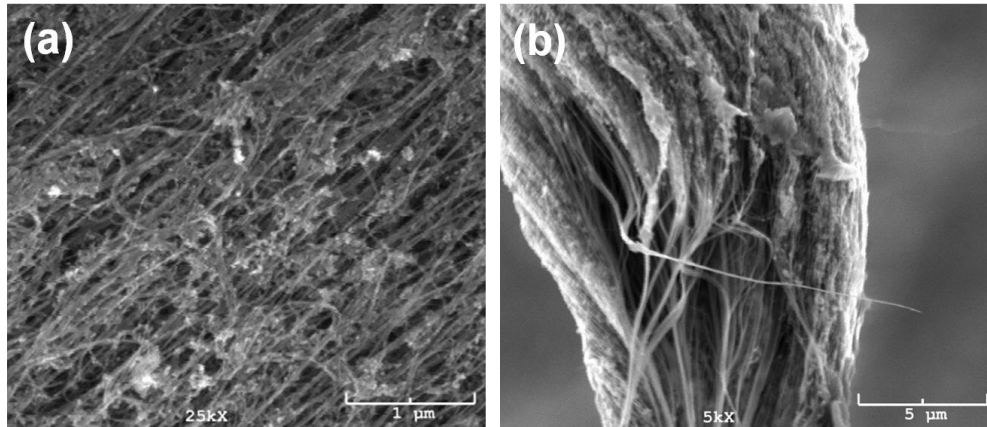


Figure 7: SEM image of (a) the surface of the yarns pointing to the CNT alignment achieved in *in-situ* fabrication; (b) the cross section of a fracture yarns. The internal structure of the in-situ-spun yarns is found to be very clean and highly aligned.

3. Nanomanufacturing and Characterization of Polyacrylonitrile (PAN) and Carbon Nanofilaments.

Polyacrylonitrile (PAN) and carbon nanofilaments were produced in the Dzenis group by electrospinning. Process parameters were varied to manufacture fibers in broad diameter range. The as-spun nanofibers were oxidized and carbonized using several thermal treatment regimes. Nanofiber structure was studied using SEM, XRD, and Raman spectroscopy and compared with the structure of a commercial carbon fiber. XRD results indicated that carbon nanofibers had lower crystallinity and smaller grain size than commercial microfibers. Raman spectra indicated apparent higher content of defects in carbon nanofilaments compared to commercial microfibers. Long (~1cm) specimens of individual PAN, stabilized PAN, and carbon nanofibers were manufactured and tested utilizing NanoUTM testing system. Load-displacement diagrams were recorded and the diameter-dependence of nanofiber mechanical properties was analyzed. As-spun nanofibers exhibited classical elasto-plastic behavior with distinguishable yield point and strain-hardening phase. Stabilized PAN nanofibers showed non-linear deformation with smaller elongations. Carbon nanofilaments deformed nearly linearly to failure. It was

shown that mechanical properties of all three types of nanofibers increased dramatically with the decrease of their diameters. Both stiffness and strength of PAN, stabilized PAN, and carbon nanofibers increased with the diameter decrease below about 500 nm. The improvement didn't show any tendency for saturation in the diameter range studied (200 nm - 1 μ m – see Figure 8a,b, and Figure 9). The highest recorded strength of carbon nanofilaments (Figure 8 a) was approximately one third of the strength of a commercial high-strength carbon fiber. Elongation at failure of the as-spun PAN nanofibers decreased slightly with the decrease of diameter. However, elongation at failure of stiffer stabilized PAN and carbon nanofibers increased with the diameter decrease (Figure 8 c). The latter effect is very unusual in structural materials and might be due to fine grain nanocrystallinity. If confirmed, the effect can be exploited to design ultrastrong filaments that are also ultratough. The detailed mechanisms of this effect are being currently investigated in collaboration with Espinosa's group.

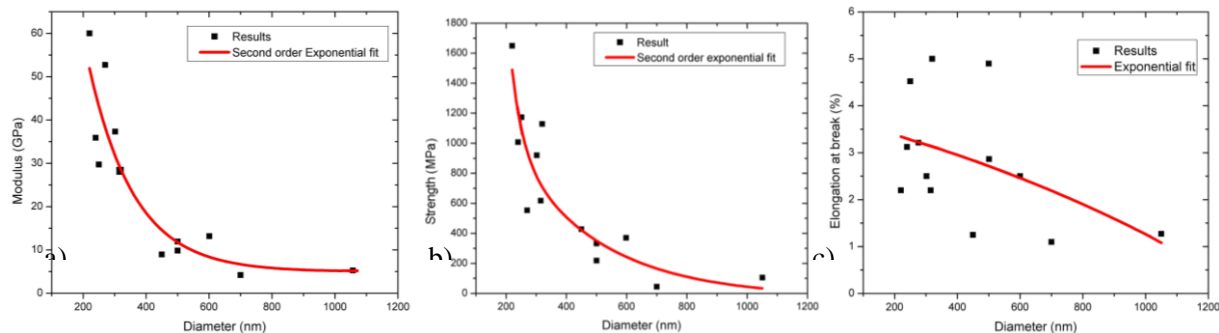


Figure 8: Variation of mechanical properties of carbon nanofibers with diameter: (a) Modulus (b) Strength (c) Elongation at break

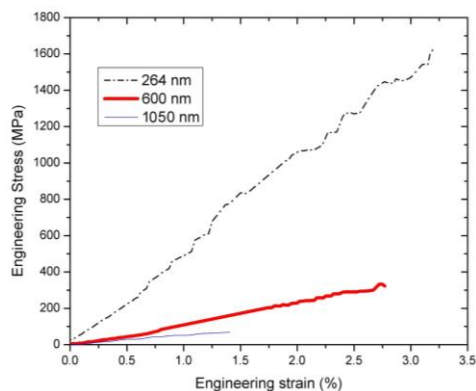


Figure 9: Representative tensile stress-strain curves of carbon nanofibers with different diameters.

Extensive parametric studies were conducted to establish the ways to further controllably reduce the nanofiber diameter. It was shown for the first time quantitatively that certain process parameters result in bimodal diameter distributions. The mechanisms of this phenomenon are being currently investigated. Nanofiber diameter control will be assisted by recent breakthrough on electrospinning modeling in Dzenis' group. The latest coupled process model incorporated solvent evaporation as a crucial phenomenon leading to jet solidification and controlling final nanofiber diameter and structure. The first paper on the subject has been prepared and submitted. In addition, new process modification that can potentially result in highly uniform ultrafine continuous nanofilaments has been invented and is being currently explored experimentally (patent disclosure in preparation).

4. Fabrication of Modified Carbon Nanofiber Precursors.

In an attempt to modify carbon nanofiber precursors, graphene nanoparticles received from Nguyen's group were successfully incorporated into PAN nanofibers by the Dzenis group for the first time. Electrospun solution composition was varied and the effect of polymer concentration, solvent, and additives were studied. Graphene nanoparticles were clearly observed inside the fiber by SEM. First observations show that nanoparticles might be crumpled by the compressive forces in the polymer jets during jet thinning and solvent evaporation (Figure 10). Further investigations are under way in collaboration with Nguyen's and Espinosa's groups.

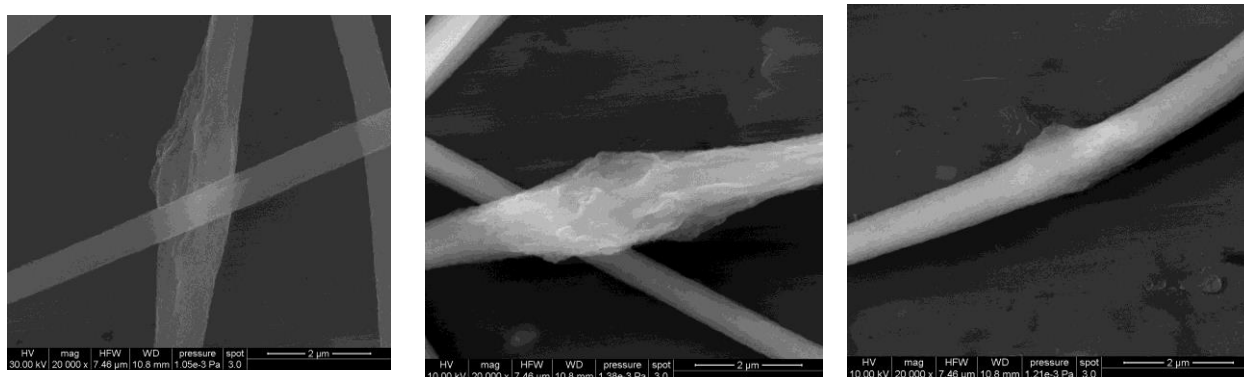


Figure 10: SEM images of nanomanufactured PAN nanofibers with embedded graphene nanoparticles.

An attempt was also made to incorporate DWNT into continuous nanofibers. Purified DWNT were received from MER Corp. Nanofibers were electrospun from solutions with various compositions with and without added surfactant. Fibers with very broad diameter distributions were observed, with the smallest nanofibers as thin as 40 nm (Figure 11). It appeared that at least some DWNT were agglomerated and might have been expelled from the polymer nanofibers (see right image in Figure 11). Work on better dispersions of DWNT in solution are in progress in collaboration with researchers from MER Corp. Graphene nanoparticles and DWNT may alter carbon nanofiber structure through templated carbonization (modeling effort is discussed below).

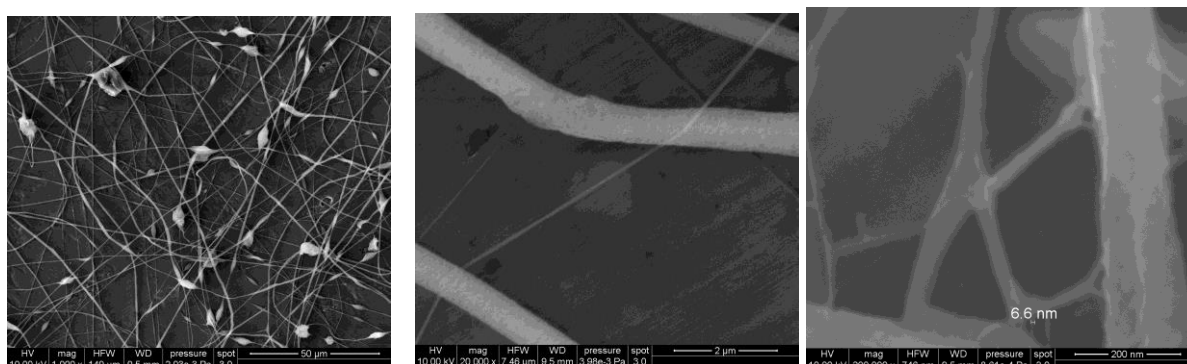


Figure 11: SEM images of nanomanufactured PAN nanofibers with embedded DWNT.

Finally, an attempt was also made to increase carbon yield and produce high-modulus nanofibers similar to pitch-based carbon fiber. Several precursors were used (mesophase pitch, phenolic solid powder, liquid carbon coke), some of which were obtained from MER Corp. Multiple solvents and solution compositions were utilized and electrospinning was performed at room and elevated temperatures. SEM analysis showed that most solutions produced droplets/particles instead of fibers. Melt electrospinning produced thick continuous filaments (Figure 12).

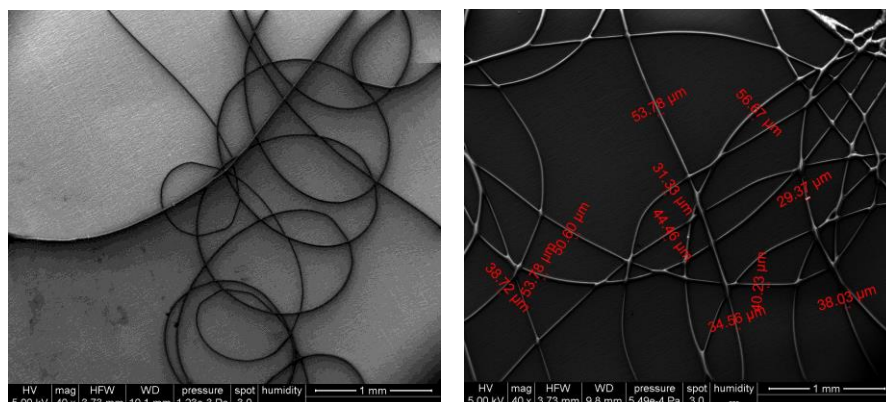


Figure 12: SEM images of melt-electrospun thick pitch filaments.

5. Manufacturing and Carbonization of Nanofilamentary Yarns.

We have also began work on nanomanufacturing of nanofilamentary yarns. Initial work was conducted to control yarn structure via variation of alignment in the precursor nanofilamentary sheets. Carbonization of PAN nanofilamentary yarns was also explored and multi-step method was developed. It was shown that yarns carbonized under the developed multistep regime retained nanofilamentary architecture (Figure 13).

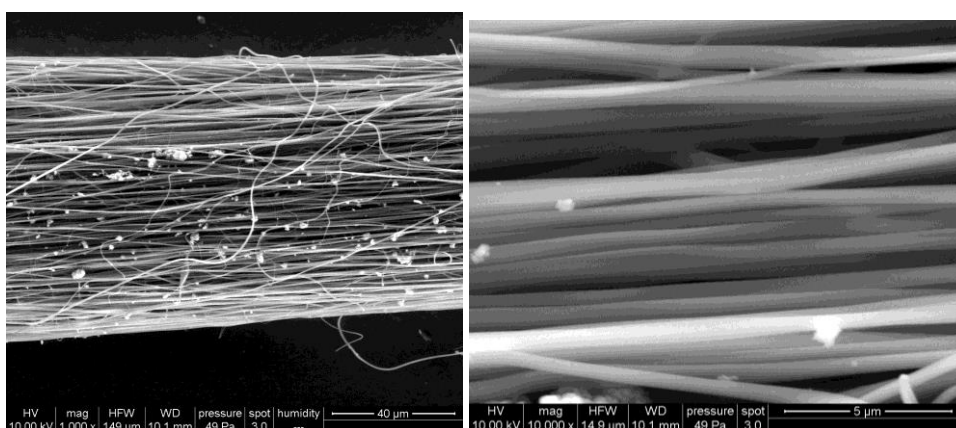


Figure 13: SEM images of electrospun yarns carbonized using multi-step process.

6. Modeling stabilization and carbonization of polymer/CNT fibers.

This effort was started in June 2010, so the Schatz group is still developing models and doing preliminary calculations. The overall goal is to use electronic structure calculations and reactive force fields combined with Monte Carlo and molecular dynamics calculations to examine steps that have been hypothesized as being involved in the conversion of polyacrylonitrile polymers to graphitic carbon (stabilization and carbonization). Ultimately, this work will be aimed at understanding the interactions of the polyacrylonitrile interactions with CNTs that are embedded in the polymer matrix during electrospinning with the goal of determining if the stabilization and carbonization steps can play a role in enhancing the lateral interactions between CNTs and the graphitic phase, as this would be a route for producing high performance fibers.

7. Alternative Nanofiber Manufacturing Techniques

Several methods of high-rate nanomanufacturing are being explored and developed by the Dzenis group. Rates 3-to-4 orders of magnitude higher than the standard single-spinneret production rate have been demonstrated. High-rate nanomanufacturing will enable rapid materials screening and optimization

in the later stages of this project. Hollow nanofibers were also produced from a variety of precursors and control of nanofiber diameters and wall thickness was explored. Thin wall of hollow continuous nanofilaments can provide yet another scale and structural optimization parameter and can lead to further enhanced properties.

A modified electro-spinning process was also used to produce and study continuous ceramic nanofilaments. Such filaments may be explored as an alternative to carbon in the later stages of this project.

8. Modeling CNT collisions with a silicon surface (relevant to CNT spraying experiments).

The Schatz group has used classical molecular dynamics with a reactive force field to model recent CNT spraying experiments (at Florida International Univ) in which the velocity of the sprayed multiwall nanotubes was high enough (supersonic speeds) that shattering of the tubes was detected after impingement on a silicon surface. The calculations show that shattering is to be expected for nanotubes above a certain velocity that is easy to obtain in the experiments. This result is important in our search for CNT processing conditions that are needed to product high performance fibers.

Multi-scale experimental and computational studies of the mechanical behavior of CNT/polymer bundles and yarns

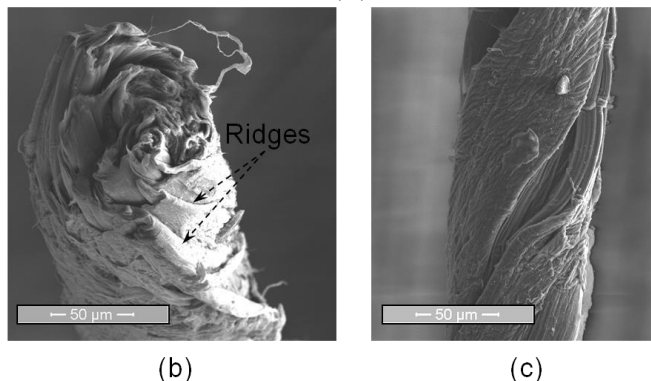
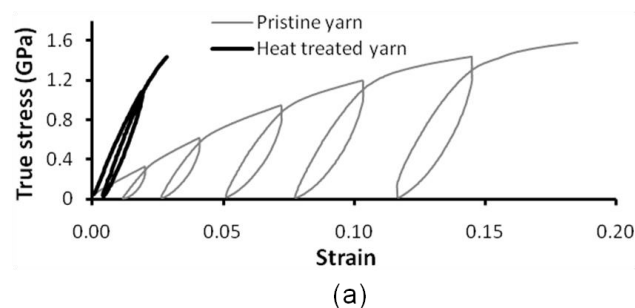


Figure 14: (a) True stress as a function of engineering strain in DWNT-based yarns. (b) The post-mortem SEM images of the fractured surface of the yarns clearly points to the buckled structure of the mat formed during spinning. (c) SEM image of the heat-treated yarns. The removal of the polymer coating reduces the interaction between layers of the mat in the yarns causing partial unfolding.

1. In-situ SEM mechanical testing of DWNT/Polymer yarns.

In-situ SEM mechanical characterization of CNT based yarns was carried out by the Espinosa group using a tensile testing stage, allowing for simultaneous measurement of the mechanical behavior of samples and identification of mechanisms of deformation and failure of the material.

A typical true stress-engineering strain curve of a DWNT-based yarn obtained in this study is shown in Figure 14a. In this case, the yarn was fabricated from a 1/8" wide ribbon of a DWNT mat, and the sample gage length was ~1 cm. The sample fails at a true stress of ~1.56 GPa, which translates to ~1 Ntex⁻¹. It also demonstrates a large ductility of ~20% engineering strain. The energy to failure of this specific sample is ~118 J per gram of the DWNTs weight. Subsequent to the removal of inherent polymer coating, the sample strength does not change significantly, while the ductility and energy to failure substantially drop, Figure 14a. The results shown in Figure 14a were typical of the yarns made out of ribbons with the same ribbon width (1/8"), as will be discussed further in this section.

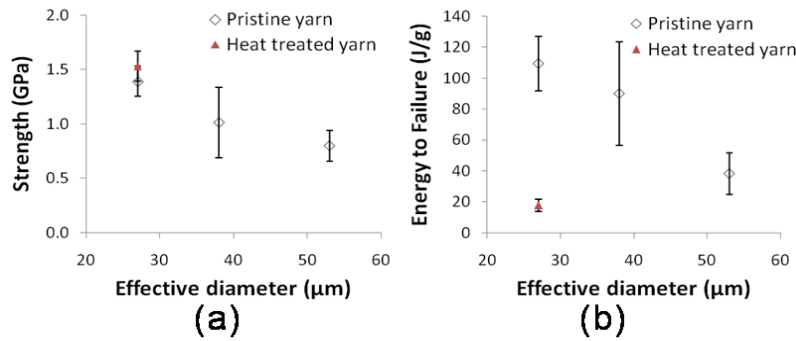


Figure 15: Plots of (a) strength and (b) energy-to-failure as a function of diameter for the pristine and heat treated yarns.

coating binds the wrinkled layers of the yarn, thus enhancing its structural stability and integrity. This feature becomes apparent when monitoring the structure of heat treated yarns (no polymer coating) in which the stacked wrinkled layers of the mat are partially unfolded at several locations along the yarn due to loss of binding, Figure 14c.

The *in-situ* SEM experiments reveal the mechanisms of deformation of the yarns. The axial deformation of the pristine yarns (before heat treatment) is accompanied by aligning the ridges of the buckled wrinkles with the loading direction. In addition, sample stretching is accompanied by the twisting of the yarns. A consequence of the combined stretching and twisting is the enhancement of lateral confinement during axial loading, noticed by significant shrinkage of the yarn diameter (negative Poisson's ratio) during in situ SEM mechanical experiments.

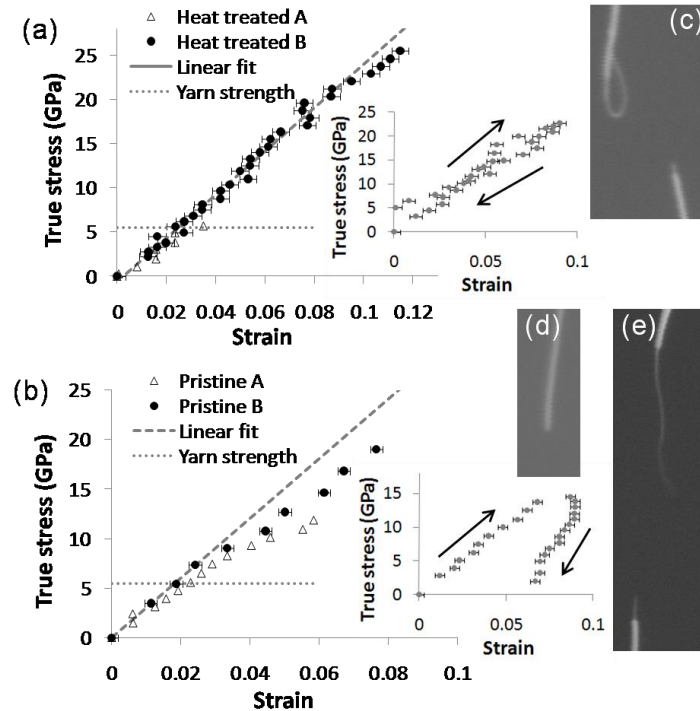


Figure 16: Stress-strain curves recorded for DWNT bundles with (a) and without (b) heat treatment. The insets show loading and unloading curves revealing plastic behavior for pristine bundles and nearly elastic behavior for heat treated bundles. (c) Sword-in-sheath failure of heat treated bundle. Complete fracture (d) and telescopic failure (e) of pristine bundles.

SEM images of the fracture surface reveal the true structure of these yarns. As shown in Figure 14b, the filament like structures observed on the surface of the yarn are wrinkled layers of the original ribbon used to fabricate the yarn. This morphology is a consequence of successive buckling of the mat during spinning which result in ridges similar to those formed in thin cylinders after being twisted to the post buckling regime. It is important to note that the polymer

coating binds the wrinkled layers of the yarn, thus enhancing its structural stability and integrity. This feature becomes apparent when monitoring the structure of heat treated yarns (no polymer coating) in which the stacked wrinkled layers of the mat are partially unfolded at several locations along the yarn due to loss of binding, Figure 14c.

Another aspect of the mechanical behavior of the yarns is their size dependent mechanical properties. The strength and energy to failure of the pristine yarns (with inherent polymer coating) as a function of effective diameter are shown in Figure 15a and b, respectively. Each point in these figures represents an average of a minimum of 3 measurements. The graphs point to a monotonic decrease of the mechanical properties of the yarns with effective diameter increase. The origin of the enhanced mechanical performance of the thinner yarns is the higher degree of twist in thinner ribbons, as the precursors of thinner yarns. The higher capability of narrower ribbons to be spun without failure allows for the development of a higher compactness, and thus it induces stronger interactions between the CNT bundles inside each yarn.

Figure 14a and Figure 15a and b also point to the significant differences between the mechanical behavior of pristine (with inherent polymer coating) and heat treated

yarns. As shown in Figure 14(a), after the removal of polymer, the yarns appear to be significantly stiffer and more brittle. These differences in the mechanical behavior of the yarns suggest increased short range interactions between bundles as a result of the removal of the polymer coating. The increased short range interactions between bundles are the result of a more compact structure of heat treated yarns as evidenced by ~15% shrinkage of their diameter.

2. In-situ SEM/TEM mechanical testing of isolated DWNT-polymer bundles

Mechanical testing of isolated bundles was conducted by the Espinosa group and was aimed at understanding both the intrinsic properties of the DWNTs within the yarns as well as the effect of polymer coatings and crosslinking on the behavior at the bundle level. In particular, in-situ tests can provide valuable information on the location of polymer crosslinks and load transfer within bundles.

To facilitate in-situ testing, nanomanipulation techniques for in-situ SEM have been developed to isolate individual DWNT bundles from the MER mat material which contain 10-100s of DWNTs in a hexagonal packing. Electron beam-induced etching and carbon deposition techniques have been adopted to manipulate and secure bundles to testing devices. Studies of isolated DWNT bundles, with and without polymer coatings, have been conducted, revealing that while the presence of the polymer does not significantly affect the elastic loading regime it does increase the plastic regime through an additional toughening mechanism. Figure 16 shows the stress-strain response of several isolated DWNT bundles tested in-situ SEM. Unloading curves just prior to failure reveal the enhancement in plasticity in the case of bundles coated in polymer. In addition, in-situ SEM images demonstrate a telescopic failure mechanisms for DWNT/polymer bundles in which several layers of inner DWNTs pull out after initial failure. Pullout tests of individual bundles have allowed quantification of the forces required to pullout inner tubes with respect to outer tubes. In the case of bundles with polymer removed, a force normalized by the number of nanotube-nanotube shear interactions of ~2 nN/CNT pair was measured. This is comparable to simulation performed in the Schatz group of sliding between tubes with OH functional groups. Work is undergoing to quantify the pullout forces in the case of polymer coated bundles and initial experiments suggest much stronger interactions.

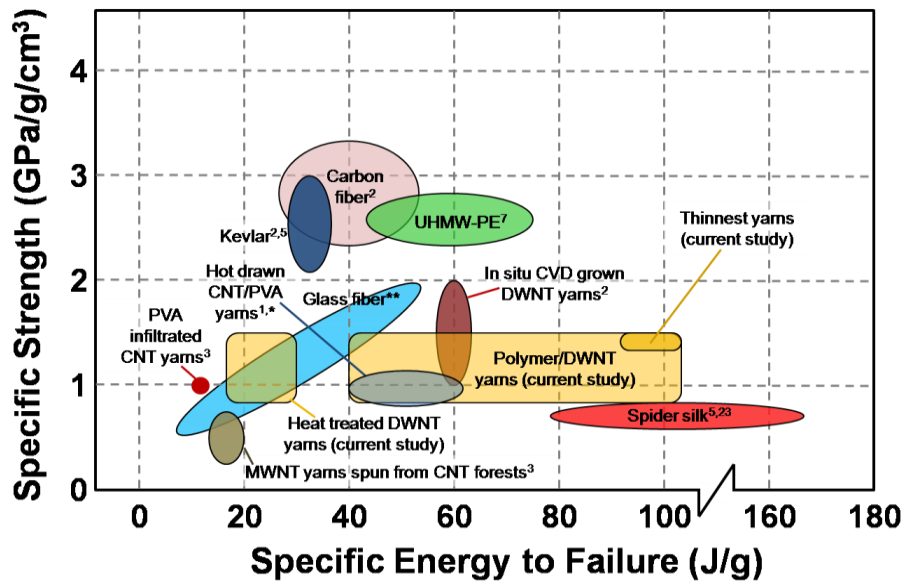


Figure 17: Specific Strength as a function of specific energy to failure for advanced yarns and fibers. Stano *et al.* have reported a relatively high strength of 8 GPa/g/cm³ for *in-situ* CVD grown yarns at small gage lengths of ~ 1 mm, but no strain to failure or toughness has been reported in the literature. Therefore, their study is not included here. The upper limit for the ductility of the materials presented here is roughly taken as ~10-20% which roughly corresponds to the ductility of the spider silk at room temperature, pointing to the high energy to failure of a hierarchical material system in nature.

(*) In this case, the density of the sample is estimated as the ratio of the area under the stress-strain curve to the reported toughness per unit mass. (**) The data for glass fibers is obtained from www.AGY.com

Work is undergoing to quantify the pullout forces in the case of polymer coated bundles and initial experiments suggest much stronger interactions.

It is interesting to note from Figure 17, that the heat-treated

yarns reported in this study exhibit similar energy to failure as MWNT yarns spun directly from forests. In both cases, we expect mainly VDW interactions between CNTs and do not expect collapsed CNT structures given the geometries of individual tubes within the yarns (2.2 nm DWNTs [this study]). In contrast, both the polymer-coated yarns in this study, and *in-situ* CVD-grown CNT yarns with collapsed geometries (Windle group) exhibit higher energy to failure presumably due to higher shear interactions between CNTs. It is also interesting to compare the results obtained in this study, with the relatively high mechanical properties of nature materials, such as spider silk, shown in Figure 17. While the yarns that we have fabricated are stronger than spider silk, their toughness, measured in terms of energy to failure, is only half of the toughness of the spider silk, pointing to the significance that a hierarchical design can play in achieving high-performance materials.

3. Modeling the lateral interactions between CNTs using atomistic simulations

As part of this work, the Schatz group has developed a software package which enables us to build one or more single- or double-walled CNTs and then to model a CNT pull-out experiment in which one tube is pulled next to another, or a tube is pulled out of a nanotube bundle, or several nanotubes are pulled out

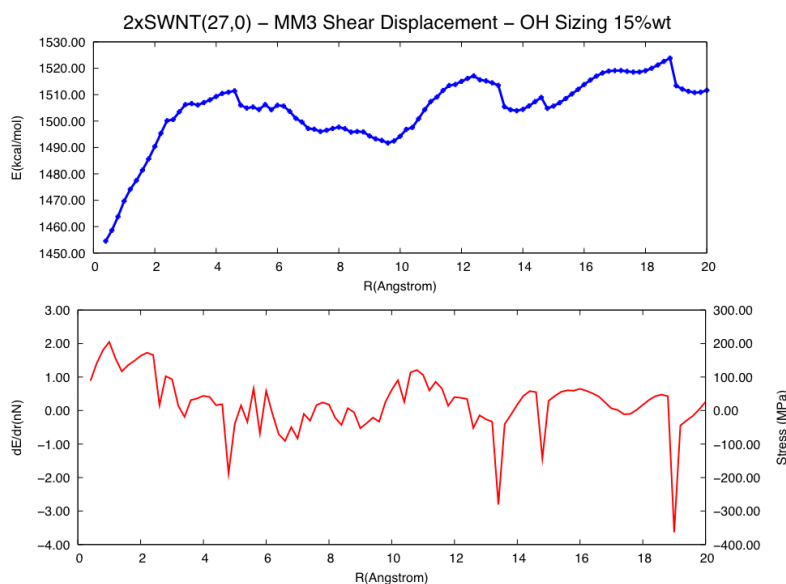


Figure 18: Energy versus strain (top) and force versus strain (bottom) associated with shear interactions between the two nanotubes in Figure 2.

of a larger bundle to another to determine shear properties of the functionalized nanotubes. Figure 18 shows an example of two single-walled tubes coated with OH groups (corresponding to 15% sizing) based on this code. Figure 18 shows energy versus strain results and force versus strain results that are based on the structure in Figure 2 and the MM3 force field (a high quality empirical force field). In this case, the lateral interactions between the tubes lead to a maximum force of about 2 nN for the nanotube pair, which is comparable to results measured by the Espinosa group in pull-out experiments. We have generated similar results using tubes that are unfunctionalized, or functionalized with atomic hydrogen, and the peak force is much lower, indicating that the sizing associated with the MER nanotube bundles involves interactions that are more like OH functionalization than H or no functionalization. We continue to do studies of this type to provide bounds on the lateral interactions between nanotubes.

4. Development, validation and application of a carbon nanotube coarse-grain model.

The Buehler group has further developed a novel *in silico* assembly procedure based on a coarse-grained model of carbon nanotubes, used here to attain a representative mesoscopic buckypaper model that circumvents a need for probabilistic approaches, see Figure 19. By variation in assembly parameters, including the initial nanotube density and ratio of nanotube type (single-

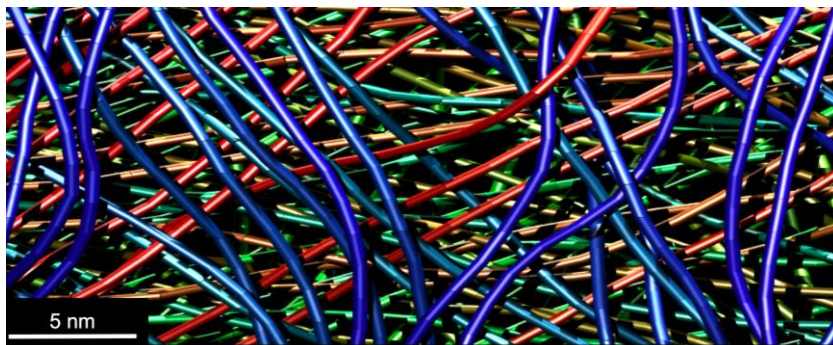


Figure 19: Visualization of carbon nanotube buckypaper, simulated using the new coarse-grained model.

and double-walled), the porosity of the resulting buckypaper can be varied threefold, from approximately 0.3 to 0.9. Further, through simulation of nanoindentation, the Young's modulus is shown to be tunable through manipulation of nanotube type and density over a range of approximately 0.2 to 3.1 GPa, in good agreement with experimental findings of the modulus of assembled carbon nanotube films. In addition to carbon nanotubes, the coarse-grain model and assembly process can be adapted for other fibrous

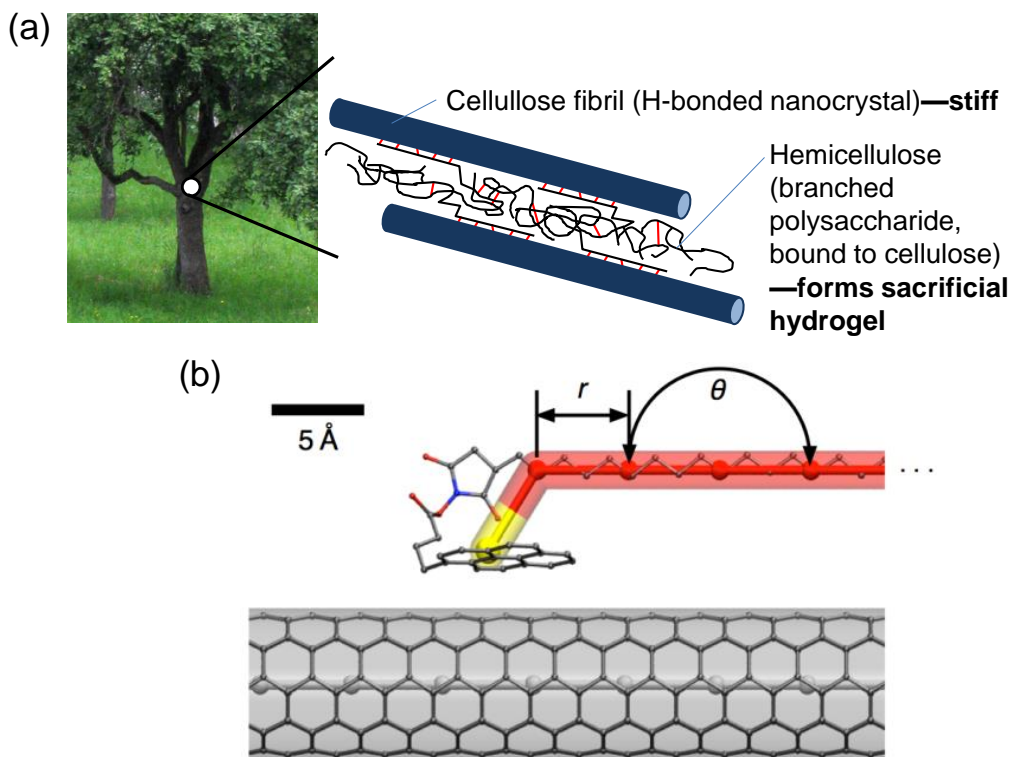


Figure 20: Schematics of a wood fibril, and the noncovalently crosslinked CNT bundle model. (a) Nanostructure of wood. Strong cellulose fibrils, H-bonded nanocrystals, wrap the wood cell and carry most of the load while soft, sacrificial hemicellulose and lignin between cells transfer load. (b) Wood's sacrificial hydrogel is mimicked here by terminating each end of a short, unbranching polyethylene chain with PSE in order to noncovalently adsorb polymer crosslinks to the CNT sidewall. The bead-spring model, superimposed to scale over the atomistic model, shows the computational advantage of coarse-grain techniques in the reduced number of particles, N , and the reduced number of parameters, *i.e.* spring length r and angle ϑ .

nanostructures such as electrospun polymeric composites, high performance nonwoven ballistic materials, or fibrous protein aggregates, facilitating the development and characterization of novel nanomaterials and composites as well as the analysis of biological materials such as protein fiber films and bulk structures.

1. Bioinspired non-covalently crosslinked 'fuzzy' carbon nanotube bundles with superior toughness and strength studied by coarse grain modeling

Carbon nanotubes (CNTs) constitute a prominent example of structural nanomaterials, with many potential applications that could take advantage of their unique mechanical properties. Utilizing the inherent strength of CNTs at larger length-scales is, however, hindered by the inherently weak inter-tube bonding interactions, allowing slippage of nanotubes within a bundle before large macroscopic stresses are reached. Many lamellar biological materials crosslink stiff fibrous components via the introduction of a soft binding matrix to achieve a combination of high strength and toughness, as seen in cellulosic wood, silk, or collagenous bone fibrils. The Buehler group has carried out atomistic-based multi-scale simulation-studies of bundles of carbon nanotubes with the inclusion of a binding polymer (polyethylene chains with functional end groups) to demonstrate the control of mechanical properties via variations of polymer structure, content and fiber geometry (Figure 20 for geometry and model setup).

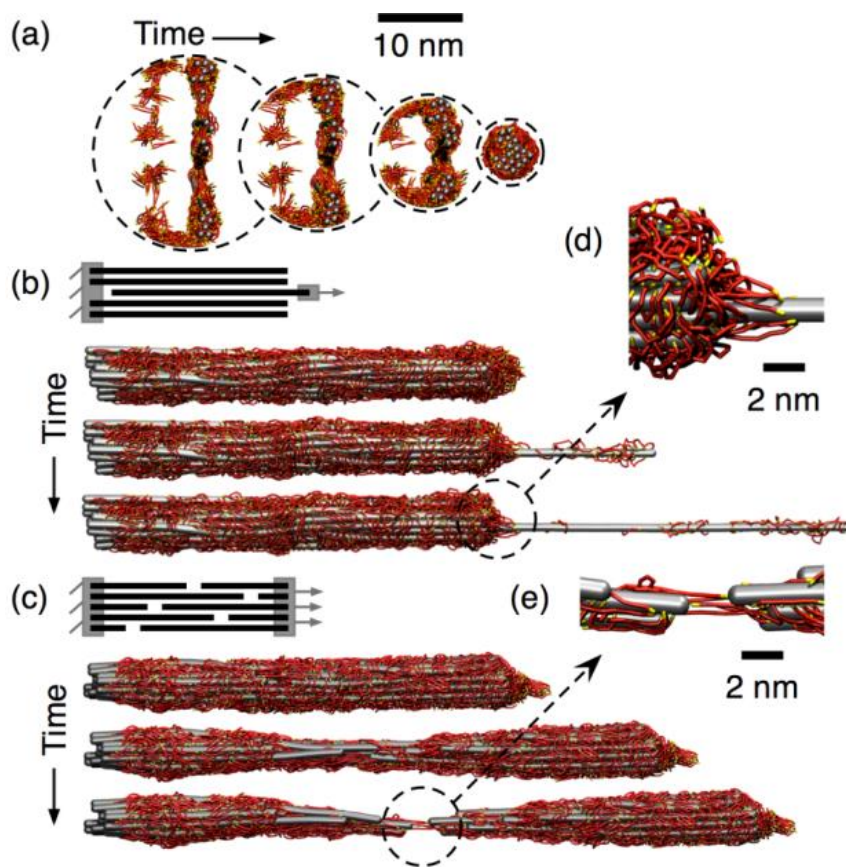


Figure 21: CNT bundle formation and testing procedure overview. (a) First, a sheet of parallel CNTs and PSE/PE chains is relaxed into a bundle using a time-dependent radial pressure. Either a pull-out test or a tension tests is then performed. (b) A pull-out test uses SMD to ramp a force on the end bead of a single nanotube. (c) A displacement-control tension test is performed by stretching the simulation box. Gaps are introduced in each nanotube so that crosslink shearing is the major failure mechanism. (d,e) By observing the crosslinks at failure points, we see that while the crosslinks are important in bridging gaps, the PSE deadsorbs before the PE is strained to failure. While PSE adsorption is not as strong as covalent intertube crosslinking, deadsorption is much more favorable than crosslink fracture in creating a damage-resistant and self-repairing bundle.

To carry out the aforementioned study, a hierarchical approach (coarse-grain molecular modeling) is implemented to develop a framework that can successfully integrate atomistic theory and simulations with material synthesis and physical experimentation, and facilitate the investigation of such novel bioinspired structural materials. This model is based on the buckypaper work described above but explores here for the first time how the addition of a soft polymer phase will influence the findings. Using two types of nanomechanical tests, analogous to those performed by the Espinosa group, we explore the

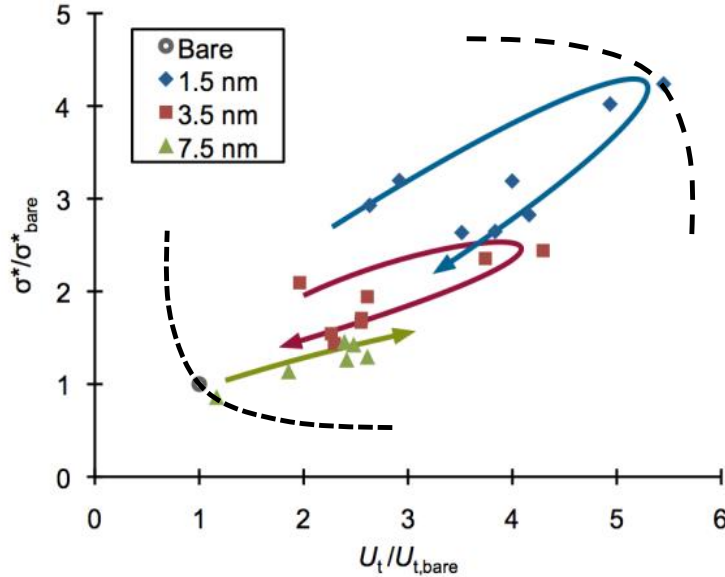


Figure 22: Ashby-plot of the normalized strength versus toughness shows that certain material parameters provide the structural basis for both high strength and high toughness. The crosslink permutation that optimizes both strength and toughness is 1.5-nm length crosslinks at 17 wt%. The arrows show the direction of increasing crosslink density. For the same strength enhancement, tougher bundles can be achieved using higher crosslink densities. This result demonstrates that the material has the capacity to combine disparate material properties, providing a structural basis for the inverse banana-curve behavior (wide dashed line). This is in contrast to the properties of many engineered materials, which show a banana-curve behavior (narrow dashed line) where high strength is achieved on the expense of high toughness.

effects of crosslink length and concentration on the ultimate tensile stress and modulus of toughness of a carbon nanotube bundle (Figure 21).

We demonstrate that the ultimate tensile stress can be increased four-fold, and the modulus of toughness five-fold, over an uncrosslinked bundle with the inclusion of 1.5 nm long crosslinking polymer at 17 wt% concentration, providing the structural basis for a fibre material that combines high levels of stress at high levels of toughness. These non-covalently crosslinked carbon nanotube bundles exhibit residual strengths after initiation of failure that depends on the crosslink length, and are similar to plastically sheared wood cells. Our work demonstrates the implementation of a wood-inspired carbon nanotube based fibre material with superior mechanical properties, specifically fibers that combine high strength and high toughness (Figure 22). We note that the selection of a polyethylene and functional groups was guided by the availability of data in the literature, which made the development of a hierarchical model possible in the first year of this program. This development will be used to assess various yarn materials being investigated under this project in subsequent years.

6. Nanofilamentary mechanics of networks of electrospun nanofibers.

The Dzenis group has begun developing numerical models of nanofilamentary assemblies and networks with explicit nanofiber and contact representation. An example of the computed stress-strain behavior of a random nanofiber network is shown in Figure 23. The results compare well with the observed non-linear experimental behavior of networks. Explicit models of nanofilamentary networks and assemblies can be integrated with atomistic calculations of others in the team and used to optimize nanofiber contacts and lateral interactions.

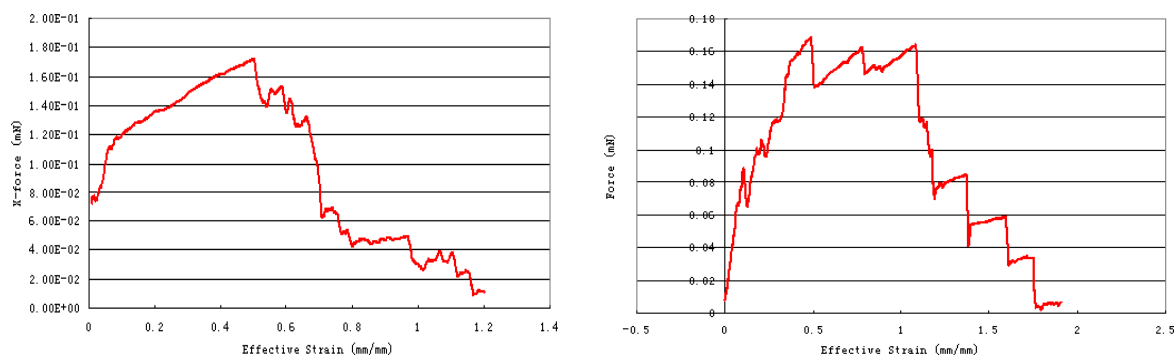


Figure 23: Comparison of simulated (left) and experimental (right) behavior of random nanofiber network.

Engineering lateral interactions within CNT yarns and fibers through crosslinking

1. Borate as a covalent cross-linker in graphene oxide thin films.

The Nguyen group has concentrated on covalently cross-linking adjacent graphene oxide nanosheets within a well-characterized thin-film model system. In this system, borate anions are trapped between graphene sheets during filtration, where they form strong hydrogen bonding interactions with the load-bearing graphene oxide nanosheets. Upon dehydration of the paper at low temperature (90 °C), the previously established hydrogen-bonded borate network reacts with hydroxyl moieties on the basal plane of graphene oxide via condensation reactions (Figure 24). This creates a covalently bound network of boron esters, which drastically increases the mechanical strength of the paper. Initial studies have shown that borate concentration in graphene oxide thin films is easily tunable, with the stiffness of the paper directly correlated to borate concentration. Very few cross-links are necessary for to improve load-transfer between nanosheets, as very low concentrations (~ 0.05 wt%) afford increases in film stiffness of over 250% (Figure 24) while still maintaining the good flexibility of the parent film. While stiffness continues to increase at higher borate concentrations (~ 1 wt%), these films becomes brittle as the covalently bound intersheet network loses translational freedom.

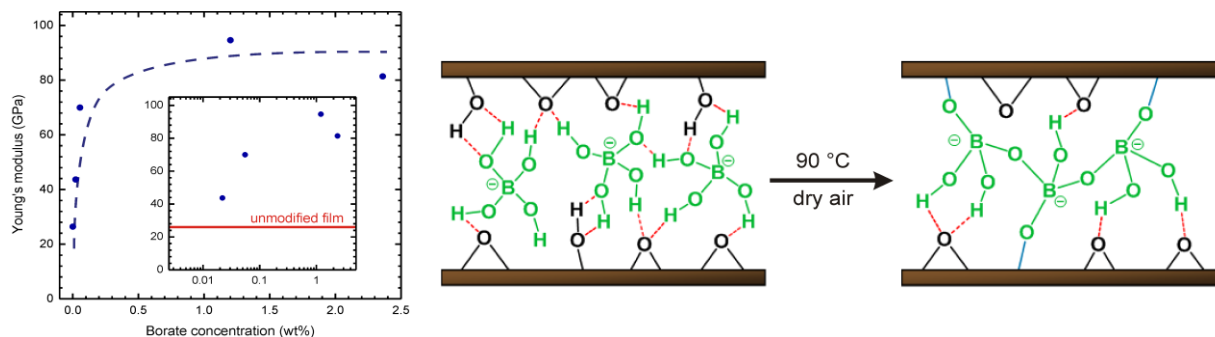


Figure 24: Left: the tunability of graphene oxide thin film stiffness as borate concentration is varied. Right: Schematic of borate cross-linking within a graphene oxide thin film. Borate ions (green) initially form hydrogen bonds (dashed red lines) with epoxide and hydroxyl groups (black) on the graphene oxide basal plane, forming a hydrogen-bonding network within the intersheet gallery. Upon annealing, covalent borate ester bonds (solid blue lines) form via condensation reactions with surface-bound hydroxyl moieties.

In collaboration with the Espinosa group, we have begun transferring the borate cross-linking chemistry to the MER carbon nanotube bundles. Our expectation is that borate introduced during spinning of nanotube yarns will penetrate and incorporate into the yarn structure (Figure 26). Subsequently, hydrogen-bonding between the oxygen containing moieties in the “sizing” polymers and molecules that surround the nanotubes will enhance load transfer between nanotubes and bundles. In parallel with this

work, we have begun studying the composition of the sizing to determine the relative amounts and importance of polymers and small molecules that may compose the sizing.

2. Graphene oxide/polymer nanocomposite films

In addition, we have prepared graphene oxide/polymer nanocomposite films to evaluate the interaction between the oxygen-containing functional groups on a nanoparticle and pendant groups on a polymer chain. Nanocomposites were fabricated via co-filtration of graphene oxide and polymer in a common solvent (Figure 25), where hydrogen bonds would form between the oxygen-containing groups on each component. This technique affords a well-ordered film with distinct separation of the nanosheet and polymer components (Figure 25). Incorporation of hydrophilic poly(vinyl alcohol) into the graphene oxide film structure increased film stiffness over 100%, as the covalent backbone of the polymer offered improved load transfer. Hydrophobic poly(methyl methacrylate) exhibited less interaction with the hydrophilic graphene oxide surface and did not improve stiffness over that of the parent film. The Buehler group has just begun to theoretically model both pure graphene oxide and nanocomposite films to determine how load transfer occurs between nanosheets in the presence and absence of polymer.

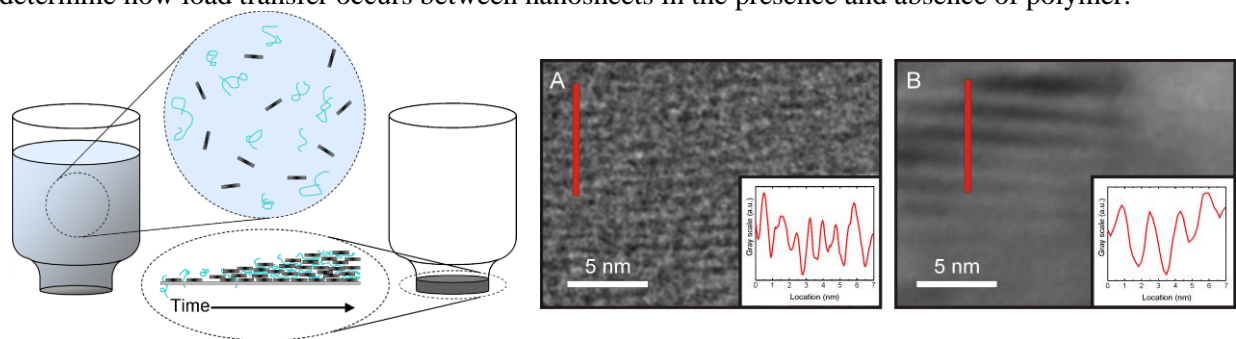


Figure 25: Left: Scheme for the fabrication of nanocomposite films from a solution containing both graphene oxide nanosheets and dissolved polymer. The filter immobilizes graphene oxide sheets, which in turn inhibit the ability of polymer to pass through. Right: TEM images perpendicular to the width of a film sample of (A) graphene oxide and (B) a composite comprising 34 wt% PVA and 60 wt% graphene oxide. The inset shows the variation in the gray scale along the line scan denoted in red on the image, clearly demonstrating the increased interlayer spacing of the composite. The alternating dark and light stripe patterns in each image represent the graphene oxide nanosheets and the intergallery space, respectively.

Complementary to the theoretical work performed by the Buehler group, the Espinosa group will examine differences in the fracture mechanisms between pristine graphene oxide and polymer composite films. Films will be viewed at high magnification in a scanning electron microscope while an *in-situ* dynamic mechanical analyzer applies stress to the samples. Interaction between graphene and polymer in a confined space will also be studied by the Dzenis group. Functionalized graphene nanosheets with lateral dimensions ranging from 50 nm to 1 μm will be electrospun with polyacrylonitrile. The nanosheets will reinforce the nanoscale-diameter electrospun fibers, whose mechanical properties will be evaluated by the Espinosa group.

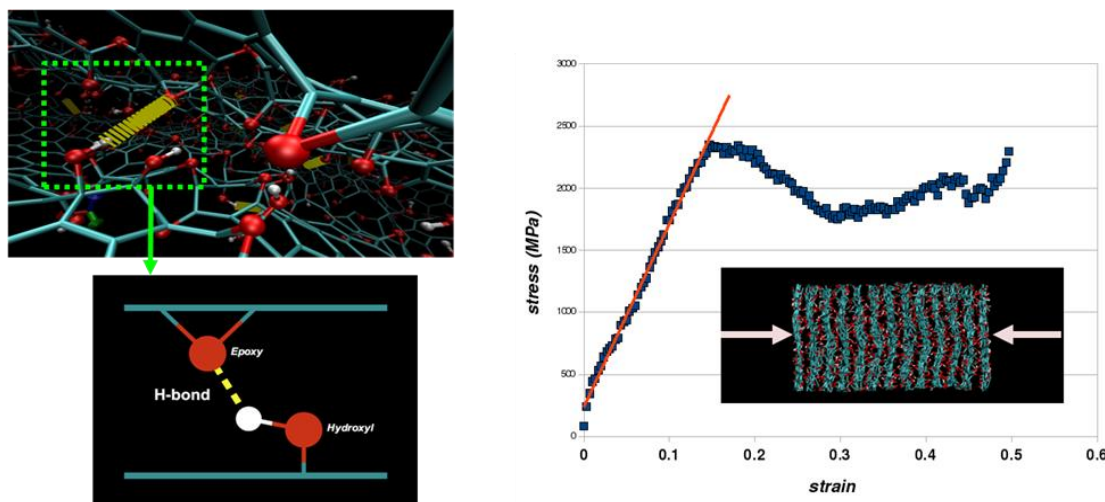


Figure 26: Reactive force field model of graphene oxide, a model system to enable an in-depth view on the structure and mechanics of carbon nanotube-based fibers (left, geometry; right, mechanical analysis under compression). The study has thus far resulted in preliminary assessment of the Young's modulus, estimated to be approximately 15 GPa.

3. Modeling the interaction of graphene sheets after chemical functionalization.

This work is aimed at explaining experiments from the Nguyen group that suggest that borates are able to chemically tether graphene sheets, producing a graphitic material with possible applications as high performance fibers. This project started May, 2010 so the Schatz group is still developing models and testing methods, but the basic approach involves using electronic structure calculations or reactive force field calculations to compare borate tethers with other tethers that we have already studied (as described above) which involve hydrogen bonds or electrostatic interactions.

4. Reactive force field based analysis of graphene oxide paper

Motivated by our desire to develop a test bed for carbon nanotube-sizing interactions, the Buehler group started a joint experimental-theoretical analysis of the graphene oxide papers synthesized by the Nguyen group. We have developed a first principles-based reactive force field (ReaxFF) model of this material to allow us to characterize their structural and mechanical properties. Thus far, we have achieved the setup of a basic model of graphene oxide with the chemical structure determined by Nguyen group, implemented a mechanical characterization approach (different loading conditions), and performed some first validation studies. This model will now be used to probe in a systematic approach how variations of water content between two layers of graphene and as such the density of H-bonds would affect the structure and mechanical properties, concurrent with experimental efforts. The goal is to elucidate the mechanisms of preliminary experimental results, which have demonstrated potential optimization of water content (in terms of mechanical stiffness). This insight will be crucial to develop a fundamental understanding of the interfacial properties associated with interfaces between carbon layers.

5. Modeling the resonance Raman (RR) spectra of functionalized double wall carbon nanotubes.

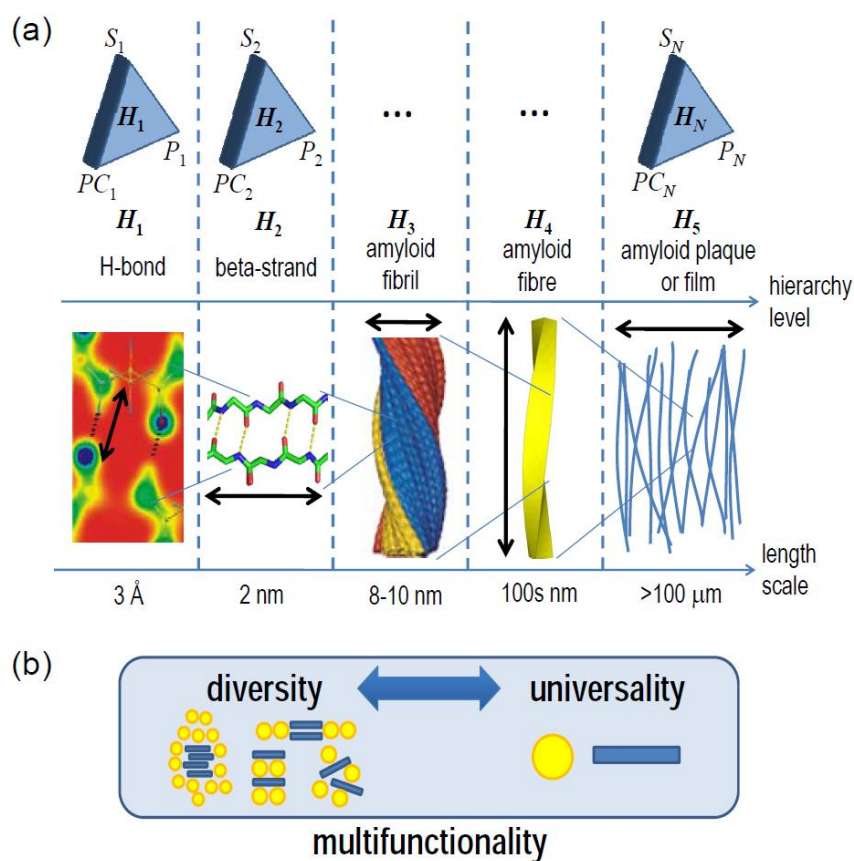
The Schatz group is using a recently developed electronic structure calculations (time-dependent density functional theory with resonant widths included in the optical response function) to evaluate resonance Raman spectra for a variety of CNT structures that are relevant to our project. The code for these calculations is derived from the ADF (Amsterdam Density Functional) program, and we have now demonstrated that it is able to determine resonance Raman intensities for a variety of single and double wall structures that are superior to what are usually done for CNTs due to the inclusion of many coherently interacting excited states in the calculations. Our work on chemical functionalization is just starting, but the goal is to determine if RR spectra are sensitive to the type of functionalization, as this will be helpful in interpreting experiments which are planned in the Espinosa group. Collaborations with

Yuhuang Wang (University of Maryland) are included in this study as Yuhuang has already measured the RR spectra for DWNT structures similar to what we are doing for the MURI project.

Synergistic activities supported by other DoD projects

1. Electron irradiation induced covalent crosslinking of DWNT bundles

As a complementary or alternative route to engineering load transfer within DWNT bundles, the Espinosa group has been exploring the utilization of electron irradiation to create covalent crosslinks between both shells and adjacent tubes. Crosslinking between outer and inner shells of the DWNTs and between DWNT bundles is unlikely to be possible via chemical polymer infussion whereas irradiation is a proven method. Through in-situ TEM irradiation and mechanical testing using MEMS devices, developed within the Espinosa group, we have demonstrated that irradiation can increase both the effective tensile



strength and modulus of bundles by up to an order of magnitude. This result is particularly important given that initial simulation performed in the Buehler group have demonstrated the necessity to crosslink to inner tubes within bundles and atomistic models by the Schatz group have suggested that very little of the polymer coating is likely to have been formed inside of bundles during the CVD fabrication. Therefore, alternative approaches, such as electron irradiation, to crosslink adjacent tubes in the core of bundles will be needed to enhance the mechanical performance of yarns.

2. Bottom-up analysis of biological materials.

Together with related activities in the Buehler lab, we have pursued studies geared to identify how natural fibers derive superior functionality and in particular mechanical properties, specifically aiming to understand how these properties are achieved under constraints of inferior building blocks, low energy, or small material volume. This research thrust has provided

Figure 27: Universality-diversity paradigm, as a general design approach to biological fibers. (a) General view of hierarchical structural formation from levels H_1 to H_N . At each hierarchical level there exists a compartmentalized interplay of structure (S_i), processes (P_i) and properties (P_i), resulting in a particular hierarchical function/requirement. Each hierarchical level contributes to the system's entire materiome. The lower part shows the hierarchical structure exemplified through amyloid protein material, from weak hydrogen bonding to beta-strand structures, fibrils to fibers, and ultimately plaques. (b) Schematic illustration of the interplay of diversity and universality. The integration of diverse and universal features provides the structural basis to achieve multifunctionality without the need to introduce new building blocks (M. Buehler, *Nature Nanotechnology*, 2010).

us with important insight into the nanoscale and hierarchical design of fiber materials. Our findings have explained how in spite of the intrinsic mechanical weakness of ubiquitous molecular bonds in protein materials such as spider silk, H-bonds, this material can reach heightened levels of strength, toughness and resilience, exceeding the properties of most engineered materials including steel.

We have achieved this by systematically quantifying the role of length-scales, defects and material hierarchies in defining the mechanical properties of natural fiber materials (e.g. silk) by using a combination of simulation and theory, and validation through experimental studies. This has resulted in the development of the universality-diversity paradigm, which will play an important role for the analysis and design of carbon nanotube based disruptive armor materials (Figure 27). Figure 28 displays recent work from Buehler's lab on multi-scale modeling of spider silk, showing excellent agreements between multi-scale models and experimental results.

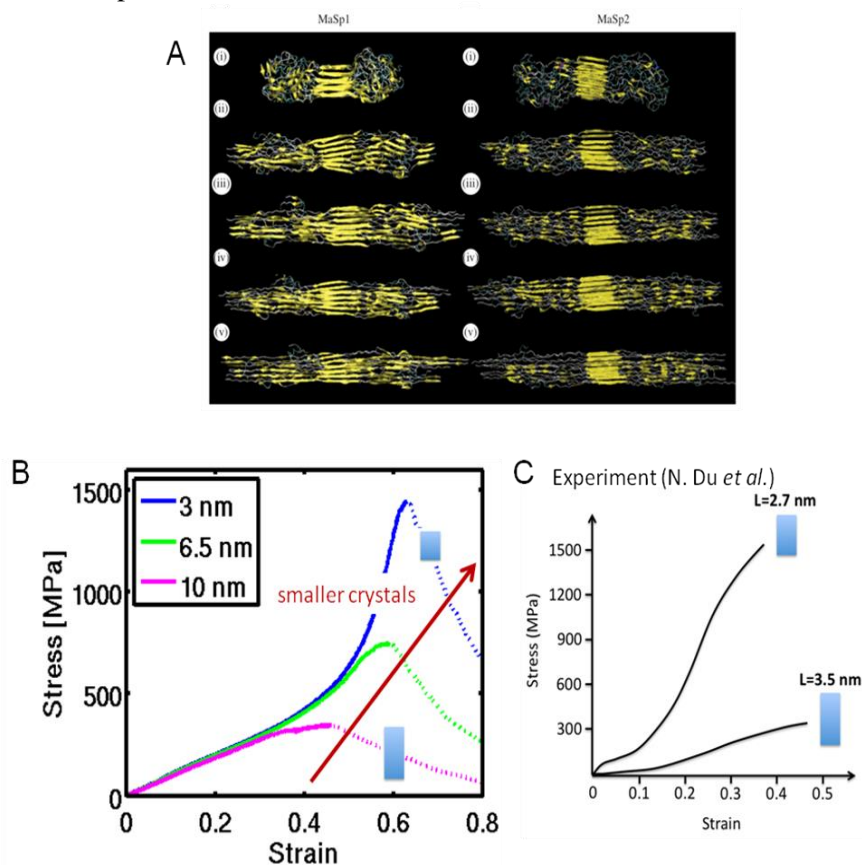


Figure 28: Multi-scale mechanics of a complex hierarchical biological fiber, here exemplified for spider silk. Panel A shows molecular modeling, specifically including structure prediction of assembly of silk proteins based on a Monte Carlo Replica Exchange approach to bridge to long time-scales. Panel B shows simulation results of stress-strain curves based on multiscale modeling for different nanocrystal sizes, and panel C shows corresponding experimental curves (by N. Du *et al.*)

Scientific Progress and Accomplishments (description should include significant theoretical or experimental advances)

Status of Work:

The primary activities of the **Espinosa group** were to *conduct multiscale testing of DWNT/Polymer and electrospun yarns including nanoscale testing of their constituents*. DWNT/Polymer Yarns are fabricated in collaboration with **A. Moravsky** and the **Nguyen group** using DWNT mats produced by MER Corp and electrospun fibers fabricated by the **Dzenis group**. In situ SEM/TEM multiscale mechanical testing methods are used to investigate the mechanical behavior at the individual CNT, CNT bundle, and macroscopic yarn hierarchical levels. Tensile and pullout experiments on individual CNTs and bundles are being directly compared to atomistic calculations in the **Schatz group**, which focus on tube-tube interactions of nanotubes with surface and end functional groups, and larger scale coarse grained calculations in the **Buehler group** that model entire polymer crosslinked CNT bundles. The methodologies developed for testing DWNT materials are being translated to study electrospun fibers by the **Dzenis group**.

As part of the aforementioned activities, we have performed characterization of the shear interactions within individual bundles and between adjacent bundles of DWNTs in the material from MER Corp described in detail in last year's progress report. Through multiscale experiments, and comparison to atomistic and course-grain modeling, we have elucidated a number of effects that contribute to shear in the as produced material. In addition we have investigated engineering the shear interactions between DWNTs within bundles and between adjacent bundles through different crosslinking approaches. In situ SEM and TEM mechanical testing experiments of crosslinked materials have been performed. At the individual bundle level electron irradiation induced crosslinking has been shown to increase the effective stiffness and strength of bundles by approximately an order of magnitude. In situ TEM studies have confirmed that this type of covalent crosslinking modifies the failure mechanisms of the bundles in which a greater fraction of load is transfer to inner DWNTs and shells in the bundles. At the CNT-CNT and yarn level we have investigated the influence of Hydrogen bond crosslinking. Our nanoscale studies indicated the substantial role of hydrogen bonds in enhancing the interactions between CNTs. Similarly, in the macroscale, in particular on in situ CVD functionalized CNTs infiltrated with PVA, pointed to the effectiveness of hydrogen bonds in developing tough, yet strong CNT yarns.

The primary activities of the **Schatz group** were to *model the structural and mechanical properties of functionalized carbon nanotubes and nanotube bundles and model the carbonization process of templated PAN nanofibers*. The nanotube bundles that are modeled include DWNTs and polymers that are present in the MER Corporation (**A. Moravsky**) synthesis. The carbonization modeling emulates the environment used to heat treat electrospun PAN fibers by the **Dzenis group**, which incorporates graphitic templating elements (such as graphene sheets and CNTs) to enhance the carbonization process. Both electronic structure and empirical force field methods are used, with electronic structure theory providing validation for the empirical force fields. This work relates directly to experiments being done in the **Espinosa group**, and it provides calibration for the larger scale calculations that are being done by **Buehler**. In addition, related studies (described below) are useful for characterizing graphene and polymer/CNT structures that are relevant to the **Nguyen** and **Dzenis** experiments.

ReaxFF Molecular Dynamics (MD) simulations of the carbonization process have provided initial demonstrations into the mechanisms of graphitic ring formation at high temperatures. Simulations that include graphene and CNT template elements have revealed an influence of these structures on the formation of additionally well-ordered graphitic structures during carbonization. Theoretical investigations into shear interactions within DWNT bundles via Molecular Mechanics (MM) simulations and density functional theory calculations based on the Perdew-Burke-Ernzerhof functional with a double zeta plus polarization orbital basis set (PBE/DZP) have reveal insights into the nature of the interaction forces. MM predictions of bare CNTs revealed that van der Waals (VDWs) forces alone cannot explain

the experimentally measured pullout forces. PBE/DZP calculations showed that functional groups terminating the ends of fractured CNTs also contribute to the pullout forces, in accordance with experiments suggesting that dissipative forces also play a significant role.

The primary goal of the **Buehler group** is to *bridge the length and time scale gaps between experiments and simulations, by performing coarse grain models that are informed by atomistic simulations* conducted by the **Schatz** group. The main objective of the models developed by the Buehler group is to develop a description of the nanoscale experimental assemblies, such that they are computationally efficient and large enough in size compared to experiments. The Buehler group has developed a coarse grain model of the DWNT bundles (mimicking the DWNT bundles grown by **Moravsky** at MER), which includes the polymer coating grown on in MER. In collaboration with the **Espinosa** group, the **Buehler** group has applied their model to investigate the shear interactions between DWNT bundles. Their new model is especially important for developing high performance CNT yarns. Moreover, the **Buehler** group has investigated the role of clustering dispersive bonds in the enhancement of the shear interactions between CNTs, which ties in with the efforts of **Espinosa** and **Nguyen** to establish methodologies to develop CNT yarns with remarkable mechanical performance.

The **Nguyen group** has worked on *functionalization of CNTs and the development and application of polymer binders to enhance the interactions between CNTs*. Nguyen has worked on understanding and enhancing the chemical rationale behind load transfer and mechanical properties in hierarchical materials with organic nanostructures as load-bearing units. In collaboration with **Espinosa**, Nguyen has studied the mechanical properties of carbon nanotube-polymer nanocomposite yarns to determine the role of hydrogen-bond donating and accepting functionalities in controlling their mechanical behavior. Together with **Buehler**, Nguyen's group has carried out a combined experimental-theoretical study of the role that hydrogen-bonding networks play in transferring mechanical load between nanostructures, both through water molecules and matrix polymers. With the **Espinosa** and **Schatz** groups, Nguyen's group has begun analyzing how the mechanical properties at the interface between two carbon nanotubes can be tuned based on the chemical interactions between them.

The goal of the **Dzenis group**'s research is to *design, manufacture, and demonstrate high-performance disruptive fibers based on continuous nanofilaments fabricated via electro spinning*. The focus in this reporting period was on individual carbonized nanofilaments that utilize graphitic templates to enhance the structural order in the resulting fibers. **Nanomanufacturing and characterization of both poly(acrylonitrile) (PAN) and Carbon Nanofilaments has been carried out. In particular, the mechanical behavior of these nanofilaments was found to be strongly dependent on fiber diameter.** Carbon nanofiber precursors were modified in collaboration with the **Nguyen** group by incorporating graphene nanoparticles into PAN nanofibers for the first time. Purified DWNTs fabricated by **A. Moravsky** at MER Corp were also incorporated into continuous nanofibers. Ultrathin PAN and Carbon Nanofilaments have been tested by the **Espinosa** group via in situ SEM/TEM mechanical testing methods. Carbonized PAN fibers which utilize DWNTs as template elements have proven to be most effective in enhancing graphitization in the fibers. Electron diffraction and Raman spectroscopy measurements have revealed a dramatic increase in ordered graphitic regions in the fibers as a result of the templating effect by the DWNT elements. The structure and characteristics of electrospun and carbonized PAN fibers are being compared to initial simulations (conducted by the **Schatz** group) to gain a better fundamental understanding of how the carbonization process unfolds and what mechanisms are involved in graphitizing local regions in the fibers.

The goals of the **Moravsky group** at MER Corp are to *develop the methodologies to fabricate DWNT-based yarns* in close collaboration with the **Espinosa** group and *to incorporate DWNTs as template elements into carbonized electrospun PAN fibers* in close collaboration with the **Dzenis** group. The focus was on fabricating DWNT yarns and further development of spinning capabilities of DWNT yarns in situ the CVD reactor. This includes developing methods to facilitate the in situ application of different chemical crosslinking treatments on the yarns as well as optimization of the processing characteristics of the yarns such as CNT overlap length. These efforts are closely linked to the multiscale

mechanical characterization done by the **Espinosa** and **Nguyen** groups, in which further treatments are applied on the in situ CVD spun yarns to obtain flaw resistant yarns with relatively uniform diameters.

Scientific Accomplishments:

Fabrication/characterization/modeling of electrospun nanofibers and yarns

*1. Manufacturing of continuous polymer nanofilaments modified with nanoparticles for carbonization templating (***)**Proprietary** (***)*

Polyacrylonitrile (PAN) precursor nanofilaments modified with small quantities of nanoparticles were produced by electrospinning. The goal was to modify the carbonization and graphitization processes rather than reinforce fibers, as has been attempted elsewhere. Graphene and graphene oxide (GO) nanoparticles were received from Nguyen's group and DWNTs from MER Corporation. All nanoparticles were successfully incorporated into PAN nanofibers (Figure 1). Electrospun solution compositions were varied and the effect of polymer concentration, solvent, and additives were studied. Graphene and GO nanoparticles appeared crumpled by the compressive forces in the polymer jets during jet thinning and solvent evaporation (Figure 2a,b). On the other hand, DWNT-filled nanofibers showed high uniformity under the optimized fabrication conditions. Good quality DWNT-filled nanofibers were fabricated for the first time (Figure 2c). All nanofibers were carbonized and analyzed using a number of analytical techniques. An evidence of strong templating was uncovered for the first time (see details in experimental section below). In addition, nanofibers with different GO nanoparticle sizes were fabricated and analyzed. It was expected that smaller GO nanoparticles would result in better dispersion and more uniform nanofibers. The results so far showed limited effect of the GO nanoparticle size on the structure of the carbonized nanofilaments. Finally, as spun nanomodified nanofibers were carbonized at various temperatures and their structure analyzed. It was discovered that the DWNT-templated nanofibers showed significant changes in structure at lower temperatures, but further increase of temperature produced insignificant structural changes. The latter effect shows promise for the control of graphitic structure of continuous nanofilaments by templating at low temperatures.

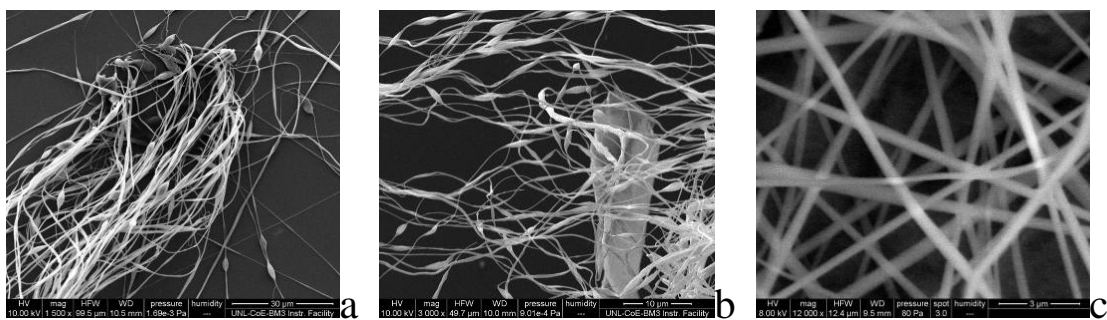


Figure 1. Nanomanufactured PAN nanofibers with embedded graphene (a), GO (b), and DWNT (c) nanoparticles.

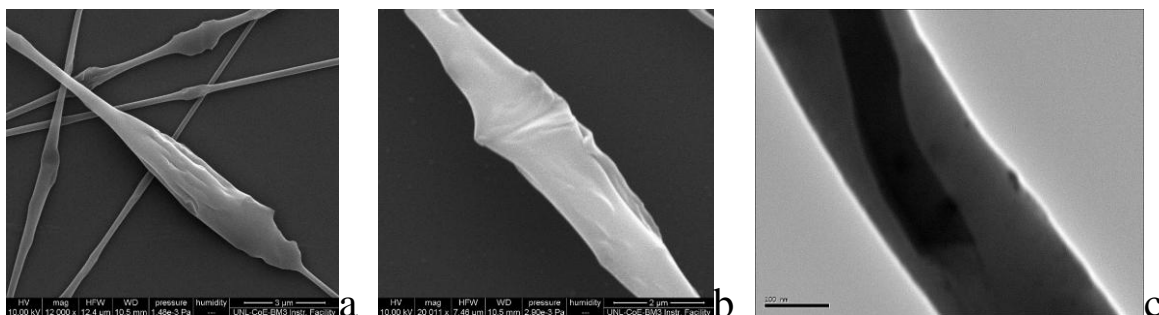


Figure 2. High-resolution SEM (a,b) and TEM (c) images of nanomodified PAN nanofibers with embedded graphene (a), GO (b), and DWNT (c) nanoparticles. DWNTs and graphene particles are not readily discernible in TEM images due to their low contrast with carbon filament. However, they can be viewed in the fracture surfaces, for instance look at Figure 6.

The Dzenis group's continued work on nanofiber yarn manufacturing. In addition to high-productivity methods, high-precision methods have been explored. This work was informed by the results of pioneering numerical simulations of jet instabilities and nanofiber deposition on substrates (paper published in MNL). Methods of control of nanofiber interactions at contacts were also explored (see section on lateral interactions below).

2. Analysis of scale effects and their origins in nanofilamentary precursors

Dzenis group continued to study scale effects in individual nanofilaments. Long (~1cm) specimens of PAN nanofibers were manufactured and tested using specially developed protocols. Tensile load versus displacement measurements were recorded and the diameter-dependence of the mechanical properties was analyzed. It was confirmed that both strength and modulus of nanofibers increased dramatically with the decrease of their diameters with no sign of saturation (Figure 3a,b). Moreover, their elongation at failure, though scattered, did not appear to show the tendency to decrease with the strength and modulus increase (Figure 3c). This led to dramatic increases in toughness of ultrafine nanofibers (Figure 3d). This behavior is very unusual in structural materials. Typically, the strain at failure and toughness decrease with the increase of strength and stiffness. When properly understood, this effect can be exploited to design ultrastrong filaments and fibers that are also ultratough. TEM analysis of individual fine nanofilaments did not show any discernable nanostructure. Electron diffraction analysis of these filaments was not possible as the nanofibers burned under the focused electron beam. XRD analysis of multifilament samples with different average diameters showed that polymer nanofiber crystallinity decreased with the decrease of average diameter. However, the response of a multifilament sample with distributed filament diameters is likely dominated by the thickest nanofibers in the sample thus providing little information on the thinnest fibers of interest. In an attempt to prove that reduced crystallinity may be responsible for high strain at failure, the Dzenis group changed nanofiber crystallinity by several methods and tested the resulting nanofibers. In one series of experiments, crystallinity of nanofibers was changed by annealing at elevated temperatures. Increase in crystallinity was confirmed by XRD experiments. Such nanofibers exhibited size effects for strength and modulus similar to the ones observed in untreated nanofibers (described above), but produced regular (classic) low strains at failure in the whole diameter range. Modeling of possible strength increase is performed in collaboration with Buehler group. Fundamental analysis of scale effects in PAN, stabilized PAN, and carbon nanofilaments continues and is expected to lead to better understanding of the observed unusual effects and to inform future material designs.

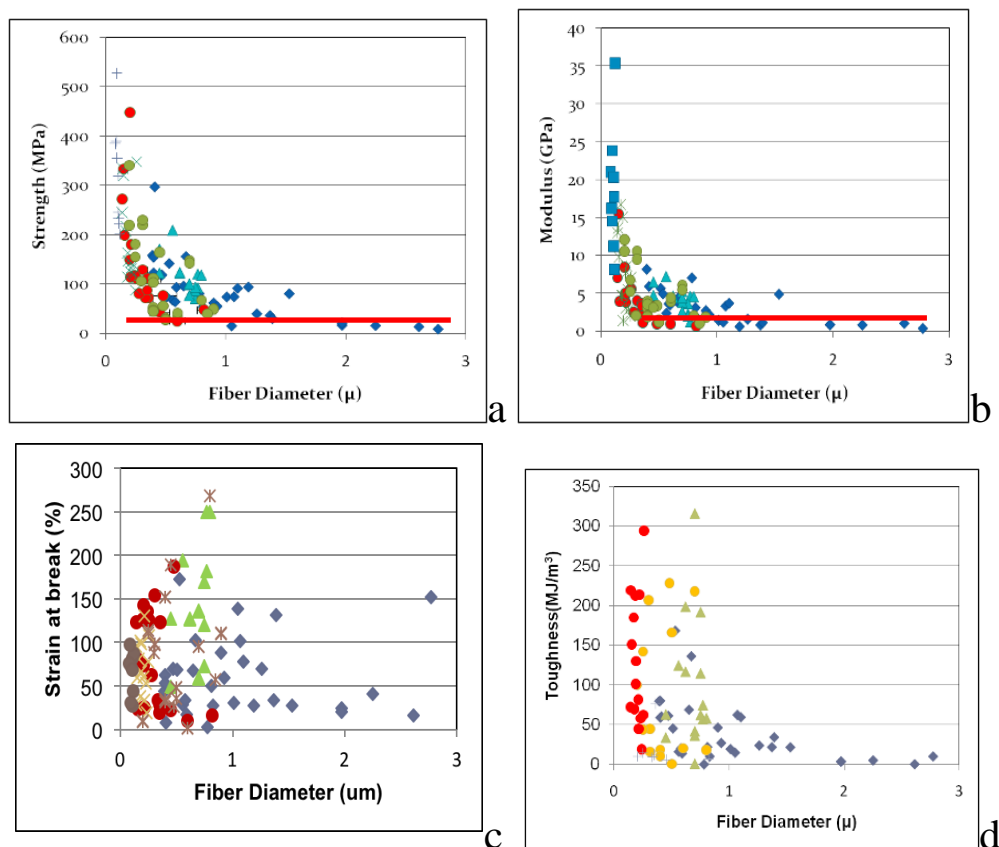


Figure 3. Scale effects: diameter dependence of strength (a), stiffness (b), strain at failure (c), and toughness (d) of individual PAN nanofilaments.

3. Evaluation of feasibility of templated carbonization

The Dzenis group continued studies of feasibility of templated carbonization of long carbon nanofilaments using small quantities of graphene, GO, and DWNT nanoparticles, in collaboration with the Nguyen group and MER Corp. Work on better dispersion of DWNT in solution performed in collaboration with researchers from MER Corp resulted in good quality of DWNT-modified continuous PAN nanofibers. The as-spun nanofibers modified with several different nanoparticles (see above) were oxidized and carbonized using several thermal treatment regimes. Nanofiber structure was studied using SEM, XRD, TEM/ED, and Raman spectroscopy and compared with the structure of unmodified carbon nanofibers. Raman spectra indicated a dramatic increase in the order/disorder peak ratio in carbon nanofilaments modified with a small quantity of DWNTs and carbonized at low temperature (Figure 4a). In order to prove that this signal does not simply come from the DWNTs themselves, but represents a true templating of the carbonized nanofiber structure, similar spectra were taken from the non-carbonized DWNT-modified polymer filaments (Figure 4b). The comparison shown in Figure 4b shows significant enhancement of the graphitic order/disorder ratio in the carbon fibers mediated with DWNTs (blue curve) that far exceeds the signal from the embedded DWNTs themselves (red curve). In addition, sophisticated quantitative electron diffraction studies (Figure 5) showed that the templating effect appears to be global (i.e., it spreads away from the immediate vicinity of the nanoparticles). Figure 5 shows limiting orientation angles (orientation spread) of the graphitic planes measured in the vicinity of and away from nanoparticles. It can be observed that incorporation of DWNTs results in globally reduced angles (i.e., improved orientation) even for thicker nanofibers. This effect is very promising as it is likely to result in considerable changes in carbon nanofibers mechanical performance. These experimentally discovered

templating effects are being now investigated theoretically by the Schatz group. Two other studies on templating effects were initiated: the investigation of the effects of GO nanoparticle size (collaboration with Nguyen's group), and theoretically inspired (Schatz group) study of the effects of higher carbonization temperatures. Some promising initial results are being now analyzed experimentally and theoretically.

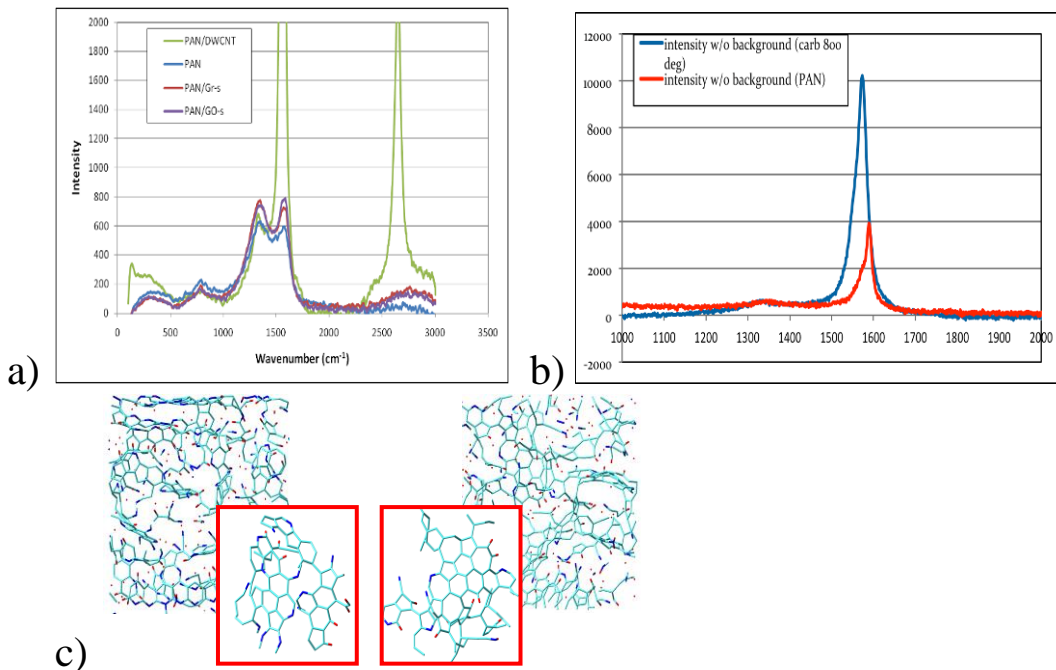


Figure 4. (a) Raman spectra from carbonized nanofibers prepared with different nanoparticles. (b) Comparison of Raman spectra from carbonized and non-carbonized DWNT-modified nanofibers. (c) ReaxFF simulations by Schatz group.

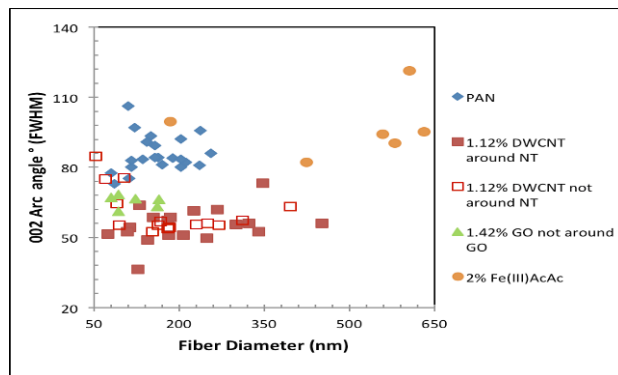


Figure 5. Improved orientation of graphitic planes in carbon nanofibers with templating: variation of limiting orientation angle (angle spread) of graphitic planes with nanofiber diameter for carbon nanofibers prepared from virgin and nanoparticle-modified PAN nanofilaments. ED measurements taken in the vicinity of and away from DWNT inclusions are distinguished. Smaller angles indicate increased order.

4. Analysis of mechanical behavior of templated carbon nanofilaments

Virgin carbon nanofibers and nanofibers templated with DWNTs were tested mechanically through failure. The Dzenis group tested long (~1cm) specimens of individual carbon nanofibers utilizing a NanoUTM testing system and specially designed protocols. Load-displacement behavior was recorded,

and the diameter-dependencies of the nanofiber mechanical properties were analyzed. The scale effect in the pristine carbon nanofibers was further investigated. First experiments on DWNT-templated carbon nanofibers were also performed. In addition to long specimens tested by the Dzenis group ex-situ, Espinosa's group performed in situ testing utilizing specially developed MEMS-based testing devices. DWNT bundle pullout was observed in many nanofibers break points (Figure 6a,b). An attempt to evaluate the DWNT adhesion to the carbon matrix was also recently performed (Figure 6c,d). These experiments are expected to provide detailed understanding of the mechanisms of deformation and failure in these novel promising materials and will enable their multiscale modeling and optimization.

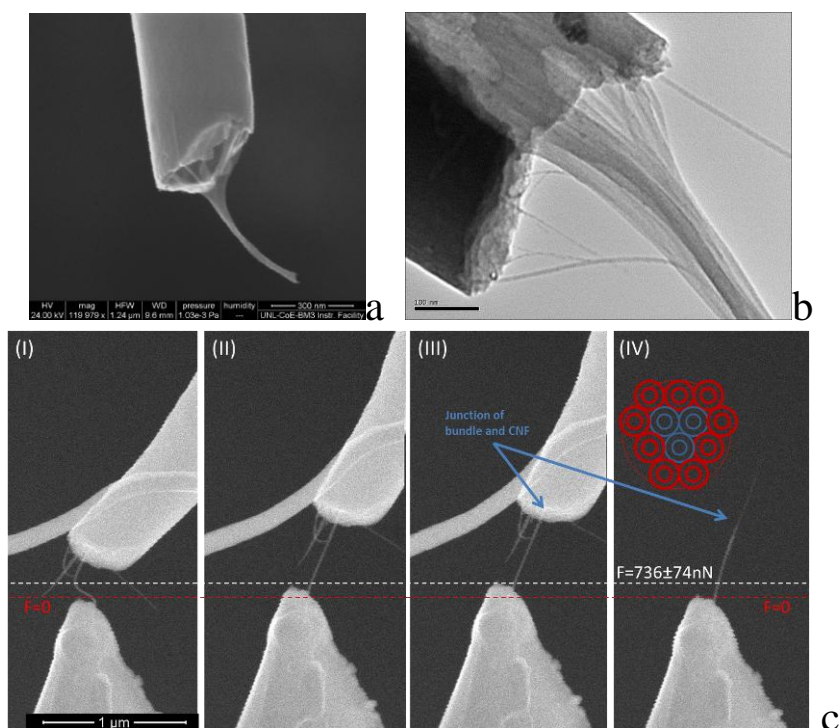
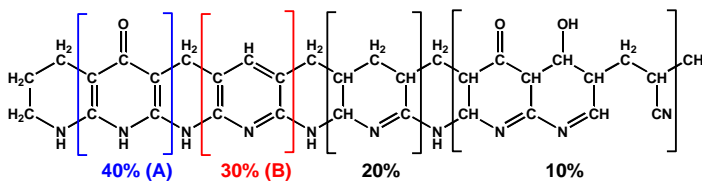


Figure 6. DWNT pullout from nanofiber fracture surfaces (a,b). Successive images of an attempt to pullout one of the DWNTs from the fractured surfaces of a template carbonized PAN, using an AFM cantilever as the load sensor (c). The test points to a strong bond between DWNT bundles and carbonized PAN, confirming the integrity of the interface between the two. The sample shows a sword in sheath failure, with the outer layer of DWNTs failing and the inner ones pulling out.

5. Modeling stabilization and carbonization of polymer/CNT fibers (**Proprietary**)

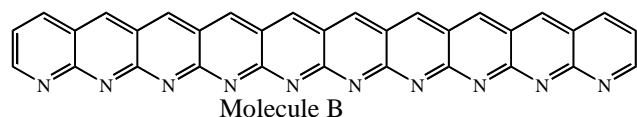
(Relevant to the Dzenis electrospinning project): The overall goal is to use electronic structure calculations and reactive force fields combined with Monte Carlo and molecular dynamics calculations to examine steps that have been hypothesized as being involved in the conversion of polyacrylonitrile polymers to graphitic carbon: stabilization and carbonization. Ultimately this work will be aimed at understanding the interactions of the polyacrylonitrile with CNTs that are embedded in the polymer to determine if the stabilization and carbonization steps can play a role in enhancing the lateral interactions between CNTs and the graphitic phase, as this would be a route for producing high performance fibers.



Scheme 1: Structure for PAN stabilized in air (Proposed by Morita et al., 1986)

Polyacrylonitrile (PAN) is used as precursor for about 90% of the carbon fiber production around the world [1]. A heat treatment technique is used to convert the PAN precursor to carbon fiber, starting initially with stabilization at $\sim 500\text{K}$ and followed by carbonization at $\sim 2000\text{K}$. An understanding of the oxidative and thermal treatments during conversion processes is crucial for the production of high strength and high modulus fibers. Commercially, stabilization of the PAN fiber is done in an oxidizing medium, which is typically air, and it is reported that a polymer back-bone containing oxygen-bearing groups that evolves into the PAN ladder structure provides greater stability to sustain the high temperature carbonization treatment [2] that follows stabilization. The mechanism of stabilization is not very clear, with some dispute about crosslinking and cyclization. Recently, cyclization that leads to the formation of six-membered rings seems to have become accepted, though the evidence still remains circumstantial [3, 4]. Morita et al. proposed a structure, Scheme 1, for PAN stabilized in air, although it is, in reality, a more complex three dimensional structure [5].

Understanding the details of carbonization, with H_2O , NH_3 and HCN being evolved, is not yet very clear albeit much progress has been made during the last several decades for the production of PAN based carbon fiber. In this work we will investigate the mechanism of carbonization by means of ReaxFF molecular dynamics simulations. We considered a model system (Scheme 2), that starts with several



Scheme 2: Stabilized PAN model (dehydrogenated)

molecules B ($\text{C}_{32}\text{H}_{14}\text{N}_{10}$) and which is subjected to high temperature conditions. This molecule is likely to be 30% of the structure formed during the stabilization step, and which therefore serves as the starting point for carbonization.

The model system is heated gradually up to 2800 K. Two sets of annealing simulations were performed at temperatures 2500 K and 2800 K for 500 ps. For each temperature ten trajectories were simulated. The data is analyzed during the course of simulations by estimating the number of species evolved, the number of ring breaking and formation events, hybridization types of carbon, carbon content in the growing structure, elementary reactions of small species formation and formation and growth mechanism of sp^2 -type carbon structures. A representative snapshot showing adjacent 5- and 6-membered rings formed from the initial structure is shown in Figure 7. Carbon atoms with sp -type hybridization are associated with this structure. Further ring condensation and growth occurs around this kind of structure. Ring breaking starts to occur at $\sim 2500\text{K}$ and subsequently small molecules, like N_2 , H_2 , HCN and NH_3 , are formed in addition to other species. The formation of these species are tabulated and shown in Figure 8. It is apparent from this figure that formation of N_2 and H_2 are more likely than other gaseous species and that N_2 formation starts to occur earlier than H_2 formation. N_2 formation occurs via three distinct stages as observed in these simulations: (i) CN-bond breaking – 6-membered rings break, (ii) NN-bond formation – N with dangling bond reacts with N on a neighbor molecule, and finally (iii) subsequent CN-bond breaking helps to form N_2 . The newly formed rings consisting of carbon atoms only are counted and shown in Figure 9. In general 5-membered ring formation occurs first as during N_2 formation the 6-membered ring of the seed molecules break and the carbon atoms in the same B unit with a dangling bond in the newly formed structures reacts to form 5-membered rings. Initially 5-membered ring formation is prominent but in the latter stage 6-membered ring formation is also prominent. Conversion of 5- and 7-membered rings into 6-membered rings stabilizes the structure, providing a thermodynamics driving force for this structure. It is to be noted that the formation of 5-membered rings in the mechanism of carbonization is reported here for the first time.

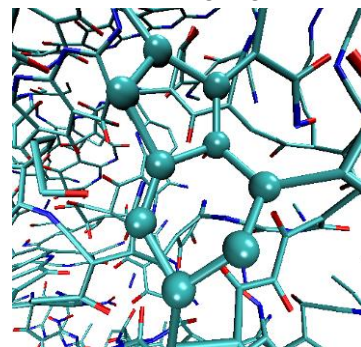


Figure 7: Initial structure formation

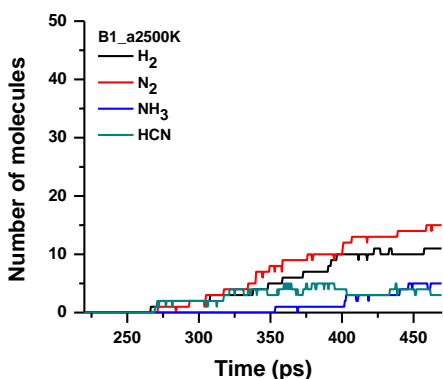


Figure 8: Species formation at 2500 K

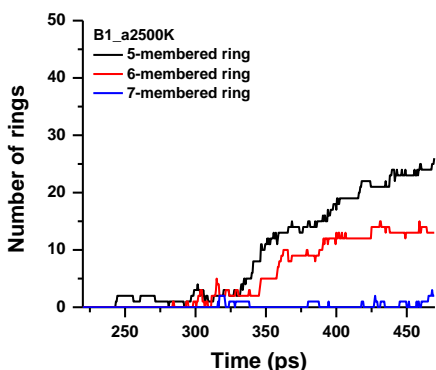


Figure 9: Ring formation consisting of carbon only

As stated above, initially structures consisting of 5- and 6-membered rings are formed. Short polyyne-like structures (with carbon atoms in the backbone) are also formed due to ring breaking and N_2 and H_2 formation. These linear polyyne-like structures may entangle themselves to form new 5-, 6- and 7-ring structures consisting of carbon atoms only. Once a cluster consisting of 5-, 6-membered rings forms, it acts as a nucleus and further ring condensation occurs around it. The newly formed initial structures consisting of 5- and 6-membered rings on different units may also react among themselves to form larger structures consisting of 5-, and 6-membered rings with carbon atoms in the backbone. Thus a three dimensional structure consisting of 5- and 6-membered rings and mainly sp^2 -carbon is formed as shown in Figure 10. Upon continuing annealing the 5- and 7-membered rings may convert to more stable 6-membered rings. Thus from the present ReaxFF simulations, the following distinct stages are observed in the carbonization mechanism: (i) formation of small structures consisting of carbon atoms only via N_2 evolution and 5- and 6-membered ring formation on the same unit, (ii) ring condensation – further ring formation occurs due to entanglement of small sp -type carbon structures attached with these rings, and (iii) cluster

growth – small clusters on different units react to form larger clusters (e.g. H_2 , HCN , NH_3).

6. MEMS based testing of PAN electrospun nanofibers

Polyacrylonitrile (PAN) nanofibers, with diameters ranging from approximately 300nm to 1400nm, were manufactured using electrospinning by the Dzenis group. These fibers were mechanically tested by the Espinosa group using MEMS-based tensile testing devices, pictured in Figure 11a. Testing was performed under an optical microscope using a piezoelectric actuator to extend the fiber at a strain rate on the order of 0.01 s^{-1} . During each test, images were recorded at 1Hz by a digital camera integrated into the microscope. These images were analyzed using Digital Image Correlation to measure the deflection of the load sensor beams and the extension of the fiber gauge section.

A size-effect of increasing strength and modulus with decreasing diameter was observed, as shown in Figure 11-b and c. The strain to failure data was scattered, and did not illustrate a trend with diameter. The specific toughness was calculated for samples with a diameter 400nm and below, and more tests are being performed to investigate this trend. A study on the mechanical behavior of thinner samples is ongoing in order to further investigate the observed size effect in the regime of diameters below 300nm.

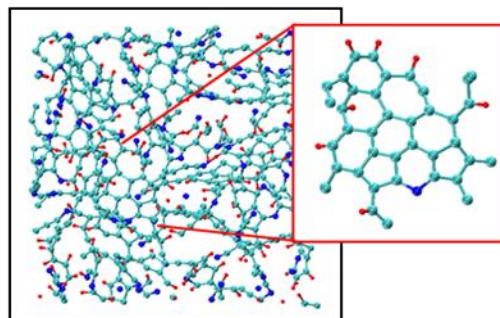


Figure 10: Cluster growth and formation

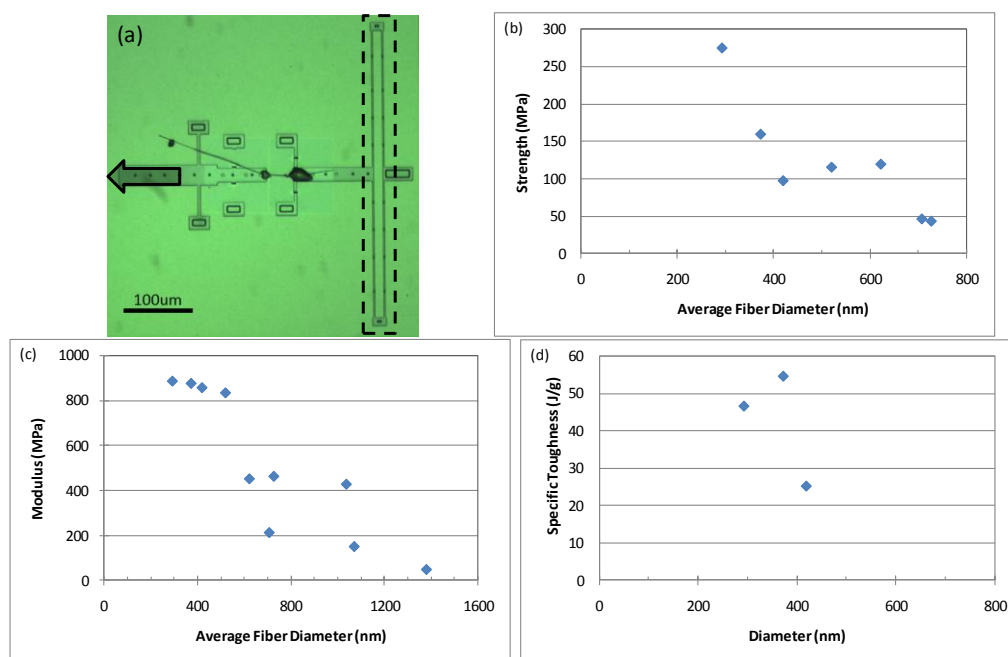


Figure 11. (a) Optical image of MEMS-based testing stage with PAN fiber glued between the two shuttles. The actuator shuttle is displaced during the test, as indicated by the arrow, while the load sensor shuttle expands with the deflection of the load sensor folded beams (indicated by dashed lines). Experimental results of PAN testing: (b) strength as a function of fiber diameter, (c) modulus as a function of fiber diameter, and (d) specific toughness as a function of fiber diameter (assuming a linear density of 1.2g/cm^3).

7. Development of DWNT yarns directly spun from the CVD Reactor

The basic technique established in the project and utilized by Espinosa's, Nguyen's and Moravsky's groups for manufacturing high quality yarns consists of cutting the nanofiber mats into narrow ribbons that are twisted and stretched while subjected to appropriate chemical and thermal treatments. The uniformity of the mat areal density determines the consistency of the yarn mechanical properties. To make the yarns of smaller linear density, which display higher strength and stiffness, the starting mats should be as thin as possible, yet retain uniformity. MER's DWNT mats, obtained by collecting the nanotube aerosol exiting the CVD reactor on the fine mesh grid, can be made of submicron optically uniform thickness to meet these requirements. No other known technique could form nanotubes in semi-transparent self-standing mats with highly uniform areal density that can be as low as 10 microgram/cm^2 . A US Patent No.7771784 of 08/10/2010 has been recently granted to MER's technique of thin mat formation from nanotube aerosol.

Despite its many advantages in developing high performance yarns, manufacture of yarns from the DWNT mat ribbons has intrinsic limitations in terms of the yarn size, nanotube alignment and presence of structural defects, which are reflected in the lower than could be expected mechanical properties and reproducibility of the measured parameters. It has been established by the Espinosa and Moravsky groups that DWNT yarns of smaller diameter display progressively enhanced mechanical properties. A substantial increase in the strength and the modulus is anticipated for yarns that would be thinner than $\sim 25\text{ micrometer}$ diameter, which for the present yarning technique appears to be the smallest that can be made because of the high fragility of the thinnest ribbons. The extreme length of MER's DWNTs is one of the main factors contributing to the high mechanical properties of the twisted yarns. High degree of entanglement and a large density of contacts between the nanotubes in as-produced DWNT mats impede the nanotube alignment during the stretching of ribbons. The structural defects on

the ribbon edges are augmented by the stretching and twisting processing and transferred in the twisted yarn structure.

An alternative approach toward fabrication of CNT based yarns is to use the nanotube aerogel as a starting material instead of DWNT mat ribbons. Under certain conditions, the CNT aerosol can condense into an aerogel in the form of a semi-transparent hollow cylinder inside the hot zone of the CVD reactor. This aerogel “sock” does not have side edges, it contains poorly connected nanotubes that undergo therefore an easy mutual displacement, and can sustain a very low linear density, thus providing the yarns of very small diameter. Upon verifying these attractive opportunities in our DWNT generating system, we have developed the capability to fabricate the DWNT yarns directly from the aerogel inside the CVD reactor.

This technique has attracted much attention due to very high mechanical properties of yarns obtained and good prospects for a continuous production process. A set of serious experimental challenges should be met to make direct spinning possible. Hydrodynamics in the CVD reactor should be neatly tuned to ensure formation of a mobile and fragile aerogel “sock” consisting of loosely interconnected pure nanotubes. Nanotube production rate should be made very high (~ 300 mg/h for a laboratory scale reactor), while maintaining high purity of nanotubes. An advanced mechanical system is required for spinning and harvesting of ~ 5 -30 micron in diameter yarns, and it should operate in a hermetic environment. To meet these challenges, one of the DWNT producing CVD reactors has been substantially modified. A new catalyst vaporization scheme was developed, and the temperature profile in the reactor appropriately changed. Composition of carbon feedstock and other reagent concentrations have been adjusted for adequately high production rate of DWNTs, while keeping amorphous carbon production suppressed. An effective hermetic mechanical system for catching and spinning the sock into yarn was designed and set to work.

The direct spinning system enabled production of much thinner yarns, down to 10-15 micron in diameter, which have displayed outstanding mechanical properties upon compositing with high performance polymer matrices (see following sections for details), thus confirming most of the expectations. However, the exploration of the system has revealed a set of problems that could hardly be resolved with the present experimental reactor, including a short length of yarns that can be produced, the non-uniform diameter of yarns along the length, and therefore inadequate reproducibility of results, the presence of structural defects and high porosity despite a better alignment of nanotubes in the yarn, high catalyst contents, low production rate, the persistent tendency of thermophoretic adhesion of the sock to the reactor walls, and difficulty to measure the linear density of very thin and short yarns. Based on the knowledge acquired on the mechanism of nanotube and sock formation, a new reactor specialized for direct spinning of nanotube yarns was designed, that would produce extended length and highly uniform diameter yarns composed of very long nanotubes coated with sizing of controlled composition, in a continuous process. The reactor will feature optimum length of the nanotube synthesis zone, a short thermophoretic zone, the injection of sub-micron droplets of catalyst solution directly in the high-temperature zone, will possess an adequately increased production rate, and equipped with a hermetic system for driving and harvesting the yarn outside the reactor tube. The construction of the reactor is in progress and close to completion. Upon shortly setting to work, it will significantly enhance the material base of the program, by producing the yarns of substantially higher quality.

Directly spun DWNT yarns are highly porous structures. The volume and shape of voids, and the apparent diameter of yarns is changing upon application of stress during tensile testing. Therefore, the specific strength and modulus of yarns are usually related to their linear density. However, the weight of the tensile test samples of the in situ DWNT yarns of ca. 10 μ m diameter and ca. 20mm length is less than 1 microgram and cannot be measured precisely. The load bearing cross section of the porous yarns was more accurately estimated from the SEM images. For the hexagonal packing arrangement of the aligned DWNT bundles of diameter “d” and average separation between the axes of bundles “D” the fraction of the yarn cross section occupied by bundles V_f is given by the expression $V_f = (\pi/2\sqrt{3})(d/D)^2$. For example, in a typical case for the present yarns, when the open space between two bundles is equal to the bundle diameter ($D = 2d$), the true cross section, or the volume fraction of bundles in the yarn V_f is equal to

22.7%. When the open space is twice the diameter ($D = 3d$), the $V_f = 10.1\%$. This is about the span of V_f observed for the as-produced yarns. The accuracy of d/D ratio determination from the SEM images can be assessed as $\sim \pm 20\%$, which corresponds to an accuracy of $\sim \pm 50\%$ in V_f and in the values for the specific strength and modulus thus obtained. The resulting optical diameter of the samples that do not contain an external matrix was in the range of 13-15 nm, and the volume fraction of the DWNT bundles was assessed from SEM images to be near 20%, which value was accepted for calculation of their specific strength and modulus. Thus, defined true values of the strength and the modulus are expressed in conventional SI units, enabling direct numerical comparison to values similarly determined in the literature reports and in our previous effort for yarns produced by other techniques and from different nanotubes and components.

The DWNT yarns directly spun from the CVD synthesis zone display outstanding mechanical behavior that match and outperform the best results obtained in the category of the carbon nanotube based fibers made without using a binder. Subject to comparison are data obtained at a large enough gauge length, typically in the range 3-20 mm. Measurements performed at a short gauge length of approximately 1mm can produce unusually high values for the strength and the modulus, as shown by Koziol et al., 2007 [6]. This enhancement was due to the practical absence of the large size defects in the yarn at a length range of 1 mm, and is not observed in yarns measured at larger gauge lengths because they contain such defects and consequently reveal much lower strength. The several times enhancements of mechanical properties refer to “intrinsic” mechanical properties of the yarns, ones that have not yet been obtained for the long yarns. These intrinsic properties point to a great potential of CNTs to develop yarns with remarkable mechanical performance. The tensile strength of our in situ twisted and stretched DWNT yarns appears to be in the range from 1 to 2 GPa for most of samples, which is comparable to or slightly exceeds the literature values for untwisted yarns made of thin-walled nanotubes and of twisted yarns made of MWNT forests, all of which were measured at a large gauge length. The modulus was measured at 40 to 150 GPa, which is comparable to the range reported for untwisted thin-walled nanotube yarns and twisted MWNT yarns. The elongation to break in our highly twisted in situ DWNT yarns is higher than in twisted and untwisted nanotube yarns reported in literature, and can reach 30% in the most stretchable samples. The energy to failure of DWNT yarns much exceeds the literature values for matrix-free nanotube yarns, and can reach 200 J/g at an elongation of $\sim 30\%$. It is however to be emphasized that the reported mechanical properties are based on the estimated DWNT volume fraction of 10%. Further studies to more accurately measure the mechanical properties of yarns are currently on the way. Another direction of this research is to develop CNT-polymer hybrid yarns with polymer molecules as cross links between CNT, as discussed in the following section.

8. Directly spun DWNT PMC yarns with polycarbonate matrix

The directly spun uniform DWNT yarns of very small diameters ($\sim 10\text{-}13\ \mu\text{m}$) and highly twisted ($\alpha \sim 35^\circ$, Figure 12) have been used to manufacture Polycarbonate PMC yarns by the diluted solution impregnation. That small diameter is unattainable by manufacture from DWNT mat ribbons, and is supposedly conducive to higher mechanical performance of yarns. Polycarbonate is sufficiently soluble in a set of common laboratory solvents, of which N-methylpyrrolidone (NMP) has been chosen for preparation of the impregnation solution. Upon impregnation with a solution, the solvent should be removed by evaporation to prepare the porous sample for the next impregnation cycle so as to deposit more of matrix inside the yarn. This evaporation should be very slow; otherwise back-flow of the solution from inside of the porous yarn to the surface occurs, and polymer matrix is deposited predominantly in the surface layer, thus also blocking the permeation of the solution in the following impregnation cycle. The NMP has the lowest vapor pressure among good solvents for polycarbonate, and to adjust the slow evaporation poses fewer problems. The 2 wt.% polycarbonate solution in NMP has been used in impregnation cycles. A fragment of the yarn was affixed at the ends on an SEM fiber sample holder and immersed in the solution for 10 min, which was found sufficient time for solution to penetrate to the center of yarn. To facilitate filling of micro-pores and possible permeation into the bundles, the ultrasonic

treatment of the identical samples was employed during the 10 min long soaking. The soaking in neat NMP solvent was also performed for comparison. After soaking, the samples have been dried at room temperature in a vacuum box under gradually reduced pressure for a total of ~ 24 hours, and the cycle repeated five times. No further heat treatment of the dried samples has been undertaken.

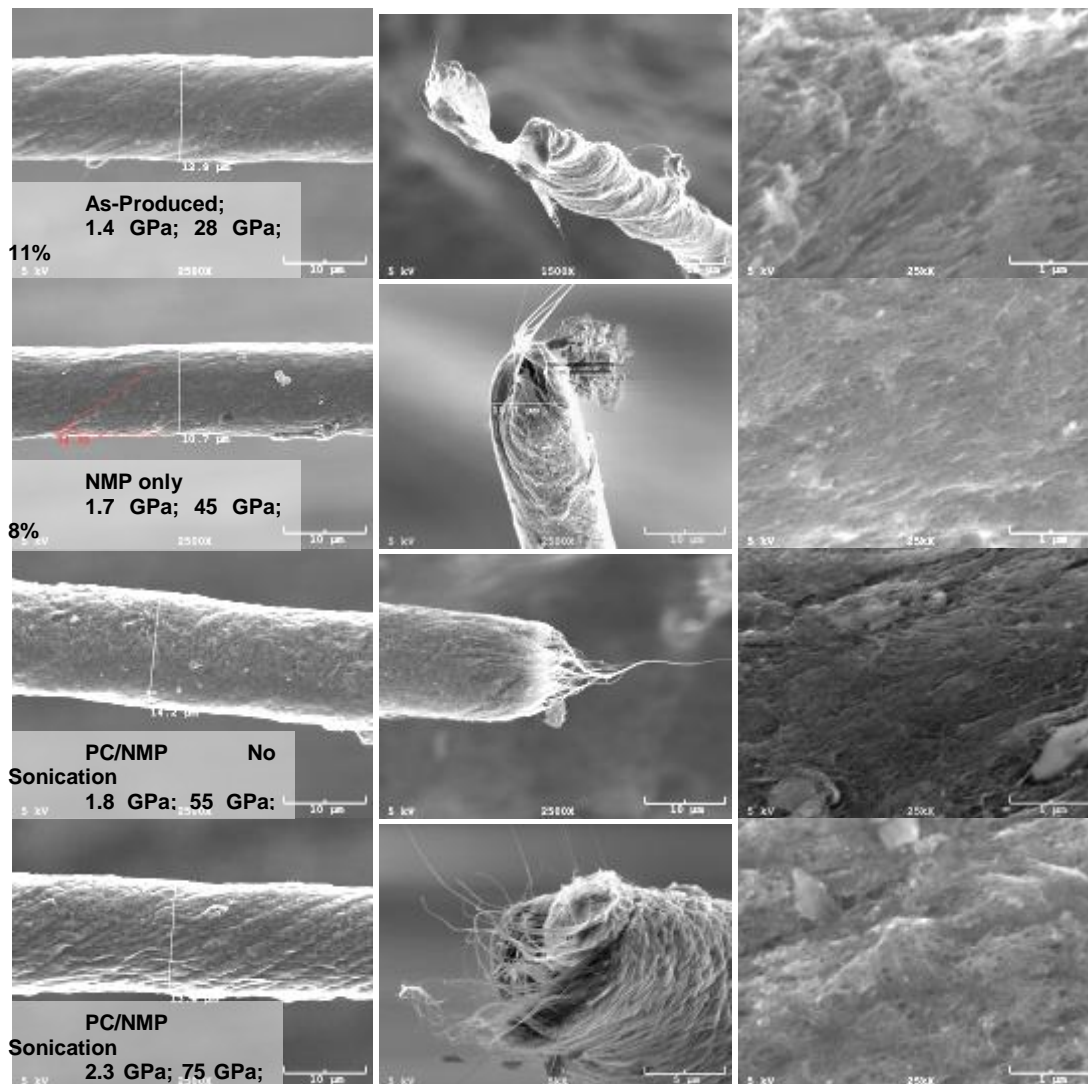


Figure 12. As-produced directly spun yarns and infiltrated with Polycarbonate (left column), tensile fractured ends (middle column) and side surface (right column).

The as-produced, neat NMP treated and impregnated with polycarbonate yarns have been examined with SEM at various stages of composite processing and after the tensile testing (Figure 12). Wetting with NMP has led to ~ 20% contraction of the yarn diameter, thus attesting to dissolution and redistribution of the intrinsic sizing matrix in the yarn, with concomitant rearrangement of thus rendered mobile bundles into a more compact structure with better aligned bundles. The yarn surface became less porous, and irregular radial distortions upon stretching less pronounced. Accordingly, the strength and the modulus have notably increased. Impregnation with polycarbonate has led to diameter swelling by about 5-10% both in sonicated and non-sonicated samples, due to incorporation of polymer. The density of yarns has increased, while the volume fraction of DWNTs did not change. The pores on the side surface became merely clogged with polycarbonate in the sample that was not treated with ultrasound, while in

the treated sample some pores remain open, thus suggesting a better transfer of matrix into the yarn interior. The strength and the modulus of polycarbonate PMC yarns have substantially grown, especially for the ultrasonically treated sample (Figure 12). This confirms the usefulness of sonication for improving solution infiltration in the dense nanotube network.

Directly spun DWNT/polycarbonate yarns demonstrate an extended elastic deformation to up to 4%, and fail at strains of as high as 12%, thus revealing an appreciable growth of dissipated strain energy relative to PC matrix-less yarns. The bundle pullout from the PC matrix consumes more energy and develops higher shear stress in response to tension than in the samples with the intrinsic sizing matrix, thus explaining better mechanical performance of the PC matrix composite yarns. The pulled out DWNT bundles protruding from the ends of fractured yarns are aligned in the tension direction, thereby supporting the mutual slippage as the principal load transfer mechanism between the bundles that serve as the main load bearing elements in the twisted PMC yarns.

Multi-scale experimental and computational studies of the mechanical behavior of CNT/polymer bundles and yarns

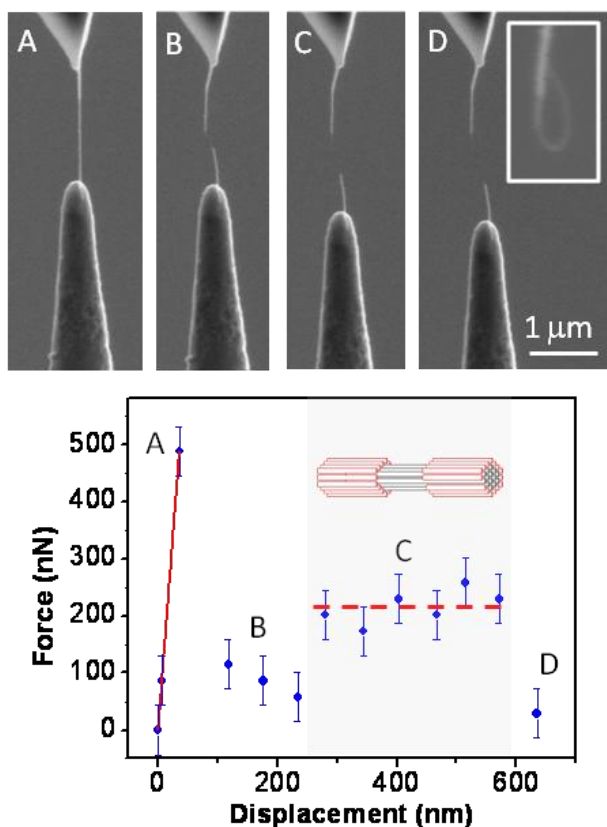


Figure 13: (Top) Sequential SEM images recorded during shear testing of an isolated bundle of DWNTs. The inset shows a smaller inner bundle of DWNTs which pulled out of an outer shell of DWNTs. **(Bottom)** Force vs displacement curve recorded during the pullout experiment. The labels indicate the different stages: **A** – Tensioning of original bundle, **B** – re-straightening after initial failure, **C** – pullout of inner bundle from outer shell of DWNTs, and **D** – final failure of DWNT bundle.

1. Experimental studies of shear interaction within individual DWNT bundles (**Proprietary**)

The shear interaction between inner DWNTs within the bundles was investigated by the Espinosa group using an in situ scanning electron microscopy (SEM) testing setup with a Si cantilever based force sensor described in detail previously [7]. Pullout experiments were conducted on individual DWNT bundles, which measured the force as a function of sliding displacement for inner DWNTs sliding with respect to an outer shell of DWNTs.

To investigate the shear interactions between DWNTs within bundles, the isolated bundles were first deformed in tension until failure of the outer shell of the DWNTs occurs, as indicated by point A in Figure 13 (*i.e.* a sharp increasing in force due to the stiff DWNTs). At the point of this initial failure a smaller inner bundle was found to partially pullout of the outer shell in a sword-in-sheath failure mechanism accompanied by the corresponding recoil of the cantilever based load sensor. The difference between the diameters of the initial and pulled out bundles measured in SEM was about twice the diameter of the DWNTs, ~ 2.2 nm, suggesting that the failure of the DWNTs has only occurred on the outmost layer of bundles. Subsequent to the initial failure, one end of the bundle was then further displaced to reduce the resulting slack and re-tension the bundle (point B in Figure 13). A pullout experiment was then

conducted in which the force was measured as a function of the relative sliding displacement between the inner and outer shell of DWNTs. The force was found to increase to a plateau (pullout force of ~ 215 nN) during sliding (point C in Figure 13) and then drop to zero upon complete failure (point D in Figure 13). After failure the free end of the inner bundle that was pulled out was found to snap back and form a loop (inset in Figure 13).

Experiments were conducted on several isolated DWNT bundles, which all revealed a similar force-displacement relationship to that shown in Figure 13. For each experiment the number of tube-tube interactions in the shear interface was estimated in order to normalize the pullout force and allow a better comparison of the shear interactions for pullout of bundles with different diameters. A justification of this method of normalization of the force is discussed in detail in the context of results of the MM analysis in the next section. The number of tube-tube interactions, $N_{CNT-CNT}$, was estimated using a geometrical model of hexagonally packed DWNTs yielding:

$$N_{CNT-CNT} = 2N + 6,$$

where N is the number of DWNTs on the perimeter of the inner bundle. This can be estimated from the inner bundle diameter [7], which is measured from SEM images. Results from pullout experiments on three DWNT bundles with different diameters revealed similar normalized pullout forces of 1.7 ± 1.0 nN/CNT interaction. It is important to note that the pullout force was found to be independent of the overlap length of the inner bundle and outer sheath of DWNTs. This finding in particular will be discussed in detail later in context with MM simulations.

Pullout experiments were also attempted on polymer coated DWNT bundles prior to heat treatment. Here the bundles were found to undergo nearly complete failure at the initial failure point (A in Figure 13) and did not exhibit a further increase in force (C in Figure 13), which would otherwise correspond to the pullout of an inner bundle. This nearly complete initial failure was confirmed by TEM imaging, which revealed a fractured region with a staggered diameter, or telescopic failure, in which multiple layers of DWNTs within the bundle had failed. This type of telescopic failure mechanism was also previously observed by the authors in SEM testing of similar polymer coated bundles [7]. Such a failure mechanism may be the result of higher external pressure acting on the bundles as a result of the polymer coating, and will be a topic for future investigations.

2. Atomistic carbon nanotube bundle mechanical property modeling

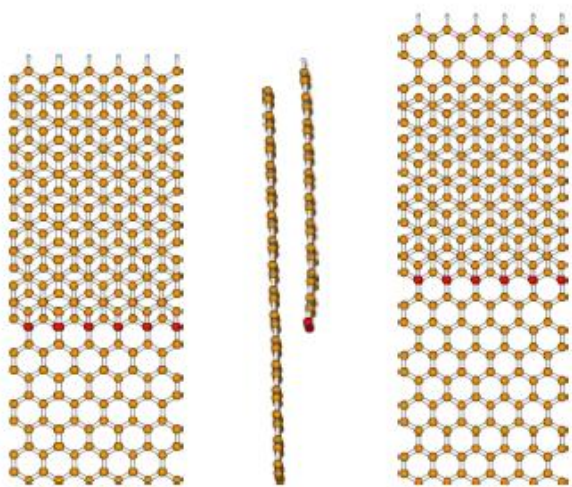


Figure 14: Top and side views of the zigzag edge model. The top view of the model after the partial sheet has been displaced one periodic distance is also shown (right panel). The free edge is functionalized with carbonyl groups. Carbon, hydrogen and oxygen atoms are shaded yellow, white, and red, respectively.

An important activity of the Schatz group was to model the structural and mechanical properties of functionalized carbon nanotube nanotube bundles, including DWNTs and sizing that are modeled on the MER Corporation synthesis. Both electronic structure and empirical force field methods are used to model nanotube pullout experiments, with electronic structure theory providing validation for the empirical force fields. This work relates directly to experiments being done in the Espinosa group, and it provides calibration for the larger scale calculations that are being done by Buehler. In addition, related studies (described below) are useful for characterizing graphene and polymer/CNT structures that are relevant to the Nguyen and Dzenis experiments. The previous year's report described our initial attempts to model

carbon nanotube pullout using QM and MM methods. In this section we describe new work that we have done that is concerned with the effect of dangling bonds in the fractured nanotubes.

When the outer tubes of the bundle fracture in the first stage of the pullout experiment, dangling bonds will be created. In Ref. [8], the authors used simulations to examine the pullout of an inner tube from a multi-walled CNT, and showed that significantly more force is necessary to extract an inner tube with an end consisting of dangling bonds than one with a fullerene-like cap. This suggests that end-effects are an important consideration for this type of situation. However, even though our experiment is performed in a vacuum of 9.26×10^{-6} Torr, the diffusion rate of gas molecules on the surface will be sufficiently large that the bonds will quickly become functionalized. The barrier to diffusion of O_2 is less than 3 kcal/mol.[9, 10] When an O_2 molecule is placed near the dangling bonds of the type that are expected experimentally, PBE/DZP-based simulations suggest that it dissociates to form a pair of carbonyl groups. This observation motivated sets of PBE/DZP-based simulations in which carbonyls were added to zigzag and armchair edges of graphene sheets, and then moved across intact sheets of graphene. The zigzag model is shown in Figure 14. Periodic boundary conditions were used, and hydrogen atoms were used to terminate what would otherwise be dangling bonds. The armchair model is analogous (not shown).

The partial sheets were moved one periodic distance, i.e., 4.3 and 2.5 Å for the models of the zigzag and armchair edges, respectively. The resulting energy versus displacement behavior for the zigzag model is shown in Figure 15a. The interaction is a combination of the dipole-induced dipole interactions between the carbonyl groups and the neighboring sheet, and the dispersive interactions between the carbon atoms of the adjacent graphene sheets. It is well-known that density functional theory

is generally unable to accurately predict the energy and thus the forces due to dispersion. Therefore, calculations were repeated in which the oxygen atoms were replaced by hydrogen atoms. In this latter set of calculations, all atomic positions were fixed except for those of the newly-added hydrogen atoms. The resulting energy versus displacement behavior for the zigzag edge model is shown in Figure 15b. By subtracting off the contribution from dispersion ($1.4 - 0.85 = 0.55$ eV), and using the fact that this energy change takes place over a pullout distance of approximately 2 Å, this gives a force of 0.275 eV/Å or $1100 \times 2 \times 0.275 / 14.8 = 40.9 \text{ eV/Å}$ at the bundle level, where an inner bundles circumference of $25 \times 14 = 1100 \text{ Å}$ has been assumed. 14.8 Å is the width of the unit cell used in the PBE/DZP calculations. The factor of two comes from the fact that two such carbonyl-functionalized ends will be moving over the surfaces of intact tubes as the pullout takes place. This translates to a force of 65.4 nN. To take into account the curvature of the tubes, a multiplication factor of 0.6 can be used, which is an estimate based on the 2.7 nm tubes of Ref. [11] and is consistent with Ref. [12]. This gives $\sim 40 \text{ nN}$ as the force.

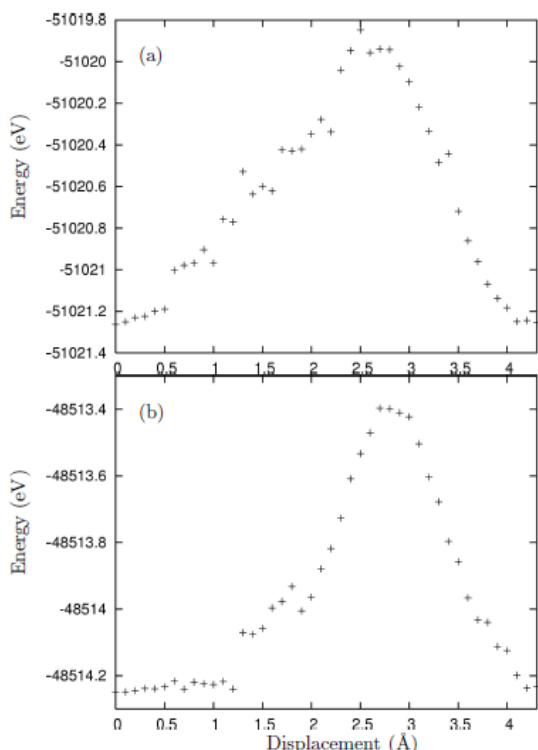


Figure 15: Energy versus displacement associated with the zigzag model with (a) carbonyl groups and (b) hydrogen atoms at the edge.

The force was calculated as the average slope of the energy versus displacement curve between the position of the energy minimum and energy maximum.[13] Interestingly, the addition of carbonyls to the armchair edge (not shown) did not increase the resistance to sliding beyond that due to dispersion. The carbonyl groups are also likely to cause enhanced local tube flattening, which will increase the amount of energy necessary to perform the pullout, and thus will further increase the pullout force. This is something we are currently examining using MM3-based simulations.

3. Comparing electronic structure results and molecule mechanics force field results for nanotube pullout

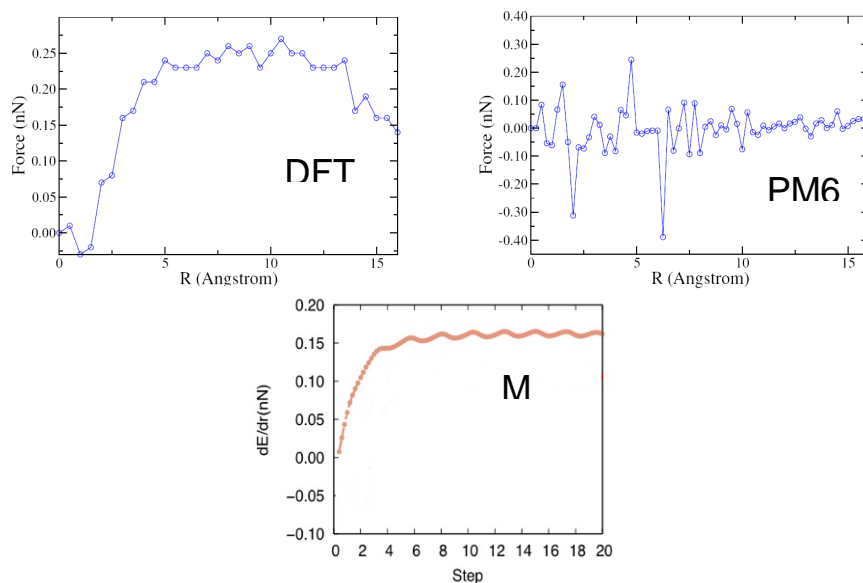


Figure 16: Force versus displacement curves for unfunctionalized 1.5 nm SWNT(5,5), comparing DFTB, PM6, and MM3.

Due to the large computational effort associated with quantum calculations, in the case of DFTB, we can only consider model systems that are much smaller than the actual MER CNT samples. In addition, all calculations refer to single wall CNTs; DFTB comparisons for DWNTs show no effect due to the inner wall so this has been left out.

Figure 16 shows a comparison of force versus displacement results for unfunctionalized SWNTs. The PM6 method does not include dispersion interactions, so the force is effectively zero. However the DFTB and MM3 include dispersion, and the results are similar, with the plateau force being 0.25 nN for DFTB and 0.16 nN for MM3. These comparisons provide an indication of the quality of the MM3 force fields. Similar results have been obtained for functionalized tubes.

4. Modeling the resonance Raman (RR) spectra of functionalized double wall carbon nanotubes

The optical properties of carbon nanotubes, which are found to be very sensitive to their physical (diameter and chiral indices) and chemical (degree of functionalization) structures, are studied using the Time-Dependent Density Functional Theory (TDDFT). A purely quantum-chemical calculation of the full range of frequencies of Raman spectra has never before been investigated. We used the SCM's Amsterdam Density Functional (ADF) program. The differential Raman scattering cross section is obtained from:

$$\frac{d\sigma}{d\Omega} = \frac{\pi^2}{\epsilon_0^2} (\omega - \omega_p)^4 \frac{h}{8\pi^2 c \omega_p} [45\bar{\alpha}'_p{}^2 + 7\gamma'_p{}^2] \frac{1}{45(1 - \exp(-hc\omega_p/k_B T))}$$

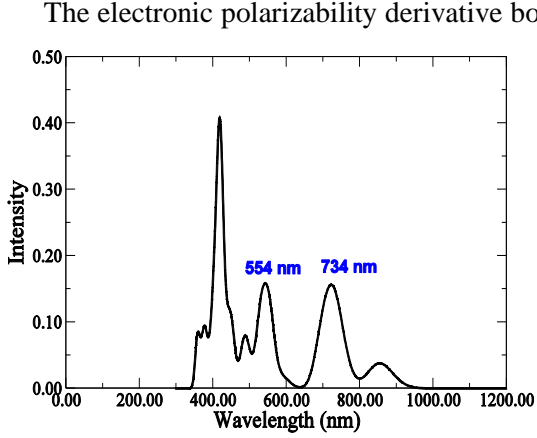


Figure 17: TDDFT optical spectrum of capped SWNT(5,5) tube using BP86/DZP.

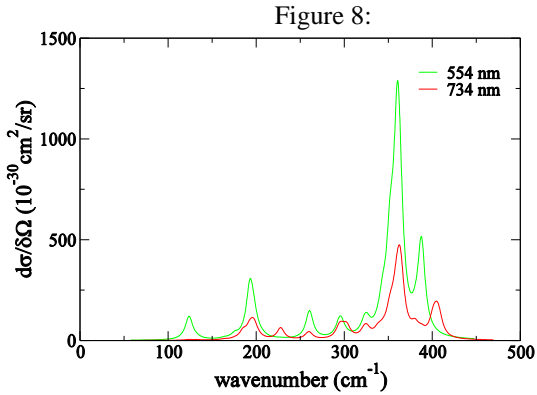


Figure 18: TDDFT Resonance Raman spectra of SWNT(6,5) at different incident wavelengths using BP86/DZP.

The electronic polarizability derivative both on and off resonance is calculated by including for the finite lifetime of the electronic excited states using a special version of TDDFT developed in the Schatz group. The polarizability derivatives are calculated by numerical three-point differentiation with respect to the normal mode displacements.

The optical spectrum at the BP86/DZP level of theory for an 8-10 Å long SWNT(6,5) tube in which the terminal carbons are capped with hydrogens (a total of 112 atoms) is shown in Figure 17. As has been demonstrated by several experiments and shown for the radial-breathing mode region in Figure 18, there is strong excitation wavelength dependence of the Raman intensity of SWNTs resulting from the proximity of the laser wavelength to the transitions between electronic states. The incident wavelengths at 554 nm gives higher intensities compared to those generated at 734 nm. Slight shifts in the frequencies are sometimes observed due to differences in intensity patterns.

Figure 20 shows the Raman spectra of carbon nanotubes at 554 nm. The radial breathing mode (RBM) region shows a peak at 361 cm^{-1} that is expected for this tube diameter. The D mode is generally observed around 1340 cm^{-1} and is attributed to disordered graphitic material associated with the short tube we studied. Lastly, the G mode, which shows at $1550\text{--}1600\text{ cm}^{-1}$, corresponds to the stretching mode of the C-C bonds in the graphite plane. The ratio between G and D intensities indicate the quality of the carbon nanotubes, and in the case of the calculated results, it is clear that the short tube length and hydrogen end-capping results in a highly defected tube. The experiment by Yuhuang and co-workers shows that as the tube become more functionalized, the D mode intensity rapidly increases (Figure 19). The MER sample shows that the G/D ratio is consistent with few defects in the outer wall (Figure 19).

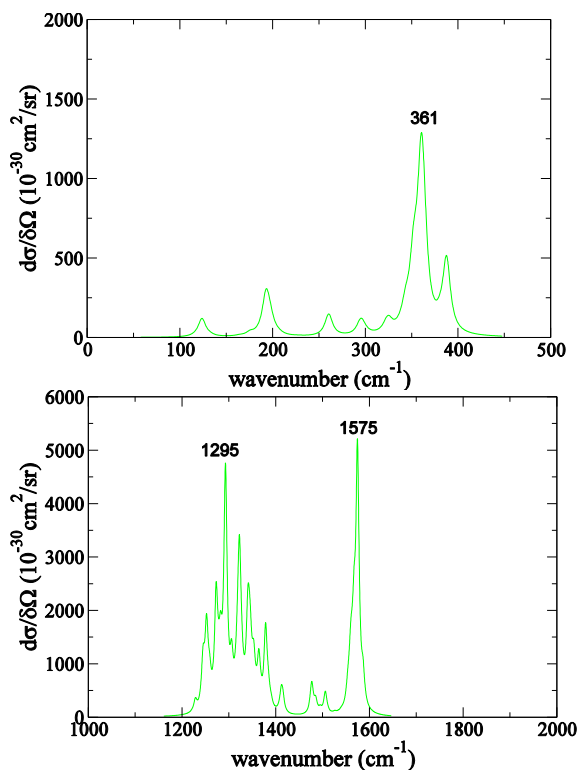


Figure 20: TDDFT Resonance Raman Spectra of SWNT(6,5) at 554 nm incident wavelength.

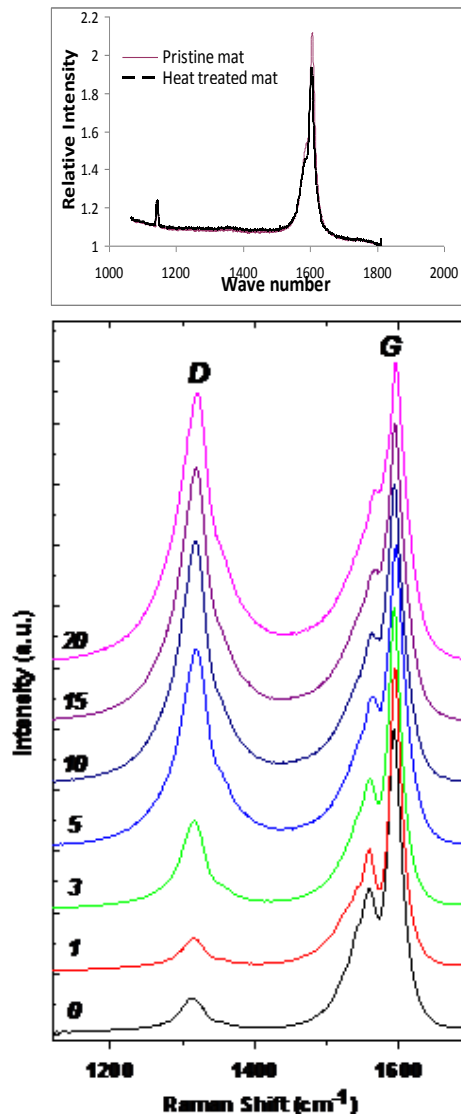


Figure 19: Comparison of D and G modes obtained from (a) MER CNT Material; and (b) from Shunliu Deng, Yin Zhang, Alexandra H. Brozena, Parag Banerjee, Maricris Lodriguito Mayes, Wen-An Chiou, Gary W. Rubloff, George C. Schatz, Yuhuang Wang, “Confined Propagation of a Covalent Chemistry in an Electron Sea”, *Nature Commun.* **2**, 382 (2011).

5. Experimental characterization of shear interactions between functionalized DWNT bundles (***Proprietary***)

As has been pointed out by numerous studies, a fundamental limitation in developing CNT based nanocomposites and yarns with mechanical properties comparable to those of CNTs is the weak shear interactions between CNTs [14, 15]. One promising approach to improve the shear interactions between CNTs has been through introducing functional groups on the surface of CNTs by physical or chemical functionalization of as produced CNTs [16-22]. These functional groups are chosen to be more active than pristine surfaces of CNTs, and thus, result in enhanced interactions between CNTs. While chemical functionalization typically results in stronger bonds between CNTs and the functional groups (due to the formation of covalent bonds between the two), it disrupts the sp^2 bonds between carbon atoms in CNTs, resulting in loss in their mechanical properties.

In this research, the Espinosa group has investigated the shear interactions between CVD grown DWNT bundles (fabricated by MER Corp) that are functionalized with substituted acrylic acid groups (inherent polymer coating). Unlike typical methods of chemical and physical functionalizations of CNTs, such as acid treatments of as produced CNTs, the DWNT bundles in our study are functionalized in situ the CVD reactor and during their synthesis, by introducing ethyl alcohol as the hydrocarbon feedstock. Our preliminary studies suggests that the inherent polymer coating is strongly attached to CNTs, potentially through covalent bonds or pi-pi interactions between aromatic groups of the polymer coating and the surfaces of bundles. Moreover, Raman spectroscopy points to a very low defect density in

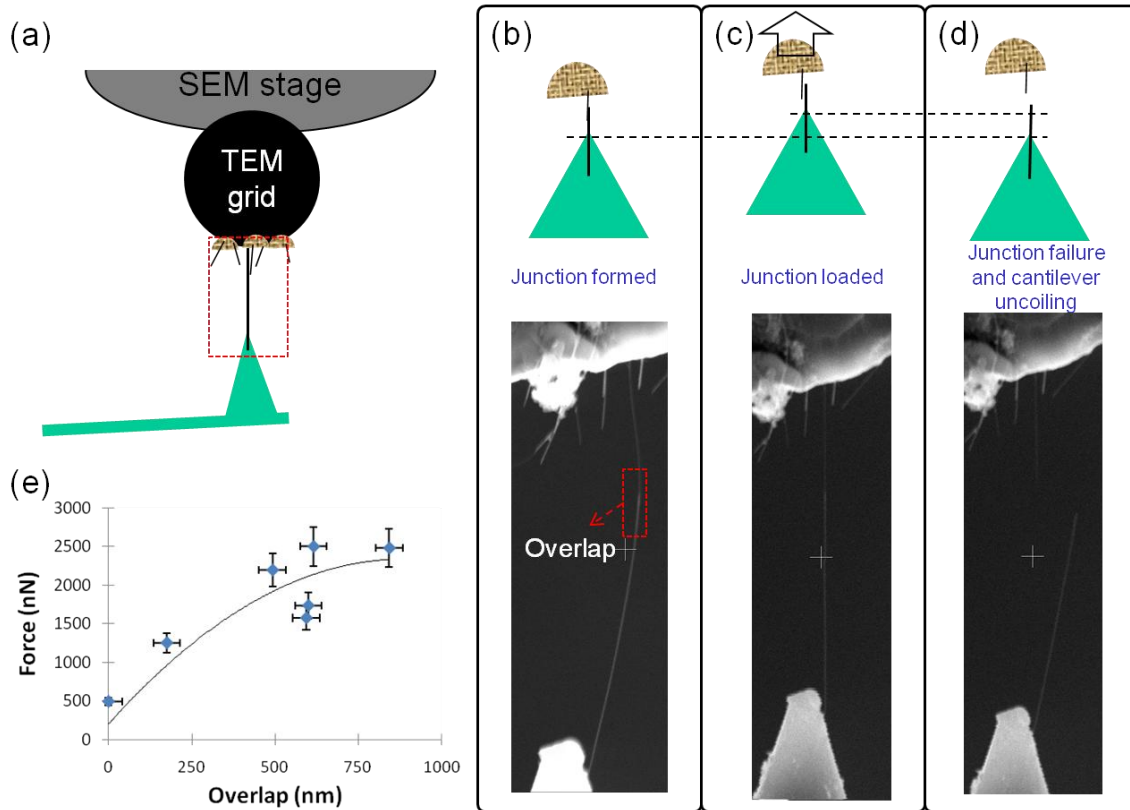


Figure 21: (a) Schematic of the experimental setup. One DWNT bundle is mounted on the tip of an AFM cantilever, which serves as the load sensor. The other bundle is mounted on a substrate. The two are brought in contact to form a junction (b). The junction is loaded (c), until the two bundles are pulled apart (d). Junction force capacity as a function of overlap length for two DWNT bundles with outer diameter of ~27 nm and 37 nm (e).

DWNTs (D/G peak $\sim 2\%$), suggesting low density of covalent bonds between DWNTs and polymer coating.

To measure the interfacial shear interactions (IFSS) between DWNT bundles, sufficiently long (several microns) DWNT bundles were picked from the edge of a TEM grid and mounted on the tip of an AFM cantilever with a known stiffness. The samples were then brought in contact with another DWNT bundle to form junctions with known contact lengths, in the range of 100 nm to 800 nm. The DWNT bundle junctions were then loaded in shear until failure. A schematic of the experiment is shown in Figure 21 (a)-(d). All the experiments were carried out in an SEM and the deformation of the DWNT bundles and the cantilever were recorded. In all experiments, junction failure was catastrophic, and no sliding between the two bundles was observed, potentially due to the limited resolution of deformation measurement in SEM. This observation is in accordance with the coarse grain models of the experiment (see following Section), in which after initial yielding of the junction, the relative displacement between the two bundles grows rapidly with applied force.

Figure 21e shows the variation of the junction rupture force between two bundles as a function of the initial overlap length. As shown in this figure, the in situ CVD functionalization, results in junction force capacity of as high as 2.5 μN for overlap lengths of ~ 600 nm. This value of junction force capacity is several times higher than the force capacity between unfunctionalized MWNTs and MWNTs functionalized with carboxylic groups with similar diameters (section 1), pointing to the remarkable contribution of in situ functionalization of MWNTs in enhancing the load transfer between them.

Moreover, normalizing the forces by contact area, estimated as the product of the initial overlap length and the contact width, results in IFSS of 300 ± 147 MPa, which is substantially higher than IFSS between unfunctionalized graphitic surfaces [23, 24], further elucidating the role of proper functionalization in the enhancement of load transfer between CNTs.

6. Coarse grain modeling of the shear interactions between functionalized DWNT bundles (***Proprietary***)

The Buehler group developed a coarse-grained CNT model (Figure 22) that is based on atomistic simulation results, enabling us to reach large scales up to micrometers and realistic bundle geometries. Key features of the model are:

- Created [(10,10)@(16,16)] DWNT in Materials Studio to represent an atomistic model
- Consider weight of 1 C atom = 12.01 Da; coarse grain at 4,264 C atoms (51,200 Da) per 10 nm
- Resulting DWNT bead spacing is 1 nm, so DWNT bead is 5,120 Da
- Based on prior work with sidewall defects, harmonic spring rate equivalent to $E = 1$ TPa
- Dimensions that can be achieved; 113 tubes results in a bundle diameter = 28 nm
- Diameter of each CNT = 2.2 nm; center-to-center = 2.5 nm; longitudinal bead distance = 1 nm; length = 0.1 – 1 μm

Figure 23 shows the process of how parameters are transferred from atomistic scales to the coarse-grained model, via parameter fitting. We constructed a full-atomistic model of the sizing chemistry informed from experiment and used to obtain CNT-CNT interaction parameters via the sizing chemistry, which is appropriately reflected in the coarse-grained model by using a bead-chain model of the polymer. Figure 24 shows parameter training and validation through the comparison between CNT bundles with all atom models and coarse grained approach, including a force-displacement curve that illustrates the direct comparison.

The coarse-grain model described in the previous paragraph is now used to build larger-scale bundle-bundle models that correspond to those geometries studied by the Espinosa group. Figure 25 shows the geometry of these studies, including key geometrical parameters. The polymer sizing is placed on the outside of the bundle as seen in experimental studies. Figure 26 shows a detailed view of the molecular structure at the interface of two bundles and an associated applied force-displacement curve.

The setup now provides a powerful tool to explore varied geometries of overlapping bundles, fitting those scales investigated in experimental studies as shown in Figure 27. Figure 28 depicts snapshots as the bundles undergo deformation, used here to highlight the potential insight that can be gained by these studies. By making a link with experiment via the force-displacement curves and associated mechanical data (Figure 29), we can garner valuable insight into detailed mechanisms. Current analyses revealed a competition between sliding, bundle rupture and potential CNT rupture under different boundary conditions and geometries, and are currently being analyzed rigorously against the experimental results. We have already demonstrated that in both experiment and simulation the mechanical properties of bundles change drastically under varied overlap length, and direct comparison with experimental studies suggests reasonable agreement.

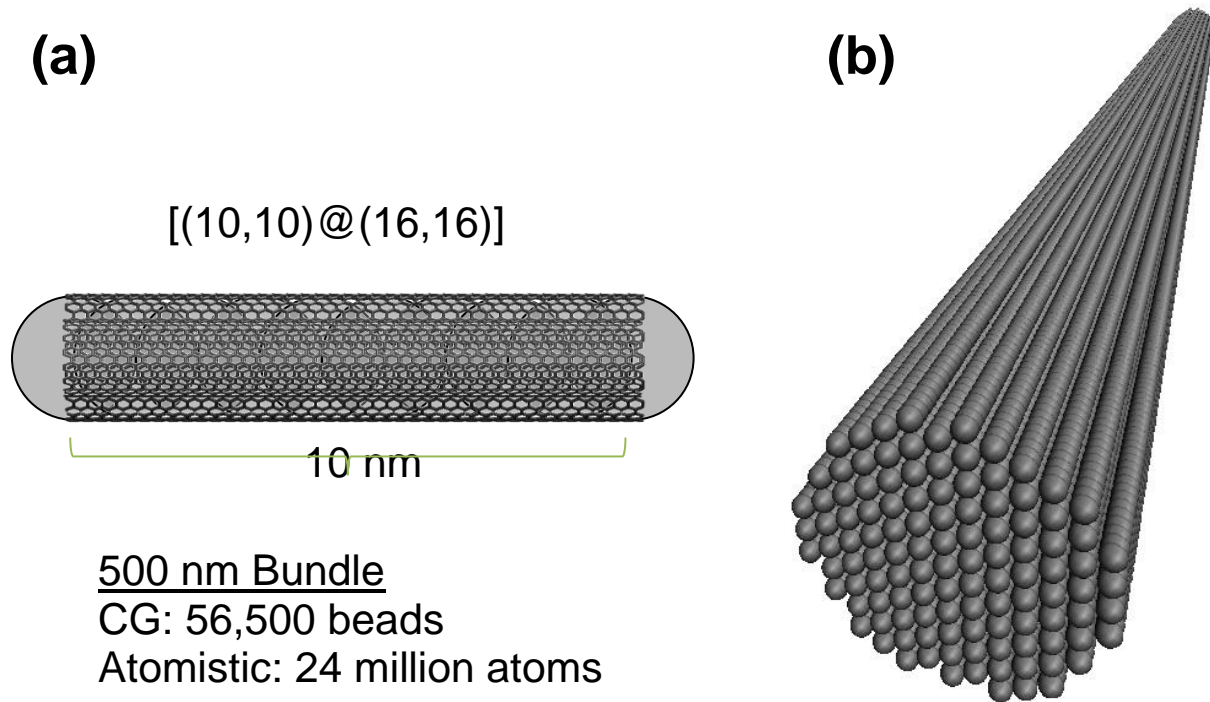
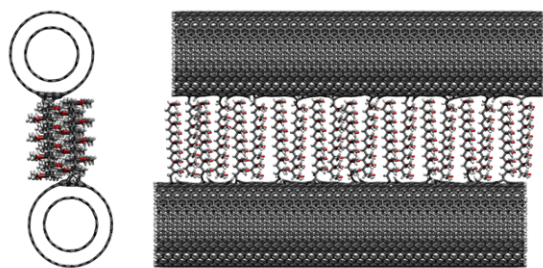


Figure 22. Summary of model development approach, from atomistic to CG scale.

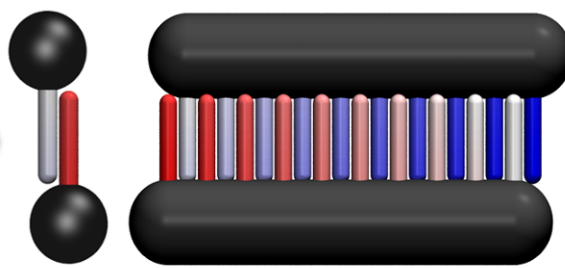
Full Atomistic with ReaxFF



$L = 10 \text{ nm}$

$N = 11,176$

Bead-Spring CG

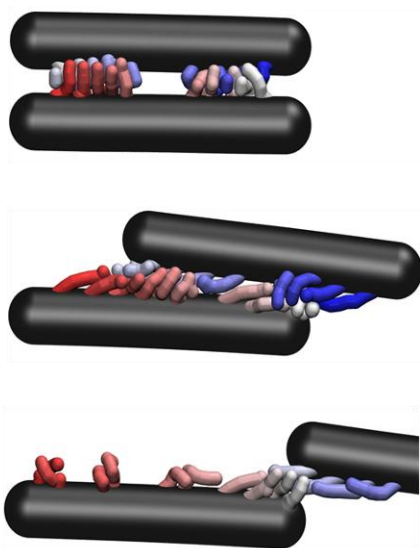


$L = 10 \text{ nm}$

$N = 180 \text{ (1.6\%)}$

Figure 23. Development of the coarse-grain model of CNT and polymer sizing. The two levels of modeling integrate full-atomistic with ReaxFF towards the bead-spring coarse-grain model, seamlessly.

Harmonic Bead-Spring CG



Full Atomistic with ReaxFF

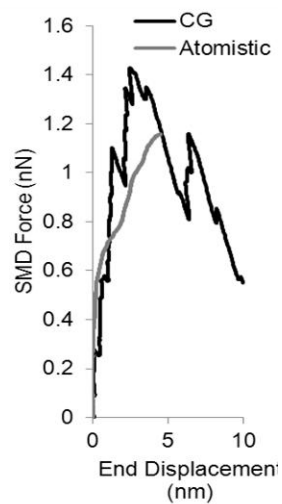
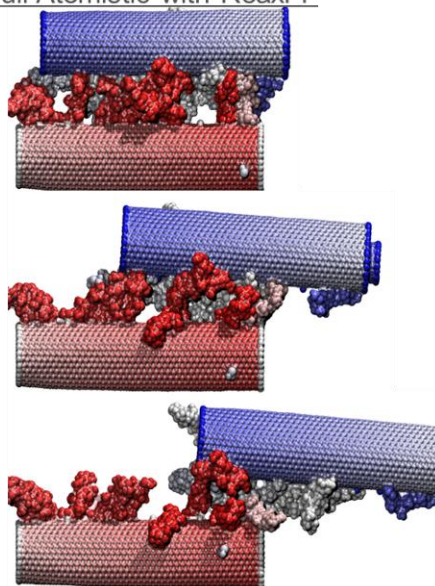


Figure 24. Parameter training and validation through the comparison between CNT bundles with all atom models and coarse grained approach.

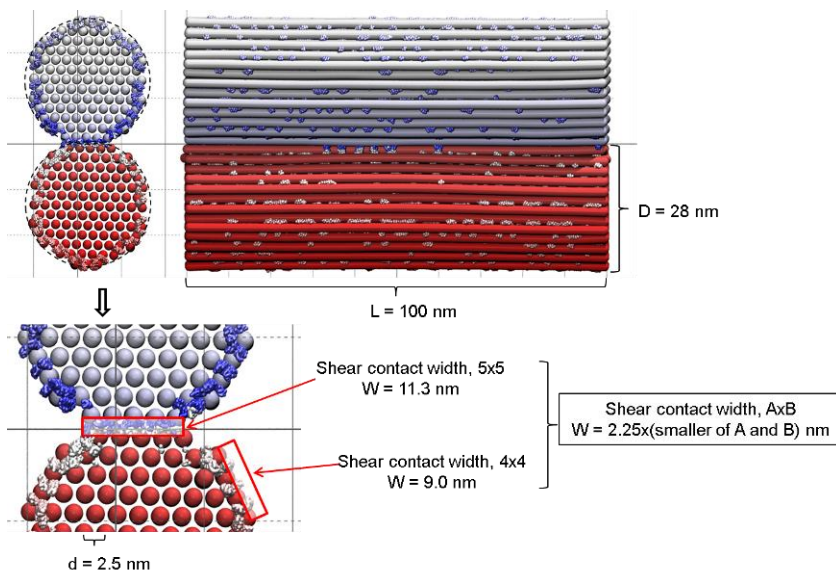


Figure 25. Detailed view of the CNT bundle geometry.

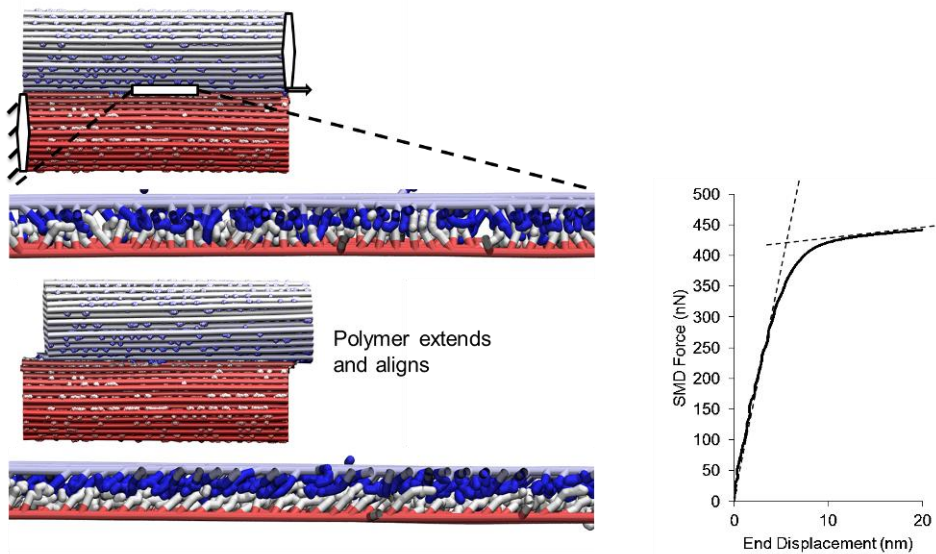


Figure 26. Molecular structure at the interface (before and during deformation) of two bundles (left) and associated force-displacement curve (right).

100 nm, P4 and P8



500 nm, P4 and P8



1000 nm, P4 (P8 still running)



Figure 27. Different cases treated in our model, with varied overlap length reaching micrometer length-scale.

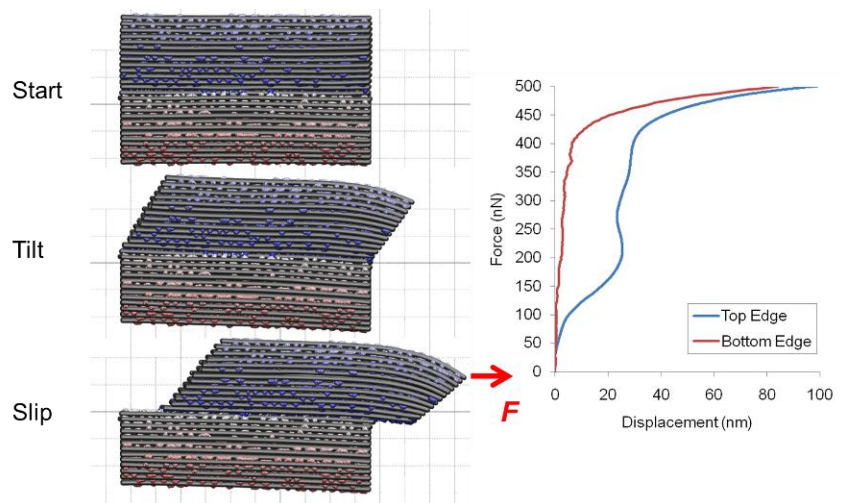


Figure 28. Snapshots of deformation obtained using the CG bundle model.

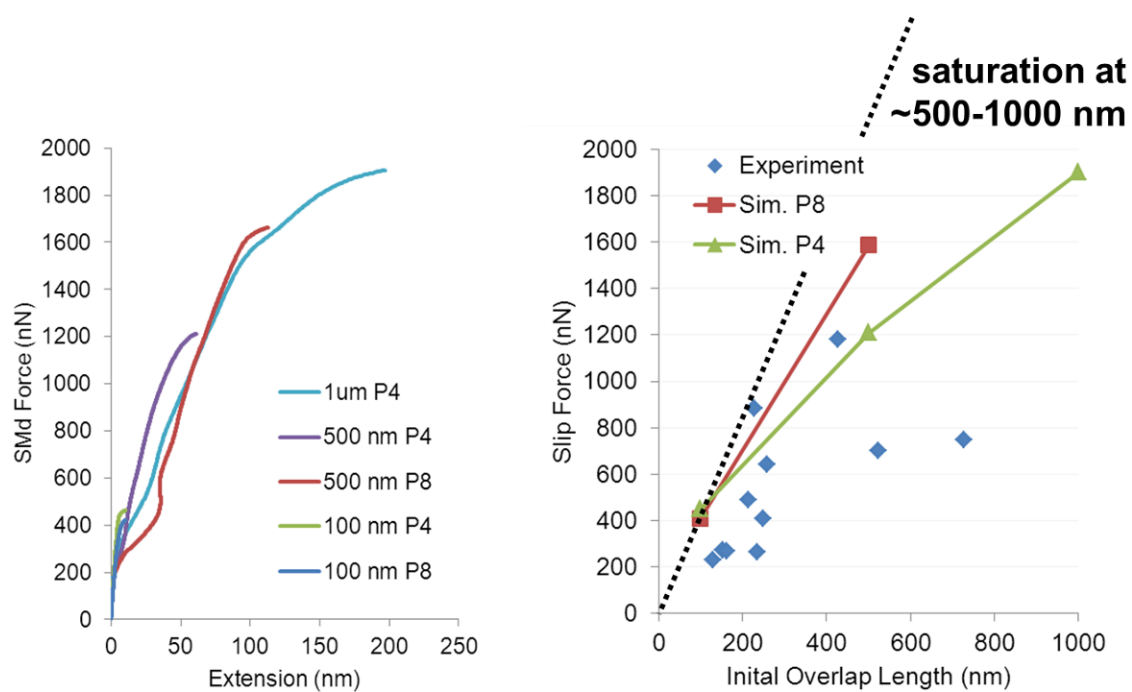


Figure 29: Mechanical properties of bundle mechanics for varied overlap length, and direct comparison with experimental studies from the Espinosa lab.

Engineering lateral interactions within CNT yarns and fibers through crosslinking

1. A Nanomechanical study of the Chemo-mechanics of crosslinking molecules (***Proprietary***)

In the last decade, CNT yarns and nanocomposites with high contents of carbon nanotube (CNT) have received considerable attention. The significance of these materials lies in the fact that high CNT content is a prerequisite to develop macroscale nanocomposites with physical properties comparable to those of CNTs. In these emerging materials, interactions between neighboring CNTs controls the mechanical performance of the macroscale material. In this study, we have developed a nanomechanical experimental approach to investigate the load transfer mechanisms between CNTs in various loading conditions including shear and peeling at various angles, mimicking the loading modes of CNT junctions present in CNT composites. Therefore, these experiments provide us with a deeper understanding of load transfer mechanisms between CNTs. Moreover, the methods developed here enable us to evaluate the efficiency of different cross linking techniques in the enhancement of interactions between CNTs.

To study CNT-substrate interactions, in mode I and mixed mode, MWNTs were mounted at the tip of an AFM cantilever, which served as the load sensor. The MWNT was then brought in contact with a graphite (graphene oxide) substrate and peeled off at different angles *in situ* a SEM, where both the shape of the MWNT and the deflection of the cantilever were recorded. When the CNT is pulled away normal to the surface, debonding happens in mode I, while at lower contact angles mixed mode fracture is observed, and as the peeling angle increases, mode II failure becomes more dominant, resulting in a substantial increase in peeling force, as shown in Figure 30 (a) and (b). Given the sp^2 structure of both CNT and substrate material, the experiment is expected to mimic the interactions between neighboring CNTs in loaded CNT yarns. Moreover, this experiment demonstrates that inducing CNT alignment should be considered as an effective strategy to enhance the load transfer between CNTs in CNT yarns. Assuming that bending stiffness of CNTs compared to its axial stiffness is negligible, the peeling force, P , as a function of peeling angle, θ , can be described as [25]:

$$P = \frac{G}{1 - \cos \theta}$$

where G is the adhesion energy per unit length between CNT and graphite. Fitting the above equation to experimental results, the value of G is measured to be 18.6 nJ/m. The future directions of this experiment will include the functionalization of MWNTs and replacing the graphite substrate with graphene oxide to mimic the interactions between two functionalized MWNTs. The values of G as a function of different MWNT surface treatments relative to the value measured for MWNTs on graphite will allow for a quantitative assessment of the effectiveness of different functionalizations in the enhancement of mechanical properties of CNT nanocomposites.

In the limit, when the contact angle reaches zero, fracture occurs in mode II (shear). In view that small angles ($< \sim 40^\circ$) are not practical within the current setup, shear experiments between two MWNTs were carried out. The experimental method to investigate the shear interactions between CNTs is similar to the method explained in Figure 21a-d, which was used to measure the shear interactions between functionalized DWNT bundles. The junction force capacity as a function of overlap length for unfunctionalized MWNTs is shown in Figure 30c. The overlap length between the two MWNTs was maintained below 1 μm , and the outer diameter of MWNTs is in the narrow range of 17-27 nm. At sufficiently small overlap lengths (below 300 nm) the force capacity of the junctions increased with overlap length, reaching a plateau at overlaps above 300 nm, which continued to ~ 500 nm. However, further increase of the overlap resulted in sudden increase of the junction force capacity, typically leading to MWNTs failure instead of their junctions. This latter trend is believed to be a result of lateral shear stresses which develops between two graphitic surfaces, when the contact is loaded parallel to the axis of the CNTs. The lateral shear is due to the tendency of contacting graphitic surfaces to establish AB

stacking. Our preliminary studies suggests that such lateral shear stresses in sliding graphitic surfaces develops in all cases, with the exception of the two AB stacked graphene layers when loaded in their armchair direction. This lateral shear between two MWNTs in contact, at sufficiently large overlap length, may result in MWNTs twisting and wrapping around each other, thus enhancing the interactions between them. This matter is currently under further investigations.

A similar qualitative trend in the force junction capacity as a function of overlap length was observed when MWNTs were functionalized with carboxylic groups (MWNT-COOH). However, in the latter case, the force junction capacity corresponding to the saturation regime was, on average, more than doubled, potentially due to the hydrogen bond interactions between -COOH groups on functionalized MWNTs, Figure 30d, mimicking nature materials such as spider silk [26]. Moreover, the sudden increase in the junction force capacity was delayed to overlap lengths of ~700 nm, potentially due to the shielding of the graphitic surfaces of the two MWNTs from each other by the functional groups, and thus reduced effect of lateral shear stresses between the two graphitic surfaces.

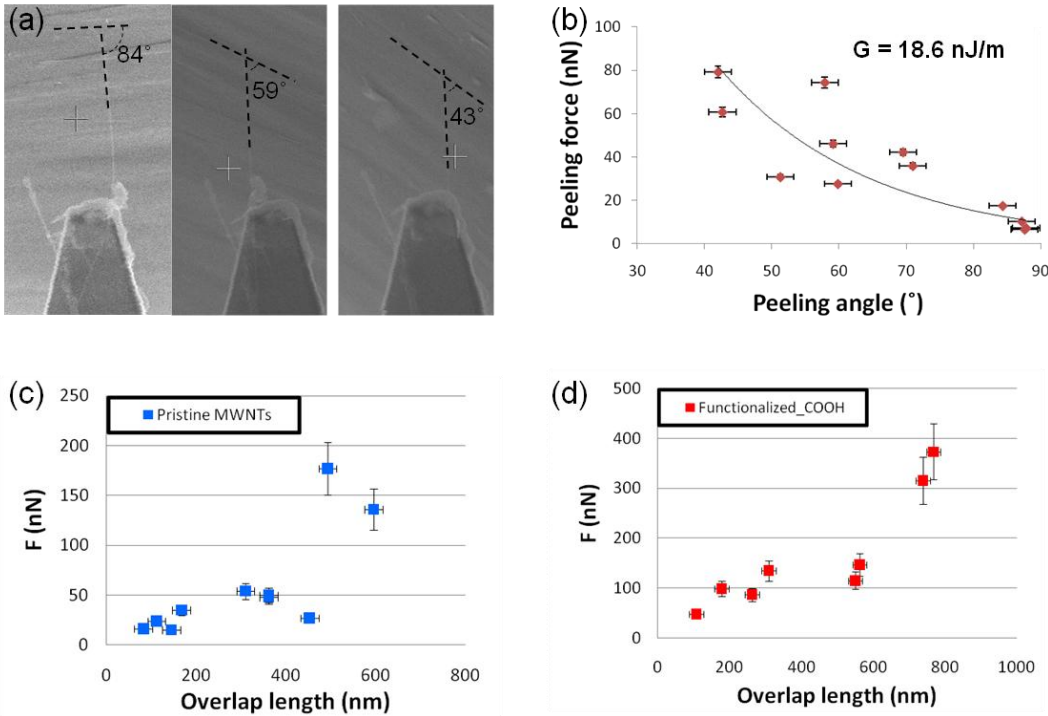


Figure 30. (a) Setup of the peeling experiments from nearly normal peeling (mode I) to higher angles (mixed mode I & II), (b) peeling force as a function of peeling angle, corresponding to adhesion energy per unit length between CNTs and graphite of 18.6 nJ/m. Shear junction force as a function of overlap between pristine MWNTs (c) and MWNTs functionalized with carboxylic groups (d).

Given the saturation of the junction force capacity below ~500 nm and ~700 nm overlaps for as produced and functionalized MWNTs, respectively, a shear lag model was adopted to the experimental results to estimate the IFSS of the CNT-CNT junctions. In this model, IFSS can be related to junction force capacity, F , interfacial shear modulus between CNTs, G , CNTs elastic modulus, E , diameter of MWNTs, d , the spacing between them, h , the thickness of CNT shells, t , and the width of the CNT junctions, w , as:

$$IFSS = \frac{F\lambda}{2w} \times \frac{1}{\tanh\left(\frac{L}{2}\right)} \quad \text{with} \quad \lambda = \sqrt{\frac{2G}{Eh} \left(\frac{w}{\pi d} \right)} \quad (2)$$

Using this model, the IFSS of as produced and -COOH functionalized MWNTs is estimated to be 56 ± 15 MPa and 164 ± 21 MPa, pointing to 2.9 times increase in shear strength between MWNTs due to Hydrogen bond interactions between MWNTs.

2. Functionalized carbon nanotubes for interfacial chemical bonding control and mechanical property measurement and simulation

In collaboration with the Espinosa and Schatz groups, the Nguyen group is planning to examine the mechanical consequences of the types and densities of chemical bonding interactions with a peeling experimental system that can measure the shear interactions at an interface between a functionalized CNT and a functionalized graphene surface or two functionalized CNTs (Figure 30). For this study, we have successfully purified and functionalized polymer-coating-free multiwall carbon nanotubes made from arc-discharging carbon electrodes. Analysis of these carbon nanotubes by SEM and Raman spectroscopy show that these nanotubes are longer, contain fewer defects, and possess superior purity in comparison with commercial sources. The surface area of these nanotubes was $80 \text{ m}^2/\text{g}$ by N_2 gas adsorption, a base value that will allow us to subsequently estimate the surface density of functional groups in concurrence with elemental analyses by XPS. After functional group modifications, the resulting functionalized CNT will be used in the aforementioned peeling experiment and the resulting data will be directly fed into the modeling work of Schatz, which will aid us in understanding mechanical measurements of Espinosa.

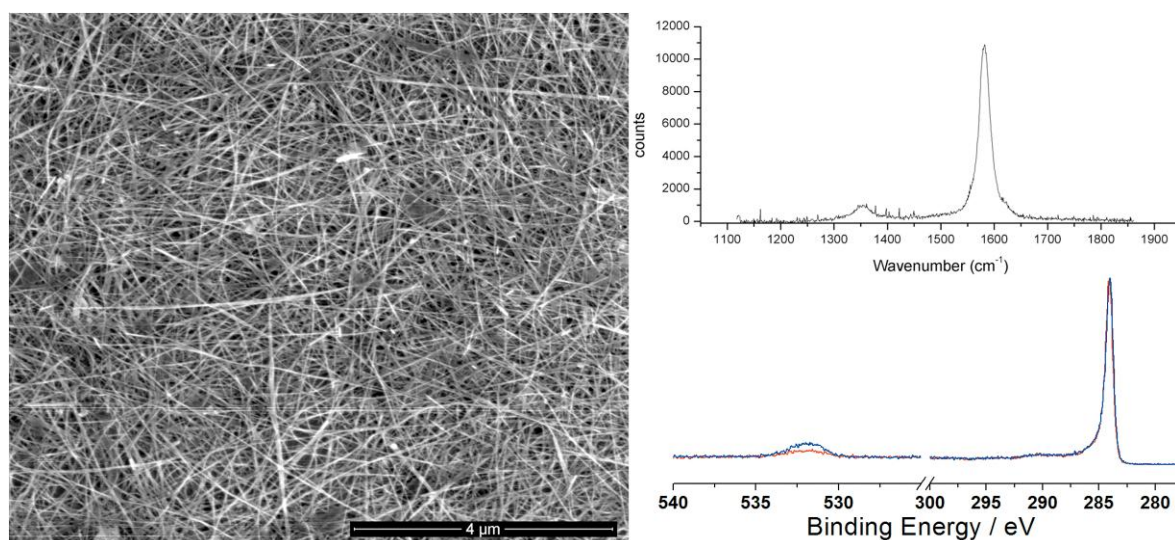


Figure 31. Left: SEM image of purified multiwall carbon nanotubes showing very few carbonaceous impurities. Top Right: Raman spectrum of these nanotubes showing that they are relatively defect-free. Bottom right: Overlaid XPS spectra of two samples of functionalized carbon nanotubes showing that the relative oxygen functional group density (through the O1s region at 530-535 eV) can be controlled.

3. Bioinspired hierarchical fibers: Size effects and synergies

The Beuhler group has also focused on detailed analyses of CNT tube-tube interaction mechanisms under varied types of interactions at the chemical scale, starting with a simple model setup shown in Figure 32. This model setup considers a range of different chemical bonds (varied strength, stiffness, length etc.) of bonds arranged between a stiff backbone, here reflecting the CNT structure. The analysis as shown in Figure 33 provided fundamental insight into the size of process zone, cooperativity, etc. A fundamental challenge in engineering biologically inspired materials and systems is the identification of molecular structures that define fundamental building blocks. The insight developed here provided a

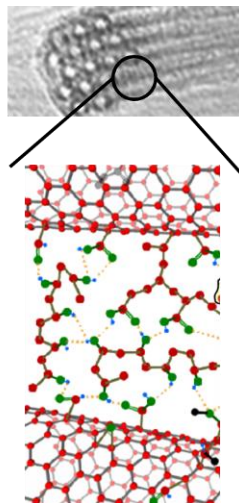
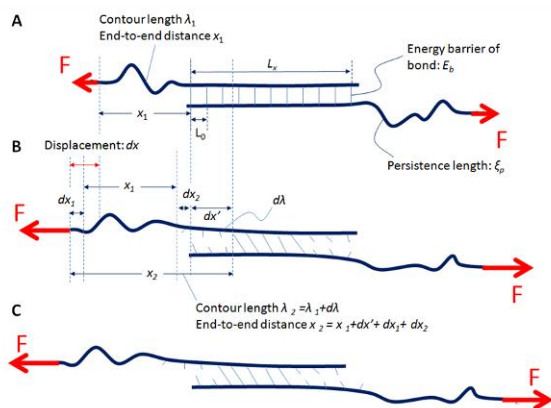


Figure 32. Model setup of the CNT-CNT bundle system, used here to study the effect of varied chemical composition on shear strength and other key mechanical properties.

systematic study of the effect of the energy of chemical bonds on the mechanical properties of molecular structures, specifically their strength and robustness.

By considering a simple model system of an assembly of bonds in a cluster we demonstrate that weak bonding, as found for example in H-bonds, results in a highly cooperative behavior where clusters of bonds operate synergistically to form relatively strong molecular clusters. The cooperative effect of bonding results in

an enhanced robustness since the drop of strength due to the loss of a bond in a larger cluster only results in a marginal reduction of the strength. Strong bonding, as found in covalent interactions such as disulfide bonds or in the backbone of proteins, results in a larger mechanical strength. However, the ability for bonds to interact cooperatively is lost, and as a result, the overall robustness is lower since the mechanical strength hinges on individual bonds rather than a cluster of bonds. In summary, the key findings were:

1. Weaker bonds are more cooperative
2. Thus, the cluster is more robust
3. Stronger bond are less cooperative, thus loose robustness
4. Strength is gained but at cost of robustness
5. Weak bonds can break & reform (stick-slip)

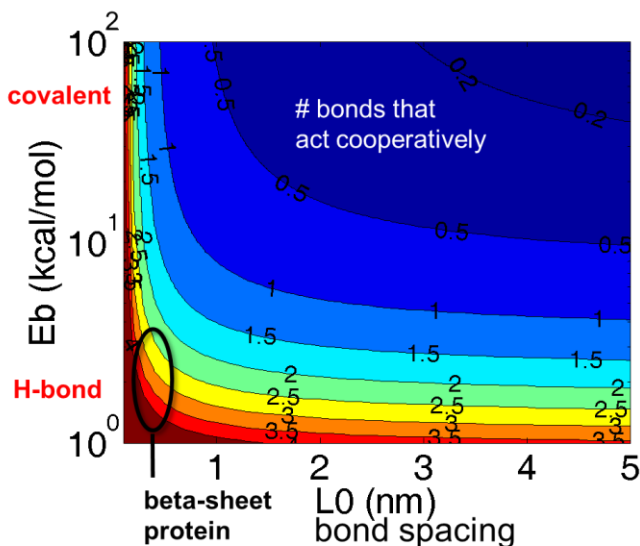


Figure 33. Weaker bonds can be more cooperative, and their clustering is more robust.

The systematic analysis presented here provides general insight into the interplay of bond energy, robustness and other geometric parameters such as bond spacing. We conclude our analysis with a correlation of structural data of natural protein structures, which confirms the conclusions derived from our study.

The results of the finding demonstrated the need for weak interactions in defining greater cooperativity for larger process zones, as well the onset of stick-slip motion to provide a mechanism of high energy dissipation under very large deformation. These desirable features provide a rigorous basis for the design of CNT bundles using polymer sizing and demonstrate why many earlier attempts to increase the strength,

toughness, resilience of CNT bundles and composites did not succeed in scaling up properties.

We then transferred these concepts to a specific CNT-CNT system in which we design the chemical interactions of the functionalization in a targeted way, as shown in Figure 34. These extended studies were made possible by using advanced MD sampling methods, in particular Metadynamics (M. Bonomi et al., Comput Phys Commun. 180(10):1961–1972; A. Barducci et al. PRL, 2008) to develop a systematic approach to explore the free energy landscape of CNT-based systems at the chemical scale without the limitations of MD time-scales. The objectives of these efforts are:

- (a) To study the cooperative deformation of functionalized CNT (both random and random in group of 3 cases, Figure 34 c, under shear and peeling loading conditions. These configurations (arrangement of functional groups) correspond to what experimental groups can make in the laboratory, as established in collaborative efforts with Espinosa's and Nguyen's laboratories for synthesis and testing.
- (b) To simulate two test cases of micromechanical boundary conditions of CNT-CNT interfaces, and specifically shearing and peeling of functionalized CNTs for the random case and random groups of three. The computed energy difference between the two configurations will determine if the grouping of functional groups in CNT will improve the mechanical strength. This will indeed guide the experiments for the manufacturing and testing of the systems.

To achieve the above objectives, we model the CNTs as flat graphene sheets with functional groups (carboxyl acid) attached to each sheet. The dimension of graphene sheet for this study is chosen as 40 Å x

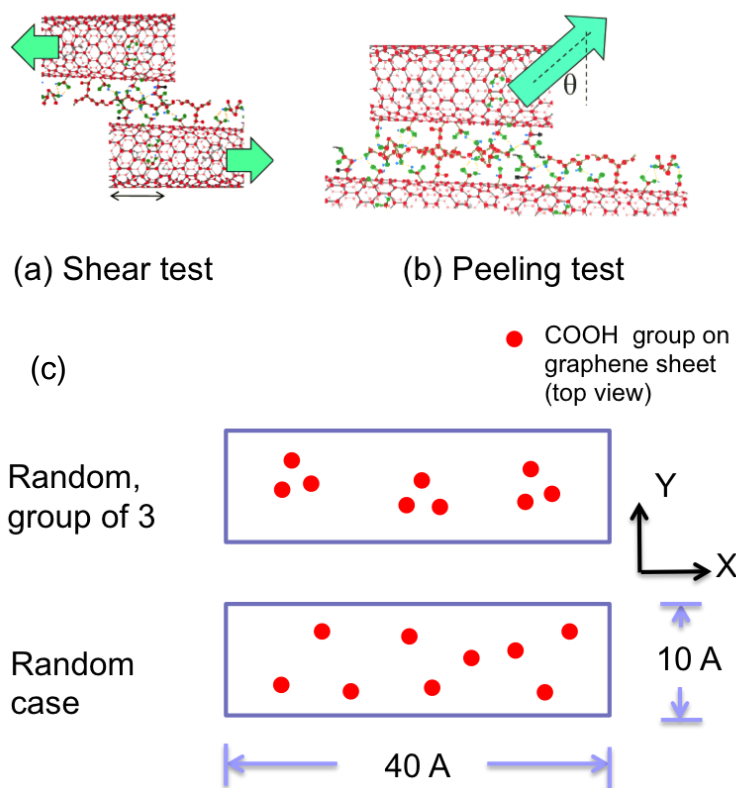


Figure 34. Illustration of cases considered here, e.g., showing the comparison of random grouping of functional groups versus a hierarchical organization. These setups were developed in close collaboration with Nguyen, Espinosa *et al.* to ensure a direct comparison with systems that can be synthesized experimentally.

10 Å and is periodic in the X- and Y- directions, respectively. The carboxyl groups from each graphene sheet form H-bonds. We use the ReaxFF (reactive force field) and LAMMPS (DOD funded molecular dynamics package developed at Sandia National Lab) to minimize and equilibrate the two configurations at 300 K under a microcanonical (NVT) ensemble. The equilibrated structure is then used to start the Metadynamics calculations to determine the free energy profile. For the Metadynamics calculations PLUMED (plugin for free energy calculations in molecular systems) was used along with LAMMPS. The free energy profile is determined along the control variable space. The system explores the free energy landscape by the adding Gaussian hills to the current energy state. Here we choose the position of a set of atoms as the control variable. The set of atom are moved by applying a bias potential till the system reaches

the final state, which corresponds to the final position of these atoms.

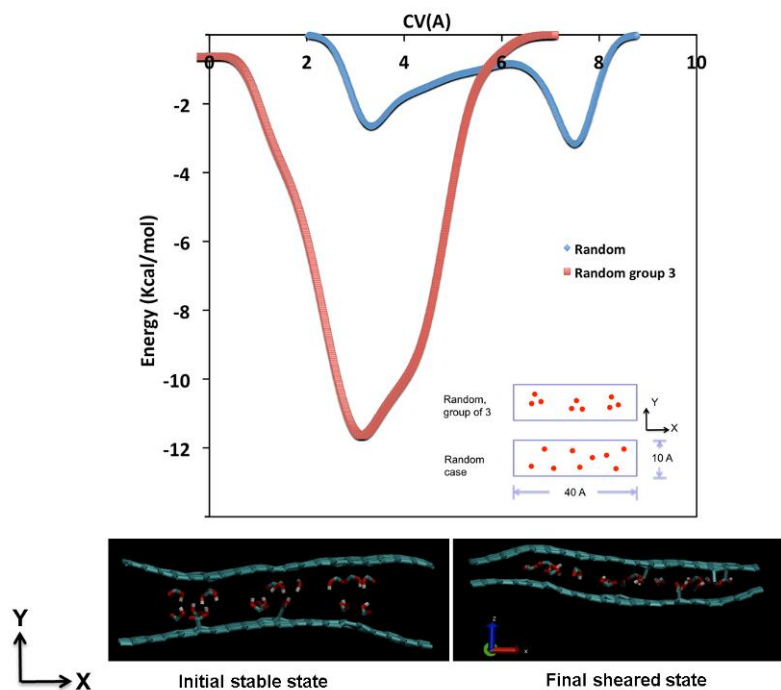


Figure 35. Free energy landscape of CNT-CNT interaction modeled as a graphene sheet here, for two nanoscale arrangements of chemical groups. Difference in adhesion energy for both cases is 8.98 kcal/mol.

The results obtained for several test cases show a significant difference in the tube-tube interaction depending on the details of the nanostructural placement at the CNT level. The shearing test was conducted for both configurations by applying a bias potential along the X direction on a group of atoms on the top graphene sheet at $T = 300\text{K}$ from the initial stable state. The Gaussian height is chosen as 0.1 kcal/mol. During the simulation it is observed that the random case goes from the initial stable state to the sheared state for energy of 2.6 kcal/mol, while the random group of three requires 11.58 kcal/mol. In the shearing test case simulations predict a difference in adhesion energy for both cases is 8.98 kcal/mol, which provides clear evidence for the importance of the chemical design of sizing (see Figure 35 for detailed results).

4. Coarse-grain model for functionalized CNT-CNT interactions (**Proprietary**)

Functionalized carbon nanotubes have tremendous potential for nanotechnology applications such as in the fabrication of polymeric carbon fibers, which break down the length limit of single carbon nanotubes or to use as a probe for detecting biological species. Experiments carried out on CNTs have demonstrated the capability to control the material property by grouping the functional agents. It is known from the study of biological materials such as spider silk that the cooperative deformation and nanoscale confinement of functional agents can improve the mechanical strength. The outstanding mechanical property of spider silk inspires us to design novel materials based on CNT and functional agents. However, the cooperative deformation of functionalized CNTs is still elusive, which prevents us from creating large-scale fibers with good mechanical properties still on the same level of single carbon nanotube. In this study we present an elastic structural model of CNTs connected by carboxyl groups (COOH) through H-bonds for a two CNT system (Figure 36). The CNT is modeled as graphene sheet of stiffness K_1 and the H-bonds (each red line in Figure 36 b corresponds to 2 H-bonds) have stiffness K_2 . The H-bonds are spaced at a distance of b and the force is applied at $x=0$. We fit an exponential function to the deformation profile to determine the characteristic length. Through this analysis we predict the optimal grouping of H-bonds on CNT to obtain maximum resistance to shear deformation.

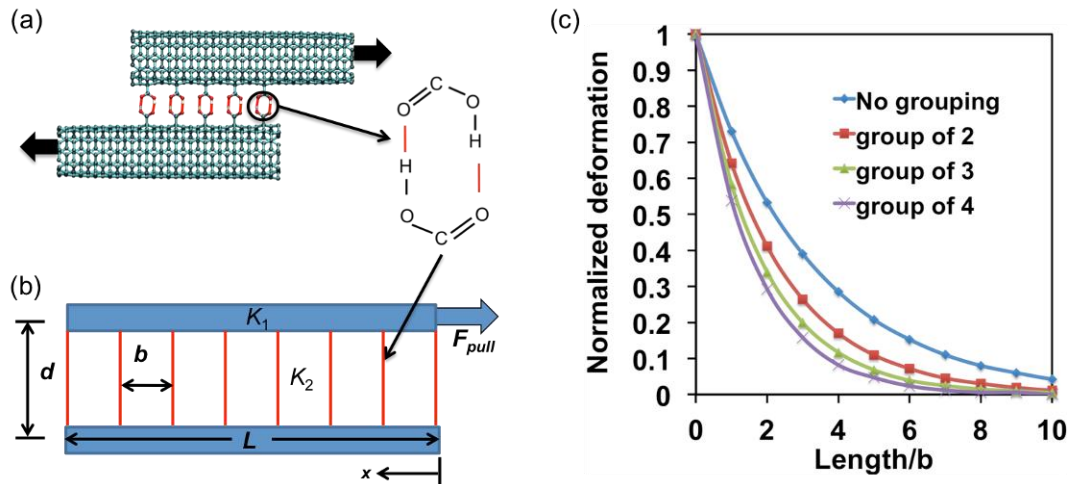


Figure 36: (a) Carbon nanotube functionalized with carboxyl group under shear loading. (b) A one-dimensional elastic structural model of functionalized CNT. Where CNTs are modeled as graphene sheets of stiffness K_1 and are connected by H-bonds (each red line corresponds to 2 H-bonds) of stiffness K_2 between them. The graphene sheets are at a distance of d and of length L . The H-bonds are separated by a distance b between them and the structure is under an applied load F_{pull} . (c) Deformation of H-bonds normalized with maximum deformation for each grouping case with respect to normalized length. As the grouping of H-bonds increases the deformation is more uniform

5. The role of hydrogen bonding networks in determining mechanical stiffness: An experimental-computational approach

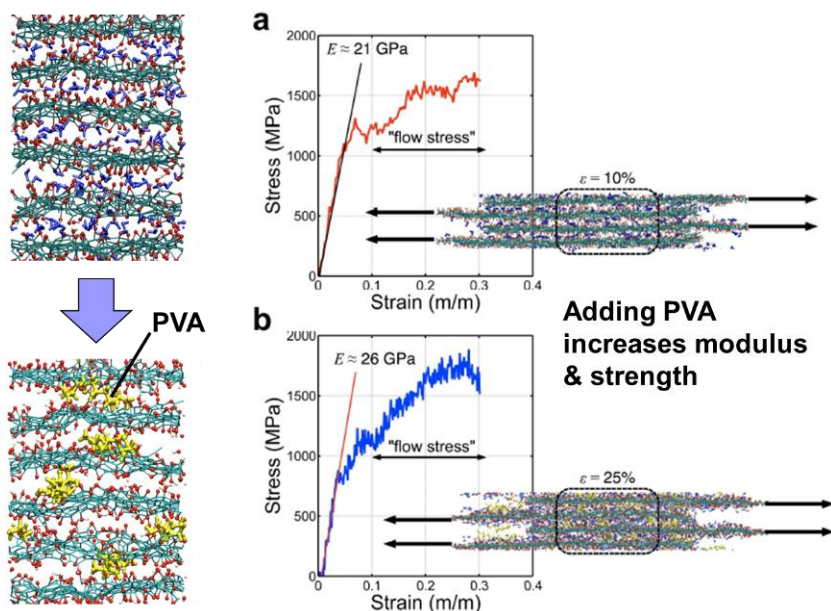


Figure 37. Left: Model snapshots of: a) a stack of pristine graphene oxide nanosheets with intercalated H₂O (10% water content shown) and a PVA-GO composite (5.5 wt% polymer content shown). These lamellar models were subjected to equilibration, with the equilibrium spacing (seq) determined by averaging the five gallery spacings. The plots on the right show an analysis of the mechanical properties.

In addition to using chemical bonds to mediate load transfer interactions in the fabrication of carbon nanotube yarns, the Nguyen group has continued to expand our understanding of hydrogen-bonding networks through a fundamental study of such networks in graphene oxide papers and graphene oxide-PVA composite papers in collaboration with the Buehler group who conducted ReaxFF-based molecular dynamics simulations (see Figure 37) to elucidate the role of water molecules in modifying the mechanical properties of both pristine and nanocomposite graphene oxide papers. Based on our

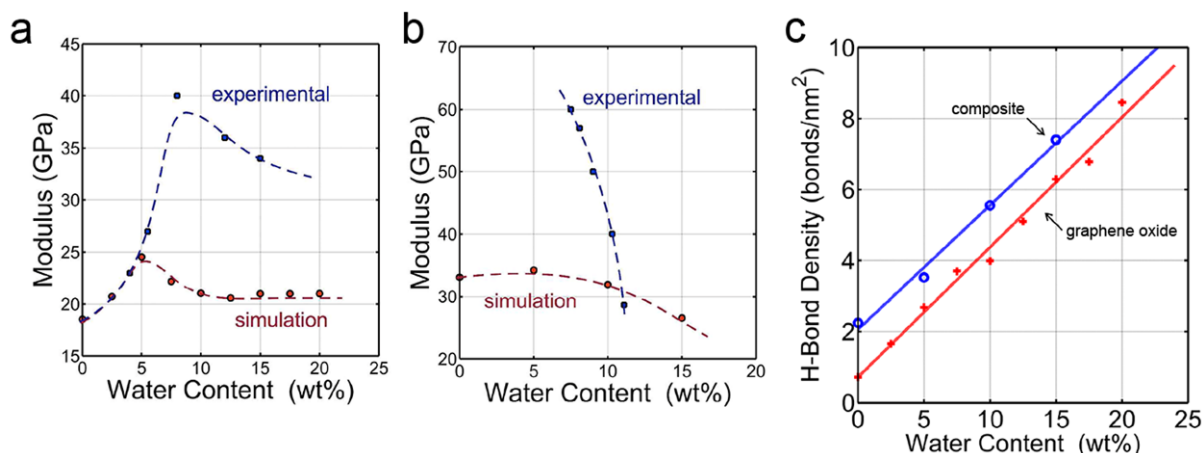
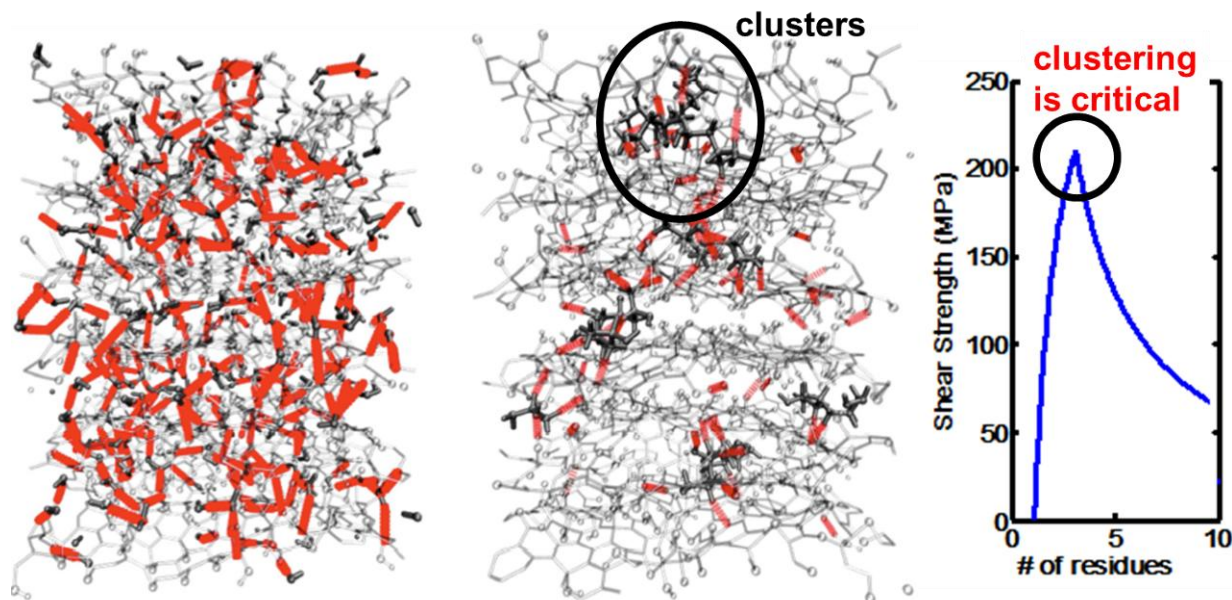


Figure 38: a) Experimental (blue) and simulated (red) stiffness of graphene oxide papers as a function of water content. b) Experimental (blue) and simulated (red) stiffness of graphene oxide-poly(vinyl alcohol) composites as a function of water content. c) Hydrogen bond density of graphene oxide papers (red) and graphene oxide-poly(vinyl alcohol) composites (blue) as a function of water content.

analysis of the stiffness of these materials as a function of water content and hydrogen-bond density, we have found that the maximum stiffness occurs at a proper combination of hydrogen bond between the graphene sheets in the paper structure and the hydrogen-bond carrier between these sheets. For example, saturation of constructive hydrogen-bonding interactions between graphene oxide sheets in pristine graphene oxide paper yielded the stiffest structure at ~7 wt% water (Figure 38a); at lower water content, this structure is much weaker due to the presence of fewer load-transferring hydrogen bonds that can be mediated by water molecules. At the other extreme, papers with more water are also weaker in spite of having an overall higher hydrogen-bond density (Figure 38c) since most of these are non-bridging water-water hydrogen bonds that weakened the structure. A similar effect was found in our graphene oxide-PVA composites, where the polymer and water cooperatively mediate load transfer between adjacent graphene oxide sheets. In this system, we found that for a PVA loading of 22 wt%, stiffness maximizes at ~7 wt% water, where water molecules aid in mediating load transfer in polymer cavities and filling underutilized interlayer connections. While we were not yet able to determine if there is a turnover behavior at lower water content, simulations indicate this may be the case (Figure 38b). These findings will aid us in designing future CNT-polymer or graphene-polymer nanocomposite systems featuring an optimized hydrogen-bonding network.

In combination, these experimental-computational studies reveal a delicate relationship between the stiffness of these papers and the water content in their lamellar structures. ReaxFF-based molecular dynamics simulations elucidate the role of water molecules in modifying the mechanical properties of both pristine and nanocomposite graphene oxide papers, as bridge-forming water molecules between adjacent layers in the paper structure enhance stress transfer by means of a cooperative hydrogen-bonding network (Figure 37 and Figure 38). For graphene oxide paper at an optimal concentration of ~5 wt% water, the degree of cooperative hydrogen bonding within the network comprising adjacent nanosheets and water molecules was found to optimally enhance the modulus of the paper without saturating the gallery space. Introducing PVA chains into the gallery space further enhances the cooperativity of this hydrogen-bonding network, in a manner similar to that found in natural biomaterials, resulting in increased stiffness of the composite (Figure 39). No optimal water concentration could be found for the PVA-graphene oxide nanocomposite papers, as dehydration of these structures continually enhances stiffness until a final water content of ~7 wt% (additional water cannot be removed from the system even after 12 h of annealing).



Cooperativity explains increase in modulus & strength (24% increase)

Figure 39: Model snapshots highlighting the hydrogen-bonding networks between the graphene oxide nanosheets in: a graphene oxide paper (left) and a ~5.5 wt% PVA-graphene oxide nanocomposite paper (right). While water molecules are included in the simulations for both models, water molecules were not shown in the snapshot of the composite model to emphasize the clusters of hydrogen bonds that form between PVA and the nanosheets in this system.

6. *Effect of non-covalent Hydrogen-bond (H-bond) interaction on the mechanical properties of DWNT-polymer yarns*

As-produced DWNT mats were provided by A. Moravsky at MER Corporation. They were highly porous (with a density of 0.03 g/cm^3) in which DWNTs are well-dispersed and retain dispersion when infiltrated within a matrix. As synthesized, MER's DWNT mat contains 10-15 wt% of an intrinsic polymer coating on the walls of the DWNT bundles. Based on NMR, MS, and FTIR analysis, this inherent polymer coating contains following components: (i) esters of acrylic acid ($\text{CH}_2=\text{CHCOOR}$), (ii) substituted acrylates ($\text{R}'\text{CH}=\text{CHCOOR}$, $\text{CH}_2=\text{C}(\text{R}')\text{COOR}$), and (iii) oxygen-containing aromatics ($\text{R}'\text{C}_6\text{H}_4\text{COOR}$, $\text{R}'\text{C}_6\text{H}_3(\text{COOR})_2$). We hypothesized that subjecting this polymer coating to an aqueous base (NaOH) treatment would generate hydrogen-bond (H-bond) donating and accepting carboxylic acid groups on the CNT surface, substantially increasing the capability of the bundles to form H-bonds with polymers such as polyvinyl alcohol (PVA), given the H-bond donating and accepting nature of the pendant hydroxyl groups. This was indeed the case: the Espinosa group subsequently found that PVA nanocomposites of the NaOH-treated MER DWNT bundles show enhancement in both strength and toughness. In collaboration with the Espinosa group, this year the Nguyen group has extended the research on the interaction between polymers and DWNT bundles to include CNT-polymer nanocomposite yarns of polyacrylonitrile (PAN) and poly(methylmethacrylate) (PMMA), which are supposed to interact with the NaOH-treated MER DWNT bundles only via H-bond accepting nitrile and acrylate groups. It is expected that these polymers will not interact with the MER's DWNT bundles as

efficiently as PVA chains and will only play a minor role in the mechanical enhancement of the polymer nanocomposite yarns.

The yarns were fabricated from 1/4" wide ribbon of a DWNT mat by a spinning apparatus fabricated in Northwestern University by the Espinosa group. During the spinning process, ribbons of DWNT mats buckle successively due to the twisting process, through which they are converted into a yarn. To prepare our nanocomposite yarns, a *N,N*-dimethylformamide (DMF) solution of polymers (PAN or PMMA) was sprayed on the CNT ribbon during the spinning. The aforementioned lateral contraction pushes almost all of the excess DMF molecules (solvent) out of the final yarn filament. The yarn was then dried under vacuum at 80°C for 24 h to remove the excess solvent.

The yarn morphology was investigated by scanning electron microscopy. The fracture-surface morphology shows that the DWNT bundles are uniformly coated with polymers, PAN in Figure 40, at different polymer concentrations. At 47.0 wt% loading of CNTs (Figure 40d, e, and f.), the network of DWNTs is found to be less porous compared to the 92.0 wt% CNT-PAN yarn (Figure 40a, b, and c). Similar morphology was observed for CNT-PMMA composite yarns (Figure 41): at 72.0 wt% CNT loading, the yarn shows significant polymer impregnation compared to that at 90 wt% loading. Reducing the CNT loading results in visibly thick white PMMA films on the yarn surface so these samples were not studied further.

The mechanical behavior of spun polymer nanocomposite yarns was measured using a microtensile tester at a strain rate of $\sim 1.6 \times 10^{-3} \text{ s}^{-1}$ for a typical gage length of 1 cm. The crosshead deformation of the yarns normalized by the initial length of the yarn is reported as the sample's strain with a typical resolution of $\sim 0.01\%$. The true stress in the yarn was computed by dividing the measured force by the true cross-section of the yarn. The specific modulus, specific strength, and energy-to-failure as a function of CNT concentration are shown in Figure 42 where each point represents an average of three measurements or more. The mechanical properties of these composite yarns decrease monotonically with decreased CNT concentration, in contrast to PVA. This can be explained by assuming that the polymer component becomes the major contributing factor in controlling the mechanical properties of the composite yarns as CNT concentration decreases. As both PAN and PMMA are mechanically weaker component than CNT in the matrix, in the absence of interactions such as H-bond donating and accepting as in the case of PVA, the mechanical properties deteriorate with decrease in CNT content or increase in polymer composition. These data support the importance of having both H-bond donors and acceptors presence in both components of CNT-polymer yarns produced using MER's DWNT, if the mechanical properties of these yarns are to be enhanced.

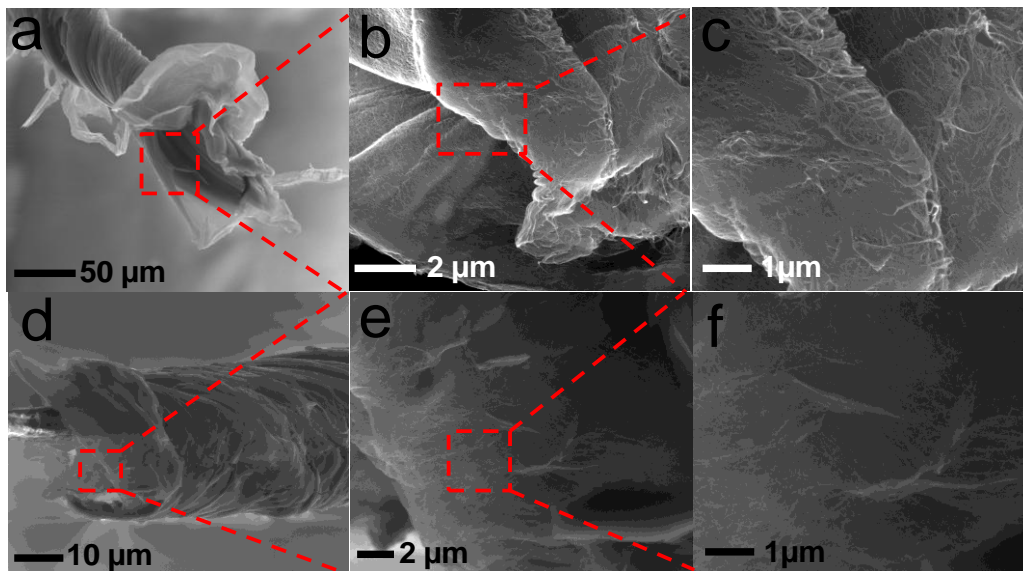


Figure 40. SEM images of CNT-PAN nanocomposites at 92.0 wt% CNT (a, b, c), and 47 wt% CNT concentrations (d, e, f). Images b, c, e, and f are high-resolution images of the selected portion of the nanocomposite yarns.

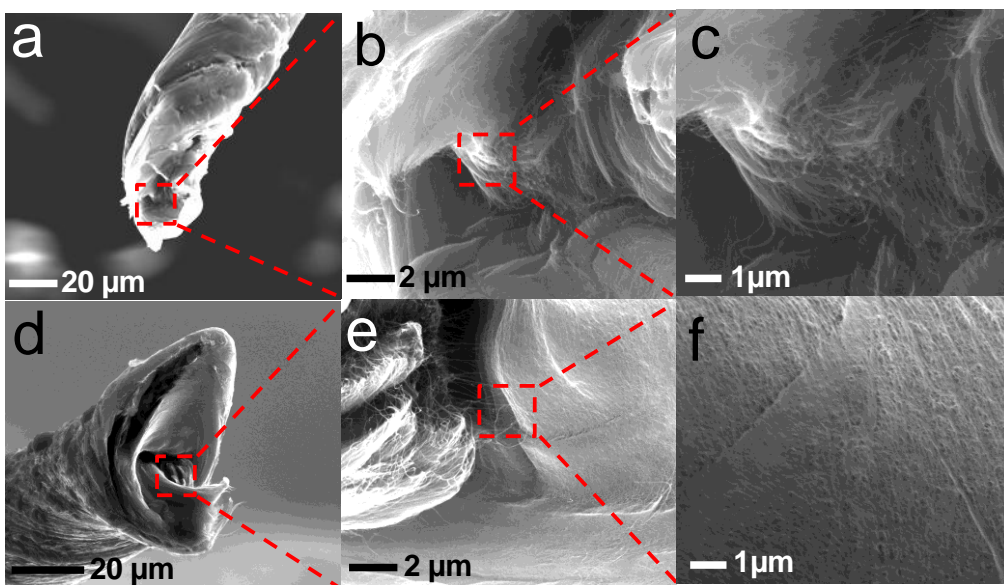


Figure 41. SEM Images of CNT-PMMA nanocomposites at 90.0 wt% CNT (a, b, c), and 72.0 wt% CNT concentrations (d, e, f). Images b, c, e, and f are high-resolution images of the selected portion of the nanocomposite yarns.

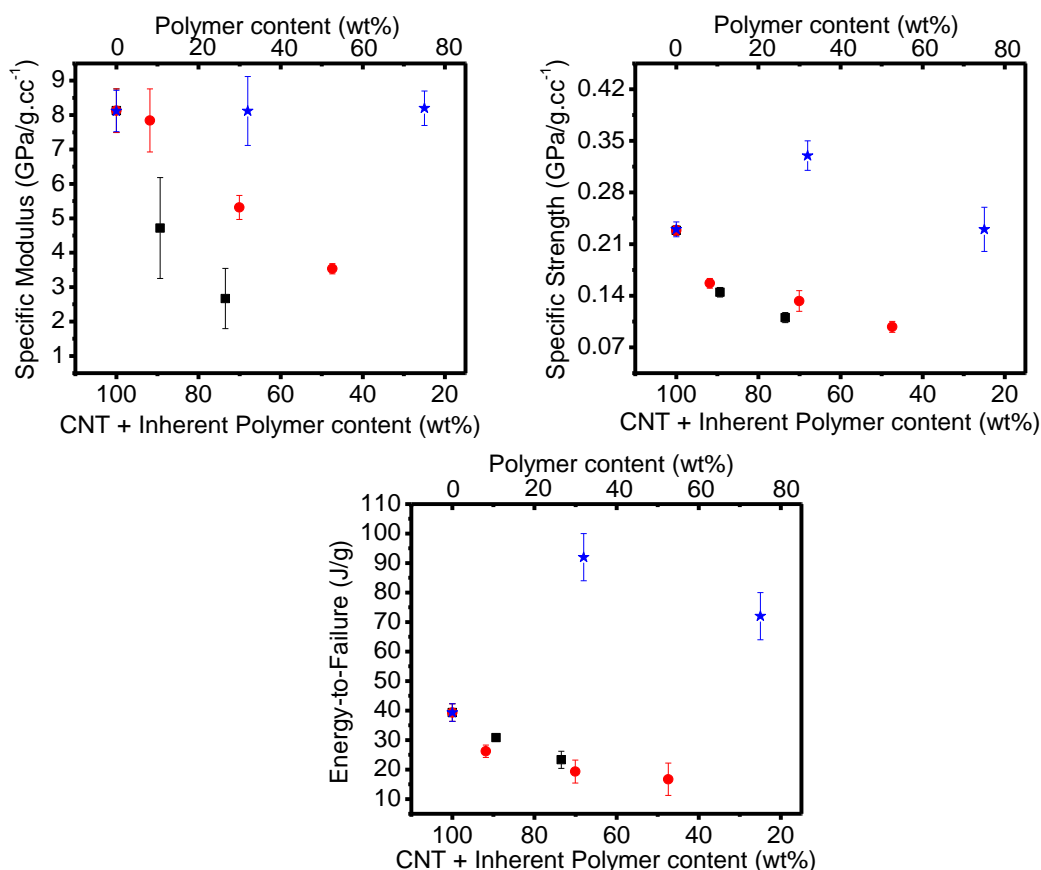


Figure 42. Plots of the mechanical properties of CNT-polymer nanocomposites as a function of different CNT concentrations. Blue, red, and black dots are the corresponding data for yarns fabricated from DWNT-polymer composites of PVA, PAN, and PMMA, respectively.

Our current effort has focused on the incorporation of poly(paraphenylene terephthalamide) (PPTA), commonly known as Kevlar[®], into DWNT yarns. PPTA is hypothesized to interact with the CNT bundles via a combination of π - π stacking and H-bond donating and accepting functionalities (Figure 43a), which should subsequently improve the mechanical properties. For this purpose, PPTA was synthesized in the Nguyen lab following literature procedure from solutions of p-phenylene diamine and terephthaloyl chloride in NMP as solvent. The polymer was characterized by TGA and Raman spectroscopy, although the molecular weight could not be determined at this time.

The nanocomposite yarns were fabricated from our synthesized Kevlar and a commercially available Kevlar[®] sample from DuPont following a similar strategy as described above with one exception: instead of spraying, a dipping technique was adopted to infiltrate the oleum solution of PPTA into the DWNT yarn. This measure is adopted for safety reasons due to the lack of spraying and ventilating equipment that can properly handle oleum. At 55 and 69 wt% CNT, the fracture morphology of the composite yarn content shows moderate incorporation of Kevlar into the DWNT mat with some porosity (Figure 43b).

The CNT-Kevlar nanocomposite yarns were subsequently tested for their mechanical properties (Figure 43c). Disappointingly, they show a decrease in both strength and modulus compared to the pristine DWNT yarn. Additionally, the mechanical properties of the CNT-Kevlar yarns are also much lower than the values reported for K-29 Kevlar[®] fiber. We suspect that this may be attributed to the inability of the infiltrated Kevlar chain to make all the proper H-bonds to the intrinsic polymer coating outside the MER DWNT bundle. One explanation for this could be that the Kevlar loading is too high to properly allow for the PPTA chains to optimize the various interactions between themselves and the

intrinsic polymer coatings on the MER DWNTs—future experiments will need to be carried out to examine this hypothesis. However, a second explanation could be that the PPTA backbone is too rigid to be able to adjust to the functional groups in the DWNT intrinsic polymer coating. A third explanation is the limitation of our processing method: our nanocomposite yarns are produced under low-stretch conditions in comparison to the Kevlar® fibers, which are obtained at high stretching conditions followed by rapid cooling from hot solutions that induce a crystallization of Kevlar® polymer chains and form high-strength fibers. In the next year, we will attempt to optimize the composition and processing conditions for the DWNT-Kevlar composite to obtain high-strength composite yarns.

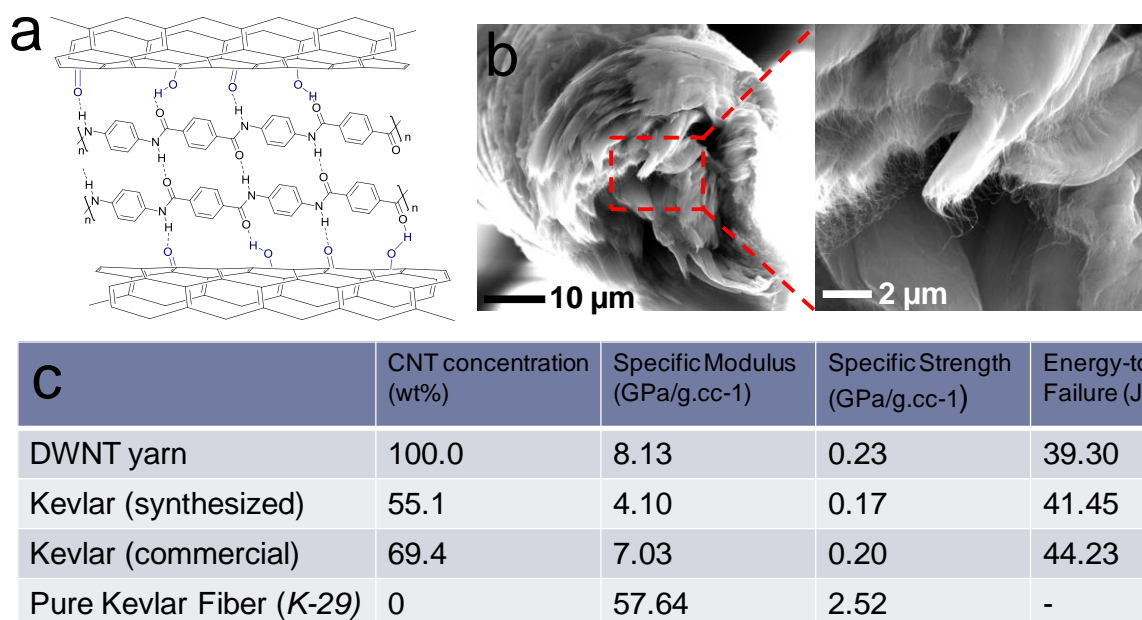


Figure 43. (a) Proposed π - π stacking and H-bond donor and acceptor interaction between Kevlar® and DWNT bundles. (b) SEM images of DWNT-Kevlar nanocomposites at 55.1 wt% CNT concentrations. (c) Tabulated data of mechanical properties of DWNT-Kevlar nanocomposite yarns.

Synergistic activities supported by other DoD projects

1. Electron irradiation cross linking of DWNT bundles

One approach to address the limitation of weak interlayer shear between graphitic layers, is the introduction of crosslinking bonds between adjacent sheets via high energy electron irradiation at energies above the knock on requirement to remove carbon atoms and create covalent crosslinking defects. Irradiation by high energy particles, such as ions, electrons, or neutrons, to induce modifications to carbon nanostructures has been predicted and demonstrated to result in the creation of vacancy and interstitial defects that can bridge adjacent atomic layers [27, 28]. This has proven to be a unique method to greatly enhance the effective properties of both MWNTs and CNT bundles. Quantum mechanics calculations have demonstrated that irradiation leads to the formation of divacancy, interstitial, and Frenkel pair defects resulting in covalent bonds being formed between adjacent graphitic sheets [28]. Molecular mechanics simulations have shown that only a low density (~ 0.2 - 0.4 defects/ \AA) of such defects is required to approach theoretical limits of load transfer between adjacent graphitic sheets, such as inner and outer shells in DWNTs [29, 30]. This approach towards achieving efficient load transfer facilitated by crosslinking defects has been applied to address load transfer at multiple lengths scales within our DWNT

based material. The first two hierarchical length scales are shell-shell interactions within individual DWNTs and tube–tube interactions between adjacent outer shells within DWNT bundles.

The Espinosa group has conducted in situ TEM tensile testing on DWNT bundles exposed to high

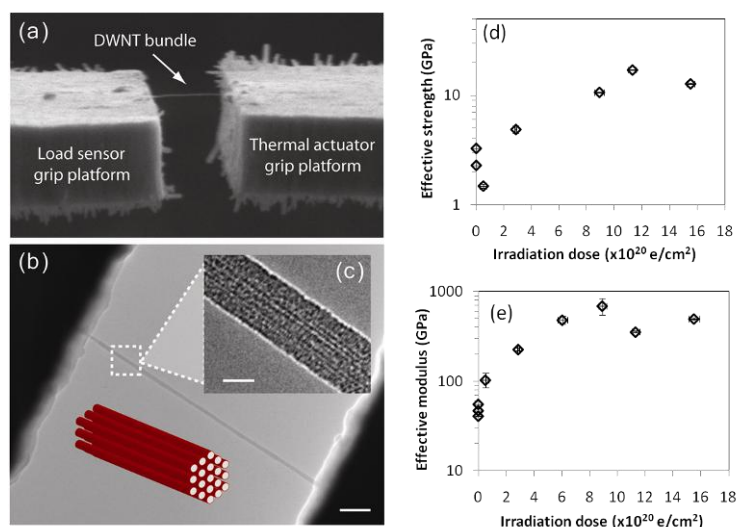


Figure 44: Irradiation induced covalent crosslinking enhancements in DWNT and SWNT bundles. (a-c) In situ TEM tensile testing of DWNT bundles. (d-e) Enhancements in effective strength and modulus for DWNT bundles as a function of irradiation dose.

energy electron irradiation. In this case both levels of hierarchy, inter tube shell-shell interactions as well as inter bundle tube-tube interactions, are present and crosslinked via irradiation [31]. Here it was found that both the effective strength and stiffness of the DWNT bundles was increased by irradiation up to 17 GPa and 693 GPa respectively (see Figure 44). HRTEM images of the DWNT bundles revealed that in the case of minimally irradiated bundles (0.5×10^{20} e/cm²) the outer tubes within the bundles failed during the tensile test and slid with respect to the inner bundle of DWNTs, akin to the sword-in-sheath failure observed for MWNT shells. However, at optimal irradiation doses ($\sim 9\text{--}11 \times 10^{20}$ e/cm²) the bundles were found to fail across the entire cross section of shells and tubes confirming

effective load transfer to the entire inner core of material. Although these studies have demonstrated that irradiation-induced crosslinking is effective at improving load transfer within DWNTs and DWNT bundles, they have also identified that there is a limit in the achievable mechanical properties as the complexity of the material is increased due to the inherent mechanisms of introducing structural defects into the material.

References

1. Rahaman, M.S.A., A.F. Ismail, and A. Mustafa, *Polymer Degradation and Stability* 2007. **92**: p. 1421-1432.
2. Rangarajan, P., V.A. Bhanu, D. Godshall, G.L. Wilkes, J.E. McGrath, and D.G. Baird, *Dynamic oscillatory shear properties of potentially melt processable high acrylonitrile terpolymers*. *Polymer*, 2002. **43**(9): p. 2699-2709.
3. Usami, T., F. Keitoku, H. Ohtani, and S. Tsuge, *Characterization of Poly(2,6-Dimethyl-1,4-Phenylene Ether) by High-Resolution Pyrolysis-Gas Chromatography (Hr Pygc)*. *Polymer*, 1992. **33**(14): p. 3024-3030.
4. Bashir, Z., *A Critical-Review of the Stabilization of Polyacrylonitrile*. *Carbon*, 1991. **29**(8): p. 1081-1090.
5. Morita, K., Y. Murata, A. Ishitani, K. Murayama, T. Ono, and A. Nakajima, *Characterization of Commercially Available Pan (Polyacrylonitrile)-Based Carbon-Fibers*. *Pure and Applied Chemistry*, 1986. **58**(3): p. 455-468.
6. Koziol, K., J. Vilatela, A. Moisala, M. Motta, P. Cuniff, M. Sennett, and A. Windle, *High-Performance Carbon Nanotube Fiber*. *Science*, 2007. **318**(5858): p. 1892-1895.

7. Naraghi, M., T. Filleter, A. Moravsky, M. Locascio, R.O. Loutfy, and H.D. Espinosa, *A multiscale study of high performance double-walled nanotube-polymer fibers*. ACS Nano. **4**(11): p. 6463-76.
8. Xia, Z. and W.A. Curtin, *Pullout forces and friction in multiwall carbon nanotubes*. Physical Review B, 2004. **69**(23).
9. Sorescu, D.C., K.D. Jordan, and P. Avouris, *Theoretical study of oxygen adsorption on graphite and the (8,0) single-walled carbon nanotube*. Journal of Physical Chemistry B, 2001. **105**(45): p. 11227-11232.
10. Lee, J., J.Y. Chung, K.H. Lee, D. Troya, and G.C. Schatz, *Multi-walled carbon nanotubes experiencing electrical breakdown as gas sensors*. Nanotechnology, 2004. **15**(11): p. 1596-1602.
11. Qian, D., W.K. Liu, and R.S. Ruoff, *Load transfer mechanism in carbon nanotube ropes*. Composites Science and Technology, 2003. **63**(11): p. 1561-1569.
12. Windle, A.H., J.J. Vilatela, and J.A. Elliott, *A Model for the Strength of Yarn-like Carbon Nanotube Fibers*. ACS Nano, 2011. **5**(3): p. 1921-1927.
13. Persson, B.N.J., J. Surf. Sci. Rep., 1999. **33**: p. 183.
14. Naraghi, M., T. Filleter, A. Moravsky, M. Locascio, R.O. Loutfy, and H.D. Espinosa, *A Multiscale Study of High Performance Double-Walled Nanotube-Polymer Fibers*. ACS Nano, 2010. **4**(11): p. 6463-6476.
15. Vilatela, J.J., J.A. Elliott, and A.H. Windle, *A Model for the Strength of Yarn-like Carbon Nanotube Fibers*. ACS Nano, 2011. **5**(3): p. 1921-1927.
16. Velasco-Santos, C., A.L. Martinez-Hernandez, F.T. Fisher, R. Ruoff, and V.M. Castano, *Improvement of thermal and mechanical properties of carbon nanotube composites through chemical functionalization*. Chemistry of Materials, 2003. **15**(23): p. 4470-4475.
17. Sahoo, N.G., H.K.F. Cheng, J.W. Cai, L. Li, S.H. Chan, J.H. Zhao, and S.Z. Yu, *Improvement of mechanical and thermal properties of carbon nanotube composites through nanotube functionalization and processing methods*. Materials Chemistry and Physics, 2009. **117**(1): p. 313-320.
18. Koval'chuk, A.A., V.G. Shevchenko, A.N. Shchegolikhin, P.M. Nedorezova, A.N. Klyamkina, and A.M. Aladyshev, *Effect of Carbon Nanotube Functionalization on the Structural and Mechanical Properties of Polypropylene/MWCNT Composites*. Macromolecules, 2008. **41**(20): p. 7536-7542.
19. Cao, X.D., H. Dong, C.M. Li, and L.A. Lucia, *The Enhanced Mechanical Properties of a Covalently Bound Chitosan-Multiwalled Carbon Nanotube Nanocomposite*. Journal of Applied Polymer Science, 2009. **113**(1): p. 466-472.
20. Wang, W., P. Ciselli, E. Kuznetsov, T. Peijs, and A.H. Barber, *Effective reinforcement in carbon nanotube - polymer composites*. Philosophical Transactions of the Royal Society a-Mathematical Physical and Engineering Sciences, 2008. **366**(1870): p. 1613-1626.
21. T. Filleter, R.A.B., S. Li, and H. D. Espinosa, *Ultrahigh Strength and Stiffness in Cross-Linked Hierarchical Carbon Nanotube Bundles*. Adv. Mater., 2011. **vol. 23**: p. 2855-2860.
22. Kis, A., G. Csanyi, J.P. Salvetat, T.N. Lee, E. Couteau, A.J. Kulik, W. Benoit, J. Brugger, and L. Forro, *Reinforcement of single-walled carbon nanotube bundles by intertube bridging*. Nature Materials, 2004. **3**(3): p. 153-157.
23. Yu, M.F., B.I. Yakobson, and R.S. Ruoff, *Controlled sliding and pullout of nested shells in individual multiwalled carbon nanotubes*. Journal of Physical Chemistry B, 2000. **104**(37): p. 8764-8767.

24. Bhushan, B., X. Ling, A. Jungen, and C. Hierold, *Adhesion and friction of a multiwalled carbon nanotube sliding against single-walled carbon nanotube*. Physical Review B, 2008. **77**(16): p. -.
25. Molinari, A. and G. Ravichandran, *Peeling of Elastic Tapes: Effects of Large Deformations, Pre-Straining, and of a Peel-Zone Model*. Journal of Adhesion, 2008. **84**(12): p. 961-995.
26. Buehler, M.J. and T. Ackbarow, *Fracture mechanics of protein materials*. Materials Today, 2007. **10**(9): p. 46-58.
27. Banhart, F., *Irradiation effects in carbon nanostructures*. Reports on Progress in Physics, 1999. **62**(8): p. 1181-1221.
28. Telling, R.H., C.P. Ewels, A.A. El Barbary, and M.I. Heggie, *Wigner defects bridge the graphite gap*. Nature Materials, 2003. **2**(5): p. 333-337.
29. Peng, B., M. Locascio, P. Zapol, S. Li, S.L. Mielke, G.C. Schatz, and H.D. Espinosa, *Measurements of near-ultimate strength for multiwalled carbon nanotubes and irradiation-induced crosslinking improvements*. Nature Nanotechnology, 2008. **3**(10): p. 626 - 631.
30. Locascio, M., B. Peng, P. Zapol, Y. Zhu, S. Li, T. Belytschko, and H.D. Espinosa, *Tailoring the Load Carrying Capacity of MWCNTs Through Inter-shell Atomic Bridging*. Experimental Mechanics, 2009. **49**(2): p. 169-182.
31. Filleter, T., R.A. Bernal, S. Li, and H.D. Espinosa, *Ultrahigh Strength and Stiffness in Cross-Linked Hierarchical Carbon Nanotube Bundles*. Adv. Mater., 2011. **23**(25): p. 2855-2860.

Scientific Progress and Accomplishments

Status of Work:

The **Espinosa** group has conducted *multiscale mechanical testing of CNTs*, from performing nanoscale peeling and shear experiments on individual CNTs to elucidate the interfacial failure properties between CNTs, to performing tests to determine CNT bundle-bundle interfacial properties, to microtensile tests on macroscale DWNT/polymer yarns. Thus, they have performed experiments at all hierarchical levels of macroscopic CNT yarn. The DWNT mats used to make yarns were fabricated by **MER**, and the DWNT/polymer yarns were fabricated in collaboration with the **Nguyen** group and **A. Moravsky**. The mechanisms of the macroscale yarn mechanical behavior are being simulated by the **Buehler** group, using fully atomistic MD models. In addition, the **Espinosa** and **Dzenis** groups have collaborated on the mechanical testing of electrospun carbonized nanofibers produced by the **Dzenis** group, with the **Espinosa** group performing in situ TEM tests on the nanofibers. In situ SEM peeling and shear tests performed to investigate mechanical properties of functionalized nanotubes are being simulated by the **Schatz** and **Buehler** groups, while the functionalized tubes are being fabricated by the **Nguyen** group. Finally, the bundle-bundle shear experiments performed by the **Espinosa** group were simulated using coarse grained methods by the **Buehler** group.

MER has *fabricated and delivered an adequate amount of DWNTs in various forms*, including DWNT mats and yarns, as-produced and purified DWNT bulk powder, solutions and suspensions of DWNTs, DWNT bucky papers, with composition, density and morphology characterized by TGA, TMGA and SEM to **Espinosa**, **Nguyen** and **Dzenis** groups for further use as starting materials in the project work

The work by the **Buehler** group focused on *atomistic and mesoscale modeling of carbon nanotubes and carbon nanotube based materials*. Both reactive and nonreactive simulations have been carried out, and scaled up to larger time- and length-scales using coarse-grain simulations. All activities were closely integrated with experimental efforts in the MURI team. In the scientific accomplishments below we highlight three major areas of activities: I) coarse-grain modeling of fiber-level mechanics; II) atomistic and coarse grain modeling of CNT fibers, and III) size effects of carbon fibers. Additional work, not reviewed explicitly here, focused on fundamental questions of fiber and web mechanics in the context of structural stability, strength and robustness, and on the development of mathematical theories to transfer insight about mechanisms between different material systems. The **Buehler** group also made several fundamental contributions to the mechanics of carbon materials, including graphene and carbon nanotubes and derived fibers and materials.

The primary activities of the **Schatz** group were to *model DWNT bundle pull-out experiments, model the peeling experiments for functionalized tubes, and model the carbonization process of templated PAN nanofibers*. The **Schatz** group has continued to research the origins of the force resisting the extraction of the inner bundle of carbon nanotubes from the outer sheath of tubes in experiments previously performed by the **Espinosa** group. In addition, the **Schatz** group is performing MM3 calculations to simulate the MWCNT peeling experiments performed by the **Espinosa** group. In particular, these studies will provide benchmark results for comparison with experiments that can be used to differentiate mechanistic issues concerning the origin of the adhesive interaction between the CNT and the flat graphene sheet, the nanotube deformation on the graphene surface, and the influence of graphitic deposits present on the outer shell of the MWCNTs being tested. Finally, the **Schatz** group has continued to work on MD modeling of the initial stages of template carbonization in PAN based carbon nanofibers to emulate the heat treatment of the electrospun PAN fibers by the **Dzenis** group, incorporating both graphene sheets

and CNTs to investigate the possible templating effect that these nanofillers have on the fibers. This work relates to mechanical experiments being performed in the **Dzenis** and **Espinosa** groups.

The **Nguyen** group has worked on ***fabrication of macroscale DWNT/polymer yarns with increased H-bond interactions between CNTs, functionalization of CNTs for mechanical interrogation, and the development of graphene oxide papers as a macroscopic model for DWNT-based yarns.*** The **Nguyen** group has worked on understanding and enhancing the chemical rationale behind load transfer and mechanical properties in hierarchical materials with organic nanostructures as load-bearing units. In collaboration with the **Espinosa** group, the **Nguyen** group has studied the mechanical properties of carbon nanotube-polymer nanocomposite yarns to elucidate the role of hydrogen-bond donating and accepting functionalities in controlling their mechanical behavior. The **Nguyen** group has also identified promising chemistries for increasing load transfer between MWCNTs, and functionalized the surfaces of MWCNTs with these chemistries, thereby providing samples with which the **Espinosa** group performs MWCNT-MWCNT shear and MWCNT-graphene shear tests to evaluate the strength of the interfaces under a range of mechanical boundary conditions. Finally, the **Nguyen** group has fabricated graphene oxide papers with different cross-linking to join adjacent graphene oxide nanosheets. These papers will be used as a macroscopic test bed for identifying particular chemistries that effectively transfer mechanical loads between adjacent sheets. These graphene oxide papers will be mechanically tested by the **Espinosa** group.

The **Dzenis** group aims to ***design, manufacture, and demonstrate high-performance disruptive fibers based on continuous nanofibers fabricated via electrospinning.*** The focus in this reporting period was on evaluating the mechanisms of graphitic structure templating and size effects in continuous nanofibers. The activities included nanomanufacturing process optimization, controlled fabrication of nanofibers of various diameters containing graphene oxide (**Nguyen** group) or DWNT (**MER**) nanocarbon inclusions, CNF carbonization under various temperatures and regimes, mechanical testing of the precursor and carbon nanofilaments, and evaluation of mechanisms and modeling (with **Buehler** and **Schatz** groups) of observed templating phenomena and size effects. Macroscopic specimen testing in the **Dzenis** group was coordinated with in situ MEMS testing in the **Espinosa** group. Remarkable improvements in graphitic structure were demonstrated in both GO- and DWNT-templated CNF systems. Significantly, the largest templating effects were recorded at low carbonization temperatures, promising a new route to low-cost high-quality nanostructured continuous carbon. Dramatic simultaneously increases in strength, modulus, and energy to failure were demonstrated for polymer precursor and carbon nanofilaments with reduction of their diameter. Variation of properties and size effects in precursor nanofibers were explained based on structural analysis and mechanical evaluation of altered (annealed) nanofibers. Initial results from mechanical testing of templated CNFs in **Dzenis** and **Espinosa** groups showed promise for further improved mechanical properties and enhanced control of structure and properties of nanofibers. The resulting strong and tough continuous nanofibers will be readily available for Department of Defense safety-critical applications.

Scientific Accomplishments:

Fabrication and characterization of microscale DWNT composite yarns

1. Studies of macro-scale modeling of DWNT yarns mechanics

Analysis of the DWNT yarns mechanics in the frame of an appropriate analytical model could provide the required but still missing link between the macroscale and nanoscale experimental and computational studies, thus strengthening the multiscale approach pursued in the project. Preliminary examination of Hearle's textile fiber model¹ revealed its applicability for analyzing DWNT yarns of the project (**Figure 1-Figure 3**). In particular, it could quantitatively verify the

effectiveness of the major factors contributing to the advanced mechanical properties of DWNT fibers, first of all the dominating aid of DWNT length (aspect ratio) to their improvement, as well as the role of other important aspects, including porosity, alignment and bonding between the composite fiber constituents, leading to recommendations for practical engineering of disruptive fibers for flexible armor.

In the preliminary analysis, the DWNT bundle was recognized as the main tensile load bearing element, whose geometry, strength and external friction properties determine the strength and the modulus of the twisted yarns. The length of the DWNT bundles is a critical parameter for achieving the highest possible strength in twisted yarns. It was revealed that the strength of the optimally twisted yarns grows exponentially with the bundle length (**Figure 2**). A certain degree of twist is a universal means to strengthen yarns compacted by any other means. The friction born from the lateral interaction of the bundle with the polymer matrix can be included in the model to provide a semi-quantitative treatment of the PMC microfiber mechanics, which enables the following conclusions. The tensile strength of ~ 2 GPa that was measured for microfibers is too high to be supported by van der Waals friction between the bundles. Involvement of a polymer matrix in the inter-bundle load transfer is a necessity. The interfacial shear strength between the nanotube and the polymer, commonly determined to be at the level of ~ 75 MPa, appears sufficient to ensure sharing of a tensile load of ~ 2 GPa between the realistically long ($\sim 100 \mu\text{m}$) DWNT bundles in the microfiber. Therefore, the mutual slippage of the bundles imbedded in the polymer matrix provides a plausible mechanism for generating the mechanical properties observed in microfibers.

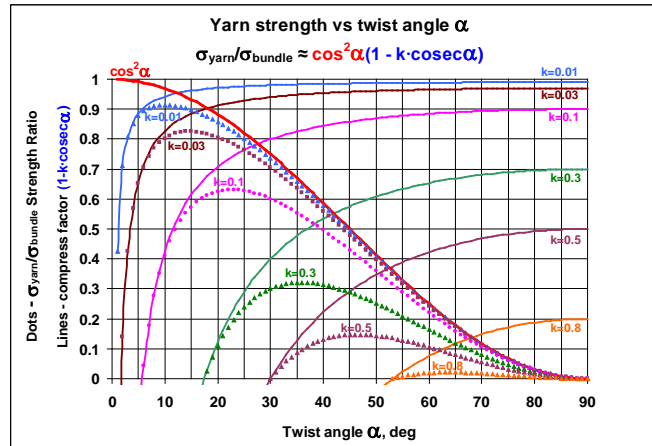


Figure 1. Dependence of the tensile strength of yarns on the twist angle, which has an optimum value for the maximum strength, and is determined by the bundle properties.

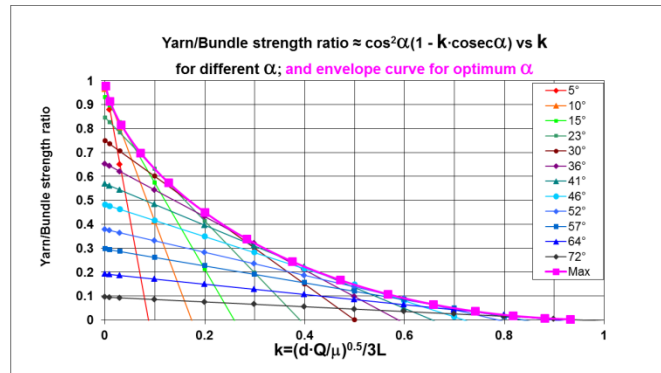


Figure 2. Linear dependence of the yarn strength on the bundle length at a given twist angle, and exponential growth of the optimized yarn strength with the bundle length.

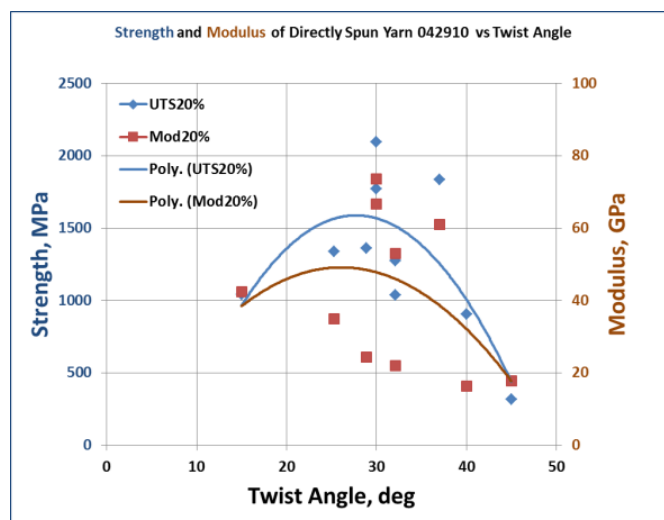


Figure 3. Dependence of the strength and the modulus of the directly spun DWNT yarns on the twist angle. A common maximum near 25-30° is characteristic of k-factor value of ~ 0.2 (Figure 1), thus corresponding to the optimum strength of yarns of about one third of the DWNT bundle strength, which was measured in the project at the ~ 5-6 GPa level.

2. Effect of non-covalent Hydrogen-bond (H-bond) interaction on the mechanical properties of DWNT-polymer yarns

As-produced DWNT mats were provided by **MER Corporation**. They are highly porous (with a density of 0.03 g/cm³) in which DWNTs are well-dispersed and retain dispersion when infiltrated within a matrix. As synthesized, MER's DWNT mat contains 10-15 wt% of an intrinsic polymer coating on the walls of the DWNT bundles as determined from thermogravimetric analysis (TGA, **Figure 4d**). Based on NMR, XPS, and FTIR analysis (**Figure 4a, b, and c**), this inherent polymer coating contains mixture of following components: (i) acrylic acid (CH₂=CHCOOH), (ii) esters of acrylic acid (CH₂=CHCOOR), (iii) substituted acrylates (R'CH=CHCOOR, CH₂=C(R')COOR), and (iv) oxygen-containing aromatics (R'C₆H₄COOR, R'C₆H₃(COOR)₂). We hypothesized that hydrogen-bond-donating and -accepting carboxylic acid groups on the CNT surface, could substantially increase the capability of the bundles to form H-bonds with polymers such as polyvinyl alcohol (PVA), given the H-bond-donating and -accepting nature of the pendant hydroxyl groups. This H-bond interaction would subsequently show enhancement in both strength and toughness. We also hypothesized that given the intrinsic polymer content of about 10-15%, the mechanical properties could show an improvement up to a critical dosage of external polymer added, which is PVA in this study.

To realize our hypothesis, we concentrated on the DWNT yarns as the macroscopic model. The yarns were fabricated by the **Nguyen group** from 1/4" wide ribbon of a DWNT mats by a spinning apparatus constructed at Northwestern University by the **Espinosa group** (**Figure 5**). During the spinning process, ribbons of DWNT mats buckle successively due to the twisting process, through which they are converted into a yarn. To prepare our nanocomposite yarns, a dimethyl sulfoxide (DMSO) solution of PVA was sprayed on the CNT ribbon during the spinning. The aforementioned lateral contraction pushes almost all of the excess DMSO molecules (solvent) out of the final yarn filament. The yarn was then dried under vacuum at 150°C for 24 h to remove the excess solvent. Polymer content of each sample tested for mechanical properties was determined from the weight loss after pyrolysis of the samples at inert argon (Ar) atmosphere at 800 °C at a ramp rate of 10 °C/min.

The yarn morphology was investigated by scanning electron microscopy (SEM). The fracture-surface morphology shows that the DWNT bundles are uniformly coated with polymers. Fracture surfaces of DWNT yarns show a semi-brittle fracture, where the folded mat material breaks off along a single plane perpendicular to the axis of the fiber. The fracture surface of a 9 wt% PVA yarn

shows more of a shear failure, where neighboring mat surfaces appear to have pulled other surfaces along, with this cooperation between layers leading to higher strain to failure and energy to failure than the 0 wt% PVA yarns. At 31 wt% PVA impregnation, the failure surface does not show any empty space within the yarn, as the PVA has filled the gaps between the layers of bundles of mats.

The mechanical behavior of spun polymer nanocomposite yarns was measured using a microtensile tester at a strain rate of $\sim 2 \times 10^{-4} \text{ s}^{-1}$ for a typical gage length of 16 mm. The crosshead deformation of the yarns normalized by the initial length of the yarn is reported as the sample's strain with a typical resolution of $\sim 0.01\%$. The true stress in the yarn was computed by dividing the measured force by the true cross-section of the yarn. The specific modulus, specific strength, and energy-to-failure as a function of CNT concentration are shown in **Figure 7** where each point represents an average of three measurements or more. As a function of PVA loading, the trends of the energy to failure and modulus of these composite yarns increase up to an optimal PVA content of approximately 10 wt%, after which these values decrease. The ultimate engineering strength of the yarns is not significantly affected by the PVA content. These data indicate that up to a certain concentration, the increasing concentration of H-bond donors and acceptors in the PVA interact readily with those available on the MER's mats of DWNT bundles, providing increased shear interactions between bundles and therefore superior yarn. This trend in mechanical properties is currently being investigated by modeling in collaboration with the **Buehler group**. In addition, we have prepared iodine-functionalized DWNT bundles to be used in the evaluation of the microstructure of these PVA nanocomposite yarns by nano-CT at **Argonne National Laboratory**.

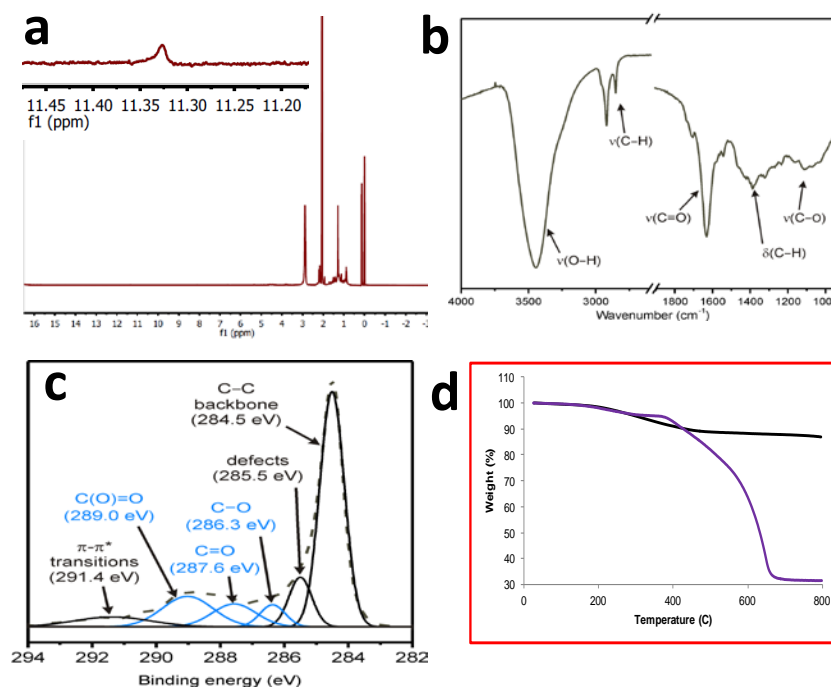


Figure 4. (a) NMR, (b) FTIR, (c) XPS, and (d) TGA data for the extracted polymer coating on DWNT bundles.

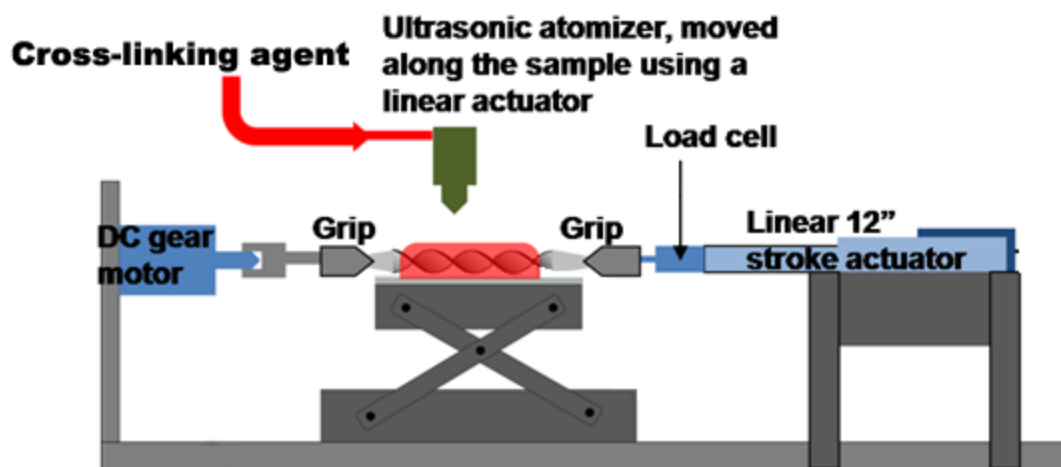


Figure 5. Schematic illustration of a yarn-spinning apparatus that allows for the incorporation of cross-linking agent (polymer in the present case). The atomizer moves along the yarn during spinning, spraying a solution of PVA in DMSO.

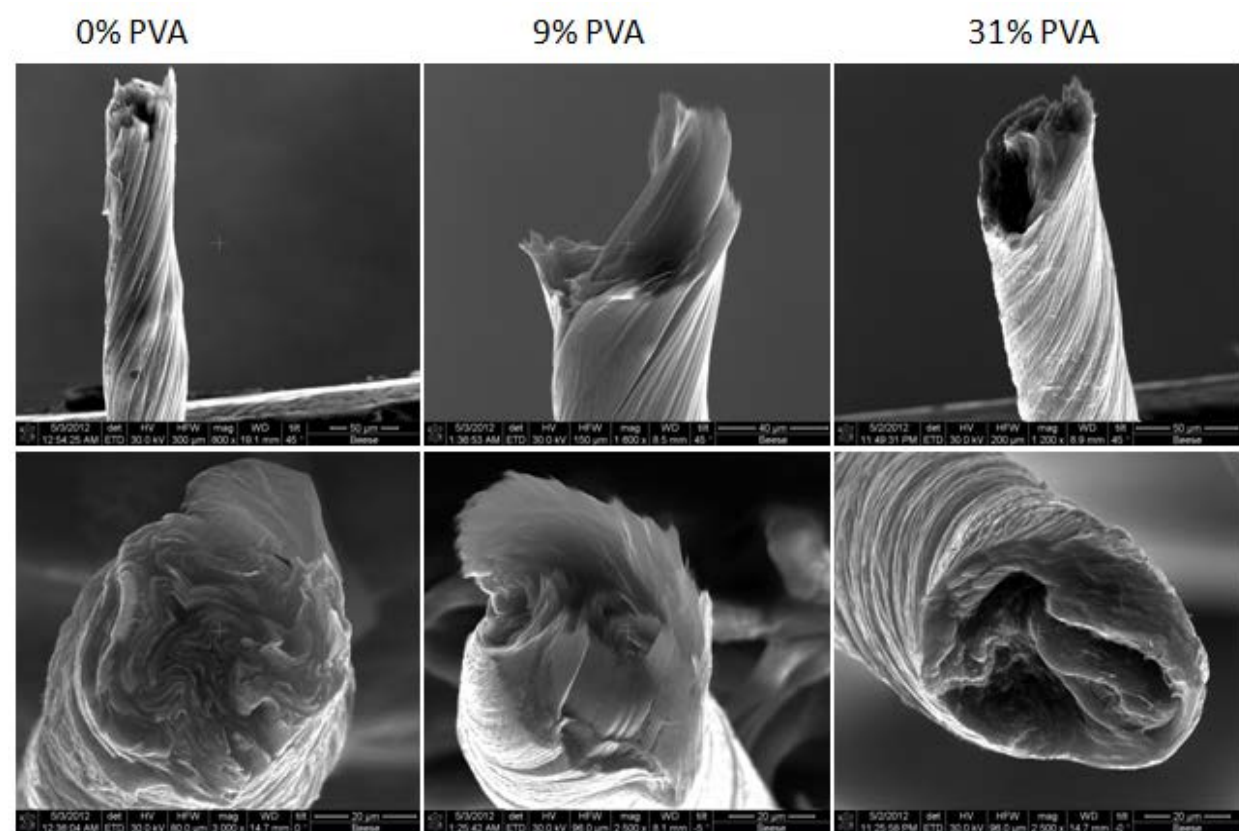


Figure 6. SEM images of DWNT yarns impregnated with (a) 0 wt% PVA, (b) 9 wt% PVA, and (c) 31 wt% PVA.

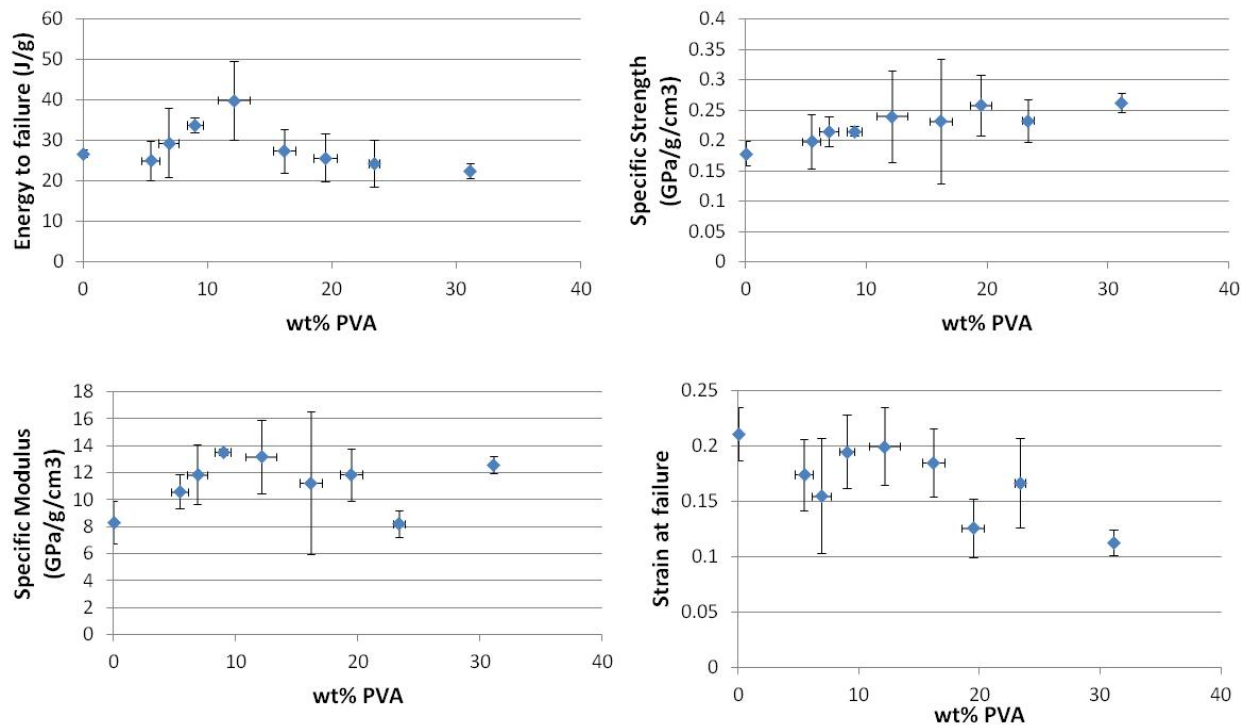


Figure 7. Mechanical properties of the CNT-PVA yarns as a function of PVA content. The average mechanical properties for each PVA content are shown, with the standard deviation of the measurements shown with error bars.

3. Structure characterization of yarns using nano-CT (nano-computed tomography)

In order to produce a fiber with superior mechanical properties, the mechanical performance of the DWNT yarns must be understood completely. In the yarns, the DWNT bundles are recognized as the main tensile load-bearing element, whose geometry, strength, and lateral shear interactions largely affect the magnitude of the yield stress and ultimately the tensile strength of the twisted yarns. It was shown that the strengths of twisted yarns are dependent upon bundle length and migration length (distance along the yarn over which the bundle shifts from the yarn surface to the deep interior and back again) by a model for a filamentous twisted yarn that was introduced by Hearle,¹ for an arbitrary friction, or shear interaction, between the filaments. To calibrate this model, the bundle length and migration length need to be obtained experimentally. Nano-CT can be used to obtain these parameters experimentally.^{2,3} X-ray nano-CT is a non-destructive imaging technique, which provides distortion-free 3D images of both the surface and the internal features of the sample. From the 3D images obtained from the nano-CT, the distribution and alignment of DWNT bundles in yarns will be semi-empirically calculated.

The measurements of the yarns' mechanical properties are based on estimates of the yarns' cross section. To calculate the yarns effective diameter, the cross-sectional area of the DWNTs in the yarns is determined from the mass of the CNTs within the sample and the density of the CNTs in a hexagonally close-packed bundle structure. The latter effective density of the CNT bundles, an estimate obtained using the diameters of the outer and inner CNT tubes and the density of graphite,⁴ is equal to the density of the yarns and mats when the pores between the bundles are excluded. Using the 3D structure of the yarns obtained from nano-CT, the effective density of the CNT bundles will be qualitatively investigated and a porosity value will be calculated. This value will be compared against the above mentioned method of estimating porosity. Furthermore, it was found that one of the common denominators leading to the outstanding balance between strength and toughness in natural composite materials, especially "brick and mortar" like structures, is the lateral interactions between adjacent reinforcement constituents. Critical overlap length scales

between adjacent reinforcements is found to directly control the strength and toughness of the material. This model has been used to interpret load-transfer capabilities in DWNT yarns.⁵ The overlap length between CNT bundles inside the yarns is another parameter expected to be obtained from the 3D nano-CT images.

In order to get these 3D images, the Advanced Photon Source (APS) at Argonne National Labs will be used. The APS has the brightest storage-ring generated X-ray beams in the western hemisphere, which will be used in nano-CT imaging. These bright beams are required for imaging the CNT yarns because the resolution required for imaging CNT bundles in yarns is approximately 15 nm and this is the only instrument with hard X-rays capable of outputting this high resolution.² This quality, along with the phase contrast and absorption-based imaging, are needed to provide better contrast in the nano-CT imaging of CNT yarns, as the constituents of the yarn, the polymer, and the CNT bundles are made out of similar homogeneous materials and this generally translates to low contrast between the constituent materials in the 3D structural images obtained. To further improve imaging quality, iodine infusion will be used to enhance the contrast between the homogeneous constituents of the yarn.

Two types of CNT yarns that are being fabricated in this project will be imaged using nano-CT. *Sample i) Yarns made from twisting and stretching narrow ribbons cut from CNT mats, with and without external polymer matrix.* These yarns will first be mechanically tested by the **Espinosa group** at Northwestern University and then imaged using nano-CT. These samples will be imaged initially without iodine infusion because there are Fe(0) particles (from the manufacturing process in the CVD reactor) coating the walls of the CNT bundles, which are expected to enhance the contrast between the polymer and the CNT bundle. Initially, 5 to 7 samples will be imaged to better understand the feasibility and quality of the imaging. If the resolution and contrast obtained from these images are sufficient, then approximately 15 more samples will be imaged further. *Sample ii) CNT yarns fabricated using nanotube aerogel as a starting material instead of DWNT mat ribbons.* These in situ yarns are fabricated, with and without an infused external polymer matrix, from the in situ CVD reactor at MER Corporation. The yarns will first be mechanically tested at MER Corporation. The tested yarn samples will also be imaged initially without iodine, again relying on the Fe(0) particle coating on the CNT bundle walls to provide the necessary contrast. After understanding the feasibility of imaging these samples, approximately 15 more samples will be imaged. *Sample iii) Iodine-infused spun yarns.* To identify the effect of iodine infusion on the improvement of contrast, the DWNT mats will be infused with iodine to coat the walls of the CNT bundles. The iodine-infused DWNT mats will be cut into ribbons and then stretched and twisted into yarns. These yarns will be imaged using nano-CT, and depending upon the results obtained, iodine infusion will then be applied to Sample i) and possibly Sample ii).

Multi-scale experimental and computational studies of the mechanical behavior of CNT/polymer bundles and yarns

1. Nanomechanical experimental characterization of DWNT bundle junctions

The experimental nanomechanical characterization of double-walled CNT bundle junctions was carried out using both *in situ* SEM and TEM by loading a bundle pair junction in shear mode. In SEM, an AFM cantilever with known stiffness was used as the load sensor, as shown in **Figure 8a**. One double-walled CNT bundle was mounted on the AFM cantilever. Using a nanomanipulator inside an electron microscope, the bundle on the cantilever tip was brought near, and approximately parallel to, another cantilevered bundle protruding from a TEM grid. When the distance between the bundles was sufficiently small, the bundles slightly bent toward each other, likely due to electrostatic interactions within the SEM chamber, and formed a junction. **Figure 8b-d** shows subsequent SEM images of a shear experiment including the formation of a bundle-bundle junction (**Figure 8b**), pulling the two bundles apart from each other and loading the junction (**Figure 8c**)

until junction failure (**Figure 8d**). Using the above protocol, each DWNT bundle will be in tension, while their junction will dominantly experience a shear stress parallel to the interface.

The force on the bundles as a function of overall average axial strain is shown in **Figure 8e**, where the average strain is calculated as the total axial deformation of the bundle pair with respect to its initial length. The initial slack of the sample is excluded from the total deformation to calculate the average axial strain. For the experimental data plotted in **Figure 8e**, the failure force was measured to be ~ 250 nN. In all of the SEM experiments, the overlap length between the two bundles was systematically varied but kept below $1\text{ }\mu\text{m}$, since at higher overlap lengths bundle failure rather than failure of the junctions was observed. Because the experiment is performed under load control, in all cases the junction failure was abrupt, and no sliding was detected prior to failure.

Because *in situ* SEM lack the resolution needed to capture the predicted sliding (below ~ 7 nm) between the two bundles prior to junction failure, we also undertook *in situ* TEM studies. For this purpose, a pair of bundles with an overlap length of $\sim 1.4\text{ }\mu\text{m}$ were mounted on the gripping pads of a MEMS-based tensile stage,⁶⁻⁸ as shown in **Figure 9a-b**. Upon actuating the device, the gripping pads were moved apart from each other, loading the junction in shear. Using image correlation to track the relative motion between the two ends of the bundle junction, the sliding between the two bundles was measured to be ~ 10 nm, consistent with the simulation predictions on a shorter junction (**Figure 9e**). We note that while the TEM experimental set up allows for much higher image resolution, the *in situ* SEM set up was found to be more suitable for investigation of the shear interactions between bundles as a function of overlap length. Indeed, mounting DWNT bundles on the MEMS platform with controlled overlap lengths proved to be difficult and low yield.

A complete set of *in situ* SEM-based experimental measurements and associated multiscale simulation results is presented in **Figure 10**. In this figure, the critical junction force, *i.e.* slip force, is normalized by the contact width to allow for a direct comparison of experimental and simulation results obtained from shearing bundles with different diameters. Following the multiscale simulation results of the bundle interactions, **Figure 9d**, the contact width between the bundles is taken as ~ 0.40 of the average of the bundle pair diameter. The contact width is also used to estimate the average shear strength, as the ratio of the critical junction force to contact area. Each data point in **Figure 10** corresponds to the junction failure force for a particular experiment. As shown in this figure, the junction slip force does not scale linearly with overlap. At small overlap length, below ~ 250 nm, the junction failure force per unit width vs. overlap length can be approximated by a straight line (using the least square method), with a slope of $\sim 330 \pm 80$ MPa, regarded as the average interface shear strength of the junction. Note that the failure force for a given overlap length is expected to have a statistical variation and this is exactly what the experimental data shows. Part of this variation can also be attributed to the experimental errors.

In summary, we have carried out a combined experimental and multiscale simulation study to investigate the effect that intrinsic acrylate oligomer coatings have on the mechanical interactions between double-walled CNT bundles. The experiments have elucidated the role of overlap length, quantified the interface failure force, and served as benchmarks to verify the simulations presented below.

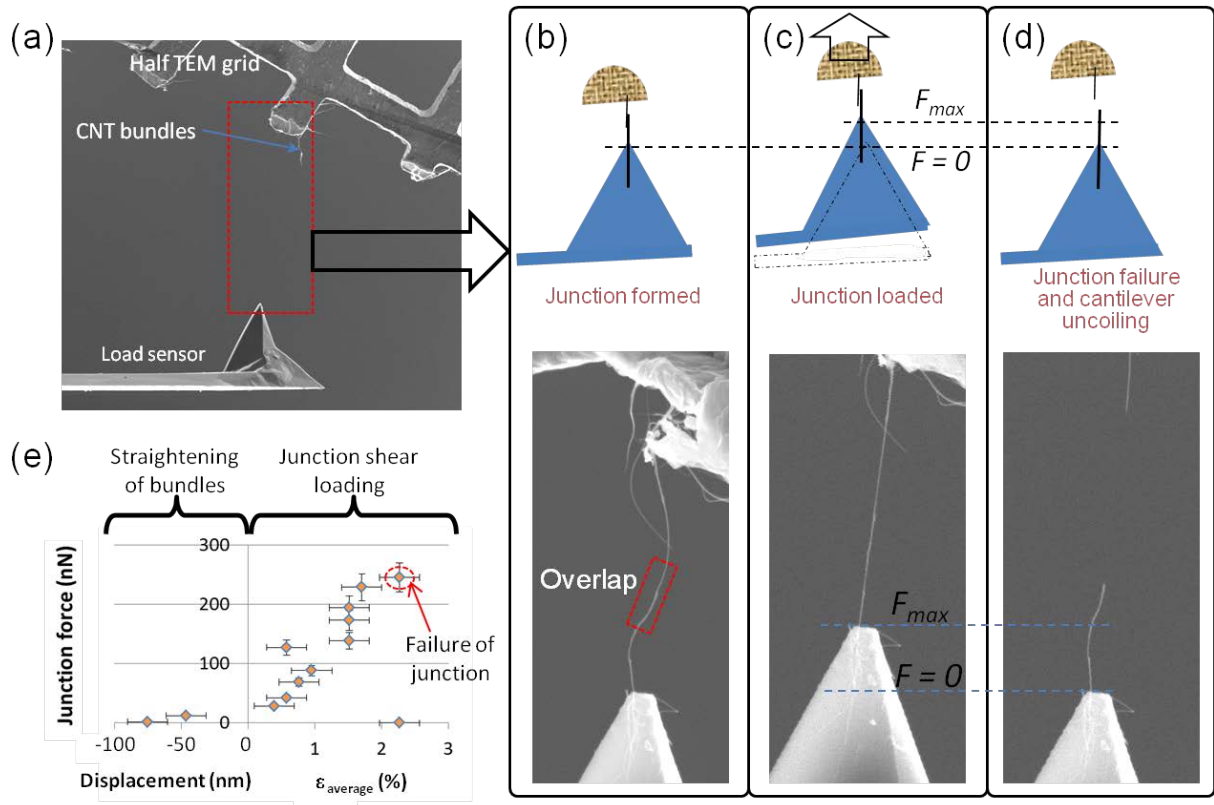


Figure 8. (a) *In situ* SEM testing setup used to investigate the shear interactions between DWNT bundles. (b-d) The junction between the bundles is formed inside the SEM with a range of overlap lengths up to 1 μm (b), followed by loading the junction in shear mode (c), until junction failure occurs (d). The dash lines indicate the location of the cantilever tip under maximum load and zero load configurations. (e) Plot of junction force as a function of the stage motion and average axial strain in the bundles.

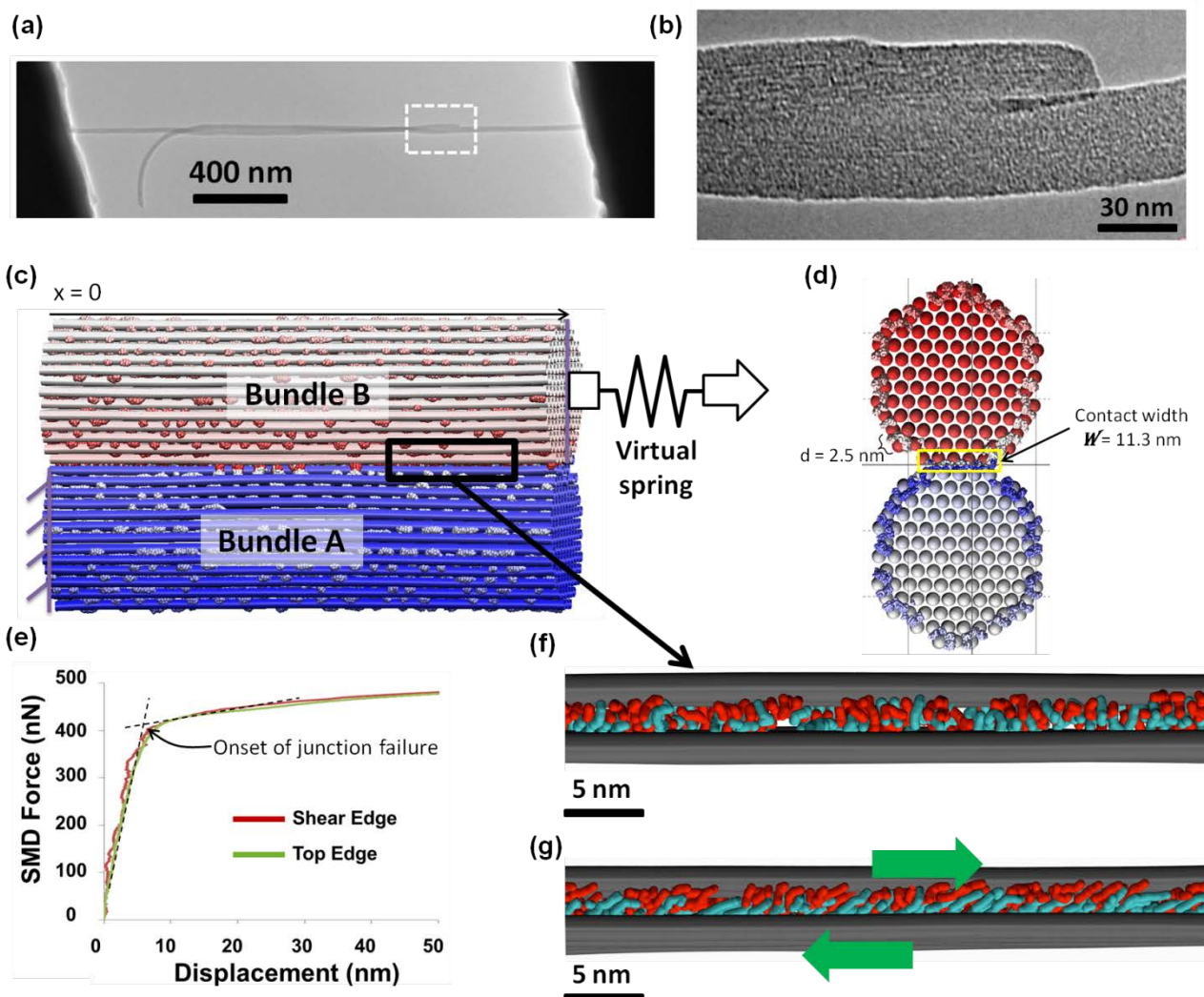


Figure 9. (a) TEM image of two overlapping DWNT bundles mounted on a MEMS testing stage. (b) High-resolution TEM image of the end of one of the DWNT bundles (from region indicated in (a)). (c-d) Side view (c) and cross-section (d) of the coarse-grain model of bundle pair used in the multiscale simulations. The diameter of each bundle is ~ 26 nm. (e) The SMD sliding force as a function of the relative displacement between the two bundles. (f-g) The oligomers at the shear surface are well-mixed at zero load (f) and elongate and align when the bundle pair is sheared (g).

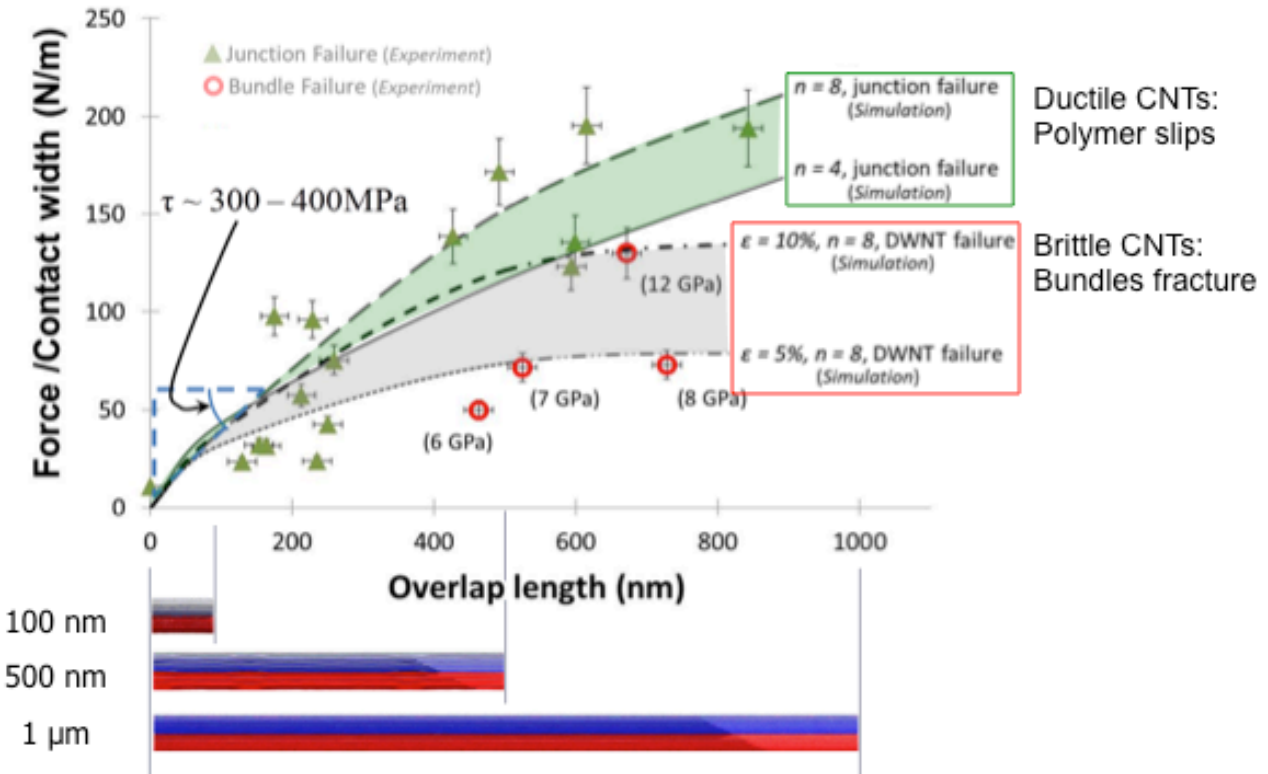


Figure 10. Comparison of coarse-grain bundle-bundle shear behavior with experiment. The shear strength of simulated bundles with 4—8 monomer cross-links encompass that of experiments at several overlap lengths. When simulated bundles are limited to 5—10% failure strain, the weakened she behavior also encompasses that of presumably defective experimental materials.

2. Coarse-grain modeling of fiber mechanics

The coarse-grain model developed by the **Buehler group** has been used to build larger-scale bundle-bundle models that correspond to those geometries studied by the **Espinosa group**. **Figure 11** shows the geometry of these studies, including orders of magnitude of length scales encompassed by the coarse-grain models. The polymer cross-links and nanotubes are assembled as separate components into bundles matching the size and polymer content of experiments. **Figure 12** shows the computational expense that is saved by using a coarse-grain model instead of traditional atomistic force fields. While the atomistic model with reactive force field and 10^4 atom count must be run on multiple processors, the coarse-grain models can be simulated much faster and on fewer processors, despite simulating 10—100 times the particle count, due to simplified parameters. This allows much larger length scales and/or longer time scales approaching those of the experiments to be conveniently studied.

Figure 10 shows good agreement between simulation and experiment. Bundles are simulated with 4 to 8 monomer cross-links to investigate upper and lower bounds of the experimentally determined range, as well as several overlap lengths between 100 nm and 1 μ m. The range of bundle interface shear strengths observed in the simulations encompasses the upper bound observed in experiments. When brittle nanotubes are simulated, the weakened shear strengths encompass the lower bound observed in experiments and serve as an explanation for the upper and lower experimental bounds. Bundles with ductile nanotubes fail by sliding at the interface, while bundles with brittle nanotubes fail when nanotubes at the interface fracture, and the interior tubes of the bundles are revealed, termed "unsheathing."

Figure 13 shows shear strengths that are accessible by tuning the overlap length and cross-link length as predicted in simulation. The range of predicted shear strengths forms a design space. For cases of both ductile and brittle nanotubes, the shear strength is greatest for shorter overlaps and cross-links near 8-monomers. The shear strengths for bundles with brittle tubes drastically weakens at longer overlaps, no matter the cross-link length. Areas of "missing strength" at longer overlaps may be accessible by controlling other variables and warrants further simulation in this area.

Figure 14 shows a shear lag prediction for a shear interface (representing the cross-link interface) between two compliant slabs (representing the nanotubes at the shear surface). Shear load transfer is predicted to decrease (*i.e.* "lag") around the midpoint of overlap. This behavior is observed directly in simulation and becomes more drastic for overlaps greater than approximately 250 nm, near the lower bound of experimentally observed overlaps. This explains the weaker total shear strength at longer overlaps and the "missing strength" region of the design space. Controlling other variables may be able to overcome the effects of the shear lag and enable much greater shear strengths between bundles.

The setup now provides a powerful tool to explore varied geometries of overlapping bundles, fitting those scales investigated in experimental studies. By linking experiments and simulation, we can garner valuable insight into detailed deformation and failure mechanisms and work to overcome inherent weaknesses like the shear lag behavior. Current analyses revealed a competition between sliding and nanotube fracture under different boundary conditions and geometries, and other variables are currently being analyzed rigorously to supplement the experimental results. We have already demonstrated that in both experiment and simulation, the mechanical properties of bundles change drastically under varied overlap length and average cross-link length, and direct comparison with experimental studies suggests reasonable agreement.

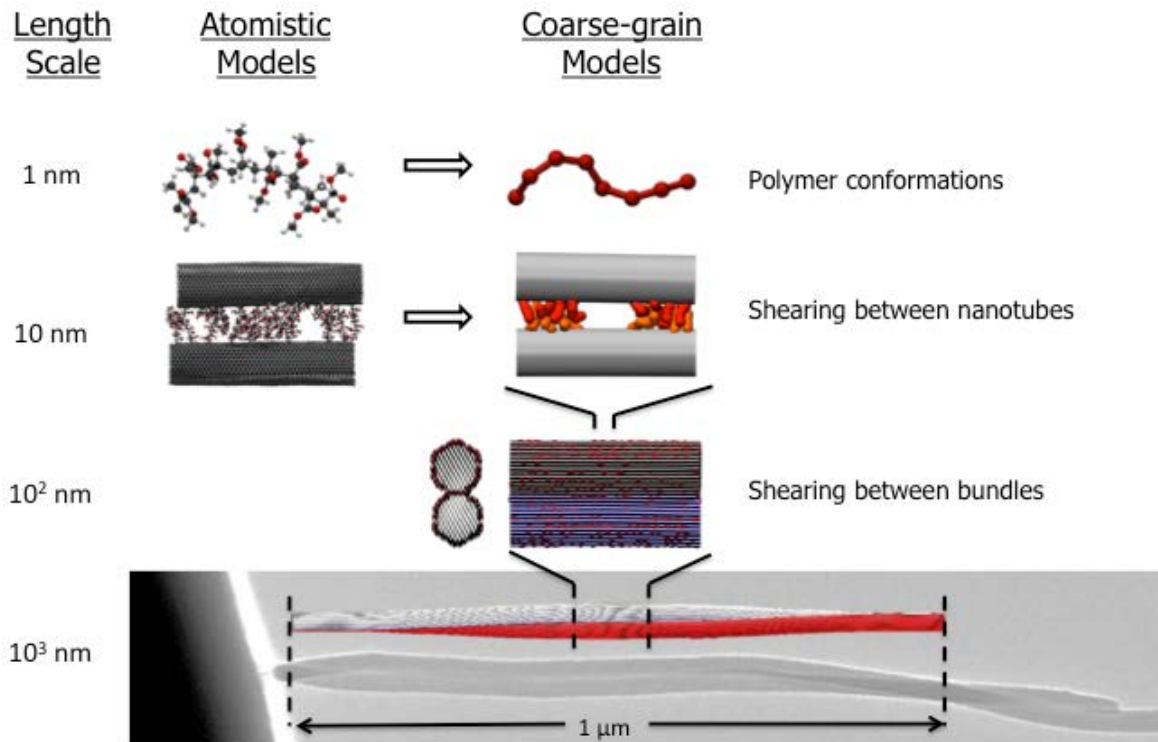


Figure 11. Multiple length scales of the coarse-grain models. The kinetics and adhesion of the short polymers and carbon nanotubes are represented as separate bead-spring components. These components are assembled into physically inspired geometries up to the micrometer scale of the experiments.

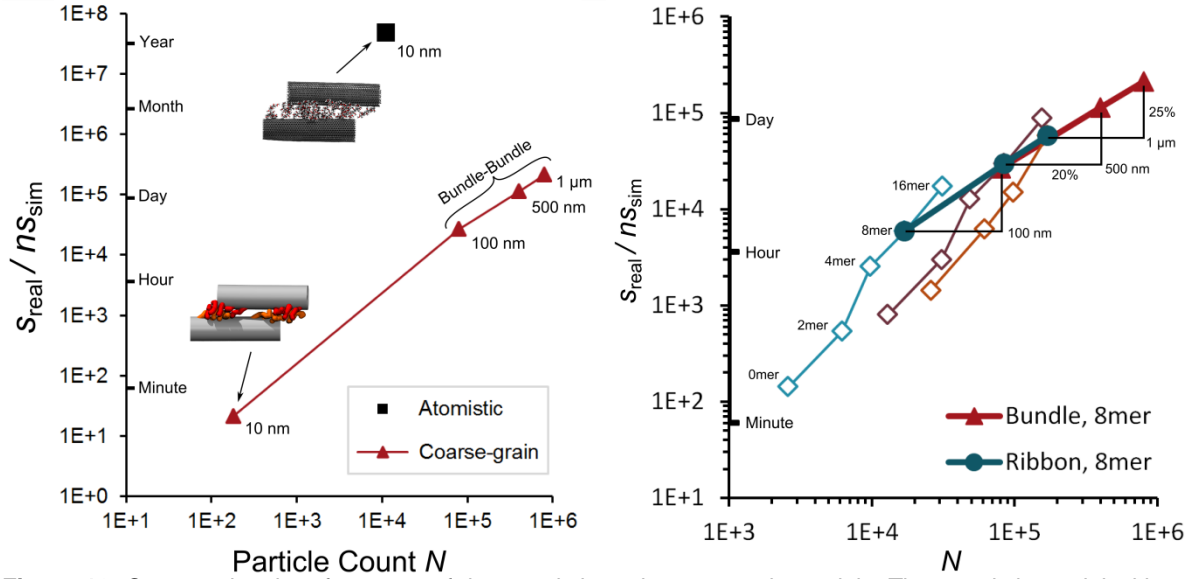


Figure 12. Computational performance of the atomistic and coarse-grain models. The atomistic model with reactive force field and 10^4 atom count must be run on multiple processors to be computationally convenient. The coarse-grain models can be simulated much faster, despite 10-100 times the particle count, due to simplified parameters.

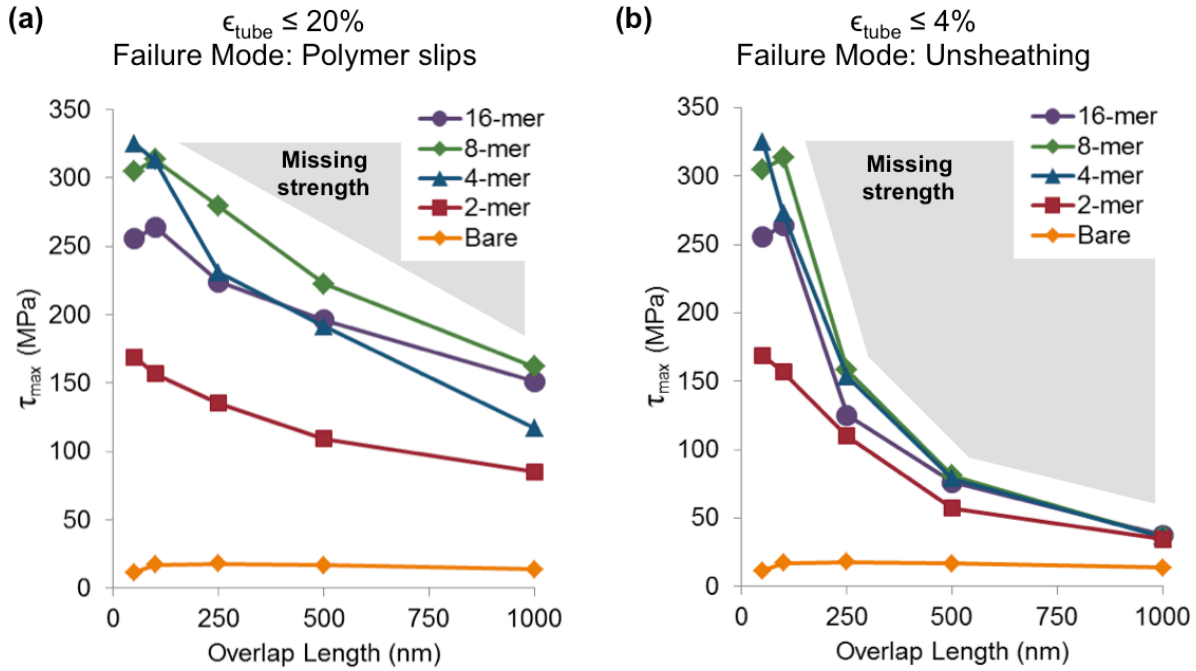


Figure 13. Shear strength design space by controlling overlap length and cross-link length. (a) The bundle interface shear strength using ductile tubes is strongest at shorter overlaps and a cross-link length near 8-monomers (i.e. the experimental value), and begins to decrease with increasing cross-link length. (b) Simulating brittle tubes, shear strength at shorter overlaps is nearly unaffected, but severely weakens at longer overlaps. The region of “missing strength” in the design space may be reached by adjusting other parameters such as bundle diameter.

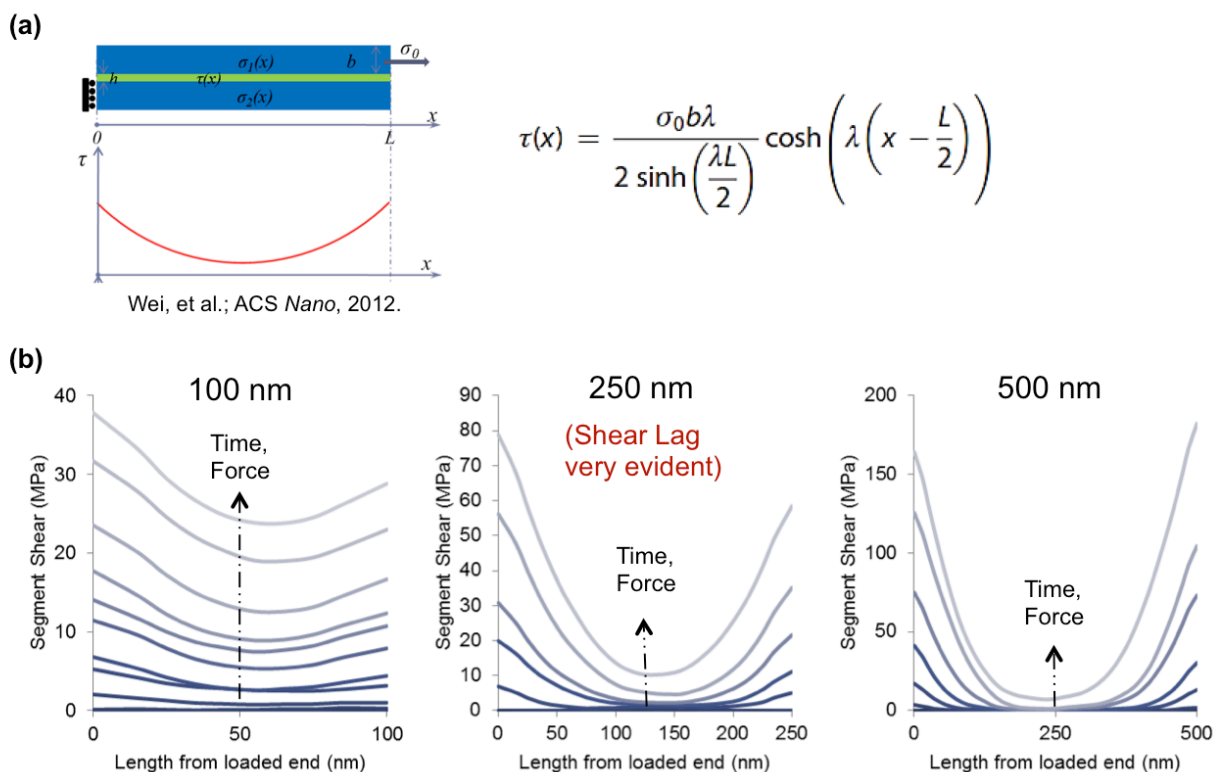


Figure 14. Shear lag prediction is observed in simulation. (a) The shear lag model predicts a decrease (i.e. lag) of shear load transfer around the midpoint of the overlap. (b) The shear load transfer at the bundle interface simulated with 8-monomer cross-links shows the predicted shear lag behavior. The shear lag is especially evident for overlaps greater than approximately 250 nm.

3. Understanding shear forces in DWNT bundle pull-out experiments

Work to understand the origins of the force resisting the extraction of the inner bundle of carbon nanotubes from the outer sheath of tubes in the experiment by Espinosa et al. have continued from the previous reporting period. MM3 simulations were performed to determine the origins of the pullout force (see **Figure 15**). We found that it was necessary to revise the methods used to tether the end atoms, to more accurately determine the force (see **Figure 16**). Once this was perfected, we were able to provide a detailed assessment of the origin of the pull-out force for the double wall nanotube bundles, leading to a joint publication with the **Espinosa group** in Nano Letters.⁹

A surprising result of these calculations and experiments is that dissipation was found to play a major role in the results, being responsible for at least half of the pullout force and possibly much more. We are now working to understand the possible impacts of pressure on this pullout force. There is significant evidence that the bundles are under pressure before heat treatment; the pressure is presumably caused by the polymer coating. Heat treatment removes some of the polymer, but evidence suggests about 20% of the polymer remains after the treatment. A polymer coating can apply a pressure as large as 100 MPa without cracking.¹⁰ Pressure is also of interest because twist is applied during the production of the yarns. This twist results in pressure within the bundles in the yarns, in excess of what was present when they were produced, and especially in those bundles close to the centers of the yarns. Twist and the resulting pressure are critical for effective load transfer between bundles. These pressures could be well in excess of 100 MPa, so we are also investigating larger pressures.

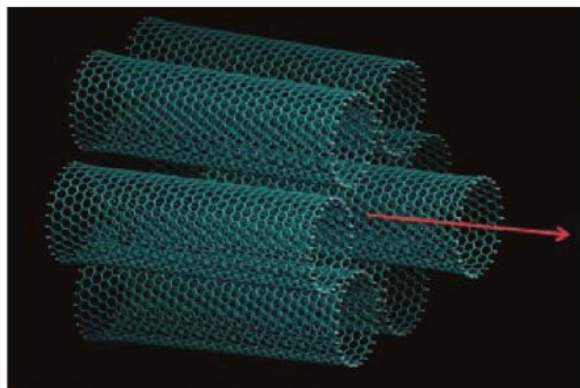


Figure 15. The seven-tube CNT bundle used in the MM3 simulations.

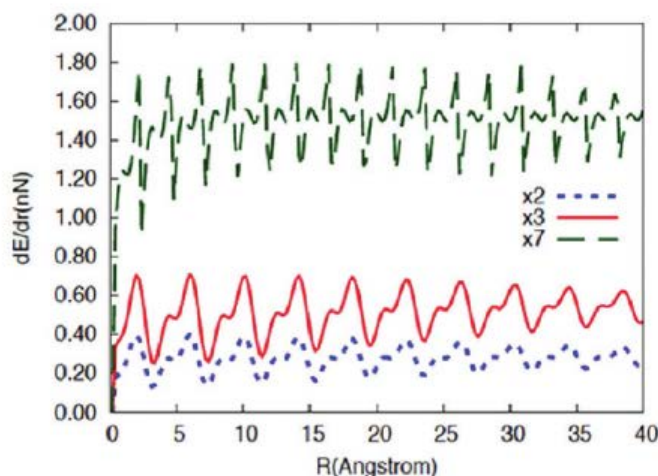


Figure 16. Force versus displacement for the CNT bundle shown in Figure 15 (top curve) and for dimer (bottom curve) and trimers (middle curves).

4. *In situ* SEM Multiwalled Carbon Nanotube (MWCNT) shear experiments

It is well-established that individual CNTs can slide past each other relatively easily due to relatively weak van der Waals forces.^{11,12} These weak inter-tube interactions pose a significant obstacle in the development of macroscale fibers, as interfaces between tubes may fail prematurely and, thus, never take full advantage of individual tubes' exceptional strength. One way to address this issue is to add functional groups onto the outermost shells of multi-walled carbon nanotubes (MWCNTs). By introducing additional chemical interactions beyond van der Waals tube-tube interactions, the interfaces may improve load transfer between carbon nanotubes throughout a fiber. As a first step toward understanding the enhancements afforded by these functionalizations at the nanoscale, we have developed methods to investigate shear and peeling properties of MWCNTs through *in situ* scanning electron microscope (SEM) testing. The following sections will describe each of these methodologies, the results obtained to-date, and the next steps being considered in these ongoing investigations.

In the context of fracture mechanics, CNT-CNT interfaces within a yarn can fail in shear (Mode II) or peeling (Mode I). Here, we investigate the mechanical properties in both of these failure modes through nanoscale *in situ* SEM experiments. As indicated in the **Espinosa group's** research into the shear lag model,⁵ investigating the shear behavior of functionalized MWCNTs can provide

insight into the load transfer that could be expected within a CNT-based fiber. By evaluating the Mode II fracture properties of functionalized interfaces between MWCNTs, an understanding of the improvements afforded by functionalization can be ascertained.

In this study, we investigate the shear strength of junctions *in situ* an SEM between functionalized and un-functionalized arc-discharge MWCNTs prepared by the **Nguyen group**. To do this, we attach a CNT to an AFM cantilever, and bring it into contact with a CNT fixed (to a TEM grid). When the two CNTs are sufficiently close to one another, they snap together, forming an overlap that can be directly measured in the SEM. If the overlap between the CNTs is sufficient and the two tubes are well-aligned, the SEM stage is pulled away at a constant rate. As the stage pulls away, the AFM cantilever acts as a force sensor—its deflections can be converted into forces exerted on the CNT using Euler-Bernoulli beam equations. Ultimate shear force is defined as the maximum force before failure, which can be measured from the deflection of the cantilever of known stiffness before and after failure. Provided no permanent deformations are observed on the CNTs, the shear test can be repeated with increasing overlap lengths.

To-date, four types of MWCNTs have been investigated through these *in situ* SEM shear tests. In addition to bare as-produced MWCNTs, tubes functionalized with approximately 3% carboxylic acid (COOH), 5% COOH, and 17% benzoic acid have been investigated in shear. These percentages are defined as the ratio of functional groups to carbon atoms as evaluated from XPS data taken by the **Nguyen group**. The 3% COOH and 5% COOH functional groups were chosen in an effort to explore the effect of changing functionalization on the tubes' shear properties. However, the maximum functionalization that can be achieved with COOH is relatively low. While the benzoic acid structure is slightly different from the carboxylic acid structure, they are both fairly short functional groups that promote hydrogen bonding at the interfaces between tubes. As such, for this preliminary investigation, the forces and overlaps attained for tubes with each of these functionalizations have been evaluated and compared to the baseline, un-functionalized tubes. The force vs. overlap data obtained for these different sets of tubes are shown in **Figure 17**.

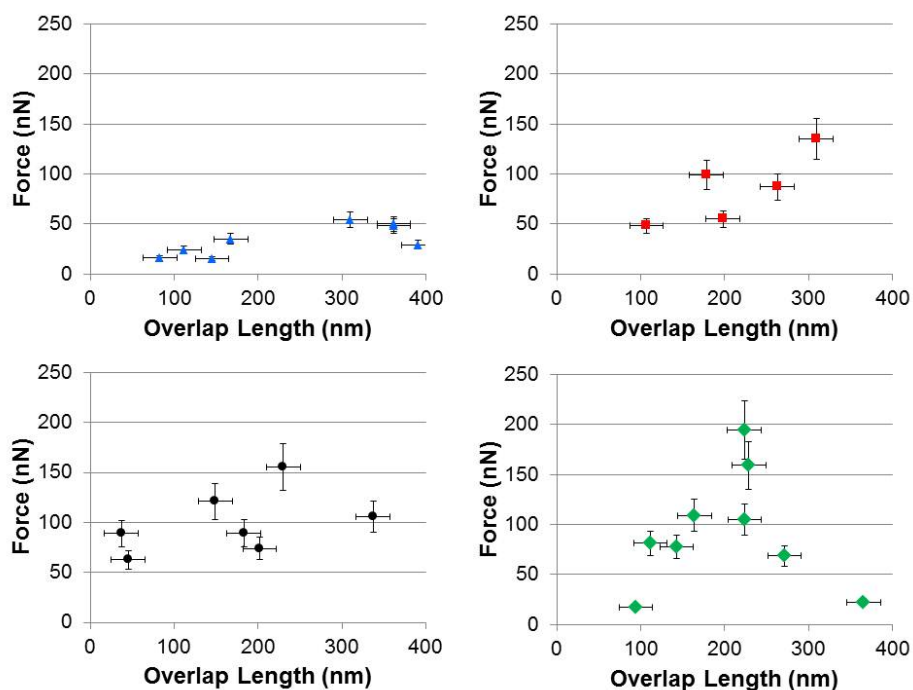


Figure 17. Force vs. Overlap Data for In situ SEM Shear Experiments. Top left (blue): Bare, as-produced MWCNTs. Top right (red): MWCNTs functionalized with 3% carboxylic acid. Bottom left (black): MWCNTs functionalized with 5% carboxylic acid. Bottom right (green): MWCNTS functionalized with 17% benzoic acid.

In **Figure 17**, the experimental data is plotted for each functional group with uniform scale bars, with overlaps ranging from 0-400 nm and forces ranging from 0-250 nN. The number of data points acquired to-date may not be sufficient to establish a statistically significant difference between the forces attained for different functionalizations. However, within the small overlap range of less than 400 nm, each of the functionalized groups generally withstands higher forces than their bare nanotube counterparts. The data also reveals, especially for the benzoic acid case, dependency on water content. A correlation was found between the time the samples were left inside the SEM chamber under high vacuum and the measured force. The **Espinosa group** is working to acquire additional experimental data to substantiate this preliminary trend. In particular, we will develop a protocol to minimize variability associated to different water content.

In addition to these data acquired to-date, there are two experimental observations that merit discussion: first, there may be onset of twisting at large overlaps, which leads to additional enhancements in forces; and, second, some failure modes beyond complete interface failure (such as the data points plotted in **Figure 17**) may provide additional insights into these functionalizations. In regards to twisting, in some cases, the maximum attainable forces tend to plateau and then rise again at increasing overlap lengths. For example, among the as-produced tubes, a maximum force of approximately 100 nN appears to be consistent for overlaps ranging from nearly 200 to 400 nm, as in **Figure 17**. At larger overlap lengths, though, the forces rise dramatically, with a peak force of roughly 480 nN for an overlap length of 930 nm. A similar trend may be observed for the 3% COOH-functionalized tubes. One possible reason for this increase in force is the onset of twisting. When overlap lengths are large, CNTs may be more likely to twist around each other, causing additional adhesion as compared to straight tube-tube interfacial adhesion. Such additional interactions would then have to be overcome before slipping in shear. In light of this behavior as a potential artifact in the experiment, we plan to focus on acquiring force-versus-overlap data for smaller overlap lengths (e.g., less than 500-700 nm) in the future.

While failure is occasionally observed in a single CNT or at one of the fixed ends, only data obtained from tests where the junction failed are reported here. The various types of shear failure observed in these *in situ* SEM studies are also noteworthy. The most directly useful mode is a complete interface failure. In this failure mode, the tubes are continuously loaded until one tube suddenly slides entirely past the other tube. This appears as a sudden drop in the deflection of the AFM cantilever and, consequently, provides a direct measure of sustained force for the particular overlap.

While we aim to learn more about these functionalized interfaces through experiments, we also aim to promote further scientific understanding with respect to other studies we have done within the MURI project. For example, establishing a more well-defined trend among the data sets would be of interest, particularly by incorporating the shear-lag model to determine shear strength τ_f and shear modulus G .⁵ This will require some additional input from both experiments and modeling. As an example, MD simulations of idealized shear interactions between two graphene sheets exhibiting the same functionalizations as these CNTs could be developed to estimate the shear moduli of the functionalized tubes. By establishing values for G through modeling and acquiring more force-versus-overlap data points through experiments, shear strength τ_f can also be estimated for each type of functionalization. The functionalization that provides the highest shear strength and lowest modulus would be characterized as the most desirable, as it achieves high strength while effectively inducing interactions along the largest interaction areas of the tubes.⁵ As such, an integrated experimental-computational approach can quantitatively define an optimal functionalization among this set which could, potentially, be integrated into larger-scale CNT-based fiber studies.

In addition to finalizing our investigations with these functionalizations, in collaboration with the **Nguyen group**, we also plan to investigate the shear behavior of additional functionalizations with longer and more compliant crosslinks. In particular, we aim to experimentally measure force-

versus-overlap trends for nanotubes functionalized with propionic and tri-propionic acid. These functionalizations can be compared directly to the benzoic acid studies, as they each bridge carbon bonds to benzene rings that terminate in hydrogen bonds, albeit with different carbon chain lengths and functional group densities. Schematics of each functionalization are shown below.

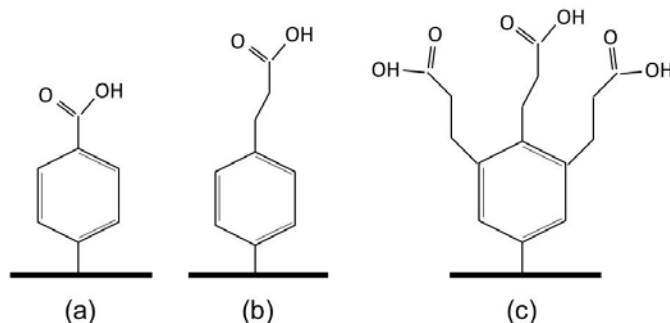


Figure 18. Schematic of functionalizations to be investigated through in situ SEM testing. (a) Benzoic acid. (b) Propionic acid. (c) Tri-propionic Acid. Thick black lines correspond to the outer shells of MWCNTs in these schematics.

By studying each of these functionalizations, we can determine whether longer carbon chains improve interactions (in terms of strength and ductility) with respect to the relatively short benzoic acid functional groups. Furthermore, by distributing propionic acid groups and comparing their shear properties to tri-propionic acid groups (at equivalent chemical concentrations), we may gain additional insights into the effect of grouping versus distributing functionalizations. Preliminary investigations into the effect of grouping have been performed in MD peeling simulations by the **Buehler group**. Adapting such simulations to investigate shear with matching functional groups and concentrations, combined with experimental studies, may provide valuable insights into optimizing shear interfaces between carbon nanotubes.

5. *In situ* SEM MWCNT peeling

As noted earlier, in the context of fracture mechanics, studying the peeling behavior of carbon nanotubes can provide insights into their Mode I fracture properties. In addition to evaluating Mode I versus Mode II properties, there are several other distinctions between the MWCNT shear and peeling tests that merit discussion. While the shear tests have incorporated several types of functionalized tubes, the peeling tests have focused on bare tubes and graphene to-date, with investigations of functionalized systems as a next step to consider. Furthermore, while the shear studies are designed to measure shear forces for different tube-tube overlap lengths, the MWCNT peeling studies aim to acquire estimates of surface energy. We will compare the experimentally determined surface energy of the interface between a MWCNT and a graphene surface, and compare this with empirical and theoretical values for graphite.¹³ This, in turn, can serve as a valuable baseline for experiments with functionalized samples in the future. In a broader context, studying the peeling failure of individual MWCNTs at the nanoscale is a complement to the aforementioned MWCNT shear studies. The goal of this study is to acquire insights into the peeling behavior that could be expected within a CNT-based yarn and propose methods of inhibiting peeling failure.

Peeling behavior of carbon nanotubes and carbon nanotube bundles has been studied before, both experimentally and computationally.¹⁴⁻²⁰ Many of the experiments rely on atomic force microscopy (AFM) to investigate peeling behavior for various reasons, such as the instrument's high spatial resolution, precise force resolution, and excellent experimental repeatability.¹⁴⁻¹⁶ However, an *in situ* SEM study enables direct visualization of CNT peeling, which the AFM cannot

provide.^{17,18} This study aims to provide two key contributions to the area of carbon nanotube peeling. First, by testing both bare and functionalized carbon nanotubes, we aim to demonstrate the mechanical benefits of functionalization in Mode I through direct quantitative comparisons. In addition, by recording experimental peeling behavior and performing simulations with the **Schatz** and **Buehler groups**, we aim to evaluate various components of interaction energy, providing a more comprehensive understanding of the nature of peeling to be expected within a CNT-based fiber.

In this study, as-produced arc-discharge MWCNTs are placed on a TEM grid. A sample of primarily monolayer graphene is also placed into the SEM chamber. A CNT is brought into contact with an AFM cantilever of known stiffness, and attached to the AFM cantilever via amorphous carbon deposition. A schematic of the process is shown below in **Figure 19**.

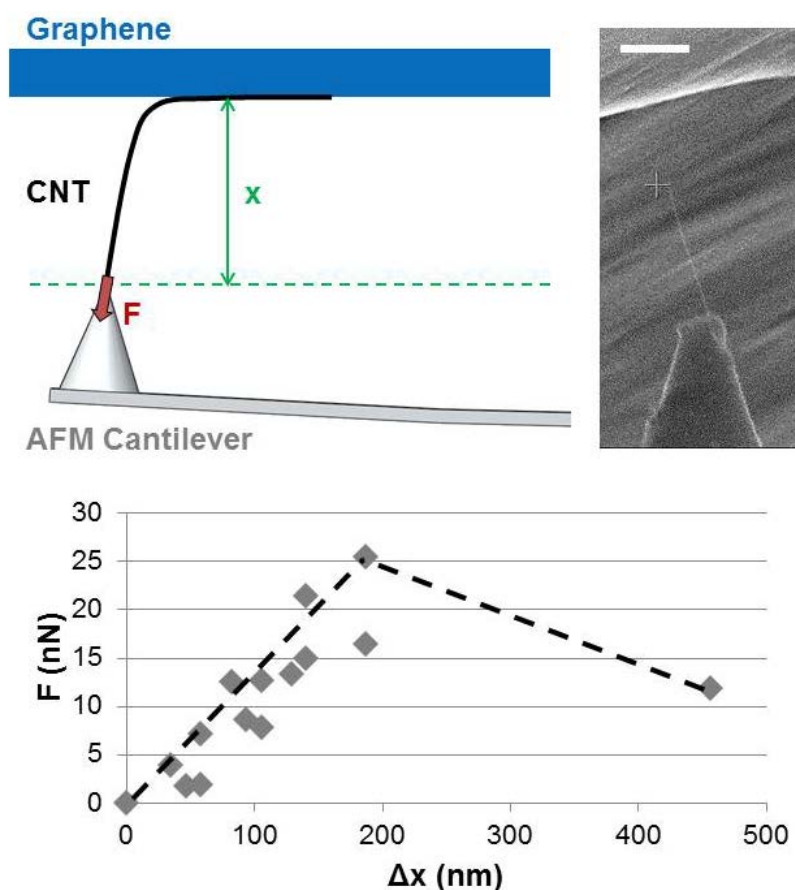


Figure 19. In situ SEM MWCNT Peeling Experimental Overview. Top left: schematic of MWCNT peeling procedure. Top right: SEM picture of AFM cantilever peeling CNT from graphene. Scale bar: 1 μm . Bottom: sample force-vs.-displacement curve based on SEM images recorded at various points throughout a peel test. Dashed line is a guide for the eye.

By manipulating the cantilever and the SEM stage, the CNT is brought into contact with the graphene and gently pushed down onto the surface, forming a “line contact” between the CNT and the graphene.²⁰ The stage is then pulled away at a constant rate. As the stage pulls away, changes in the shape of the carbon nanotube are recorded as a means to estimate bending energy at different stages. Simultaneously, the AFM cantilever acts as a force sensor whose deflections throughout the test can be converted into forces exerted on the CNT. Successive peels of the carbon nanotube are typically observed until the tube transitions from a “line contact” to a “point contact” and, ultimately,

a free cantilevered tube, as predicted by simulations.²⁰ Provided no permanent deformations are observed on the CNT, the peeling test is repeated in new regions of the graphene substrate.

Analysis of these peeling tests principally relies on the classical work of Kendall.²¹ Kendall assumed that an elastic, inextensible material peeled from a rigid substrate would maintain a consistent shape during peeling, leading to a differential relation between energy components at the onset of peeling:

$$\delta W_{ext} = \delta E_{adhesive} + \delta E_{elastic}$$

where δW_{ext} refers to external work exerted on the CNT, $\delta E_{adhesive}$ denotes adhesive energy (i.e. the energy required to create additional interface area), and $\delta E_{elastic}$ represents the change in stored elastic energy. Applying Kendall's formula to our CNT-graphene system, we obtain

$$F(1 - \cos(\theta)) = Gw - \frac{F^2}{2E\pi dt}$$

where F stands for the applied force, θ refers to the peeling angle with respect to the surface, G corresponds to the Mode I energy release rate of the material, w signifies the contact width between the CNT and the graphene, E is the modulus of the CNT (here assumed to be 1 TPa⁷), d stands for the CNT diameter, and t denotes the thickness of the CNT (here assumed to be 0.34 nm, the accepted value for graphene interlayer spacing).

While we can rearrange this equation to solve for the energy release rate, G , we ultimately want to experimentally determine the surface energy, γ , of the CNT-graphene interface. γ is a material property that can be compared to established values in the literature: in particular, the surface energy of graphite has been experimentally determined to be 0.2 Joules per square meter.¹³ If we assume that the MWCNT peeling can be characterized as an infinitesimal crack propagation in a linear elastic material,²² then the energy release rate and surface energy can be related by

$$G = 2\gamma$$

In other words, the energy release rate equals the energy required to create two new surfaces in this study: one on the graphene and one on the MWCNT. The mathematical relations between all these terms can be summarized as follows.

$$\gamma = \frac{1}{2}G = \frac{1}{2w} \left\{ (F(1 - \cos(\theta)) + \frac{F^2}{2E\pi dt}) \right\}$$

While the Kendall analysis is regarded as an established peeling analysis,¹⁷ we recognize that some of the assumptions in Kendall's formula may not hold for our CNT peeling. For example, the carbon nanotubes do not always maintain a self-similar shape before and after peeling, so changes in bending energy may be important. The effects of radial deformation and amorphous carbon deposition on the CNTs are also being investigated in collaboration with the **Schatz group**. In light of these possible discrepancies with respect to the Kendall analysis, it is worth noting that an alternative, integration-based method is also being investigated. By simply integrating the force-vs.-displacement curve from *in situ* SEM images from the moment before peeling to the moment after peeling (i.e. between sequential frames), an upper bound estimate of surface energy can be estimated. Such an analysis is an upper bound because it assumes a steady decline in force during peeling and combines all potential energy dissipation sources into surface energy. Nevertheless, comparing the two forms of analysis may provide additional insights into the role of other sources of energy dissipation.

In an effort to summarize the data acquired thus far, we will use the Kendall analysis to plot surface energy γ as a function of peeling angle θ for bare MWCNTs peeling from non-functionalized graphene. These results are plotted in **Figure 20**.

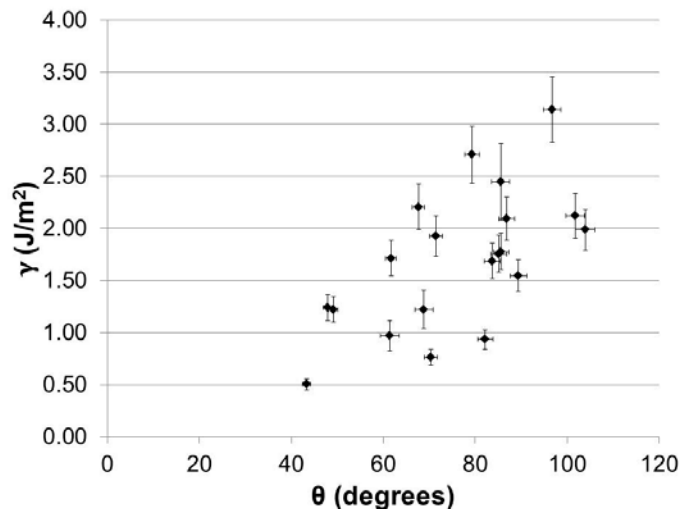


Figure 20. Surface Energy (γ) vs. Peeling Angle (θ) from in situ SEM Experiments. Preliminary analysis suggests that surface energy calculated with Kendall's formula increases with peeling angle. Statistical analysis and, perhaps, additional tests are required to establish this more conclusively.

Although a thorough statistical analysis and, perhaps, additional repeated tests are required to establish a more substantive relationship between these parameters, preliminary results suggest that surface energy increases with peeling angle. This stands in contrast to the notion that surface energy is a material property—in other words, surface energy should be constant regardless of the peeling angle. This initial trend, however, suggests that there may be some additional sources of energy dissipation that become especially prevalent at higher peeling angles. As such, it is possible that our initial assumptions—that the peeling process can be treated as infinitesimal crack propagation within a linear elastic material—may not hold for this study. While additional tests may improve confidence in the results, it is worth noting that low peeling angles are difficult to obtain experimentally due to potential interference between the AFM cantilever and the graphene substrate (see **Figure 19**).

In addition to remaining questions regarding the trend of γ versus θ , there is also some uncertainty regarding the values of γ obtained to-date. All of these values are well above the theoretical value of γ (0.2 Joules per square meter) reported in the literature.¹³ In this regard, the primary remaining uncertainty with respect to analyzing the value of γ is the contact width of the CNT-graphene surface. While we initially regarded the MWCNT as a rod with limited flattening for our analysis, MD simulations by the **Schatz group** have suggested that the tubes under consideration may flatten significantly, increasing the effective contact width as defined in Kendall's formula. Increasing the effective contact width would, in turn, decrease the measured surface energy γ , essentially decreasing each of the values reported in **Figure 20** by a factor of 5-10. Consequently, for the purposes of comparing the measured surface energy with the established standard for graphite, obtaining a reliable estimate of contact width is an essential next step we are currently pursuing.

In summary, the **Espinosa group** has successfully demonstrated a novel method of *in situ* SEM peeling of multiwalled carbon nanotubes from graphene surfaces. This experiment can be used to provide an estimate of surface energy and will serve as a valuable baseline study for measuring the improvements in adhesion afforded by chemical functionalization. The contributions of other energy factors still need to be more thoroughly evaluated. Through collaborations with the **Schatz** and **Buehler groups** who are also performing MD simulations of carbon nanotubes in peeling, we aim to produce a comprehensive understanding of nanoscale CNT peeling, offering insights into optimal functionalization architectures to be used in larger-scale CNT-based fibers.

6. Atomistic modeling of peeling functionalized CNTs

Functionalized carbon nanotubes have tremendous applications in the fabrication of polymeric carbon fibers. However, approaches to design carbon nanotube (CNT) structures by using functional groups as 'glue' and carbon nanotubes as stiff 'backbone', aimed at enabling superior mechanical strength and toughness at the fiber level with limited amount of materials, remains poorly understood. Inspired by the outstanding mechanical properties of spider silk, here we explore a bio-inspired structural model of carbon nanotube based fibers connected by weak hydrogen bonds (H-bonds) formed between functional carboxyl groups as the molecular interface. Here a systematic study of the deformation of H-bonds in functional groups is carried out to assess how it is affected by the structural organization of the carboxyl groups. We perform full atomistic simulations using the first principles based ReaxFF force field to show how the grouping of functional groups can significantly improve the interface mechanical properties of CNTs.

We carry out peeling of functionalized CNTs for random and grouped cases as shown in **Figure 21a-b**, where the random case corresponds to carboxyl groups randomly distributed on each CNT and grouped case corresponds to combining 3 carboxyl groups at a single node for each CNT. The density of functional groups is one functional group per 65 carbon atoms for the random case, and is consistent with the experimental values reported by **Nguyen group**. Simulations are carried out at 300 K with bottom CNT fixed and force applied to top CNT end as shown in **Figure 21a-b**. The force-displacement data is plotted as shown in **Figure 21b** for a peeling angle of 90 degrees. Force-displacement for grouped case shows plateau regions before failure indicating cooperative H-bond deformation. Force-displacement for random case shows abrupt failure. These results clearly indicate that grouping improves the interface mechanical properties of CNTs functionalized with carboxyl groups.

The key findings of the simulations that will aid the experiments (to be conducted by **Espinosa group**) is that the spacing of functional groups in random case needs to be ≥ 10 Å (for 3-5% water content) in order to distinguish the mechanical properties of grouped vs. random distribution of carboxyl groups. Higher water content (>5%) will lead to clustering of functional groups in random case.

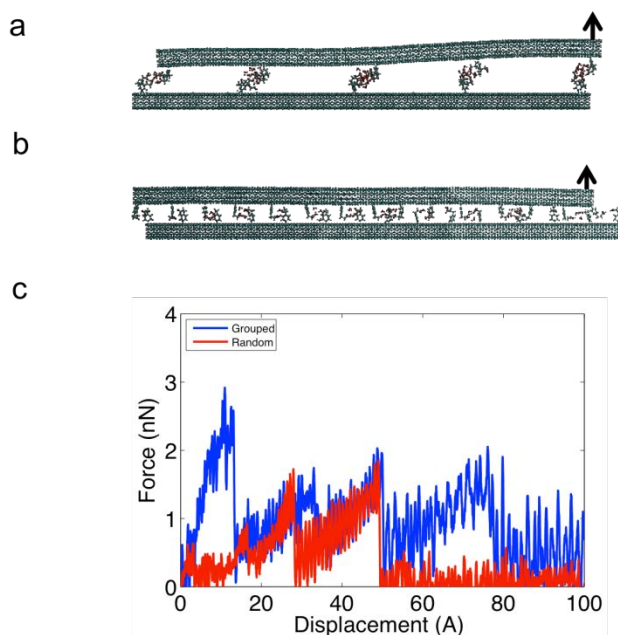


Figure 21. Distribution of carboxyl groups on CNTs for peeling test at 90 degrees, (a) Grouped case, (b) Random case. (c) Force-displacement relation for grouped and random cases at 90-degree peel angle shows abrupt failure for the random case.

7. Coarse-grain modeling

A coarse-grain model is developed for CNT functionalized with carboxyl groups, where the parameters of the model are derived from our atomistic studies, applied to study CNTs of larger diameters and lengths. By applying shear loading, we study how the deformation of H-bonds in functional groups is affected by the structural organization of the carboxyl groups, as well as by the geometry of constituting carbon nanotubes. The analysis of H-bond deformation fields is used to compute the extent of significant deformation of inter-CNT bonds, defining a region of cooperativity. We utilize an exponential function ($\exp(-x/\xi)$) to fit the deformation of H-bonds, with the cooperative region is defined by the parameter ξ , and where a higher value of ξ represents a slower exponential decay of displacements of carboxyl groups from the point where the load is applied (**Figure 22a**). Hence, the parameter ξ characterizes the number of carboxyl groups that participate in the deformation of CNTs under shear loading. The cooperativity of deformation is used as a measure for the utilization of the chemical bonds facilitated by the functional groups. The analysis of H-bond deformation fields from the coarse-grain model is used to compute the extent of significant deformation of inter-CNT bonds, defining a region of cooperativity. The cooperativity of deformation is used as a measure for the utilization of the chemical bonds facilitated by the functional groups.

Each red line in **Figure 22b** corresponds to the interaction between two carboxyl groups connected via two H-bonds. The spacing between the functional groups is b and the CNTs are separated at a distance of d from each other. We use harmonic springs to describe the tension and compression properties of the CNT segment (blue blocks of the length of b in between any two of the neighboring carboxyl groups). The stiffness of the CNT segment is $K_1 = K_g w/b$, where $K_g = 289$ N/m is the average stiffness of graphene sheet with unit width and unit length (based on atomistic-level modeling) and $w = \pi D$ is the cross-section perimeter of the CNT (D is the diameter of CNT). Another set of harmonic springs is applied to describe the two carboxyl groups connected via a pair of H-bonds (red lines of the length of d in **Figure 22b**). The shearing stiffness of these springs is K_2 and is a function of the hydrogen bond energy.

We investigate whether by varying the distribution of the density of carboxyl groups along the CNT axis; the characteristic length ξ can be increased. Here we adjust the grouping and change the grouping (N) along the axis of the CNT, making $N=N(x)$ in order to reach a decreasing K_2 as a function of the distance from the loading point. Here we take $K_2(x, x \leq L/2) = Ax^{-\alpha}$ (by controlling $N=N_0x^{-\alpha}$), where α is a positive dimensionless factor. We test different values of α with $K_1=33,890$ pN/Å and a spacing of $b=8.526$ Å and observe the cooperative length as a function of α as given by **Figure 22b**. It is shown that $\alpha = 1.5$ corresponds to the maximum cooperative length of $\xi=93$ Å (**Figure 22b**), which is approximately five times the original characteristic length ($\xi=27$ Å corresponds to $N=0$). While manufacturing such CNTs with distributed densities of carboxyl groups may be difficult, this result points to a possible engineering design that can vastly improve the performance of CNT fibers.

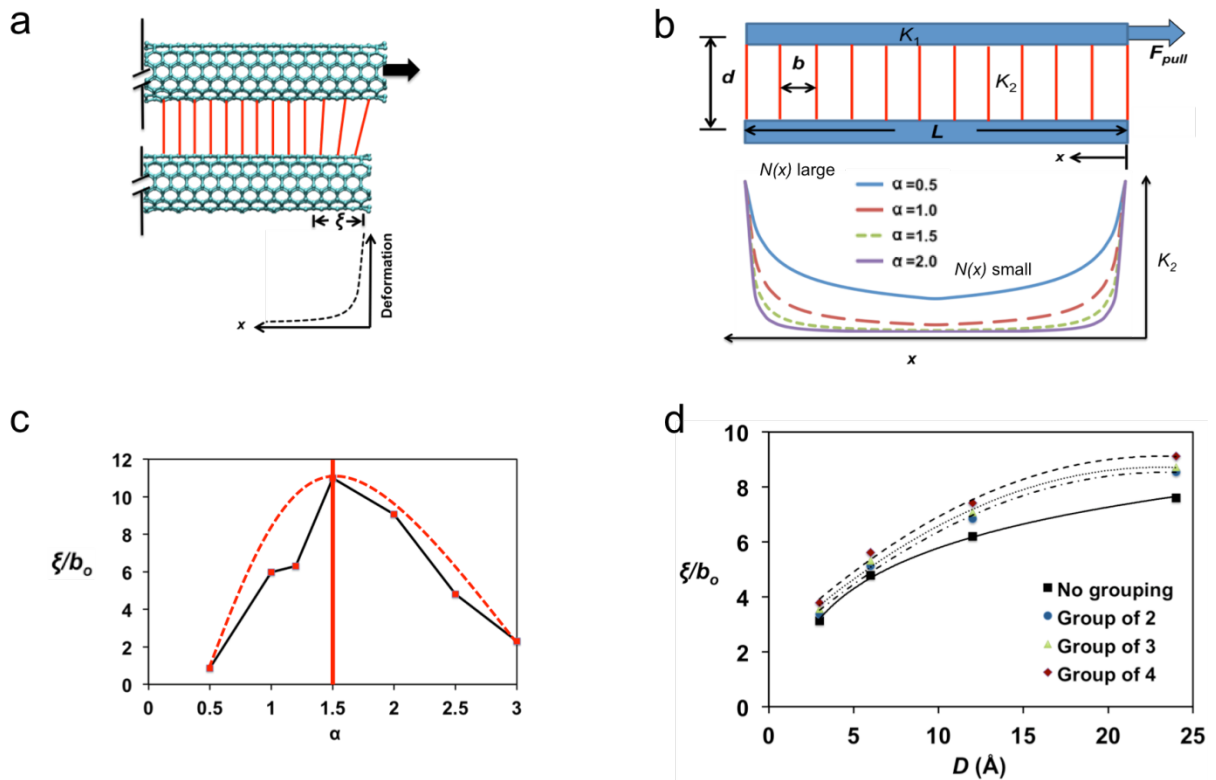


Figure 22. (a) Deformation of carboxyl groups (red lines) near the end of CNTs under shear loading. The deformation profile shows an exponential decay of displacements along x and the characteristic length ξ is also shown, (b) The variation of stiffness K_2 along the length for different alpha values for a CNT of diameter $D = 3.2$ Å. (c), Cooperative length as a function of non-uniform distribution of the clustering of carboxyl groups, achieved by making $N=N(x)$. The results show that corresponding to $\alpha = 1.5$ yields a maximum cooperative length as $\xi = 93.76$ Å, significantly increased from $\xi \approx 27$ Å for the case of no grouping and uniform distribution, (c) Variation of characteristic length for no grouping and groupings of $N= 2,3$ and 4 as a function of CNT diameter D shows that as the CNT diameter increases, the normalized characteristic length increases. As the grouping increases the normalized characteristic length also increases. This result is important since it reveals that the effect of structural organization of functional groups is not only seen in very small diameter CNTs, but that larger diameter CNTs also benefit from the effect of grouping functional groups.

We find that for ultra-small diameter CNTs below 1 nm the external force deforms H-bonds significantly only within a relatively small region on the order of a few nanometers. We find that the mechanical properties of carbon nanotube fibers are affected by the organization of H-bonds in functional carboxyl groups. Both, the grouping of functional groups into clusters, and a specific variation of the clustering of functional groups along the CNT axis are shown to be potential strategies to improve the cooperativity of deformation. This allows for a more effective utilization of functional groups and hence, larger overlap lengths between CNTs in fibers. The effect of structural organization of functional groups is not only significant in very small diameter CNTs, but also in larger diameter CNTs (**Figure 22d**) as they are most commonly used for engineering applications.

8. Modeling MWCNT peeling experiments

The MWCNT peeling experiments are of interest in determining the interactions between nanotubes and simple surfaces such as graphene. Our studies are designed to provide benchmark results for comparison with experiment that can be used to sort out mechanistic issues concerning the origin of the adhesive interaction, of nanotube deformation on surfaces, and of the influence of

graphitic deposits. Several components of this work are described below, along with some preliminary results.

a. Adhesion

Calculations to determine the origins of the adhesion force in the peeling experiments have been performed using simple models. If one considers the van der Waals energy associated with the creation of new surface as the peeling is performed, one can account for the force using known interactions for graphite. The calculations assume nearly-complete relaxation of the tubes against the graphene surface and use the interaction energy between layers in graphite. Full relaxation should be a good approximation, as the tubes are large in diameter. The use of the interaction energy in graphite should also be a good approximation, as the outer tube wall will act similarly to a graphene layer as far as van der Waals energy is concerned. The relaxation of the tube as it is peeled from the surface will reduce the energy necessary for the peel. We are performing MM3 calculations to estimate the various energies involved, and to check the full-relaxation hypothesis.

b. Radial deformation of MWCNT's during adhesion.

Recent MD studies²³ of single-walled CNTs reported that *"the adhesion energy is very close to the net vdW energy when the adhesion system is free of adhesive deformation...The degree of the radial adhesion deformation increases dramatically with increasing tube diameter."* Additional shells may reduce radial adhesion deformation of CNT and may alter value of the adhesion surface energy. Hertel et al.²⁴ show such trends for CNTs with outer diameter range from 1 to 10nm and number of shells varied from 1 to 8.

Taking into account outer diameters (~30nm) and number of shells (~10-11) in current experimental samples, one would suspect that experimental MWCNTs are not forming solid-cylinder shapes when fully adsorbed on a graphene substrate. In this case, surface energy equation for a continuum nanorod would be not applicable for post processing experimental results. Thus, we are performing a systematic study of radial adhesion deformation as a function of number of shells in pristine carbon nanotubes (see **Figure 23**). Corresponding isolated CNTs, and CNTs on a graphene surface have been fully relaxed under periodic boundary conditions. The contact width of cylinder-shaped tubes was calculated according to continuum model equation (see black line on **Figure 23**) using diameters of fully relaxed isolated samples. Real contact width values were measured from fully relaxed tubes on graphene substrate samples (blue, red, purple and green lines on **Figure 23**). Based on the four examples from the **Figure 23** one sees that for diameters comparable to the experiments (~30 nm) there is a strong likelihood that samples undergo radial adhesion deformation and no longer maintain a solid-cylinder shape. Therefore, application of solid-cylinder model for post processing will underestimate values of contact surface energies and introduce significant errors into adhesion energy measurements. The variation of radial adhesion deformation energy with diameter of the tube is also under investigation. Data available at the moment (**Figure 24**) shows a distinct gap between single-walled tubes and tubes with any other number of shells. For example, there is almost a 50% energy increase observed when moving from a single-walled tube to a double-walled tube. At the same time, a minor energy increase is observed when the number of shells increased from 2 to 3, and 3 to 4. The common trend for tube of any number of shells is that energy per unit area required to deform it becomes constant after tube reaches a diameter value of approximately 30nm.

In further work, the variation of the binding energy for tubes with number of shells up to the experimentally observed value will be computed and checked for its van der Waals, and radial deformation (due to adhesion) components. These results will be used as guidelines for selection of mathematical models during post-processing of experimental data on peeling CNTs with varying number of shells.

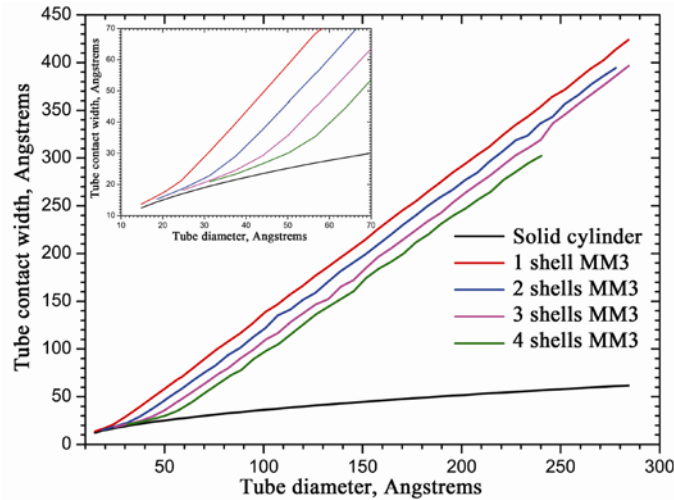


Figure 23. Contact width as a function of tube diameter. MM3 calculated values (red, blue, purple and green curves). Corresponding values calculated according to a solid-cylinder model (black curve). Solid-cylinder width= $d \cdot \sqrt{1 - (1 - 0.68/d)^2}$, where d is the outer diameter of the fully relaxed isolated tube.

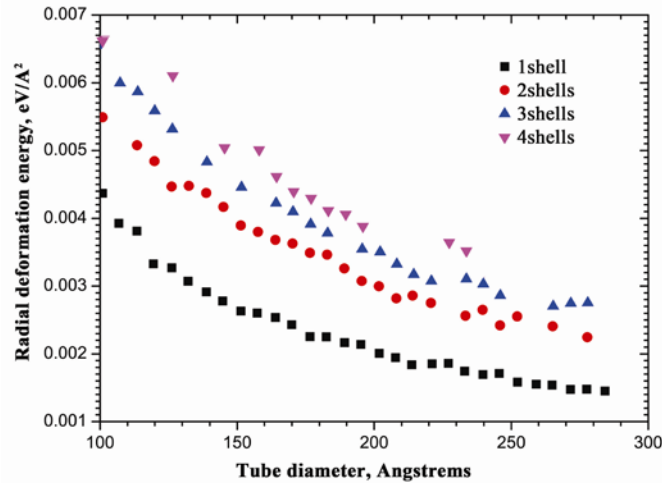


Figure 24. Radial deformation energy as a function of diameter of the tube. Value is calculated as a difference between adhesion energy and van der Waals energy.

c. Effect of carbon deposits (flakes) on MWCNT peeling

In this part of the project we are studying the effect of carbonaceous materials, including polyaromatic hydrocarbon flakes, fullerenes and onion-like structures on the peeling experiments. Such graphitized structures are always found on the surface of MWCNTs grown by arc-discharge (3000-4000°C and 25V). XPS analysis performed by the Nguyen group on the arc-discharge-produced powder show 100% carbon content, but with 40-50% of the surface of purified MWCNTs (after extraction of large onion-like structures and thermal treatment) covered with graphitized carbon deposits. Taking into account TEM data, and the insignificant intensity of the Raman D peak it appears arc-discharge-grown tubes have fewer defects than CVD-grown tubes, however the effect of the carbon deposit on mechanical behavior needs to be assessed in order to interpret the results.

Our modeling of carbon deposits for peeling tests was based on the assumption that various shaped and folded graphene flakes, as well as the tiny onion-like structures, are left on the surface after extraction of large onion-like structures. Unfortunately we have limited experimental input on the structure of these deposits, so we have developed a few model structures to generate

representative results. In order to reduce the number of dangling bonds, graphene flakes formed at the surface of CNTs during the synthesis will do one of three things: (1) become covalently attached to existing defects on the walls of the CNTs, (2) fold into onion-like structures or (3) stay semi-straight and become functionalized with hydrogen atoms at their edges. The current part of the project is dedicated to cases 2 and 3 (which are probably more common) where the graphitized carbon deposits adhere to the walls of the CNTs by means of dispersion interactions.

As a preliminary step to the peeling calculations, the adhesion energy was calculated for completely adhered tubes. Values of the adhesion energy for various carbon deposits (as described in **Figure 25**) were compared to the adhesion energy of corresponding pristine tube. Despite their structure and position, the individual graphitized structures do not significantly change the adhesion energy (by no more than 14%). The calculations suggest that the carbon deposits affect the adhesion energy by changing the adhesion surface.

We have simulated the peeling experiment by pulling a finite length nanotube from a flat graphene surface by applying a force to one end of the tube that is perpendicular to the surface. Due to the limitation of computational resources, smaller diameter DWCNTs are used in place of MWCNTs. The size of the individual graphitized carbon structures is kept to minimum from what is seen in TEM images. Due to the insignificance of end-point effects in the peeling tests, the ends of the simulated tubes were capped with hydrogen atoms. The peeling simulations were done for finite size pristine DWCNTs, DWCNTs with individual graphitized structures at different positions, and DWCNTs with some amount of randomly positioned graphene flakes and fullerene-like structures. The concentration of carbon deposit in the latter model was significantly smaller than is observed in experimental samples. However, the latter model was generated in order to see trends in the deviation of ideal single-structure carbon deposits from experimentally observed graphitized structures.

Changes in the total potential energy for each model have been monitored as a function of peeled separation starting from the fully adhesive state (see curves in **Figure 26**) and up to complete detachment. For all the nanotube structures, there is a transition (sudden change in energy) in **Figure 26** from an “S-shaped nanotube” stage, in which one end of the tube is still tangent to the surface, to a “point contact” stage in which the tube end touches the surface. **Figure 26** shows that this transition is delayed by the carbon deposit, independent of the shape and position of the carbon deposit. Thus there are small peaks in most curves at ~ 7nm compared with the peak in the black curve peak at 6.5nm for the pristine tube. This transition is even more delayed for randomly positioned structures (small peak on purple curve ~ at 8nm in **Figure 26**).

Prior to reaching the point contact position, the carbon deposit plays a small lubricating role during the peeling by smoothly sliding along the tube. This sliding reduces the energy needed to shear two graphene layers along the different registries. Shifting the deposits along the radial direction of the tube, flake flattening (which produces the large peak in the purple curve at 5 nm), and motion strictly perpendicular to the substrate surface (parts of the curves after 19.8nm) cause a dramatic increase in energy.

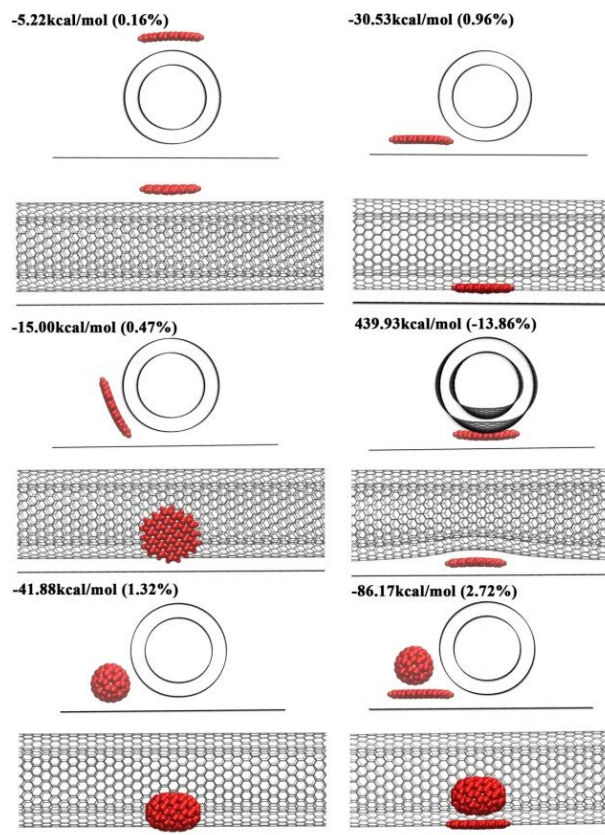


Figure 25. Effect of carbon deposit position on the relative adhesion energies of DWCNT. Values are shown at the top of each structure in kcal/mol (or %) were calculated from the following equations: $\Delta E_{adh} = E_{adh} - E_{adh}^0$; and $\% \Delta E_{adh} = 100 * \Delta E_{adh} / E_{adh}^0$. Where $E_{adh}^0 = E_{POT_tube/graphene} - E_{POT_tube} - E_{POT_graphene}$ and $E_{adh} = E_{POT_flake/tube/graphene} - E_{POT_flake/tube} - E_{POT_graphene}$.

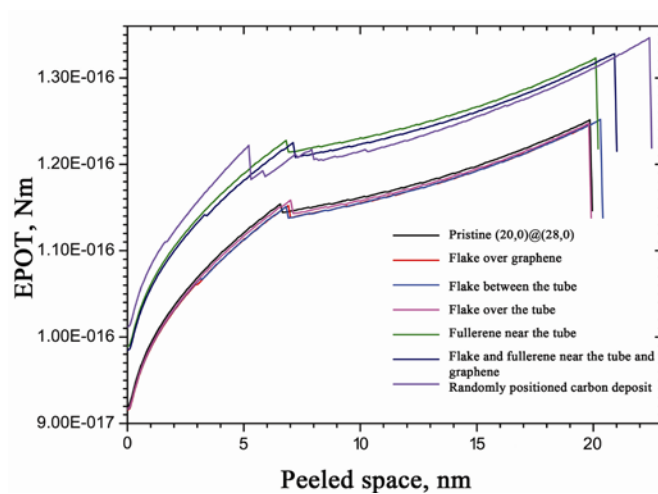


Figure 26. Variation of total potential energy of the system versus peeling separation during the peeling test simulations.

Engineering lateral interactions within CNT yarns

1. Surface Manipulation and Analysis of Multiwall Carbon Nanotubes

The **Nguyen group** is working with the **Espinosa and Buehler groups** to evaluate the chemomechanical factors that affect the properties of the interface between two MWCNTs. A necessary preliminary experiment has been characterization of the outer surface of arc-discharge MWCNTs that provide the measured mechanical interactions. With the **Espinosa group**, we have purified MWCNT using many of the procedures outlined in literature, and characterized their purity by scanning electron microscopy (SEM) and by High Resolution Transmission Electron Microscopy (HR-TEM). Despite all of the tested purification procedures affording perfectly pure MWCNT samples when examined by SEM, we found substantial impurities by HR-TEM. In addition to finding >10 nm regions of pristine outer wall surfaces, similar to images often presented in literature, at the >100 nm scale we observed substantial amounts of strongly-adhered carbonaceous impurities present on the MWCNT of each as-produced or purified sample. Interestingly, not only are these impurities stable against extremely harsh purification conditions that included multi-hour refluxes in concentrated nitric acid and high temperature calcination, but the bare regions of MWCNT outer walls also appear to be completely unaffected by the treatments. We ascribe these behaviors to the chemical similarity between the adhered impurities and the CNT and the superior crystallinity of the CNT walls, respectively. As these adhered impurities are unaffected by purification treatments, we have attempted to characterize their effects on MWCNT chemistry and on the mechanical properties of MWCNT interfaces (With the **Schatz group**).

As we have not been able to selectively remove these strongly-adhered surface impurities due to their chemical similarity with nanotubes walls, we have initiated the functionalization of the imperfect CNT surfaces with functional groups, including nitric acid oxidation and grafting of benzoic acid (**Figure 27**), and provided samples to the **Espinosa group** for mechanical analysis. Since we do not observe any damage to the outer walls of the MWCNT after harsh nitric acid oxidation, we hypothesize that the majority of the oxygen-containing functional groups introduced by this chemical treatment are located on the edges of the strongly-adhered impurities.

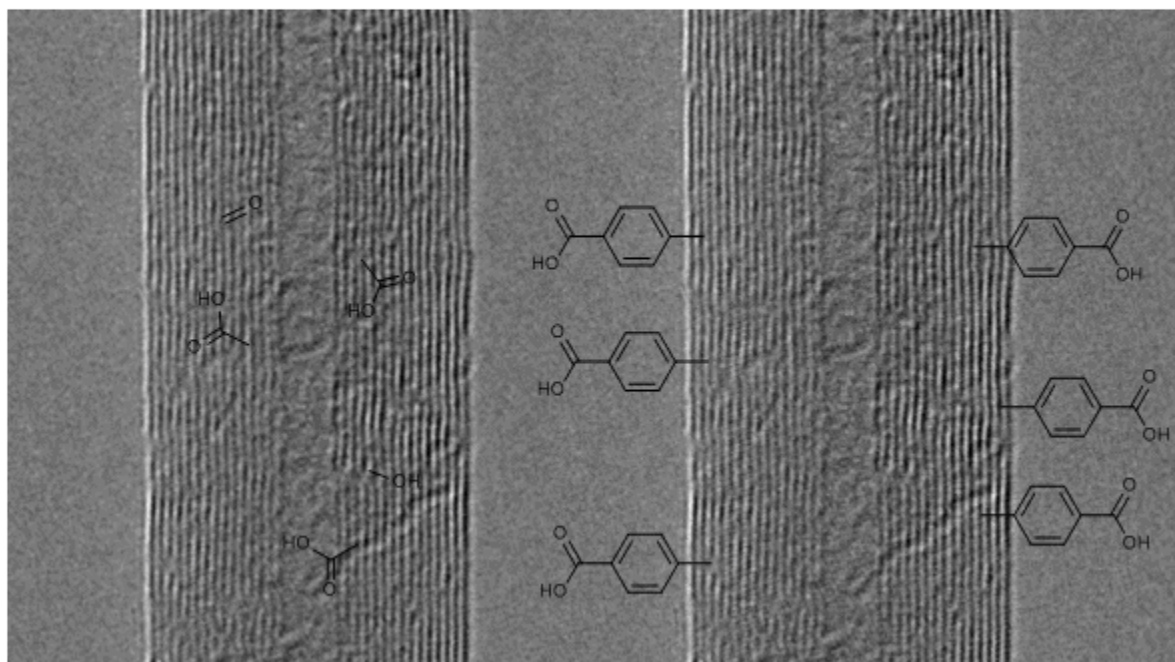


Figure 27. Schematics of functional groups on MWCNT after nitric acid-oxidation (left) and benzoic acid grafting (right).

Functionalization of graphene oxide monolayers-graphene oxide paper as a macroscopic model for DWNT-based yarns

1. Covalent crosslinking of graphene oxide

Because the functionalization chemistry of CNTs is difficult to control, we also continued a program to use graphene oxide papers as an easily manipulated macroscopic model to elucidate the best chemistry for strengthening the interface between two adjacent nanotubes or two adjacent bundles in a CNT-based yarn. Graphene oxide is a single-sheet nanocarbon material containing epoxide and hydroxyl groups on the basal plane and carboxylic acids along the edges. Under flow-directed filtration (**Figure 28a**), aqueous dispersions of these sheets can be used to fabricate paper-like materials with regularly spacing intersheet gallery space that retain all the oxygenated functional groups of graphene oxide (**Figure 28b**). The mechanical properties of these papers can thus be tuned in a facile fashion using a wide variety of chemical “crosslinking” schemes. For example, the incorporation of a small amount of tetravalent crosslinkers such as borate ions into the gallery spacing of the graphene oxide papers have significantly improved their mechanical strength and stiffness (25% and 225% respectively), albeit at the expense of their ductility. Attributing this to the presence of short and inflexible multivalent borate ester linkages, we hypothesized that divalent, flexible long carbon-chain crosslinks may afford a better combination of strength and ductility (**Figure 28c**). To evaluate this hypothesis, graphene oxide papers were functionalized with diamines of varying carbon chain lengths (C_n) length ($n = 0, 3, 6, 8, 12$; $n = 0$ represents non-functionalized graphene oxide paper) and subsequently characterized by X-ray diffraction (XRD) and Fourier-transformed infrared (FTIR) spectra.

Pristine graphene oxide paper shows a sharp intense XRD peak corresponding to an intergallery spacing of 8.6 Å. When functionalized with various diamines, the long alkyl chain can intercalate between the graphene oxide sheets as “spacers”, increasing the intergallery spacing to about 10.0 Å, 12.0 Å, 12.6 Å, and 13.0 Å for C^3 , C^6 , C^8 , and C^{12} -diamines, respectively as shown in **Figure 29**. This result is consistent with the fact that increasing alkyl chain length would progressively reduce the interactions between the adjacent sheets and increase the gallery spacing. The functionalization was also characterized by FTIR spectroscopy (**Figure 30**), which show a decrease in the carboxyl stretching at 1720 cm^{-1} along with the growth of a new peak at 1520 cm^{-1} for alkylammonium salts formed by the reaction between amine and carboxylic acid groups at the edges of graphene oxide sheets. Together with the appearance of strong alkyl stretches and deformations at 2920 cm^{-1} and 1470 cm^{-1} , the presence of N-H deformation at 727 cm^{-1} confirms the intercalation of amine molecules. Most importantly, the epoxide peak at 1250 cm^{-1} has decreased significantly due to the reaction of amine and epoxide groups at the basal planes of the graphene oxide sheets. The mechanical properties of these samples are now under investigation using DMA to evaluate the effect of this flexible divalent crosslinking. The results can then be used to elucidate the best interactions between the surfaces of two adjacent nanotubes or two adjacent bundles in a CNT-based yarn.

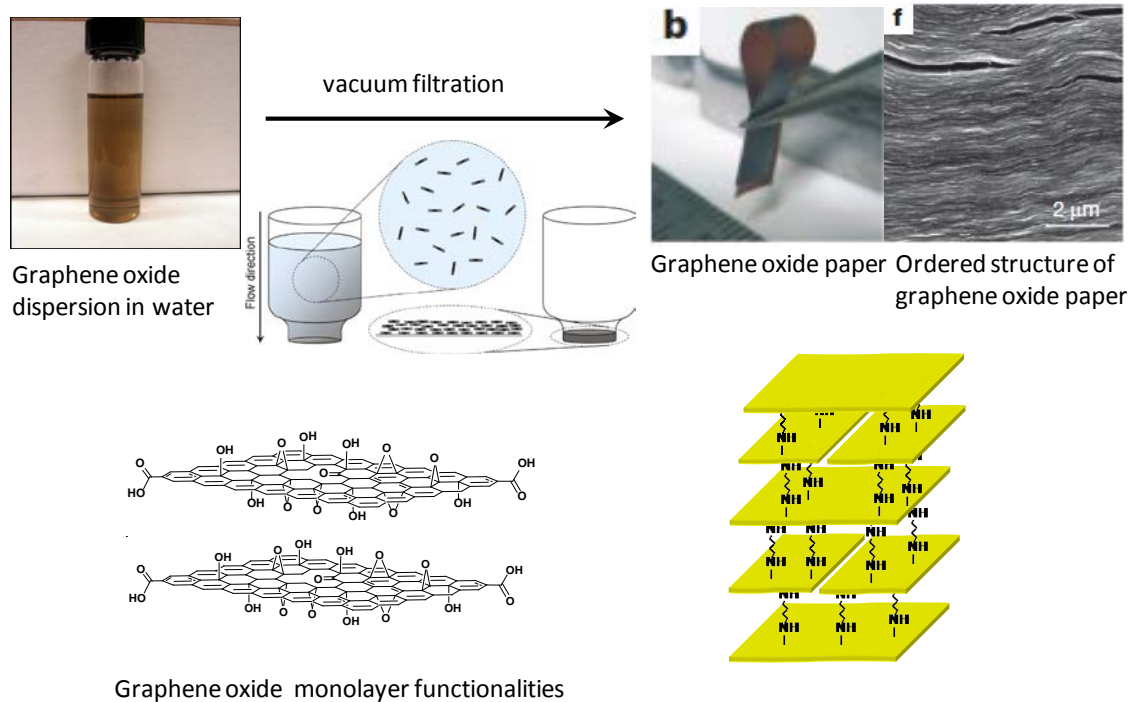


Figure 28. (a) Fabrication of self-assembled graphene oxide paper by flow-directed vacuum filtration, (b) graphene oxide functionalities, and (c) graphene oxide layered structure covalently crosslinked by flexible long carbon-chain diamines.

Figure 29. XRD spectra of GO papers functionalized with C^n -diamines ($n=0, 3, 6, 8, 12$; $n=0$ represents GO paper)

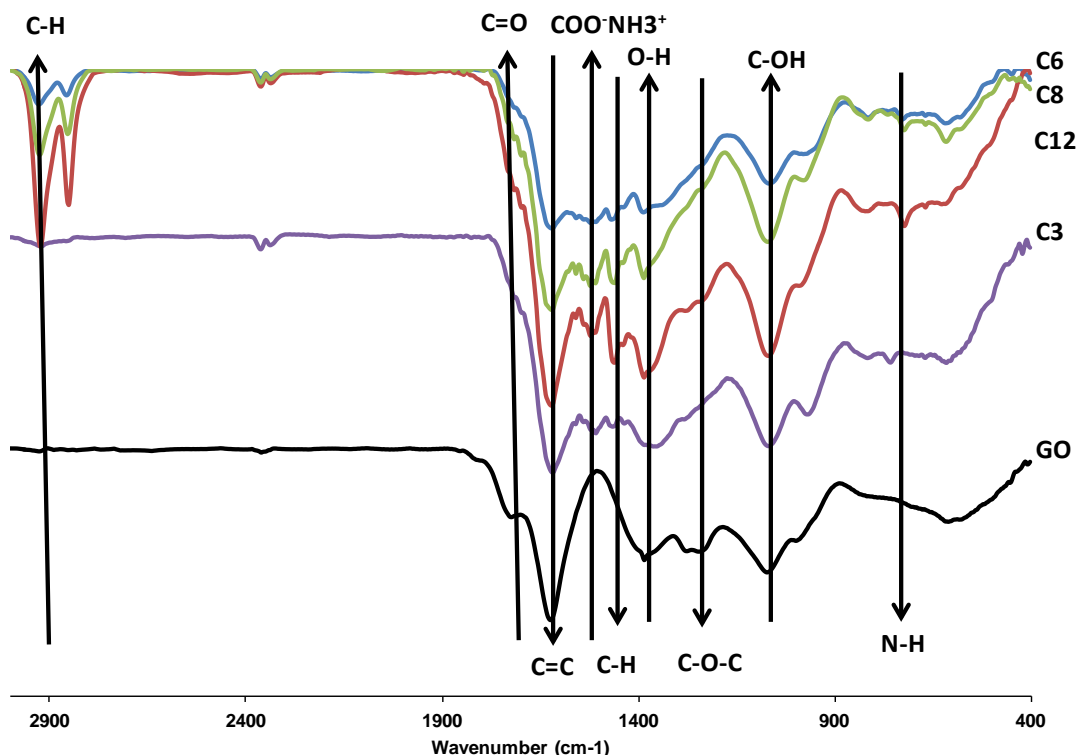


Figure 30. FTIR spectra of GO papers functionalized with C' -diamines ($n=0, 3, 6, 8, 12$; $n=0$ represents GO paper)

2. Disulfide functionalization and cross-linking of graphene oxide paper

A second type of chemistry for functionalizing graphene oxide paper is via disulfide crosslinking where the ability of disulfide bonds to reform after breaking may enhance the mechanical strength in the paper. Disulfide graphene oxide paper was prepared in a similar fashion as described above for the diamine. The thiol-functionalized graphene oxide paper is then fabricated by cleaving the disulfide crosslinks in disulfide-crosslinked graphene oxide paper with dithiothreitol (DTT) (0.1 M in methanol). The PXRD pattern for disulfide cross linked graphene oxide paper showed an increased spacing of 11.54 Å (**Figure 31**), as compared to the 8.33 Å peak corresponding to the graphene oxide paper (**Figure 32**). After DTT treatment, as the disulfide link cleaves, the PXRD peak shifts to a slightly lower value of 10.27 Å, which is expected because as the disulfide bond cleaves, the free thiol groups can spatially adjust their orientation. Elemental analysis (EA) indicates a S/C ratio of 0.078 in the disulfide crosslinked graphene oxide paper and 0.073 in the thiol-functionalized graphene oxide paper. These approximately correspond to 1S atom for 14 C atoms. The FTIR spectrum for disulfide functionalized graphene oxide paper exhibited adsorption bands for the C-N stretch of bound amine (**Figure 33**) and all expected stretches of graphene oxide. In addition, it also exhibits the peak corresponding to the disulfide bond.

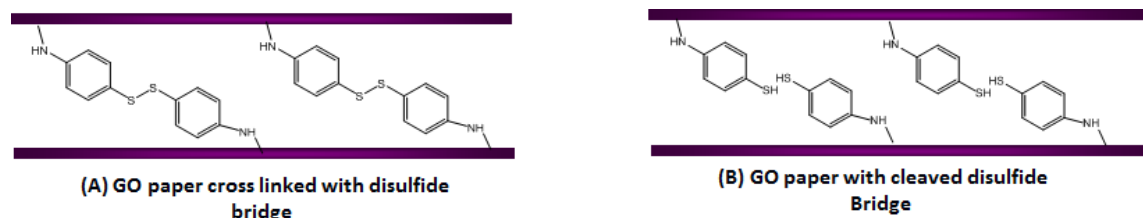


Figure 31. Schematics of graphene oxide paper crosslinked with disulfide molecules and graphene oxide paper with cleaved disulfide bridge

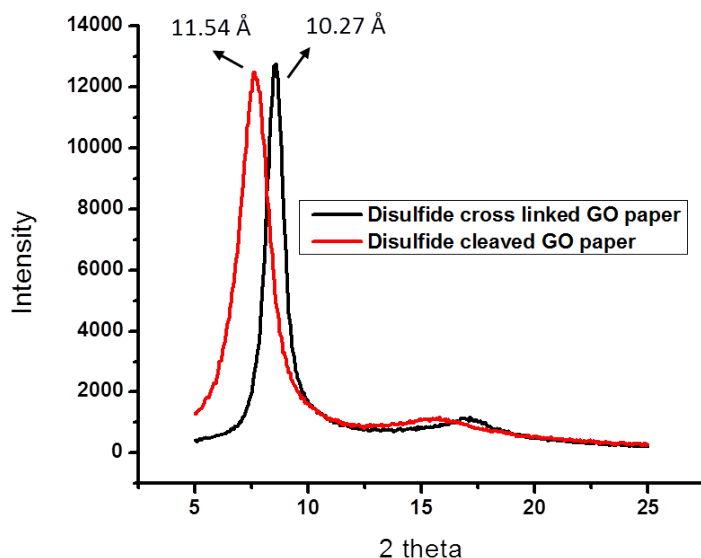


Figure 32. PXRD patterns for disulfide cross linked graphene oxide paper (black) and thiol functionalized graphene oxide paper (red). The slight reduction in the inter gallery spacing on cleaving the disulfide bonds is likely due to the formation of terminated thiol groups which have more spatial freedom as compared to the disulfide cross link

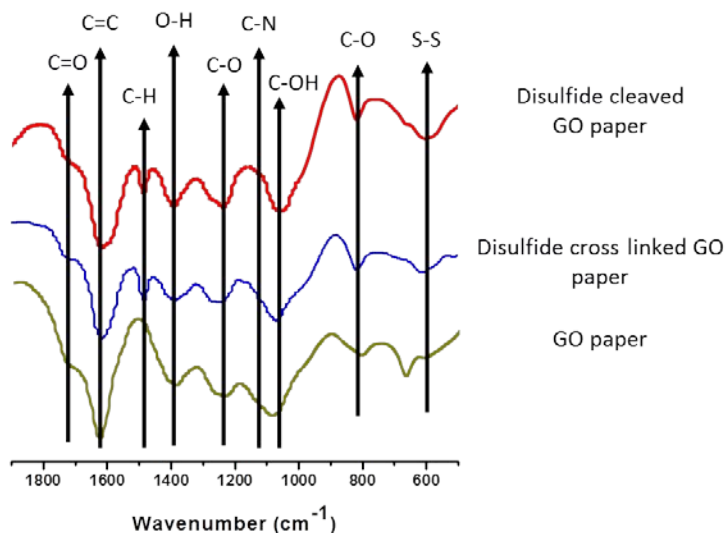


Figure 33. FTIR spectra for graphene oxide paper, disulfide cross linked graphene oxide paper and thiol functionalized graphene oxide (or disulfide cleaved) graphene oxide paper with assigned bending and stretching frequencies.

3. Preparation of disulfide-crosslinked graphene oxide composites

In addition to the aforementioned divalent molecularly crosslinked graphene oxide papers, we are preparing a paper that include both disulfide crosslinks and polymer mediator. To form the disulfide crosslinks within these composites, we are utilizing thiosulfate salts, a readily accessible and stable thiol and disulfide precursor (**Figure 34**). We synthesized poly (vinyl chloride-co-vinyl thiosulfate) from poly (vinyl chloride) by substitution of chloride groups by sodium thiosulfate, as well as prepared thiosulfate-functionalized graphene oxide *via* diazonium chemistry. Fabrication of

thin films using these materials is in progress, and we expect that they can be easily cross-linked by disulfide bonds by post-assembly oxidation using well-established thiosulfate chemistry.

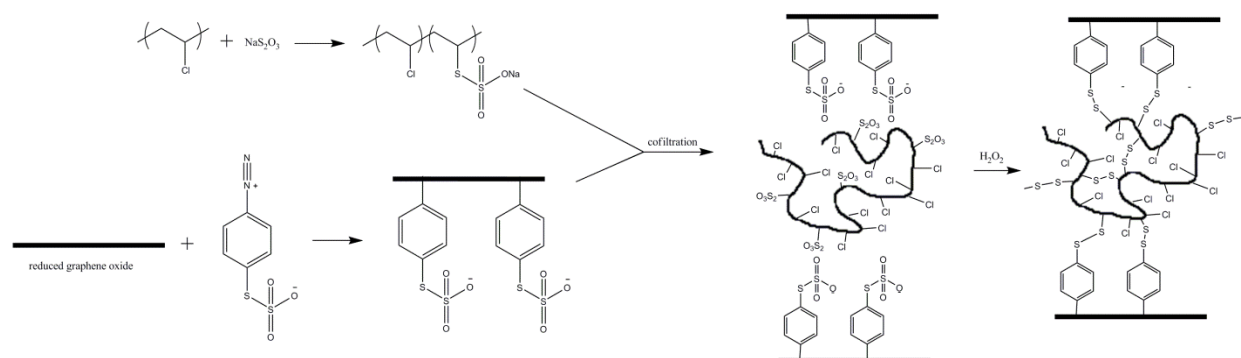


Figure 34. Synthesis pathway for preparing disulfide-crosslinked composites

4. Mechanical characterization of graphene oxide composites

The graphene oxide papers will be used as a test bed for experimentally determining the effectiveness of various interfacial chemistries in load dissipation or shear interface strengthening. In order to evaluate the effectiveness of the bonds introduced in the graphene oxide paper layers, the **Espinosa** group will perform mechanical tests on strips of the graphene paper. In particular, we will perform quasi-static monotonic tensile tests in addition to dynamic mechanical analysis (DMA), where we will subject the samples to temperature and frequency sweeps to measure the storage and loss moduli of the papers.

Fabrication/characterization/modeling of CNT/Polymer and Electrospun Nanofilaments and Yarns

1. Electrospinning process optimization and control of nanofiber diameters and diameter distributions **** proprietary ****

The **Dzenis group** worked to further optimize nanofiber manufacturing process. The goal of this activity was to controllably produce uniform nanofilaments for mechanical and structural characterization. The focus in the reporting period was on further reduction of polymer precursor nanofiber diameters and on improvement of quality of nanofibers containing templating nanoparticles. In the past, continuous nanofibers with diameters as small as low tens of nanometers were fabricated but nanofiber diameter distributions remained relatively broad. Polyacrylonitrile (PAN) precursor nanofilaments were fabricated in a broad range of diameters by varying process parameters. The variables included type of solvent, polymer concentration in solution, electrospinning voltage, electrospinning distance, the needle gauge, and additives. As a result, combinations of process parameters producing more uniform, finer nanofibers were identified (see **Figure 35**). These parameters have been already used to fabricate nanofiber samples that were tested and characterized by groups at UNL, NU, and ARL. These experiments yielded new insights into the behavior and mechanisms of size effects in these systems. Further process optimization and production of ultrafine nanofibers is under way, assisted by modeling. Previously developed in **Dzenis group** model of solvent evaporation is being further generalized and applied for fully coupled multiphysics jet modeling. Once developed, such model will be used for the analysis of jet solidification, residual stress development, and structure formation in nanofibers that are critically important for control of final nanofiber diameter and properties.

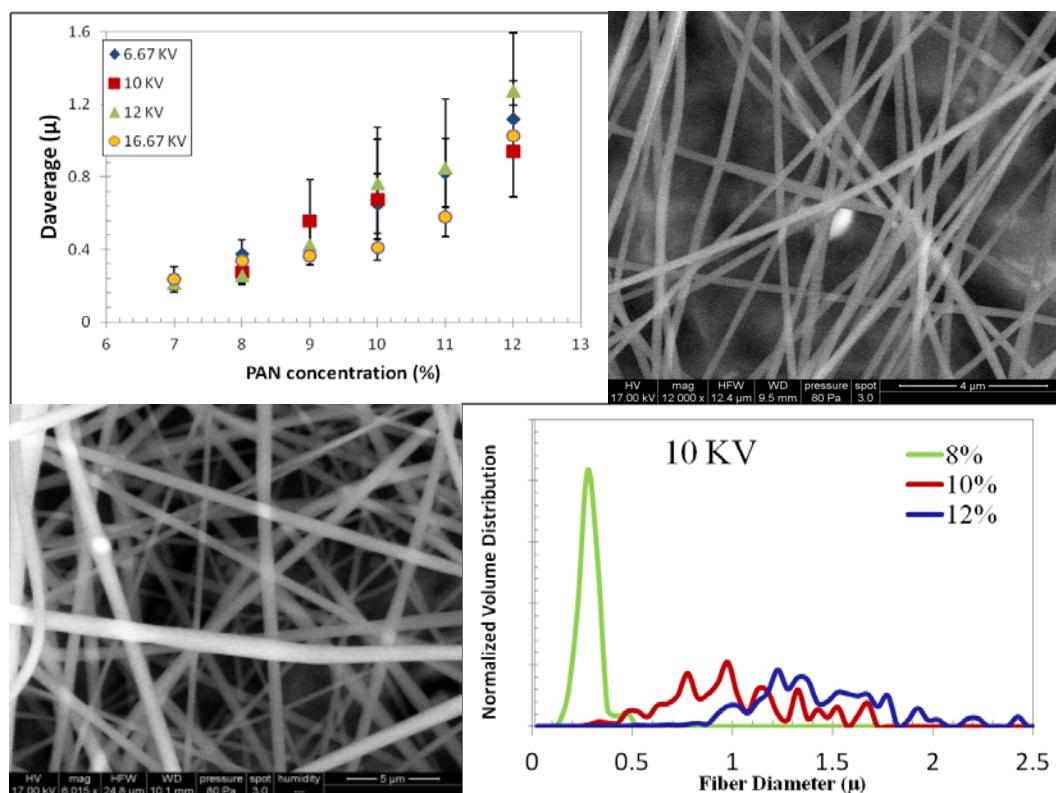


Figure 35. Variation of average nanofiber diameter and diameter distribution with polymer solution concentration and voltage.

2. Nanomanufacturing of high quality nanofilaments modified with nanoparticles for carbonization templating ****proprietary****

The **Dzenis group** continued optimization of nanomanufacturing of nanofibers templated with graphene and graphene oxide (GO) nanoparticles (from **Nguyen's group**) and DWNT (from **MER Corp.**). Earlier studies produced non-uniform GO-templated nanofibers with visible large particles in the thicker nanofiber regions. While this nanofiber morphology allowed us to study and compare the graphitic structure in the vicinity of visible GO particles with the structure in the regions without visible particles (that provided first evidence of global nature of the templating effect), the non-uniform nanofibers will most likely have inferior mechanical properties. An attempt was made to reduce the GO nanoparticle size to improve the nanofiber uniformity. Several GO batches with different nanoparticle sizes were prepared by sonication by **Nguyen's group** (**Figure 36**). A non-sonicated sample from nano graphite was also produced and utilized. All particles were incorporated into nanofibers using various processing parameters (**Figure 36**). Best samples were selected for more extensive parametric studies. An example of polymer concentration effect on nanofiber quality is shown in **Figure 37**. The resulting best process parameters are now being utilized to produce specimens for mechanical testing and structural characterization. A similar study of nanomanufacturing of DWNT-filled nanofibers allowed us to identify process parameters producing high quality, uniform DWNT-templated nanocomposite nanofibers (**Figure 38**). Analysis showed excellent DWNT alignment and length coverage with most nanofiber cross-sections containing at least one nanotube bundle. These ultra-low-volume-fraction nanocomposite nanofibers were carbonized and used in mechanical and structural analysis of templating.

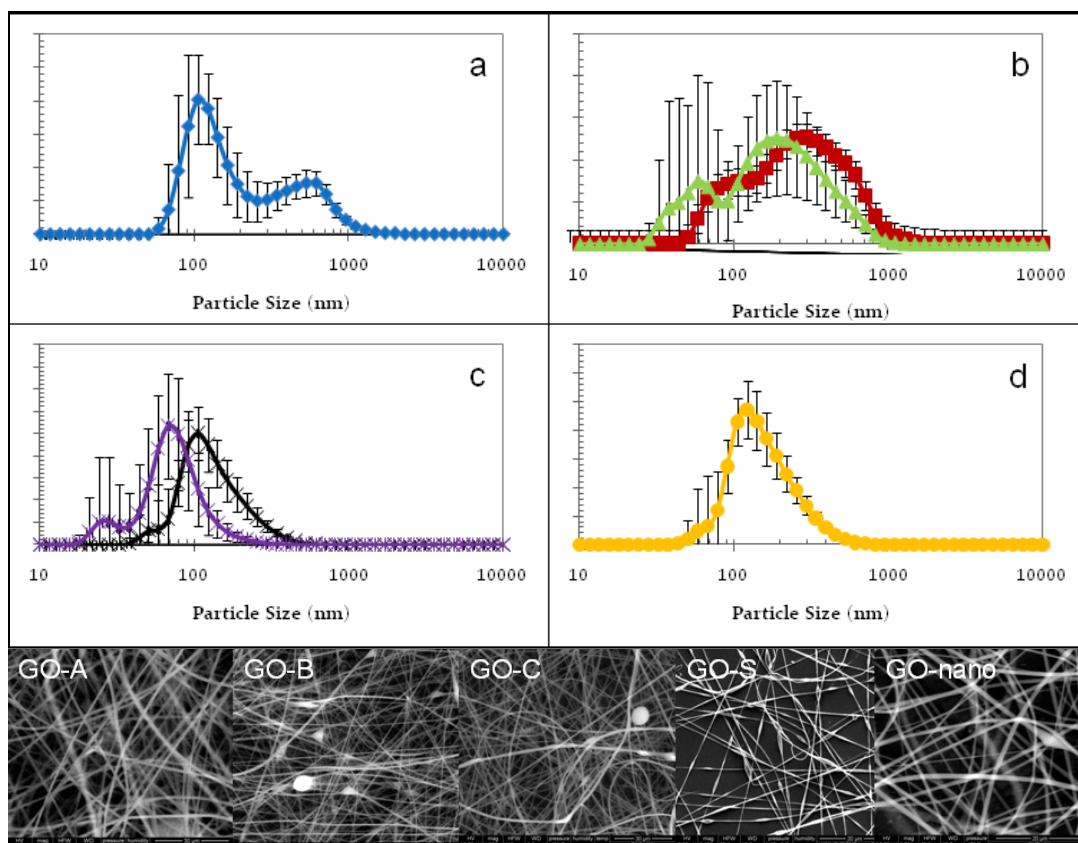


Figure 36. Particle size of different GO batches produced at NU (Nguyen) as measured by DLS; a) non-sonicated GO; b) red -- GO-A sonicated for 1 hr, green – GO-B sonicated for 2 hr; c) black – GO-C sonicated for 4hr, purple – GO-S sonicated for 6hr; d) GO-nano non-sonicated, produced from nanoscale graphite. SEM images of electrospun fibers containing different GO particle types produced at UNL (Dzenis). With the exception of the GO-S sample, which contained 1.42% wt/wt GO on PAN, all other samples contained 1% wt/wt GO on PAN.

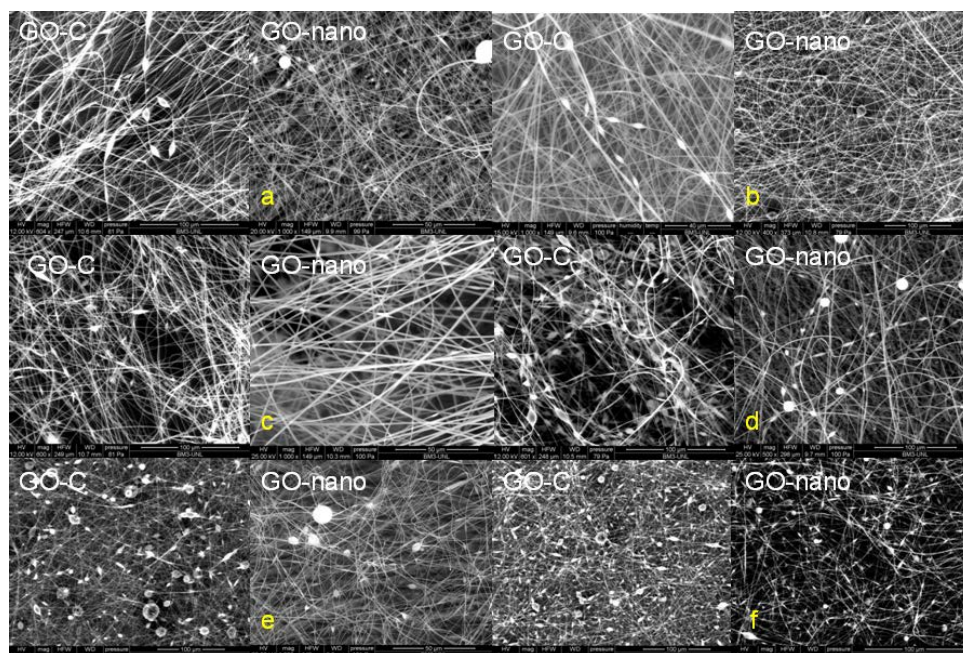


Figure 37. Electrospun nanocomposites fibers containing different amounts of GO. Every pair of micrographs compares samples with similar amount of GO-C and GO-nano. a) 0.5% wt/wt GO on PAN; b) 1% wt/wt GO on PAN; c) 2% wt/wt GO on PAN; d) 3% wt/wt GO on PAN; e) 4% wt/wt GO on PAN; f) 5% wt/wt GO on PAN.

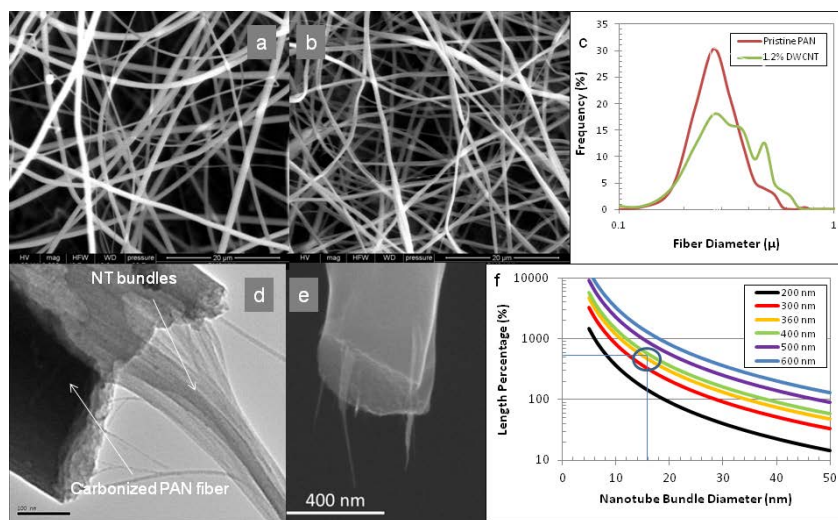


Figure 38. CNF morphology and DWNT distribution: SEM micrograph of electrospun PAN (a) and 1.2% DWNT/PAN (b) nanofibers; (c) diameter distributions for pristine PAN and 1.2% DWNT/PAN samples (as measured from approximately 200 fibers); (d) TEM micrograph of a broken edge of CNF with NT bundles; (e) SEM micrograph of the fracture surface of CNF. The pulled out DWNT bundles seemed to have uniform distribution along the length and within the cross section of the CNFs. (f) Length coverage (LC) of nanotube bundles in PAN nanofibers for different bundle and fiber diameters – average fiber diameter measured for this sample was 360 nm and the typical bundle diameter measured was 16 nm (the corresponding point is circled).

3. Modeling-based nanomanufacturing of aligned nanofiber assemblies and yarns

Improved methods for nanomanufacturing of high quality nanofiber assemblies and yarns were developed by **Dzenis group**. Both high-productivity and precision methods have been explored. Precision optimization was assisted by the previously developed numerical models of jet motion incorporating jet instabilities and nanofiber alignment and deposition on substrates. We now began using these techniques to produce specimens for mechanical testing and structural evaluation.

4. Carbonization process optimization

The **Dzenis group** began exploring optimization of the stabilization and carbonization conditions for PAN-based nanofibers. Stabilization and carbonization are known to be crucial for carbon fiber properties. We have explored several thermal treatment cycles (profiles) and carbonized both pristine and templated nanofibers at 8 different temperatures in the range from 600-1850 C in several atmospheres. Higher temperature carbonization was performed at MER Corp. The first results demonstrated different behavior of GO- and DWNT- templated nanofibers at different carbonization temperatures, with DWNTs showing stronger templating effects at lower temperatures. Further analysis will include effects of mechanical stretch during stabilization and carbonization.

5. Improving graphitic structure of CNFs as a result of carbonization templating

The **Dzenis group** performed comprehensive systematic analysis of the effects of templating on carbon nanofiber (CNF) structure. As-spun PAN nanofibers modified with several different nanoparticles (see above) were oxidized and carbonized using several thermal treatment regimes. Nanofiber structure was studied using SEM, XRD, TEM/ED, and Raman spectroscopy and compared with the structure of unmodified carbon nanofibers produced under similar conditions (controls). Significant improvements of graphitic structure quality were recorded for both GO- and DWNT-templated nanofibers based on Raman and XRD analyses. Electron diffraction analysis showed improved axial orientation of the graphitic planes in presence of inclusions (**Figure 39**). Selected area electron diffraction (SAED) analysis of nanofiber regions with and without visible nanoinclusions yielded similar structural parameters indicating global nature of the templating effects (**Figure 39**). The latter global effects were present in both GO- and DWNT-templated nanofibers. These effects are promising as they show that a very small quantity of carbon nanoinclusions can result in considerably improved graphitic structure and orientation that can lead to improvements in mechanical and other properties. Exhaustive analysis in the context of conventional carbon fiber manufacturing by the **Dzenis group** allowed us to attribute the observed beneficial effects to polymer chain anchoring on carbon inclusions. This anchoring results in better chain orientation and better graphitic structure in the templated carbon nanofibers even in absence of the stretch typically applied during stabilization and carbonization of commercial carbon fibers. The obtained experimental results are consistent with the theoretical analysis by **Schatz group**.

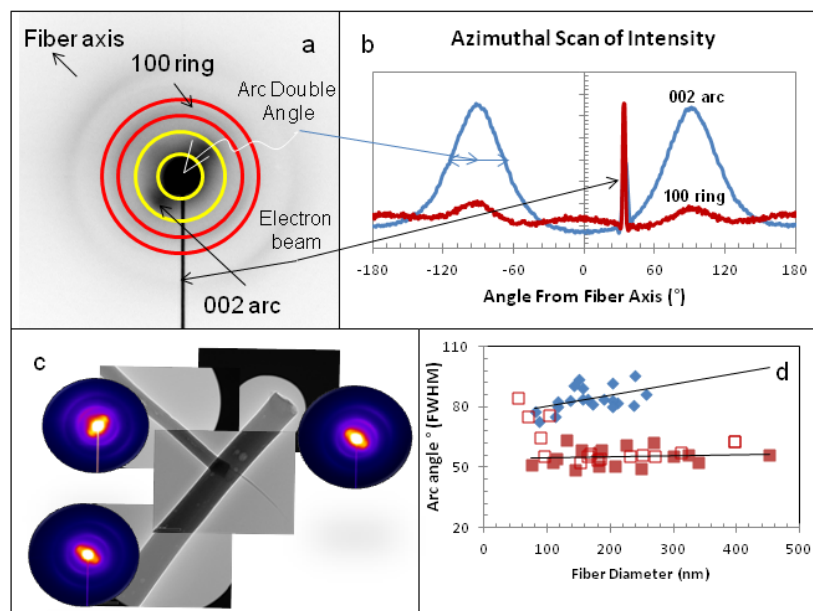


Figure 39. Electron diffraction analysis of DWNT-templated CNFs: a) Typical 2D SAED scan; b) Azimuthal variations of scattering intensities for the 002 arc and 100 ring; c) TEM micrograph and SAED diffraction patterns from carbonized DWNT/PAN nanofiber in the areas with and without visible DWNT; d) variations of 002 arc double angles with nanofiber diameter for carbonized pristine PAN (blue diamonds) and 1.2% DWNT sample from the areas with (full red squares) and without (empty red squares) visible NT bundles. Scale bars on c) are 200 nm.

6. Effect of carbonization temperature and templating

Systematic analysis effects of carbonization temperature on structure of templated CNFs was performed by **Dzenis** group. Raman analysis of GO-templated nanofibers (**Figure 39**) demonstrated accelerated carbonization process at intermediate and high carbonization temperatures as a result of GO-templating. Especially encouraging is significant improvement of graphitic structure at the intermediate temperature (1200 C). This promises high quality fibers at lower cost. These results are further supported by the SAED data (**Figure 40**). Electron diffraction patterns in this figure show major improvements in graphitic structure of templated CNFs carbonized at intermediate temperature, while the non-templated sample only showed improvements at the high temperature. In addition, comparison of SAED patterns in the second and third columns in **Figure 40** further confirms the global nature of graphitic templating and shows that it is preserved at different carbonization temperatures.

The obtained results for the DWNT-templated samples are even more encouraging (**Figure 41**). The Raman spectra for the CNFs carbonized at different temperatures (**Figure 41**) show that the DWNT-templated samples exhibited better graphitic structure (as indicated by significantly reduced I_D/I_G ratio and G band width). As expected, the graphitic structure of CNFs improved with the increase of carbonization temperature for both pristine and templated CNFs. However, this improvement was accelerated by the presence of DWNTs. Analysis of temperature variations of the extracted structural order parameters (**Figures 41c-d**) showed that the largest templating effect was achieved at lower carbonization temperatures. The templating effect reached the maximum at around 1000°C. The level of graphitic order achieved in the templated system carbonized at 1000°C was comparable to or better than the order in the pristine system carbonized at 1850°C.

These findings are significant. Increase of carbonization temperature is a common method of improving graphitic structure of carbon materials and fibers. It has been successfully used to improve graphitic structure of CNFs by graphitizing them at temperatures up to 3000°C. However,

high temperature graphitization is expensive. The cost of high-temperature post-treatment required to achieve high mechanical properties of the first commercial high-performance carbon fiber, Thornell by Union Carbide, was a competitive disadvantage that has eventually driven it out of the market. One of the main advantages of PAN-based carbon fibers is that their structure and graphitic order can be controlled by applying stretch at much lower temperatures, eliminating the need for high temperature post-treatment. Further reduction of carbonization temperature is always desirable and will further reduce the cost of carbon fiber production. Our overall data indicates that both GO- and DWNT- templating may simultaneously relax the stretch requirement and provide significant structural improvements at lower carbonization temperatures. Better graphitic structure and orientation, coupled with the previously shown by the **Espinosa group** good interfacial bonding of carbon nanoinclusions to the templated CNF matrix are likely to result in better mechanical properties. General low cost of the top-down nanofabrication process and our newly demonstrated significant graphitic improvements as a result of templating at low carbonization temperatures open up attractive new routes for controlled ultra-low cost nanomanufacturing of high quality CNFs.

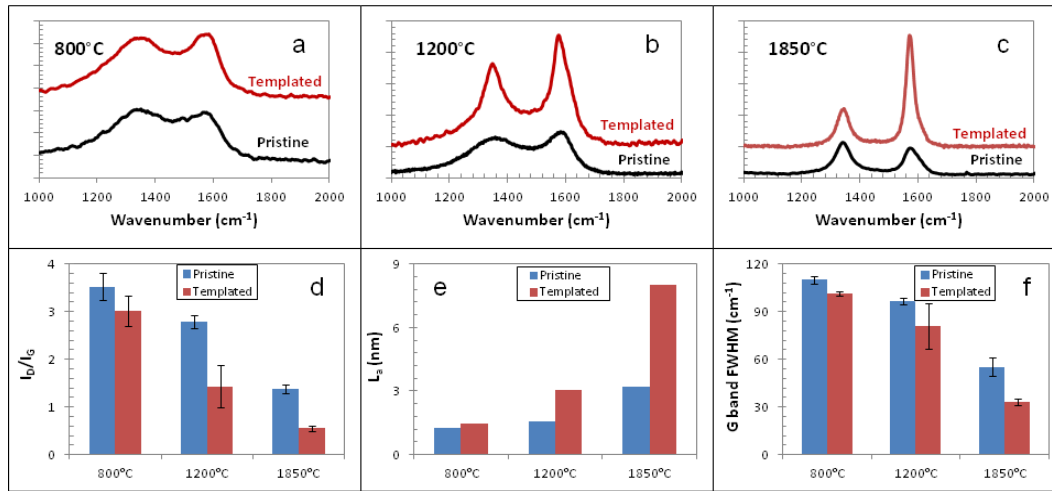


Figure 40. a-c) Raman spectra for carbon nanofibers obtained from pristine-PAN and graphene oxide templated samples that have been carbonized at 800 °C (a), 1200 °C (b) and 1850 °C (c). d) I_D/I_G ratios for the two sets of samples at different carbonization temperatures. e) L_a values for the two sets of samples at different carbonization temperatures. f) FWHM values of the G band for the two sets of samples at different carbonization temperatures.

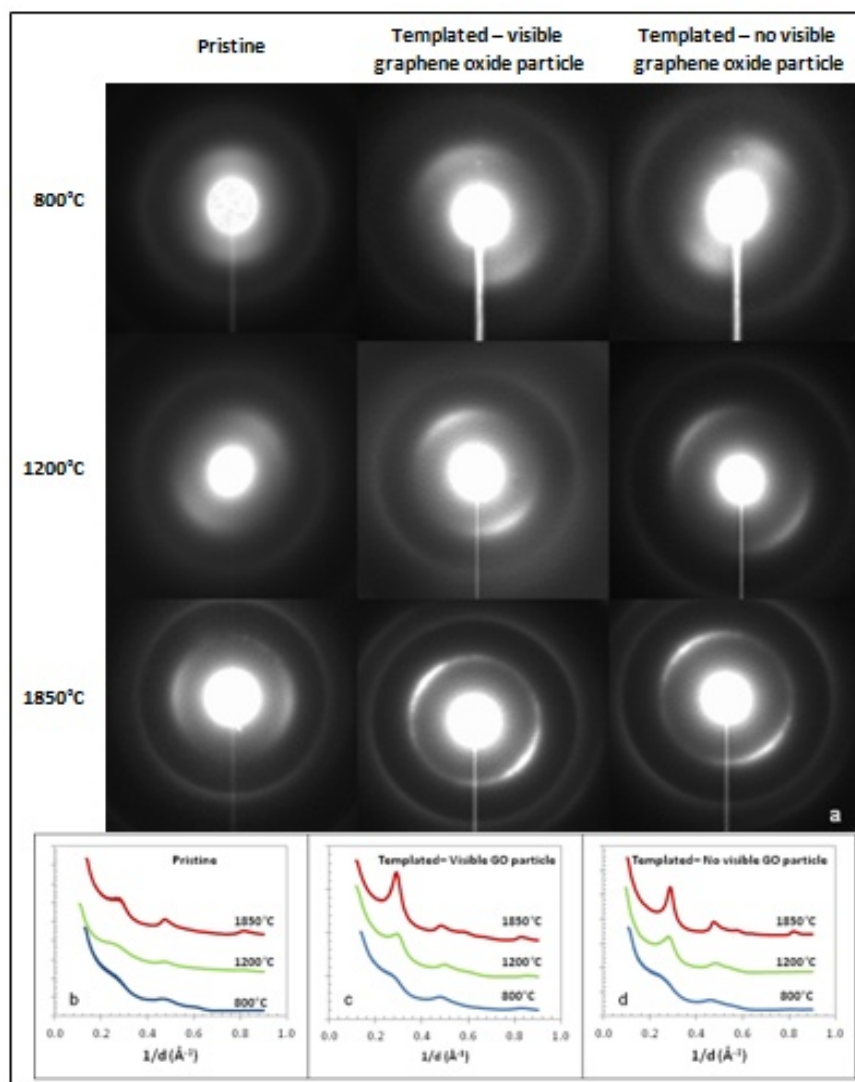


Figure 41. Electron diffraction analysis of carbon nanofibers. a) Typical 2D SAED patterns for pristine and templated CNFs (in regions with and without visible graphene oxide particles) at different carbonization temperatures. b-d) Digital intensity profiles for pristine sample (b); templated sample in the area around visible graphene oxide particle (c); and templated sample in the area with no visible graphene oxide particle (d).

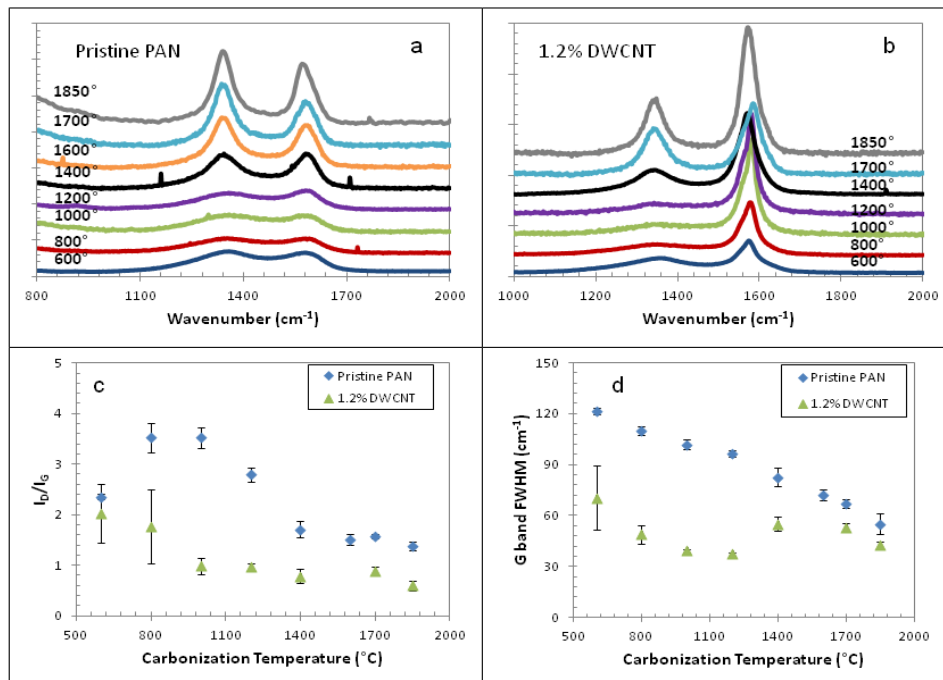


Figure 42. Analysis of the effect of carbonization temperature: a) Raman spectra of the carbonized pristine PAN sample for different carbonization temperatures; b) Raman spectra of the carbonized 1.2% DWCNT sample for different carbonization temperatures; c) I_D/I_G ratio as a function of carbonization temperature for both samples. The ratio is inversely proportional to in-plane graphitic crystal size L_a ; d) FWHM of G band as a function of carbonization temperature for both samples. Smaller band width indicates better graphitic structure.

7. Analysis of Mechanical Size Effects in Polymer Nanofilamentary Precursors **** proprietary ****

The **Dzenis** group continued systematic analysis of size effects in individual polymer and carbon nanofilaments. Previously observed size effects in as-spun PAN nanofibers were further expanded into the smaller nanofiber diameter range. Analysis of over 50 mechanical tests of long (5-10 mm) individual nanofibers demonstrated that reduction of fiber diameter from 2.8 micrometers to ~100 nanometers resulted in simultaneous increases in elastic modulus from 0.36-48 GPa, true strength from 15-1750 MPa, and toughness from 0.25-605 MPa, with the largest increases recorded for the ultrafine nanofibers smaller than 200-250 nanometers. These size effects are among the highest recorded for any material. The observed simultaneous increases in strength, modulus, and toughness are unusual in structural materials as their strength and modulus are typically improved at the expense of toughness. Previously, based on the XRD analysis of structure of as-spun nanofibers, we hypothesized that reduced crystallinity in the ultrafine electrospun nanofibers is responsible for preserving high ductility while increased chain molecular orientation caused by intense jet stretching in electrospinning is responsible for high strength and modulus. Our direct observation of fine as-spun PAN nanofibers in low-voltage TEM and electron diffraction analysis confirmed low polymer crystallinity. However, diffuse diffraction patterns did not allow quantitative structural characterization of individual PAN nanofibers. To further elucidate the role of crystallinity on mechanical behavior we performed mechanical analysis of annealed nanofibers. Annealing was used to increase the degree of crystallinity in rapidly solidified electrospun nanofibers. Wide-angle X-ray analysis confirmed the increase in crystallinity as compared to as-spun nanofibers across the range of nanofiber diameters (**Figure 43**). Evaluation of the stress-strain diagrams (**Figure 43E,F**) and comparison of the extracted properties with the properties of as-spun nanofibers (**Figure 44**) showed an increase in modulus and strength.

However, nanofiber failure strain sharply decreased. Significantly, the observed sharp reduction of strain at failure led to reduction of toughness. These results supported our hypothesis that large strains at failure and ultrahigh toughness of as-spun nanofibers were due to their low crystallinity.

It is interesting to see (**Figure 45**) that ultrafine electrospun PAN nanofibers outperformed most existing structural materials and fibers in toughness. The best recorded properties of nanofibers far exceeded the properties of conventional optimized PAN microfibers (250-400 MPa strength and 3-8 GPa modulus) and exceeded the strength of all commercial polymer textile fibers (such as polyester, Nomex, polyamide 6, and nylon 66) while exhibiting 6-10 fold higher toughness. The best recorded strengths of as-spun PAN nanofibers were on par with the high strength spider silk while showing three times higher toughness. Finally, best as-spun PAN nanofibers were as strong, but tougher than most developmental carbon nanotube (CNT) fibers. Encouragingly, all trends analyzed in our study do not show signs of saturation, indicating a strong possibility of further performance improvements. Demonstrated superior mechanical performance of polymer nanofibers is significant as it is likely to result in better mechanical properties of carbon nanofibers. Unique macro-nano nature of continuous nanofibers provides an easy way to bridge scales. We also note that our demonstrated mechanism of simultaneously high strength, modulus, and toughness challenges the prevailing 50-year old paradigm of high-performance polymer fiber development calling for high polymer crystallinity and may have broader implications in fiber science and technology. Currently, we analyze effects of plasticizers and solvents on the mechanical properties of polymer and carbon nanofibers with the goal to develop methods of robust control of their structure and properties.

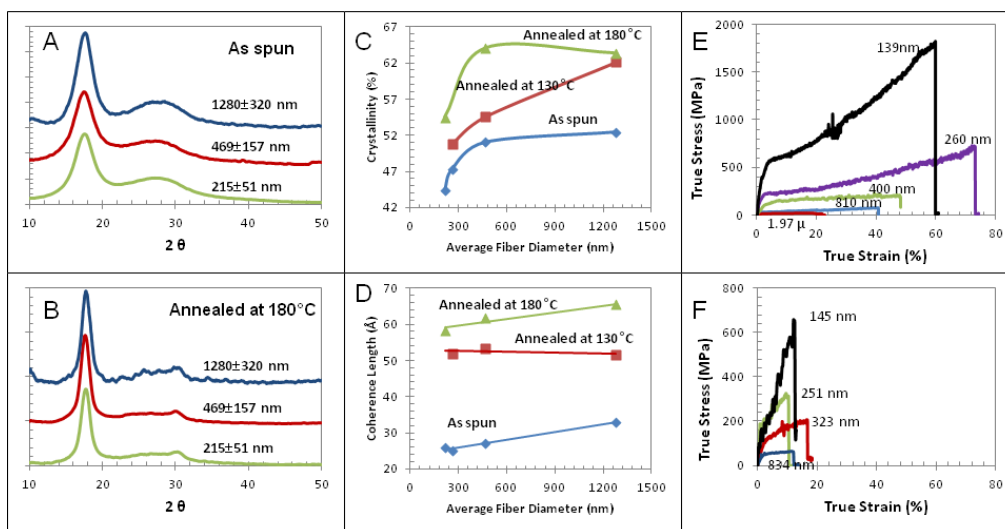


Figure 43. Effects of PAN nanofiber diameter and annealing on crystallinity and mechanical behavior: Wide-angle X-ray diffractograms for (A) as-spun and (B) annealed nanofiber mats with different average fiber diameters (XRD spectra for nanofibers annealed at 130°C and 180°C were qualitatively similar); variations of XRD crystallinity (C) and coherence length (D) as functions of average fiber diameter; representative stress-strain diagrams for as-spun (E) and annealed (B) individual PAN nanofibers of different diameters. The same strain scale was used in panels E and F for easier comparison and evaluation of annealing effect.

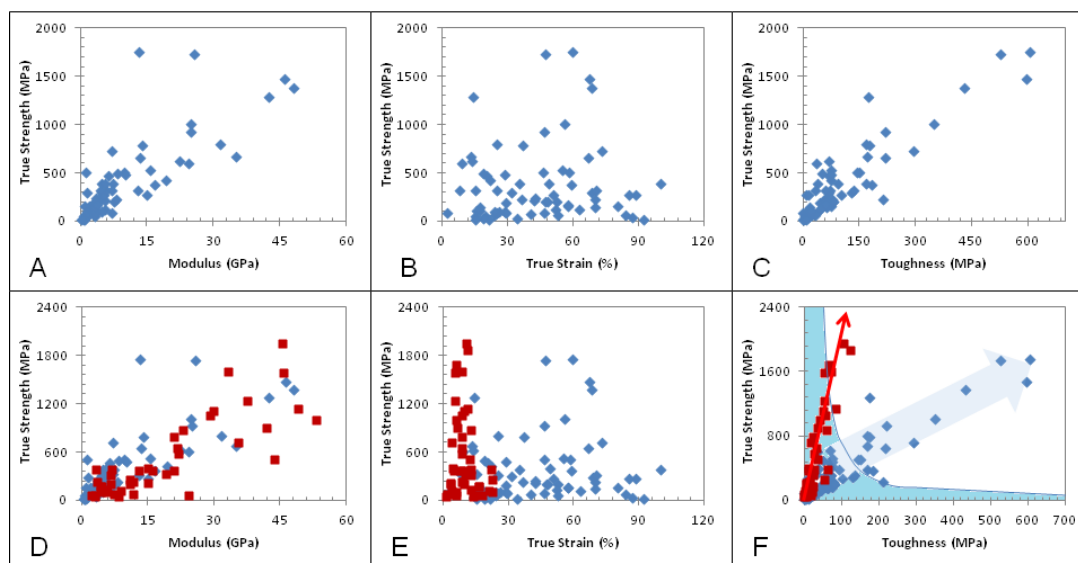


Figure 44. Correlations of mechanical properties of nanofibers of different diameters. A-C) As spun fibers – A) True strength vs. Modulus; B) True strength vs. True strain to failure; C) True strength vs. Toughness; D-E) Comparison between as-spun (blue diamonds) and 130C annealed (red squares) nanofibers – D) True strength vs. Modulus; E) True strength vs. True strain to failure; F) True strength vs. Toughness. Arrows in F) point in the directions of decreasing nanofiber diameters; the colored area represents the strength/toughness region occupied by traditional materials.

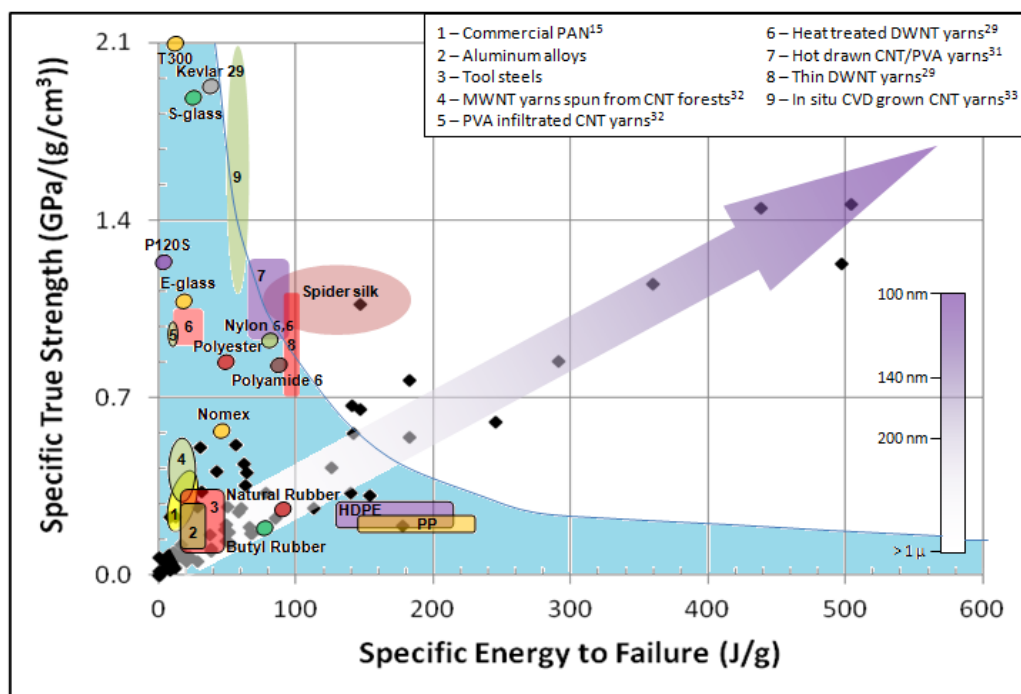


Figure 45. Comparison of specific strength and specific energy to failure of as-spun PAN nanofibers (diamonds) with typical values for commercial and developmental fibers and materials. The arrow density indicates approximate values of nanofiber diameters (see scale bar). The colored area represents the typical strength/toughness region occupied by traditional materials.

8. Mechanical properties and mechanisms of size effects in carbon nanofilaments

The **Dzenis** group continued systematic analysis of size effects in carbon nanofilaments. Previously observed variations of mechanical properties with nanofiber diameter were further expanded into the smaller nanofiber diameter range. Extensive fractographic analysis was performed to study mechanisms of failure. Several typical fracture surfaces were classified. High-resolution TEM analysis of carbon fiber structure (**Figure 46**) confirmed generally poor graphitic structure of non-templated CNFs. Some preferred orientation was visible on the FFT diffractograms (**Figure 46**) that was consistent with the SAED data. The structure of the CNFs was uniform across the nanofiber cross-section. Poor graphitic structure of the non-templated CNFs is most likely responsible for their relatively high ductility and toughness. Additional analysis is in progress. The observed scale effects in CNFs are being modeled in collaboration with the **Buehler** group.

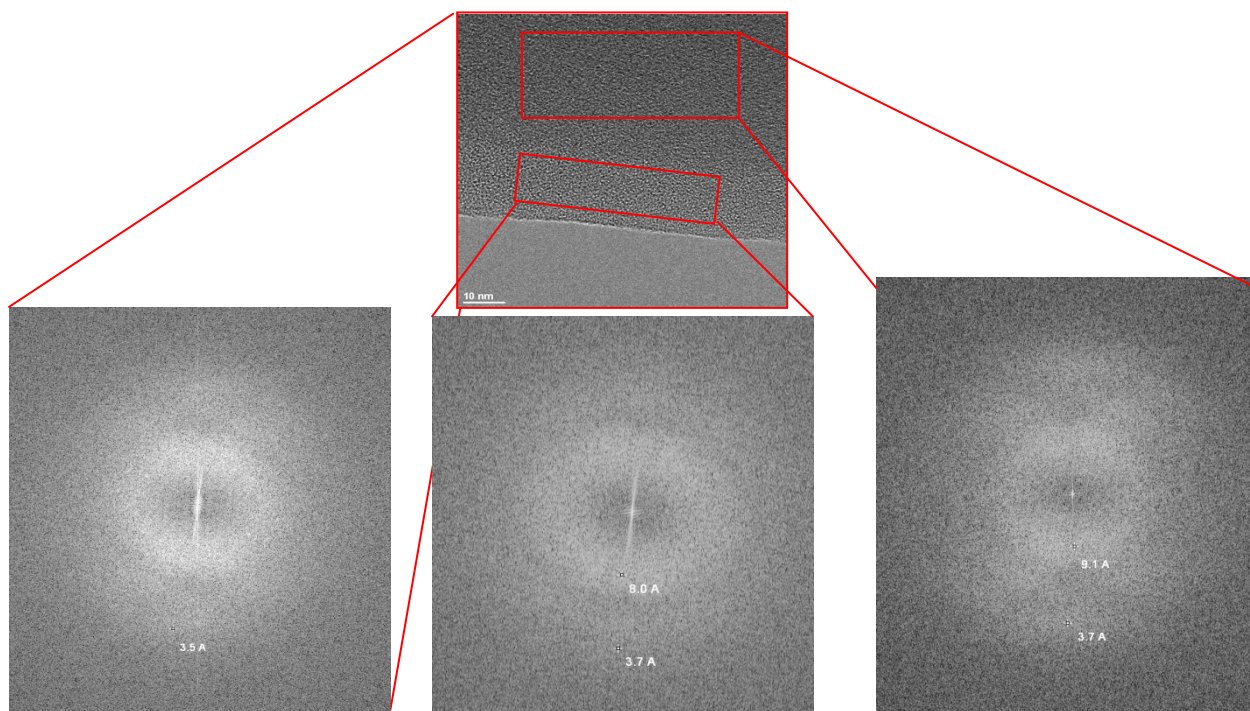


Figure 46. HRTEM imaging of CNF structure and FFT diffractograms showing weak orientation and generally poor, uniform graphitic structure.

9. Analysis of mechanical behavior of templated carbon nanofilaments

We have begun mechanical analysis of templated CNFs. Previously, in-situ study by **Espinosa** group showed good interfacial bonding between DWNT bundles and templated carbon matrix. **Dzenis** group performed first mechanical tests of millimeters-long samples of templated CNFs. The initial results show improvements in strength and modulus, compared to the non-templated CNFs (**Figure 47**). Significantly, properties of thicker nanofibers have been improved. The latter may have important practical implications, as it is easier to produce thicker nanofibers uniformly. Analysis of long specimens in the **Dzenis** group was coordinated with the in-situ TEM mechanical evaluation in the **Espinosa** group. The initial results showed good correspondence (**Figure 47**).

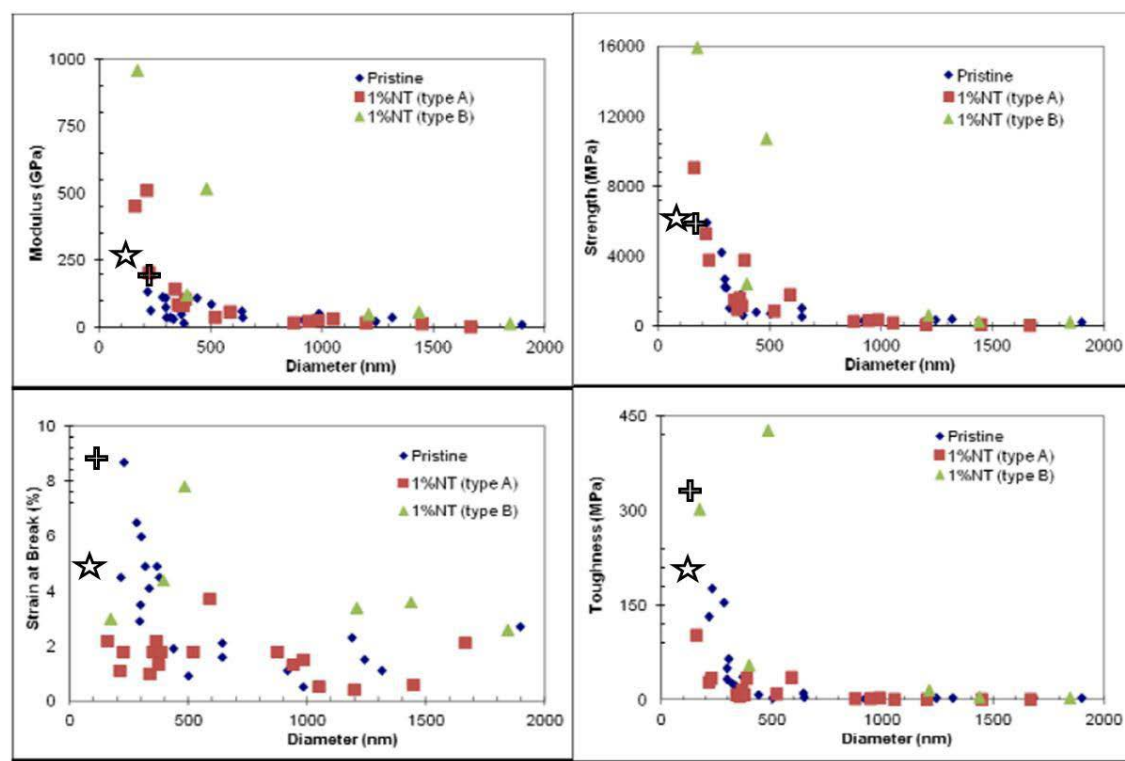


Figure 47. Variation of mechanical properties of pristine (diamonds) and DWNT-templated CNFs (squares and triangles) – preliminary results. Comparison of samples tested at the University of Nebraska and the results of in-situ TEM analysis at Northwestern University (star is for Sample 1 with D~108nm, cross is for Sample 3 with D~145nm).

10. Tensile testing using a microelectromechanical system (MEMS) in situ TEM

The **Espinosa group** is performing tensile tests on the carbonized nanofibers in situ a TEM using a MEMS device (**Figure 48**). For this technique, a nanomanipulator is used inside the chamber of an SEM to select a fiber and place it across the MEMS device shuttles. The sample is then welded to the opposing shuttles using electron beam induced deposition of carbonaceous platinum. The tests are then performed in increments of 0.1% strain up to failure. In addition to the images taken during the tensile test, we also perform high resolution imaging and selected area electron diffraction (SAED) along the length of the nanofibers before each test to obtain information on the structure of the fiber. Following each test, we also take high resolution images of the fracture surfaces (**Figure 49**).

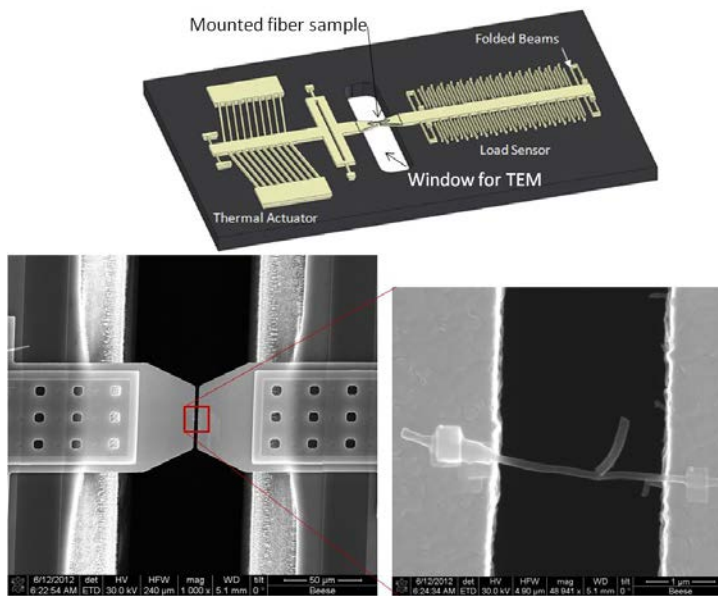


Figure 48. MEMS device for in situ TEM tensile tests, with load cell stiffness of 1623N/m or 812N/m. Top: schematic of MEMS testing device used. Bottom left: SEM mage of shuttles onto which nanofibers sample is mounted. Bottom right: carbon nanofibers mounted onto shuttles, and welded to the shuttles using electron beam induced deposition of carbonaceous platinum.

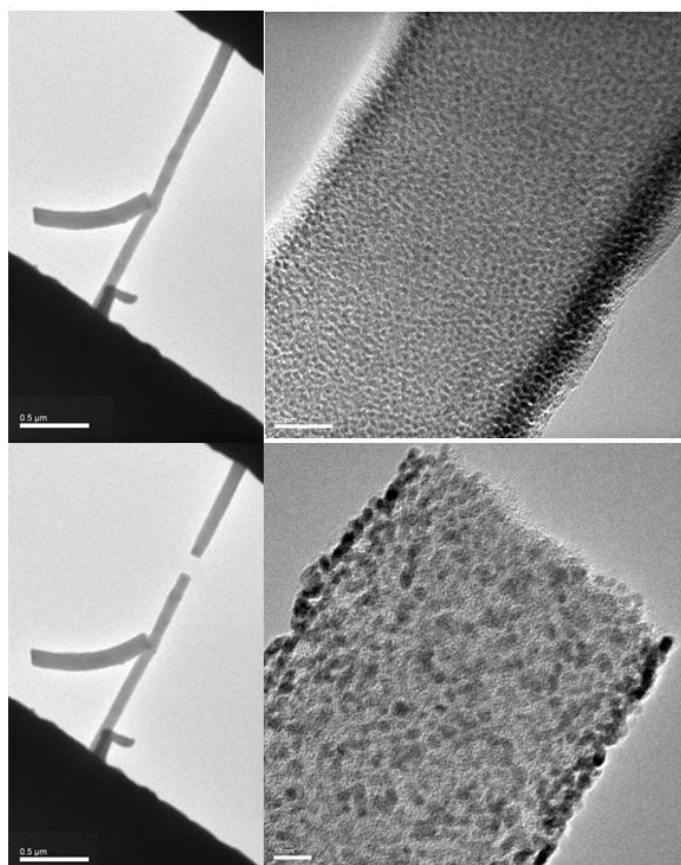


Figure 49. TEM images of carbon nanofibers mounted onto MEMS testing device for tensile test. Images of the fiber before the test (top), and after fracture (bottom).

11. Modeling of mechanical behavior of nanofilamentary yarns

A numerical model of nanofilamentary yarns with explicit nanofiber and contact representation was developed by **Dzenis** group. Initial examples of stress-strain behavior of nanofiber yarns were computed and analyzed with account for lateral interaction through friction (**Figure 50**). Explicit models of nanofilamentary yarns can be integrated with atomistic calculations of others in the team and used to optimize nanofiber contacts and lateral interactions. Effects of nanofiber fusion in nanofilamentary assemblies can also be studied. Controlled fusion may lead to optimal combination of bonding and friction at interfaces between the nanofilaments. In a related work by **Dzenis** group, PAN nanofibers with surfaces modified with inorganic nano spikes were produced by a new room temperature method. Such hierarchical structures can dramatically increase friction between nanofilaments thus providing powerful means of control of lateral interactions in nanofilamentary yarns.

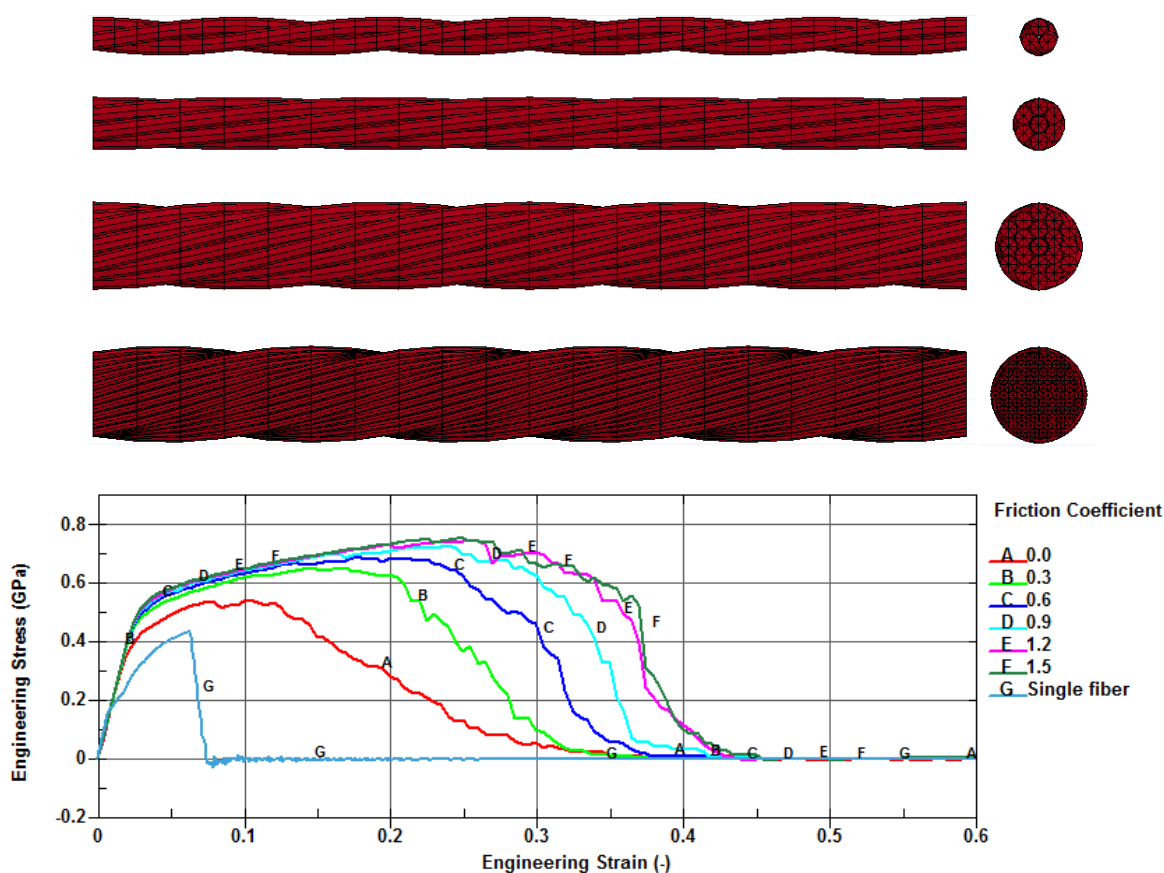


Figure 50. Explicit model of nanofiber yarn and simulated effects of friction between nanofilaments on mechanical behavior through failure.

12. ReaxFF Molecular Dynamics Simulations of the Initial Stages of Templated Carbonization in PAN-Based Carbon Nanofibers

This section describes our use of molecular dynamics (MD) simulations with a reactive force field (ReaxFF) to study the initial stages of the templated carbonization process.²⁵ More details on these simulations can be found in the recently submitted “Improved Graphitic Structure of Continuous Carbon Nanofibers via Graphene Oxide Templating,” by Papkov, D.; Goponenko, A.; Compton, O. C.; Zhi, A.; Nguyen, S. T.; and Dzenis, Y. A. Experimental observation of the complex

concurrent 3D propagating chemical reactions involved in carbonization is currently impossible, so we have been developing computational methods that can be used to understand carbonization mechanisms. Of course the simulations are limited by system size and stimulation duration, so only qualitative connections between theory and experiment are possible. However, recent molecular dynamics simulations of the initial stages of carbonization in a stabilized polyacrylonitrile (PAN) structure²⁵ have proven useful for understanding the reaction mechanisms that lead to carbonization, including the effects of temperature and density on the rates of graphitic structure formation. Here, this modeling approach is further expanded and used to simulate the effects of templates on carbonization, modeling recent experiments in the **Dzenis and Espinosa groups**. Currently, it is computationally not feasible to simulate the exact geometry of a DWNT bundle surrounded by the stabilized PAN molecules. We have therefore simulated and compared two limiting geometries, i.e. a small diameter cylindrical single wall nanotube (SWNT) and a flat graphene nanoparticle. The actual cases of the DWNTs considered here and the radially crumpled graphene particles studied in our previous work will fall in between these selected limiting geometries.

A well-oriented, stabilized PAN precursor structure is crucial for good quality carbon fibers. Experimental analysis indicates that such orientation exists and may be preserved in the templated NFs with the help from anchoring polymer molecules on the axially oriented templating particles. This preexisting orientation was modeled in the analysis below by aligning the initial ladder polymer precursor molecules along the particle surface or axis.

The simulations were performed using the ReaxFF force field.²⁶ ReaxFF uses a general relationship (i) between bond distance and bond order and (ii) between bond order and bond energy – allowing for proper dissociation of bonds to give separated atoms. Other valence terms (angle and torsion) are defined in terms of the same bond orders so that all these terms go to zero smoothly as the bonds break. It has been demonstrated in the literature that ReaxFF is suitable to study various reactions for systems consisting of C, N, O and H atoms.²⁷⁻³⁰ In another paper, we have studied the carbonization of PAN alone using molecular dynamics based on ReaxFF, and the results are consistent with known properties of the carbonization process in terms of gaseous species emitted during the process, and the types of structures that are produced, subject to constraints of the simulations that require us to use higher temperatures than in the experiments, and very short simulation times such that the carbonization process is only partially completed.²⁵

The analysis below summarizes the main templating effects. The molecular dynamics calculations show that breaking of the heterocyclic rings starts to occur at ~2500 K and subsequently small volatile molecules, like N₂, H₂, HCN and NH₃, are formed as well as new π -conjugated carbon clusters consisting of five, six and seven-membered carbon-only rings. Representative snapshots at 500 ps showing fused five- and six-membered rings structures are shown in **Figure 51** for the graphene composite system and **Figure 52** for the CNT composite. **Figure 51** shows the formation of two five-membered rings and one six-membered ring. Similarly, **Figure 52** shows the four six-membered rings. Further ring condensation and growth occurs around these clusters (i.e., these clusters serve as nuclei for further carbonization).

The populations of small molecule species formed during the simulations were analyzed and averaged over ten trajectories. The analysis shows that the formation of N₂ and H₂ is more likely than NH₃ and HCN, with N₂ formation initiating earlier than H₂ formation. The reaction initiated by the H-abstraction and then N₂ formation occurs via three distinct stages as observed in these simulations: (i) CN-bond breaking – where original six-membered heterocyclic rings break, (ii) NN-bond formation – N with dangling bond reacts with another N of a neighboring molecule, and finally (iii) subsequent CN-bond breaking helps to form N₂.

The populations of newly formed rings consisting of carbon atoms only are shown in **Figure 53**. Ring formation rate is presented in Table 1. In general five-membered ring formation occurs first as a result of N₂ formation in which the six-membered heterocyclic rings of the seed molecules break

and the carbon atoms in the same PAN (B) unit with dangling bonds in the newly formed structures react to form five-membered rings. Initially five-membered ring formation is dominant but in later stages of growth six-membered ring formation also becomes prominent. Conversion of five- and seven-membered rings into six-membered rings is observed and thus the most stable π -conjugated structures are formed. It is to be noted that the formation of five-membered rings in the mechanism of carbonization is not usually considered in carbonization mechanisms but is an obvious outcome of our simulations.

Here we concentrate on the effect of templating on the results. The analysis shows that the N_2 and NH_3 formation rates are much higher for the pure PAN(B) model than for the PAN(B) + graphene model while the rates for the PAN(B) + CNT model are intermediate between the other models except for HCN. In case of new ring formation, the six-membered ring formation rate is much higher in case of the PAN(B) model, while the five-membered and seven-membered ring formation rates are higher in the case of the PAN(B) + CNT model. The formation rate of new six-membered rings is very low for the PAN(B) + CNT model.

As stated above, initially structures consisting of five- and six-membered rings are formed. Short polyyne-like structures (with carbon atoms in the backbone) are formed due to ring breaking and N_2 and H_2 formation. These short polyyne-like structures may entangle themselves to form new five-, six- and seven-membered rings consisting of carbon atoms only. Once a small cluster consisting of five- and/or six-membered rings forms it acts as a nucleus, and further ring condensation occurs around it. The newly formed initial structures consisting of five- and six-membered rings on different units may also react among themselves to form larger structures consisting of five- and six-membered rings with carbon atoms in the backbone. Thus, three dimensional structures consisting of five- and six-membered rings and mainly sp^2 -carbon are formed. Upon continued annealing the five- and seven-membered rings may convert to more stable six-membered rings. Thus, from the present ReaxFF simulations the following distinct stages were observed in the carbonization mechanism (both with pure PAN and with the PAN + CNT and PAN + graphene composite systems): (i) formation of small structures consisting of five- and six-membered carbon-only rings via N_2 evolution, (ii) ring condensation – i.e., further ring formation due to entanglement of small sp -type carbons (polynes) that become attached to the five- and six-membered rings, (iii) cluster growth – small carbon-only ring clusters on different units react to form larger ring clusters, with formation of H_2 , HCN, NH_3 , and other species continuously occurring.

In case of simulations with the PAN + graphene composite system, the five- and six-membered rings are predominantly formed parallel to the plane of the graphene sheet – which is a direct effect of the template. This is apparent in **Figure 51**, where layers of newly formed rings are clearly visible immediately on either side of the graphene layer. This result is also consistent with past experiments involving MWCNTs.^{31,32} In some cases, more than one π -conjugated layer is formed, all being parallel to the graphene sheet. In case of the SWNT composite system, no cylindrically curved graphitic planes are observed (**Figure 52**). This can be understood as arising because the (5, 5) CNT diameter is too narrow to support templating. The experiments in ^{31,32} have been done with large diameter MWCNTs, so our studies of graphene (which can be considered as a CNT with a very large diameter) composite system may be more representative of the large diameter MWCNT-templating during carbon nanofiber production. Importantly, in both composite systems studied, there was a distinct preferred axial orientation of the planes of the newly formed rings and the early stacks. This is consistent with the experimental results described here and demonstrates how both the presence of the oriented carbon particles and the initial orientation of the stabilized PAN molecules (also influenced by the templating particles via internally constrained stabilization, as discussed above) result in improved orientation of the graphitic structure in the templated CNFs. In particular, the observed preferred axial orientation of the planes of the newly formed rings in the two limiting geometric cases considered here indicates that the improved orientation effect is general and should be observed on all intermediate template geometries. The latter include DWNT

bundles studied here and axially crumpled graphene sheets analyzed in the recently submitted Papkov, et al., “Improved Graphitic Structure of Continuous Carbon Nanofibers via Graphene Oxide Templating”.

Thus, these ReaxFF MD simulations of templated carbonization confirmed oriented graphitic growth and provided insight into mechanisms of carbonization initiation.

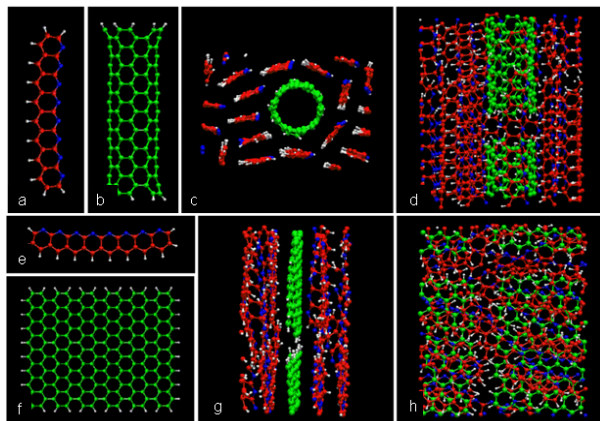


Figure 51. MD models with NT and graphene particles. (a) Model stabilized PAN molecule (B); (b) SWCNT (5, 5) of length 22 Å. Snapshots at 50 ps of the model equilibrated at 300 K; (c) view along SWCNT axis; (d) view perpendicular SWCNT; (e) Model stabilized PAN molecule (B); (f) Graphene sheet. Snapshots at 50 ps of the model equilibrated at 300 K; (g) view along parallel to graphene sheet; (h) perpendicular view. Color code: Carbon atoms on B molecules are represented by red and on graphene and on CNT by green spheres. Nitrogen and hydrogen atoms are represented by blue and white spheres, respectively.

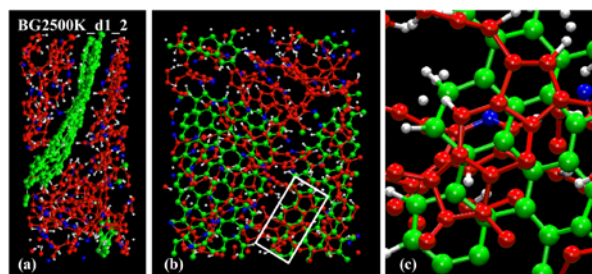


Figure 52. Snapshots at 500 ps for graphene composite system. (a) view parallel to graphene plane; (b) perpendicular view; (c) detailed view of selected part. Color code: Carbon atoms on B molecules and on graphene are represented by red and green spheres, respectively. Nitrogen and hydrogen atoms are represented by blue and white spheres, respectively.

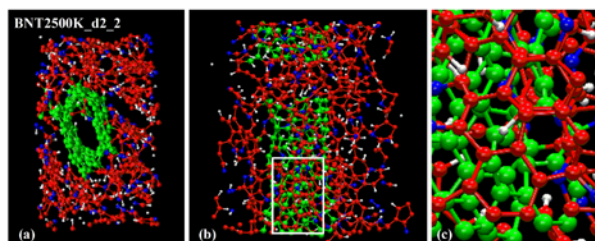


Figure 53. Snapshots at 500 ps for CNT composite system. (a) view along CNT axis; (b) view perpendicular CNT axis; (c) detailed view of selected part. Color code: Carbon atoms on B molecules and on graphene are represented by red and green spheres, respectively. Nitrogen and hydrogen atoms are represented by blue and white spheres, respectively.

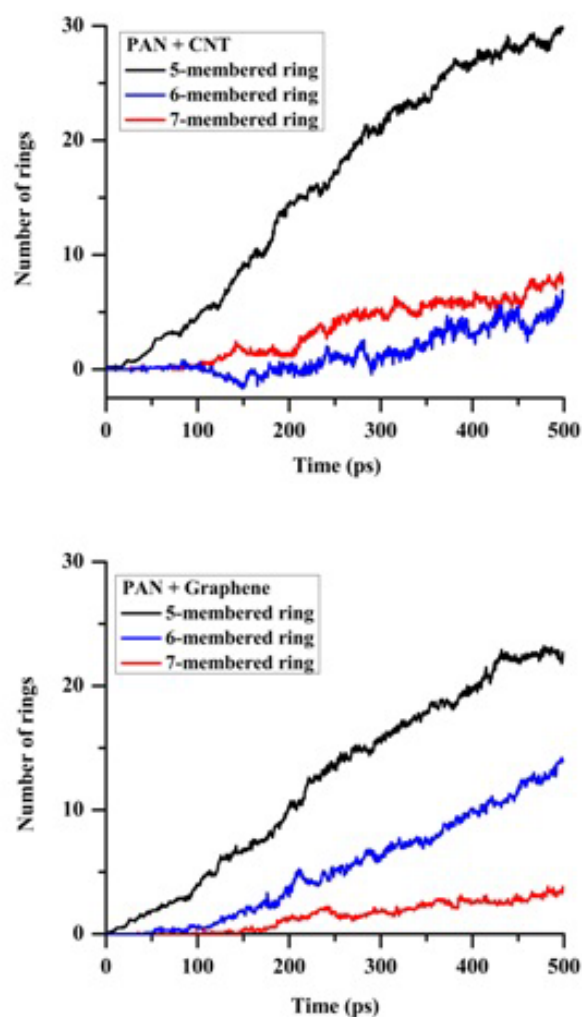


Figure 21. Number of rings formed (consisting of carbon atom only) during simulations at 2500K and with density 1.6 gm/cc. Averaged over 10 trajectories.

Table 1. Ring (consisting of carbon atoms only) formation rate (number of rings/ns) for simulations at 2500K and density 1.6 gm/cc. Averaged over 10 trajectories.

Model System	five-membered ring	six-membered ring	seven-membered ring
PAN	57.5	43.5	9.0
PAN + CNT	59.6	13.6	15.8
PAN + Graphene	44.9	26.9	6.7

13. Modeling Size effects in carbon nanofibers

a. Experimental results

Carbon nanofibers were tested by the **Dzenis** and **Espinosa** groups. The mechanical performance was recorded for fibers of different diameters and the elastic modulus, failure strength, failure strain and toughness modulus was determined for different. It can be seen in **Figure 55** that lower diameters lead to a pronounced increase in elastic modulus, failure strength and extensibility. Hence, also the toughness modulus increases significantly.

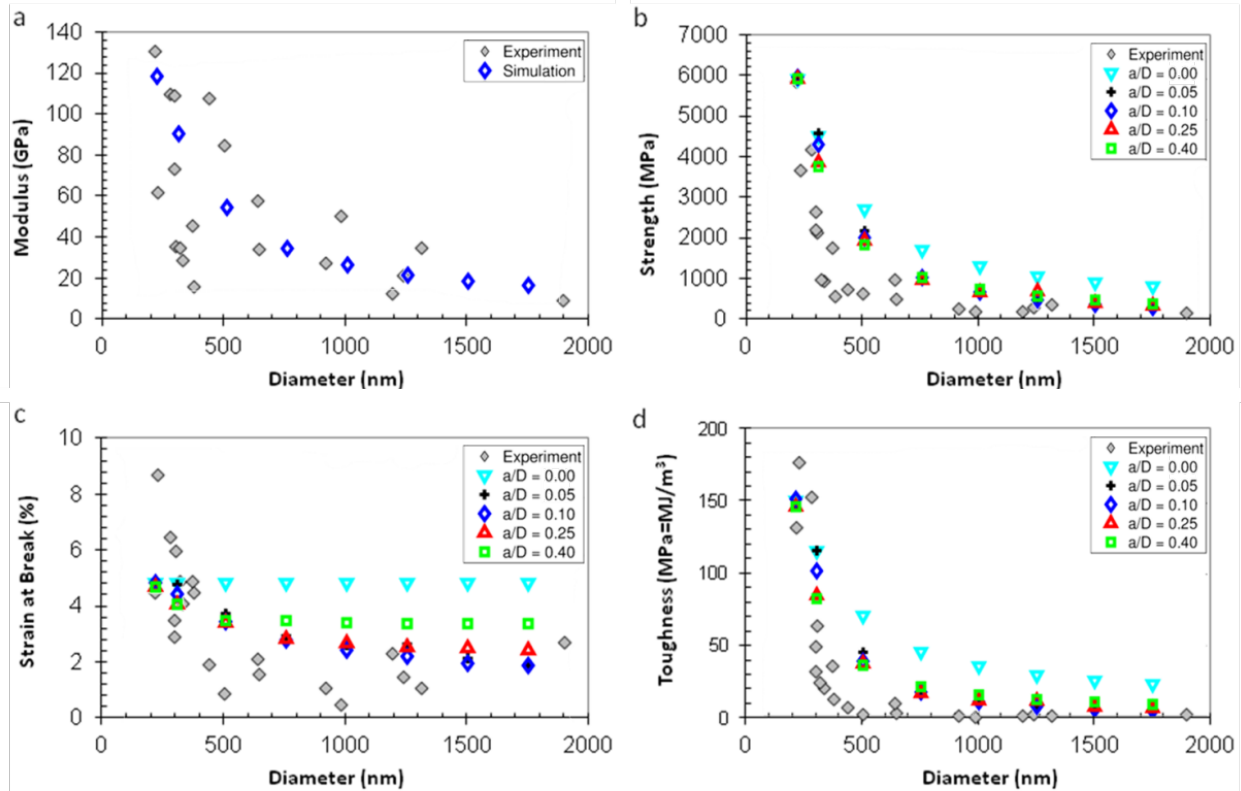


Figure 55. Experimental results and the results of the computational study; a) Elastic modulus; b) strength; c) strain to failure; and d) toughness modulus. A good match with the experimental results is found in case the model incorporates size effects of a flawed fiber ($a/D \neq 0$). Thereby, the strength does not only scale with the modulus but displays also the size-dependence of a flawed fiber as predicted by fracture mechanics, *i.e.* the strength scales with $\sqrt{1/D}$.

b. Model Setup

A plane strain coarse-grained bead-spring model is used to model the mechanical behavior of fibers and to complement the experimental analyses (see **Figure 56** for the geometry). This technique has been shown to provide a good model for size effects in fibers.^{33,34} A triangular mesh with bond distance 10 nm is used to model a flawed fiber with diameter D , length L (both much bigger than the bond distance) and a surface crack with length a . Since $D, L \gg d$ no boundary or mesh-dependent effects are anticipated. The choice of $d = 10$ nm bond distance resembles the characteristic size of the crystallites in the carbon fibers as determined from our experiments. The length of the fiber is chosen to be $L = 1.73 \mu\text{m}$.

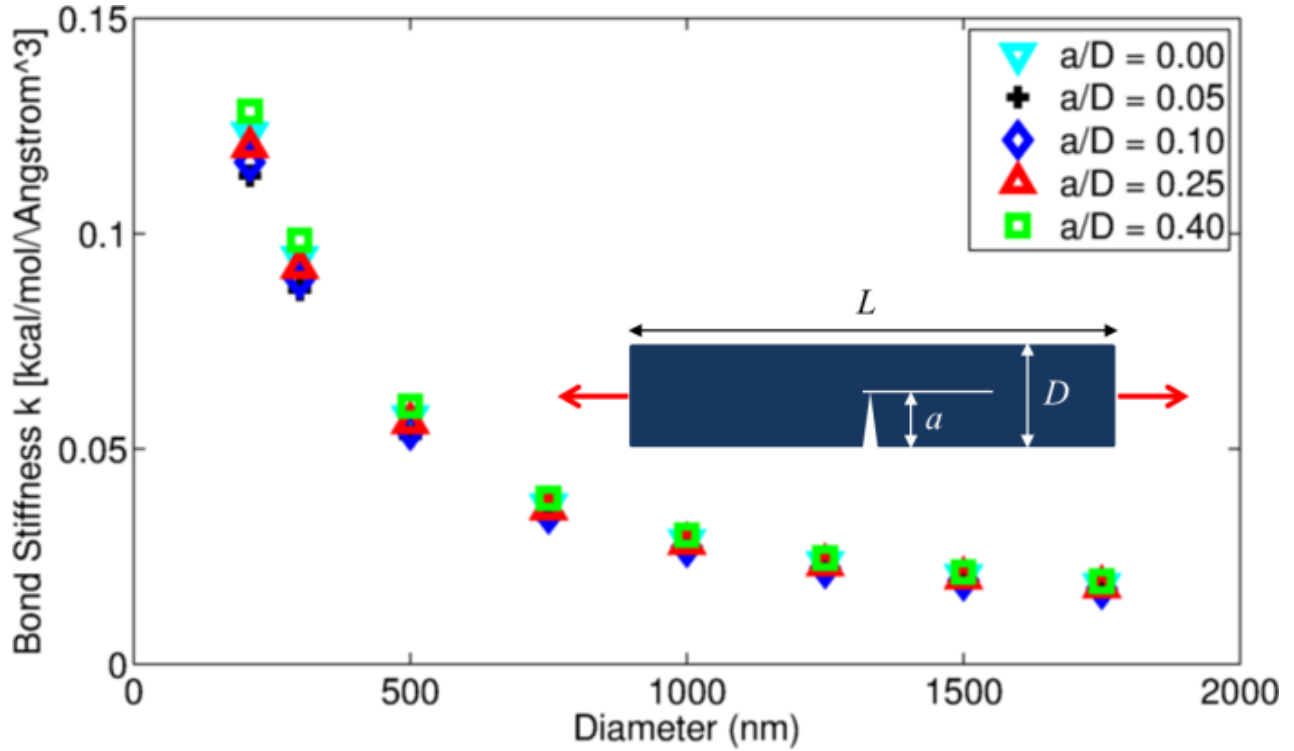


Figure 56. Plane strain fiber model with flaw and bond stiffness for different crack size ratios a/D . A triangular mesh with bond distance 10 nm is used to model a flawed fiber with diameter D , length L (both much bigger than the bond distance) and a surface crack with length a . Each crack size ratio a/D with $D = 210$ nm is associated with a different internal bond stiffness to match the experimentally observed modulus of ≈ 120 MPa.

For a variety of crack size to diameter ratios a/D , the bond stiffness k_0 and bond failure strain ϵ_0 of the harmonic potential are calibrated (individually for each ratio a/D) such that the $D = 210$ nm fiber model coincides with the experimental strength and failure strain (*i.e.*, 5% failure strain and 6,000 MPa failure strength, see **Figure 56**). This calibration is necessary as we have no knowledge of the perfect crystal cell behavior. Each crack size ratio a/D with $D = 210$ nm is then associated with a different internal bond stiffness to match the experimentally observed modulus of approximately 120 MPa (**Figure 55a**). By matching the model with experiments at the smallest diameter, we account for the nescience of typical fiber flaw sizes and the perfect crystal cell behavior. Structural changes in the material, for example crystal reorientation caused by changes in the processing conditions used to generate varied fiber diameters, cannot be directly reflected in this coarse-grained model. Hence, the modulus at all diameters is a model input and the bond stiffness of the fibers with larger diameters is adjusted according to the experimentally observed modulus (**Figure 56** and **Figure 55a**). For larger diameters $D > 210$ nm, the bond failure strain is kept constant and the bond stiffness decreases proportional to the modulus.

All simulations are carried out as molecular statics runs (at an effective zero temperature to model steady state deformation), using the molecular dynamics simulation package LAMMPS.³⁵ We use a conjugate gradient energy minimization algorithm. The failure strength (the engineering stress calculated from the virial stress), failure strain, and toughness modulus are recorded for all fiber diameters in the range of $D = 210$ nm to $1.75 \mu\text{m}$.

c. Results and discussion

For comparative reasons, the scaling behavior of strength and toughness modulus of the unflawed fiber ($a/D = 0$) is plotted in **Figure 55b-d**. The data shows that the scaling of the fiber

strength and in particular extensibility cannot be sufficiently reasoned by taking into account only the change in modulus. Specifically, the failure strain remains constant in the unflawed model (**Figure 55c**). In the case of an unflawed fiber, the drop in strength, strain and toughness with increasing diameter are not well reproduced.

A good match with the experimental results is found in the case where the model incorporates size effects of a flawed fiber, *i.e.* fibers where $a/D \neq 0$ (**Figure 55b-d**). The findings suggest that both the strength and toughness modulus scaling can be well explained by a size effect model of the cracked fiber (**Figure 55b&d**). Thereby, the strength does not only scale with the elastic modulus, but displays also the size-dependence of a flawed fiber as predicted by fracture mechanics, *i.e.* the strength scales with $\sqrt{1/D}$. In fact, the computational results are almost independent of the crack size ratio a/D . By fitting the experimental results with an assumed crack size ratio, the perfect crystal behavior, an unknown physical quantity represented by the bond failure strength and bond failure strain, is set. We then use these parameters for a simulation series of constant a/D .³⁴ The combination of structural change (represented by the change of elastic modulus) and size effect (scales with $\sqrt{1/D}$) decrease the fiber strength for larger diameters in a similar way for all a/D .

We note that the strain scaling is slightly overestimated in the flawed fiber models (**Figure 8c**). This suggests that other effects could play a role in reducing the failure strain at larger diameters, *e.g.* nonlinearities in the material behavior (the model assumes a linear bond behavior) and structural changes in the crystallites that further reduce the strain capacity of the fiber. In case the reduced extensibility for larger diameters was taken into account in the fiber model, the fit between the model results and the experimentally observed failure strength and toughness modulus would improve.

References

- (1) Hearle, J. W. S.; Grosberg, P.; Backer, S. *Structural mechanics of fibers, yarns, and fabrics*; Wiley-Interscience: New York, 1969.
- (2) Wang, Y. In *Characterization of materials*; John Wiley & Sons, Inc.: 2012.
- (3) Chinga-Carrasco, G.; Miettinen, A.; Luengo Hendriks, C. L.; Gamstedt, E. K.; Kataja, M. In *Nanocomposites and polymers with analytical methods*; Cuppoletti, J., Ed.; InTech: Online, 2011.
- (4) Naraghi, M.; Filleter, T.; Moravsky, A.; Locascio, M.; Loutfy, R. O.; Espinosa, H. D. A multiscale study of high performance double-walled nanotube-polymer fibers, *Acs Nano* **2010**, *4*, 6463-6476.
- (5) Wei, X. D.; Naraghi, M.; Espinosa, H. D. Optimal length scales emerging from shear load transfer in natural materials: Application to carbon-based nanocomposite design, *Acs Nano* **2012**, *6*, 2333-2344.
- (6) Zhu, Y.; Espinosa, H. D. An electromechanical material testing system for in situ electron microscopy and applications, *P Natl Acad Sci USA* **2005**, *102*, 14503-14508.
- (7) Peng, B.; Locascio, M.; Zapol, P.; Li, S. Y.; Mielke, S. L.; Schatz, G. C.; Espinosa, H. D. Measurements of near-ultimate strength for multiwalled carbon nanotubes and irradiation-induced crosslinking improvements, *Nat Nanotechnol* **2008**, *3*, 626-631.
- (8) Filleter, T.; Bernal, R.; Li, S.; Espinosa, H. D. Ultrahigh strength and stiffness in cross-linked hierarchical carbon nanotube bundles, *Adv Mater* **2011**, *23*, 2855-+.
- (9) Filleter, T.; Yockel, S.; Naraghi, M.; Paci, J. T.; Compton, O. C.; Mayes, M. L.; Nguyen, S. T.; Schatz, G. C.; Espinosa, H. D. Experimental-computational study of shear interactions within double-walled carbon nanotube bundles, *Nano Lett* **2012**, *12*, 732-742.
- (10) Qian, D.; Liu, W. K.; Ruoff, R. S. Load transfer mechanism in carbon nanotube ropes, *Compos Sci Technol* **2003**, *63*, 1561-1569.
- (11) Kis, A.; Csanyi, G.; Salvetat, J. P.; Lee, T. N.; Couteau, E.; Kulik, A. J.; Benoit, W.; Brugger, J.; Forro, L. Reinforcement of single-walled carbon nanotube bundles by intertube bridging, *Nat Mater* **2004**, *3*, 153-157.
- (12) Salvetat, J. P.; Briggs, G. A. D.; Bonard, J. M.; Bacsá, R. R.; Kulik, A. J.; Stockli, T.; Burnham, N. A.; Forro, L. Elastic and shear moduli of single-walled carbon nanotube ropes, *Phys Rev Lett* **1999**, *82*, 944-947.
- (13) Schrader, M. E.; Loeb, G. I. *Modern approaches to wettability: Theory and applications*; Plenum Press: New York, 1992.
- (14) Strus, M. C.; Zalamea, L.; Raman, A.; Pipes, R. B.; Nguyen, C. V.; Stach, E. A. Peeling force spectroscopy: Exposing the adhesive nanomechanics of one-dimensional nanostructures, *Nano Lett* **2008**, *8*, 544-550.
- (15) Strus, M. C.; Cano, C. I.; Pipes, R. B.; Nguyen, C. V.; Raman, A. Interfacial energy between carbon nanotubes and polymers measured from nanoscale peel tests in the atomic force microscope, *Compos Sci Technol* **2009**, *69*, 1580-1586.
- (16) Buchoux, J.; Bellon, L.; Marsaudon, S.; Aime, J. P. Carbon nanotubes adhesion and nanomechanical behavior from peeling force spectroscopy, *Eur Phys J B* **2011**, *84*, 69-77.
- (17) Ke, C. H.; Zheng, M.; Zhou, G. W.; Cui, W. L.; Pugno, N.; Miles, R. N. Mechanical peeling of free-standing single-walled carbon-nanotube bundles, *Small* **2010**, *6*, 438-445.
- (18) Ishikawa, M.; Harada, R.; Sasaki, N.; Miura, K. Visualization of nanoscale peeling of carbon nanotube on graphite, *Appl Phys Lett* **2008**, *93*.
- (19) Sasaki, N.; Toyoda, A.; Itamura, N.; Miura, K. Simulation of nanoscale peeling and adhesion of single-walled carbon nanotube on graphite surface, *e-Journal of Surface Science and Nanotechnology* **2008**, *6*, 72-78.
- (20) Sasaki, N.; Toyoda, A.; Saitoh, H.; Itamura, N.; Ohyama, M.; Miura, K. Theoretical simulation of atomic-scale peeling of single-walled carbon nanotube from graphite surface, *e-Journal of Surface Science and Nanotechnology* **2006**, *4*, 133-137.
- (21) Kendall, K. Thin-film peeling - elastic term, *J Phys D Appl Phys* **1975**, *8*, 1449-1452.

- (22) Griffith, A. A. The phenomena of rupture and flow in solids, *Philosophical Transactions of the Royal Society of London. Series A, Containing Papers of a Mathematical or Physical Character* **1921**, 221, 163-198.
- (23) Huang, P. H. Molecular dynamics for lateral surface adhesion and peeling behavior of single-walled carbon nanotubes on gold surfaces, *Mater Chem Phys* **2011**, 131, 297-305.
- (24) Hertel, T.; Walkup, R. E.; Avouris, P. Deformation of carbon nanotubes by surface van der waals forces, *Phys Rev B* **1998**, 58, 13870-13873.
- (25) Saha, B.; Schatz, G. C. Carbonization in polyacrylonitrile (pan) based carbon fibers studied by reaxff molecular dynamics simulations, *J Phys Chem B* **2012**, 116, 4684-4692.
- (26) van Duin, A. C. T.; Dasgupta, S.; Lorant, F.; Goddard, W. A. Reaxff: A reactive force field for hydrocarbons, *J Phys Chem A* **2001**, 105, 9396-9409.
- (27) Chenoweth, K.; van Duin, A. C. T.; Goddard, W. A. Reaxff reactive force field for molecular dynamics simulations of hydrocarbon oxidation, *J Phys Chem A* **2008**, 112, 1040-1053.
- (28) Kamat, A. M.; van Duin, A. C. T.; Yakovlev, A. Molecular dynamics simulations of laser-induced incandescence of soot using an extended reaxff reactive force field, *J Phys Chem A* **2010**, 114, 12561-12572.
- (29) Jiang, D. E.; van Duin, A. C. T.; Goddard, W. A.; Dai, S. Simulating the initial stage of phenolic resin carbonization via the reaxff reactive force field, *J Phys Chem A* **2009**, 113, 6891-6894.
- (30) Desai, T. G.; Lawson, J. W.; Koblinski, P. Modeling initial stage of phenolic pyrolysis: Graphitic precursor formation and interfacial effects, *Polymer* **2011**, 52, 577-585.
- (31) Prilutsky, S.; Zussman, E.; Cohen, Y. The effect of embedded carbon nanotubes on the morphological evolution during the carbonization of poly(acrylonitrile) nanofibers, *Nanotechnology* **2008**, 19.
- (32) Prilutsky, S.; Zussman, E.; Cohen, Y. Carbonization of electrospun poly(acrylonitrile) nanofibers containing multiwalled carbon nanotubes observed by transmission electron microscope with in situ heating, *J Polym Sci Pol Phys* **2010**, 48, 2121-2128.
- (33) Gao, H. J.; Chen, S. H. Flaw tolerance in a thin strip under tension, *J Appl Mech-T Asme* **2005**, 72, 732-737.
- (34) Giesa, T.; Arslan, M.; Pugno, N. M.; Buehler, M. J. Nanoconfinement of spider silk fibrils begets superior strength, extensibility, and toughness, *Nano Lett* **2011**, 11, 5038-5046.
- (35) Plimpton, S. Fast parallel algorithms for short-range molecular-dynamics, *J Comput Phys* **1995**, 117, 1-19.

Scientific Progress and Accomplishments

Status of Work:

The **Espinosa** group performed mechanical testing and characterization experiments at all hierarchical levels, in addition to theoretical modeling to complement the efforts of the Schatz and Buehler groups. They completed multiscale mechanical testing of carbon nanotubes (CNTs) including nanoscale peeling and shear experiments on individual CNTs, tests to determine CNT bundle-bundle interfacial properties, and microtensile tests on macroscale DWNT/polymer yarns. They have characterized double walled carbon nanotube (DWNT) yarns fabricated by MER Corporation and the Nguyen group. Mechanical testing of the yarns is currently being completed. The mechanisms of the macroscale yarn mechanical behavior are being simulated by the Espinosa and Buehler groups. Finally, they have determined the mechanical properties of graphene oxide (GO) composites containing polymer layers fabricated by the Nguyen group.

MER Corporation fabricated and characterized directly spun and mat-derived DWNT yarns for comparative studies of static mechanical properties and structural characterization. Characterization was completed in collaboration with the Espinosa group to determine composition, by measurements of linear mass density and by scanning electron microscopy (SEM) to determine helix angle, diameter, average porosity and surface layer porosity, and DWNTs alignment. Mechanical testing of these yarns is currently in progress.

The **Buehler** group's work focused on atomistic and bottom-up modeling of carbon nanotubes and carbon nanotube based materials. Both reactive and nonreactive full atomistic simulations have been carried out, and scaled up to larger time- and length-scales by preforming coarse-grain simulations. All activities were closely integrated with experimental efforts in the MURI team. Major areas of activities include: I) atomistic and theoretical analysis of tunable inter-CNT interactions; II) wavy CNT tuned by the interfacial interaction and mismatch strain; III) coarse-grained modeling of CNT fiber and PMMA polymer trained by atomistic simulations and its application in studying interaction between CNT-bundles; and IV) fracture mechanics and size effects in carbon fibers as collaborative work with the Dzenis group.

The **Schatz** group has focused on modeling sheer forces in DWNT bundle pull-out experiments, modeling MWCNT peeling experiments between CNTs and graphene surfaces, and modeling the chemistry of CNT functionalization. They continued to research the origins of the force resisting extraction of the inner bundle of CNTs from the outer sheath. In addition, they perform MM3 calculations to simulate the multi-walled carbon nanotube (MWNT) peeling experiments performed by the Espinosa group. These studies provide benchmark results for comparison with experiments that can be used to differentiate mechanistic issues concerning the origin of the adhesive interaction between the CNT and the flat graphene sheet, the nanotube deformation on the graphene surface, and the influence of graphitic deposits present on the outer shell of the MWCNTs being tested. Finally, the Schatz group has expanded their capabilities for MD modeling of the initial stages of template carbonization in polyacrylonitrile (PAN) -based carbon nanofibers to emulate the heat treatment of the electrospun PAN fibers by the Dzenis group.

The **Nguyen** group explored the structure-property relationship in DWNT yarns by preparing samples to investigate the effect of alignment and packing density of CNTs in mechanical properties. The Nguyen group fabricated yarns at different processing conditions, which were then characterized and evaluated for mechanical properties with the Espinosa group. Another focus was the continued study of graphene oxide paper as an easily manipulated macroscopic model to study the effect of increasing the interface between adjacent carbon-based nanofillers. They prepared

graphene oxide/CNT composite papers from aqueous dispersion by a vacuum filtration technique and characterized the relative graphene oxide/CNT ratios. To examine the effect of defects in graphene oxide composites, they studied the effects of introducing soft polymer layers into nanocomposites, which have theoretically been shown to hinder crack propagation. They found that their multilayer-laminate composites retain strength with increased sample volume due to a defect-tolerance imparted by the crack-hindering polymer layers.

The focus of the **Dzenis** group's research in this reporting period was the mechanical behavior and mechanisms of deformation and failure in individual continuous carbon nanofilaments. Size effects in continuous carbon nanofibers (CNF) were further evaluated. A possibility of tough continuous carbon filament was demonstrated for the first time. Mechanical behavior and structure of CNFs were compared to those of a range of commercial carbon fibers. Modeling of the size effects was performed in collaboration with the Buehler group. Results of extensive mechanical testing of macrolength specimens in the Dzenis group were compared with in-situ testing of micro-specimens by the Espinosa group. CNF fine structure was evaluated explicitly by HRTEM. Nanomanufacturing of DWNT- and GO-templated nanofibers was further optimized in collaboration with MER Corp and the Nguyen group. Size effects in the templated CNFs were further investigated and the highest strength of DWNT-templated CNF was recorded. Effects of mechanical constraint during CNF fabrication on their structure were evaluated. Internal constraint as a mechanism of graphitic structure improvement in templated CNFs was investigated by evaluating nanofiber shrinkage. Modeling of this mechanism was discussed with the Schatz group. Variation of properties and size effects in precursor nanofibers were further explored by fabricating, testing, and characterizing pioneering nanofibers with artificially reduced crystallinity. The nanofibers exhibited further improved mechanical strength and toughness.

Scientific Accomplishments:

Fabrication and Characterization of Microscale DWNT Composite Yarns

Fabrication of DWNT yarns

During the reporting period, MER Corporation manufactured and delivered to NU a set of 106 samples of directly spun and mat-derived DWNT yarns for comparative studies of static mechanical properties and structural characterization by WAXD and FIB techniques. The yarns have been subjected to the strictly controlled processing to provide for desirable helix angle and diameter. All samples have been characterized by TGA to precisely determine their composition, by measurements of linear mass density, and by SEM to determine helix angle, diameter, average porosity and surface layer porosity, and assess the degree of DWNTs alignment in the yarn. This data is tabulated in an interactive Excel table that upon insertion of the break Force and maximum Slope values measured in tensile testing automatically generates the values for all types of the strengths and moduli of nanotube yarns that are used in the literature reports.

A fundamental structural conclusion is suggested by the table data. The table generates a precise value for the average porosity of the full-component yarn from the values of linear density, optical diameter, percentage and densities of yarn components (DWNT bundles, sizing, iron particles, amorphous carbon and graphite). This can be compared to the presented in the table value of the surface porosity of the yarn assessed from the SEM images by the formula: Porosity (vol%) = $100(1 - (\pi/2\sqrt{3})(d/D)^2)$, where "d" is the average diameter of DWNT bundles, and "D" is the average separation between the bundle axes. The surface porosity slightly exceeds in value the average porosity in most cases of these external matrix-free yarns. This comparison shows that the bundles are more densely packed inside the yarn than in the surface layer.

Structure-property relationship in DWNT yarns - a quantitative study

Although CNTs are known for their high strength and stiffness, translating their nanoscale properties into macroscopic materials such as yarns is highly challenging and requires both a high degree of CNT alignment as well as optimized interactions between neighboring individual CNTs or bundles. Studies have indicated that maximal alignment and packing in CNT-based yarns is highly desirable to maximize the contact efficiency between neighboring CNTs and thus the efficiency of load transfer. To investigate the effect of alignment and packing density of CNTs in mechanical properties of DWNT yarns, we attempted to make yarns at different processing conditions, in collaboration with MER Corporation, and then characterize and evaluate the mechanical properties with Espinosa group. Three different kinds of yarns are fabricated: (1) quickly spun yarn from DWNT mat at NU (~5 min), (2) slowly spun yarn (~2 h) from DWNT mat, (Figure 1a), and (3) directly spun yarn from CVD reactor both at MER Corp. (Figure 1b). The yarns were then characterized for structural morphology and packing by focused-ion beam (FIB).

While directly spun yarns from the reactor have DWNTs that appears to be well aligned, they have highly porous morphology (Figure 1a). Quickly spun yarns are similarly porous but do not have good CNT alignment (Figure 2c). Slowly spun yarns have a very different morphology: with intermediate CNT alignment that is slightly better than that of quickly spun yarns, but are highly compact in nature. Apart from few voids where DWNT mats did not collapse properly, in most parts these yarns are densely packed. The alignment of these yarns is being investigated at Argonne National Laboratory using wide-angle X-ray diffraction (WAXD), which will allow us to quantify the alignment or orientation factor and be able to distinguish these yarns from structural point-of-view. The mechanical properties of the yarns are currently under investigation by Espinosa group.

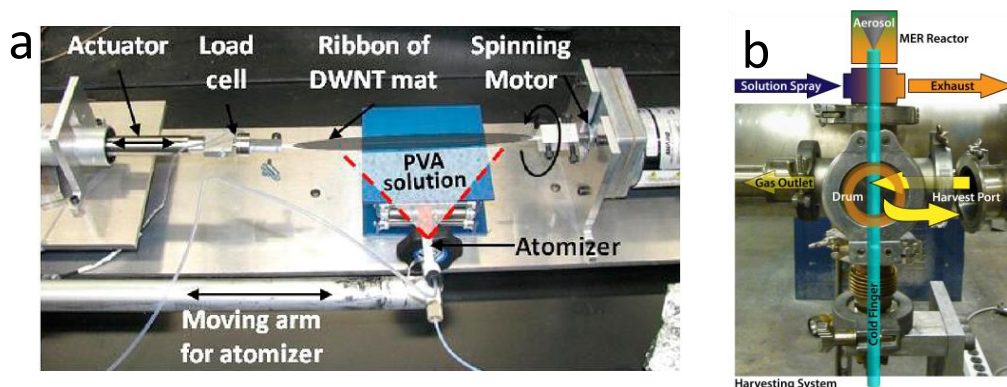


Figure 1. (a) Fabrication set-up for quickly and slowly spun DWNT yarns, and (b) directly spun yarn from CVD reactor.

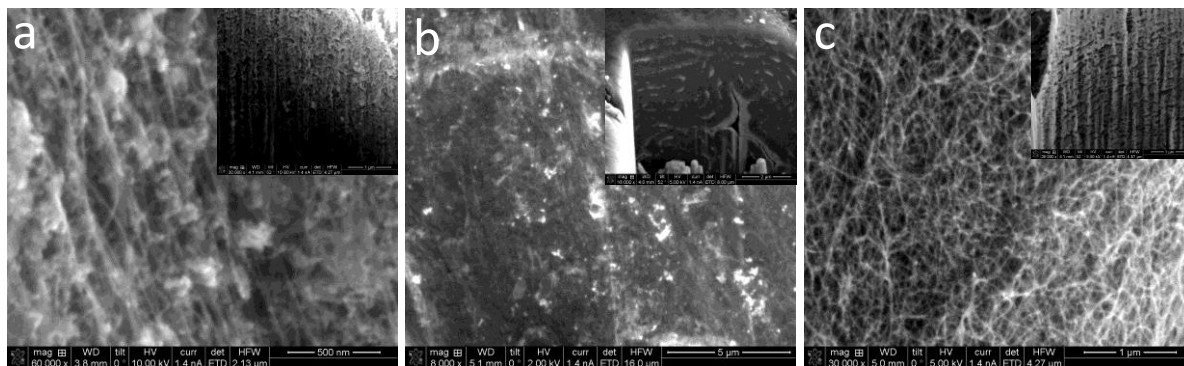


Figure 2. FIB images of (a) directly spun, (b) slowly spun, and (c) quickly spun DWNT yarns.

Mechanical testing and analysis of yarns

Thus far, a total of 28 samples have been tested, among which the results of 16 samples have been analyzed: six quickly-spun, six directly-spun, and four slowly-spun samples. In calculating mechanical properties from load-displacements, cross sectional area plays a key role. There are different ways to estimate cross sectional area depending on which components of the yarn are considered to be load bearing. The first is taking the cross section based on SEM images. First, the strength and modulus were calculated based on the cross section of the samples measured in SEM. So far, the results show that the slowly spun yarns have a 2x higher strength and modulus than the other two types of yarns as shown in Figure 3. Ductility does not depend on the method of cross section calculation and is roughly the same for the three kinds of yarns (Figure 3).

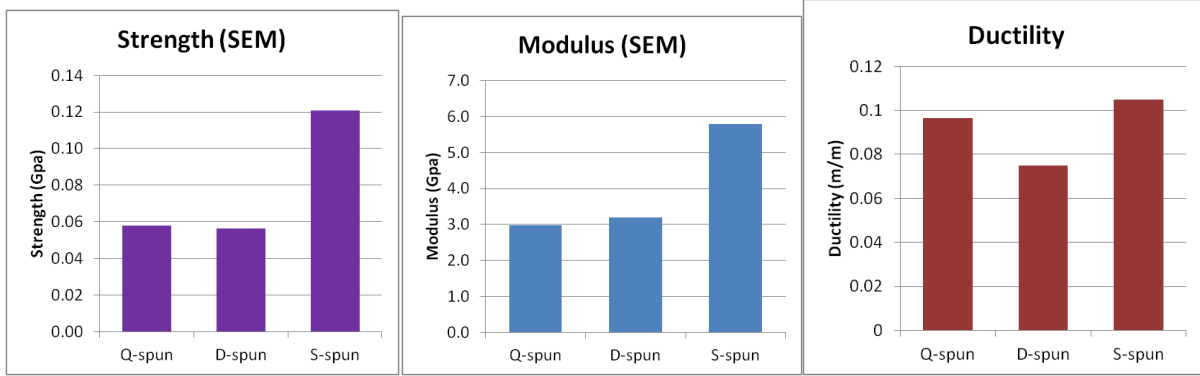


Figure 3. Comparison of strength, modulus, and ductility for quickly spun, directly spun, and slowly spun yarns.

The second method considers the cross section based on the linear density of the whole yarn. After the failure of each sample, the length and weight of the two pieces of the sample were measured based on which the linear densities of the whole yarn were calculated. The cross sectional area then would be counted as $A^{yarn} = \frac{\lambda^{yarn}}{\rho^{yarn}}$. The linear densities were used to consider the porosity in the cross-section calculations. In this case, quickly spun yarns show higher mechanical properties, mostly due to the fact that this method considers porosity and the quickly spun samples are more porous than the other two types (Figure 4).

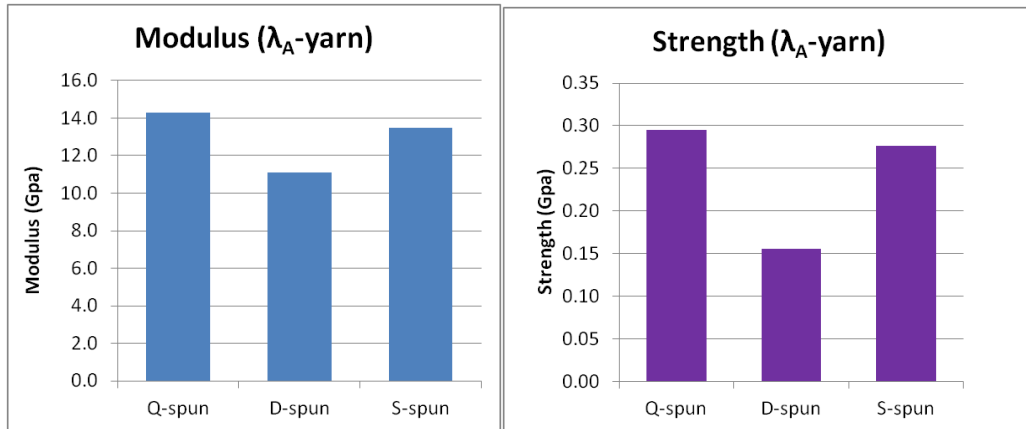


Figure 4. Comparison of strength and modulus as determined by analyzing the cross section based on the linear density of the whole yarn for quickly spun, directly spun, and slowly spun yarns.

The third method considers the CTNs as the only load bearer and neglects other components in the cross section calculations. Considering the CNTs as the only load bearer and calculating mechanical

properties based on their fraction of the cross section is a means of assessing the effectiveness of load transfer to CNTs within the yarn. In this context, the cross sectional area would be counted as $A^{CNT} = \frac{\lambda^{CNT}}{\rho^{CNT}}$ where λ^{CNT} is the linear density of the carbon nanotubes, and ρ^{CNT} is the volume density of carbon nanotubes, assumed from close hexagonal packing estimations reported in the literature. The results show that the relative behavior of the three types of yarns remains the same as the ones calculated using the last method. The values are about 2x higher since the components other than nanotubes are neglected in cross section calculations, resulting in lower area and higher mechanical properties.

Fracture surfaces of DWNT yarns have also been investigated using SEM. Complementing mechanical testing data, qualitative analysis of fracture surfaces can provide insight into the way in which the yarns failed. Preliminary analysis of the fracture surfaces suggests that directly spun yarns (Figure 5a) undergo significant local deformation near the failed region, as the initially circular cross section appears to be stretched into a different conformation. A slowly spun sample (Figure 5b) shows fanning out near the fracture surface, as evidenced by the larger diameter toward the bottom end of the dark gray region. Sword-in-sheath type failure, in which the outermost bundles separate from one another, may also play a role, as suggested by the light white region extending from the end of the yarn. Quickly spun samples (Figure 5c) often show brittle fracture surfaces, which matches well with the results of our previous study when 0% PVA content was used. Additional characterization of the SEM fracture surfaces will be conducted, with emphasis on the best-performing and worst-performing yarns, in order to obtain additional insights into the structure-property relationships of these CNT-based yarns.

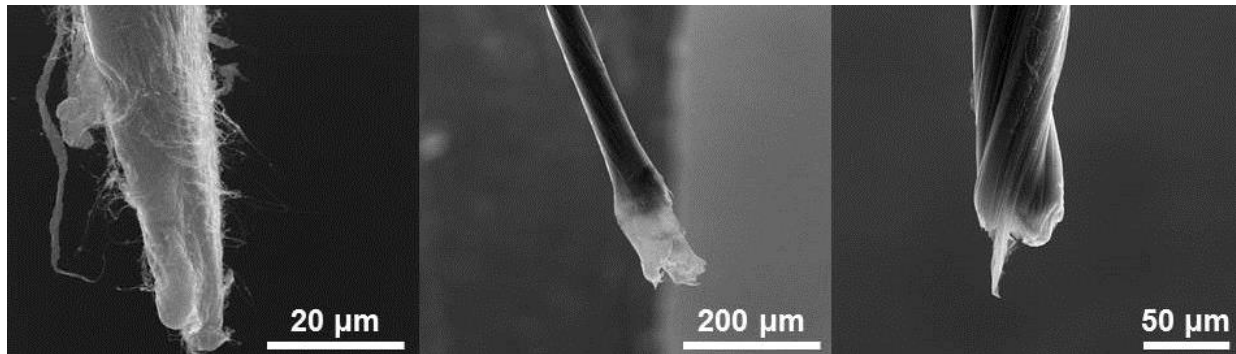


Figure 5. SEM images of fracture surfaces of (left) directly spun, (center) slowly spun, and (right) quickly spun DWNT yarns.

Multi-scale Experimental and Computational Studies of the Mechanical Behavior of CNT/Polymer Bundles and Yarns

Multiscale Modeling

The Espinosa, Buehler, and Schatz groups have developed a multi-scale modeling framework for predicting the strength of CNT yarns. In previous studies, we have accurately characterized the mechanics of each component of our yarns, including the fracture strength of DWNT bundles and interface shear strength between two DWNT bundles (see Figure 6). The goal of the modeling effort is to develop a realistic, accurate model for the mechanics of carbon nanotube yarns at length scales ranging from a macroscopic yarn down to an individual carbon nanotube and to synthesize our knowledge of the mechanics of nanoscale components into a unified predictive framework. From the experiments, we noticed that there are three factors which have significant effects on the yarn performance:

1. The bundle will rupture under tension,
2. The bundle-bundle interface will fail under shear,
3. The transversal pressure developed inside a twisted yarn under tension will stabilize the bundle-bundle interface.

Thus, we developed load-sharing Monte-Carlo model to investigate, in our yarns, which of these three aspects will be the predominant factor for determining the composite strength. The following sections discuss how these factors are incorporated in the models.

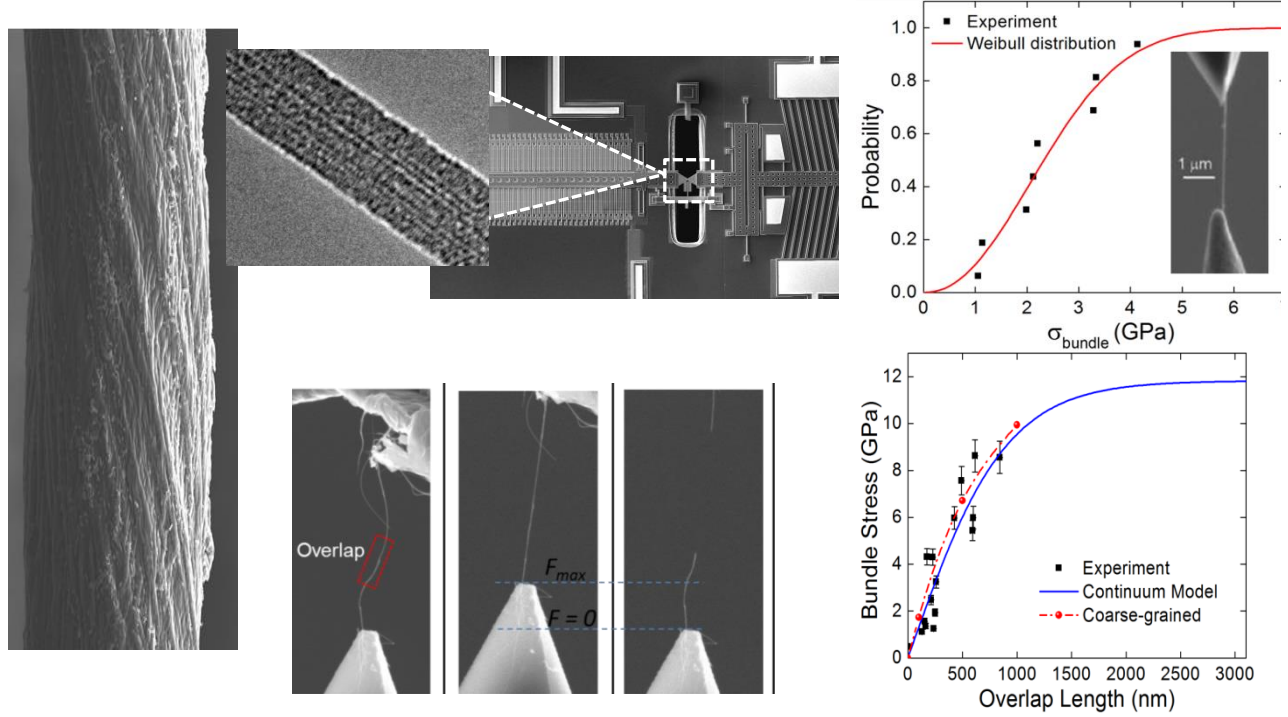


Figure 6. A macroscopic DWNT yarn (Left) exhibits unique structures at disparate length scales. The tensile strength of DWNT bundles (Top middle) and interface shear strength (Bottom middle) have been studied by experimental and computational methods. The results from these studies are interpreted with accurate models, and applied in a unified computational framework to predict the strength of macroscopic yarns.

Bundle rupture strength

The tensile strength of DWNT bundles is taken from experiments by Filleter *et al.* [1] and interpreted using Weibull statistics (see Figure 6 (top right)). The rupture strength of bundles is assumed to be randomly distributed according to

$$F(\sigma) = 1 - \exp\left\{-\left(\frac{\sigma}{\sigma_0}\right)^m\right\}$$

where $F(\sigma)$ is the probability of failure at stress σ . It is important that the scale factor σ_0 is only valid for specimens of the same length as the specimens tested. In order to assign strengths to each node, it is necessary to determine how strength scales with size.

Bundle-bundle interface without transversal pressure

Since the bundles are discontinuous, the load carried by a bundle at a location where the bundle is broken must be zero. The load may be recovered over some characteristic distance from the break through shear-transfer from its neighbors. The axial stress distribution near a break is approximated with a bi-linear law fitted to the shear-lag model. This strategy captures the essential load-saturation effect measured in bundle-bundle shearing experiments, never accounted for in any

other computational model in the literature. In addition, the equilibrium constraint is satisfied exactly at each yarn cross-section.

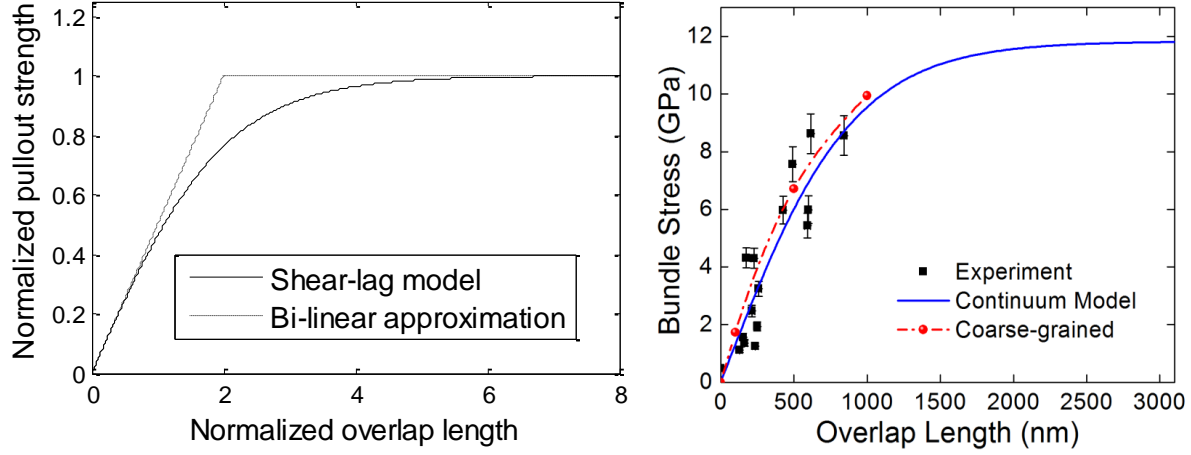


Figure 7. The pullout strength of bundles is approximated from the shear-lag model, which gives excellent agreement with experiments.

Due to the assumption that bundle-bundle interfaces undergo perfect plasticity, the load-sharing Monte Carlo model yields an upper bound on the yarn strength. A lower-bound is obtained using the recently-developed statistical shear-lag model.

Effect of transversal pressure on the bundle-bundle interface

As the yarn is loaded axially, a radial pressure develops within the yarn due to the yarn twist. Each concentric layer of fibrils contributes to the radial pressure, which attains its maximum at the center of the yarn. The increment in pressure is determined by modeling each layer of fibrils as a twisted filament under constant tension. From equilibrium, the pressure increment is

$$\delta P = \sigma_f \left(\frac{A_f}{d_f^2} \right) \frac{\sin^2 \alpha_r}{r} d_f$$

where σ_f , A_f , d_f , α_r and r are the fibril stress, fibril cross-sectional area, fibril diameter, twist angle, and radial position, respectively. The fibril stress is assumed to follow the relation $\sigma_f = \sigma_y (E_f/E_y) (\cos^2 \alpha - \nu \sin^2 \alpha)$. Since a macroscopic yarn consists of many concentric layers of fibrils, the incremental equation above is converted to a continuum approximation by integrating through the radius of the yarn, letting $d_f \rightarrow dr$, the radial increment. The pressure at any point within the yarn is given by

$$P_{radial}(r) = \sigma_y \left(\frac{E_f}{E_y} \right) \left(\frac{A_f}{d_f^2} \right) \int_r^{r_o} (\cos^2 \alpha_r - \nu \sin^2 \alpha_r) \frac{\sin^2 \alpha_r}{r} dr$$

where α_r depends on r as noted earlier.

The transversal pressure will affect the tube-tube contact number between bundles and enhance the shear strength of the polymer coating between bundles. To check the effect of the transversal pressure on the contact between bundles, we adopted the coarse-grain molecular dynamic model developed by Buehler group for DWNTs with PMMA polymer coating. In order to determine the change in contact area between two DWNT bundles as pressure is applied, we have developed a model system consisting of seven close-packed DWNT bundles. Figure 8 (left) represents the geometry of the system, as generated by the Buehler group. In this geometry, two types of beads are present. Red beads represent PMMA polymers adhering to bundle surfaces in as-fabricated yarns.

Grey beads represent segments of carbon nanotubes, which have been parameterized by fitting of mechanical properties and force – displacement curves.

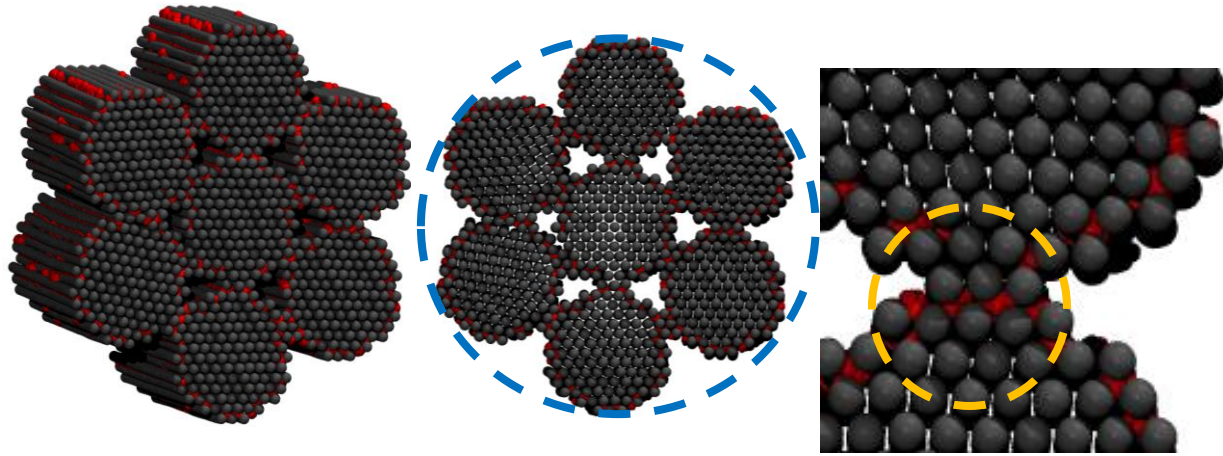


Figure 8. (Left) Coarse-grained representation of yarn system. Red beads represent PMMA groups, and grey beads represent segments of carbon nanotubes. This model was parametrized with experimental data generated by the Espinosa group. The model is able to accurately represent peeling and shearing interactions. (Center) Coarse-grained representation of yarn system, contained within the potential energy surface. This surface will produce a force of magnitude $F = -k(r-R)^2$ inwards, generating pressure effects in the system. This will lead to compression of the yarn, and in direct consequence, the bundles. (Right) Sample schematic of contacting tubes. In this case, three beads from the top bundle are in direct contact with four beads from the bottom bundle. This leads to $N_{\text{Contact}} \approx 4$. It is expected that this quantity will have a strong variation with pressure.

Starting from this model, a harmonic force is applied to atoms that lie within an infinitely long cylinder that contains the exterior radii of the yarn. This force pushes atoms inwards, simulating pressure effects. An example of the system within the force generating cylinder is shown in Figure 8 (center). Under different pressure ranges, the number of contacting nanotubes in adjacent bundles is determined to understand the pressure transfer mechanisms that occur between bundles. These results will directly input into the Monte Carlo model to study the behavior of CNT yarns. Figure 8 (right) shows an example of the criteria utilized for contacting tubes between bundles. This model will inform the Monte Carlo, complemented by simulations performed by the Buehler group in which the force transfer as a function of pressure is studied. This set of simulations will directly describe the force transfer mechanisms in contacting nanotubes that are part of yarn bundles, leading to an informed description of the behavior of yarns during experiments.

In addition to the axial stress in bundles and shear stress between bundles, radial pressure in the yarn can play an important role in the mechanical properties of yarns. Radial pressure can arise during axial loading due to yarn twist, or due to ballistic impact. In order to integrate these effects into the multiscale model, we have run simulations at multiple length and time scales to quantify the effect of radial pressure on CNT-bundle strength and CNT-bundle network deformation.

Predictions by load-sharing Monte-Carlo model

The load-sharing Monte Carlo model is a computational method to estimate the strength of carbon nanotube yarns, incorporating the effects of bundle failure, load recovery, yarn twist, and radial pressure. The Monte-Carlo algorithm starts with an idealized helical yarn with some stochastic parameters, including tensile strength of bundles and spatial distribution of bundle ends. As the load on the yarn is increased, bundles fail in a random fashion depending on their tensile strength.

The stress distribution in the yarn is determined by solving force equilibrium in the axial direction, using a simplified rule for distributing load amongst broken fibers. The core of this method is the load sharing rule which determines how load lost near broken bundles is redistributed to other bundles in the cross section, and how load is recovered along the bundle axis by shear load-transfer.

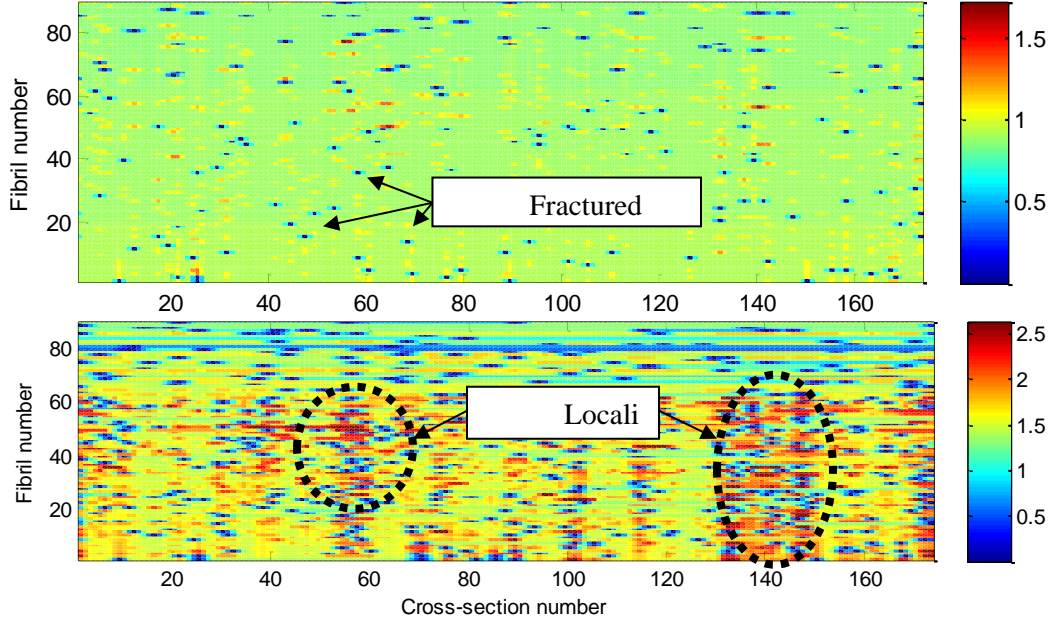


Figure 9. Incremental loading of the yarn causes a progression of bundle failures (above) until finally the stress concentrations near failed bundles cause localized failure of an entire cross-section of the yarn. Color scale corresponds to axial stress in GPa.

Atomistic and theoretical analysis of tunable inter-CNT interactions

Functionalized carbon nanotubes have tremendous potential for nanotechnology applications such as in the fabrication of polymeric carbon fibers. However, approaches to design carbon nanotube structures by using functional groups as glue and carbon nanotubes as stiff building blocks to reach superior mechanical strength and toughness at the fiber level with limited amount of materials remains poorly understood.

Inspired by the outstanding mechanical properties of spider silk, we have investigated the bio-inspired structural model of carbon nanotube based fibers connected by weak hydrogen bonds (H-bonds) formed between functional carboxyl groups as the molecular interface. We have systematic studied the deformation of H-bonds in functional groups and investigated how it is affected by the structural organization of the carboxyl groups, as shown in Figure 10.

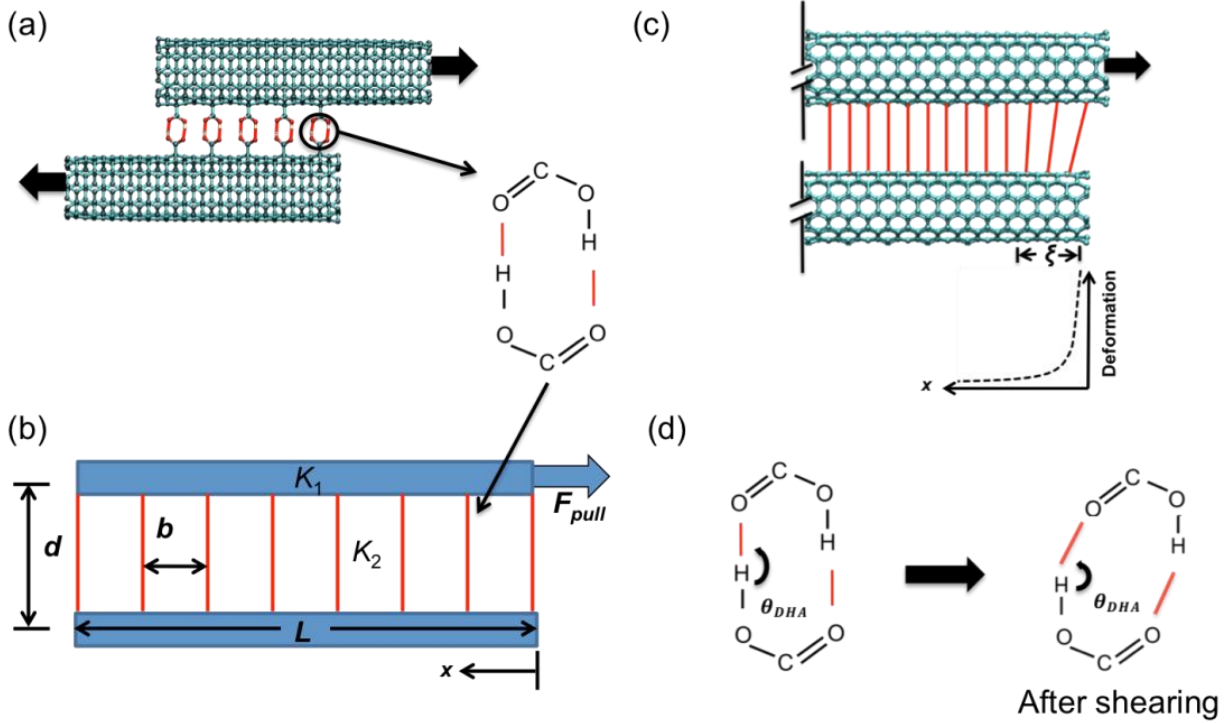


Figure 10. Geometry of the model considered here. (a) Carbon nanotube functionalized with carboxyl groups under shear loading. (b) A one-dimensional elastic structural model of functionalized CNT, where CNTs are modeled as sheets of stiffness K_1 and are connected by H-bonds of stiffness K_2 between them. The H-bonds realized by the functional groups are separated by a distance b and the structure is subject to an applied load. Each red line corresponds to two H-bonds as shown in the chemical structure. (c) Deformation of carboxyl groups near the end of CNTs under shear loading. The deformation profile shows an exponential decay of displacements. (d) The carboxyl group before and after deformation.

We introduce a simple elastic structural model for CNTs functionalized with carboxyl groups, and study the interaction between CNTs from the perspective of H-bonds formed between the carboxyl groups on each CNT surface. In this mesoscale model, each CNT is modeled as a truss with its stiffness corresponding to the diameter of the CNT. The two H-bonds (from the carboxyl group) that connects the CNTs is also modeled a truss element, where the stiffness of the truss corresponds to two H-bonds.

We calculate the bond energy of each single H-bond to derive the stiffness of each carboxyl group (of two H-bonds) based on the Dreiding force field model, in which the H-bond energy is given by the distance and angle between the donor and acceptor. We study the cooperative deformation of H-bonds by grouping the carboxyl groups in pairs of two, three and four on two CNTs, as illustrated in Figure 11.

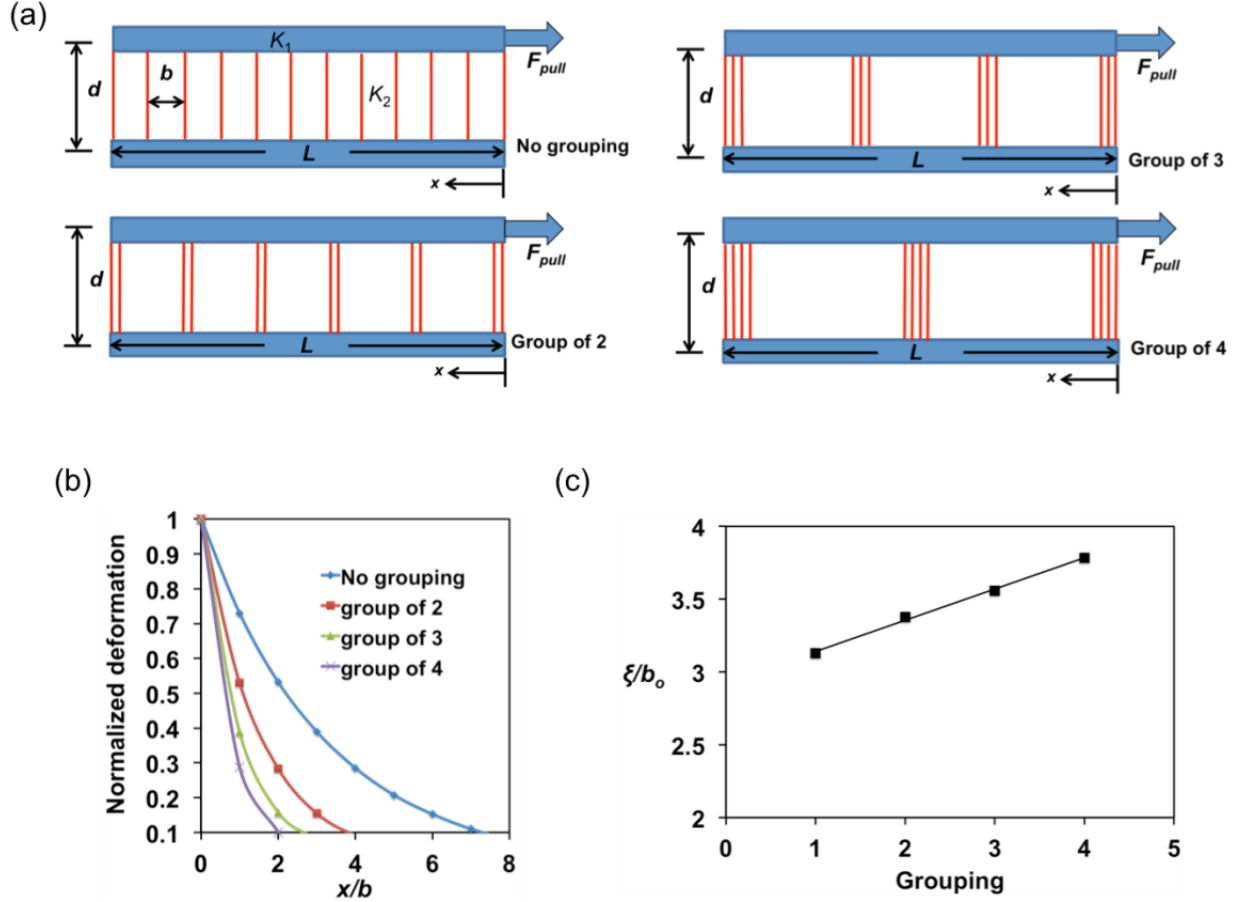


Figure 11. (a) Variation of geometry, where the grouping is changed from no grouping to groups of $N = 2, 3$ and 4 . Each carboxyl group comprises of a pair of two H-bonds; indicated as a red line in the figure. The total number of carboxyl groups per unit length is constant. (b) Comparison of normalized deformation of H-bonds for different cases of carboxyl groups shows how deformation drops as the grouping increases. (c), Variation of the normalized characteristic length as N is increased shows that the normalized characteristic length increases as the grouping increases. The value of n increases as the grouping is increased, from 27 \AA for $N=2$ to approximately 39.22 \AA for the case of $N=4$, marking a 44% increase.

We find that the carboxyl group deformation is non-uniform (Figure 11b) with the maximum deformation near the applied force, whereas it drops to smaller values for the inner bonds. It is also observed that as the grouping of carboxyl groups increases from no grouping to $N = 2, 3$ and 4 , the maximum deformation of carboxyl groups drops while the applied force is constant, with the inner bonds deforming more uniformly. The characteristic length provides a measure for the “ideal” overlap length between the CNTs, and when the CNT length is greater than this characteristic length there is limited cooperative deformation among the carboxyl groups. By computing the characteristic length for $N = 2, 3$ and 4 cases, it is observed that the grouping of carboxyl groups increases the normalized characteristic length as shown in Figure 11c. Which means that even the glue material keeps at a constant level, by changing its distribution can effectively alter the interaction force between two CNTs. For example, comparing to $N=2$, $N=4$ involves 44% more interfacial materials in deformation, yielding larger shear modulus and strength (Figure 11d).

Our study demonstrates that for ultra-small CNTs the external force deforms H-bonds significantly only within a relatively small region on the order of a few nanometers. To have stronger shear strength, we need to increase the CNT diameter or by integrate several of CNTs in the form of bundle. Moreover, our result shows that grouping of functional carboxyl groups (act as inter-CNT

“glue” here) can be used to control the characteristic length in CNT fibers. We may tune the shearing strength and stiffness by designing the distribution of those functional groups. Indeed, this result demonstrates that to improve the mechanical performance of CNT fibers, we need to have functional groups that is able to involve more H-bonds than this simple carboxyl group.

Wavy CNT tuned by the interfacial interaction

The ability to control the morphology of nanomaterials is critical for manufacturing as well as for utilizing them as functional materials or devices. However, the manipulation of such materials remains challenging, and effective methods to control their morphology remain limited. Here, we propose to mimic a macroscopic biological system—the gut—as a means to control the nanoscale morphology by exploiting the concept of mismatch strain, as illustrated in Figure 12. We show that, by mimicking the development of the gut, one can obtain a controlled wavy shape of a CNT. Our study illustrates the possibility of downscaling macroscale phenomena to the nanoscale using continuum mechanics theory.

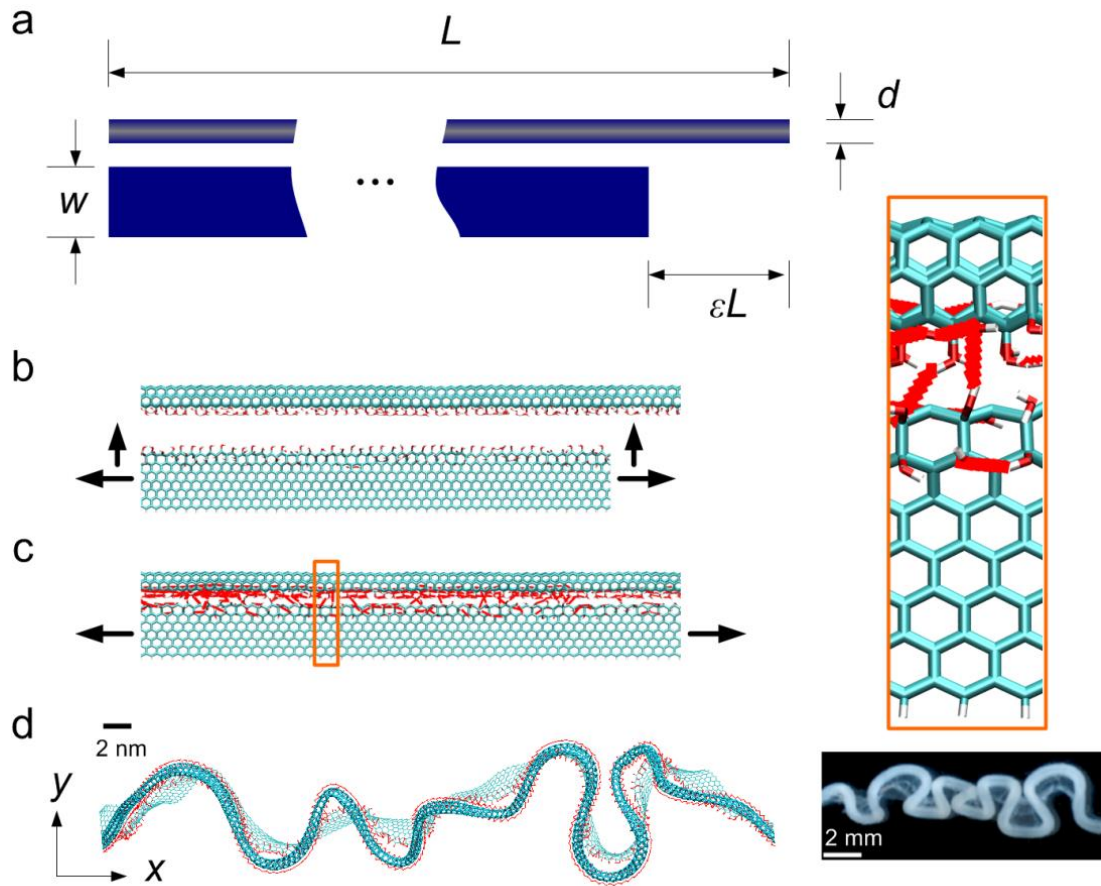


Figure 12. Simulation set up and procedure. (a) Schematic figure of the system composed of a combination of a graphene ribbon and a CNT. The step-by-step simulation procedure is summarized in panels b-d. (b) As the simulation starts, the graphene ribbon is subjected to tensile strain, such that it reaches the same length as the CNT. (c) We fix the two ends of the graphene ribbon and relax other parts of the system. The inset shows a segment with details. (d) Geometry after all constraints are removed and the system is fully relaxed. The inserted figure on the right shows the morphology of loops in the chick's gut at embryonic day 12, at a length-scale 106 times larger than our nano-gut CNT system.

We measure two characteristic geometric parameters: the wave length and magnitude, which are similar to what is found in the gut's loops, to characterize the wavy geometry of CNT. These parameters are computed from the geometry of the CNT axis, which deforms following the profile of the entire CNT, as shown in Figure 13a for a (3,3) CNT. The root mean square deviation of all the axis beads converge within 200 ps, indicating that there is no further conformational change by the end of equilibration simulation. The relationships between the combination of the CNT diameter and applied strain and the characteristic parameters of the wavy geometry are depicted in Figure 13. We note that the wave length monotonically increases with increasing diameter until 5.4 Å. However, for larger diameter this relationship is not monotonic, as the stiffness becomes much smaller than the predicted result. For the magnitude of the wave, it is also seen that, for large diameter the relationship is not monotonic. We analyze our simulation result and reveal that the reason for the deviation from the monotonic curve is buckling of CNTs in their cross-section profiles. The bending moment in the CNT before buckling is primarily caused by the deviation of the compression force direction from the tube axis, which alters the cross-sectional profile of the CNT. For small-diameter CNTs, this effect is not significant, since van der Waals interactions lead to repulsive forces as the opposite walls get too close to one another, while, for large-diameter CNTs, the van der Waals interactions result in attractive forces between opposite walls.

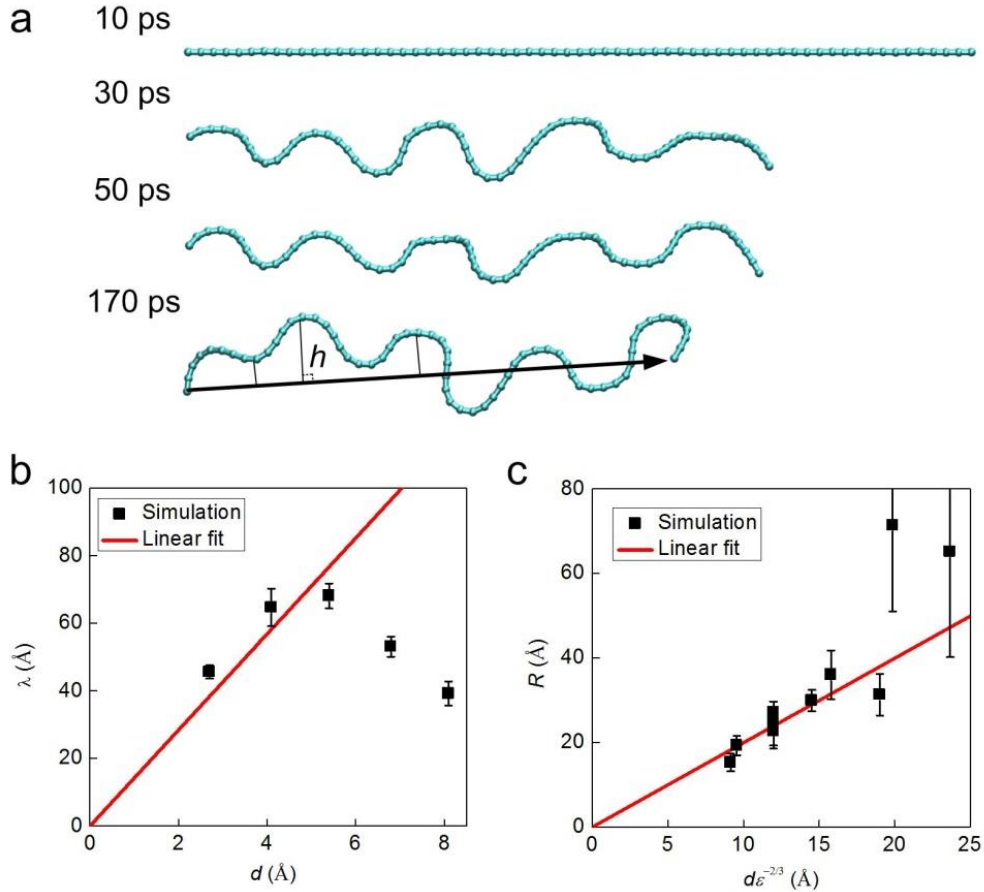


Figure 13. (a) Snapshots of the evolution of the geometry of the (3,3) CNT during equilibration. The CNT axis is represented by a series of beads. The coordinate of each bead is given by the mass center of 50 neighboring carbon atoms. (b) Wave length of a loop period as a function of the CNT diameter. (c) Magnitude of the wave at the maximum amplitude as a function of the CNT diameter and prescribed strain.

In this study we demonstrate that by adding hydroxyl groups on CNTs, they can act as a glue to combine those nanoscale components and achieve controllable wavy conformations. Our result also shows that, for large CNTs, cross-sectional buckling is a mechanism that significantly decreases the wave length of a loop and leads to irregular shape of the waves. Our study illustrated the potential to use nanoscopic carbon materials in order to fabricate biomimicking nanodevices by exploiting prescribed mismatch strain and the particular mechanical features of nanoscale structures. CNTs with a gut-like geometry may also be used as building blocks for building hyperelastic and stretchable CNT fibers and could be a platform for other MURI activities.

Coarse-grained model of CNT fiber and PMMA trained by atomistic simulations

We utilized an atomistically trained coarse-grained simulation approach that allowed for the investigation of the structural and mechanical properties of the polymer-coated CNT bundles. While molecular-level interactions of adjacent carbon nanotubes has been extensively investigated using atomistic methods, bundles and fibers consisting of a large number of CNTs, as studied here, become too computationally expensive at the atomistic level. Moreover, simulating polymer crosslinks further adds to the computational cost. Hence, mesoscopic “bead-spring” methods were employed as a viable approach to simulate arrays of CNTs that can reach the same scales as those investigated in our experimental studies. A “fine-trains-coarse” multiscale approach was implemented to produce a mesoscale model derived from atomistic calculations.

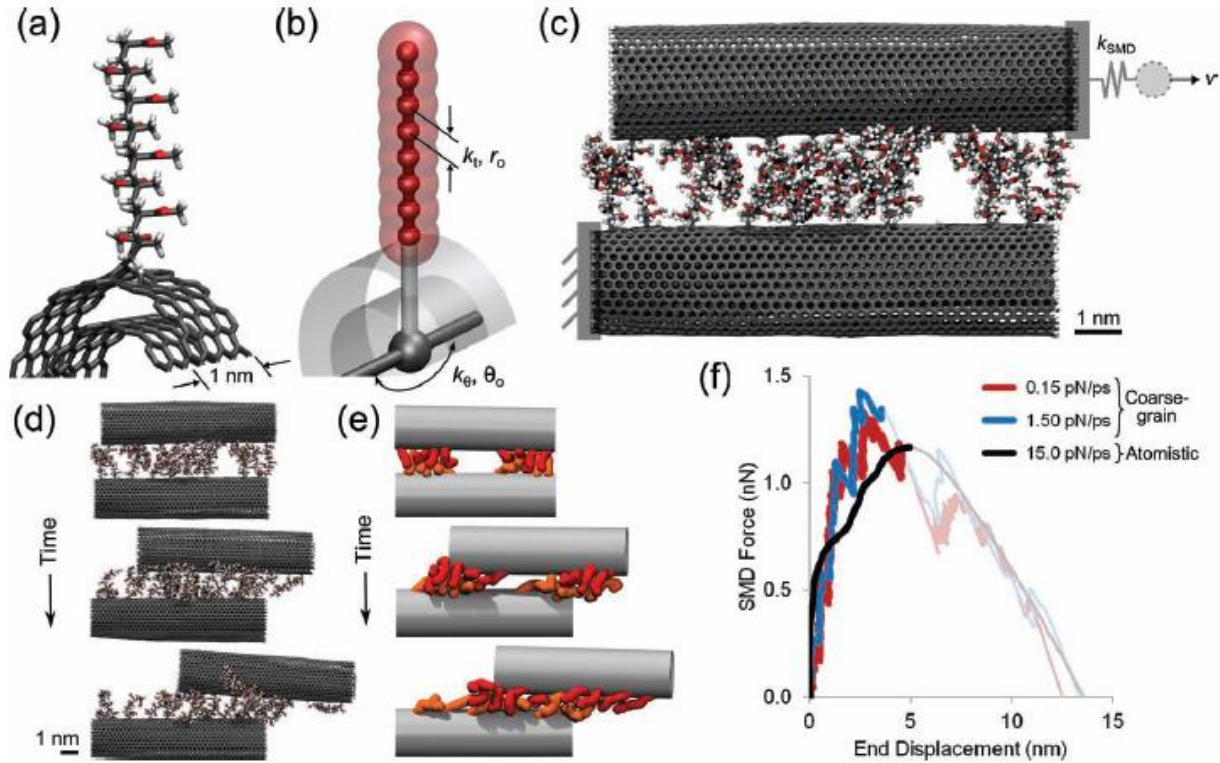


Figure 14. Validation of the coarse-grain model by comparison with atomistic shear behavior at the same length scale. (a) Components of the bundle: ultrashort PMMA oligomer covalently bonded to the sidewall of a DWNT. (b) Coarse-grain (bead-spring) representation of atomistic components, with effective physical dimensions derived from intermolecular adhesion parameters (Non-dimensional beads and springs are shown as opaque, while physical dimensions are shown as translucent). (c) Setup of the SMD, showing virtual springs and dummy atoms. (d,e) Snapshots of the atomistic (d) and coarse-grain (e) shearing of the “oligomer-crosslinked” interface during the molecular simulation. (f) Force–displacement profiles show loading (solid line) and free acceleration after slipping (faded line), indicating good agreement between the atomistic and coarse-grained models.

The dimensions of the modeled bundles and the density of polymer chains on the surface were identified experimentally. The polymer chains on bundles were modeled as poly(methyl methacrylate) (PMMA) oligomers with lengths of 4 or 8 repeating units based on their similarities to the chemical structure of the inherent polymer coating obtained through XPS, FTIR and NMR spectroscopy, and TGA-MS analysis. The choice of polymer length in simulations was guided by gel-permeation chromatography (GPC) analysis that yields a PMMA chain with an average degree of polymerization of 5. This polymer chain, as shown in Figure 14a, provides many possible sites for forming H-bonds and they are glued in one chain to enhance the adhesion strength.

We applied simple shear force to the “oligomer-crosslinked” interface via steered molecular dynamics, whereby the atoms of one tube, at the end, are held fixed in space, and the center of mass of the group of atoms at the other end of the second tube is connected by a harmonic spring potential to a massless “dummy atom” that moves at a constant velocity in the longitudinal direction. During the shearing simulations of the atomistic and coarse-grain (Figures 14d and e) models, it was observed that the “crosslinks” aggregate via weak interactions, then become elongated and more aligned in parallel as the pulled DWNT displaces. Plotting the force in the SMD spring potential against the end displacement of the pulled tube allows direct comparison of the “crosslinked” interface shear behavior between the atomistic and coarse-grained models (Figure 14f). The force-displacement profile shows good agreement with coarse-grain models of multiple orders of magnitude of loading rate.

The shear strength values calculated so far from simulations correspond to the case when five double-walled CNTs on each bundle are along the interface. However, depending on the initial orientation of the bundles with respect to each other, less energetically favorable junctions can also form between bundles in which a lower number of double-walled CNTs (three to four) from each bundle lie along the bundle-pair interface, as shown in Figures 15a and b. The coarse-grain model allows us for the investigation of the effect of contact width for a given bundle diameter on the shear interactions between bundles. In such cases, and for the 8-mer long PMMA chains and an overlap length of 100 nm, the multiscale simulations predict that the critical junction force is reduced by ~20%, which corresponds to a loss of the interface shear strength of ~8%, as shown in Figure 15c. Therefore the experimental uncertainty in the number of double-walled CNTs along the interface in the shear experiments, which stems from the SEM resolution, may lead to a scatter range of ~20% in the experimentally measured slip forces.

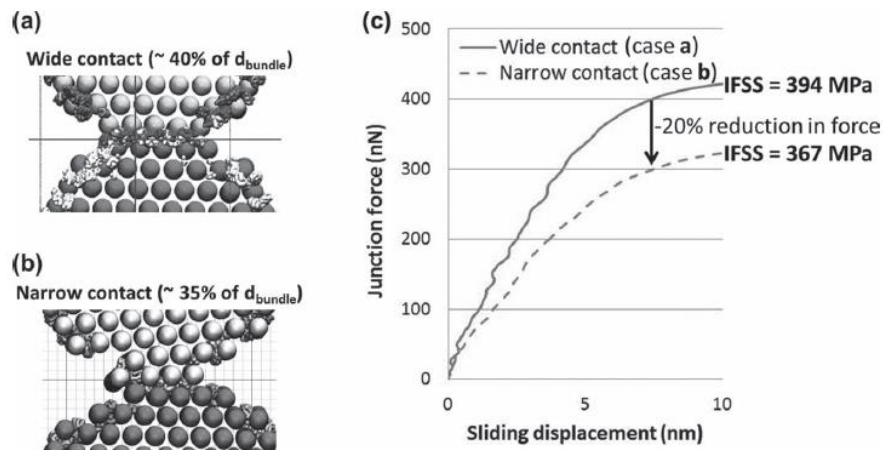


Figure 15. Due to the uneven surfaces of the bundles, the number of DWNTs along the interface of the bundles depends on the initial orientation of the bundles with respect to each other. (a,b) Two cases with 5 (a) and 3–4 (b) DWNTs along the interface. (c) The higher number of DWNTs along the interface promotes interactions between the bundles, enhancing the slip force of the junction.

Using the coarse-grained model developed here we investigated the interfacial shear strength, the equilibrated conformation between two CNT bundles as well as the experimental uncertainty and possibility of bundle failure. The model and simulations have provided detailed description of interactions between the bundles beyond the spatial resolution of the experiments. Both the experimental and the simulation studies point to a substantial enhancement of the interfacial shear strength between bundles to as high as 400 MPa, which is among the highest values reported in the literature, and an order of magnitude higher than the shear strengths that can be reached by pure van der Waals interactions between pristine CNTs. The model and multiscale method should be applicable to many similar materials, including single- and multiwalled carbon nanotubes, their corresponding bundles, as well as any other nanoscopic fibrous materials.

Understanding shear forces in DWNT bundle pull-out experiments

This section describes the work that we have been doing to investigate the sources of dissipation in the carbon nanotube pullout experiments of Espinosa *et al.* In previous work, we identified a number of contributors to the force associated with the withdrawal of an inner bundle of tubes from an outer sheath of tubes. Some of the forces were identified as being due to an increase in the potential energy of the system, while at least half was found to be due to dissipation. A satisfactory explanation as to the details associated with the potential energy was developed, as was an explanation for some of the dissipation, but there was a significant amount of dissipation that was unaccounted for.

Additional studies of the literature led to clues to the probable source of the missing dissipation. We used the empirical force field MM3 to explore the contribution of the corrugation due to the graphitic van der Waals (vdW) registry for Ref. [1]. This is one of the highest-quality force fields available for this type of problem. However, recent work by Lebedeva *et al.* [2] suggests that MM3 underestimates the barrier associated with moving from one minimum in the graphite vdW registry to the next by a factor of ~ 35.2 . This work also suggested that another popular force field, AIREBO, similarly underestimates the barrier. An underestimate of this barrier will be associated with an underestimate of the force. We have been working to confirm the Lebedeva *et al.* results. Also, there is a method that incorporates more advanced dispersion corrections than those used by Lebedeva *et al.* (PBE-D3). We have also used it to estimate the size of the barrier. The goal is to establish a means of capturing the size and shape of the energy barrier, so we can more accurately model force during the shearing of graphitic materials.

A summary of our findings is presented in Figure 16a. It is the barrier marked “SP” that is associated with moving from one vdW minimum to the next in the registry. Using PBE-D2 and a plane wave basis set, Lebedeva *et al.* [2] predicted that this barrier is approximately 2 meV/atom. We confirmed that MM3 and AIREBO predict this barrier to be substantially lower, as shown in Figure 16a, and in Figure 16b, which is a blow up of the SP region. Lebedeva *et al.* used the VASP code for their calculations. The D3 correction is not available in VASP, so we used CP2K. This means D2- (from VASP) and D3- (from CP2K) corrected PBE-based data in Figure 16 needs to be compared with caution, due to differences in basis sets. The VASP code uses plane waves and the projector augmented wave method (PAW), while CP2K uses Gaussian-type orbitals and plane waves (GPW). As a result, our CP2K PBE-D2 calculation (not shown) suggests a significantly higher barrier at SP than the VASP PBE-D2 result. Work continues on the resolution of this issue. Regardless, work so far supports the conclusion of Lebedeva *et al.* that MM3 and AIREBO significantly underestimate the barrier.

Predictions were also made using a number of other methods. PM6 and DFTB are semi-empirical methods that we used to calibrate our MM3 results for Ref. [1]. As can be seen in Figure 16, they

also underestimate the barrier compared to PBE-D2 and PBE-D3. The “pbc”, “mio” and “3ob” acronyms represent three different sets of DFTB parameter files, which do affect the size of the barriers as shown in Figure 16b, although the barriers are all low as compared to the PBE results. PM7 is an improved version of PM6, and PM7 does predict the barrier to be higher than PM6 as shown in Figure 16b, but the barrier is still low compared to PBE. So, it appears that a number of force-field-based and semi-empirical methods significantly underestimate this barrier. Therefore, we plan to make modifications to the AIREBO potential to correct its behavior in this regard, once we are satisfied we have established the best possible estimate for the barrier.

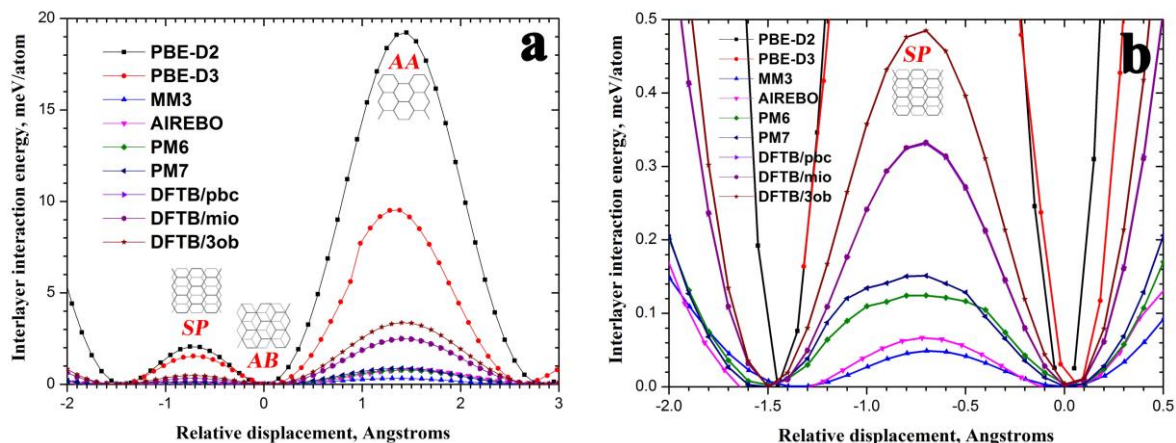


Figure 16. (a) Energy as a function of relative sheet position for a pair of graphene sheets. (b) Expanded y-axis scale for the region that includes the lowest-energy barrier to sheet motion.

We have also been exploring the saturation in the force necessary to pull out the inner bundle. Beyond a certain inner bundle-outer sheath overlap length, the force necessary to pull out the inner bundle is a constant, [1] consistent with the expected shear-lag behavior. MM3 simulations performed for Ref. [1] suggested that this length is approximately 12 nm. However, more recent experiments using pairs of carbon nanotubes that suggest much larger lengths (~300 nm), in conjunction with the uncertainties associated with MM3 discussed above, motivated additional studies of this issue. The AIREBO results for achiral tubes shown in Figure 17 suggest a length of approximately 60 nm. This value can be rationalized using a shear-lag model. Investigations continue in relation to chiral tubes, the type of tubes expected to have been present in the experiments resulting in the ~300 nm lengths.

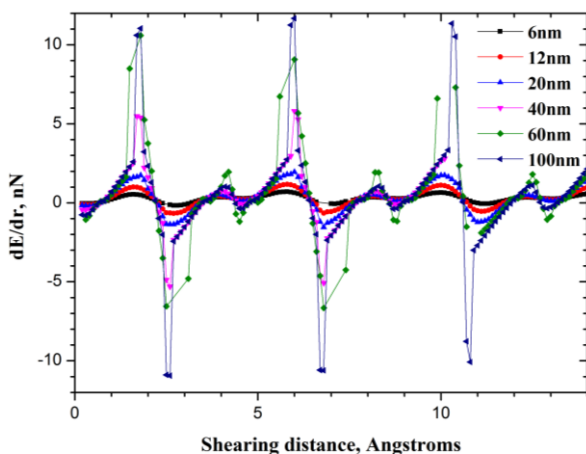


Figure 17. Force saturation as a function of length of nanotube overlap.

Bare multiwalled carbon nanotube peeling

Recently, the development of CNT-based macroscopic yarns with high strength-to-weight ratios has been an area of great interest in the scientific community. Researchers have synthesized CNT yarns through various processes (e. g. [3-11]) but none of the methods have been able to produce yarns with the exceptional mechanical properties of individual tubes [12-13]. One challenge is the need to enhance tube-tube interfacial interactions within a yarn, as the van der Waals interactions between

individual tubes are very weak compared to the sp² bonding between carbon atoms within a single CNT. These tube-tube interfaces within a yarn can debond via shearing and peeling. If CNTs were perfectly aligned with one another, along the axis of the fiber, shearing would be expected to be the predominant mode of failure. However, as perfect alignment of all of the CNTs within a yarn cannot be achieved, it is important to also characterize peeling.

Here we report an *in situ* experimental peeling technique (developed by the Espinosa group) that can be used to investigate the effects of various chemical functionalizations of CNT surfaces on tube-tube interfacial interactions and the resulting material properties. Specifically, we present an approach combining *in situ* SEM peeling experiments and theoretical computations. This study focuses on evaluating the surface energy of individual MWNTs peeling from a graphene substrate. The direct visualization of the peeling process through *in situ* SEM testing, combined with force measurements, provides fundamental insights into the nanoscale interactions between these materials. When combined with an analytical model, finite element simulations (by the Espinosa group), and atomistic calculations (by the Schatz group), the approach also enables the estimation of energy contributions within the framework of fracture mechanics. The method presented here is envisioned as a technique that can be used to evaluate the enhancements in nanoscale interactions between CNTs afforded by chemical functionalizations, with the results presented here serving as baseline values for interactions between non-functionalized CNTs.

In the peeling tests conducted by the Espinosa group, as-produced MWNTs were attached to, and then peeled from, a substrate of graphene on copper (Figure 18) in order to experimentally evaluate the surface energy between the CNT and graphene. Within an SEM chamber, a MWNT was attached to the tip of an AFM cantilever of known stiffness that extends from a nanomanipulator. The MWNT was manipulated such that it lied down on a graphene substrate mounted on an SEM stage. After a line contact formed between the tube and the monolayer graphene, the stage was pulled away from the fixed cantilever to peel the MWNT from the graphene substrate. Images of the peeling process were recorded to track both the profile of the MWNT and the deflection of the AFM cantilever. The vertical peeling forces were calculated by visually tracking the cantilever deflection and profile of the tube during peeling.

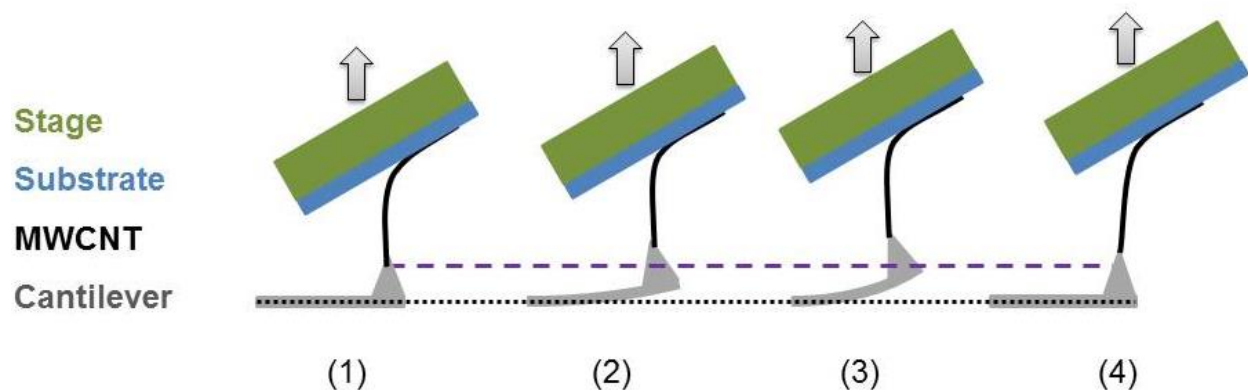


Figure 18. *In situ* SEM peeling schematic. A carbon nanotube adhered to a cantilever (force sensor) is brought into contact with a graphene-on-copper substrate attached to the SEM stage. The stage is pulled away as shown in (1) – (4). The deflection of the cantilever and profile of the tube are monitored throughout this process.

MWCNT peeling studies were analyzed using the classical peeling formula developed by Kendall [14], which assumes that an elastic film peels from a rigid substrate under a constant axial load, incrementally progressing the peel front without changing the shape of the film. The corresponding energy balance yields:

$$F(1 - \cos(\theta)) = 2\gamma w - \frac{F^2}{2E\pi dt} \quad (1)$$

where F is the applied force, θ is the angle of the applied force with respect to the substrate (see Figure 18), γ is the interface surface energy, w is the contact width between the two surfaces, E is the elastic modulus of the CNT ($E = 1$ TPa [13, 15-16]), d is the outer diameter of the CNT, and t is the single wall thickness ($t = 0.34$ nm, as we assume only the outer wall carries the tensile load). The term on the left-hand side of the equation corresponds to the external work of the cantilever acting on the CNT, while the first and second terms on the right-hand side of the equation denote changes in adhesion energy and changes in strain energy, respectively.

While Kendall's formula is used in this study to calculate surface energy, Kendall's assumption of shape constancy during peeling does not apply in the experiments, as the cantilever restricts the motion of the CNT. Hence, during a small but finite advancement of the peeling front, the shape of the CNT changes slightly. The effect of this discrepancy between the experimental and analytical boundary conditions on adhesion energy is investigated using finite element analysis (FEA) by the Espinosa group.

In the FEA calculations, a carbon nanotube was modeled as a 1-D beam with a cylindrical cross-section matching that estimated from experiments. Three-node quadratic beam elements were used to account for the tensile and bending deformation of the carbon nanotube. As in Figure 19a, in the initial state (1), the CNT is straight and slack: no external loading is applied, and thus there is no strain energy in the system. At the left end of the CNT, displacement and rotation are constrained, and at the right end, a spring element with a spring constant equivalent to that of the AFM cantilever used in the peeling experiments, is connected to the CNT. Note that during peeling, the AFM cantilever does not move horizontally but can move in the vertical direction. Hence, to obtain an initial shape consistent with the experiment, the spring element is progressively displaced until the position of the right end of the CNT coincides with the position of the CNT, right before peeling, in an experiment (see Figure 19b). The FEA simulation predicts a tube profile that closely matches the experimental observation (see Figure 19b). At this configuration, the force applied at the right end of the CNT, F , as well as the strain energy stored in the tube, F , are obtained.

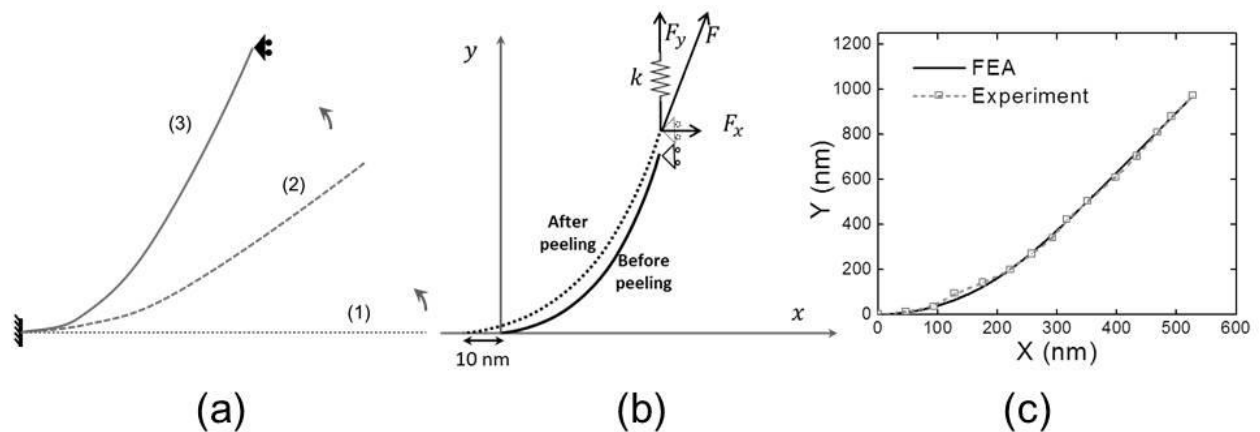


Figure 19. FEA simulations. (a) Schematic of the FEA simulation setup. An initially-flat CNT with length matching that measured in the experiment is bent from (1) to (2) to (3), with the left end held fixed. The right end in configuration (3) corresponds to the experimental measurement. A roller is added to the right end after (3) to prevent the tube from translating horizontally during peeling. (b) Schematic of the FEA peeling model. The spring with constant k corresponds to the cantilever elasticity. The solid line represents the CNT configuration right before peeling and the dashed line represents the CNT configuration after peeling 10 nm. (c) Comparison of the CNT shapes right before peeling obtained from the FEA simulation and experimental observation.

To compute the energy release rate numerically, a virtual motion of the peeling front (10 nm in length) is assumed. After the system equilibrates, the strain energy of the tube after peeling, E_{final} , is obtained. Also, integrating the cantilever force versus cantilever displacement yields the external work, W_{ext} , applied on the tube. Thus, according to Griffith's analysis [17], the energy release rate, G , during peeling can be obtained numerically, namely,

$$G = W_{ext} - (E_{final} - E_{initial}) \quad (2)$$

To compare, Kendall's formula can also be applied to calculate the energy release rate. By inputting the cantilever force, F , and the peeling angle, θ , extracted from the simulation result right before peeling, the energy release rate given by Kendall's model is

$$G = F(1 - \cos(\theta)) + \frac{F^2}{2E\pi dt} \quad (3)$$

The Espinosa group performed FEM calculations on multiple peeling experiments (varying tube length and peeling angle) and consistently found only a 5% overestimation of the energy release rate by Kendall's model compared to Griffith's analysis. Thus, Kendall's analysis is used to compute the energy release rate from which γ is obtained.

Experimental results for six in situ SEM peeling tests conducted by the Espinosa group are reported in Table 1. The tubes employed in the experiment had diameters in the range 19-30 nm. Surface energy was calculated for each test using Kendall's formula (Equation 1). The average surface energy for the six peel tests is 0.13 J-m⁻² with results ranging from 0.04 J-m⁻² to 0.24 J-m⁻². In addition, the results of two peels with applied loads and peeling angles similar to those reported with the graphene-on-copper substrate are 0.20±0.07 J-m⁻² and 0.09±0.03 J-m⁻² (Table 1). The variation among these results could stem from multiple sources, which merit a detailed discussion.

One such source of experimental uncertainty is the presence of amorphous carbon. For example, while MWNTs developed through arc discharge only contain carbonaceous materials, amorphous carbon is present on the outermost layers of the tubes, either directly from fabrication or due to induced amorphous carbon deposition by the electron beam in the SEM chamber. As this amorphous carbon lacks the well-ordered sp² bonding structure of carbon nanotubes and graphene surfaces, it may introduce additional interactions beyond what would be expected for idealized peeling between atomically-smooth graphitic surfaces. [18]

Another source of scatter in the measured surface energy might be the roughness of the graphene surface. Due to the different thermal expansion properties of the copper foil and graphene membrane, the substrate inevitably exhibits some wavy regions after processing. [19-22] The rippled graphene will inherently affect the contact area at the interface. While limitations in SEM resolution prevent highly precise in situ characterization of peeling surfaces, deviations in surface roughness may also contribute to the measured surface energy.

The presence of molecules such as water in the SEM chamber may also affect the surface energy measured in this study. While in situ SEM tests were conducted in stable vacuum (~10⁻⁵ Torr) after several hours of equilibration, molecules such as water may remain on both the carbon nanotube and graphene surfaces. When the surfaces come into contact, molecules on each surface may interact with one another and introduce additional interaction energy components. However, even if it were possible to conduct these tests in higher vacuum, this would present other challenges, e.g. the time required for cutting the tubes, during sample preparation, would increase, [23] resulting in additional exposure of the CNT to the electron beam. The combinations of voltage and current conditions used during peeling and tube cutting in this study, as well as the equilibration pressure

conditions, reflect attempts to establish a compromise among the factors that must be considered in *in situ* SEM experiments.

Table 1. Experimental Measurements and Calculated Surface Energy Values For Graphene-on-Copper and HOPG Substrates.

<i>Substrate</i>	<i>Tube #</i>	<i>Test #</i>	<i>Peel Angle, θ</i> [degrees]	<i>Force, F</i> [nN]	<i>Outer Diameter</i> [nm]	<i>Assumed # of Walls</i>	<i>Contact Width, w</i> [nm]	<i>Surface Energy, γ</i> [J-m ⁻²]
Graphene	1	1	66	14	30	37	32	0.13 ± 0.04
Graphene	1	2	58	15	30	37	32	0.11 ± 0.03
Graphene	1	2	56	13	30	37	32	0.09 ± 0.02
Graphene	2	1	66	9	20	22	18	0.15 ± 0.05
Graphene	3	1	68	2	19	21	16	0.04 ± 0.02
Graphene	3	1	61	16	19	21	16	0.24 ± 0.08
HOPG	1	1	69	12	21	24	19	0.20 ± 0.07
HOPG	1	1	49	10	21	24	19	0.09 ± 0.03

Modeling MWNT peeling experiments

This section describes the work we have been doing to understand the details of the forces involved in interactions between carbon nanotubes and graphene surfaces, when the tubes are peeled from the surfaces. An understanding of such forces is critical for the systematic design of high-performance nanocomposites. Preliminary work on this was described in last year's report. The work involves molecular mechanics simulations using MM3 as well as analytical work to carefully consider the implications of the vdW interactions. Note that we confirmed that MM3 estimates a surface energy in good agreement with experimental estimates for graphite, a property that is distinct from corrugation.

Carbon nanotubes, especially those with significant void space in their interiors, can undergo flattening against surfaces (see Figure 20). This behavior is well understood for single- and double-walled tubes of small diameter, but not for large multi-walled tubes. The degree of flattening is a function of the number of walls within the tubes (sometimes referred to as shells) and tube diameter, and affects the contact width between the tubes and surfaces with which they are brought into contact. Accurate estimates of these contact widths are necessary to accurately estimate the force per unit area of interaction between the tubes and surfaces. We used MM3 to estimate these contact widths.

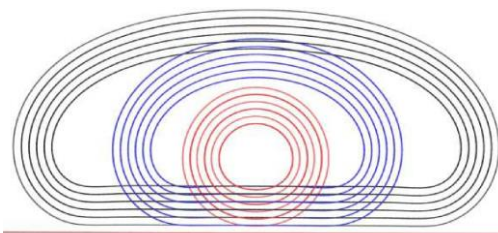


Figure 20. Carbon nanotubes relaxing against a surface.

Width estimates as a function of (outer) diameter of isolated tube, for tubes with increasing numbers of shells, are shown in Figure 4. As the figure suggests, there is a linear relationship between isolated tube diameter and contact width. As the number of shells increases, the degree of flattening decreases. The contact width associated with a solid cylinder is also shown, and it illustrates how dramatic the flattening can be. The tubes used by Espinosa et al. for their peeling experiments had diameters of approximately 20-30 nm and ~20-40 shells. The modeling of such large tubes using MM3 is not possible with our (substantial) computational resources, so we developed a formula with which we extrapolated to the experimental system sizes, using the data in Figure 21.

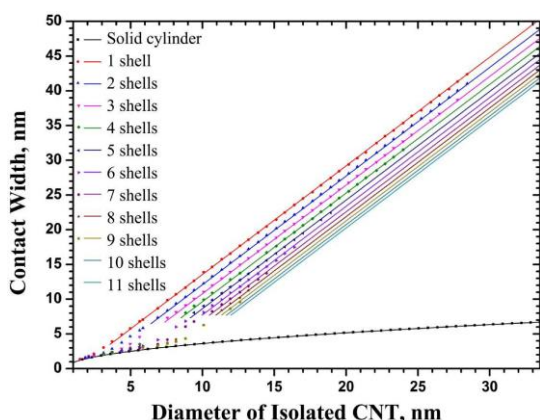


Figure 21. Carbon nanotube contact width as a function of number of walls (shells) and diameter of isolated tube.

atom at the vdW minimum (~ 3.4 Å). Also, not all atoms within 6.8 Å of the graphene sheet contribute equally. Those at the minimum make a full contribution, and those at larger separations make a contribution scaled appropriately with distance. By extending the work of Steele, [24] we developed a formula that accurately accounts for these differences. With this, we were able to rigorously define contact widths. We also showed by way of consideration of the full dielectric response of the material (Casimir effects) that the Lennard-Jones-based approach is valid for this case.

By combining the flattening and vdW formalism, we were able to provide a set of results that was used in the interpretation of the experiments of Espinosa et al. Reference [25] that describes the work has been submitted (May, 2013) for publication.

Functionalized in situ SEM peeling

Building on the previous bare tube-graphene peeling study, the Nguyen group has synthesized highly ordered pyrolytic graphite (HOPG) and carbon nanotubes functionalized with propionic acid. Compared to the bare tube-graphene system, this system will introduce hydrogen bonding as well as additional van der Waals interactions resulting from the alkyl chain extending from the benzene ring. Both of these bond types are expected to make some contribution to the change in adhesion compared to the bare peeling case. The Espinosa group has characterized the functionalized HOPG surface using atomic force microscopy (AFM). They have also been conducting in situ SEM peeling tests with these propionic acid-functionalized materials.

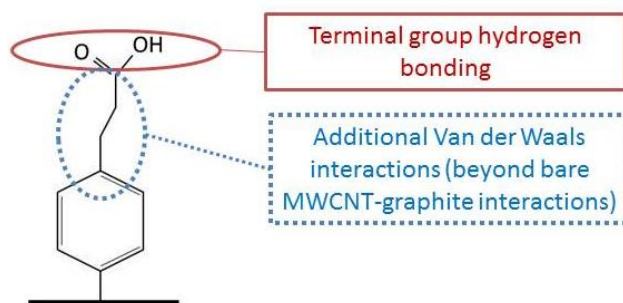


Figure 21. Propionic acid schematic.

In order to induce additional van der Waals interactions at the interfaces of these CNT-graphite surfaces, the Nguyen group has also investigated the possibility of adding long alkyl chains to the

We also developed an analytical formalism for understanding the vdW interactions between the tubes and surfaces. The adhesion energy and contact surface is a function of the radial deformation of the multi-walled carbon nanotube. To determine this contact surface, we needed to define the operational range of the vdW forces associated with contact between the tube and surface. A complete treatment of vdW forces would include Casimir effects. However, the less-general Lennard-Jones potential was found to be sufficient for our purposes. This is because significant portions of the tubes are in close contact with the surfaces during peeling. We showed that tube atoms 6.8 Å from the graphene sheet each contribute ~ 3 % of the energy of an

surfaces of CNTs and HOPG. This approach, inspired by ultrahigh molecular weight polyethylene (UHMWPE), may also yield enhanced chemical interactions and, thus, changes in surface energy. The Nguyen group has conducted preliminary attempts to functionalize the surfaces of these materials with such long alkyl chains, and the work is still ongoing. This may be a future direction for the Espinosa group in subsequent peel tests if the chemical synthesis and characterization are expected to yield significant improvements in adhesion.

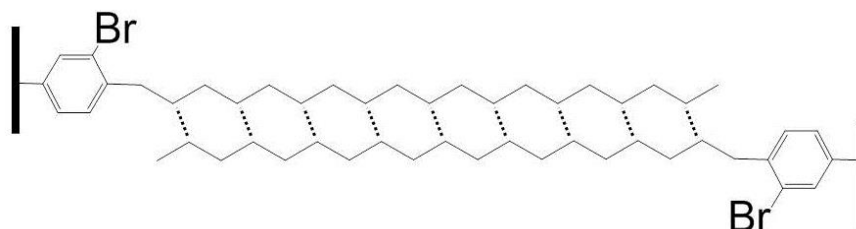


Figure 22. Long alkyl chain functionalization schematic.

Engineering Lateral Interactions within CNT Yarns

Studies of CNT functionalization

In this project we are trying to understand the chemistry of carbon nanotube functionalization involving alkylcarboxylation and arylation as performed using the Billups and diazonium reactions, respectively. These chemistries are crucial to the peeling and pullout experiments described earlier, and we plan to use our results to model these experiments in future work, however the focus of the present work has been on the influence of these chemistries on CNT structures and optical properties. The main focus this year was on alkylcarboxylation using the Billups-Birch alkylation reaction. Previously we demonstrated that this reaction selectively alkylates nanotubes starting at defects, and then propagates outward following chains of carbons on the CNT surface with reactivity determined by the unpaired electron densities on carbon atoms that are near to previously alkylated sites. Work completed this year demonstrated that the alkylcarboxylation of a (6,5) single walled CNT leads to red-shifted emission at a localized site in the vicinity of the radical site. Figure 23 shows some typical data from these measurements, all of which are consistent with electronic structure calculations that we have done. This work was published in: "Propagative sidewall alkylcarboxylation that induces red-shifted near-IR photoluminescence in single-wall carbon nanotubes", Yin Zhang, Nicholas Valley, Alexandra H. Brozena, Yanmei Piao, Xiaoping Song, George C. Schatz, Yu Huang Wang, *J. Phys. Chem. Lett.*, 4(5), 826-830 (2013).

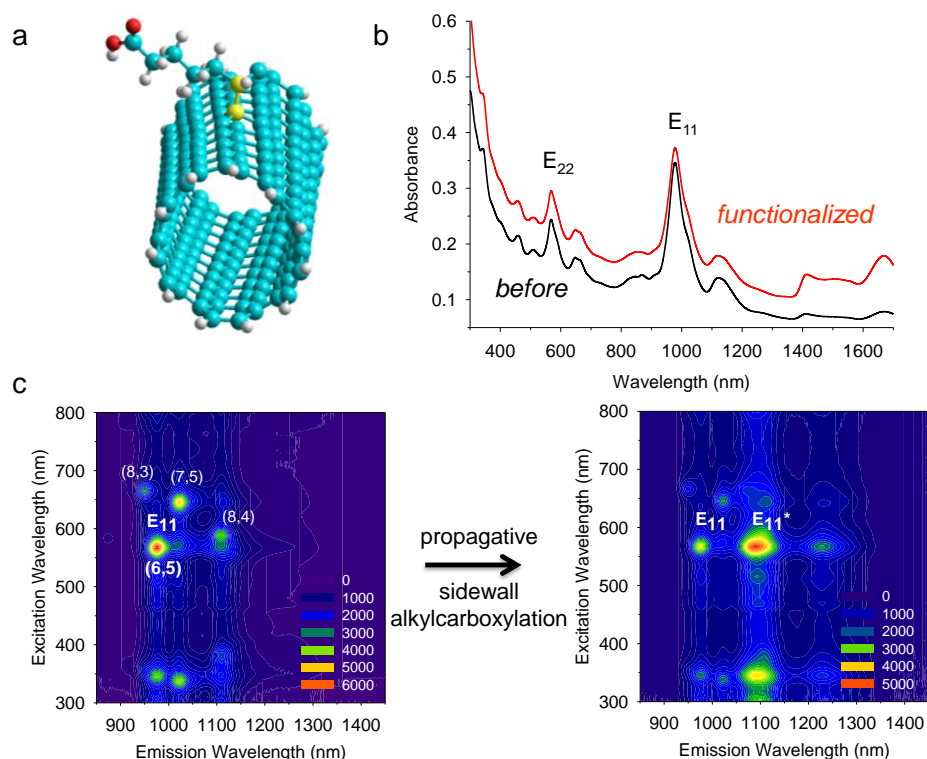


Figure 23. Propagative sidewall alkylcarboxylation induces a red-shifted emission peak in (6,5)-SWCNTs. (a) A molecular model of (6,5)- $(\text{CH}_2)_5\text{COOH}$. (b) visible near-infrared absorption spectra of CM(6,5) before and after the sidewall alkylcarboxylation. (c) Excitation-emission PL maps. A new PL peak, E_{11}^* , is created after sidewall alkylcarboxylation of CM(6,5) SWCNTs. This new emission is red-shifted from (6,5) E_{11} PL by 117 nm (136 meV). The nanotubes were individually dispersed in 1 wt.% SDBS- D_2O .

Graphene Oxide Composites

Effect of carbon nanotubes on the mechanical properties of graphene oxide paper

During this reporting period we continued to employ graphene oxide paper as an easily manipulated macroscopic model to study the effect of increasing the interface between adjacent carbon based nanofillers. To supplement the peeling experiment between CNT and graphene, we have studied the effect of CNT as a potential additive that can interact via π - π interaction with the aromatic regions graphene oxide in its structure. Studies have shown that CNTs, which cannot be dispersed into water due to strong van der Waals interaction, can readily go into dispersion in aqueous solution with the help of graphene oxide. Hence we attempted to use this strategy to make graphene oxide/CNT composite paper from an aqueous dispersion by vacuum filtration technique and subsequently study the mechanical properties of these papers in collaboration with the Espinosa group. The dispersion was achieved by ultrasonication technique followed by centrifugation to remove unstabilized CNTs and the supernatant was vacuum-filtered to obtain nanocomposite paper. The papers were then characterized by Fourier-transformed infrared (FTIR) spectra, X-ray diffraction (XRD), and thermogravimetric analysis (TGA). Incorporation of CNTs was confirmed by FTIR spectroscopy (Figure 24a), which shows C=C stretches from CNTs at 1560 cm^{-1} and alkyl stretches at 2920 cm^{-1} typically observed in CVD-grown CNTs. As expected, both these peaks decrease as the graphene oxide:CNT ratio increases from 1:1 to 4:1 in the composites. Also with increase in graphene oxide:CNT ratio from 1:1 to 4:1, intergallery spacing of graphene oxide

sheets decreases from 9.2 Å to 8.7 Å, typically the spacing for vacuum-filtered graphene oxide paper. Increasing intensity of (002) reflection corresponding to the graphitic planes at $2\theta = 25.3^\circ$ confirms the presence of CNTs in composites.

Thermogravimetric analysis (TGA) was used to quantify CNTs in each of these composites. Pristine graphene oxide at 800 °C reduces to ~35% graphene-like carbonaceous materials. As we expected, when CNTs are added, the % carbon yield increases from ~35% in graphene oxide to ~ 58.2% in 1:1 graphene oxide/CNT composites (see table in Figure 25 for detailed compositions). CNT compositions were then calculated using the following equation:

$$x * (\% \text{carbon} / \% \text{GO}) + ((100 - \% \text{H}_2\text{O TGA}) - x) = \text{total carbon content},$$

where $x = \% \text{GO}$ in the composite mixture.

It can be seen that the %CNT content increases from 28.2% to 36.0% as the graphene oxide:CNT ratio decreases from 4:1 to 1:1.

The mechanical data for graphene oxide/CNT papers of different compositions (Figure 26, top) suggests that both modulus and strength of these materials are much smaller than those of pure graphene oxide paper. However, there are not much difference in the mechanical properties for the three compositions that we examined, suggesting that these properties are probably dominated by defects from the insertion of CNT into graphene oxide lamellar (Figure 26, bottom).

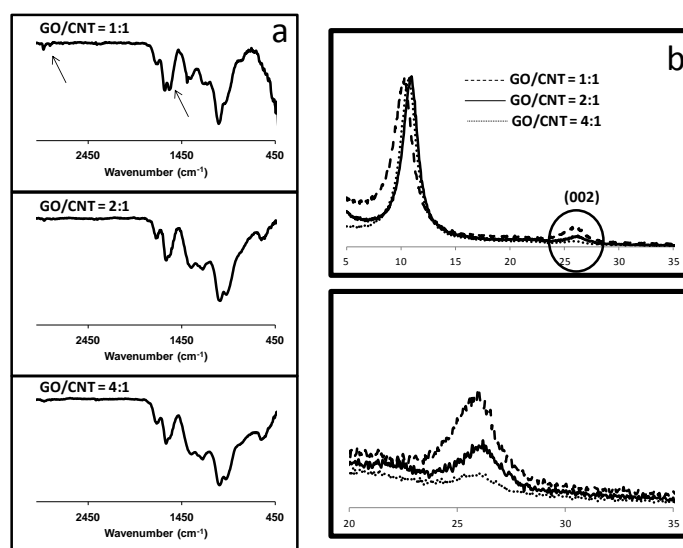
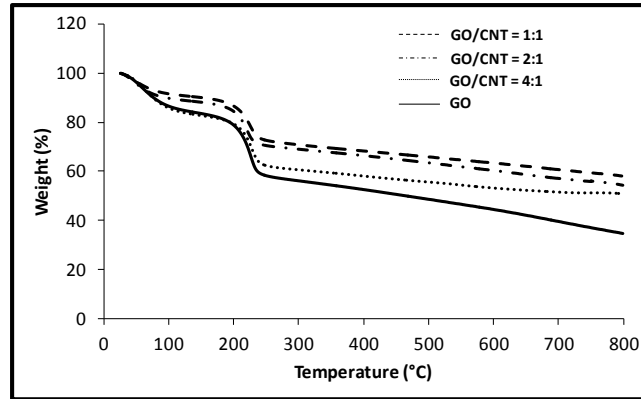


Figure 24. (a) FTIR spectra, and (b) XRD pattern of GO/CNT nanocomposite papers.



Sample	% H ₂ O	% GO	% CNT	Total C
GO	13.8	86.2	0.0	35.0
4:1	15.1	56.7	28.2	51.0
2:1	10.3	59.0	30.7	54.3
1:1	8.5	55.5	36.0	58.2

Figure 25. TGA and %CNT analysis table of graphene oxide (GO)/CNT nanocomposite papers.

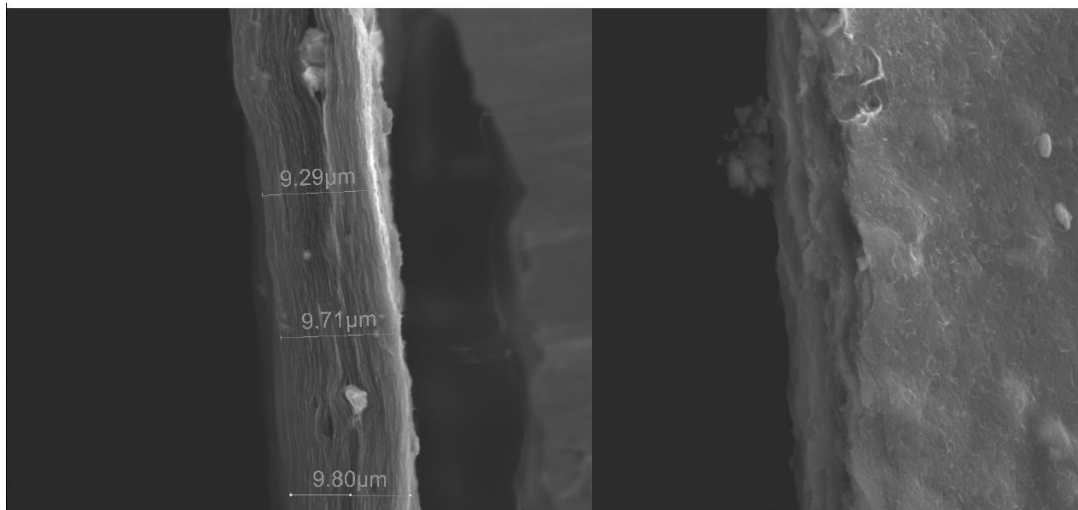
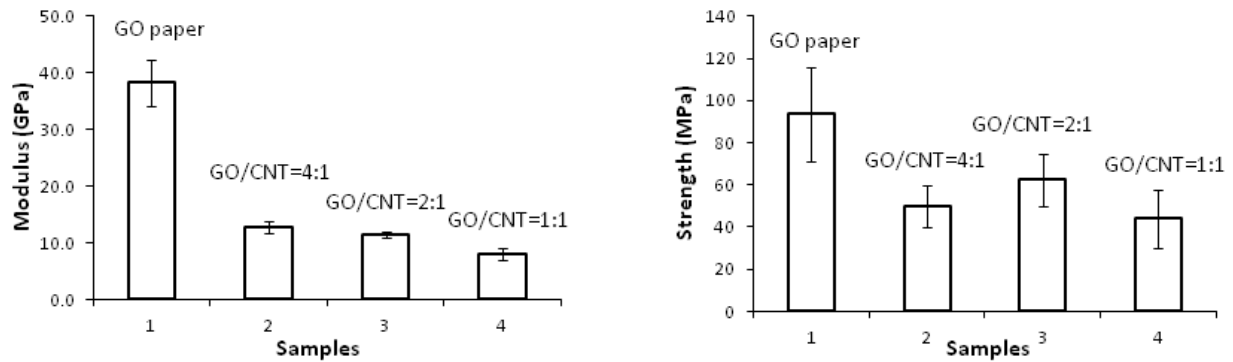


Figure 26. Top: Modulus and strengths of graphene oxide (GO)/CNT nanocomposite papers. Bottom: scanning electron micrographs of the GO/CNT composite fabricated from a starting graphene oxide:CNT ratio of 4:1.

Defect-tolerant graphene oxide composites

Stiff composites comprising carbon nanofillers such as CNTs, graphene, or graphene oxide typically display brittle behavior, where the composite fractures at very low strains, much lower than the strength of the individual nanofillers, and display a strong inverse volume-strength relationship. Such behavior is classically explained by the presence of defects, which fail at low stresses, creating a crack that rapidly propagates through the rest of the material, leading to catastrophic failure, thereby preventing access to the composite's theoretical strength. Such defects can have many forms in a nanocomposite, including defects in the nanofillers themselves, whose individual mechanical properties can vary greatly and display non-uniform surface chemistry, and defects in the composite, where alignment, nanostructure dispersion, and overlap length distribution are still difficult to control. Therefore, we set out to introduce defect-tolerant mechanisms into composites, with the goal of discovering a generalizable approach that can bring the strengths of currently defect-dominated composites closer to their theoretical maximum strengths.

During this reporting period, we have studied the effects of introducing soft polymer layers into nanocomposites, which have theoretically been shown to hinder crack propagation. In this way, cracks that form when a defect fails are localized, preventing catastrophic failure, which allows the remainder of the material to continue bearing load. Specifically, we, with the Espinosa group, have studied graphene oxide-PMMA multilayer laminate films prepared by spin-assisted layer-by-layer deposition of alternating graphene oxide and PMMA layers. The effectiveness of this structure in hindering crack propagation is visible in images of their fracture surfaces (Figure 27). Fracturing the monolithic graphene oxide films results in a flat surface that is characteristic of a crack propagating through the entire material, breaking individual nanostructures as it extends. In contrast, the fracture surface of the new graphene oxide-PMMA composites clearly shows terraces and pull-out of the individual layers, which is indicative of a crack-deflection mechanism.

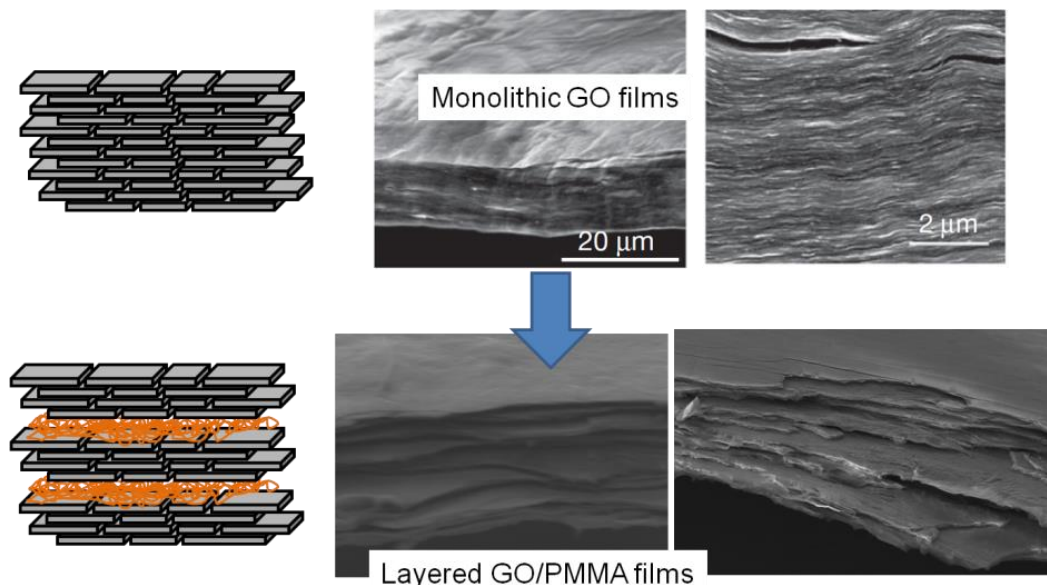


Figure 27. Schematic and SEM images of fracture surfaces of monolithic graphene oxide films (top) or multilayer laminate graphene oxide-PMMA films (bottom).

By keeping the graphene oxide layer thickness constant at 380 nm and the total number of layers constant at 20 layers, while varying the polymer layer thickness, we found an optimum polymer thickness of 36 nm, which maximizes both the stiffness and strength of our films (Figure 28). At this polymer thickness, the strength and stiffness of the composite film increase by 90% and 115%, to

38 GPa and 280 MPa, respectively. We note that this value of strength already approaches the best reported for graphene oxide-based composite films to date, solely by modifying the film's structure.

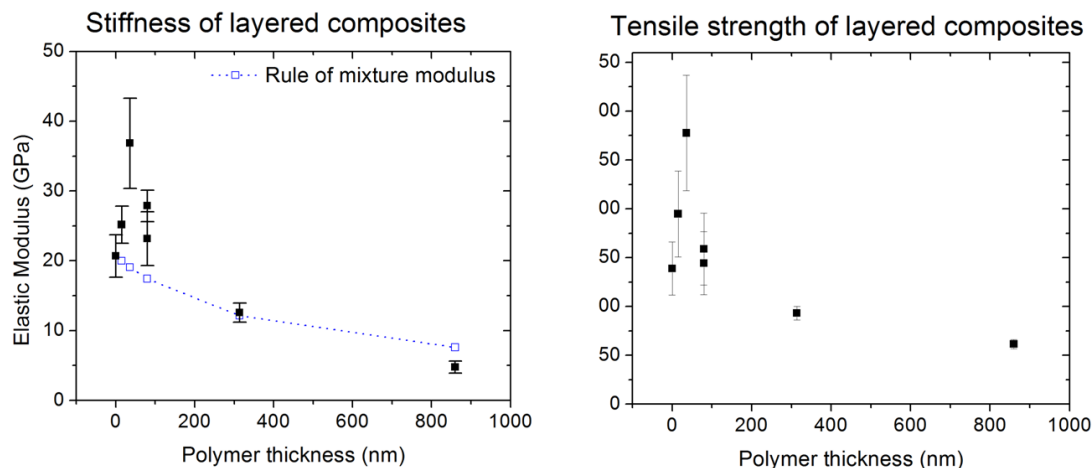


Figure 28. Mechanical properties of graphene oxide-PMMA multilayer composites

Focusing on films comprising the 36 nm PMMA layer, we increased the total thickness of our composites, and thus the total sample volume, by increasing the number of layers while keeping the width and volume of each layer constant. As previously mentioned, a composite with brittle behavior and defect-dominated strength will show diminished strength as the sample volume increases. In contrast, we found that our multilayer-laminate composites actually retain their strength with increased sample volume due to the defect-tolerance imparted by the crack-hindering polymer layers (Figure 29). Therefore, this approach of inserting soft, crack-hindering polymer layers into a composite effectively renders that composite defect-tolerant. Importantly, this method of modifying the composite through structure should be readily applicable to a broad range of composite system, and is a generalizable method for producing defect-tolerant composites.

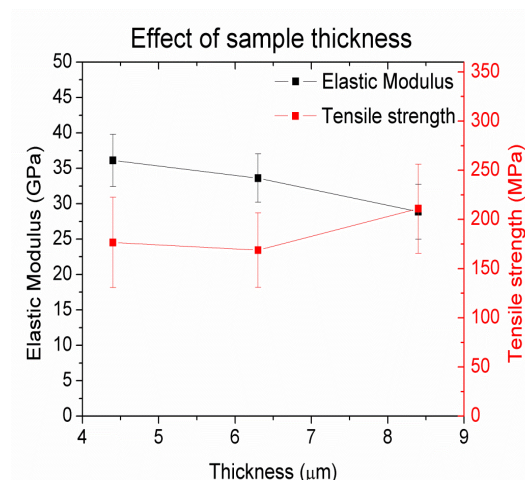


Figure 29. Mechanical properties of multilayer laminate films as thickness and sample volume increases stay relatively constant.

Graphene oxide/PVA papers

In addition to studies performed with GO/PMMA papers, the Nguyen Group and Espinosa Group have also initiated studies with polyvinyl alcohol (PVA) instead of PMMA as the polymer additive. As PVA is a hydrogen bond donor and acceptor, it may yield enhanced interactions between GO and the polymer constituents versus PMMA, which is only a hydrogen acceptor. In addition to incorporating PVA, we also aim to build on the previous study by extending the work to three-level hierarchies. This is a bioinspired approach stemming from several materials seen in nature, which have shown that multilayered structures with significantly different elastic moduli among the layers can arrest cracks and, thus, inhibit failure within the material [26-29]. Applying this finding

from nature to GO-based papers may yield insights into ways to prepare lightweight crack-resistant composites in the future.

To date, the Nguyen group has synthesized monolithic samples with a range of GO content, ranging from 0.5 wt% to 20 wt%. They have also prepared samples with two and three levels of hierarchy using layer-by-layer assembly techniques. The Espinosa group has conducted tensile testing, using a Fullam microtensile tester and SEM characterization of samples after testing, to investigate the fracture surfaces and their thicknesses. Sample results are shown below in Figures 30 and 31.

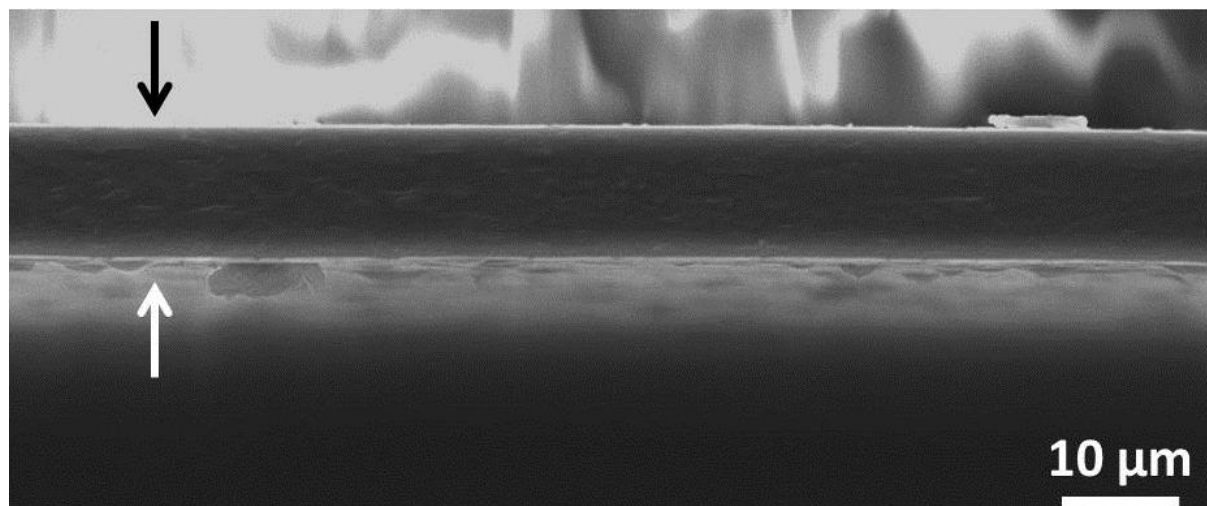


Figure 30. Sample graphene oxide/polyvinyl alcohol (GO/PVA) cross section using SEM. For a given type of sample, thicknesses were measured using SEM by taking the average of multiple thickness measurements in different regions of the paper. One such thickness measurement could be made between the two arrows shown above.

The next major step envisioned for this project is the synthesis, characterization, and testing of samples with higher GO percentages than those used to-date. Theoretical studies have shown that changes in moduli of approximately a factor of five are required to see substantial improvements in crack inhibition [26]. The most brittle samples to-date (20 wt% GO) do not have moduli with such a degree of difference to-date. If a higher proportion of GO (e.g. 50 wt%) yields this factor of 5 improvement, then this will be incorporated into multilayer hierarchies for additional testing and characterization.

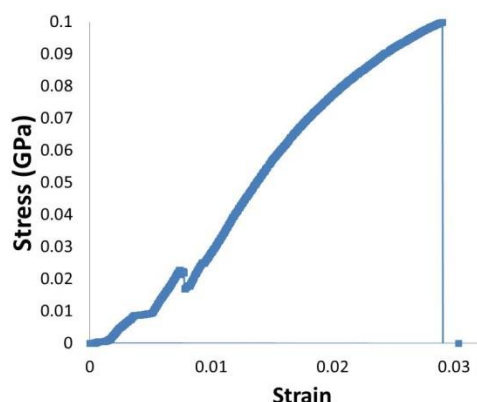


Figure 31. Sample stress-strain curve for GO/PVA paper with 5 wt% GO. Force-displacement outputs from the Fullam microtensile tester are converted into stress-strain curves based on loading conditions and sample geometry.

Fabrication/Characterization/Modeling of CNT/Polymer and Electrospun Nano-Filaments and Yarns

In situ TEM/SEM of carbon nanofibers

Tensile tests were performed on carbon nanofibers *in situ* TEM using a microelectromechanical system (MEMS) tensile testing device. The carbon nanofibers tested in this study were produced via the electrospinning of polyacrylonitrile (PAN) into fibers, which are subsequently stabilized in an oxygen environment at 270 °C and carbonized in nitrogen at 800 °C. To investigate the relationship between the fiber molecular structure, diameter, and mechanical properties, nanofibers with diameters ranging from ~100 to 300 nm were mounted onto a MEMS device using nanomanipulation inside the chamber of a SEM, and subsequently tested in tension in situ a TEM (Figure 32).

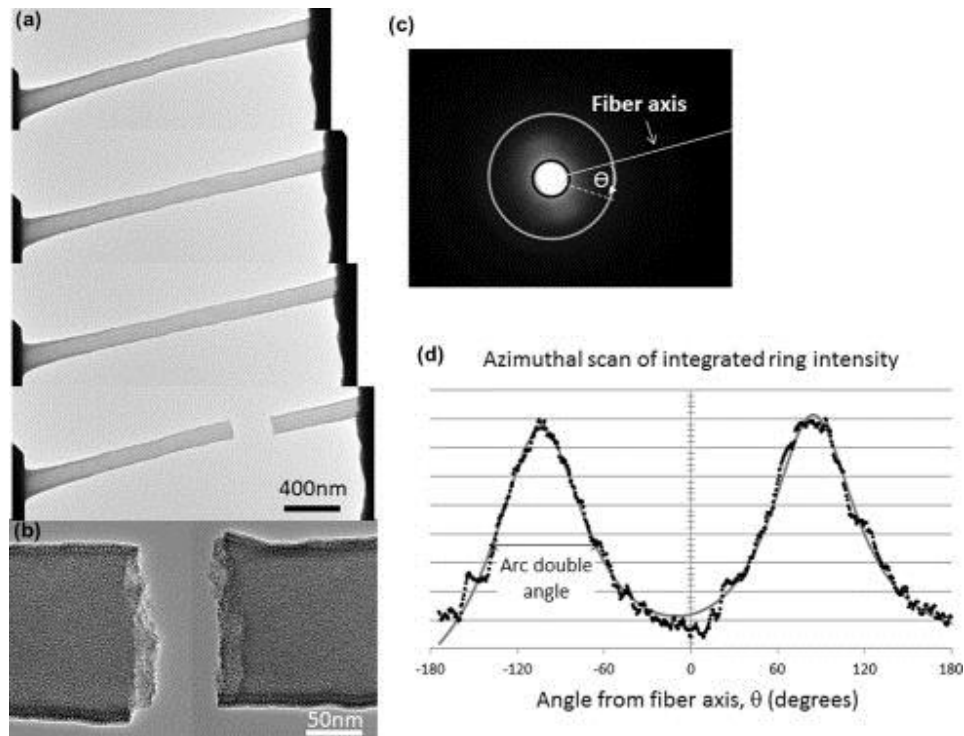


Figure 32. (a) Sequential TEM images during a tensile test. (b) High resolution image of the fracture surface in (a). (c) Example SAED pattern with fiber axis direction indicated, along with the angle from the fiber axis, θ . A schematic overlay of white and black circles indicates the ring of 0 0 2 graphitic plane signal. (d) Integrated intensity of the 0 0 2 signal ring of the SAED pattern in (b) as a function of the angle from the fiber axis (data points represented by solid symbols with solid line indicating best fit line), with the full width at half maximum, or arc double angle, indicated.

The results show the dependence of strength and modulus on diameter, with a maximum modulus of 262 GPa and strength of 7.3 GPa measured for a 108 nm diameter fiber. The dependence of fiber strength on diameter was studied in various fibers, and it has been shown that a decreasing diameter, resulting in smaller fiber volume, also results in a decreased number of initial defects or cracks in a material, and thus a decreased probability of failure in brittle materials (Figure 33).

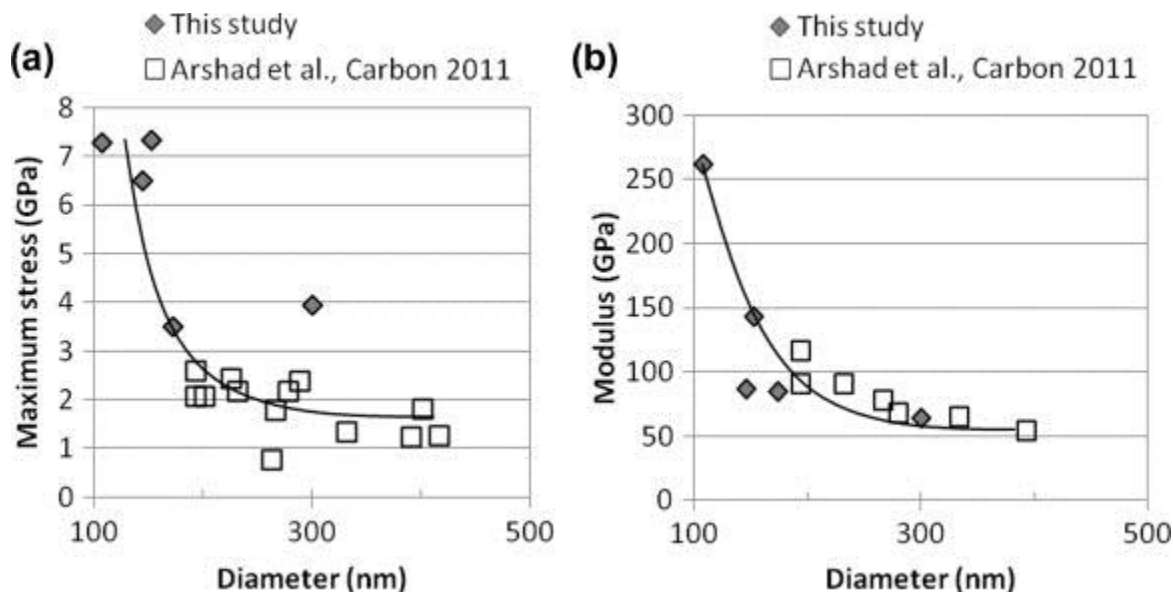


Figure 33. Stress (a) and modulus (b) versus carbon nanofibers diameter measured in this study (solid diamonds) compared with data from Arshad et al (Carbon 2011) (open squares), with the same carbonization temperature. Solid black curves are a guide for the eye to show the mechanical property trends with diameter.

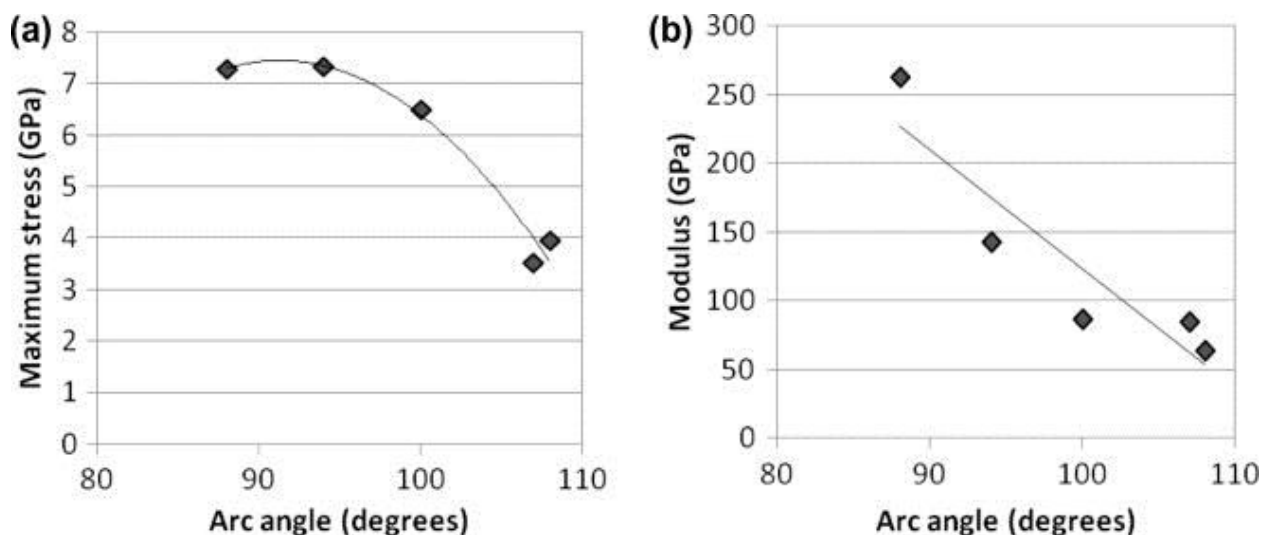


Figure 34. Maximum stress (a) and modulus (b) versus 0 0 2 double arc angle of fiber, with trends indicated with solid black lines.

Through TEM evaluation of the structure of each individual nanofiber immediately prior to testing, we elucidate a dependence of mechanical properties on the molecular orientation of the graphitic structure: the strength and stiffness of the fibers increases with a higher degree of orientation of the 0 0 2 graphitic planes along the fiber axis, which coincides with decreasing fiber diameter. It was found that the strength increases with decreasing double arc angle, or increasing molecular orientation of the graphitic planes along the fiber tensile axis (Figure 34). The strength appears to saturate around 7.3 GPa. In addition, the modulus increases with decreasing double arc angle. Thus, a decrease in diameter results in an increase in the molecular orientation of the 0 0 2 graphitic planes along the fiber axis, which in turn manifests into increased mechanical properties of the fiber, namely strength and stiffness.

Currently, another batch of carbonized nanofibers which were pre-stretched during the carbonization process is being tested in situ SEM/TEM. The motivation for this work, is the expected better molecular alignment of the 0 0 2 graphitic planes along the fiber axis due to the pre-stretch, which would in turn result in a stiffer and stronger fiber. As the previous work, these fibers will be mechanically tested using the MEMS devices insitu SEM/TEM and the molecular alignment will be ascertained using SAED studies on the TEM.

ReaxFF molecular dynamics simulations of the initial stages of templated carbonization in PAN-based carbon nanofibers

This section describes our use of molecular dynamics (MD) simulations with a reactive force field (ReaxFF) to study the initial stages of the templated carbonization process. Our first attempts to do this were described in last year's report, and this led to a joint publication in which the effects of DWNTs and graphene to template the growth of graphitic structures in carbon fibers was presented ("Extraordinary improvement of the graphitic structure of continuous carbon nanofibers template with double wall carbon nanotubes", Dmitry Papkov, Allison, M. Beese, Alexander Goponenko, Yan Zou, Mohammad Naraghi, Horacio D. Espinosa, Biswajit Saha, George C. Schatz, Alexander Moravsky, Raouf Loutfy, Sonbin T. Nguyen, Yuris, Dzenis, ACS Nano, 7, 126-42 (2013)). During the past year we have expanded our capabilities for doing ReaxFF calculations of carbonization processes with the release of ReaxFF in the Lamps code. This makes it possible for us to increase the number of atoms being studied by about a factor of 10 (from 1000 to 10000) while at the same time increasing the time duration of the integration from 500 ps to a few ns. Figure 35 shows some of the results of these calculations, here referring to a DWNT embedded in a PAN carbon fiber precursor at the beginning of the simulation. This shows results similar to those obtained in our

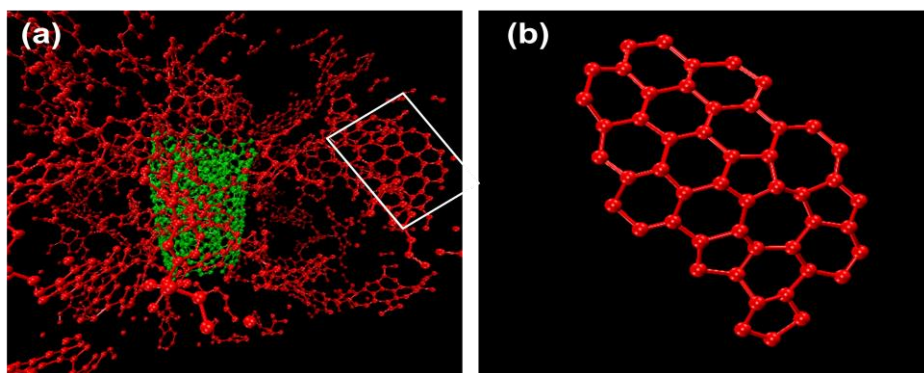


Figure 35. (a) snapshot at 3.25 ns after annealing at 2800K. (b) selected part of the system showing formation of graphene like structure. Only sp^2 C atoms are shown and N and H atoms are also removed for clarity. Color code: C (PAN) – red, C (DWNT) – green.

earlier calculations in which graphitic sheets have nucleated close to the DWNT, consisting of 5, 6, and 7 membered rings. However here we see that 6 membered rings are the most abundant. Figure 36 shows ring abundance as a function of time, and it is clear that

these longer simulations are able to achieve the expected limit where 6 membered rings are dominant. Another new result is that little covalent linking is observed with the NT wall, even at the high temperatures of the simulations. This indicates that the templating effect is mostly a physical templating rather than nucleation that is induced by covalent bonds to the template material.

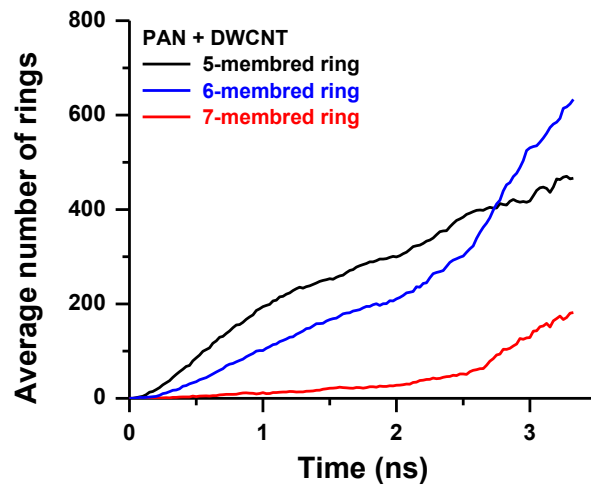


Figure 36. Rings (consisting of C atoms only) formation during annealing simulations. Annealing simulation up to 2.0 ns was performed at 2200K, 2.0 to 2.5 ns at 2500K and 2.5 ns onwards at 2800K.

Strong and tough continuous carbon nanofibers ** proprietary **

The Dzenis group continued evaluation of size effects in continuous CNFs. Uniform long carbon nanofilaments of varying diameters were controllably produced. Extensive mechanical testing was performed on the macroscopic (5 mm long) specimens. The results (Figure 37) indicate a pioneering possibility of simultaneously strong and tough carbon filaments.

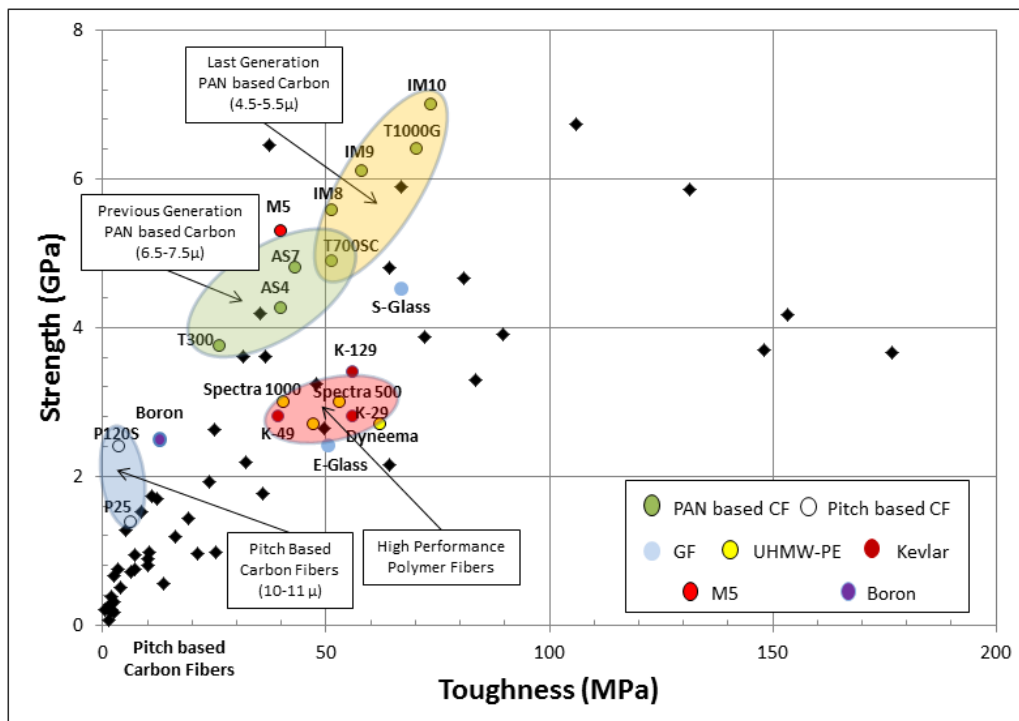


Figure 37. Strength/toughness correlation in individual CNFs and comparison with commercial advanced fibers.

Previous structural analysis of the unconstrained CNFs was augmented by fabrication and analysis of CNFs that were mechanically constrained during stabilization and carbonization. The resulting structural data (Figure 38) was correlated with mechanical behavior (Figure 37).

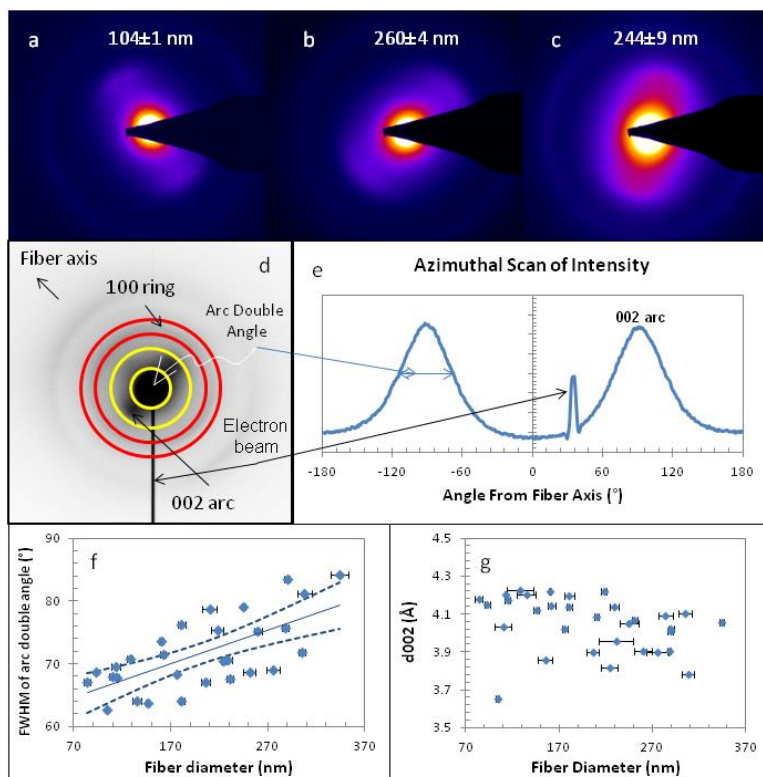


Figure 38. Updated ED data for constrained CNFs.

The results of structural and mechanical investigations of CNFs were also compared with the data obtained from a range of commercial carbon fibers. An example of ED comparison is shown in Figure 39. A layer of T310J fiber prepreg was polished and ion milled. An ED was taken from the thin longitudinal area near the edge of the hole created by ion milling.

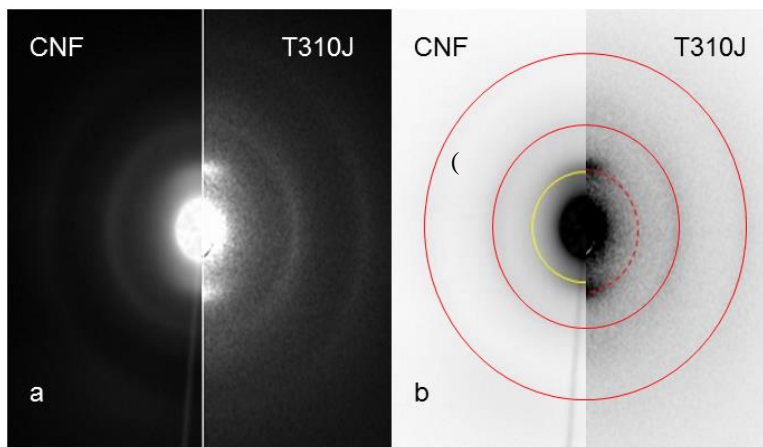


Figure 39. ED comparison between a (~220nm) CNF and a commercial carbon fiber T310J. (a) Unadjusted ED comparison; (b) adjusted (for visual effect) ED comparison.

It can be seen that the (002) arc for the commercial fiber is significantly sharper and the double angle of the arc is significantly smaller than for the CNF, indicating both better structure and orientation of “graphitic” crystallites. As the visual comparison in Figure 39b shows (the red and the yellow semi-circles for the (002) arcs) the d_{002} -spacing in the commercial fiber is also significantly smaller, again indicating better graphitic structure.

XRD examination was also performed and the results for CNFs, PAN-based, and pitch based commercial fibers were compared (Figure 40 and Table 2).

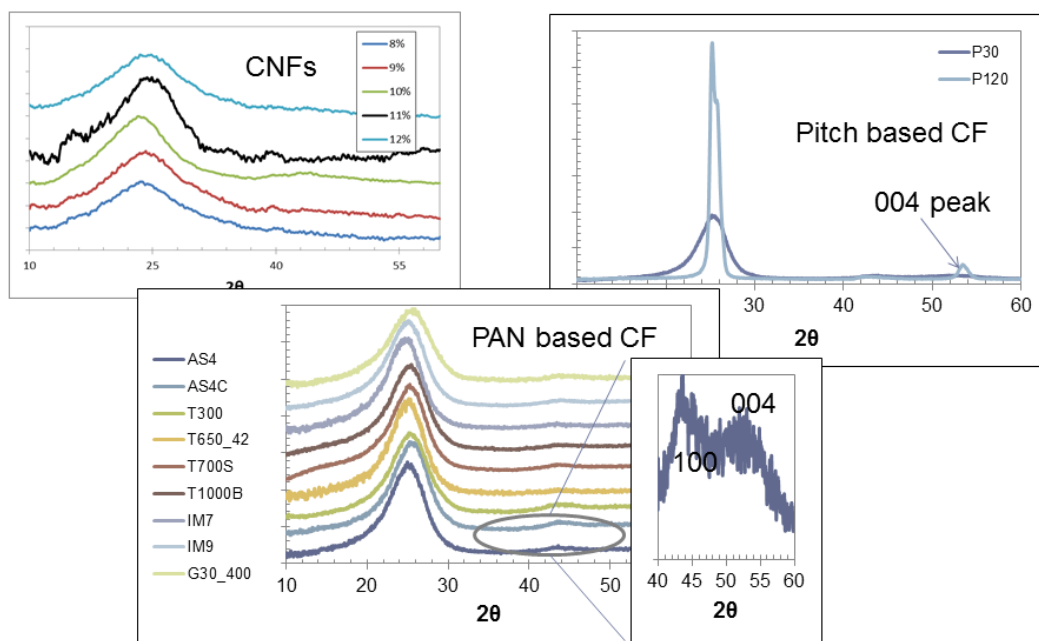


Figure 40. Comparison of XRD patterns for CNFs and different commercial carbon fibers. Commercial carbon fibers exhibited better graphitic structure than the CNFs (with the pitch based fibers exhibiting the best graphitic structure) described by a sharper (002) peak and visible (100) and (004) peaks.

Table 2. Comparison of parameters extracted from XRD patterns for CNFs and commercial carbon fibers.

Fiber	Precursor	d_{002} (Å)	d_{004} (Å)	d_{002} from 004 peak	d_{100} (Å)	L_c (Å)	L_a (Å)
CNFs	PAN	3.71 ± 0.06	No visible peak	n/a	No visible peak	9.5 ± 2.9	n/a
AS4	PAN	3.61	1.76	3.52	2.09	15.8	40.8
AS4C	PAN	3.52	1.73	3.46	2.04	16.1	37.1
T310J	PAN	3.51	1.75	3.5	2.04	19.6	54.3
T300	PAN	3.54	1.73	3.46	2.06	14.9	28.6
T650/42	PAN	3.58	1.72	3.44	2.04	16.8	37.2
T700S	PAN	3.56	1.74	3.48	2.06	15.3	35.7
T1000B	PAN	3.56	1.73	3.46	2.03	15.3	39.1
IM7	PAN	3.64	1.74	3.48	2.06	16.2	45.4
IM9	PAN	3.60	1.73	3.46	2.04	15.3	42.5
G30/400	PAN	3.54	1.71	3.42	2.04	13.3	28.6
P30	Pitch	3.53	1.74	3.48	2.08	23.4	44.8
P120	Pitch	3.51	1.71	3.42	2.08	82.4	32.7

Raman spectroscopy was performed using a 532 nm laser and the results for CNFs and commercial fibers were compared (Figure 41).

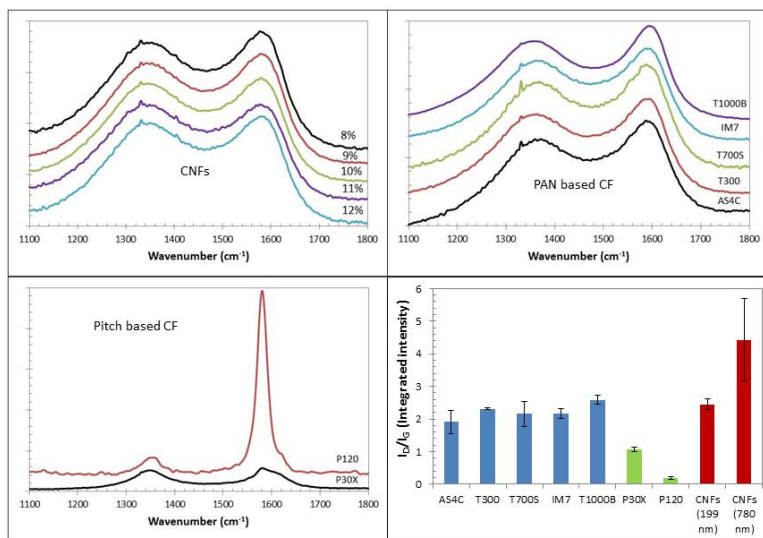
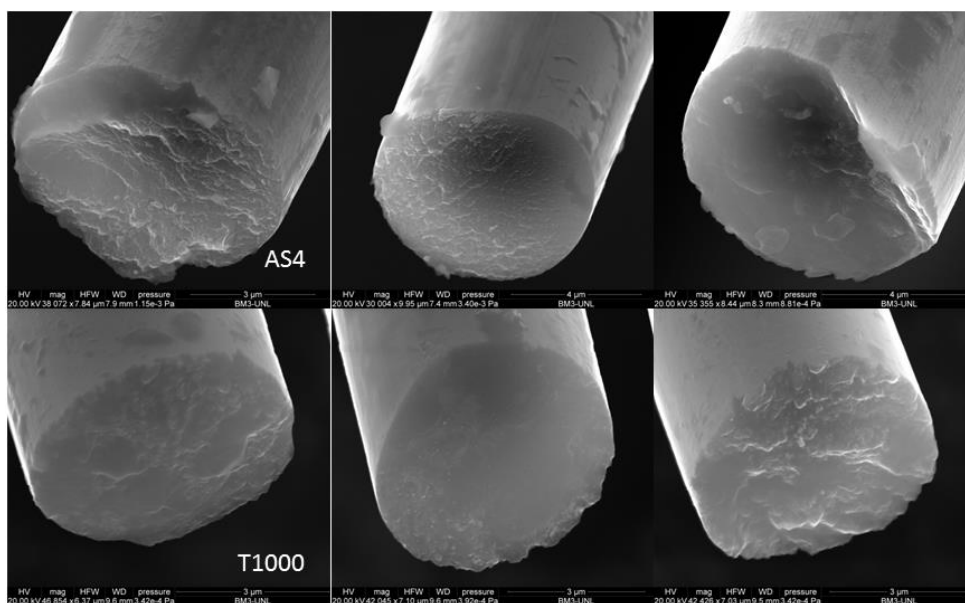


Figure 41. Comparison of Raman spectroscopy results for CNFs and commercial carbon fibers (blue and green columns are for PAN and pitch based commercial fibers respectively).

The commercial carbon fibers exhibited better structure as expressed by the lower I_D/I_G ratio (inversely proportional to L_a crystal size), with Pitch based fibers (as expected) exhibiting the best structure. The ratio for CNFs decreased with the decrease in average diameter of the mat, with the thinnest CNFs exhibiting Raman pattern similar to the high-performance T1000 commercial fiber.

A range of commercial carbon fibers was tested mechanically and their fracture surfaces were compared to CNF fracture surfaces (Figure 42).



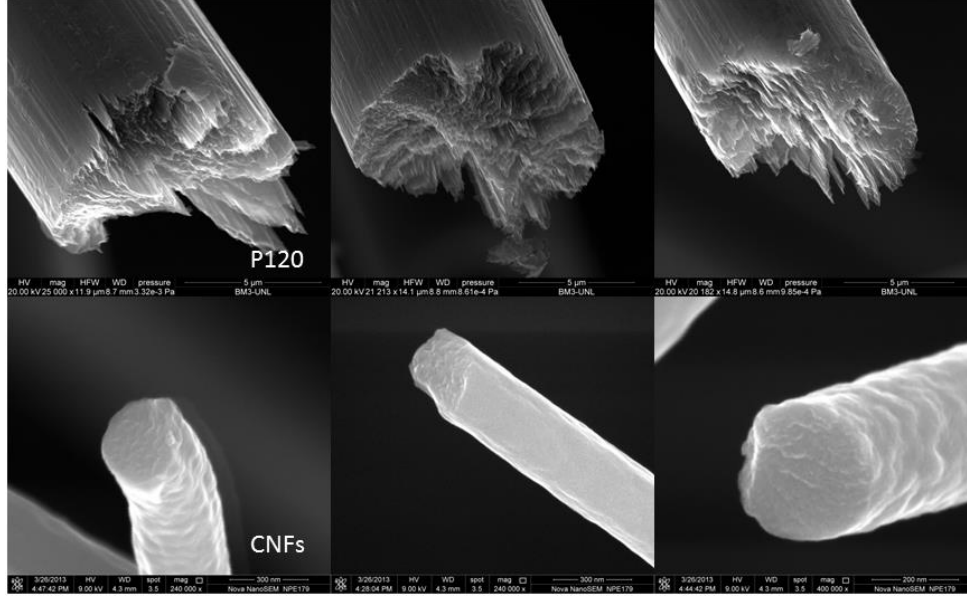


Figure 42. Comparison of fracture surfaces of CNFs and commercial carbon fibers.

Results of experimental investigation of the CNF size effects in Dzenis group were submitted to the Buehler group for modeling and simulation. A plane strain coarse-grained bead-spring model was used to model the mechanical behavior of individual carbon nanofilaments (Figure 43). The internal bond stiffness was calibrated to matches the experimentally observed modulus (Figure 44a). Variations of fiber properties with size were computed for several different crack to diameter ratios $a/D = 0.05, 0.10, 0.25, 0.40$ (Figure 44). The results show good correspondence with experimental data.

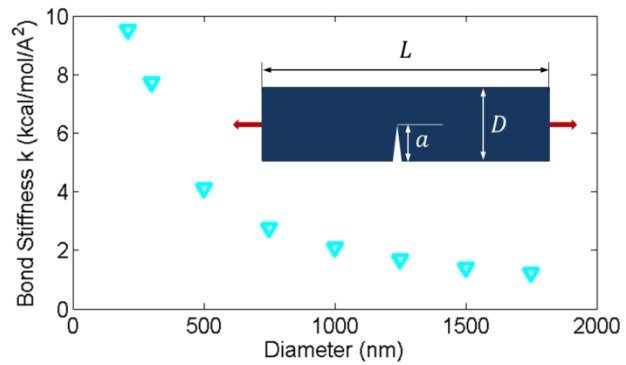


Figure 43. Plane strain fiber model with flaw and bond stiffness for different crack size ratios a/D . A triangular mesh with bond distance 10 nm is used to model a flawed fiber with diameter D , length L (both much bigger than the bond distance) and a surface crack with length a . Each crack size ratio a/D with $D = 210$ nm is associated with a different internal bond stiffness to match the experimentally observed modulus of ≈ 150 GPa.

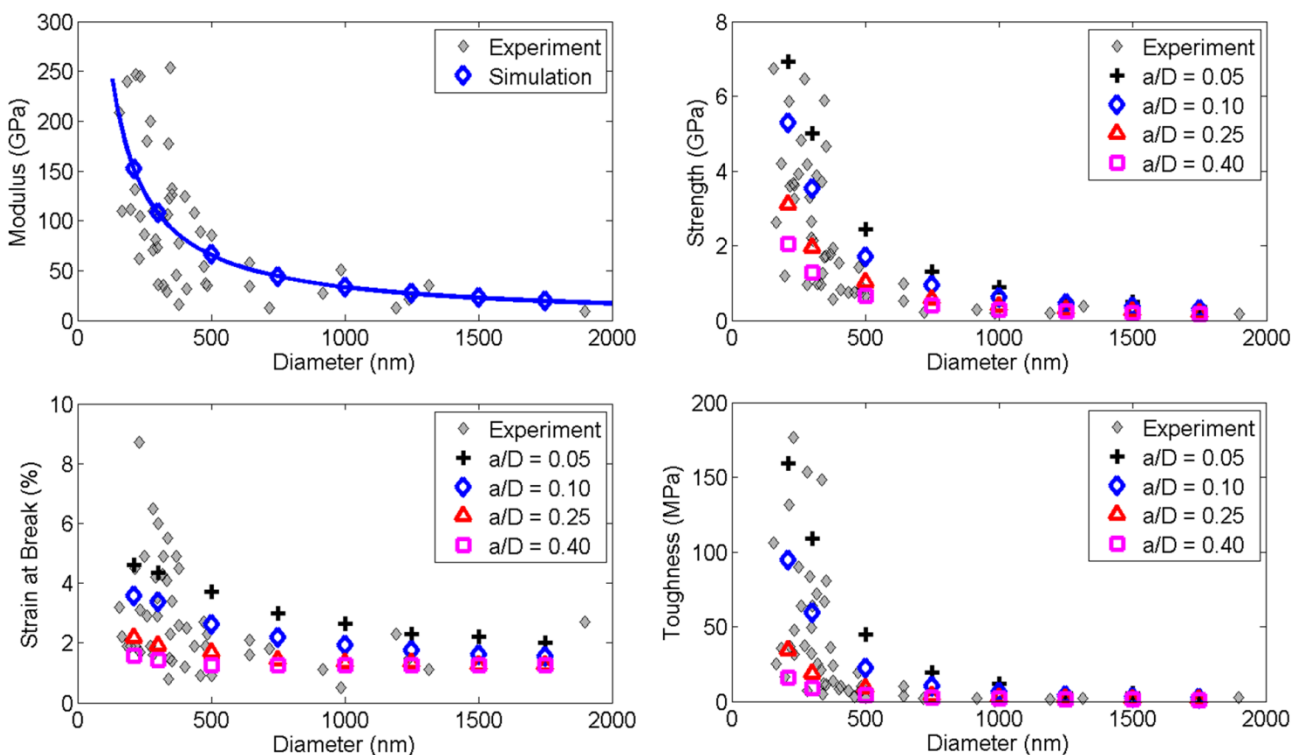


Figure 44. Comparison of experimental results to the results of the computational study; a) Elastic modulus; b) strength; c) strain to failure; and d) toughness modulus.

A good match with the experimental results is found in case the model incorporates size effects of a flawed fiber ($a/D \neq 0$). Thereby, the strength does not only scale with the modulus but displays also the size-dependence of a flawed fiber as predicted by fracture mechanics, *i.e.* the strength scales with $\sqrt{1/D}$. This means that the mechanical properties at high diameters may be attributed to the existence of stress concentrators (e.g. flaws) in the order of 5% or more of the fiber diameter and structural changes cannot be solely accounted for the dramatic change in mechanical performance.

High resolution TEM (HRTEM) analysis of CNFs was performed by Dzenis group. The investigation was undertaken to explicitly observe nanocrystalline structure and orientation in CNFs as well as to confirm the unusually large d_{002} spacing in the crystallites observed in ED and XRD. The images (Figures 45 and 46) revealed a generally poor graphitic structure with small crystallites roughly aligned along the fiber axis (verified by both visual examination and FFT analysis), consistent with the ED measurements. Explicit (manual) measurements confirmed large d-spacings consistent with the XRD and ED data.

Overall, the results of the CNF analysis allow to conclude that the generally poor graphitic structure of CNFs might be responsible for their large deformation at failure. Coupled with the size effect, this may lead to simultaneously strong and tough ultrafine carbon fibers.

Ultrahigh-performance DWNT-templated carbon nanofibers **proprietary**

The Dzenis group continued the analysis of the size and templating effects in the DWNT-templated CNFs. New data were accumulated in the broad range of CNF diameters (Figure 47). The world's strongest continuous nanofiber was demonstrated for the first time. The results for the smaller diameter nanofibers were consistent with the *in situ* testing data on UNL samples by Espinosa group. The HRTEM analysis of the templated CNFs is in progress. The current results show high promise for the ultrahigh-performance continuous carbon nanofilaments templated with a very small amount of DWNT.

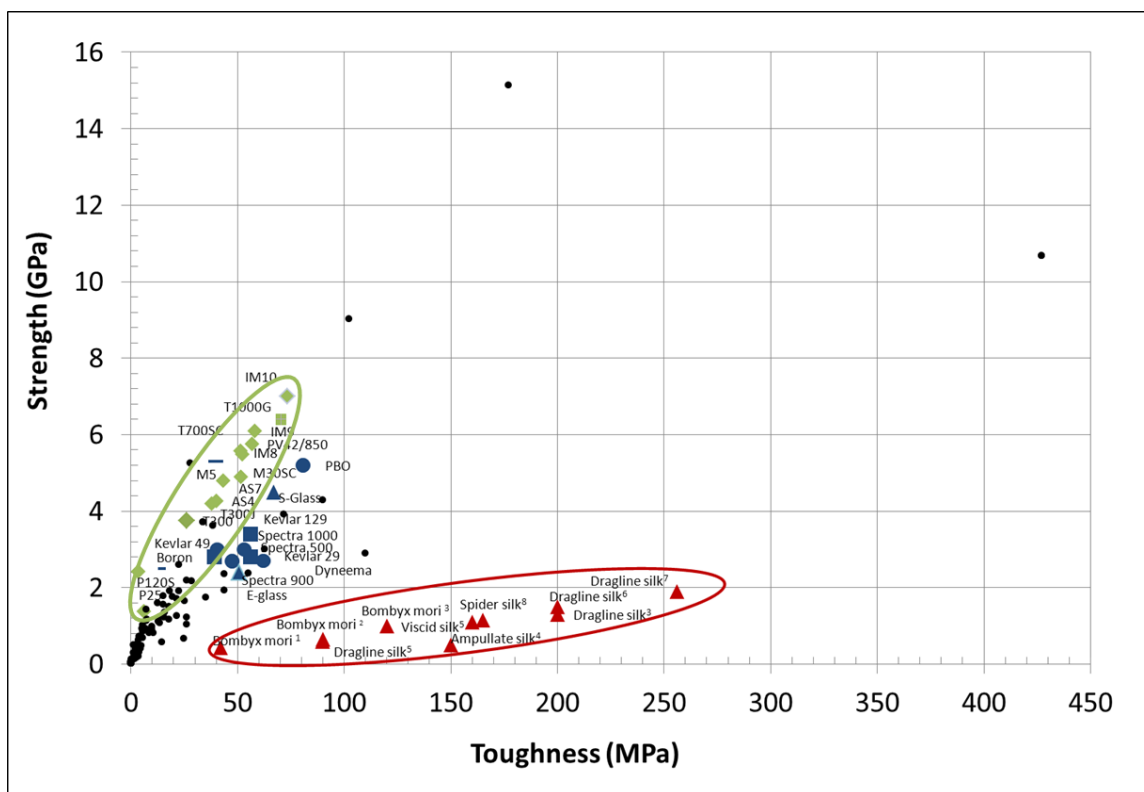


Figure 47. Strength-toughness correlation for DWNT-templated CNFs and comparison with advanced commercial and silk fibers. The results show promise of the ultrahigh strength and toughness of the continuous CNFs.

The Dzenis group continued optimization of nanomanufacturing of nanofibers templated with GO nanoparticles in collaboration with Nguyen's group. The resulting best process parameters are now being utilized to produce specimens for mechanical testing and structural characterization.

Evaluation of the effects of mechanical constraint during CNF stabilization and carbonization

The effect of constraint during carbonization on the structure of CNFs was examined by ED and Raman spectroscopy in Dzenis group (Figure 48).

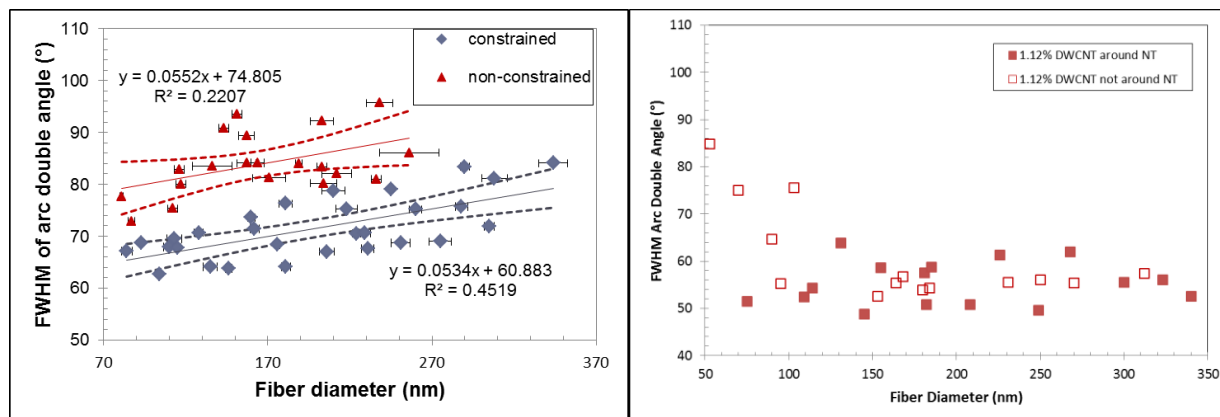


Figure 48. Comparison of graphitic crystal orientation as measured by the (002) double angle from ED for CNFs constrained and non-constrained during carbonization. Figure on the right shows similar measurements for templated samples.

It was found for the first time that the constrained sample exhibited significantly better crystal orientation across the examined diameter range. Raman spectroscopy was performed using 514nm laser (Figure 49).

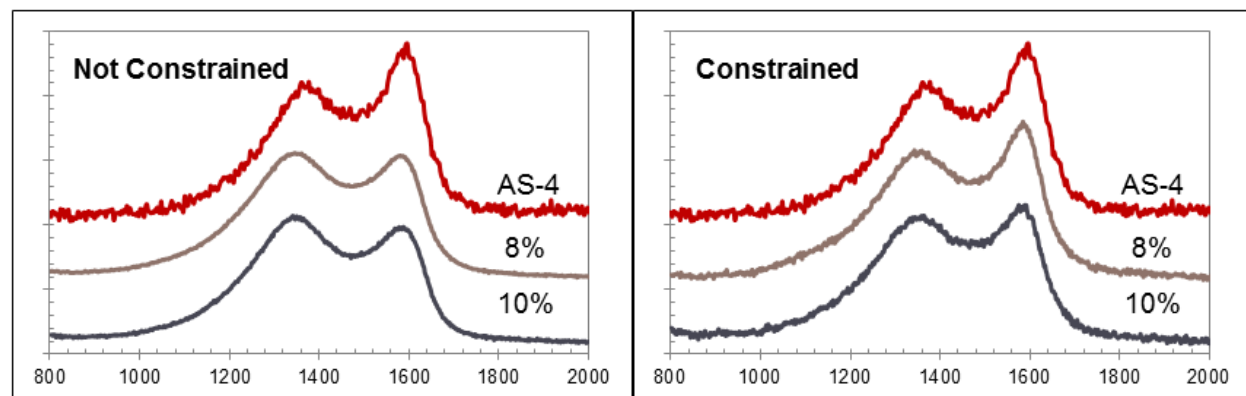


Figure 49. Comparison of Raman spectra for constrained and non constrained CNFs. In both figures the spectra for CNFs is compared to a commercial AS4 fiber.

It was found that the constrained samples show better graphitic structure as indicated by the sharper G band, and smaller I_D/I_G ratio (inversely proportional to L_a crystal size). It is also apparent that the improvement in the structure for the thinner CNFs (lower polymer concentration during electrospinning) was significantly more pronounced in the case of constrained CNFs, with 8% sample exhibiting the spectrum similar to the AS4 fiber.

These results indirectly support our previously articulated hypothesis that internal constraint imposed by the aligned nanocarbon particles (DWNT and crumpled GO) might be responsible for the observed improvements in graphitic structure and properties. Constrained and unconstrained CNF specimens were fabricated by the Dzenis group and sent to Espinosa group for comparative mechanical evaluation (in progress).

Further evaluation of hypothesis of internal constraint in DWNT-templated CNFs
*****proprietary*****

To further analyze the internal constraint hypothesis, the Dzenis group studied nanofiber shrinkage behavior during stabilization and carbonization. Several new approaches were developed. Nanofiber diameter evolution was studied on individual nanofibers in a broad diameter range.

Individual, long (~25mm) NFs were placed on a quartz slide and fixed at the edges with epoxy. The NFs underwent standard stabilization and carbonization process (carbonization temperature was 800°C). Diameter was measured at each step at several locations on the fiber separated by several millimeters. In each location, several micrometers in size, five measurements of fiber diameter were performed. The data was analyzed to get an average diameter of the fiber at each step and the change in diameter. The tests were performed on three nanofiber families – pristine and composite with 1% DWNT and 1% GO-nano.

From Figure 50b it appears that the diameter change decreases for all families as a result of a decrease in initial fiber diameter. This decrease is steeper for the composite NF families (with the family containing DWNTs having the steepest decrease in diameter shrinkage). As a result, the decrease in diameter for the pristine NFs is larger than for the composite ones at lower initial diameters. From Figure 50c it appears that the diameter change in the composite NFs is roughly independent of initial diameter, while for pristine NFs it decreases for smaller initial diameters.

In addition to the analysis of individual nanofibers, average NF diameters for the three families were measured on nanofiber mats before and after carbonization (carbonization was performed on non-constrained mats). Average fiber diameters for the pristine and 1%DWNT NF families were similar, while the average diameters for the family with 1% GO-nano was smaller throughout the whole concentration range both before and after carbonization. The diameter distribution was also narrower for this nanofiber family.

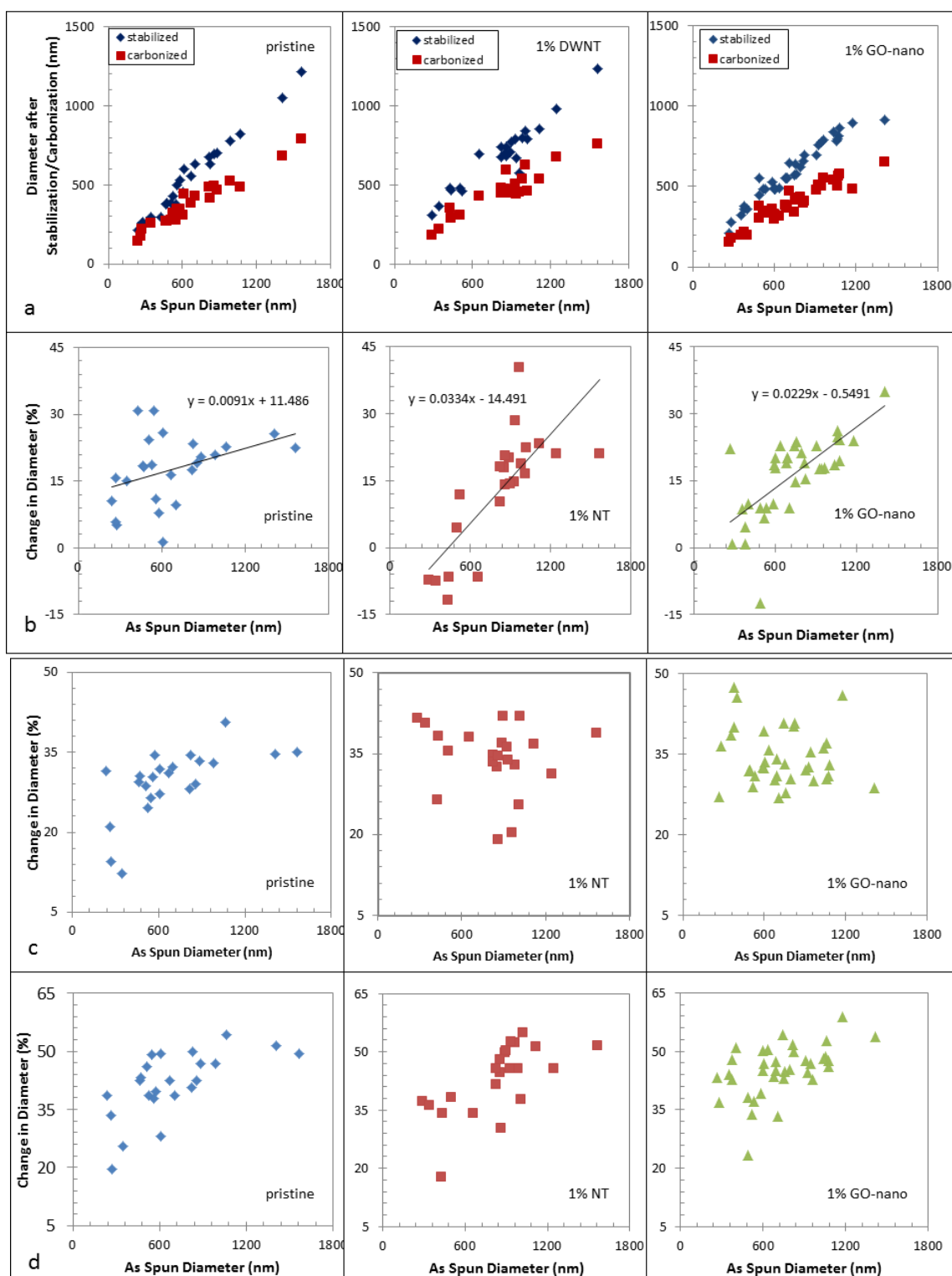


Figure 50. Diameter evolution for the different nanofiber families during carbonization. (a) diameter after stabilization and carbonization vs. initial diameter; (b) diameter change during stabilization; (c) diameter change during carbonization; (d) total diameter change.

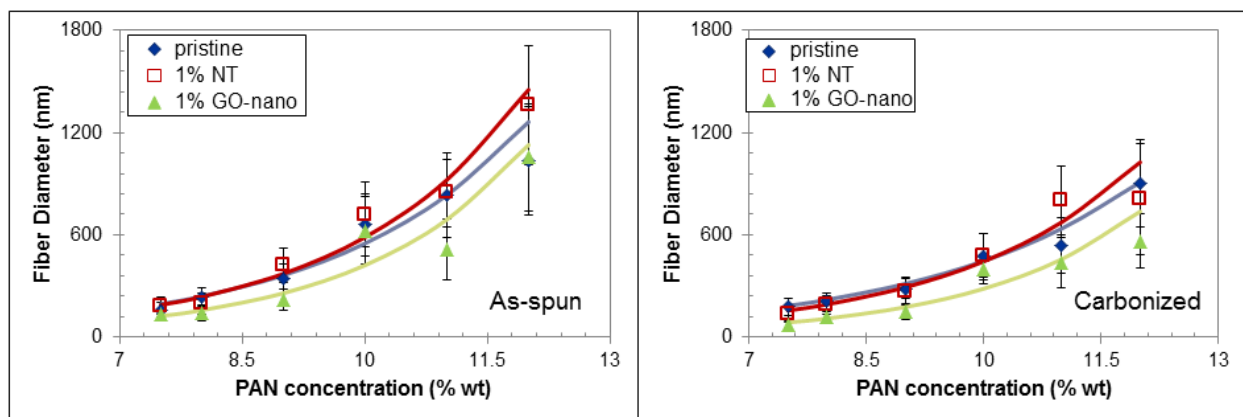
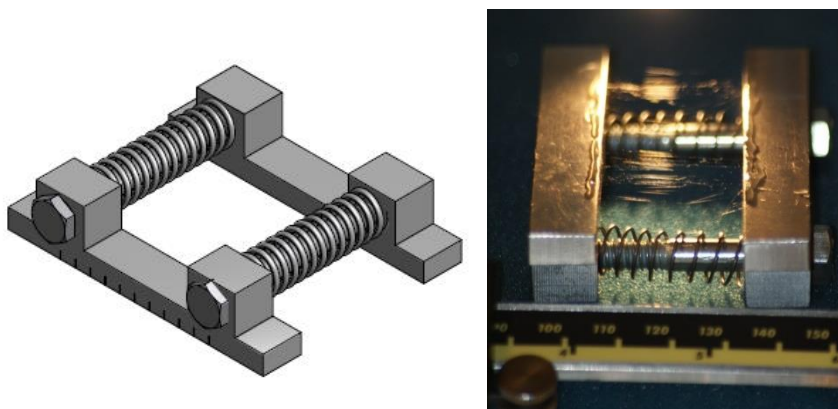


Figure 51. Average nanofiber diameters for the three nanofiber families before and after carbonization as a function of PAN concentration. The lines correspond to an exponential fit and the error bars are standard deviation within each concentration.



A new fixture (above) was developed for controlled length shrinkage experiments that are currently in progress in Dzenis group. The fixture will be also used for fabrication of unconstrained CNFs for mechanical analysis in Dzenis and Espinosa groups.

Size effects in modified PAN precursor nanofibers

In the previous reporting period, the Dzenis group showed that increasing nanofiber crystallinity of PAN nanofibers by annealing led to significant decrease in strain to failure and toughness. The current study was intended to manipulate the crystal structure in the opposite direction and to examine the effect of reduced crystallinity on mechanical properties.

Morphology of the NFs produced with a different solvent (DMAc) and plasticizer (ethylene carbonate) were examined, and the average diameters were compared for the same PAN concentrations (Figure 52).

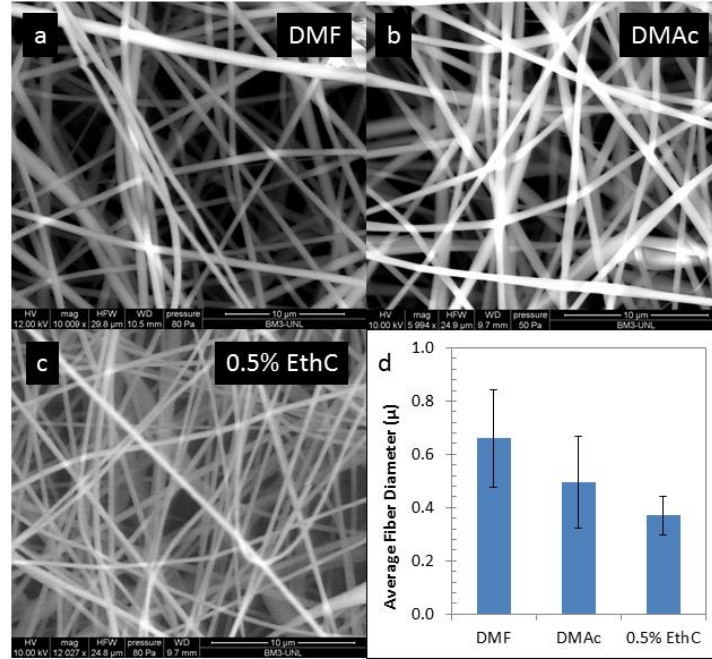


Figure 52. (a)-(c) Nanofiber morphology for the different NF families produced from 10 wt% PAN solutions; (d) Average NF diameter (error bars are standard deviations).

Both the use of DMAc as a solvent and the use of plasticizer resulted in thinner NFs. In addition, the plasticized NF family exhibited narrower diameter distribution. Mechanical properties were measured for individual NFs and compared with the previous results for the DMF-spun nanofibers (Figure 53).

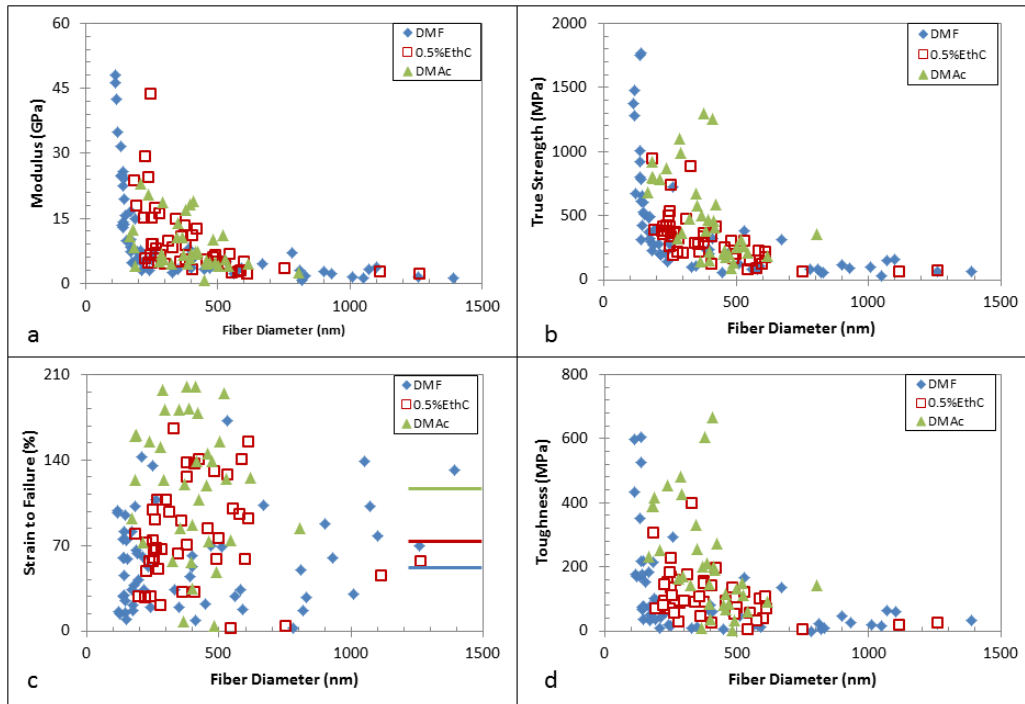


Figure 53. Mechanical properties of different NF families. (a) Modulus; (b) True strength; (c) Strain to failure (the lines on the left are average values for the different families); (d) Toughness.

The new NF families exhibited significantly higher strength and modulus in the intermediate diameter range (250-500 nm) at times almost reaching the highest values obtained previously for the ultra-fine DMF-spun PAN fibers. The strain to failure increased significantly (with the DMAc giving a two fold increase) and resulted in elevated toughness in the intermediate range, with the best results even exceeding those previously reported for the ultrafine DMF-spun NFs.

NF crystal structure was studied by XRD. The new NF families exhibited lower crystallinity than the ones examined in the past. The structural and the mechanical data are consistent with the previous explanation for the ultrahigh toughness and large strain to failure of nanofibers resulting from low crystallinity, and high strength and modulus resulting from better polymer chain alignment.

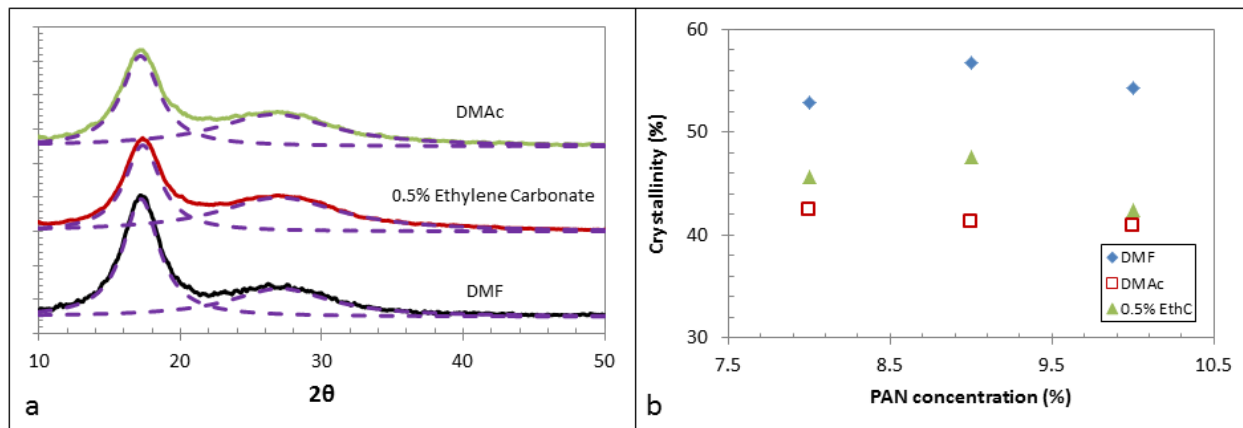


Figure 54. XRD analysis of PAN nanofiber structure. (a) XRD patterns for different nanofiber families spun from 10 wt% PAN solutions; (b) variation of XRD-crystallinity with PAN concentration for different nanofiber families.

Correlations of properties were also examined (Figure 55) and it was shown that the choice of solvent as well as small amounts of additives can be effectively utilized to tailor nanofiber property variations in the strength/modulus and strength/toughness spaces.

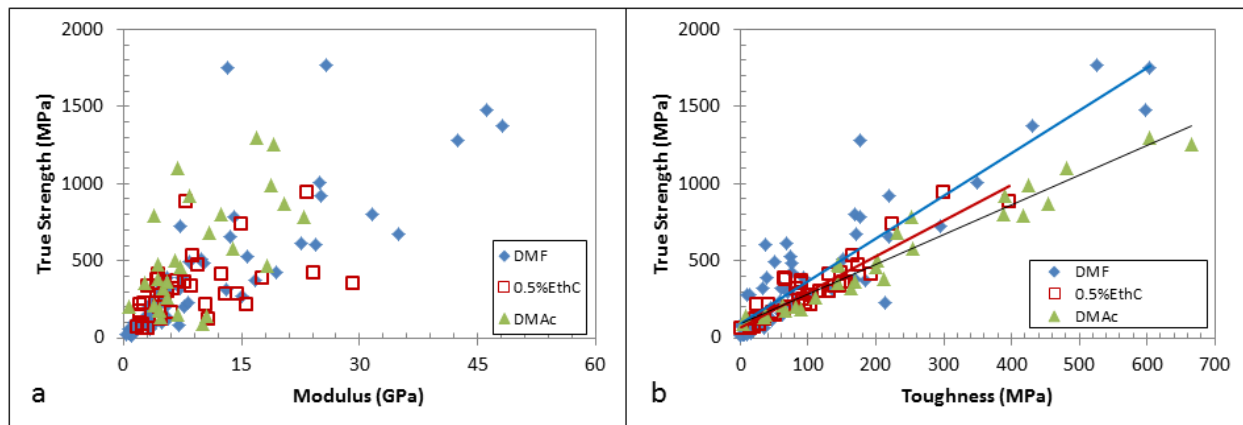


Figure 55. Correlations of mechanical properties of continuous nanofibers: (a) Strength/modulus and (b) strength/toughness correlations for different nanofiber families.

Further experiments are in progress with the goal to determine whether the increases in mechanical properties extend into the ultrafine diameter range.

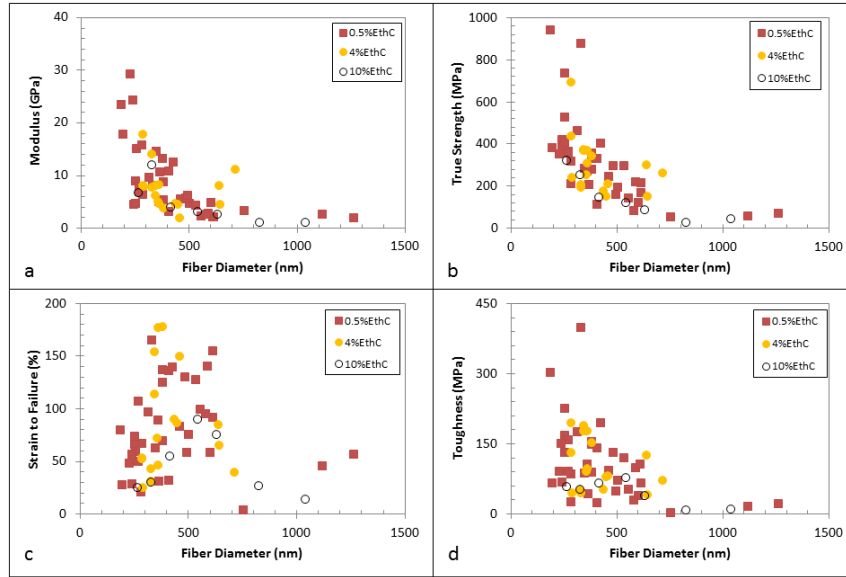


Figure 56. Effect of plasticizer content on mechanical properties. (a) Modulus; (b) True strength; (c) Strain to failure; (d) Toughness.

Evaluation of mechanical behavior of nanofiber assemblies and yarns

Numerical analysis of nanofilamentary networks and yarns with explicit nanofiber and contact representation was continued in the Dzenis group. Extensive parametric studies were conducted. It was shown that individual nanofiber properties can be further significantly enhanced in the yarn assembly (Figures 57 and 58). Scaling of yarn properties with nanofiber diameter was analyzed for the first time. The pioneering results (Figure 59) show that the enhancements of nanofiber properties as a result of lateral interactions in the nanofilamentary yarn depends on the nanofiber diameter, with finer nanofibers exhibiting larger relative enhancements. This result is significant as it provides guidance for nanofiber assembly design and promises further improvements of already spectacular properties of individual nanofibers.

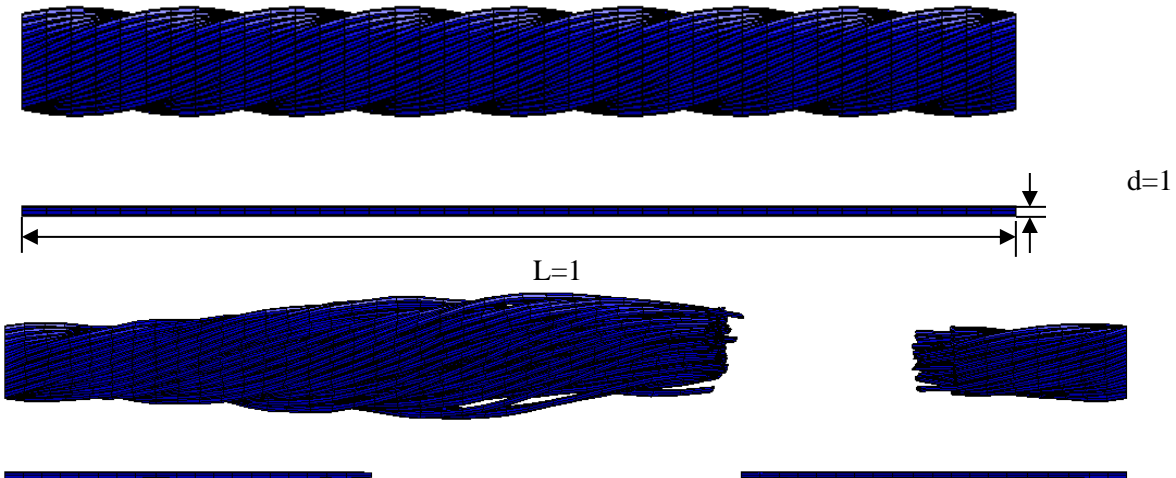


Figure 57. Yarn model and comparison of yarn and single nanofiber deformations at yarn total failure point.

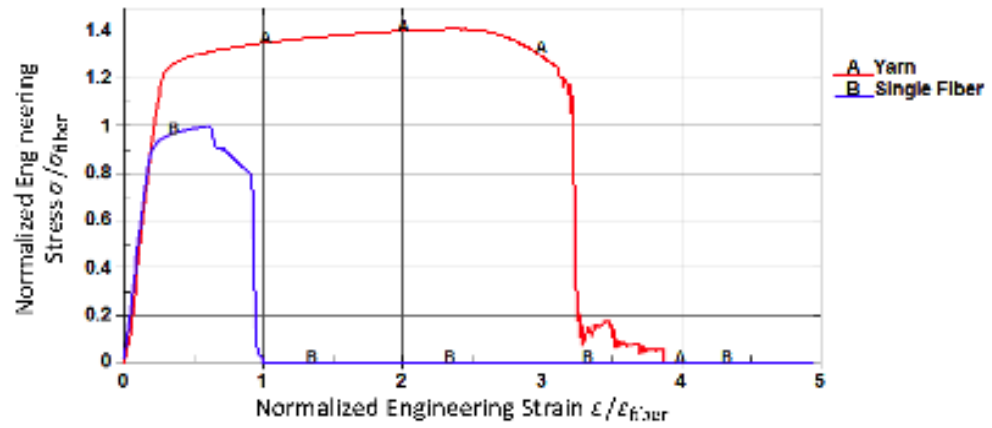


Figure 58. Normalized engineering stress – strain curves of yarn and single fiber.

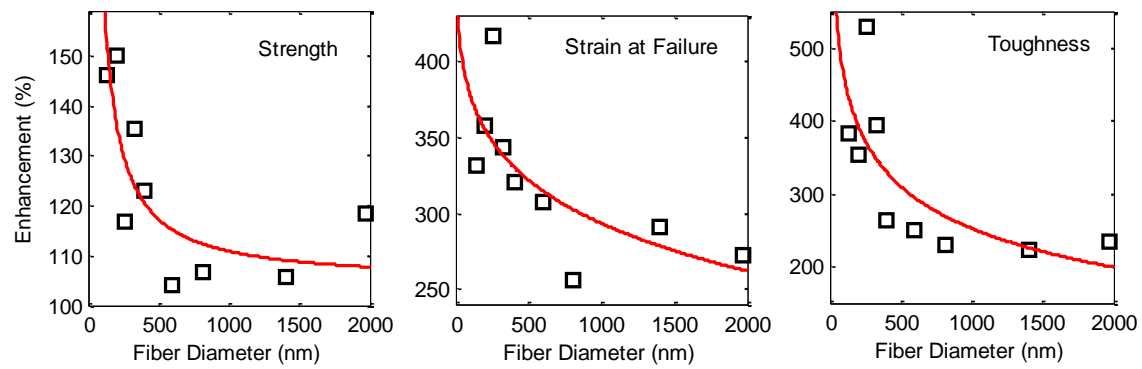


Figure 59. Variation of percent enhancement of yarn properties over single fiber as a function of fiber diameter. Data points were curve fitted with power function.

References

- [1] Filleter, T., Yockel, S., Naraghi, M., Paci, J. T., Compton, O. C., Mayes, M. L., Nguyen, S. T., Schatz, G. C., & Espinosa, H. D. (2012). Experimental-computational study of shear interactions within double-walled carbon nanotube bundles. *Nano letters*, **12**(2), 732-742.
- [2] Lebedeva, I. V., Knizhnik, A. A., Popov, A. M., Lozovik, Y. E., & Potapkin, B. V. (2011). Interlayer interaction and relative vibrations of bilayer graphene. *Physical Chemistry Chemical Physics*, **13**(13), 5687-5695.
- [3] Zhang, M.; Atkinson, K. R.; Baughman, R. H., Multifunctional Carbon Nanotube Yarns by Downsizing an Ancient Technology *Science* **2004**, *306*, 1358-1361.
- [4] Min, J.; Cai, J. Y.; Sridhar, M.; Easton, C. D.; Gengenbach, T.; McDonnell, J.; Humphries, W.; Lucas, S., High Performance Carbon Nanotube Spun Yarns from a Crosslinked Network. *Carbon* **2012**.
- [5] Koziol, K.; Vilatela, J.; Moisala, A.; Motta, M.; Cunniff, P.; Sennett, M.; Windle, A., High-Performance Carbon Nanotube Fiber. *Science* **2007**, *318*, 1892-1895.
- [6] Zhang, S.; Zhu, L.; Minus, M. L.; Chae, H. G.; Jagannathan, S.; Wong, C. P.; Kowalik, J.; Roberson, L. B.; Kumar, S., Solid-State Spun Fibers and Yarns from 1-Mm Long Carbon Nanotube Forests Synthesized by Water-Assisted Chemical Vapor Deposition. *Journal of Materials Science* **2008**, *43*, 4356-4362.
- [7] Tran, C. D.; Humphries, W.; Smith, S. M.; Huynh, C.; Lucas, S., Improving the Tensile Strength of Carbon Nanotube Spun Yarns Using a Modified Spinning Process. *Carbon* **2009**, *47*, 2662-2670.
- [8] Denis-Lutard, V.; Derre, A.; Maugey, M.; Mercader, C.; Moisan, S.; Zakri, C.; Poulin, P. In *New Wet Spinning Process for the Continuous Production of Polymer/Carbon Nanotubes Composite Fibers*, Recent Advances in Textile Composites: Proceedings of the 10th International Conference on Textile Composites, DEStech Publications, Inc: 2010; p 167.
- [9] Naraghi, M.; Filleter, T.; Moravsky, A.; Locascio, M.; Loutfy, R. O.; Espinosa, H. D., A Multiscale Study of High Performance Double-Walled Nanotube-Polymer Fibers. *ACS Nano* **2010**, *4*, 6463-6476.
- [10] Li, Y. L.; Kinloch, I. A.; Windle, A. H., Direct Spinning of Carbon Nanotube Fibers from Chemical Vapor Deposition Synthesis. *Science* **2004**, *304*, 276-278.
- [11] Zhang, X.; Li, Q.; Tu, Y.; Li, Y.; Coulter, J. Y.; Zheng, L.; Zhao, Y.; Jia, Q.; Peterson, D. E.; Zhu, Y., Strong Carbon-Nanotube Fibers Spun from Long Carbon-Nanotube Arrays. *Small* **2007**, *3*, 244-248.
- [12] Lu, W.; Zu, M.; Byun, J.-H.; Kim, B.-S.; Chou, T.-W., State of the Art of Carbon Nanotube Fibers: Opportunities and Challenges. *Advanced Materials* **2012**, *24*, 1805-1833.
- [13] Peng, B.; Locascio, M.; Zapol, P.; Li, S.; Mielke, S. L.; Schatz, G. C.; Espinosa, H. D., Measurements of near-Ultimate Strength for Multiwalled Carbon Nanotubes and Irradiation-Induced Crosslinking Improvements. *Nature Nanotechnology* **2008**, *3*, 626-631.
- [14] Kendall, K., Thin-Film Peeling-the Elastic Term. *Journal of Physics D: Applied Physics* **1975**, *8*, 1449.,
- [15] Yu, M.-F.; Lourie, O.; Dyer, M. J.; Moloni, K.; Kelly, T. F.; Ruoff, R. S., Strength and Breaking Mechanism of Multiwalled Carbon Nanotubes under Tensile Load. *Science* **2000**, *287*, 637-640.
- [16] Haskins, R. W.; Maier, R. S.; Ebeling, R. M.; Marsh, C. P.; Majure, D. L.; Bednar, A. J.; Welch, C. R.; Barker, B. C.; Wu, D. T., Tight-Binding Molecular Dynamics Study of the Role of Defects on Carbon Nanotube Moduli and Failure. *The Journal of chemical physics* **2007**, *127*, 074708.
- [17] Griffith, A. A., The Phenomena of Rupture and Flow in Solids. *Philosophical transactions of the royal society of london. Series A, containing papers of a mathematical or physical character* **1921**, *221*, 163-198.
- [18] Ma, X.; Wang, H.; Yang, W., Tribological Behavior of Aligned Single-Walled Carbon Nanotubes. *J. Eng. Mater. Technol.* **2004**, *126*, 258-264.
- [19] Li, X.; Cai, W.; Colombo, L.; Ruoff, R. S., Evolution of Graphene Growth on Ni and Cu by Carbon Isotope Labeling. *Nano letters* **2009**, *9*, 4268-4272.

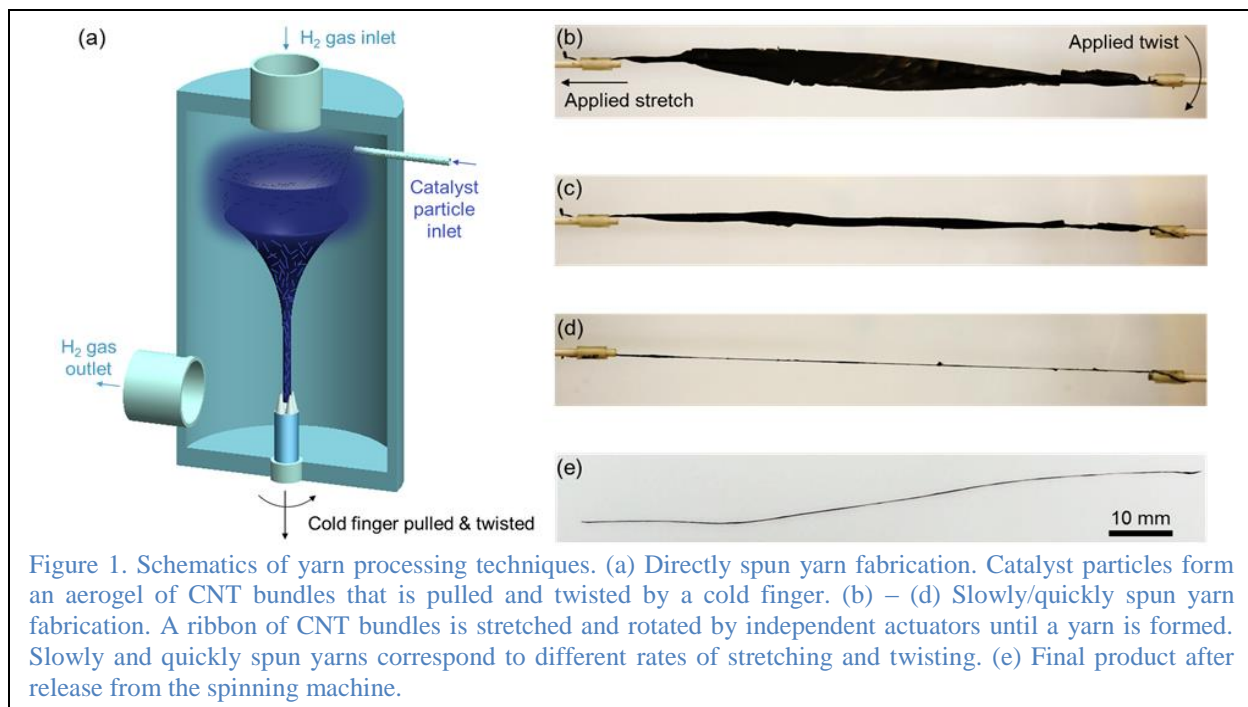
- [20] Cai, W.; Piner, R. D.; Stadermann, F. J.; Park, S.; Shaibat, M. A.; Ishii, Y.; Yang, D.; Velamakanni, A.; An, S. J.; Stoller, M., Synthesis and Solid-State Nmr Structural Characterization of ¹³C-Labeled Graphite Oxide. *Science* **2008**, *321*, 1815-1817.
- [21] Obraztsov, A.; Obraztsova, E.; Tyurnina, A.; Zolotukhin, A., Chemical Vapor Deposition of Thin Graphite Films of Nanometer Thickness. *Carbon* **2007**, *45*, 2017-2021.
- [22] Mattevi, C.; Eda, G.; Agnoli, S.; Miller, S.; Mkhoyan, K. A.; Celik, O.; Mastrogiovanni, D.; Granozzi, G.; Garfunkel, E.; Chhowalla, M., Evolution of Electrical, Chemical, and Structural Properties of Transparent and Conducting Chemically Derived Graphene Thin Films. *Advanced Functional Materials* **2009**, *19*, 2577-2583.
- [23] Yuzvinsky, T. D.; Fennimore, A. M.; Mickelson, W.; Esquivias, C.; Zettl, A., Precision Cutting of Nanotubes with a Low-Energy Electron Beam. *Applied Physics Letters* **2005**, *86*, 053109-3.
- [24] Steele, W. A., *The interaction of gases with solid surfaces*, 1974: Paragon Press, Oxford.
- [25] *In situ* SEM Peeling to Quantify Surface Energy between Multiwalled Carbon Nanotubes and Graphene, M. R. Roenbeck, X. Wei, A. M. Beese, M. Naraghi, A. Furmanchuk, J. T. Paci, G. C. Schatz, H. D. Espinosa, ACS Nano, to be published.
- [26] Fratzl, P., Gupta, H. S., Fischer, F. D., & Kolednik, O. (2007). Hindered crack propagation in materials with periodically varying Young's modulus—lessons from biological materials. *Advanced Materials*, *19*(18), 2657-2661.
- [27] Kolednik, O., Predan, J., Fischer, F. D., & Fratzl, P. (2011). Bioinspired Design Criteria for Damage-Resistant Materials with Periodically Varying Microstructure. *Advanced Functional Materials*, *21*(19), 3634-3641.
- [28] Dunlop, J. W., Weinkamer, R., & Fratzl, P. (2011). Artful interfaces within biological materials. *Materials Today*, *14*(3), 70-78.
- [29] Fischer, F. D., Predan, J., Fratzl, P., & Kolednik, O. (2012). Semi-analytical approaches to assess the crack driving force in periodically heterogeneous elastic materials. *International journal of fracture*, *173*(1), 57-70.

Scientific Progress and Accomplishments

Fabrication and Characterization of Microscale DWNT Composite Yarns

In this study, we examine the fabrication-structure-mechanical property relationships in CNT yarns made through three distinct fabrication approaches. “Directly spun” yarns were fabricated by extracting the aerogel from a CVD reactor while the CNTs were being produced, which was expected to result in well-aligned CNTs. “Quickly spun” and “slowly spun” yarns were fabricated from ribbons cut from disordered mats of CNTs. All yarn types were then characterized for structural features of interest (e.g. porosity and alignment) and mechanical performance. The results of this study yielded significant insights into structural and processing factors that limit yarn mechanical strength, thus suggesting next steps to be taken in the development of CNT-based yarns. This work has been submitted for publication and is currently under review.

All yarns were composed of bundles of DWNT prepared by MER Corporation using a CVD reactor. The yarns we refer to as ‘directly spun’ were fabricated from the CVD reactor as the CNTs are being produced. A hollow cylindrical shaped aerogel of loosely connected CNTs was formed in the hot zone of the vertical CVD reactor and carried downstream by the flow of gas (Figure 1). A “cold finger” spindle was inserted through the vacuum port in the lower flange of the reactor tube to contact the aerogel, which was stretched and twisted into a yarn by driving the spindle downward while rotating it. Following removal from the reactor, directly spun yarns were stretched and twisted to further compact the yarns. Typical stretching and twisting rates were 0.08 mm/min and 3 turns/min, respectively.



Both slowly spun and quickly spun yarns were prepared from porous CNT mats with an apparent thickness of 50 μm . Strips of constant width were cut from the mat, with one end of the strip then connected to a linear actuator to stretch the mat and the other end to a rotating actuator to twist the mat into a yarn. The slowly spun yarns were stretched at a rate of ~ 0.1 mm/min and twisted at

a rate of ~ 0.5 turn/min, while the quickly spun yarns were stretched at a rate of ~ 1.2 mm/min and twisted at a rate of ~ 60 turns/min. Thus, the slowly spun yarns were fabricated over a period of a few hours, while the quickly spun yarns were fabricated over a period of ~ 5 minutes. This variation in fabrication rates leads to differences in alignment and compaction of the yarns.

Following synthesis, yarns were further twisted and stretched, and a solvent was applied to the yarn to aid its compaction.

Multiscale Experimental and Computational Studies of the Mechanical Behavior of CNT Bundles and Yarns

Processing-structure-property relationships in CNT yarns

Carbon nanotubes (CNTs) have long been envisioned as potential filaments in macroscopic composites in light of their exceptional nanoscale properties, including tensile strengths and elastic moduli of 100 GPa and 1 TPa, respectively [1, 2]. In particular, there have been extensive efforts to develop yarns comprised of CNTs [3-5]. The strongest yarns reported to-date achieved tensile strength of 8.8 GPa [6]. While impressive, this strength is far lower than the 100 GPa exhibited by individual carbon nanotubes, suggesting there is still significant room for improvement in CNT-based fiber design. In addition, it is difficult to draw comparisons among the trends and properties obtained in different studies to guide optimized design, as vastly different constituents and fabrication techniques have been used [3]. A comprehensive study that integrates processing conditions, nanoscale properties, and macroscale structural features to guide effective design of CNT yarns is critical for future studies in this area.

Over the course of this MURI project, we have put significant effort into characterizing properties of CNT yarn constituents and the nanoscale interfaces between them [7-11]. At the macroscopic yarn level, we have compared the performances of DWCNT bundles and yarns fabricated from mats developed by MER Corporation [12]. We have also explored the effect of polyvinyl alcohol (PVA) infiltration on the mechanical performance of MER yarns [13]. In this current study, we aim to build upon the knowledge accrued through our previous studies to explore this topic more deeply. In particular, we explore processing-structure-property relationships in CNT yarns developed with different fabrication techniques. We also develop a computational model to study properties that could be obtained with an ideal yarn and use this model to assess several ways to improve yarn performance. Over the past year, we have used this study to acquire a more holistic understanding of the key factors that contribute to yarn performance.

Structural characterization of quickly, directly, and slowly spun yarns was performed using scanning electron microscopy (SEM), focused ion beam (FIB), and wide angle x-ray diffraction (WAXD). SEM images of the yarns reveal the organization of the CNT bundles on the surface of the yarns, and qualitatively provide insight into whether the bundles are well-aligned with the yarn principal axis or randomly oriented. However, visualization of the surface cannot provide information on the organization of the CNTs inside the yarns. To gain insight into the nature of the internal porosity of the yarns, we used FIB to mill wells into the yarns. Finally, we used WAXD to quantify the degree of CNT alignment through the entire cross section of the yarns.

Inspection of the surfaces of the three types of yarns through SEM imaging (Figure 2) reveals contrasting CNT orientations. Quickly spun yarns have a random distribution of orientations of the CNTs on the surface of the yarns, where the organization of CNTs still resembles the original disorganized mat structure. This is expected since these yarns were made quickly by twisting and moderately stretching ribbons of the mat, introducing an effective tensile strain of only about 6%

toward untangling and orienting the CNTs with the yarn's tensile axis. The directly spun yarns have the highest degree of CNT alignment on the surface of the yarns. Since these yarns were fabricated by pulling the CNTs out of the CVD reactor while they are made, it is expected that this fabrication technique should result in a high degree of alignment. However, wavy strands of CNT bundles are present on the surfaces of all yarns. The slowly spun yarns have an intermediate degree of CNT alignment on their surfaces. It is expected that the alignment of CNTs in these yarns, fabricated from the same disordered mats of CNTs as the quickly spun yarns, should be higher than that of the quickly spun yarns. A larger axial strain is introduced (~12%) over the much slower, and therefore longer, processing time, which gives time for the network of CNTs to relax as tension is applied.

The overall porosity, p , of the yarns can be calculated using the following equation:

$$p = 1 - \left(\frac{D_{\text{effective}}}{D_{\text{outer}}} \right)^2 \quad (1)$$

where $D_{\text{effective}}$ corresponds to the diameter from linear density assuming a 'filled' circular cross section, and D_{outer} is the outer diameter of the yarn as measured in the SEM. The average porosities of representative directly, quickly, and slowly spun yarns was found to be ~77%, ~72%, and ~55%, respectively.

To determine the nature of the porosity, FIB was performed to visualize the internal structure of each type of yarn. The FIB studies reveal that the directly spun yarns have a large amount of microporosity, defined here as having pores with characteristic dimensions of less than 0.2 μm , distributed throughout the diameter of the yarns. The slowly spun yarns are very compact, and have a very small amount of microporosity, but have large voids (defined as having characteristic dimensions of 1 μm or more) present where the folds of the initial ribbon of mat have not fully come into contact. The quickly spun yarns have both large pores present and a large amount of microporosity.

Beyond structural characterization, CNT yarns were tested in tension using a microtensile tester in accordance with the methods described in our previous paper [13]. For each test, a yarn was clamped at both ends into a screw-driven micro-testing frame (Fullam, 2000 lb test frame) and stretched in tension, while the load was recorded with a 250 g load cell (Honeywell, Model 31, resolution of 2 mg) and the elongation of the yarn was recorded using a linear variable differential transformer (Allison Model HS50, resolution of 1 μm). The gauge lengths of the yarns varied from 5 to 20 mm. Quasi-static tests were performed with strain rates on the order of $2 \times 10^{-4} \text{ sec}^{-1}$.

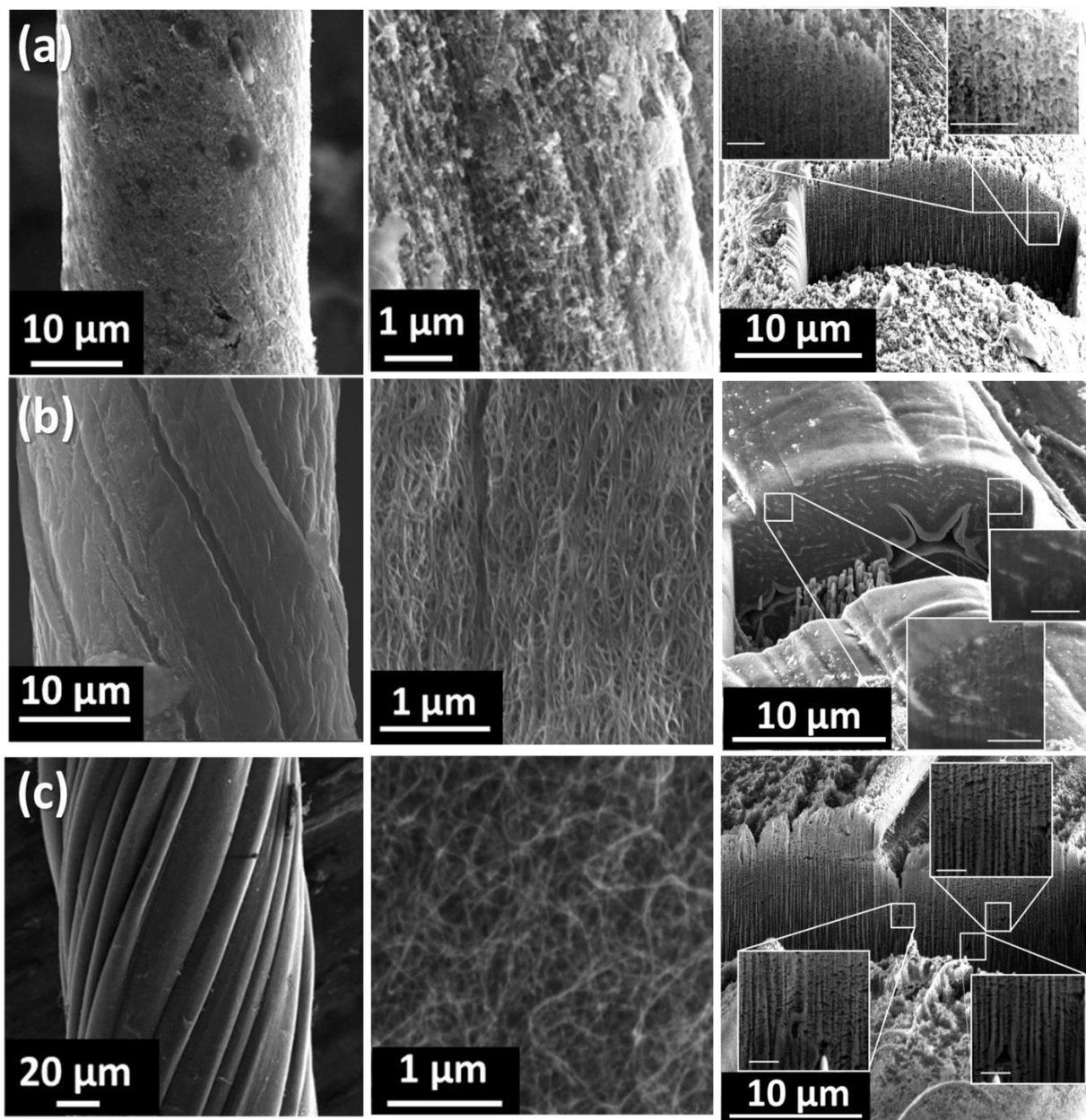
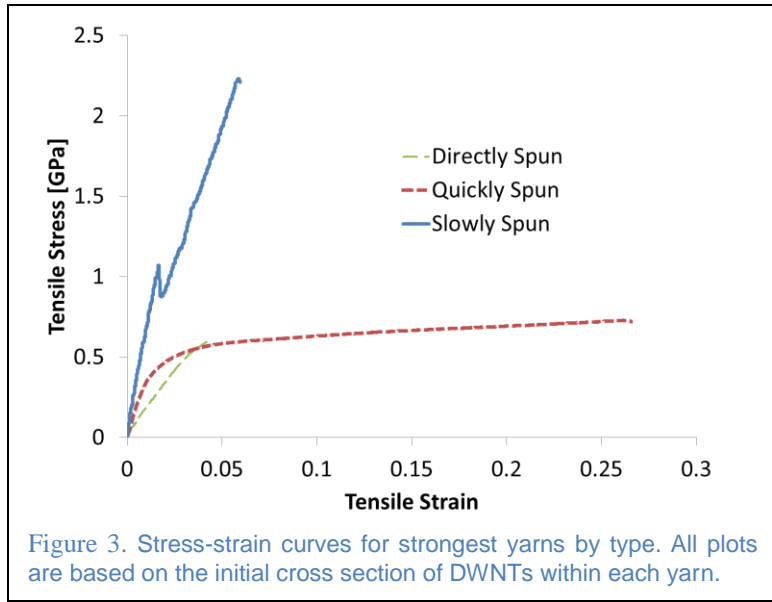


Figure 2. Structural Characterization. SEM images of (a) directly spun, (b) slowly spun, and (c) quickly spun yarns, where the first column shows the yarn morphology, the second shows the arrangement of CNT bundles on the surface of the yarn, and the third column shows wells machined into the yarns using FIB to reveal the internal porosity and morphology of the yarns. Inset scale bars are 1 μm .

Stress-strain curves are presented in Figure 3 for the strongest of each of the three types of yarns. For each yarn, the modulus was calculated as the initial slope of the stress-strain curve, the strength was calculated as the maximum stress value, and the energy to failure was calculated as the area under the force-strain curve, normalized by the linear mass density of the yarn. Modulus and energy to failure are reported in terms of engineering values using the initial cross section of the DWNTs within the yarn, while true strength values are reported in terms of the cross section of the DWNTs in the yarn before failure.

As shown in Figure 3, the stress versus strain behavior for the directly spun yarns was approximately linear to failure. The strain to failure in directly spun yarns was always less than 11%, compared to maximum strains of 27% for quickly spun, and 22% for slowly spun yarns. This supports the previous assertions that the directly spun yarns contain at least a shell of well-aligned CNTs that support the load until failure. The stress-strain curves for the slowly and quickly spun yarns exhibit an initial linear regime followed by a nonlinear response in which the strength continues to increase



with strain. For the quickly spun yarn, the slope of the non-linear regime is low. This large deformation response corresponds to a major rearrangement of the network of misaligned CNTs , which results in much higher failure strains than for the directly spun yarns, in which the aligned CNTs at the surface carries the load until abrupt failure without large CNT network rearrangement. The slowly spun yarns presented, in general, a much stiffer behavior in the non-linear regime, which is consistent with a denser, more aligned CNT structure leading to a more brittle behavior when compared to the quickly spun yarns.

The mechanical properties are summarized in Table 1. The average strengths of the directly, quickly, and slowly spun yarns were found to be 0.24 GPa, 0.55 GPa, and 0.95 GPa, respectively. The average modulus values of the directly, quickly, and slowly spun yarns were found to be 12.1, 27.3, and 79.4 GPa, respectively. Thus, in terms of strength and modulus, the better surface alignment of the directly spun yarns was outweighed by the high porosity and possible internal misalignment. Any misaligned or ineffective CNTs add weight without adding strength to the yarn. The slowly spun yarns had the highest strengths, as they had increased alignment over the quickly spun yarns and they were significantly more compact than the other two types of yarns. We also note that the CNT bundles in the directly spun yarn are $\sim 7 \mu\text{m}$ long, compared to the $\sim 60 \mu\text{m}$ in the slowly and quickly spun yarns, which has been shown to be an important parameter in yarn properties, with longer CNTs resulting in higher properties. Regarding the energy to failure (ETF), a measure typically associated to material toughness, we found that the slowly and quickly spun from mats yarns achieved higher values (18.4 J-g⁻¹, and 40.1 J-g⁻¹, respectively) than the directly spun yarns (5.3 J-g⁻¹) for the reasons previously discussed.

Table 1. Summary of WAXD Results and Mechanical Properties by Yarn Type. (Note that the HOF values with an asterisk correspond to values with waviness.)

	Parameters	Experimental Yarn Type		
		<i>Directly</i>	<i>Quickly</i>	<i>Slowly</i>
WAXD Results	HOF _{avg}	0.325 (0.049*)	0.338	0.346
	HOF _{max}	0.464 (0.072*)	0.390	0.368
	HOF _{min}	0.193 (0.014*)	0.306	0.324
Mechanical Properties	E _{avg} [GPa]	12.1 + 7.3	27.3 + 10.9	79.4 + 44.0
	E _{max} [GPa]	24.8	42.7	208.3
	σ _{avg} [GPa]	0.24 + 0.15	0.55 + 0.11	0.95 + 0.40
	σ _{max} [GPa]	0.626	0.773	2.375
	ETF _{avg} [J-g ⁻¹]	5.3 + 2.9	40.1 + 25.3	18.4 + 15.3
	ETF _{max} [J-g ⁻¹]	9.8	89.6	71.4

In summary, through this work, we have explored the processing-structure-property relationships among yarns fabricated with very different manufacturing techniques, and we have gained valuable insights into how CNT yarns can be improved. The need for processing techniques that yield compact, well-aligned CNT constituents of substantial length is apparent, as we have shown how trends in strength and other mechanical properties vary with these structural features. The results of this study have been submitted to *ACS Nano* for review.

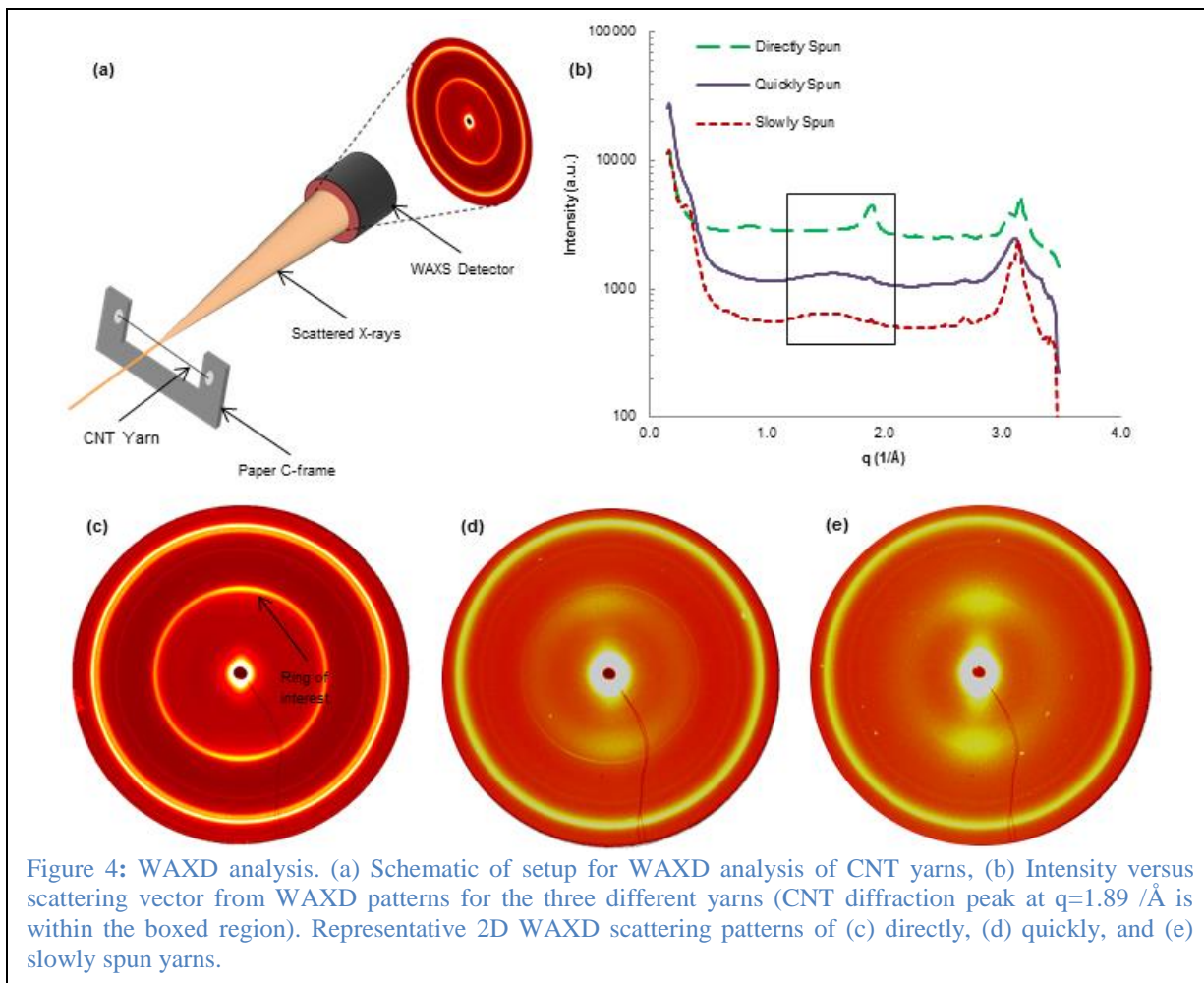
Building on the results of this study, a future area of interest would be to systematically explore the mechanical properties of smaller systems, such as sets of few joined CNT bundles. Probing systems at this size scale would provide several advantages over continued yarn-level studies and provide additional insights. For instance, one of the primary challenges in studying CNT yarns is the vast difference in size scales that can be obtained with simulations versus those that can be used in experiments. Additionally, small sets of bundles would enable investigation of inter-filament interactions and nanoscale failure mechanisms while eliminating the possibility of macroscopic features (such as macroscopic voids) that can dominate over nanoscale deformation mechanisms. Through finer control and processing of sets of pristine bundles, the upper limits of mechanical properties of yarns could be more effectively explored through computations and experiments.

Wide angle X-ray diffraction (WAXD) testing of CNT yarns

Wide angle X-ray diffraction (WAXD) was used to quantify the degree of CNT alignment through the entire cross section of the yarns. The WAXD studies were performed at Argonne National Laboratory's Advanced Photon Source (APS beam line 5ID-B). The synchrotron X-rays were produced with an APS standard undulator A. The beamline's double Si(111) monochromator was set for 17.4 keV (wavelength of 0.71 Å). The WAXD patterns were recorded with a MAR165 CCD X-ray detector, with a sample to detector distance of 19.2 cm and a square spot size of 250 μm defined by collimating slits. In the 2-dimensional diffraction patterns produced by the CNT yarns, a reading at $2\theta = 9.98^\circ$ corresponds to the 002 planes of the CNTs perpendicular to their longitudinal axes, and the azimuthal spread of those reflections indicates how aligned the CNTs are with the yarn axis.

WAXD provides information about the alignment of the CNTs within the yarns through the entire cross section of each yarn. The 2D WAXD scattering patterns of the CNT yarns and their respective 1D data, obtained by summing the intensities along the azimuthal scan and plotted as a function of scattering vector q , are shown in Figure 4. The diffraction peak at a scattering vector of $q = 1.89 \text{ /Å}$, corresponding to the DWCNT internal wall spacing ($d = 3.32 \text{ Å}$), is pronounced for the directly spun yarns, but in the cases of the quickly and the slowly spun yarns, the peaks at this scattering vector are much less pronounced (Figure 4b). Instead there are broad, diffuse peaks around $q = 1.54 \text{ /Å}$,

which could correspond to the spacing between adjacent CNTs within a bundle ($d = 4.08 \text{ \AA}$). Thus, for directly spun yarns in which the diffraction peak is concentrated at $q = 1.89 / \text{\AA}$, we believe that the CNTs in the bundles are in close contact with each other throughout the bundle, and that their inter CNT distance is similar to the DWCNT interlayer spacing. Conversely, in the bundles of the slowly and quickly spun yarns, the CNTs may be convoluted inside the bundle, meaning that they are not in close contact along the length of the bundles, and thus their inter CNT spacing varies throughout the bundle, producing a diffuse and shifted peak at $q = 1.54 / \text{\AA}$.



We note that there is peak broadening in the WAXD studies, as shown in Figure 4, where the full width at half maximum is 0.4 degrees at $2\theta = 9.98^\circ$ in the slowly and quickly spun yarn. Peak broadening in an X-ray diffraction can occur due to several factors, including residual strain in the walls of the CNTs, variations in the crystallite size, and a random distribution of the spacing between CNTs inside bundles [14].

Regarding whether residual strain can explain the peak broadening seen in these studies, the classical equation of peak broadening (Equation (2)) suggests that the radial strain within the CNTs would be 12% if the FWHM of 0.4 degrees was accounted for by this factor alone. However, as this translates to a highly unstable graphitic interlayer distance of 3.6 \AA , the peak broadening cannot be due to residual strains [15].

$$t = 2\varepsilon \tan(\theta_B) \quad (2)$$

where t is peak full width at half maximum (in q space), ε is radial strain and θ_B is the Bragg angle.

In our current study, variations in crystal size correspond to variations in the diameters of CNTs within the bundles. From TEM inspection and previous studies by the co-authors, it is believed that the CNT bundle diameters vary between 10 nm and 30 nm. The Scherrer equation (Equation (3)) indicates that a crystallite size of 10-30 nm can account for peak broadening of 0.12 – 0.36 degrees; thus the peak broadening of 0.4 degrees cannot be attributed to only variations in crystallite sizes.

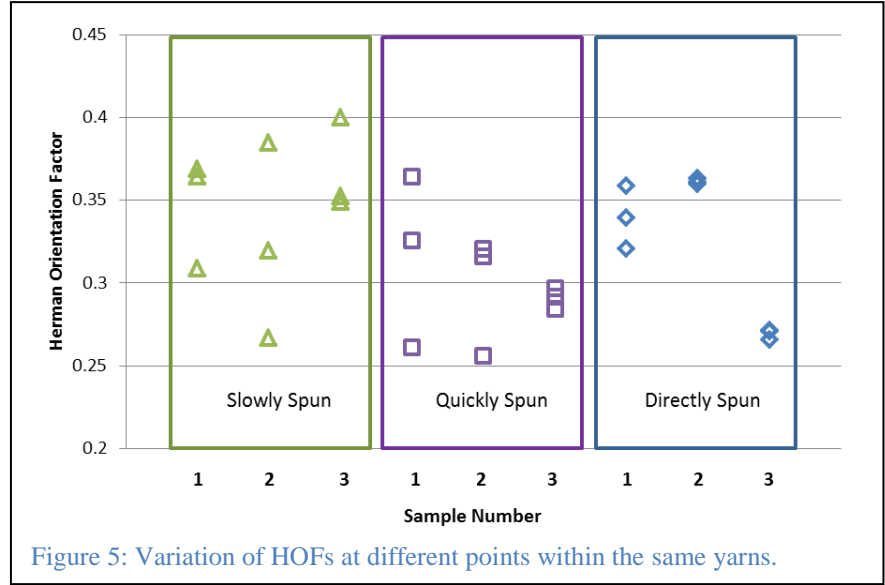


Figure 5: Variation of HOFs at different points within the same yarns.

$$t = 0.9 \lambda / (D \cos(\theta_B)) \quad (3)$$

where λ is the wavelength of the x-ray beam, D is crystallite thickness, and t is in radians. Thus, the final possible explanation for the peak broadening is that there is a random distribution of the spacing between the CNTs within the yarn (except the directly spun samples, where the majority of CNTs inside the bundle are separated by a distance similar to the graphene interlayer distance, seen

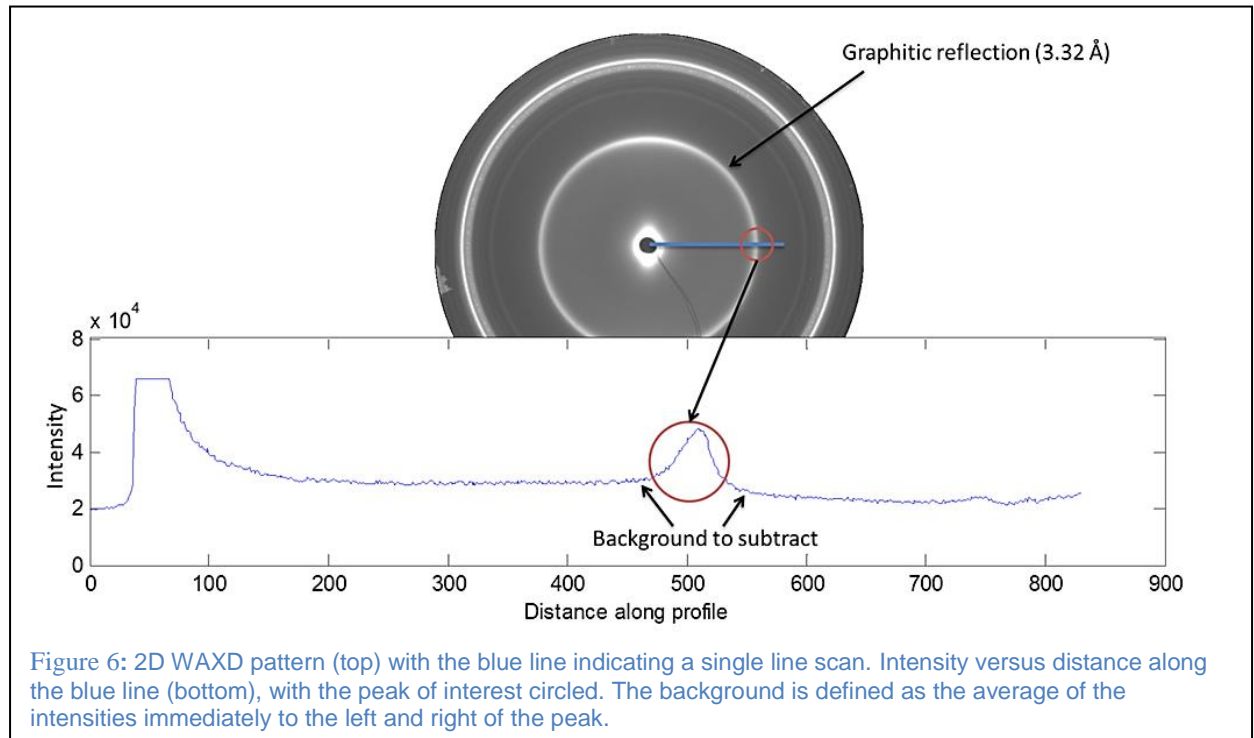


Figure 6: 2D WAXD pattern (top) with the blue line indicating a single line scan. Intensity versus distance along the blue line (bottom), with the peak of interest circled. The background is defined as the average of the intensities immediately to the left and right of the peak.

by the sharp peak at $q = 1.89 \text{ /}\text{\AA}$ ($d = 3.32 \text{ \AA}$) in Figure 4b). This conclusion is further validated by studying the variations of the Herman orientation factor at different points in the same yarn, as shown in Figure 5. For the directly spun samples, the variation of HOF in the same yarn is small, proving the fact that the CNTs are spaced out evenly. We note that the HOF value itself is small in these yarns, due mainly to the large porosity, which results in wavy bundles within the yarn that can skew the HOF value [16]. Conversely, in the slowly and quickly spun samples, the variation of HOF in the same yarn is large, indicating that the CNTs inside the yarn are randomly separated from each other and also possess wavy bundles, yet the HOF values obtained are high. This can be explained by the fact that these yarns are less porous, thus the waviness in the samples does not affect the HOF values significantly [16].

Azimuthal intensity scans were extracted from the 2D WAXD patterns by integrating the intensities of the line scans along the azimuthal ring [17]. The intensities at the q -ranges to the left and right of that of the peak of interest (graphitic reflection $d = 3.32 \text{ \AA}$) are averaged and subtracted from the intensity of each line scan as the background, as shown in Figure 6.

Azimuthal integrated scans of the intensity of the $2\theta = 9.98^\circ$ ring, corresponding to the spacing of the two walls comprising each DWCNT within the bundles, were obtained from each 2D image. To quantify the degree of preferred orientation of the CNTs within the yarns, we calculate the Herman orientation factor (HOF) for each yarn using the following equations:

$$f_H = \frac{2\langle \cos^2 \phi \rangle - 1}{2} \quad (4)$$

$$\langle \cos^2 \phi \rangle = \frac{\int_0^{\frac{\pi}{2}} I(\phi) \cos^2 \phi \sin \phi d\phi}{\int_0^{\frac{\pi}{2}} I(\phi) \sin \phi d\phi} \quad (5)$$

where ϕ is the angle between the axis of interest (CNT axis) and the reference direction (the yarn axis) [18, 19]. For a perfectly aligned sample, the HOF would be 1 and for a yarn where the CNTs are randomly oriented, the HOF would be 0.

For each yarn, WAXD patterns were obtained for three to four points along the length of the yarn. The incident X-ray beam conditions were kept constant for all data points, but the exposure times were varied for each type of yarn (100 s for directly spun, 15 s for quickly spun, and 4 s for slowly spun yarns) to account for the disparate masses of each yarn type. The average values of the HOF across these points were calculated for each yarn and are tabulated in Table 1. The directly spun samples have low HOF values (Average HOF = 0.049) compared to the slowly spun (Average HOF = 0.346) and quickly spun samples (Average HOF 0.338).

We hypothesize that since the directly spun samples are more porous than the slowly and quickly spun samples, the waviness of the CNTs within the samples affect the WAXD results of the directly spun sample significantly. We note that the linear densities of directly spun yarns ($\sim 0.7 \text{ }\mu\text{g/mm}$) are about 3-5 times lower than the quickly ($\sim 1.9 \text{ }\mu\text{g/mm}$) or slowly spun yarns ($\sim 3.4 \text{ }\mu\text{g/mm}$); thus, if a small amount (e.g., $0.1 \text{ }\mu\text{g/mm}$) of wavy CNTs is incorporated into or on the directly, quickly, and slowly spun yarns, that amount will more heavily influence the data for the directly spun yarns.

In order to evaluate and remove the effect of waviness from the WAXD analysis of directly spun samples, a second set of analyses were performed in which the intensities were first integrated over the azimuthal ring, and then the background, taken as the baseline intensity over the entire $2\theta = 9.98^\circ$ ring, was subtracted (Figure 7). Once the effect of waviness is removed with this approach, the HOFs increase significantly (to an average HOF of 0.325 for directly spun yarns), correlating with the previously drawn conclusions from SEM imaging and mechanical testing. Thus, we hypothesize that at least the shell of the directly spun yarns contains well-aligned CNTs, whereas the porous core may contain some misaligned CNTs that do not directly support the tensile load.

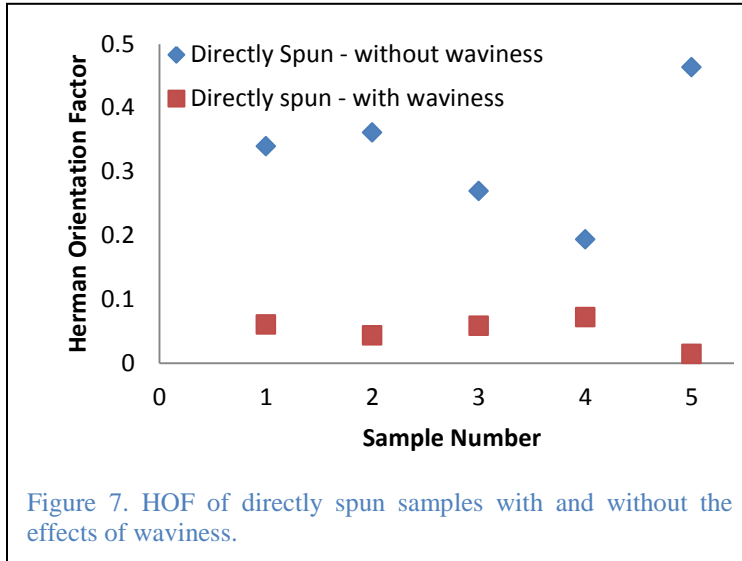
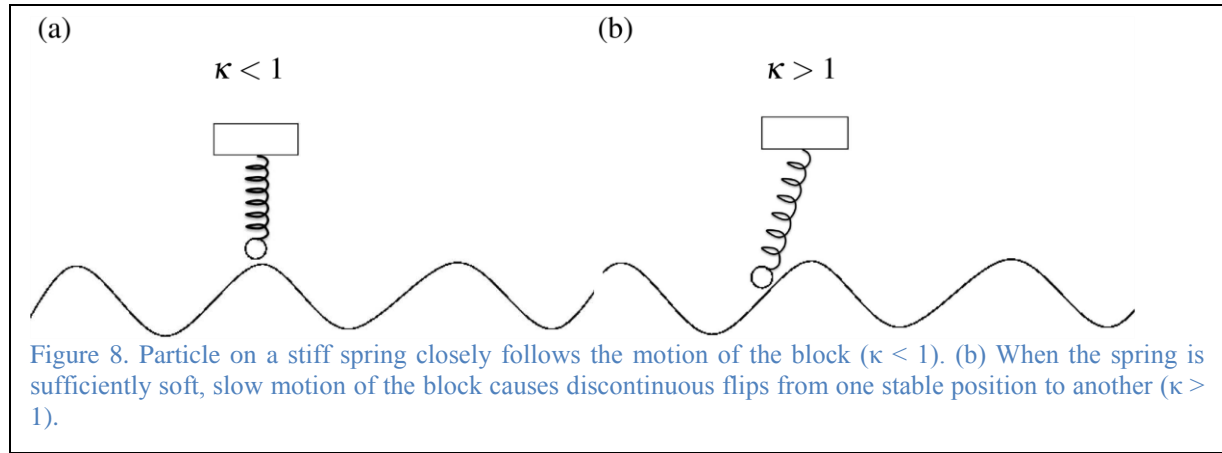


Figure 7. HOF of directly spun samples with and without the effects of waviness.

Understanding shear forces in CNT bundles and yarns

This section describes the continuation of work we started last year to investigate the sources of dissipation in the carbon nanotube pullout experiments of Espinosa et al. In previous work,[8] we identified a number of contributors to the force associated with the withdrawal of an inner bundle of tubes from an outer sheath of tubes. Some of the forces were identified as being due to an increase in the potential energy of the system, while at least half was found to be due to dissipation. A satisfactory explanation as to the details associated with the potential energy was developed, as was an explanation for some of the dissipation, but there was a significant amount of dissipation that was unaccounted for.

Additional studies of the literature led to clues to the possible source of the missing dissipation. We used the empirical force field MM3 to explore the contribution of the corrugation due to the graphitic van der Waals (vdW) registry. This is one of the highest-quality force fields available for this type of problem. However, recent work by Lebedeva et al. suggests that MM3 underestimates the barrier associated the AB stacking arrangement of the graphite vdW registry by a factor of ~ 35 . An underestimate of this barrier could be associated with an underestimate of the force. We confirmed the Lebedeva et al. results. Also, we evaluated the accuracy with which a number of semi-empirical methods predict this barrier. In addition, we performed a detailed density functional theory assessment of the factors that determine shear interactions between carbon nanotubes (CNTs) within bundles, and in related CNT and graphene structures including yarns. This provided an explanation for the shear force measured in the recent experiments [8].



The potential energy barriers separating AB stacked structures were found to be irrelevant to the shear analysis for bundles and yarns due to turbostratic stacking, and as a result, the tube-tube shear strength for pristine CNTs is estimated to be < 0.24 MPa, i.e., extremely small. Instead it is pinning due to the presence of defects and functional groups at the tube ends that primarily cause resistance to shear when bundles are fractured in weak vacuum ($\sim 10^{-5}$ Torr). Such defects and groups are estimated to involve 0.55 eV interaction energies on average, which is much larger than single-atom vacancy defects (approximately 0.039 eV). Furthermore since graphitic materials are stiff, they have large coherence lengths, and this means that push-pull effects result in force cancellation for vacancy and other defects that are internal to the CNTs. Another important factor is the softness of cantilever structures relative to the stiff CNTs in the experiments, as this contributes to elastic instability transitions (see Figure 8) which account for significant dissipation during shear that has been observed. The application of these results to the mechanical behavior of yarns was explored, providing general guidelines for the manufacture of strong yarns composed of CNTs.

A Monte Carlo model for predicting the mechanical strength of fiber yarns

We developed a Monte Carlo model for hierarchical fiber yarns from the understanding of the statistics of individual fiber strength and the shear load transfer between pairs of discrete fibers. Adopting the solution for shear stress distribution from the shear lag model, a new load transfer law was implemented in the Monte Carlo model. Simulations were performed on two types of yarns made of different CNT resources to validate the predictive capability of the model. The key inputs for the Monte Carlo model, that is, the mechanical properties of building blocks (fibers and interfaces) were obtained directly from tensile and shear experiments on fibers at the nanoscale.

For the stochastic Monte Carlo model, a twisted fiber yarn consisting of fibers in a hexagonal close packing structure was assumed (Figure 9). Axial positions of individual fibers are randomly placed to account for a random distribution of overlap lengths. Each fiber is discretized into series of 1D elements along the fiber axis, thus the normal stress in a fiber is uniform in the thickness dimension and only varies as a function of axial positions. A random strength value is assigned to each element to simulate bundle rupture. The strength values are chosen from a probability distribution that ensures that the bundle rupture strengths follow Weibull statistics:

$$P(\sigma) = 1 - \exp \left[-\frac{L_b}{L_0} \left(\frac{\sigma}{\sigma_0} \right)^m \right] \quad (6)$$

where σ is the applied stress, σ_0 is a scale factor, m is the shape parameter, \bar{L} is the bundle length, L_0 is a reference bundle length, and $P(\sigma)$ is the failure probability of the bundle under stress σ .

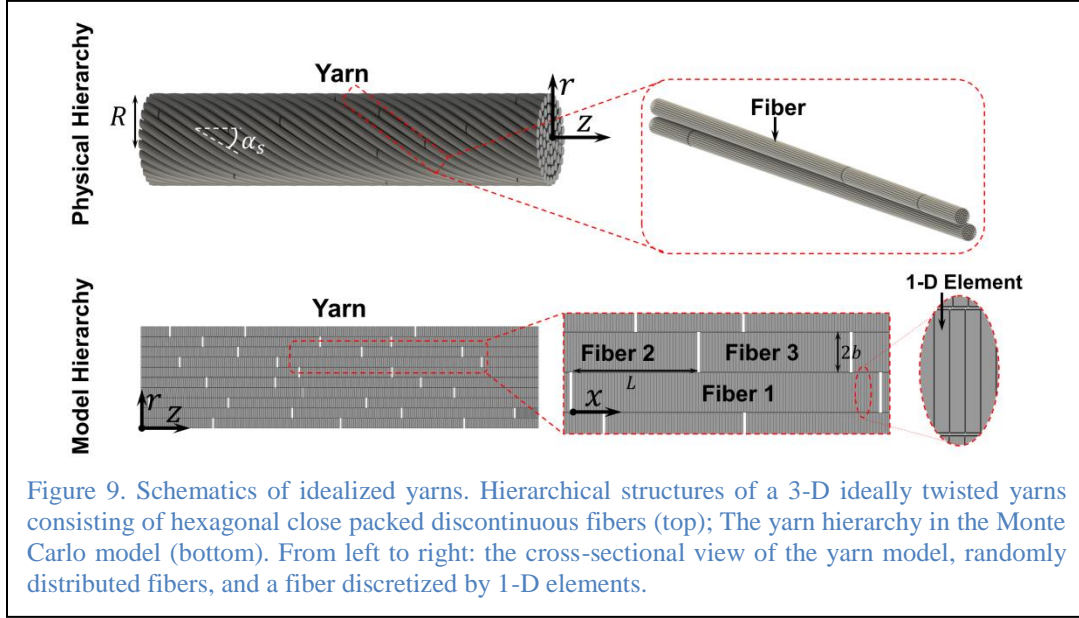


Figure 9. Schematics of idealized yarns. Hierarchical structures of a 3-D ideally twisted yarns consisting of hexagonal close packed discontinuous fibers (top); The yarn hierarchy in the Monte Carlo model (bottom). From left to right: the cross-sectional view of the yarn model, randomly distributed fibers, and a fiber discretized by 1-D elements.

In a twisted yarn, it is necessary to transform fiber strains between the individual fiber axis and yarn axis along which the external load is applied. As pointed by Hearle et al. [20], the relationship between the applied yarn strain ε_y and the fiber strain ε_f at radial position r is given by

$$\varepsilon_f(r) = \varepsilon_y \left(\cos^2 \alpha_r - \nu_T \sin^2 \alpha_r \right), \text{ where } \alpha_r = \tan^{-1} \left(\frac{r}{R} \tan \alpha_s \right) \quad (7)$$

where R is the yarn radius, α_s is the twist angle at the yarn surface, α_r is the twist angle of the fiber at radial position r , and ν_T is the Poisson's ratio of the yarn.

Unlike the static friction law in previous models [21, 22], the load transfer between fibers in the current model is through interfaces that have well-defined mechanical properties, i.e., shear modulus G and shear strength τ_f . It is worth to note that load transfer does not occur within all pairs of adjacent fibers. An algorithm was implemented in the model to discriminate “effective” and “ineffective” contacts between two adjacent fibers based on their relative positions: (1) If a fiber is shorter than the adjacent fiber, and both ends of the first fiber are completely enclosed by the adjacent fiber, the contact is defined as “ineffective,” and the load transfer through this contact is neglected (for example, the contact between fibers 1 and 3 in Figure 9). (2) If one end of a fiber lies between the two ends of the adjacent fiber, the contact is defined as “effective” (for example, the contact between fibers 1 and 2 in Figure 9), meaning that load can be effectively transferred between the two adjacent fibers through their interface. For an “effective” contact, the elastic solution for the shear lag model was used to calculate the maximum tensile stress distribution in each fiber along the overlap region L that can be transferred via the interface:

$$\sigma(x) = \frac{2\tau_f}{b\lambda} \frac{1}{\cosh\left(\frac{\lambda L}{2}\right)} \sinh\left(\frac{\lambda x}{2}\right) \cosh\left(\frac{\lambda(L-x)}{2}\right) \quad (8)$$

where $\lambda = \sqrt{2G/(Ebh)}$, E is the fiber elastic modulus, G is the interface shear modulus, τ_f is the interfacial shear strength, h is the interface thickness, and $2b$ is the equivalent fiber thickness. For fibers with a circular cross section, the equivalent fiber thickness in the shear lag mode is defined as $2b = A/(nw)$, in which A is the cross-sectional area, w is the contact width and n is the total number of effective contacts for a fiber with its nearest-neighbors. Moreover, we note that non-zero porosity in actual yarns will impair the load transfer ability by reducing the effective interactions between fibers. Since load is transferred between adjacent fibers through shear forces, reducing the density of nearest-neighbor fibers leads to a reduction in the load-bearing capacity of the material. We model distributed micro-porosity by decreasing the maximum shear stress between fibers by a multiplication factor of $(1-p)$, for a yarn with porosity p .

The elastic shear lag solution in Equation (8) gives the maximum tensile stress the elements along the overlap distance can carry before the interface slides (i.e. the shear stress at the interface reaches τ_f). On the other hand, the true maximum tensile stress that can be applied on the elements is limited by the fiber strength. This brings another important failure mode – fiber rupture – into the model. CNT strength is extremely sensitive to the inherent defects from manufacturing processes. Experimental studies [23-25] have shown that the CNT strength can be described by a Weibull distribution function expressed in Equation (6) in which the scale factor (the strength at which approximately 63% CNT samples fail) depends on gauge length. Therefore, to take into account the variation in fiber strength and know the initiation and progression of fiber fragmentation, a random strength value needs to be assigned to individual element. According to Equation (6), the element strength values should be picked from a reservoir generated by a Weibull

distribution function with the same shape factor m and a new scale factor of $\sigma_0 \left(\frac{L_0}{L_e}\right)^{1/m}$ in which

L_e is the 1-D element size. Yet, there is an issue of the element size dependence. For example, for an extremely small element size, the scale factor of the Weibull function might be even greater than the theoretical strength of the fiber σ_{th} , which is unphysical. To avoid this issue, a minimum length

scale $L_{\min} = -L_0 \left(\frac{\sigma_0}{\sigma_{th}}\right)^m \log 10^{-2}$ was used to limit the scale factor in the Weibull function that

creates the element strength reservoir. L_{\min} has a physical meaning of the maximum average distance between defects. It assures that only 1% element strength values exceed the theoretical fiber strength, so that the Weibull scaling will not affect the fiber fragmentation progression significantly.

Apparently, the maximum stress an element can carry should be the minimum of these two values – the maximum stress that can be transferred through the interface before sliding, and the assigned element strength. During simulation, an increasing load is applied to the yarn in steps and the stress was distributed on the elements of fibers according to Equation (8). In each step, the distributed stress will be compared with the maximum allowable stress of each element to determine whether interface sliding or fiber rupture occurs. If rupture happens in a fiber, two new fibers will be

created and the stress at the fragmentation location will be set to zero. The model re-evaluates the effectiveness of each new fiber with their nearest-neighbors and redistributes the stress. The iteration stops when no new fiber breaks occur in the current step and equilibrium is satisfied at all cross sections. Then an increasing load will be applied on the yarn in the next step. The yarn is deemed as having failed when no additional load can be supported. It should be noted that a full description of load transfer within a yarn requires solving equilibrium and compatibility at each point simultaneously. In the current model, to reduce computational cost, the load-sharing rules implemented only ensure force equilibrium. The fiber deformation and interface sliding are not solved for. Thus, the model output contains the yarn stress, but no yarn strain.

The goal of this study is to develop a Monte Carlo model from the micro/nanomechanics of building blocks to predict the average value and the dispersion of fiber yarns. Therefore, accuracy of the statistical results has been evaluated carefully. Model results show that the yarn strength distribution approaches a Gaussian distribution function as the simulation times increase. The mean and standard deviation converges for more than 100 simulations. In addition, we found that the model result becomes mesh independent when the element size is less than $0.5\lambda^{-1}$ where $\lambda = \sqrt{2G/(Ebh)}$. In this report, the element size of $0.2\lambda^{-1}$ was used and 100 simulations were performed for each case to obtain the mean and standard deviation of yarn strength.

To demonstrate the model's predictive capabilities, case studies were performed on two types of yarns fabricated from different CNT resources. The first type of yarns were manufactured by dry spinning from double-walled carbon nanotube (DWCNT) mats produced by MER Corp. and characterized at Northwestern University (denoted as "NU yarns") [12]. The second type is the multi-walled carbon nanotube (MWCNT) yarns fabricated using the "wet-spinning" method at Rice University, here termed "Rice yarns" [26].

Figure 10 shows the hierarchy of the NU yarn down to individual fibers (i.e. DWCNT bundles in this case). Each DWCNT bundle consists of tens of hexagonally closed-packed DWCNTs and bundle diameter ranges from 10-30 nm. Individual DWCNTs have an outer diameter of 2.2 nm. X-ray photoelectron spectroscopy (XPS) and Fourier transform infrared (FTIR) spectroscopy characterizations have shown that an inherent polymer coating (approximately 2.5 nm thick) exists on the bundle surface [27]. The mechanical properties of individual DWCNT bundles and bundle-bundle interfaces were characterized through nanoscale experiments and atomistic computations. Weibull analysis on the tensile experimental results reported in our previous studies on individual DWCNT bundles (30 nm diameter and 5 μm length in average) yields a scale factor $\sigma_0 = 2.8$ GPa and a shape factor $m = 2.2$ (see Figure 11a) [7, 12, 27, 28]. It should be noted that the stress here is defined as the load on the bundle divided by the cross-sectional area of all DWCNTs within the bundle. It should be discriminated with the "true stress" that is defined as the load divided by the cross-sectional area of only the DWCNTs on the outer layer of the bundle. The interface properties were obtained from in-situ scanning electron microscope (SEM) shear experiments on pairs of parallel bundles. According to the shear lag model analysis, the applied stress that causes the bundle-bundle junction to slide is a function of the overlap length L :

$$\sigma_{\text{junction}} = \frac{2\tau_f}{b\lambda} \tanh\left(\frac{\lambda L}{2}\right) \quad (9)$$

Fitting the shear experimental [27] results with Equation (9) reveals an effective shear modulus of $G = 10$ MPa and shear strength $\tau_f = 350$ MPa (Figure 11b).

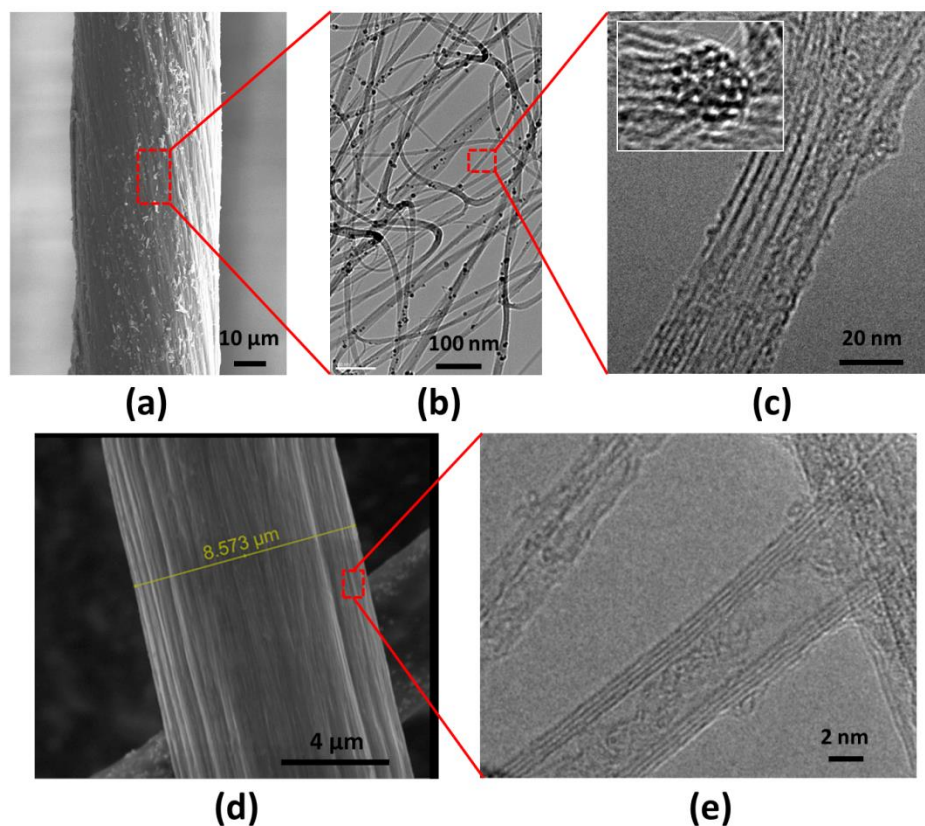


Figure 11. (top) From left to right: Hierarchy of DWCNT yarns studied at Northwestern University. (a) SEM image of a NU yarn. (b) TEM image of interconnected DWCNT bundles picked from mats. (c) TEM image of individual DWCNT bundle. Top inset: cross section of individual bundle. (bottom) From left to right: Hierarchy of MWCNT yarns studied at Rice University (images are adapted from [26]). (d) SEM image of a Rice yarn. (e) TEM image of individual MWCNT.

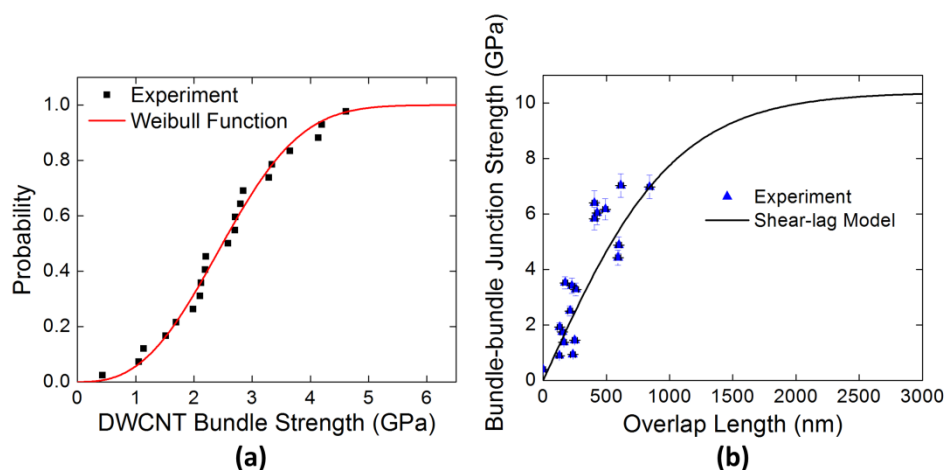


Figure 10. Mechanical properties of building blocks for NU yarns. (a) Weibull analysis on the individual DWCNT bundle strength. (b) Fitting the shear experimental results on pairs of parallel DWCNT bundles using the shear lag model.

In Rice yarns, the constituent fibers are individual MWCNTs with an average length of 5 μm and an average diameter of 3.2 nm. The properties of these MWCNTs have not been studied, and have to be approximated from independent studies. Tensile tests on MWCNTs performed by Yu et al. [29] yield a scale factor of 31.5 GPa (note that the stress in reference [29] was defined by assuming only the outer shell of a MWCNT bears the load) and a shape factor of 2.4. Converting the stress value to an effective stress by accounting for the cross-sectional area of all of the shells, the scale factor for the MWCNTs in Rice yarns is approximated as 14.8 GPa, and the shape factor remains the same. The interface properties between MWCNTs were estimated from the in-situ SEM shear experiments on pairs of parallel bare MWCNTs [9]. Adopted from the results in reference [9], the interfaces between MWCNTs in Rice yarns are assumed to have a shear strength of 60 MPa and a shear stiffness of 100 MPa.

The properties of fibers and interfaces for NU and Rice yarns are summarized in Table 2. The theoretical strength of a 30 nm diameter DWCNT bundles in NU yarns was estimated by assuming that the outer shells of the DWCNTs on the outer layer of the bundle fail at 100 GPa, the theoretical strength of a single shell of CNT [2]. Similarly, the theoretical strength of a MWCNT in Rice yarns was estimated by assuming that the outer shell of the MWCNT fails at 100 GPa.

Table 2 Mechanical properties of fibers and interfaces for NU and Rice yarns.

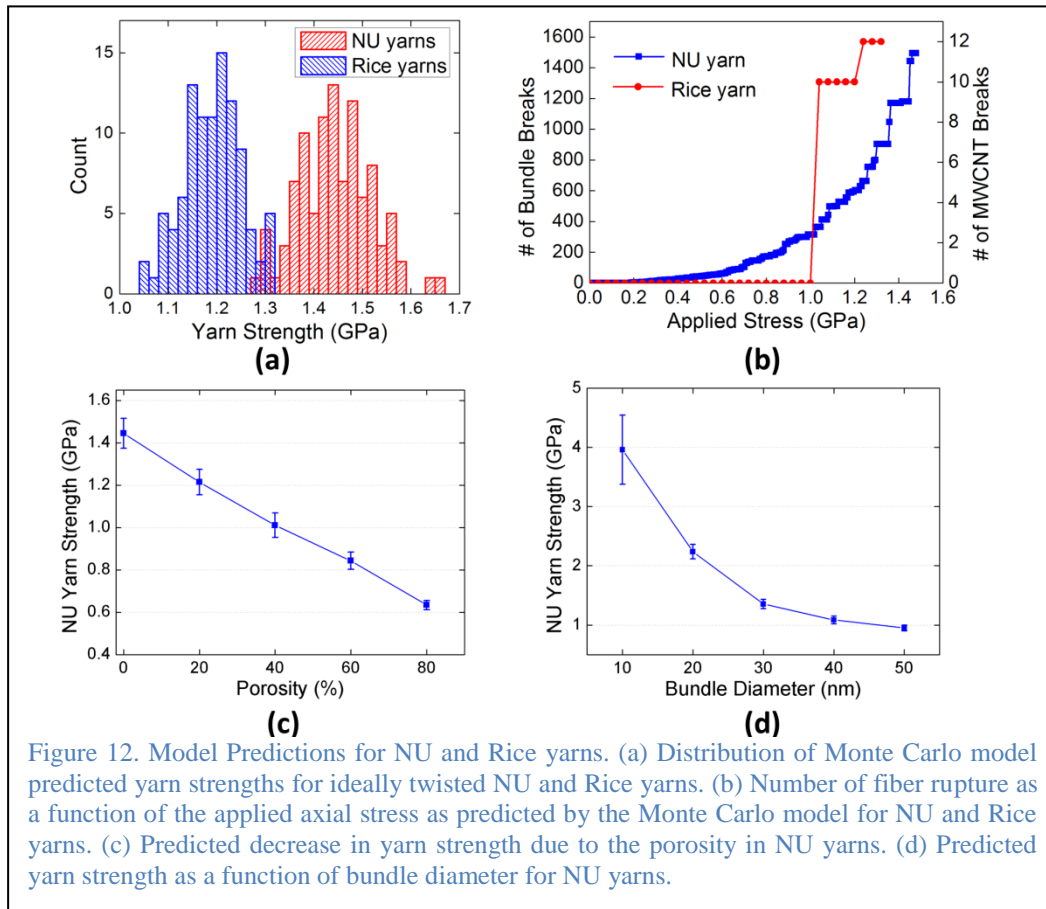
	Fibers	Fiber diameter (nm)	Fiber length, L_b (μm)	E (GPa)	σ_0 (GPa)	m	σ_{th} (GPa)
NU yarns	DWCNT bundles	10-30	≥ 5	60	2.9	2.7	20.2
Rice yarns	MWCNTs	2-6	5	400	14.8	2.4	42.3
	Interface thickness (nm)		Effective interface shear modulus (MPa)		Interface shear strength (MPa)		
NU yarns	2.5		10		350		
Rice yarns	0.34		100		60		

Simulations were performed on both types of yarns. Each yarn in the simulation was composed of 10 fibers along the yarn radius and 4 fibers along the yarn axis, that is, a total of 320 fibers. The dimensions of DWCNT bundles in NU yarns have wide variations. For each system, 100 Monte Carlo simulations were performed, and the average and standard deviation of the yarn strength and standard deviation were calculated from these results.

X-ray and electron microscopy studies on Rice yarns showed 5 μm long MWCNTs aligned nearly perfectly along the axial direction, with no appreciable yarn porosity[26]. Therefore, the actual microstructure in Rice yarns is very close to the idealized yarn structure assumption presented here. However, NU yarns have much more complicated microstructures that feature DWCNT bundle misalignment and entanglement, as well as non-negligible yarn porosity ranging from 50%-80%. In addition, the bundle geometries have noticeable variations. The majority of the bundle diameter is approximately 30 nm, but it can be as small as 10 nm. It is hard to characterize the bundle length distribution precisely, but it is speculated to range from 5 μm up to 60 μm . Apparently, it is impractical to consider all these variations in the model. To provide useful insights to NU yarns design, the model only selectively took into account critical factors. In this study, simulations were performed on NU yarns with ideal helical twisted geometries first to predict an

upper bound of average yarn strength by neglecting the complexity from material preparation (such as bundle misalignment and entanglement). As a baseline, 30 nm bundle diameter and 5 μm bundle length were assumed in the model. Then the model examined the effects of porosity and bundle size on NU yarn strength. As shown in Figure 11b, the load transfer between bundles tends to saturate at an overlap length of 1.5 μm , therefore the 5 μm bundle length assumption in the baseline simulations was appropriate. Simulations performed on 60 μm long bundles did not yield any appreciable difference.

Model predicts the average strength of Rice yarns as 1.2 ± 0.07 GPa. For the ideally twisted NU yarns consisting of 30 nm diameter and 5 μm long bundles, the predicted yarn strength was 1.45 ± 0.07 GPa. Shown in Figure 12a are the distributions of predicted yarn strength for NU and Rice yarns, suggesting for both materials the strength distribution is virtually normal. Even though the predicted strength values for both yarns were similar, the model reveals different dominant failure mechanisms. As shown in Figure 12b, for the ideal NU yarn, the first bundle rupture occurred very early, at a small applied stress of 0.2 GPa, and the rupture rate accelerates gradually until the yarn fails. In the end, a total of approximately 3000 new bundles were generated due to rupture, almost 10 times the number of bundles originally. This suggests that in the idealized NU yarns, the bundle strength is the bottleneck that limits the yarn performance. In contrast, MWCNT rupture in Rice yarn occurred much later, at a high large applied stress of 1.0 GPa, and the total number of ruptured tubes only reached tube rupture number reaches 12 when yarn failure happens occurred due to tube sliding and pull-out. This suggests that the interface strength is the bottleneck that limits the Rice yarns' performance.



As discussed before, the effective shear strength between fibers will be affected by yarn porosity. FIB and SEM characterizations on NU yarns indicate that the porosity ranges from 50%-80% (60% in average). Figure 12c shows that the predicted NU yarn strength drops almost linearly with yarn porosity up to 80%. As the porosity increases, the effective interface shear strength weakens because individual bundles have fewer bundle-bundle contacts. Thus, the dominant failure mechanism becomes interface sliding. For example, the final number of bundle ruptures for 60% porous NU yarns is only 382 at an ultimate stress of 0.84 GPa compared with 1494 for the ideal helical NU yarns at an ultimate stress of 1.45 GPa; thus, more porous yarns result in less effectively accessing the full bundle strengths within the yarns.

Finally, the effect of bundle diameter was examined. As noted by Filleter et al., since the DWCNTs on the outer layer of the bundle carries the load, the effective bundle strength, which is defined by the load divided by all the cross-sectional area of the DWCNTs, highly depends on the bundle diameter. When the bundle diameter reduces, the ratio of the number of external to internal tubes will increase. Therefore, the effective bundle strength will increase. Figure 12d predicts that the average yarn strength could reach 4 GPa if the bundle diameter were reduced to 10 nm.

The model prediction is compared with the experimental measurement in Table 3. The model prediction for Rice yarns (1.2 ± 0.07 GPa) agrees very well with the experimental measurement (1.0 ± 0.2 GPa). For NU yarns with 60% porosity, the predicted yarn strength (0.84 ± 0.04 GPa) also agrees well with the experimental measurement (0.95 ± 0.4 GPa). The model-predicted standard deviations for both materials are larger than the experimental values, especially for NU yarns. This is expected for this simplified model in which complexity such as fiber misalignment, entanglement, and waviness were not considered.

Table 3. Comparison between experimentally measured and model predicted strength for NU yarns and Rice yarns

	Surface twisting angle, α_s	Porosity, $p \varphi$	Experimental yarn strength	Predicted yarn strength
NU yarns	$\sim 15^\circ$	$\sim 60\%$	0.95 ± 0.4 GPa	0.84 ± 0.04 GPa
Rice yarns	$\sim 0^\circ$	$\sim 0\%$	1.0 ± 0.2 GPa	1.2 ± 0.07 GPa

Overall, the model prediction agrees very well with the experimental measurements and provides valuable insights into the future possible approaches that should be explored to improve the yarn strength. However, these approaches are quite different. For NU yarns, the key to improve the strength is to: 1) reduce the yarn porosity (i.e. make yarns more compact); 2) increase the fiber (i.e. DWCNT bundle) strength. In contract, For Rice yarns, the effective way to improve the strength is to improve the interface strength. Likewise, with the mechanical properties of the building blocks characterized using multiscale experiments or computations, this model can be applied to other hierarchical composites to guide the materials design.

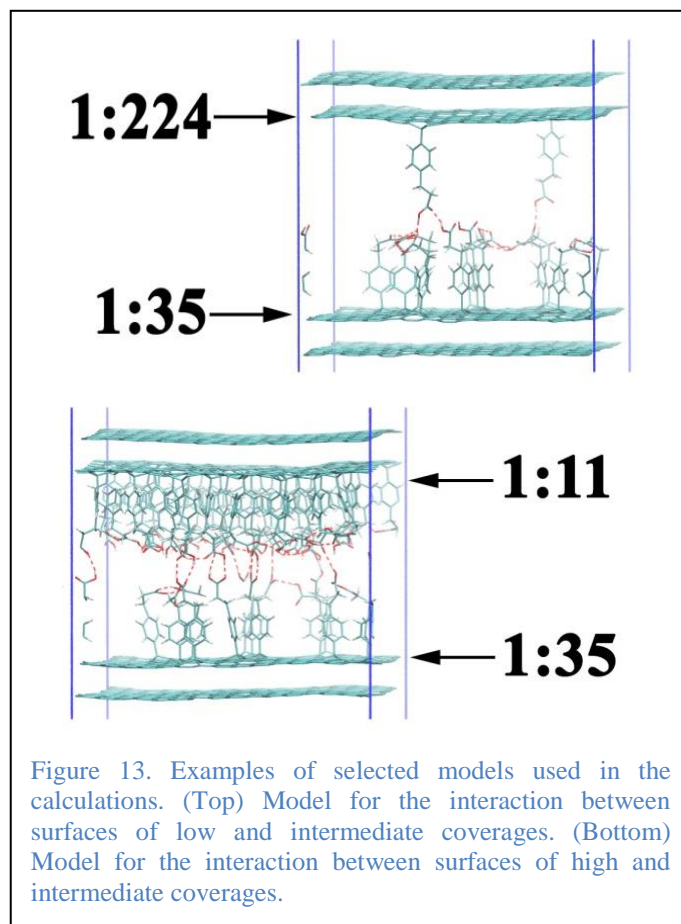
Studies of CNT Surface Impurities and CNT Functionalization

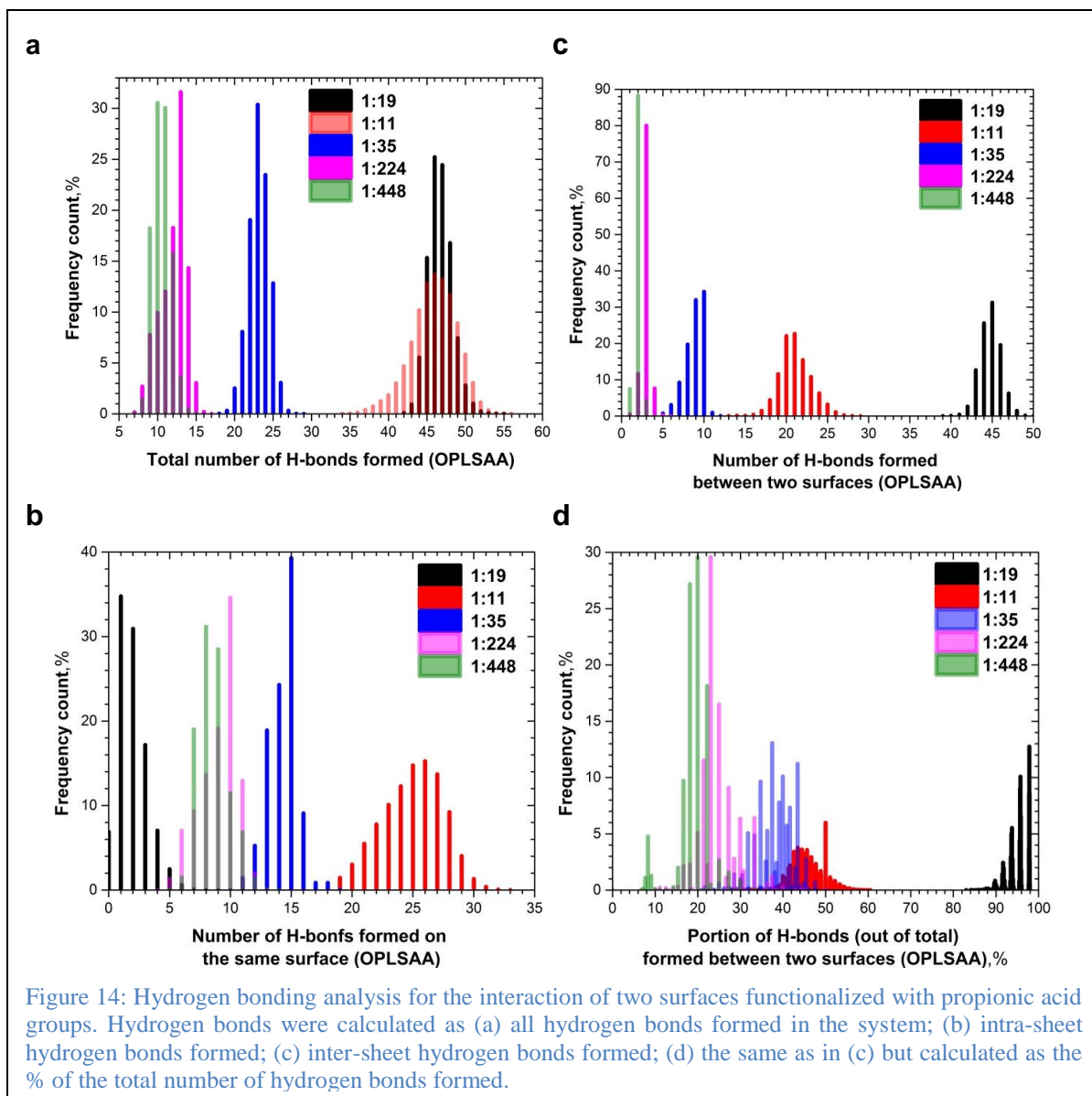
Molecular dynamics simulations of functionalized CNTs

In this section we describe the results of molecular dynamics simulations based on the OPLSAA force field. Our goal is to model the interfacial interactions between two functionalized graphitic materials such as multi-walled CNTs or HOPG. It is hoped that trends observed in our modeling will provide understanding and facilitate the generation of guidelines for the engineering of functional surfaces with predetermined adhesive properties.

Graphene bilayers were used to model each of the two surfaces, with one side of one layer functionalized with propionic acid groups (see Figure 13). For functionalized layers of graphene, a portion of the carbon atoms are sp^3 hybridized and, therefore, the layers become corrugated. We included a pristine graphene layer adjacent to each functionalized layer in order to represent the stabilization effects of the van der Waals forces in experimental multi-layered samples.

We investigated interactions between surfaces with a broad range of functional group coverages. For one set of simulations, we kept functionalization of one surface constant, while coverage of the second surface was varied. The concentration of propionic acid groups on the constant surface was chosen to be an experimentally-determined ratio of 1 functional group per 35 surface-layer graphene carbon atoms. Functional group coverages for the opposing surfaces were set to 1:11, 1:35, 1:224, and 1:448. For a second set of simulations, we used ratios of 1:19 for both surfaces. For all simulations, the graphitic layer was 3x3nm in size, and functional groups were located randomly.





Propionic acid functional groups contain carboxylic acid groups that are capable of forming hydrogen (H) bonds. We found that interactions between these acids are the dominant contributor to the adhesive properties of the surfaces. Adhesion is strong when acids are in contact with acids in functional groups on the opposing surface. Due to the length and flexibility of propionic acid, some interactions between neighboring groups on the same surface occur. When groups undergo intra-sheet interactions, groups are no longer available for interactions with the opposing surface. This leads to a loss of inter-surface interaction activity, and therefore lowers the adhesion between surfaces. We found that an analysis of H bonds is the best way to understand the coverage-adhesion relationships for these surfaces. We observed that higher coverages generated more H bonds in system where two surfaces were in contact.

At high coverage, functional groups are dense and, therefore, have little freedom to make effective H-bond contacts with neighbors on the same surface. The 1:19 on 1:19 case (black histograms in Figure 14) is one such example. Almost all functional groups are available to participate in H

bonding with other functional groups on the respective opposing surfaces. Eighty two to ninety nine percent (black histograms in Figure 14c and d) of available H bonds (black histograms in Figure 14a) form between the surfaces (inter-surface). This occurs despite the randomness of the functionalization patterns. The average separation between functional groups is larger at intermediate versus high coverages. With an increase in separation comes an increase in the probability for formation of intra-sheet H bonds (see the red versus black histograms in Figure 14b and c). Lower coverages (blue, pink and green histograms in Figure 14) mean larger average separations between groups. In these cases the separations are sufficiently large to limit intra-sheet H-bond formation. Brought into contact, such surfaces would also exhibit gaps between groups on opposing surfaces. Intra-sheet H bonding would further limit adhesion.

In peeling tests performed by Espinosa et al., analogous to our simulations, adhesion will be a function of the number of inter-sheet H bonds. Therefore, we conclude that high coverage surfaces are optimal for applications involved peeling (see the experimental data provided by Espinosa et al.). In order to provide qualitative guidance for the experiments, we first simulated interactions as would be present in ultra-high vacuum. Currently we are working on the experimental (10^{-6} Torr) humidity conditions that for such polar surfaces imply the presence of certain amounts of water. Such water molecules as well as the presence of hydrocarbons on the surfaces may alter the trends observed for systems in ultra-high vacuum conditions.

Theoretical estimation of the effect of surface irregularities on the variations in the mechanical performance of arc-discharge MWCNTs

Much of the previous work on the mechanical properties of CNTs is based on a structural model whose surface comprises a perfectly crystalline and smooth layer of graphitic carbon. However, experimentally, we have observed a thin film of randomly distributed, strongly adhered carbonaceous impurities on their surfaces (Figure 15). These surface impurities can potentially alter the interactions between a CNT and its surroundings, resulting in significant variation in mechanical behavior of the CNT-CNT or CNT-matrix interfaces within a nanocomposite. We hypothesized that the effects of these impurities can primarily be observed as scatter within a set of measurements. Indeed, our past experiments measuring the mechanical properties of a single interface between a MWCNT and graphite show scatter in surface energy of 44%, beyond the intrinsic experimental error of the technique. Further evidence is found in the literature in studies of CNTs rolling or sliding on surfaces [30-32], where the lateral force required to induce

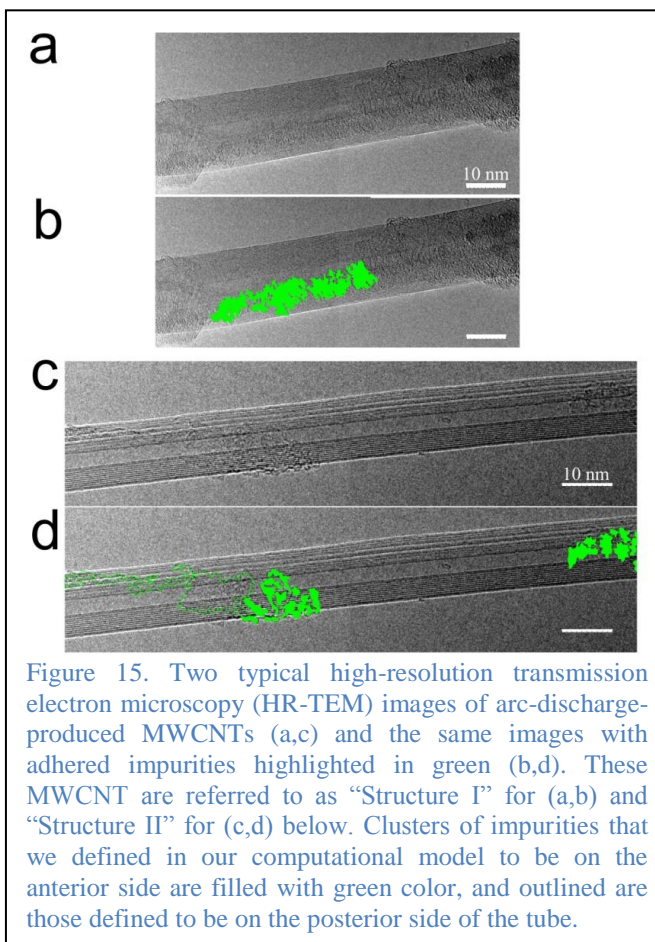


Figure 15. Two typical high-resolution transmission electron microscopy (HR-TEM) images of arc-discharge-produced MWCNTs (a,c) and the same images with adhered impurities highlighted in green (b,d). These MWCNT are referred to as “Structure I” for (a,b) and “Structure II” for (c,d) below. Clusters of impurities that we defined in our computational model to be on the anterior side are filled with green color, and outlined are those defined to be on the posterior side of the tube.

rolling shows periodicity equal to the CNT circumference, and can be correlated to the topographical mapping of adhered impurities on the CNT surface. These force peaks are likely caused by the presence of carbonaceous, surface-bound impurities over which the tube must roll. Similarly, when a single nanotube was placed on and peeled from a surface [33], peaks and dips in force far beyond experimental noise were observed and reproduced at the same location along the tube during both approach and retraction, and can be explained by the presence of impurities located on the nanotube's surface.

As the bottom-up design of an ideal nanocomposite requires a quantitative description of the mechanical behaviors of its interfaces, these observations prompted us to undertake a computational evaluation of the variations in interaction strength between a CNT and a graphitic surface in the presence of a carbonaceous coating and quantify their contributions to the scatter in experimental measurements. We elected to use arc-discharge MWCNTs as a model CNT for consistency with our previous peeling experiments.

Using HR-TEM imaging, we also evaluated the ability of several commonly reported chemical purification techniques to remove carbonaceous impurities from the outer surfaces of arc-discharged MWCNTs. MWCNT were oxidized by hydrothermal treatment, bromination, or nitric acid oxidation, then calcined. Examination of the treated MWCNT by HR-TEM found no removal of the adhered coating, despite removal of larger impurities detectable by SEM (Figure 16). We concluded that the adhered carbonaceous impurities are very chemically similar to the MWCNT itself, and therefore are extremely difficult to selectively removed via known chemical strategies. As such, design and analysis of any CNT-based nanocomposite must take these impurities into account.

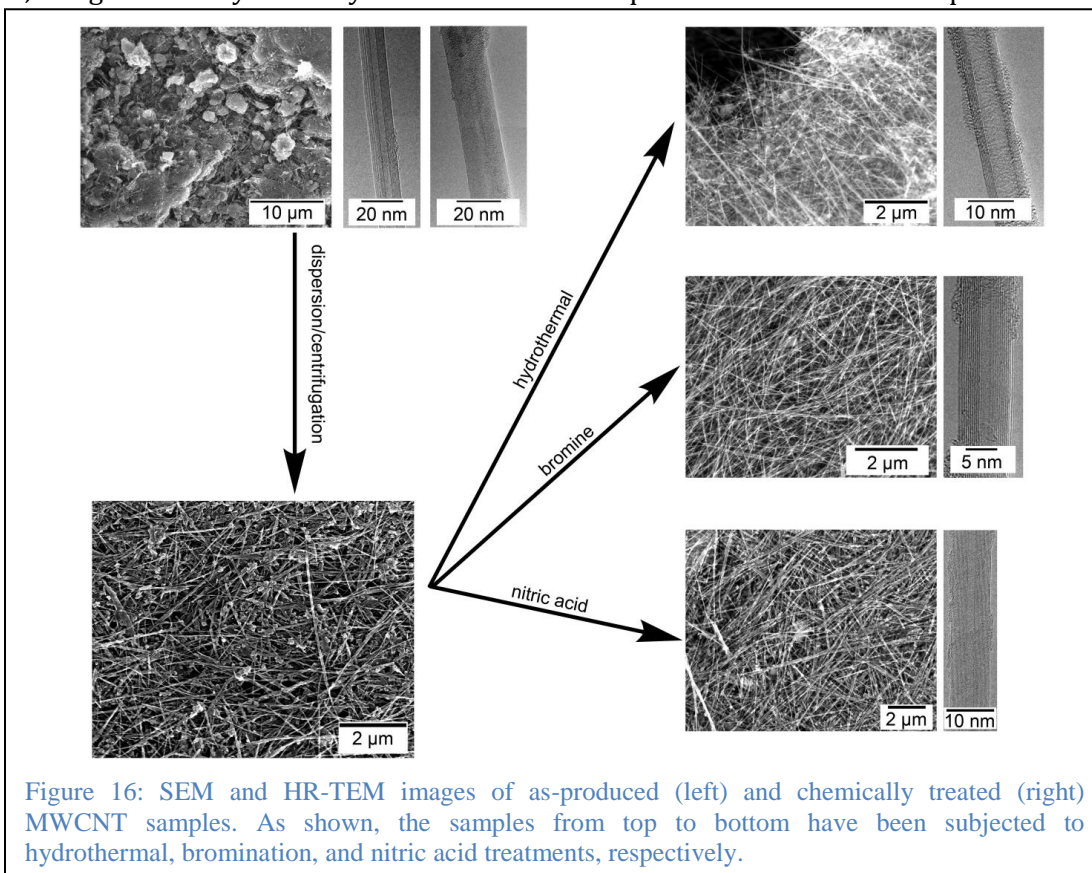


Figure 16: SEM and HR-TEM images of as-produced (left) and chemically treated (right) MWCNT samples. As shown, the samples from top to bottom have been subjected to hydrothermal, bromination, and nitric acid treatments, respectively.

This section describes our hybrid method that combines molecular mechanics calculations and analytical modeling with experimental data. Such combined approaches are crucial for understanding the sources of scatter in adhesion energy values obtained from mechanical tests. In the experiments, CNTs grown using arc-discharge were peeled from graphitic substrates. Careful study of the surfaces of the CNTs revealed irregular carbon formations on the surfaces. Based on XPS, Raman data provided by Nguyen's group, and HR-TEM data from Espinosa's groups, as well as analysis of the arc-discharge production process, we developed models of CNT surface deposits. Evidence suggests these deposits are graphitic in nature, and may resemble wrinkled graphene with some formation of onion-like structures. The latter is the optimal way to minimize the number of dangling bonds in a high vacuum environment.

Benchmark MM3 force field calculations with different models indicated the importance of deposit location as opposed to deposit/impurity structure. Therefore, for the sake of simplicity, all further modeling of carbon impurities was done with hydrogen-capped, hexagonal graphene flakes. The (20,0)@(28,0) double wall carbon nanotube (DWCNT) was chosen as a prototype nanotube as it provides the flexibility/stiffness characteristics observed in the MWCNTs employed in the experiments.

An interaction energy profile (Figure 17) as a function of the angular position, α , of the impurity around the circumference of prototype nanotube was obtained. Analytic equations that describe the relationship were derived, and are given below, where energy is measured in kcal/mol, surface in \AA^2 , and angular position in degrees.

$$f(\alpha) = (E_{\text{int}_{\text{hybrid}}} - E_{\text{int}_{\text{pristine}}}) / \text{Surface}_{\text{deposit}} = (1 - g(\alpha))f_1(\alpha) + g(\alpha)f_2(\alpha) \quad (10)$$

where

$$g(\alpha) = \frac{1}{1 + e^{-\alpha}} \quad (11)$$

$$f_1(\alpha) = -0.1795 + (-0.01686 + 0.1795) \left[\frac{0.10491}{1 + 10^{0.0284(29.70667 - \alpha)}} + \frac{1 - 0.10491}{1 + 10^{-0.0883(106.79462 - \alpha)}} \right] \quad (12)$$

$$f_2(\alpha) = 4.20164 + \frac{-0.16602 - 4.20164}{1 + \left(\frac{\alpha}{142.08976} \right)^{18.62217}} \quad (13)$$

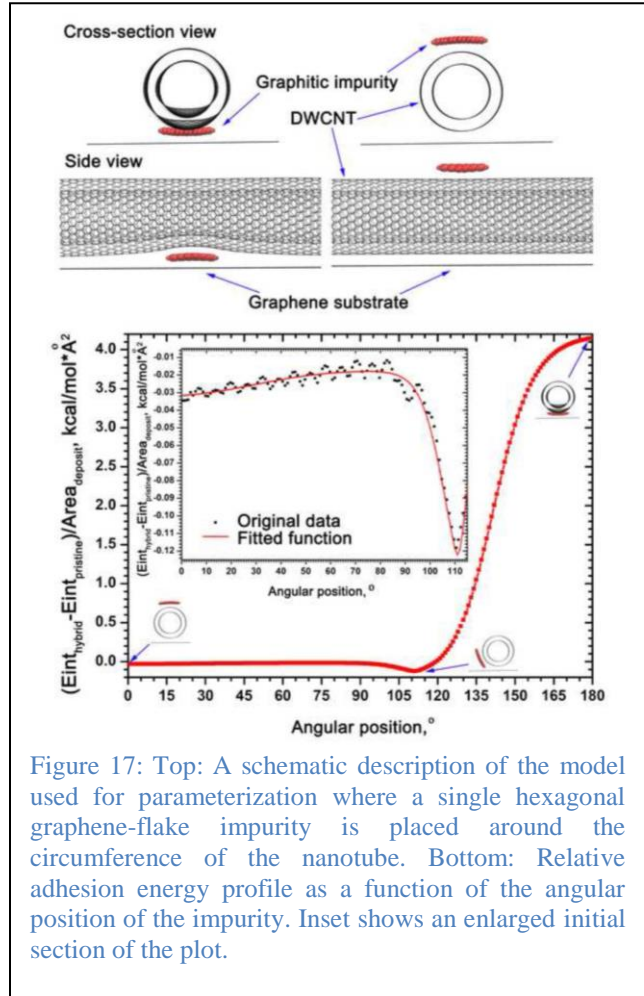


Figure 17: Top: A schematic description of the model used for parameterization where a single hexagonal graphene-flake impurity is placed around the circumference of the nanotube. Bottom: Relative adhesion energy profile as a function of the angular position of the impurity. Inset shows an enlarged initial section of the plot.

$$Eint_{pristine} = U_{DWCNT \text{ on graphene}} - U_{graphene \text{ isolated}} - U_{tube \text{ isolated}} \quad (14)$$

$$Eint_{hybrid} = U_{graphene_tube_flake} - U_{graphene \text{ isolated}} - U_{DWCNT+impurity} \quad (15)$$

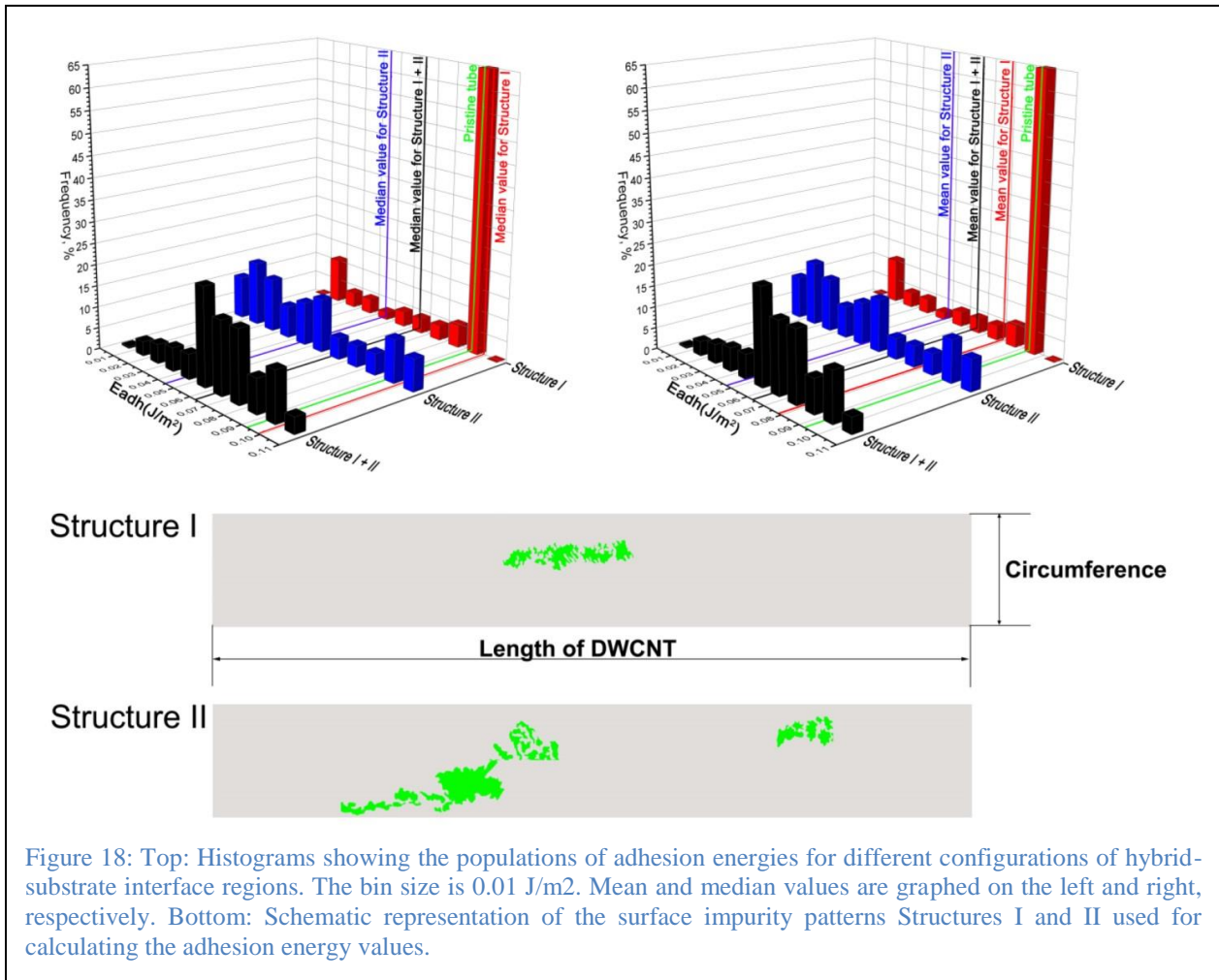
HR-TEM images were used to get the distributions of impurities on the surfaces of the experimental CNTs. Images were transformed into matrix form and then processed in such a way as to give exact pixel-by-pixel planar views of the impurities. Dimensions were rescaled using ratios of the diameters of the experimental and prototype CNTs. Final patterns were used to calculate the effect of impurity location on the adhesion of the CNTs to graphitic substrates according to the equations

$$Eadh_{hybrid} = \left| \frac{Eint_{hybrid}}{Area_{pristine}} \right| \quad (16)$$

and

$$Eint_{hybrid} = Eint_{pristine} + \sum S_i \times f(\alpha_i) \quad (17)$$

where $Eint_{pristine}$ is the interaction energy of the pristine tube and the graphitic substrate, S_i is surface area of a pixel containing impurities, α_i is the angular position of that pixel, and $f(\alpha_i)$ is a function defining the per-surface-area potential energy difference between the hybrid structure and pristine nanotube, based on its angular position.

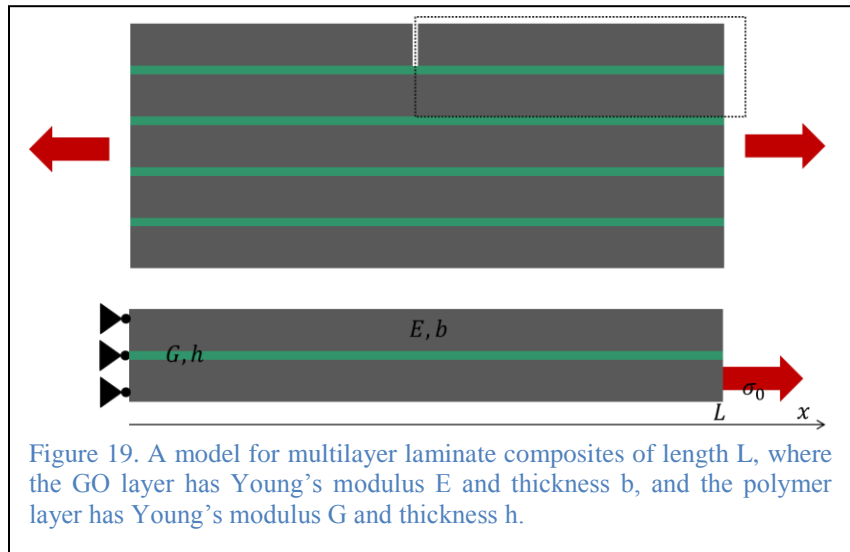


By continuously rotating patterned prototypes along their circumferences, adhesion energies could be obtained specific to the configurations of the interface regions (Figure 18, top panel). Based on HR-TEM images, we modeled localized (Structure I) and delocalized (Structure II) patterns (Figure 18, bottom panel), as well as a combination of both (Structure I+II). After computing all possible configurations of the interface region, we found that localized deposits result in a relatively small scatter in the adhesion energy (standard deviation of 38% and median absolute deviations of 0.38% of the mean/median values) during peeling from a graphene substrate. Due to the large clean CNT surface area in Structure I, the impurity resides far from the interface in many tube-on-substrate configurations, yielding adhesion energies that are similar or only slightly higher than those obtained for a pristine CNT. The scatter in adhesion energy for Structure II is larger (standard deviation of 68% and median absolute deviation 64% of the mean/median values) due to the presence of impurities near the nanotube-substrate interfaces in nearly all configurations. For Structure I + II, the standard deviation (34%) and the median absolute deviation (20%) in measured adhesion energy occurs due to variations in surface-adhered impurities. These values are close to the scatter reported in experimental measurements. It supports our initial conjecture that surface-adhered impurities can significantly alter the properties of the CNTs.

Graphene Oxide Composites

Studies with yarns fabricated from DWCNT bundles suggest that porosity, filament misalignment and overlap length of the constituents are key elements that determine the mechanical performance of the system. In the context of this approach, yarns are then able to provide interesting insight into structure-property relationships that seemingly dominate in carbon-based nanomaterials. Nevertheless, there is a clear need for strong, lightweight composites capable of providing superior mechanical properties based on tunable building blocks. Motivated by this, graphene was originally envisioned as a potential building block for composite materials. Graphene possesses incredible mechanical properties [34] and studies have reported the potential for the material to be functionalized [35]. Nevertheless, various reports show that neighboring sheets of pristine graphene can slide easily due to weak van der Waals interactions that bind them together [36]. This, in turn, leads to an extremely low intersheet shear modulus which hinders successful fabrication of nanocomposite materials [37].

Recently, and due to the observations made during studies with graphene, graphene oxide has acquired significant impetus for application in the design of nanocomposite materials. Due to the intrinsic functional groups that are located in the graphitic backbone of the material, it is expected that additional interactions will be introduced leading to enhanced intersheet properties. In this regard, graphene oxide should show



enhancement as a building block over graphene. Furthermore, the mechanical properties of graphene oxide are promising [38]. With this in mind, and based on the methodology of the existing MURI, we have studied theoretically and experimentally graphene oxide systems to assess the feasibility of designing graphene oxide-based nanocomposites showing superior mechanical performance based on fully tailorable building blocks.

A shear-lag model for predicting transition of fracture modes for GO-polymer composites

In this model (Figure 19), a multilayer laminate consisting of stiff, continuous graphene oxide (GO) layers separated by thin polymer layers is constrained on the left, while put under a tensile load towards the right. A small crack is introduced in the top layer, and the model predicts how the crack will propagate through the thickness of the material based on the dimensions and properties of the components. The shear stress in the polymer layer is given by:

$$\tau(x) = \frac{\sigma b \lambda}{2\alpha} \frac{\sinh(\lambda x)}{\cosh(\lambda L)} \quad (18)$$

where $\lambda = \sqrt{\frac{2G}{Ehb}}$ and $\alpha = \frac{\max(\sigma(x=L,y))}{\text{average}(\sigma(x=L,y))} \approx 3$ is the stress concentration factor.

The maximum shear stress is therefore given by

$$\tau_{max} = \frac{\sigma b \lambda}{2\alpha} \tanh(\lambda L) \quad (19)$$

as $L \rightarrow \infty$ for a film that's much longer than its thickness, we get $\tau_{max} = \frac{\sigma b \lambda}{2\alpha}$. Under tensile load, the interface between GO layers formed by the polymer will delaminate if the shear stress τ_{max} exceeds the polymer's shear strength (τ_f) prior to the applied stress σ exceeding the tensile strength of the GO layer (σ_f). This delamination leads to the crack moving along the interface, resulting in crack deflection/shielding. On the other hand, if the GO layer breaks prior to the interface, then the crack will extend directly through the next GO layer, leading to no crack deflection/shielding. We can write the following inequalities to describe this condition:

Crack shielding occurs if

$$\tau_f < \frac{\sigma_f b \lambda}{2\alpha} \quad (20)$$

or

$$h < \frac{\sigma_f^2}{\alpha^2 \tau_f^2} \frac{Gb}{2E}. \quad (21)$$

Otherwise, crack shielding will not occur.

Therefore, this model predicts a critical polymer thickness h for constant GO layer properties and dimensions and polymer type. For polymer layer thicknesses less than h , there is crack shielding, and the fracture surface should show a terraced morphology with steps at the interfaces. For polymer thickness greater than h , there is no crack shielding and the fracture surface should be smooth as it is in unmodified GO composite films. While it's possible to rearrange the equations (20) and (21) to isolate the other parameters for critical values, we chose to use h because it is the easiest to tune experimentally.

The model was applied to predict the failure mode transition for multilayer laminated GO-PMMA composites. $E = 40 \text{ GPa}$ and $\sigma_f = 400 \text{ MPa}$ were taken from the mechanical measurements of pure

GO paper. The thickness of each GO layer in the composites was kept as 380 nm. The shear modulus and shear strength of PMMA were taken as $G = 0.75 \text{ GPa}$ and $\tau_f = 40 \text{ MPa}$ [39]. The stress intensity factor was taken as $\alpha = 3$. With these inputs, the critical PMMA thickness $h_c = 40 \text{ nm}$ is predicted by the model. When the PMMA layer thickness decreases toward the critical thickness, the fracture propagation in the laminated GO-PMMA composites becomes difficult. Therefore, at the critical thickness h_c , the mechanical property of the laminated composites should be enhanced. This prediction agrees very well with the experimental observation in which the mechanical strength of GO-PMMA composites was greatly enhanced at PMMA thickness of 36 nm [40].

To assess the generality of the model to different polymers and/or dimensions of constituents, various cases were designed and analyzed through the use of the above shown relationships. GO-PMMA composites were again fabricated, this time varying the building block dimensions. Additionally, GO-Polystyrene composites were designed and tested. Because of its properties, $G \approx 40 \text{ GPa}$ and $\tau_f \approx 40 \text{ MPa}$, it can be expected that GO-Polystyrene composites will lead to enhanced properties and improved composite materials. Figure 20 shows the combined results from our tests, which clearly show that the model is adequate independently of the building block or composite dimensions utilized in the nanoscale. This leads to the potential for utilizing these equations in the design of thin-film based composites that may have high-performance mechanical applications in the future.

Parallel to these studies, the Espinosa and Nguyen groups also analyzed the possibility of mixing polymer and GO platelets within each building block film. For this application, (poly)vinyl alcohol (PVA) was selected. Due to its amphiprotic behavior, PVA is able to interact with both oxidized and graphitic domains in GO. Thus, it is expected that these higher interactions will lead to better overall performance from composites constructed from these mixed GO-PVA films. The next section focuses on discussing the mechanical properties of these composites in the context of loading ratios and hierarchical structures, for which this model is not apt at predicting behavior of the material.

Graphene oxide and polyvinyl alcohol (PVA) composites

In addition to the studies of other GO-polymer composites, we also investigated the mechanical performance of multilayer films composed of graphene oxide and polyvinyl alcohol (PVA). Recently, a theoretical study by Fratzl and coworkers suggested that sharp fluctuations in modulus within a multilayer composite material could lead to crack deflection which, in turn, improves the material toughness [41]. This type of structural design is also reflected in natural materials such as nacre. Nacre effectively bridges the strong but brittle abalone shell with thin layers of soft polymer, leading to significantly

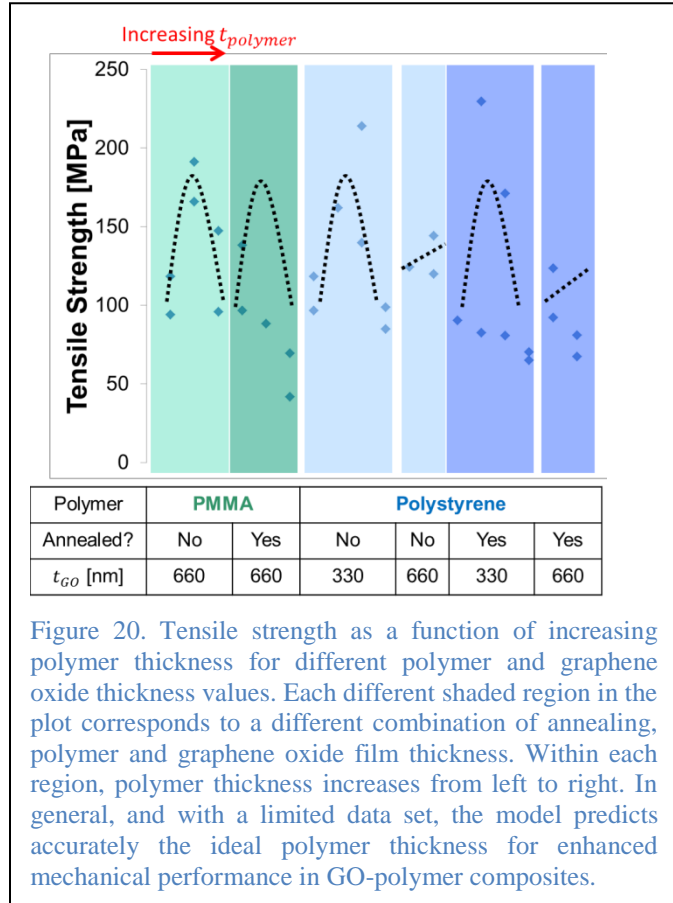


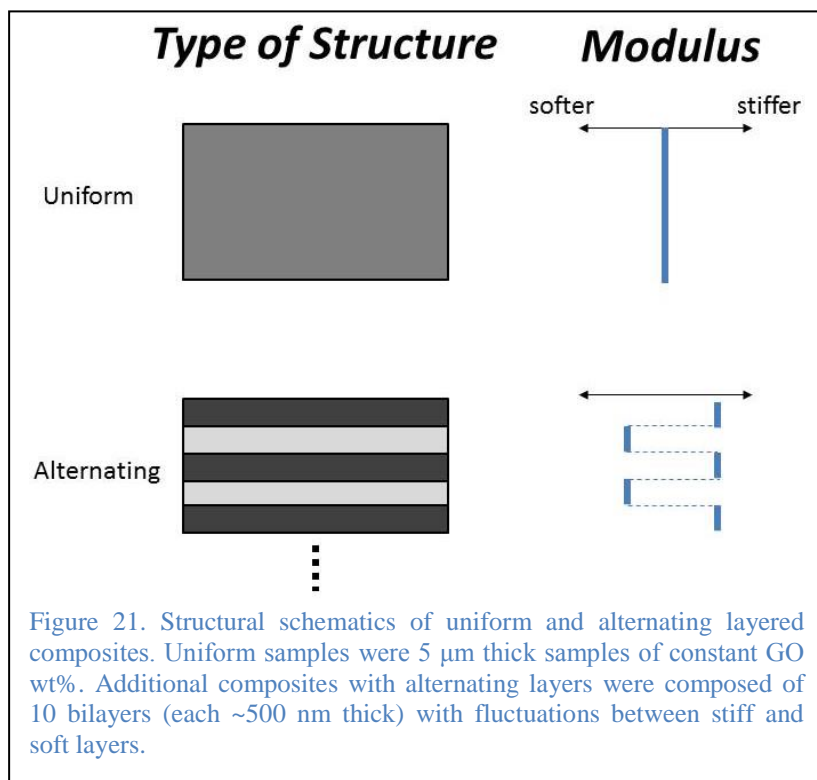
Figure 20. Tensile strength as a function of increasing polymer thickness for different polymer and graphene oxide thickness values. Each different shaded region in the plot corresponds to a different combination of annealing, polymer and graphene oxide film thickness. Within each region, polymer thickness increases from left to right. In general, and with a limited data set, the model predicts accurately the ideal polymer thickness for enhanced mechanical performance in GO-polymer composites.

higher toughness than the abalone shell alone [42]. Our previous work also demonstrated improved mechanical performance upon optimal inclusion of PMMA thickness [40]. Here, we aimed to incorporate polyvinyl alcohol due to two unique advantages it has over other polymers: i) it acts as both a hydrogen bond donor and acceptor, which should enable strong interactions with graphene oxide; ii) it can be mixed with graphene oxide in varying concentrations to allow variations in modulus of different layers.

GO/PVA composites were prepared using layer-by-layer assembly via spin coating. All composites were prepared with a thickness of roughly 5 microns, as estimated from ellipsometry and verified from SEM imaging of post-mortem fracture surfaces. This thickness was selected as a compromise between processing and handling requirements. The processing method becomes prohibitively time-intensive for larger thicknesses, but smaller thicknesses become difficult to manipulate for tensile testing. Subject to this constraint, two types of structures (Figure 21) were created:

- Uniform structures. A homogeneous structure of a given weight % of graphene oxide mixed within PVA. Mixtures of 0.5, 1, 5, 10, 20, 50, and 75 wt% GO were prepared.
- Alternating structures. Each film was composed of 10 bilayers of brittle, high weight % GO-PVA and soft, low weight % GO-PVA. Bilayers thickness was maintained constant (~500 nm). The bilayer systems explored were composed of bilayers with 50/0.5 wt% GO, 20/0.5 wt% GO, and 10/1 wt% GO.

Uniform structures were developed to assess the mechanical properties of “constituent” layers that would then be used within the alternating structures. In addition, with a global 5 wt% GO concentration applied to all alternating structures, the 5 wt% uniform structure was intended to serve as a baseline for comparison. As this uniform structure contained no fluctuation in modulus, it was expected that the alternating structures would exhibit higher strength by taking advantage of crack deflection.



Quasistatic tensile tests were conducted using a Fullam microtensile testing device as outlined in our previous publication [13]. All samples were kept in dry conditions (~20% humidity) overnight. After each sample was mounted in the tensile tester within the humidity control chamber, the sample was maintained at constant humidity (~20-25%) for at least 5 minutes prior to testing. Applied loads and displacements were recorded and converted to engineering stress-strain curves based on sample geometry.

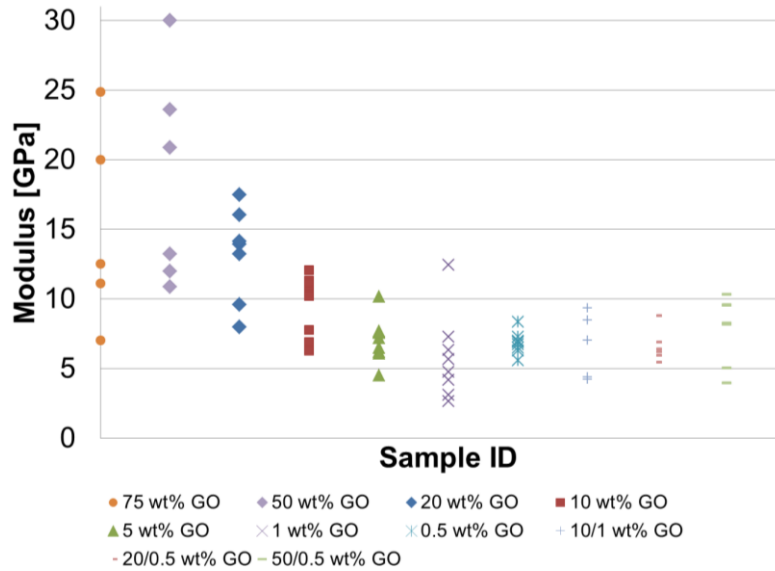


Figure 22: Elastic modulus for all sample types. As expected, samples with higher GO concentrations exhibited higher stiffness. Alternating structures (right most 3 sets) had similar elastic moduli to uniform samples with low GO concentration.

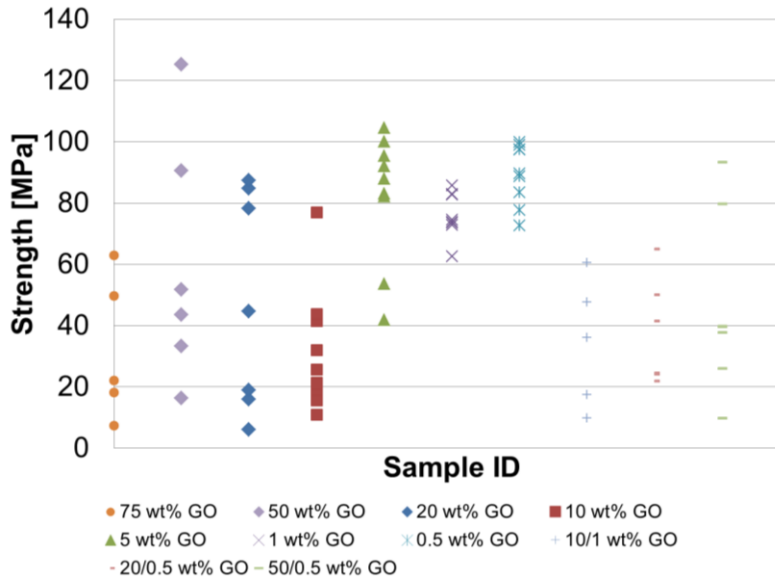


Figure 23. Tensile strengths for all sample types. Alternating layered samples (rightmost three sets) did not exhibit higher strength than uniform samples.

The elastic moduli of uniform samples (Figure 22), in general, followed the expected trend: samples with greater concentrations of brittle graphene oxide were stiffer than those with lower GO concentrations. The highest stiffness for any sample was obtained with 50 wt% GO (~30 GPa), which is approximately four to five times stiffer than the softest uniform samples. This fluctuation in stiffness is close to the difference that Fratzl and coworkers [41] predicted was required for crack deflection. Consequently, bilayer samples that exhibited a sharp change in modulus (50/0.5 wt%) were to be compared with other bilayer samples that did not have such a sharp change (20/0.5 wt% and 10/1 wt%). It is worth noting that these bilayer samples, shown at the right in (Figure 21), exhibited similar elastic moduli to uniform samples with low GO concentration. However, as crack deflection is more closely related to strength than elastic modulus (which is a measure of initial loading conditions well before failure), this value is not the primary metric of interest for comparison with uniform samples.

The tensile strength values reported in Figure 23 are divided into uniform (left) and alternating (right) sets. While the elastic modulus increased with GO concentration for uniform samples, as expected, the strength did not follow such a trend. While the single strongest sample contained 50 wt% GO, in general, samples with 5 wt% GO, 1 wt% GO, and 0.5 wt% GO were stronger than their more brittle counterparts. (This is further supported by the samples with the highest GO concentration, 75 wt%, which consistently exhibited low strength.) This result suggests that samples with alternating layers would not mimic the structure of nacre. While nacre combines strong, brittle ceramic platelets with weak, flexible polymer, the brittle components investigated here were actually weaker than their ductile counterparts. As such, it would be expected that composites consisting of alternating brittle and ductile layers with varying GO concentrations would behave differently than nacre.

Building on this point, it is worthwhile to note that the tensile strengths obtained for the composites with alternating layers were not as expected. Figure 23 shows no clear trend in strength among the three types of alternating-layer composites. While theoretical studies [41] suggested that the samples with sharp variations in modulus (e.g. 50/0.5 wt%) might perform better than those with smaller variations in modulus (e.g. 10/1 wt%), this was not consistently observed in these samples. Furthermore, these samples (with net 5 wt% GO) typically exhibited lower strength than the uniform 5 wt% GO samples, which have constant stiffness across the cross section. In addition to the low strength values, examinations of fracture surfaces within an SEM revealed that none of the samples exhibited crack deflection or “terracing” between different layers. As the mechanisms and performance predicted by theory do not translate into these composite systems, there must be many structural and processing complexities in the composites that prevent variations in modulus alone from yielding improved mechanical performance.

In order to use the results of this study to guide future design of GO-based composites, there are several difficulties with the materials and systems that merit further discussion. First, it is important to note that each of the graphene oxide layers is composed of small, inhomogeneous flakes. The interfaces between these flakes could serve as stress concentration points that lead to cracks in various locations along the sample. As the inhomogeneous nature of the material prevents cracks from being selectively placed, it is difficult to apply classical fracture theory to this system. Attempts at introducing cracks along the top and side with multiple techniques (e.g. nanoindentation and sharp razor cuts) were unable to achieve this, either, as the small dimensions of the material (~5 μm thick) dictated by processing conditions are not conducive to the introduction of small, sharp cracks. Consequently, the capabilities of introducing cracks into this system are far from ideal and are likely affected by inhomogeneous features throughout the sample.

In addition to the complications associated with flake-flake interfaces, it is also difficult to establish the properties of the flake-polymer interfaces as well as the properties of the thin polymers that comprise the composites. Characterization of polymers and polymer-fiber interactions within nanoscale systems can be very challenging both experimentally and computationally [10, 43]. Assuming bulk properties may not be appropriate, as polymers have been shown to be sensitive to size effects [44]. Furthermore, changes in polymer thickness within a given layer, as well as variations in porosity within individual layers and among different layers, may complicate the interactions even further. To address this issue, additional work needs to be done in characterizing nanoscale GO-polymer interfaces as well as thin layers of polymers. At the same time, additional processing techniques must be developed to improve the uniformity of different layers.

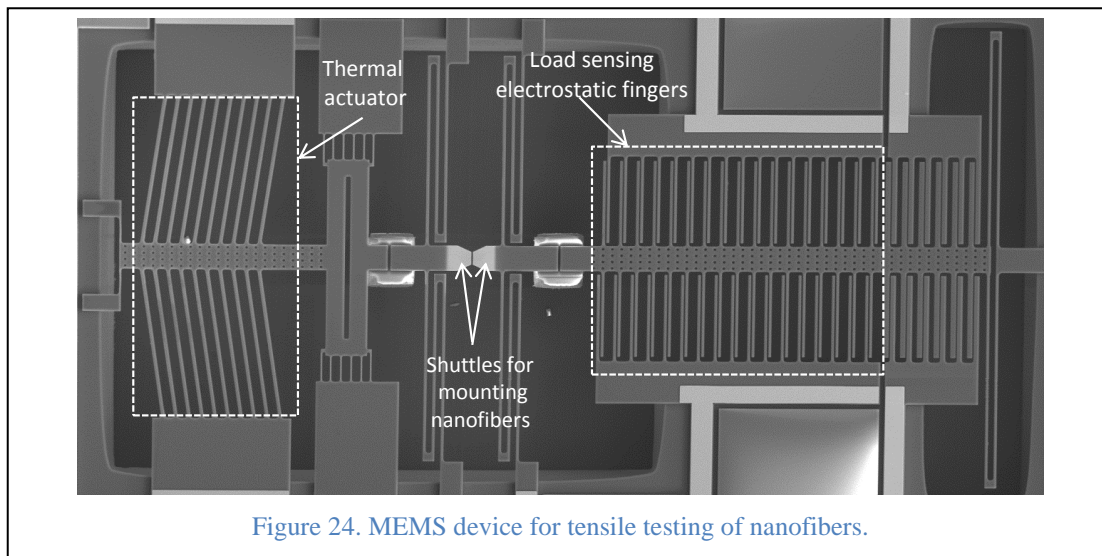
Ultimately, GO-polymer composites are extremely complicated systems that require a significant amount of future research. While further development and characterization at the composite level is one possible (and active) route, there are still many fundamental properties and behaviors to be explored among the nanoscale constituents of these materials. The effects of different processing conditions, humidity, porosity, interfaces, and constituent properties are just some components of these systems that could serve as new areas for future research.

Fabrication/Characterization/Modeling of CNT-Polymer and Electrospun Nano-Filaments and Yarns

In situ electron microscopy tensile testing of constrained and unconstrained carbon nanofibers

The carbon nanofibers tested in this study were manufactured by the Dzenis group through an electrospinning process elaborated elsewhere [28]. Polyacrylonitrile (PAN) nanofibers were produced using electrospinning at 12kV with a 0.6ml/hr feed rate, a 20 ga needle, and a spinneret-collector distance of 20 cm. The nanofibers were subsequently stabilized in an oxygen atmosphere at 270°C for 1hr. These nanofibers were then carbonized under constraint at 800°C in nitrogen at a heating rate of 10°C/min and dwell time of 1 hr, to convert them to constrained carbon nanofibers (CCNFs). The reason for the constraint was to obtain better molecular orientation, which was expected to translate to higher mechanical properties, namely strength and stiffness.

CCNFs were tested by the Espinosa group using a microelectromechanical system (MEMS) tensile testing device and in situ transmission and scanning electron microscopy (TEM and SEM). The



MEMS device, as shown in Figure 24, consists of V-shaped thermal actuator beams, shuttles across which nanofibers are mounted, and load sensing electrostatic fingers. A 600 mesh TEM grid was cut in half, and then gently scraped over the electrospun and carbonized CCNFs mats to transfer some of the CCNFs onto the half grid[12]. This grid was placed inside an SEM (FEI NovaSEM 800) chamber along with a Klocke nanomanipulator, which controls a sharp tungsten tip with nanometer resolution, and the MEMS device. Using the tungsten tip attached to the nanomanipulator the CCNFs were manipulated from the grid onto the shuttles of the MEMS device. The CCNFs were clamped onto the shuttles using electron beam induced deposition (EBID) of a carbonaceous platinum spot weld. The dimensions of the spot weld were chosen in accordance with the critical clamp width found for each CCNF diameter, as described by Qin et al. [45].

Once a CCNF was mounted across the shuttles of the MEMS device it could be pulled in tension either within a TEM or an SEM. To perform *in situ* TEM tests, the MEMS device is first loaded into a JEOL 2100 field emission HRTEM. A power supply is then used to apply an increasing voltage to the thermal actuator, providing step increases in displacement. Using digital image correlation the displacement between the shuttles versus image was obtained during each test. Thus, during the test the displacement of the CCNF is obtained and immediately after the test the thermal actuator is calibrated by unloading using the same voltage steps to obtain the displacement of the thermal actuator with no load as a function of applied voltage. The load was calculated by multiplying the spring constant of the folded beams in the MEMS device by the displacement of the load sensor. The displacement of the load sensor (d_{LS}) is calculated by subtracting the elongation of the CCNF (d_{CCNF}) during the test from the calibrated thermal actuator displacement (d_{TA}) after the test:

$$d_{LS} = d_{TA} - d_{CCNF} \quad (22)$$

The resolution of the TEM is almost 6 times higher than the SEM [46]. Consequently, while the digital image correlation as described above can be used in the SEM, it will result in a higher error, due to the low image resolution. In light of this, the *in situ* SEM method uses differential capacitive sensing of displacement to obtain the load. To perform *in situ* SEM tensile testing of the mounted CCNF, a voltage is applied to the thermal actuator using a signal generator which provides continuous displacements at $5 \times 10^{-3} \text{ s}^{-1}$ strain rate. However, instead of using digital image correlation to calculate the load, this method uses the differential capacitive load sensing [47]. The capacitive load sensor consists of another shuttle suspended by a series of flexible folded beams functioning as a spring in series with the specimen, which can be thought of as another spring. Given that the load sensor experiences the same force as the specimen, the force in the specimen can be known by measuring the displacement of the load sensor shuttle from equilibrium. The folded beams spring constant is known from beam theory, geometry, and the properties of the device material (silicon), or from calibration. The measurement of displacement is carried out electronically, by a series of capacitors (otherwise known as interdigitated fingers) formed between the moving shuttle and electrodes (or fingers) fixed to the substrate. Movement of the shuttle generates a capacitance change that can be detected electronically by a commercial integrated circuit and correlated to the displacement change [48]. Thus, contrary to the *in situ* TEM method, during the *in situ* SEM tests the displacement of the load sensor is obtained through changes in capacitance. The thermal actuator is calibrated again by digital image correlation immediately after the test, by unloading using the same voltage profile. The displacement of the CCNF (d_{CCNF}) is obtained by subtracting the displacement of the thermal actuator (d_{TA}), obtained from calibration, and displacement of the load sensor (d_{LS}), obtained during the test: (Equation 2).

$$d_{CCNF} = d_{TA} - d_{LS} \quad (23)$$

In order to understand the molecular alignment in the CCNFs, Selected Area Electron Diffraction (SAED) studies were performed *in situ* TEM along the length of the CCNFs on a TEM grid with diameters varying from 40 to 185 nm. The diffraction patterns of the 002 graphitic planes were

studied to qualify the degree of molecular orientation in the CCNFs. A diffuse 002 diffraction ring would indicate random orientation of the 002 crystal planes in the fiber, whereas discrete spots would indicate preferential alignment in a certain direction with respect to the fiber axis.

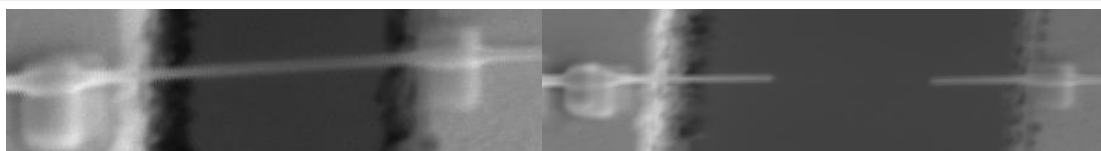


Figure 25. Example of a CCNF before and after (left and right, respectively) an in situ SEM tensile test.

In situ TEM tensile tests were performed on two CCNFs and in situ SEM tensile tests were performed on four CCNFs. The diameters of the CCNFs varied from 90 to 250nm. Figure 25 shows an image of the CCNF before and after an in situ SEM tensile test. It should be noted that the EBID platinum spot welds used to clamp the CCNF to the shuttles can diffuse to the gauge region and additionally the SEM/TEM imaging of the CCNF electron beam induced carbon deposition. However, following the calculations done by Filletter et al. [8], we find that the error in modulus will be less than 5%.

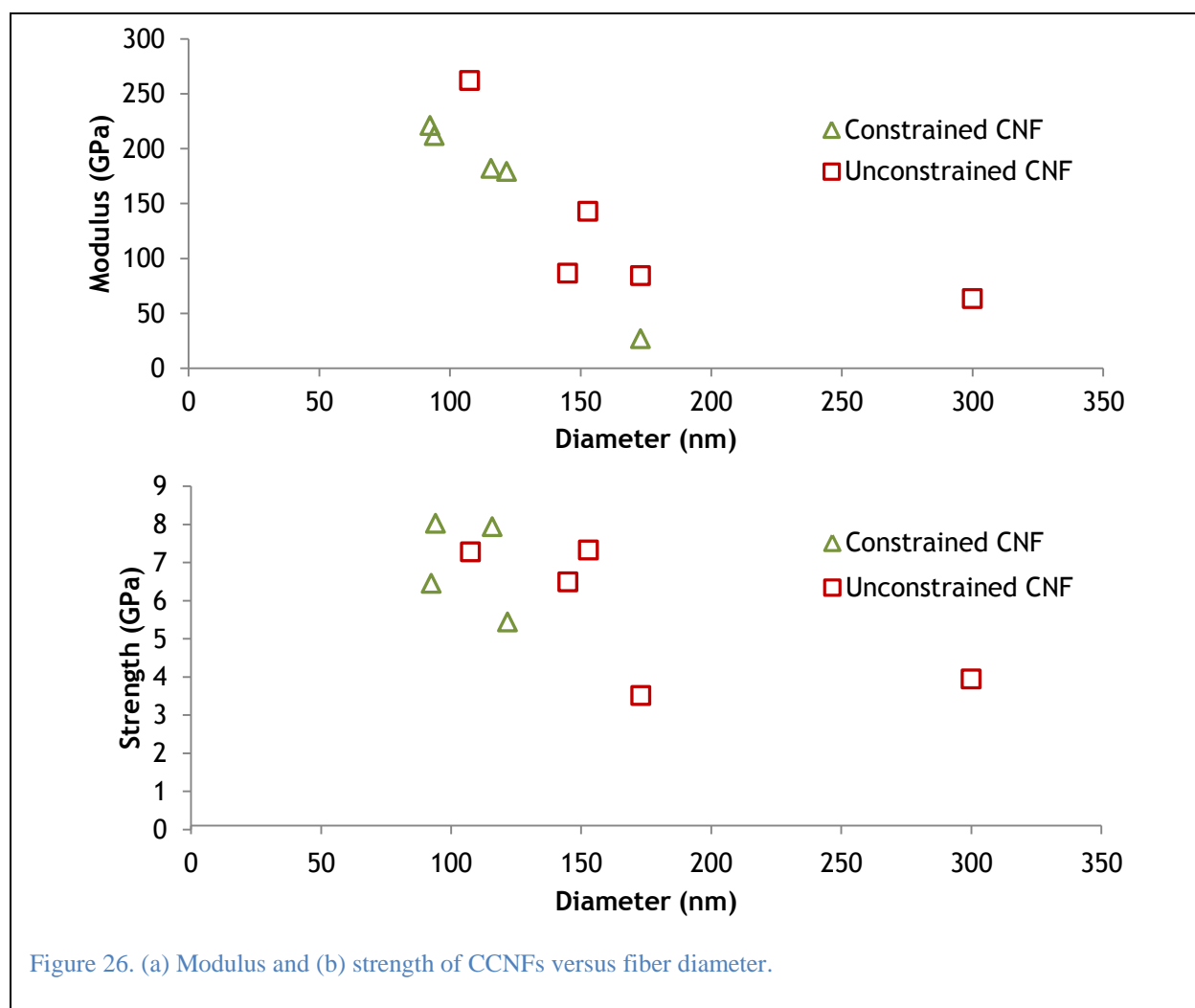


Figure 26. (a) Modulus and (b) strength of CCNFs versus fiber diameter.

Previously Beese et al. performed tensile tests on unconstrained CNFs using MEMS devices [49]. To compare the enhancement in mechanical properties due to the constraint during fabrication of the CCNFs, the results of the current study are plotted against the previous study with unconstrained fibers, as shown in Figure 26a and b, where the modulus and maximum stress values are plotted against the fiber diameters, respectively.

The modulus and maximum stress values of the CCNFs are higher than values obtained for unconstrained CNFs tested by Beese et al., though they follow the same trend where modulus decreases with decreasing diameter. As the diameter decreases below 100 nm, there is a significant increase in the modulus and maximum stress values. It should be noted that the carbon fibers in general are brittle and have intrinsic defects which leads to scatter in the maximum stress data. Thus the outlier in CCNF data for maximum stress for 250 nm diameter can be explained by the hypothesis that, that particular fiber was particularly pristine and had significantly lower defects than the other tested fibers. Since this fiber was tested using the in situ TEM technique, this hypothesis is validated by the high resolution TEM images of this fiber.

Our previously explained hypothesis was that that pre-stretch leads to a better molecular alignment within the fibers, and therefore, better properties. In order to determine if the molecular alignment was indeed better in the CCNFs compared to the unconstrained CNFs, Small Area Electron Diffraction (SAED) studies were conducted in situ TEM separately on a TEM grid with CCNFs. SAED patterns for CCNFs with diameter varying from 40 to 185 nm were obtained. To quantify the molecular alignment, which qualifies the various fiber internal structures, the Full Width Half Maximum (FWHM) of the integrated intensities (calculated as a function of angle from the fiber axis using QPCED2 software) of the 002 arc was obtained for all of the fibers examined in TEM. A higher value of the FWHM corresponds to a more random orientation of the 002 planes, while smaller values point towards increased alignment of these planes within the fibers. The FWHM was calculated for the two peaks in each SAED pattern and several SAED data points along the same fiber were obtained. The average of all these values was taken as the FWHM or the arc double angle for each fiber. From Figure 27 it can be seen that the constrained fibers do indeed have better molecular alignment compared to the unconstrained CNFs reported by Beese et al. [49].

Since it was not possible to conduct SAED studies on the particular tested fibers, as some of the tested were conducted in

the SEM instead of the TEM, a curve fit was generated to describe the arc double angle values from the separate TEM imaging studies, and this fit was used to interpolate the arc double angles for the fiber diameters tested inside the SEM. This allows us to obtain the structure-property relationships of the CCNFs and to compare them with these relationships obtained for the unconstrained fibers, as shown in Figure 28a and b. These clearly demonstrate that as the arc double angle decreases, and thus the molecular orientation increases, the strength of the fiber increases. In addition, these figures show that the CCNFs, which have increased molecular orientation of the graphitic basal planes compared to the orientation within unconstrained CNFs, have higher modulus and

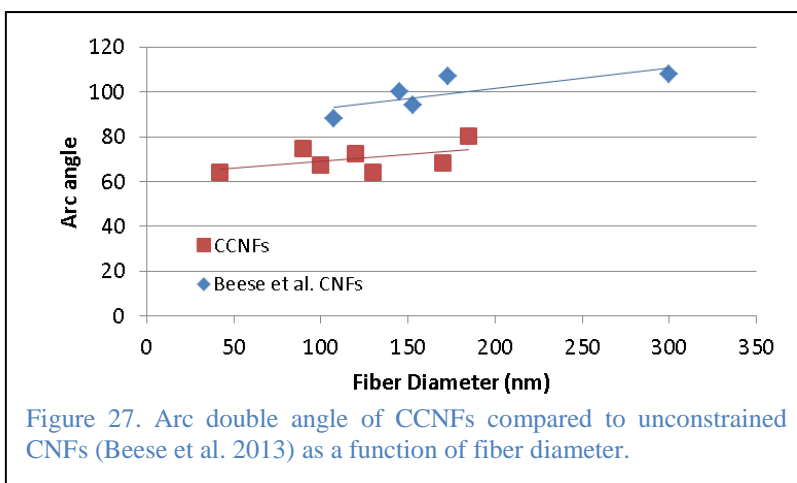
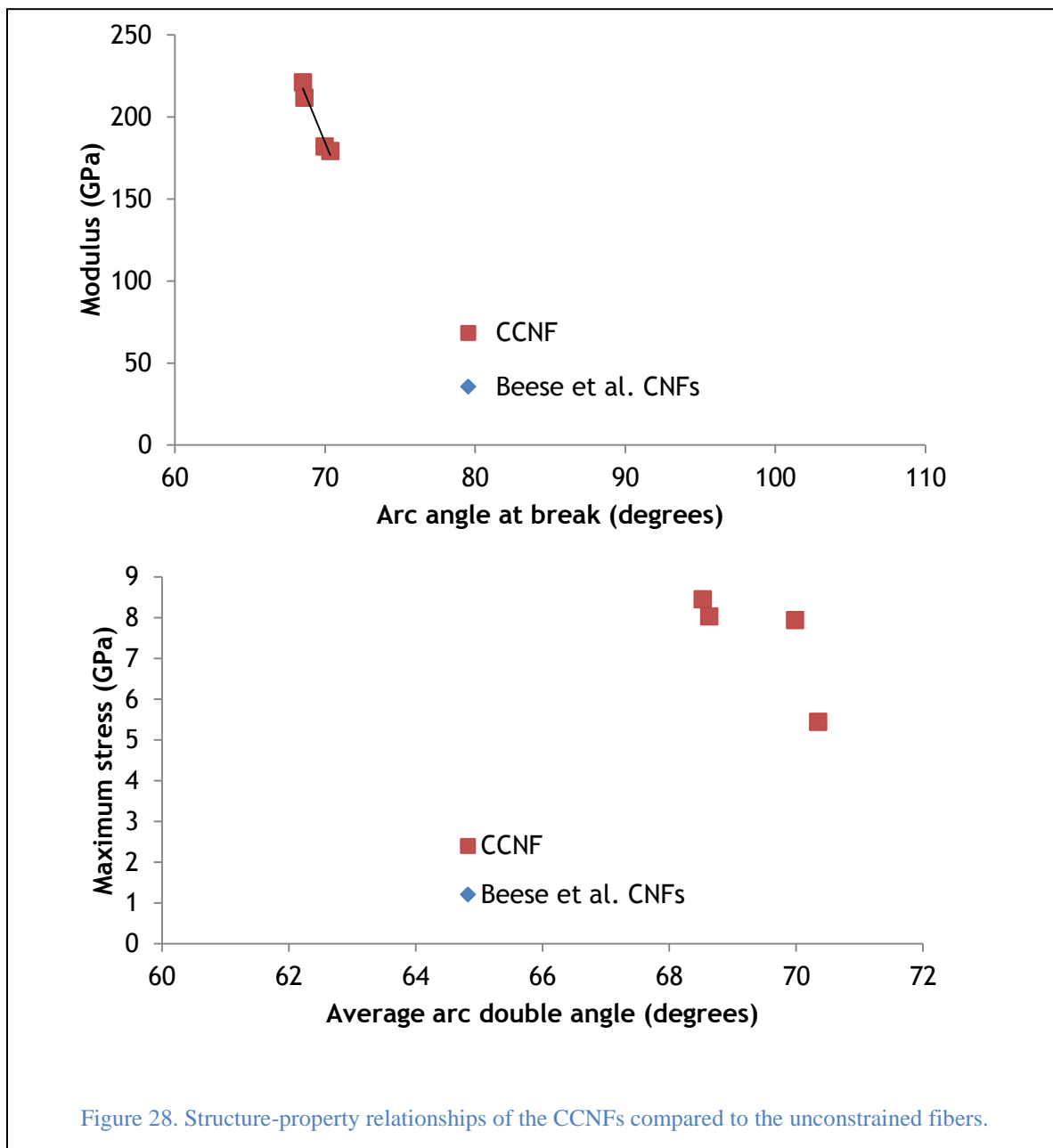


Figure 27. Arc double angle of CCNFs compared to unconstrained CNFs (Beese et al. 2013) as a function of fiber diameter.

maximum stress to failure than the unconstrained CNFs. Though the modulus follows the same trend as the unconstrained CNFs when plotted against the arc double angle, more data points need to be collected to obtain a trend for the maximum stress.

Thus, two features may lead to the increased strength with decreasing diameter: the decreasing volume fraction translates to decreased initial defects and thus a decreased probability to failure, especially in brittle materials [50], and the pre-stretch before carbonization improves molecular alignment resulting in stronger fibers.



In summary, *in situ* electron microscopy tensile testing of CCNFs was carried out to understand the effects of pre-stretch on the structure of nanofibers and in turn its impact on mechanical properties. We successfully tensile tested CCNFs with diameters of 90 to 250 nm and understood that the modulus and strength increases with decreasing diameter. We compared these results with the

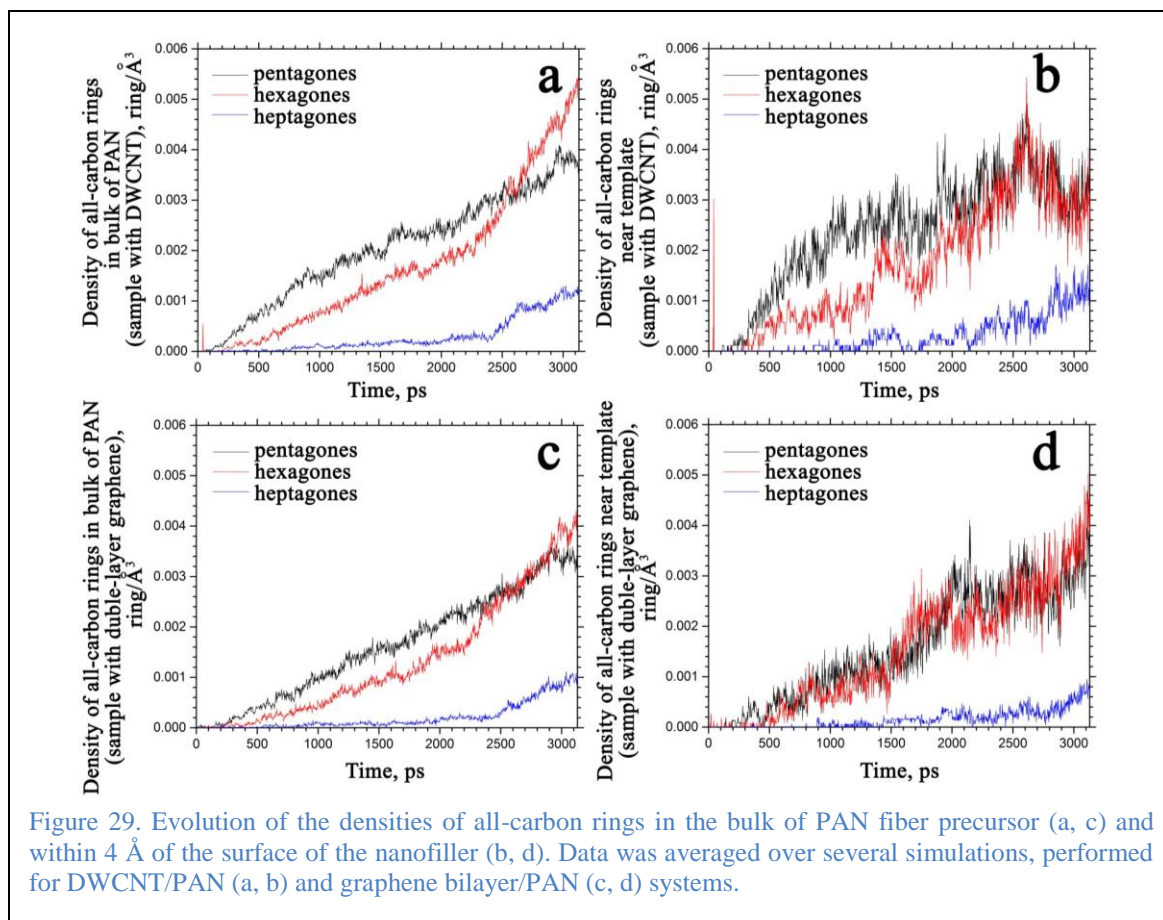
results obtained by Beese et al. on unconstrained fibers. The comparison showed that the constrained fibers are mechanically superior to the unconstrained fibers, as there is an increase of 22% in average strength and an increase of 31% in average modulus. As a method to identify and compare the structure-property relationships of the CCNFs and previously tested unconstrained CNFs, SAED studies were conducted. As predicted, the results showed that the constrained fibers have better molecular alignment than the unconstrained counterparts. The structure-mechanical property relationships show similar trends in both constrained and unconstrained cases, where decreasing diameter leads to increased strength and stiffness, though the CCNFs show better mechanical properties than the unconstrained CNFs. Thus, constraining the carbon nanofibers before carbonization will result in an increasing degree of polymer precursor alignment, especially in fibers with diameters <100 nm, and will result in 22% increase in strength and 31% increase in modulus compared to unconstrained fibers for a 0% increase in effort during manufacture.

ReaxFF molecular dynamics simulations of the initial stages of templated carbonization in PAN-based carbon nanofibers

This section describes our use of molecular dynamics (MD) simulations with the ReaxFF reactive force field to study the mechanism of carbonization of polyacrylonitrile (PAN) as templated by carbon nanotubes and graphene. This study is intended to model the experiments of Dzenis et al., which suggest improved graphitic alignment when templating is used. Last year we reported the presence of covalent linking between the CNT surfaces and thermally decomposing oligomers of stabilized PAN. At that time we speculated that templating in the presence of nanofiller was largely due to physical templating rather than nucleation. Our reasoning was based on the sporadic nature of covalent bond formation with the template material.

The purpose of the current project was to explore structure-templating effects for different nanofillers. Such information could be crucial for developing guidelines for creating future nanofiller-reinforced carbon fibers. We chose DWCNT and bilayer graphene for this study. Dzenis et al. have used CNTs in some of their templating work. The bilayer is expected to exhibit some of the properties of exfoliated graphene oxide (GO) and highly oriented pyrolytic graphite (HOPG) flakes, two other potential nanofillers. At carbonization temperatures (1700-3000°C) GO becomes reduced, and it is predicted to result in a material that may be similar to HOPG. Because we were targeting a particular stage of carbon fiber production, our simulations started with a system composed of embedded nanofiller in a PAN carbon fiber precursor.

The formation of all-carbon rings was observed when the temperature of the system reached ~1930°C. During the next 3 ns, we assessed the degree of carbonization by calculating changes in the densities of different types of all-carbon rings. Similar trends for DWCNT and bilayer graphene fillers in all-carbon ring formation were observed, in regions far from the nanofiller surfaces (Figure 29a and c). Close to the nanofillers (Figure 29b and d), the slopes of the curves in Figure 29 suggest that the relatively rigid and curved topologies of the DWCNTs promote the formation of pentagons more efficiently than that which occurs in the bulk. Bilayered graphene flakes show equal yield for all-carbon pentagons and hexagons. The overall activity of bilayer graphene is lower than for carbonization of PAN in the bulk. However, we observed a minor increase in the densities of all-carbon hexagons.



During the first 100 ps of the simulations, 13.4% of the PAN fiber precursor molecules participated in chemical transformations. The most prevalent type of reaction (7.6%) was self-decomposition of the precursor molecules. Reactions in which precursor molecules underwent condensation with large structural fragments of decomposing neighboring PAN molecules were second in prevalence (2.2%). Chemical transformations after H radical attack occurred 1.8% of the time. H radicals are a product of self-decomposition, and these atoms readily react with nearby precursors before combining with other radical species to become gas phase molecules. 0.6% of the chemical transformations in this period of time occurred at the surfaces of the DWCNT. Once decomposition is initiated, additional bonds destabilize and break, with further local heating and the influence of nearby structures.

Similar intermediates were observed at the surfaces of the CNTs and in the bulk. The CNTs provide a continuous curved graphitic surface in the “chemical soup” during carbonization. Curvature generates some deviation from sp² hybridization in the carbon atoms and, therefore, stabilizes certain intermediates during transformations. Stabilization by precursors in the decomposing bulk is heterogeneous in nature. The removal of gas molecules (performed once every 100 ps) creates cavities. This adds to the anisotropy in the reaction mixture. Such anisotropy is a key factor in the relative stability of intermediates and the alteration of reaction mechanisms. The flexible structure of the graphene bilayer is not as effective in providing homogeneous stabilization as the CNTs. Intermediate species near the surface of bilayer graphene are facing a heterogeneous environment of nearest precursor molecules most of the time. Therefore, the densities of the all-carbon rings formed (Figure 29d) are not as affected as in the presence of the CNTs (Figure 29b).

Another important topologically-defined feature of a nanofiller, is its readiness to form covalent bonds with the intermediates of chemical transformations. Bilayer graphene may form structures with significant local curvature and temporarily attach precursor fragments. However, at high temperatures such as those in the simulations such deformations are short lived (Figure 30, left panel), and they are quickly followed by counter-deformations that tend to destabilize the newly-formed covalent bonding. For CNTs, curvature is not as significant but it is permanent. Outer wall counter-fluctuations are limited due to the presence of the inner wall. Therefore, the intermediates of chemical transformations can bind more readily to the surfaces. Such bonds have higher survival probabilities (Figure 30, right panel) and, therefore, promote formation of all-carbon rings through stabilization in a homogeneous environment.

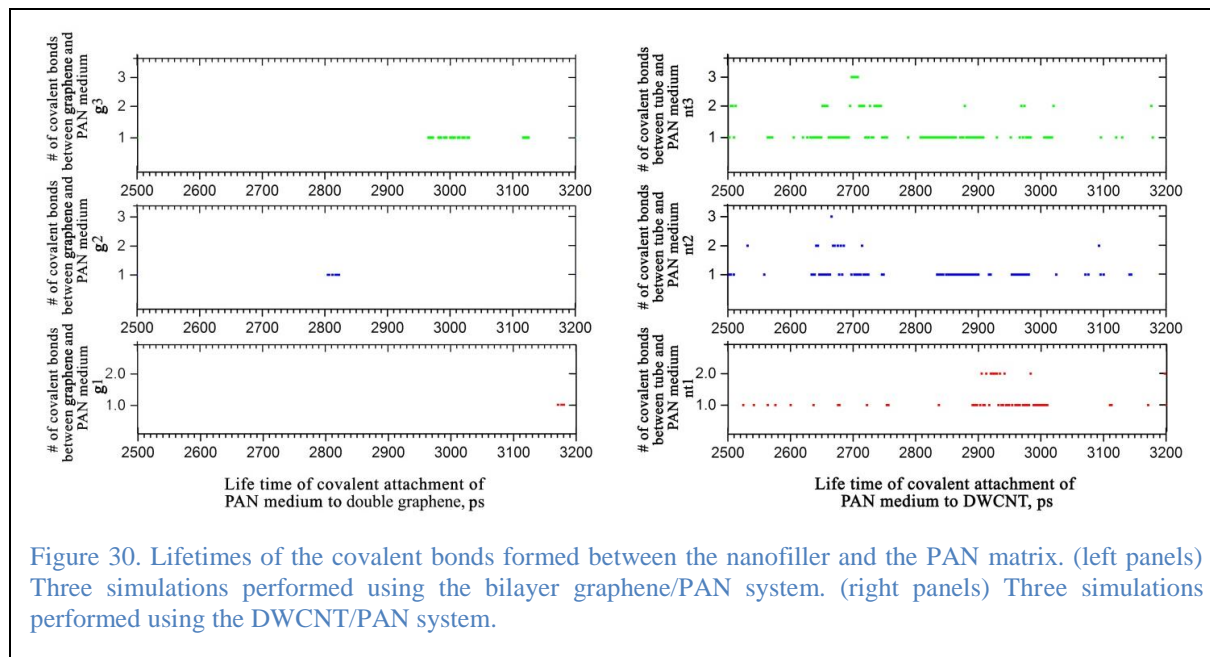


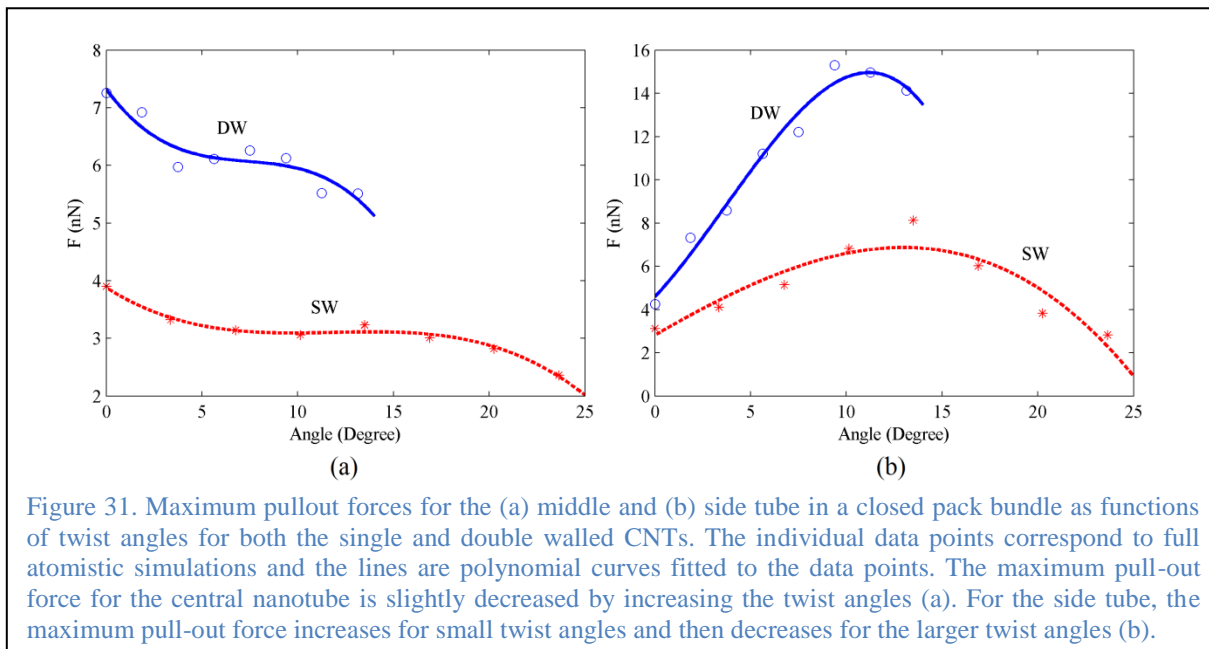
Figure 30. Lifetimes of the covalent bonds formed between the nanofiller and the PAN matrix. (left panels) Three simulations performed using the bilayer graphene/PAN system. (right panels) Three simulations performed using the DWCNT/PAN system.

Effect of twisting on the mechanics of SWCNT and DWCNT bundles and yarns

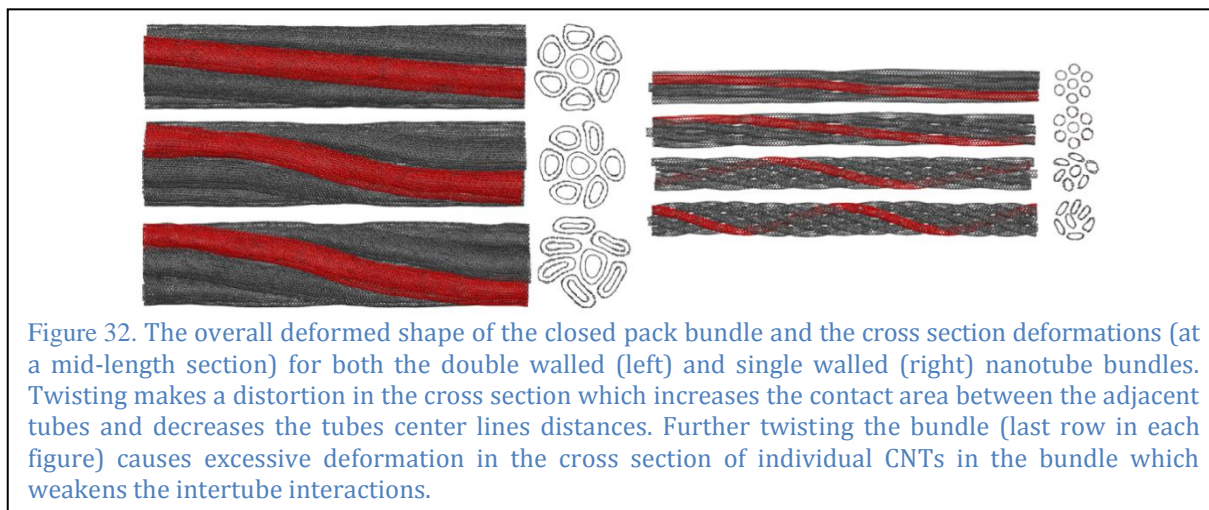
To analyze the mesoscale mechanics of carbon nanotube yarns and bundles, the Buehler group has performed atomistic and coarse grained simulations capable of providing insight into the deformation behavior of these systems. The molecular dynamics simulation package LAMMPS has been utilized to perform various tensile test experiments under displacement control conditions [51]. For atomistic simulations, a potential representation developed by Zou et al. is utilized [52]. This potential has been tested for accuracy utilizing shear test cases as the primary benchmark. To assess accuracy, results are obtained and compared between this potential and the Adaptive Intermolecular Reactive Empirical Bond Order (AIREBO) potential [53]. The simulation test cases show good agreement between both potentials. Shear has been utilized as the metric for accuracy as the predominant deformation mechanism in bundle pullout and tube sliding involve shear failure.

For simulations involving full atomistic representations, a 7-tube bundle of either SWCNTs or DWCNTs is modeled. During simulations, twisting through torsion is applied to bundle ends and equilibrated to ensure the system is stable. Then, the center of mass of the center tube or a side tube is pulled utilizing a spring connected to an artificial node (attached to the ends of the bundle) at a constant velocity. Results suggest that, for the central tube, there is a monotonic decrease in the pullout force associated with sliding the central tube out of the bundle, regardless of the bundle

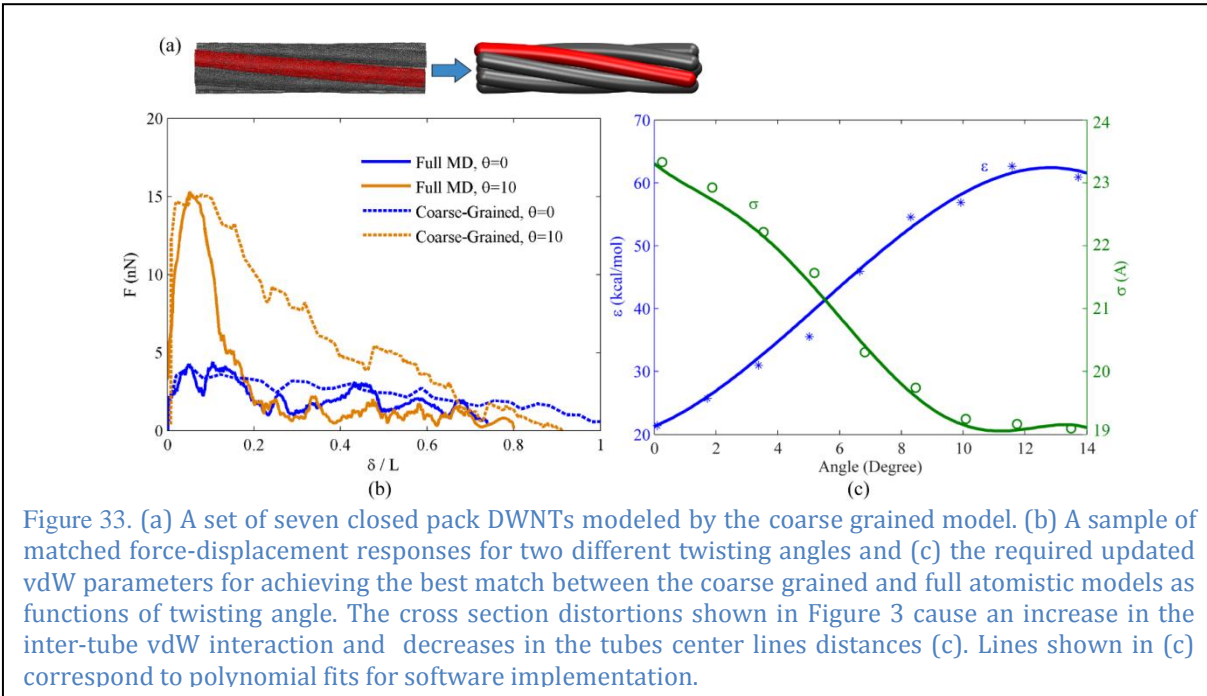
being composed of SWCNTs or DWCNTs. In contrast, when pulling a side tube utilizing the same methodology, our simulations suggest that the pullout forces associated with tube sliding are much higher. Figure 31 shows the obtained simulation results for this case.



To analyze this phenomenon, the cross-section of the bundle can be tracked as it becomes deformed. Figure 32 shows how the cross-section deformation for the bundles evolves with increasing twisting angle. Specifically, at intermediate twist angles, the distortions caused by twisting increase the contact area between adjacent tubes. Furthermore, the tubes center line distance decrease with increasing twist angle. The combination of these affects leads to an increase in the maximum shear force necessary to initiate tube pullout. Then, a critical angle is reached by which the cross-sections collapse and the highly distorted tubes become unstable. This critical angle is not explored in this report, and constitutes future work in this area.



With knowledge of how the deformation of the cross-sections of bundles affects the mechanics of tube pullout in bundles, a coarse graining strategy was implemented to study the effect of bundle pullout in yarns. The coarse grain model adjusts the effective Lennard-Jones interaction parameters as a function of twisting angle to represent accurately the mechanics of tube deformation. The dispersive distance, σ , is updated by calculating the average center-to-center distance between tubes in the full atomistic bundle simulation. The dispersive energy, ϵ , is updated by matching the force between the coarse grained and full atomistic model. After performing this procedure for various twisting angles, the set of parameters shown in Figure 33 are obtained.



To study the effect of twisting on mechanical properties at the next hierarchical level – CNT yarns – micro-yarns were generated and simulated by stacking 5 randomly oriented CNT layers. This method mimics the experimental procedure used to generate a porous film consisting of CNT bundles that become spun into yarns. These CNT stacks were spun into micro-yarns, whose ends were pulled under displacement control to simulate a tensile test. For obtaining the extent of the effect of twisting, the tensile tests were simulated with and without updating the Lennard-Jones parameters as a function of twisting angle. Results are shown in Figure 34. For comparison, untwisted yarns are also simulated.

Our simulations then suggest that the deformation of tube cross-section and the increase in contact area between tubes have a dramatic effect on the mechanical properties of CNT yarns, consistent with experimental observations shown in this report. Our model clearly suggests how there exists some optimum twisting angle, which is largely determined by the microstructure of the simulated system. In this way microstructural features such as porosity, twisting angle and overlap length play a critical role in the observed properties of CNT systems, consistent with previous and current experimental efforts like those reported in this document [54-56].

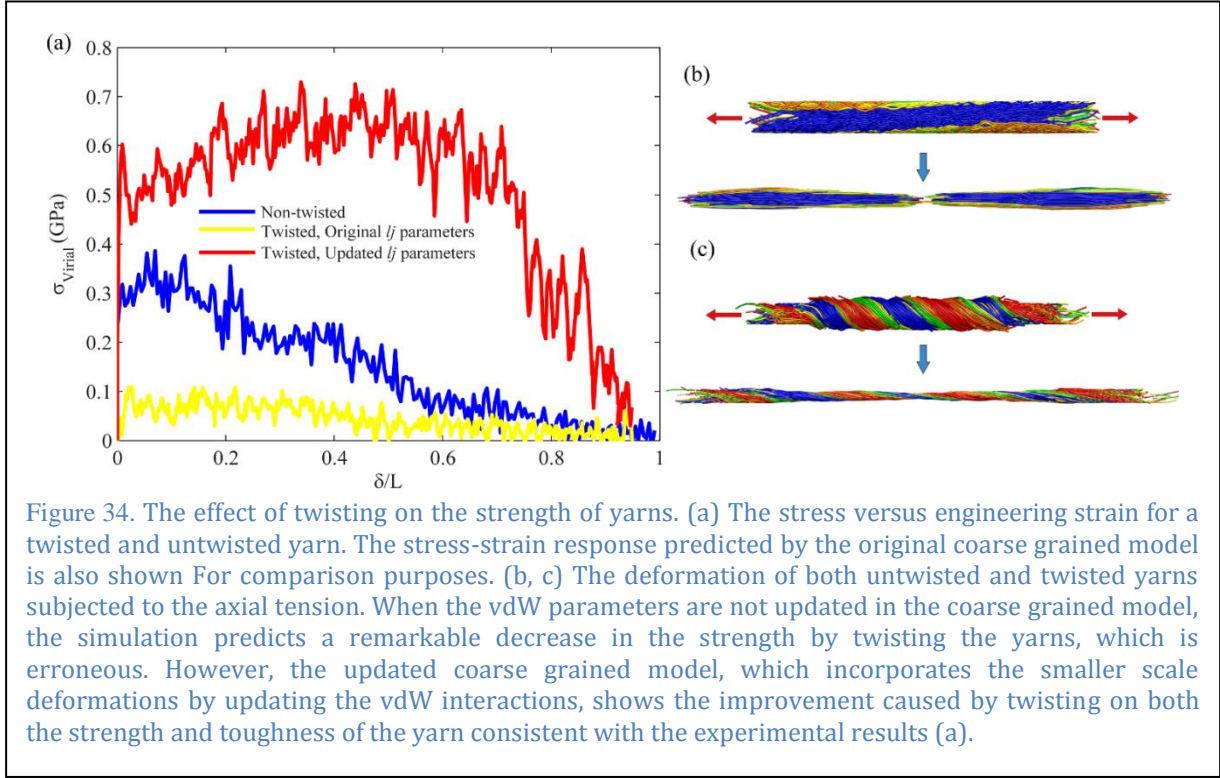


Figure 34. The effect of twisting on the strength of yarns. (a) The stress versus engineering strain for a twisted and untwisted yarn. The stress-strain response predicted by the original coarse grained model is also shown For comparison purposes. (b, c) The deformation of both untwisted and twisted yarns subjected to the axial tension. When the vdW parameters are not updated in the coarse grained model, the simulation predicts a remarkable decrease in the strength by twisting the yarns, which is erroneous. However, the updated coarse grained model, which incorporates the smaller scale deformations by updating the vdW interactions, shows the improvement caused by twisting on both the strength and toughness of the yarn consistent with the experimental results (a).

Literature Cited

- [1] Yu, M.F., O. Lourie, M.J. Dyer, K. Moloni, T.F. Kelly, and R.S. Ruoff, *Strength and breaking mechanism of multiwalled carbon nanotubes under tensile load*. *Science*, 2000. 287(5453): p. 637-640.
- [2] Peng, B., M. Locascio, P. Zapol, S. Li, S.L. Mielke, G.C. Schatz, and H.D. Espinosa, *Measurements of near-ultimate strength for multiwalled carbon nanotubes and irradiation-induced crosslinking improvements*. *Nature nanotechnology*, 2008. 3(10): p. 626-631.
- [3] Lu, W.B., M. Zu, J.H. Byun, B.S. Kim, and T.W. Chou, *State of the art of carbon nanotube fibers: Opportunities and challenges*. *Advanced Materials*, 2012. 24(14): p. 1805-1833.
- [4] Park, J. and K.H. Lee, *Carbon nanotube yarns*. *Korean Journal of Chemical Engineering*, 2012. 29(3): p. 277-287.
- [5] Baughman, R.H., A.A. Zakhidov, and W.A. de Heer, *Carbon nanotubes - the route toward applications*. *Science*, 2002. 297(5582): p. 787-792.
- [6] Koziol, K., J. Vilatela, A. Moisala, M. Motta, P. Cuniff, M. Sennett, and A. Windle, *High-performance carbon nanotube fiber*. *Science*, 2007. 318(5858): p. 1892-1895.
- [7] Filleter, T., R. Bernal, S. Li, and H. Espinosa, *Ultrahigh strength and stiffness in cross-linked hierarchical carbon nanotube bundles*. *Advanced Materials*, 2011. 23(25): p. 2855-2860.
- [8] Filleter, T., S. Yockel, M. Naraghi, J.T. Paci, O.C. Compton, M.L. Mayes, S.T. Nguyen, G.C. Schatz, and H.D. Espinosa, *Experimental-computational study of shear interactions within double-walled carbon nanotube bundles*. *Nano Letters*, 2012. 12(2): p. 732-742.
- [9] Wei, X., M. Naraghi, and H.D. Espinosa, *Optimal length scales emerging from shear load transfer in natural materials: Application to carbon-based nanocomposite design*. *ACS nano*, 2012. 6(3): p. 2333-2344.
- [10] Naraghi, M., G.H. Bratzel, T. Filleter, Z. An, X.D. Wei, S.T. Nguyen, M.J. Buehler, and H.D. Espinosa, *Atomistic investigation of load transfer between dwnt bundles "crosslinked" by pmma oligomers*. *Advanced Functional Materials*, 2013. 23(15): p. 1883-1892.
- [11] Roenbeck, M.R., X.D. Wei, A.M. Beese, M. Naraghi, A. Furmanchuk, J.T. Paci, G.C. Schatz, and H.D. Espinosa, *In situ scanning electron microscope peeling to quantify surface energy between multiwalled carbon nanotubes and graphene*. *Acs Nano*, 2014. 8(1): p. 124-138.
- [12] Naraghi, M., T. Filleter, A. Moravsky, M. Locascio, R.O. Loutfy, and H.D. Espinosa, *A multiscale study of high performance double-walled nanotube-polymer fibers*. *Acs Nano*, 2010. 4(11): p. 6463-6476.
- [13] Beese, A.M., S. Sarkar, A. Nair, M. Naraghi, Z. An, A. Moravsky, R.O. Loutfy, M.J. Buehler, S.T. Nguyen, and H.D. Espinosa, *Bio-inspired carbon nanotube-polymer composite yarns with hydrogen bond-mediated lateral interactions*. *Acs Nano*, 2013. 7(4): p. 3434-3446.
- [14] Ortiz, A.L. and L. Shaw, *X-ray diffraction analysis of a severely plastically deformed aluminum alloy*. *Acta Materialia*, 2004. 52(8): p. 2185-2197.
- [15] Savini, G., Y.J. Dappe, S. Oberg, J.C. Charlier, M.I. Katsnelson, and A. Fasolino, *Bending modes, elastic constants and mechanical stability of graphitic systems*. *Carbon*, 2011. 49(1): p. 62-69.
- [16] Ginga, N.J., W. Chen, and S.K. Sitaraman, *Waviness reduces effective modulus of carbon nanotube forests by several orders of magnitude*. *Carbon*, 2014. 66: p. 57-66.
- [17] Pujari, S., S. Rahatekar, J.W. Gilman, K.K. Koziol, A.H. Windle, and W.R. Burghardt, *Shear-induced anisotropy of concentrated multiwalled carbon nanotube suspensions using x-ray scattering*. *Journal of Rheology*, 2011. 55(5): p. 1033-1058.
- [18] Schrauwen, B.A.G., L.C.A. Von Breemen, A.B. Spoelstra, L.E. Govaert, G.W.M. Peters, and H.E.H. Meijer, *Structure, deformation, and failure of flow-oriented semicrystalline polymers*. *Macromolecules*, 2004. 37(23): p. 8618-8633.
- [19] Giboz, J., A.B. Spoelstra, G. Portale, T. Copponnex, H.E.H. Meijer, G.W.M. Peters, and P. Mele, *On the origin of the "core-free" morphology in microinjection-molded hdpe*. *Journal of Polymer Science Part B-Polymer Physics*, 2011. 49(20): p. 1470-1478.
- [20] Hearle, J.W.S., P. Grosberg, and S. Backer, *Structural mechanics of fibers, yarns, and fabrics*. Vol. 1. 1969, New York: John Wiley & Sons, Inc.

- [21] Porwal, P.K., I.J. Beyerlein, and S.L. Phoenix, *Statistical strength of a twisted fiber bundle: An extension of daniels equal-load-sharing parallel bundle theory*. *Journal of Mechanics of Materials and Structures*, 2006. 1(8): p. 1425-1447.
- [22] Porwal, P.K., I.J. Beyerlein, and S.L. Phoenix, *Statistical strength of twisted fiber bundles with load sharing controlled by frictional length scales*. *Journal of Mechanics of Materials and Structures*, 2007. 2(4): p. 773-791.
- [23] Barber, A., I. Kaplan-Ashiri, S. Cohen, R. Tenne, and H. Wagner, *Stochastic strength of nanotubes: An appraisal of available data*. *Composites science and technology*, 2005. 65(15): p. 2380-2384.
- [24] Barber, A.H., R. Andrews, L.S. Schadler, and H.D. Wagner, *On the tensile strength distribution of multiwalled carbon nanotubes*. *Applied Physics Letters*, 2005. 87(20): p. 203106.
- [25] Klein, C.A., *Characteristic tensile strength and weibull shape parameter of carbon nanotubes*. *Journal of applied physics*, 2007. 101(12): p. 124909.
- [26] Behabtu, N., C.C. Young, D.E. Tsentelovich, O. Kleinerman, X. Wang, A.W. Ma, E.A. Bengio, R.F. ter Waarbeek, J.J. de Jong, and R.E. Hoogerwerf, *Strong, light, multifunctional fibers of carbon nanotubes with ultrahigh conductivity*. *Science*, 2013. 339(6116): p. 182-186.
- [27] Naraghi, M., G.H. Bratzel, T. Filleter, Z. An, X. Wei, S.T. Nguyen, M.J. Buehler, and H.D. Espinosa, *Atomistic investigation of load transfer between dwnt bundles "crosslinked" by pmma oligomers*. *Advanced Functional Materials*, 2013. 23(15): p. 1883-1892.
- [28] Papkov, D., A.M. Beese, A. Goponenko, Y. Zou, M. Naraghi, H.D. Espinosa, B. Saha, G.C. Schatz, A. Moravsky, and R. Loutfy, *Extraordinary improvement of the graphitic structure of continuous carbon nanofibers templated with double wall carbon nanotubes*. *ACS nano*, 2012. 7(1): p. 126-142.
- [29] Yu, M.-F., O. Lourie, M.J. Dyer, K. Moloni, T.F. Kelly, and R.S. Ruoff, *Strength and breaking mechanism of multiwalled carbon nanotubes under tensile load*. *Science*, 2000. 287(5453): p. 637-640.
- [30] Lucas, M., X.H. Zhang, I. Palaci, C. Klinke, E. Tosatti, and E. Riedo, *Hindered rolling and friction anisotropy in supported carbon nanotubes*. *Nature Materials*, 2009. 8(11): p. 876-881.
- [31] Falvo, M.R., R.M. Taylor, A. Helser, V. Chi, F.P. Brooks, S. Washburn, and R. Superfine, *Nanometre-scale rolling and sliding of carbon nanotubes*. *Nature*, 1999. 397(6716): p. 236-238.
- [32] Falvo, M., J. Steele, R. Taylor II, and R. Superfine, *Evidence of commensurate contact and rolling motion: Afm manipulation studies of carbon nanotubes on hopg*. *Tribology Letters*, 2000. 9(1-2): p. 73-76.
- [33] Seydou, M., Y.J. Dappe, S. Marsaudon, J.P. Aime, X. Bouju, and A.M. Bonnot, *Atomic force microscope measurements and lcao-s-2 + vdw calculations of contact length between a carbon nanotube and a graphene surface*. *Physical Review B*, 2011. 83(4).
- [34] Lee, C., X. Wei, J.W. Kysar, and J. Hone, *Measurement of the elastic properties and intrinsic strength of monolayer graphene*. *science*, 2008. 321(5887): p. 385-388.
- [35] Dikin, D.A., S. Stankovich, E.J. Zimney, R.D. Piner, G.H. Dommett, G. Evmenenko, S.T. Nguyen, and R.S. Ruoff, *Preparation and characterization of graphene oxide paper*. *Nature*, 2007. 448(7152): p. 457-460.
- [36] Tan, P., W. Han, W. Zhao, Z. Wu, K. Chang, H. Wang, Y. Wang, N. Bonini, N. Marzari, and N. Pugno, *The shear mode of multilayer graphene*. *Nature materials*, 2012. 11(4): p. 294-300.
- [37] Liu, Y., B. Xie, Z. Zhang, Q. Zheng, and Z. Xu, *Mechanical properties of graphene papers*. *Journal of the Mechanics and Physics of Solids*, 2012. 60(4): p. 591-605.
- [38] Suk, J.W., R.D. Piner, J. An, and R.S. Ruoff, *Mechanical properties of monolayer graphene oxide*. *ACS nano*, 2010. 4(11): p. 6557-6564.
- [39] Rabinowitz, S., I. Ward, and J. Parry, *The effect of hydrostatic pressure on the shear yield behaviour of polymers*. *Journal of materials Science*, 1970. 5(1): p. 29-39.
- [40] Beese, A.M., Z. An, S. Sarkar, S.S.P. Nathamgari, H.D. Espinosa, and S.T. Nguyen, *Defect-tolerant nanocomposites through bio-inspired stiffness modulation*. *Advanced Functional Materials*, 2014. 24(19): p. 2883-2891.
- [41] Fratzl, P., H.S. Gupta, F.D. Fischer, and O. Kolednik, *Hindered crack propagation in materials with periodically varying young's modulus—lessons from biological materials*. *Advanced Materials*, 2007. 19(18): p. 2657-2661.

- [42] Espinosa, H.D., J.E. Rim, F. Barthelat, and M.J. Buehler, *Merger of structure and material in nacre and bone—perspectives on de novo biomimetic materials*. *Progress in Materials Science*, 2009. 54(8): p. 1059-1100.
- [43] Xia, W., S. Mishra, and S. Keten, *Substrate vs. Free surface: Competing effects on the glass transition of polymer thin films*. *Polymer*, 2013. 54(21): p. 5942-5951.
- [44] Landel, R.F. and L.E. Nielsen, *Mechanical properties of polymers and composites*. 1993: CRC Press.
- [45] Qin, Q.Q., F. Xu, Y.Q. Cao, P.I. Ro, and Y. Zhu, *Measuring true young's modulus of a cantilevered nanowire: Effect of clamping on resonance frequency*. *Small*, 2012. 8(16): p. 2571-2576.
- [46] Warren, J.B. and B.J. Panessa-Warren, *A comparison of nanometrology using sem and tem*. *Microscopy and Microanalysis*, 2005. 11(SupplementS02): p. 1932-1933.
- [47] Espinosa, H.D., Y. Zhu, and N. Moldovan, *Design and operation of a mems-based material testing system for nanomechanical characterization*. *Journal of Microelectromechanical Systems*, 2007. 16(5): p. 1219-1231.
- [48] Zhu, Y., N. Moldovan, and H.D. Espinosa, *A microelectromechanical load sensor for in situ electron and x-ray microscopy tensile testing of nanostructures*. *Applied Physics Letters*, 2005. 86(1).
- [49] Beese, A.M., D. Papkov, S.Y. Li, Y. Dzenis, and H.D. Espinosa, *In situ transmission electron microscope tensile testing reveals structure-property relationships in carbon nanofibers*. *Carbon*, 2013. 60: p. 246-253.
- [50] Tagawa, T. and T. Miyata, *Size effect on tensile strength of carbon fibers*. *Materials Science and Engineering a-Structural Materials Properties Microstructure and Processing*, 1997. 238(2): p. 336-342.
- [51] Plimpton, S., *Fast parallel algorithms for short-range molecular dynamics*. *Journal of computational physics*, 1995. 117(1): p. 1-19.
- [52] Zou, J., B. Ji, X.-Q. Feng, and H. Gao, *Self-assembly of single-walled carbon nanotubes into multiwalled carbon nanotubes in water: Molecular dynamics simulations*. *Nano Letters*, 2006. 6(3): p. 430-434.
- [53] Stuart, S.J., A.B. Tutein, and J.A. Harrison, *A reactive potential for hydrocarbons with intermolecular interactions*. *The Journal of chemical physics*, 2000. 112(14): p. 6472-6486.
- [54] Fang, S., M. Zhang, A.A. Zakhidov, and R.H. Baughman, *Structure and process-dependent properties of solid-state spun carbon nanotube yarns*. *Journal of Physics: Condensed Matter*, 2010. 22(33): p. 334221.
- [55] Miao, M., J. McDonnell, L. Vuckovic, and S.C. Hawkins, *Poisson's ratio and porosity of carbon nanotube dry-spun yarns*. *Carbon*, 2010. 48(10): p. 2802-2811.
- [56] Zhang, X., Q. Li, Y. Tu, Y. Li, J.Y. Coulter, L. Zheng, Y. Zhao, Q. Jia, D.E. Peterson, and Y. Zhu, *Strong carbon-nanotube fibers spun from long carbon-nanotube arrays*. *Small*, 2007. 3(2): p. 244-248.

Scientific Progress and Accomplishments

Statistical Shear Lag Model for Hierarchical Composites

This study aimed to explore size effects on the strength of bio-inspired staggered hierarchical composites and to define the influence of the geometry of constituents in their outstanding defect tolerance capability [1]. Hierarchical composite materials found in nature, such as nacre shells, collagen fibrils, and spider silk, are well known for their balanced strength and toughness [2]. Through staggered arrangements of constituents (i.e., strong and stiff filaments embedded in softer interfaces), natural composites can not only preserve the stiffness and strength of the filaments during material scale-up, but also achieve remarkable toughness. Microstructure characterizations of these natural composites reveal a critical length scale for each material that correlates to the two main failure mechanisms – filament fracture and interface sliding – to optimize macroscopic strength and toughness simultaneously [3-6]. Different continuum models have been advanced to relate critical length scales with mechanical properties of constituents, but they had assumed only a specified flaw with a predefined size and location. In practice, the location and size of flaws are randomly distributed along the strong and stiff filaments, and the number of flaws scales with the dimensions of filaments. Thus, the stochastic nature of flaw distribution needs to be taken into account in these continuum models.

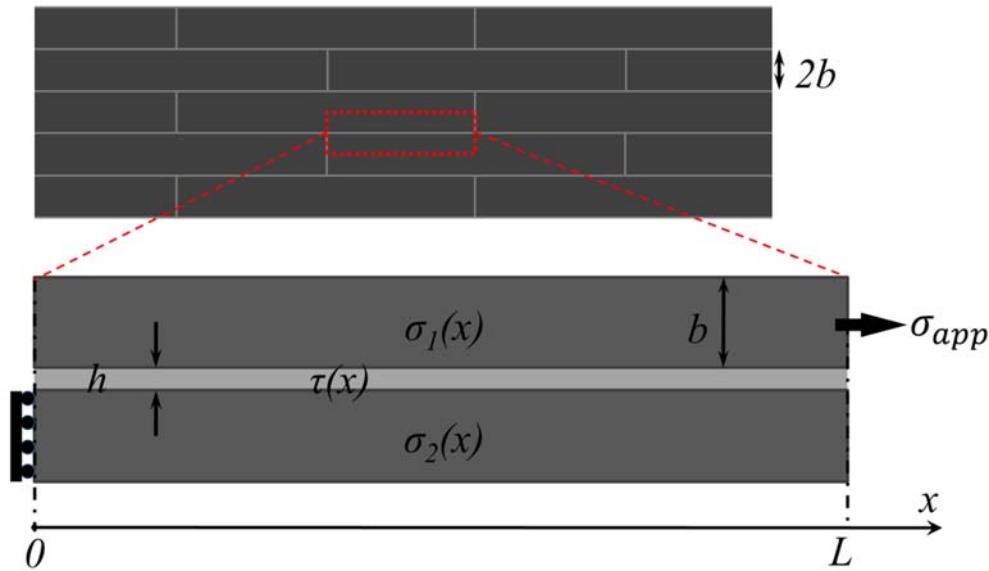


Figure 1: Schematic of the 2D unit cell used in the statistical shear lag model simplified from the brick-and-mortar structure of a hierarchical staggered composite.

In our previous study, the classical shear lag model was used to describe the optimal length scale in staggered composites that simultaneously optimize their strength and toughness [7]. As shown in Figure 1, a simplified 2D unit cell was constructed to study the load transfer efficiency between two adjacent filaments (with a thickness denoted as b) bonded by a thin soft interface layer (with a thickness denoted as h) over the length L . A tensile normal stress σ_{app} is applied at the right end of the top filament, and the left end of the bottom filament is fixed in the axial direction but is free to deform in the lateral direction. The left end of the top filament and the right end of the bottom filament are traction-free and free to displace. Assuming the filaments

and interface deform elastically, the solutions for axial tensile stress along the top and bottom filaments are expressed as

$$\begin{aligned}\sigma_1(x) &= \frac{\sigma_{app}}{\sinh\left(\frac{\lambda L}{2}\right)} \sinh\left(\frac{\lambda x}{2}\right) \cosh\left(\frac{\lambda(L-x)}{2}\right) \\ \sigma_2(x) &= \sigma_1(L-x) = \frac{\sigma_{app}}{\sinh\left(\frac{\lambda L}{2}\right)} \cosh\left(\frac{\lambda x}{2}\right) \sinh\left(\frac{\lambda(L-x)}{2}\right)\end{aligned}\quad (1)$$

respectively. In Equation (1), $\lambda = \sqrt{\frac{2G}{Ehb}}$ in which E is the elastic modulus of the filament and G is the shear modulus of the interface.

Filament rupture and interface sliding were assumed to be the only two failure mechanisms that determine the composite strength. The classical shear lag model is based on several key assumptions. First, the filaments are treated as one-dimensional springs so that the transversal stress and variations in axial stress are neglected. Second, the interfaces carry no tensile but only shear load controlled solely by the relative displacements of filaments adhered to the interface regions. Microscopic characterizations suggest that the tensile strengths of reinforcements in natural composites spread widely due to variations in dominant defects [8]. In this study, we modified the classical shear lag model to account for the statistics in the tensile strength of reinforcements while keeping the key assumptions for the classical shear lag model.

The failure probability for a filament subject to a *nonhomogeneous* uniaxial stress state can take the integral form [9, 10]:

$$P_f = 1 - \exp\left\{-\int_L \left[\frac{\sigma(\mathbf{x})}{\sigma_0}\right]^m \frac{dL(\mathbf{x})}{L_0}\right\}, \quad (2)$$

where $\sigma(\mathbf{x})$ is the distribution function of the effective uniaxial stress over the sample length L .

Clearly, Equation (2) suggests that both the material dimension and loading conditions affects the structural strength. Substituting Equation (1) into Equation (2), the probability of the rupture of any two filaments in the unit cell is given by

$$\begin{aligned}P_f(\sigma_{app}) &= 1 - \exp\left\{-\frac{2}{L_0} \int_0^L \left(\frac{\sigma_1(x)}{\sigma_0}\right)^m dx\right\} \\ &= 1 - \exp\left\{-\frac{2 \int_0^L \left(\frac{1}{\sinh(\lambda L/2)} \cosh\left[\frac{\lambda}{2}(L-x)\right] \sinh\left(\frac{\lambda x}{2}\right)\right)^m dx}{L_0} \left(\frac{\sigma_{app}}{\sigma_0}\right)^m\right\}\end{aligned}\quad (3)$$

in which L_0 is the reference length for the filament in the simplified 2D unit cell. By defining the effective length

$$L_{eff}(L) = \int_0^L \left(\frac{1}{\sinh(\lambda L/2)} \cosh \left[\frac{\lambda}{2}(L-x) \right] \sinh \left(\frac{\lambda x}{2} \right) \right)^m dx, \quad (4)$$

we can rewrite Equation (3) as

$$P_f(\sigma_{app}) = 1 - \exp \left\{ - \frac{2L_{eff}}{L_0} \left(\frac{\sigma_{app}}{\sigma_0} \right)^m \right\}. \quad (5)$$

Equation (5) suggests that the probability of the unit cell failing by filament rupture follows a Weibull distribution, which possesses the same shape parameter as the Weibull distribution of the monolithic filament rupture strengths. The new Weibull distribution for the rupture strength of the unit cell takes the form

$$P_f(\sigma_{app}) = 1 - \exp \left\{ - \left(\frac{\sigma_{app}}{\sigma_{0,uc}} \right)^m \right\} \quad (6)$$

where $\sigma_{0,uc} = \sigma_0 \left(\frac{L_0}{2L_{eff}} \right)^{1/m}$ is the scale factor for the unit cell rupture strength.

The statistical shear lag model introduced above facilitates the investigation of the statistics of unit cell rupture strengths as a function of overlap length. For a filament material whose strength has a Weibull distribution, the unit cell rupture strengths also follow Weibull statistics with a scale factor that is a function of the overlap length. The variance of the Weibull distribution for unit cell rupture strength is $\sigma_{0,uc}^2 \left[\Gamma(1+2/m) - (\Gamma(1+1/m))^2 \right]$. Alternatively, the unit cell can also fail by filament-filament sliding. For a linear elastic interface, the unit cell fails in sliding when $\sigma_{app} = 2\tau_f / (b\lambda) \tanh(\lambda L/2)$, in which τ_f is the interface shear strength [7]. Note that when scaling unit cells up to a macroscopic composite, the effective stress applied on the unit cell is $\sigma_{eff} = \sigma_{app} b / (2b+h)$. When the interface is thin (i.e., $h \ll b$), σ_{eff} equals approximately $\sigma_{app}/2$.

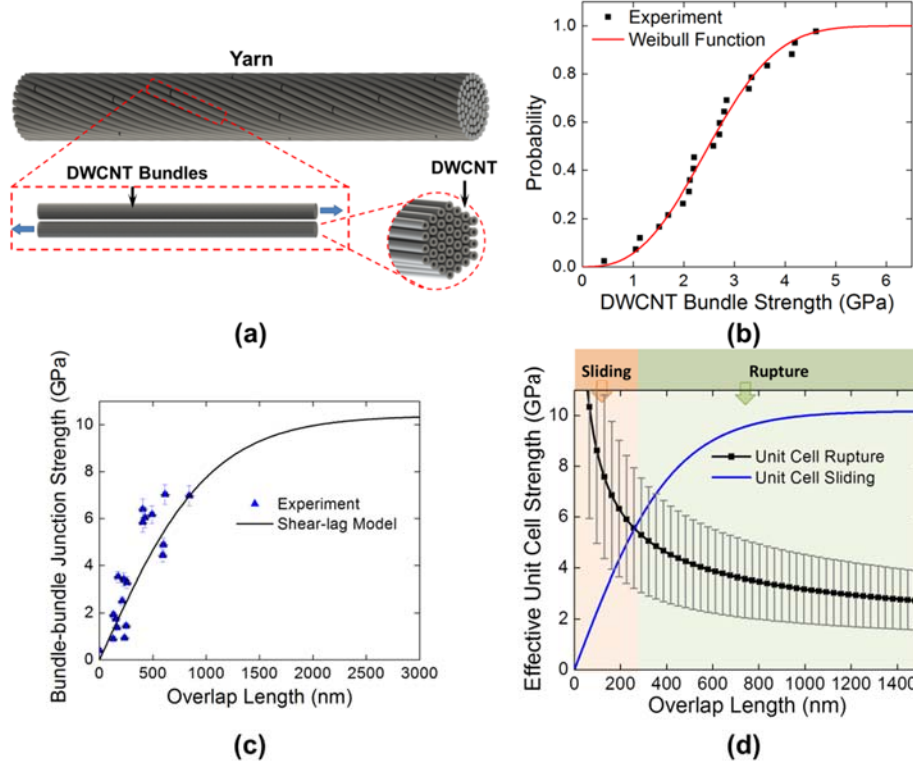


Figure 2: (a) Schematic depicting the hierarchical structure of a macroscopic DWCNT yarn. Each unit cell in the yarn consists of two parallel DWCNT bundles. (b) Weibull analysis of the individual bundle rupture strength. (c) Simulated fit using the shear lag model of experimental shear strengths measured for two parallel DWCNT bundles. (d) Plot of the effective unit cell strength as a function of the unit cell length (overlap length). The unit cell strength determined by interface sliding is plotted in blue and by bundle rupture is plotted in black. Each black square represents the scale factor of the Weibull distribution function of the unit cell rupture strength at a particular overlap length. The error is the square root of the variance for each Weibull distribution function.

To demonstrate the two competing failure mechanisms within the unit cell, a case study was performed on yarns made of double-walled carbon nanotube (DWCNT) bundles (see Figure 2a) [11]. Each unit cell contains a pair of parallel DWCNT bundles. Statistics of bundle strength have been obtained through previous in-situ SEM tensile experiments on 21 individual bundles with an average diameter of 25 nm and length of 5 μm [11-14]. After ordering 21 strength values ascendingly and defining $P_i = 100(i - 0.5)/21$ as the sample percentile ($i = 1, \dots, 21$), the set of strength values was fitted with the Weibull distribution function given by Equation (1) to yield a scale factor of $\sigma_0 = 2.8$ GPa and a shape factor $m = 2.2$ (Figure 2b). Note that the stress on a bundle in this study is defined as the load divided by the cross-sectional area of all carbon nanotube shells within the bundle. The mechanical properties of the interface were investigated through in-situ SEM shear tests on pairs of parallel bundles [13]. A pair of bundles aligned parallel to one another with various overlap lengths was pulled on the opposite ends of the bundles with the force to break the junction recorded. As shown in Figure 2c, tensile stresses required to slide 19 pairs of bundles were plotted as a function of overlap lengths. Previous coarse-grained simulations suggested that the interface between parallel bundles has a thickness $h \sim 2.5$ nm [13]. The equivalent filament thickness b is approximated as half of the bundle radius r . Fitting the results with the classical shear lag model solution $\sigma_{app} = 2\tau_f / (b\lambda) \tanh(\lambda L/2)$ yield an interface shear strength $\tau_f = 350$ MPa and an effective

interface shear modulus $G=10$ MPa. The properties of DWCNT bundles and interfaces are summarized in Table 1. Combining the results from the classical shear lag model and the statistical shear lag model, the effects of both failure modes on the unit cell strength are shown in Figure 2d. The final unit cell strength is the smaller of the two strength values predicted by the statistical shear lag model and the classical shear lag model. The critical overlap length (or unit cell size) \tilde{L} where the classical and statistical shear lag model solutions intersect gives the optimized unit cell strength and can be determined by numerically solving the following equation

$$\sigma_0 \left(\frac{L_0}{2L_{eff}(\tilde{L})} \right)^{1/m} = \frac{2\tau_f}{b\lambda} \tanh \left(\frac{\lambda\tilde{L}}{2} \right). \quad (7)$$

For unit cells smaller than \tilde{L} , the scale factor $\sigma_{0,uc}$ fails to describe the unit cell strength due to the interface sliding, and thus is invalid for weakest-link model for size-scaling the composite strength. In other words, \tilde{L} has the same physical meaning as the aforementioned fundamental link length \hat{L} . Moreover, we can show that Equation (7) is a more general solution that can be simplified to the formulations proposed previously [15, 16] under specific conditions.

When $m > 1$, the effective unit cell length L_{eff} given by Equation (4) is bounded by two limits

$$\frac{L}{m+1} > L_{eff} > \frac{L}{2^m}. \quad (8)$$

L_{eff} approaches the upper limit for a small λ (meaning the interface is very soft compared to the filament) and approaches the lower limit for a large λ . Thus, for a small λ , Equation (7) can be approximated as

$$\sigma_0 \left(\frac{L_0(m+1)}{2\tilde{L}} \right)^{1/m} \approx \frac{\tau_f}{b} \tilde{L} \quad (9)$$

Solving Equation (9) yields $\tilde{L} = \left[\frac{\sigma_0 b L_0^{1/m}}{\tau_f} \left(\frac{m+1}{2} \right)^{1/m} \right]^{m/(m+1)}$. Substituting the equivalent filament

thickness $b \sim r/2$ for cylindrical filaments into this solution suggests that \tilde{L} derived here has essentially the same functional form as the one proposed by Phoenix *et al.* with only a slight change in the coefficient [15]. It is clear that as m decreases, a larger critical link length \tilde{L} is required to apply weakest-link scaling. This is consistent with the observation in the Monte Carlo simulations by Landis *et al.* [16]. Similarly, for a large λ , Equation (9) can be approximated as

$$\sigma_0 \left(\frac{L_0 2^m}{2\tilde{L}} \right)^{1/m} \approx \frac{2\tau_f}{b\lambda} \quad (10)$$

Solving Equation (10) yields another typical solution $\tilde{L} = \left(\frac{\sigma_0}{\tau_f} \sqrt{\frac{2Gb}{Eh}} \right)^m \frac{L_0}{2}$. This solution takes

similar functional form as the one proposed by Landis *et al.*, yet includes more constituent mechanical properties and geometries [16]. Therefore, through rigorous mathematical derivation, the statistical shear lag model developed herein provides a more general solution that solves the ambiguity in the fundamental link length scale obtained in previous statistical models for fiber-reinforced composites, bridging the gap between earlier theories.

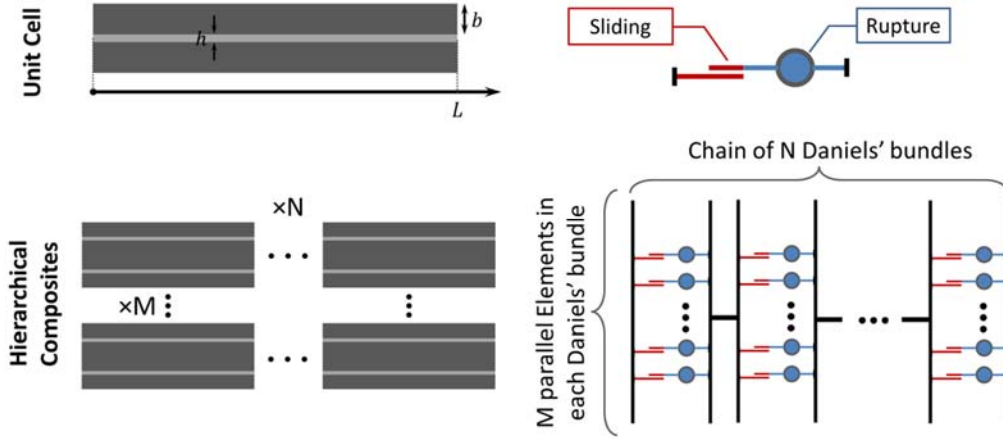


Figure 3: Schematic of the method used to scale up the statistical shear lag model. The unit cell for the shear lag model (top left) is simplified as an element (top right) that has two failure modes (filament-filament sliding or filament rupture). A macroscopic hierarchical composite consisting of $M \times N$ unit cells (bottom left) is simplified into the statistical model of $M \times N$ elements (bottom right). The cross-section is represented in the axial direction as a chain of N Daniels' bundles, and in the lateral direction as M parallel elements.

To extend the statistical shear lag model for evaluating the strengths of hierarchical composites, the following strategy was employed where the mechanical behavior of the unit cell was used as an input to investigate how the size of a macroscopic hierarchical composite is related to its strength. First, the unit cell (with length $L \geq \tilde{L}$) was simplified as an element consisting of two sub-elements connected in series; one sub-element represents filament rupture, and the other represents filament-filament sliding (see Figure 3). Therefore, a hierarchical composite consisting of $M \times N$ unit cells can be simplified into the statistical model consisting of $M \times N$ elements. The cross-section of the composite is modeled as a Daniels' bundle of M parallel unit cells aligned in the lateral direction that are evenly clamped at both ends [17]. Along the axial direction, the composite is simplified as a chain of N Daniels' bundles connected in series such that the composite has a total length $L_{comp} = N \cdot L$. Daniels' theory suggests that the strength of a bundle consisting of M unit cells whose strength distribution is a Weibull probability function exhibits a Gaussian distribution expressed as

$$G(\sigma_{eff}) = \frac{1}{2} \left[1 + \operatorname{erf} \left(\frac{\sigma_{eff} - \mu}{\sqrt{2\delta^2}} \right) \right]$$

in which,

$$\mu = \left(\frac{1}{m} \right)^{\frac{1}{m}} \exp \left(-\frac{1}{m} \right) \sigma_{0,eff} , \quad (11)$$

$$\delta^2 = \frac{1}{M} \left(\frac{1}{m} \right)^{\frac{2}{m}} \exp \left(-\frac{1}{m} \right) \left[1 - \exp \left(-\frac{1}{m} \right) \right] (\sigma_{0,eff})^2 , \text{ and}$$

$$\sigma_{0,eff} = \sigma_{0,un} \frac{b}{(2b+h)}$$

The strength of a composite consisting of N serially connected Daniels' bundles is governed by the weakest bundle and thus is distributed as

$$H(\sigma_{eff}) = 1 - \left[1 - G(\sigma_{eff}) \right]^N . \quad (12)$$

As shown by Phoenix and Raj[18], the Weibull approximation to $H(\sigma_{eff})$ takes the form

$$H(\sigma_{eff}) \approx 1 - \exp \left[- \left(\frac{\sigma}{\sigma'} \right)^{m'} \right] , \quad (13a)$$

with the composite Weibull scale factor σ' given by

$$\sigma' = \mu + \delta \left[\frac{\log(\log(N)) + \log(4\pi)}{\sqrt{8\log(N)}} - \sqrt{2\log(N)} \right] , \quad (13b)$$

and the composite shape factor m' given by

$$m' = \frac{\mu \sqrt{2\log(N)}}{\delta} + 2 \left[\frac{\log(\log(N)) + \log(4\pi)}{\sqrt{2\log(N)}} - \log(N) \right] . \quad (13c)$$

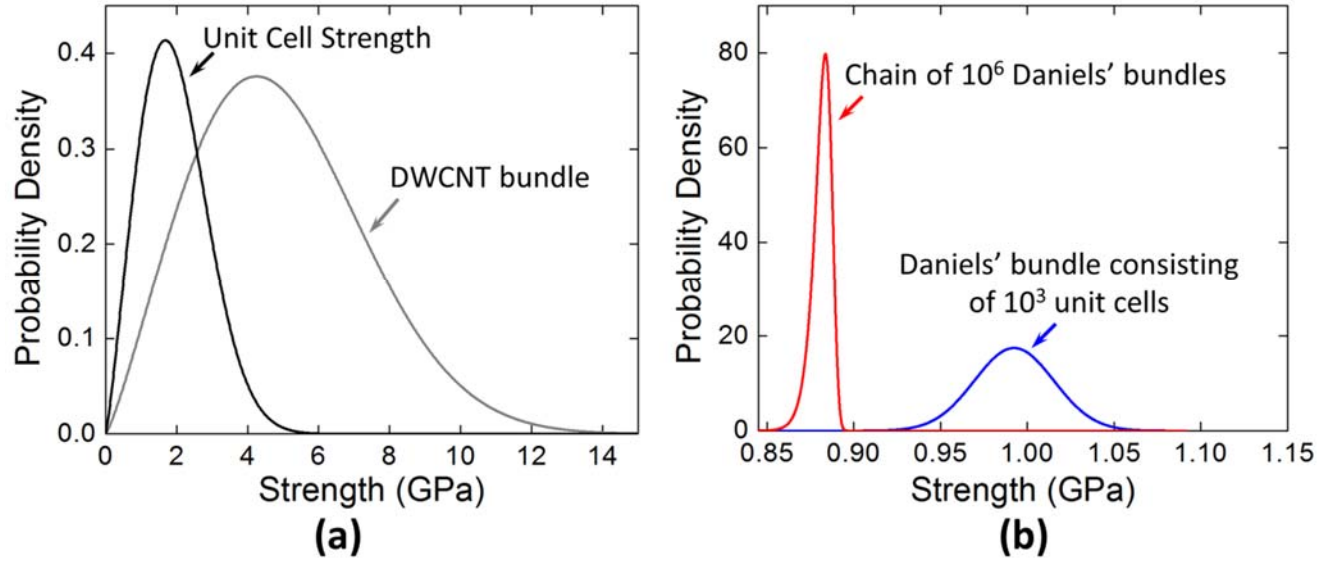


Figure 4: Probability density functions for different hierarchies in the DWCNT yarn. (a) The probability density functions of the DWCNT bundle rupture strength and unit cell strength; (b) The probability density functions of the Daniels' bundle strength (consisting of 10^3 unit cells) and the macroscopic yarn strength (consisting of 10^6 Daniels' bundles).

Clearly, there is a size effect with respect to the strength of composites with different hierarchies as a function of the filament material, the unit cell, and the composite size. To illustrate this size effect, a case study was performed on a DWCNT yarn consisting of unit cells with an overlap length of $2.5 \mu\text{m}$. The yarn contained 10^3 elements in the lateral direction and 10^6 Daniels' bundles in the axial direction. Figure 4 shows the probability density distributions for the strengths of $2.5 \mu\text{m}$ long and 30 nm diameter DWCNT bundle, a unit cell, Daniels' bundle of 10^3 elements (with a diameter of approximately $30 \mu\text{m}$), and a chain of 10^6 Daniels' bundles (i.e. a 2.5 meter long yarn). The Weibull distributions for DWCNT bundles and unit cells share the same shape factor, while the scale factor for the unit cell strength is lower than that for the DWCNT bundle strength. The strength of the yarn's cross section shows a Gaussian distribution. In contrast, the strength distribution of a chain of 10^6 Daniels' bundles exhibits a Weibull distribution function profile. Fitting the data yields a scale factor of approximately 0.9 GPa and a very high shape factor of 195 , in excellent agreement with the Weibull approximation (0.9 GPa and 203) given by Equations (13b) and (13c). This much higher shape factor as compared with that of 2.2 for individual DWCNT bundles indicates an increase in reliability as yarn length increases, which is consistent with previous reports [19].

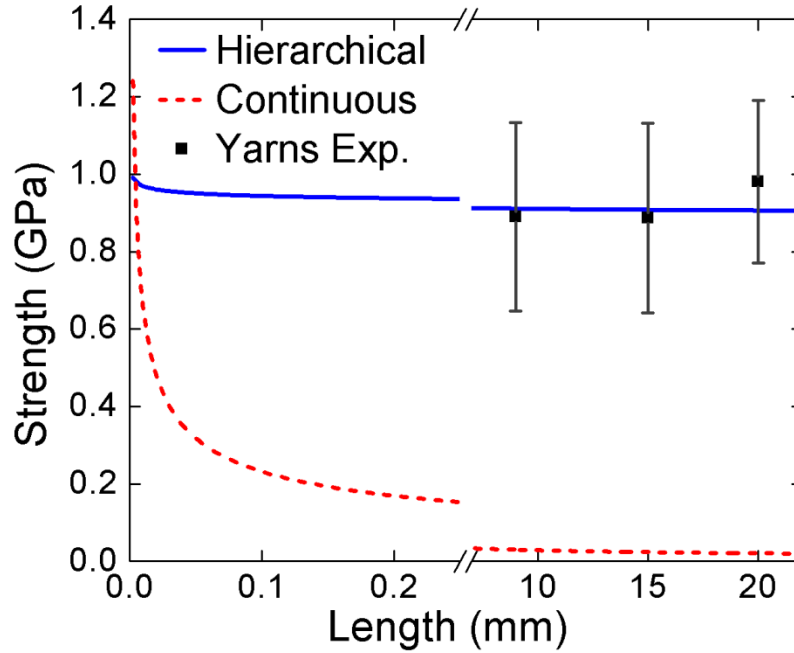


Figure 5: The predicted strength of the hierarchical DWCNT yarns as a function of yarn length demonstrates the suppressed length scale sensitivity. Experimentally measured DWCNT yarn strength at various gauge lengths are included to compare with the model prediction (the error represents the standard deviation of yarn strength).

More interestingly, the statistical model explains why a hierarchical structure is so important in material scaling up – from nanoscale constituents to macroscopic composites. Figure 5 shows that the mean strength value for the DWCNT yarn (a discontinuous hierarchical composite) depends barely on the yarn length – when the yarn length increases by 10^4 times (from $2.5\ \mu\text{m}$ to $2.5 \times 10^4\ \mu\text{m}$), the mean yarn strength drops by only 10% (from 1 GPa to 0.9 GPa). The model prediction agrees very well with the results from tensile experiments on DWCNT yarns [20]. The experimentally measured mean strengths at various yarn gauge lengths agree with the model predictions and do not show appreciable length dependence. Insensitivity of strength with respect to gauge length has also been observed in other composites containing natural or synthetic fibers, such as sisal fibers and carbon fibers [21-23], as they share the same deformation mechanisms. By obtaining the mechanical properties of the constituents through micromechanical experiments, this model could potentially be applied to those composites to gain further insights into the microstructure-property relationships. Thus, understanding why the hierarchical structures are common in most of the natural composites is straightforward – through this approach, which reveals the ability of discontinuous staggered composites to re-distribute load over characteristic length scales that are function of constituent geometry and mechanical properties. Hence, macroscopic natural composites can preserve remarkable mechanical properties when scaling up from the filaments usually in the nm or μm length scales.

A New Monte Carlo Yarn Model for Predicting Yarn Mechanical Properties

In this study, we developed a new Monte Carlo model for fiber which simulates the effects of stochastic fibril rupture and interface sliding history on the mechanical properties [24]. The interface is modeled as a soft thin layer that undergoes only shear deformation. The mechanical properties of the building blocks, fibril statistical strength and interface shear strength, are inputted from nanoscale experiments [11-13, 25]. The distinct bottlenecks for the mechanical performance of both types of yarns were identified using this model.

A twisted fiber yarn consisting of fibers in a hexagonal close-packing structure was assumed in our stochastic Monte Carlo model (Figure 1). Axial positions of individual fibers were randomly distributed to account for a random distribution of overlap lengths. Each fiber is discretized into a series of 1-D elements along the fiber axis, thus the normal stress in a fiber is uniform in the thickness dimension and only varies as a function of axial position.

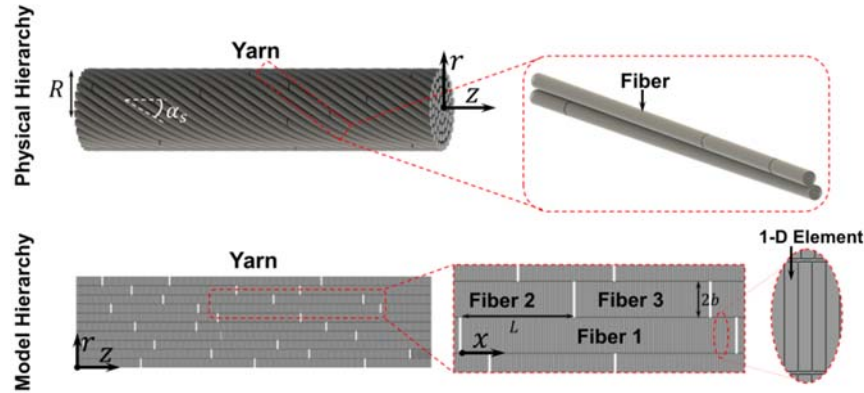


Figure 6: Schematics of idealized yarns depicting (left to right): the cross-sectional view of the yarn model, randomly distributed fibers (in this study, a fiber refers to a bundle consisting of 60 to 100 double-walled carbon nanotubes), and a fiber discretized by 1-D elements. (top) Hierarchical structure of a 3-D ideally twisted yarn consisting of hexagonal close-packed discontinuous fibers; (bottom) Yarn hierarchy in the Monte Carlo model (section view) reported here.

In a twisted yarn, it is necessary to transform fiber strains between the individual fiber axis and yarn axis along which the external load is applied. As noted by Hearle et al. [26], the relationship between the applied yarn strain ε_y and the fiber strain ε_f , at radial position r , is given by

$$\varepsilon_f(r) = \varepsilon_y \left(\cos^2 \alpha_r - \nu_T \sin^2 \alpha_r \right), \text{ where } \alpha_r = \tan^{-1} \left(\frac{r}{R} \tan \alpha_s \right) \quad (14)$$

where R is the yarn radius, α_s is the twist angle at the yarn surface, α_r is the twist angle of the fiber at radial position r , and ν_T is the Poisson's ratio of the yarn.

Unlike the static friction law in previous models [27, 28], the load transfer between fibers in the current model is through interfaces that have well-defined mechanical properties, i.e., shear modulus G and shear strength τ_f . Note, however, that load transfer may not occur within all pairs of adjacent fibers. We therefore implemented an algorithm in our model to discriminate “effective” and “ineffective” contacts between two adjacent fibers based on their relative positions according to the following rules: 1) If one end of a fiber lies between the two ends of

the adjacent fiber, the contact is defined as “effective”, meaning that load can be effectively transferred between the two adjacent fibers through their interface (for example, the contact between fibers 1 and 2 in Figure 6). For an “effective” contact, the elastic solution for the shear lag model was used to calculate the maximum tensile stress distribution in each fiber, along the overlap region L , that can be transferred via the interface [7]:

$$\sigma(x) = \frac{2\tau_f}{b\lambda} \frac{1}{\cosh\left(\frac{\lambda L}{2}\right)} \sinh\left(\frac{\lambda x}{2}\right) \cosh\left(\frac{\lambda(L-x)}{2}\right), \quad (15)$$

where $\lambda = \sqrt{2G/(Ebh)}$, E is the fiber elastic modulus, G is the interface shear modulus, τ_f is the interfacial shear strength, h is the interface thickness. The equivalent fiber thickness is $2b = A/(nw)$, in which A is the cross-sectional area, w is the contact width, and n is the total number of effective contacts for a fiber with its nearest-neighbors [7]. If a fiber is shorter than the adjacent fiber, and both ends of the first fiber are completely enclosed by the adjacent fiber (for example, the contact between fibers 1 and 3 in Figure 6), the contact is defined as “ineffective.” The load transfer through an “ineffective” contact is neglected in the present study for the following reasons: First, the main mechanism for a macroscopic yarn to carry external loads is the load transfer between two fibers that are in effective contact. In contrast, when a long fiber fully encloses a short fiber to form an ineffective contact, the load on the long fiber is just redistributed within the contact by the short fiber. This stress redistribution within an ineffective contact pair does not affect the overall load carrying capability of the macroscopic yarn significantly. Second, whether a contact is effective or not, a relative axial displacement between two fibers is essential for the load transfer or redistribution. In an effective contact, two fibers tend to slide relative to one another. By contrast, having a relative axial displacement is more difficult for two fibers in an ineffective contact. Thus, for the same axial contact length, the stress distribution is affected more by the effective contact than by the ineffective contact. In the investigated yarns, since the fibers are hexagonally close-packed, each fiber has 6 contacts with its neighbors. Therefore, even if there is one ineffective contact out of the 6 pairs, the load distribution in the fiber is still dominated by the load transfer through the remaining effective contacts.

Note that although the tensile stress distribution solution given by Equation (3) is from the shear lag analysis for two parallel fibers in an effective contact, it can be extended to twisted fiber yarns by introducing pressure dependence to the interface properties (such as shear modulus G and shear strength τ_f). When a twisted yarn is under tension, a transversal pressure between fibers will develop in the cross-section, which will affect the interfacial shear properties. By performing atomistic simulations, one can obtain the relationship between the shear modulus G (as well as the shear strength τ_f) and the lateral pressure P for fibers (e.g. CNT bundles in the present study) sliding relative to one another. With the inputs of pressure dependent shear modulus $G(P)$ and shear strength $\tau_f(P)$, the extended shear lag analysis will provide a more precise description of the stress distribution for twisted fibers than the static friction assumption in previous models [27-29].

In addition, since load is transferred between adjacent fibers through shear forces, reducing the density of nearest-neighbor fibers leads to a reduction in the load-bearing capacity of the material. We model distributed micro-porosity by decreasing the maximum shear stress between fibers by a multiplication factor of $(1 - p)$, for a yarn with porosity p .

The elastic shear lag solution gives the maximum tensile stress the elements along the overlap distance can carry before the interface slides (i.e. the shear stress at the interface reaches τ_f).

However, the true maximum tensile stress that can be applied on the elements is limited by the fiber strength. This brings another important failure mode – fiber rupture – into the model. CNT strength is extremely sensitive to the inherent defects that arise from manufacturing processes. Experimental studies [30-32] have shown that the CNT strength can be described by the Weibull distribution function expressed in Equation (1) in which the scale factor (the strength at which approximately 63% CNT samples fail) depends on gauge length. Therefore, to take into account the variation in fiber strength and define the initiation and progression of fiber fragmentation, a random strength value needs to be assigned to the individual element. Similar to the approach used in the aforementioned previous models, the element strength values are chosen from a reservoir of random numbers generated by the Weibull distribution function

$$P(\sigma) = 1 - \exp\left[-\frac{L_b}{L_0}\left(\frac{\sigma}{\sigma_0}\right)^m\right]$$

with L_b replaced by the 1-D fiber element size, L_e . However, we

note that this approach raises the element size dependence issue. For example, for an extremely small element size, the scale factor of the Weibull function might be even greater than the theoretical strength of the fiber σ_{th} , which is unphysical. To avoid this issue, a minimum length

scale $L_{min} = -L_0 \left(\frac{\sigma_0}{\sigma_{th}}\right)^m \log 10^{-2}$ was used in the model to limit the scale factor in the Weibull

function that creates the element strength reservoir. Thus, L_{min} has the physical meaning of being the average distance between defects. It assures that only 1% of element strength values exceed the theoretical fiber strength so that the Weibull scaling will not significantly affect the fiber fragmentation progression.

The maximum stress an element can carry should be the minimum of two values – the maximum stress that can be transferred through the interface before sliding or the element strength. During simulations, an increasing elongation was applied to the yarn in steps, and the strain value on individual fiber was determined according to Equation 14. Then, the stress was distributed on the elements of fibers assuming the fibers are linear elastic. In each step, the distributed stress was compared with the maximum allowable stress of each element to determine whether interface sliding or fiber rupture occurs. If rupture occurred, two new fibers were created and the stress at the fragmentation location was set to zero. The model re-evaluated the effectiveness of each new fiber with their nearest-neighbors and the stress was redistributed. The iteration stopped when no new fiber breaks occurred in the current step and equilibrium was satisfied at all cross sections. Then an increasing load was applied to the yarn in the next step. The yarn was deemed as having failed when no additional load could be equilibrated. It should be noted that a full description of load transfer within a yarn requires solving equilibrium and compatibility at each point simultaneously. In the current model, to save computational cost, the load-sharing rules, as implemented, only ensure force equilibrium. The plastic portion of the yarn deformation due to

interface sliding was not specifically accounted for. Based on this simplification, the model was aimed to predict the ultimate stress where the yarn fails rather than describe the full stress-strain response.

The goal of this study was to develop a Monte Carlo model from the micro/nanomechanics of CNT building blocks to predict the average value and distribution of fiber yarn strength. Therefore, accuracy of the statistical results was evaluated carefully. Model results showed that the yarn strength distribution approaches a Gaussian distribution function as the simulation number is increased. The mean and standard deviation converged for more than 100 simulations. In addition, we found that the model result became mesh independent when the element size was less than $0.5\lambda^{-1}$ where $\lambda = \sqrt{2G/(Ebh)}$. In this report, an element size of $0.2\lambda^{-1}$ was used and 100 simulations were performed for each case to obtain the mean and standard deviation of the yarn strength.

To demonstrate the model's predictive capabilities, case studies were performed on two types of yarns fabricated from different CNT sources. The first type was manufactured by dry spinning from double-walled carbon nanotube (DWCNT) mats produced by MER Corporation and characterized at Northwestern University (denoted as “NU yarns”) [11]. The second type were multi-walled carbon nanotube (MWCNT) yarns fabricated at Rice University using the wet-spinning method, here termed “Rice yarns” [33].

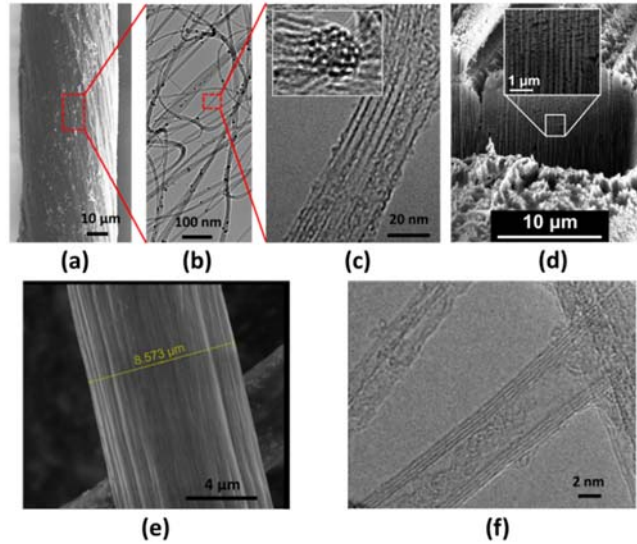


Figure 7: top) From left to right: Images displaying the hierarchy of DWCNT yarns studied at Northwestern University. (a) SEM image of a NU yarn. (b) TEM image of interconnected DWCNT bundles picked from mats. (c) TEM image of individual DWCNT bundle with the inset image showing a cross section of an individual bundle. (d) A well was micromachined into a NU yarn using focused ion beam (FIB) to reveal the internal porosity. The inset highlights the porosity in the cross-section of the yarn. (bottom) From left to right: Images of the hierarchy of MWCNT yarns studied at Rice University (images are adapted from [33]). (d) SEM image of a Rice yarn. (e) TEM image of an individual MWCNT.

Figure 7 shows the hierarchy of the NU yarn down to individual fibers (i.e. double-walled carbon nanotube (DWCNT) bundles in this case). Each DWCNT bundle consists of tens of hexagonally closed-packed DWCNTs and bundle diameter ranges from 10-30 nm. Individual DWCNTs have

an outer diameter of 2.2 nm. X-ray photoelectron spectroscopy (XPS) and Fourier transform infrared (FTIR) spectroscopy characterizations determined that an inherent polymer coating (approximately 2.5 nm thick) exists on the bundle surface [13]. The mechanical properties of individual DWCNT bundles and bundle-bundle interfaces were characterized through nanoscale experiments and atomistic computations. By pooling DWNT bundle strength data from tensile strength experimental results previously reported [11-14], Weibull analysis on individual DWCNT bundles (30 nm diameter and 5 μm length in average) yielded a scale factor $\sigma_0 = 2.8$ GPa and a shape factor $m = 2.2$ (Figure 3a). Note that the stress is defined here as the load on the bundle divided by the cross-sectional area of all DWCNTs within the bundle. This should be discriminated from the “true stress” that is defined as the load divided by the cross-sectional area of only the DWCNTs on the outer layer of the bundle. The interface properties were obtained from in-situ scanning electron microscope (SEM) shear experiments on pairs of parallel bundles [13]. According to the shear lag model analysis, the applied stress that causes the bundle-bundle junction to slide is a function of the overlap length L as:

$$\sigma_{\text{junction}} = \frac{2\tau_f}{b\lambda} \tanh\left(\frac{\lambda L}{2}\right). \quad (16)$$

Fitting the experimental shear results with Equation (16) revealed an effective shear modulus of $G = 10$ MPa and shear strength $\tau_f = 350$ MPa (see Figure 8).

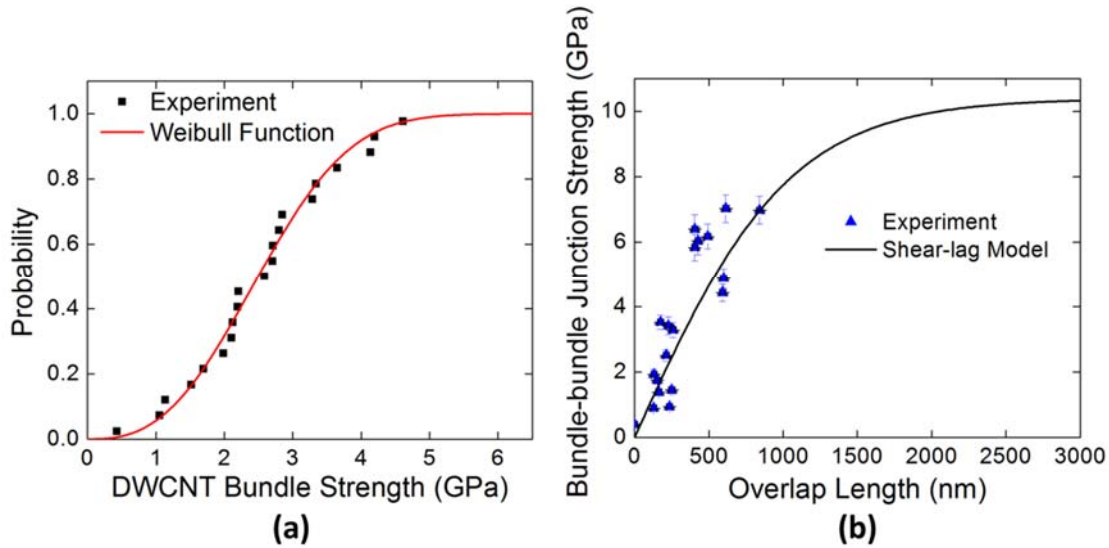


Figure 8: Mechanical properties of building blocks for NU yarns. (a) Weibull analysis on the individual DWCNT bundle strength compared to experimental values reported previously (T Filleter et al., 2011; Mohammad Naraghi et al., 2013; Mohammad Naraghi et al., 2010; Dmitry Papkov et al., 2012). (b) Fit of the experimental shear results for pairs of parallel DWCNT bundles reported previously (Naraghi, Bratzel et al. 2013) using the shear lag model.

In Rice yarns, the constituent fibers are individual MWCNTs with an average length of 5 μm and an average diameter of 3.2 nm. The mechanical properties of these MWCNTs were not characterized here, and therefore were approximated from independent studies. Tensile tests on MWCNTs performed by Yu et al. [34] yield a scale factor of 31.5 GPa, where the stress was

defined by assuming only the outer shell of a MWCNT bears the load, and a shape factor of 2.4. By converting the stress value to an effective stress by accounting for the cross-sectional area of all of the shells, the scale factor used for the MWCNTs in Rice yarns was approximated as 14.8 GPa, while the shape factor remained the same. The interface properties between MWCNTs were estimated from the in-situ SEM shear experiments on pairs of parallel bare MWCNTs [7]. Adopted from reference [7], the interfaces between MWCNTs in Rice yarns were assumed to have a shear strength of 60 MPa and a shear stiffness of 100 MPa. Note that molecular dynamics and density functional theory calculations suggest that the shear interaction between CNTs highly depends on the tube chirality and vacancy defects ([35, 36]). The shear strength between a pair of chiral tubes (i.e., a turbostratic stacking instead of AB stacking of the shells in contact) might be as low as 0.24 MPa. On the other hand, presence of vacancy defects in tubes will increase the shear strength. To have a better estimation of the interface properties for Rice yarns, shear experiments on the constituents in those yarns are needed. In this study, the interface properties reported by Wei *et al.* are used as a first approximation.

The properties of fibers and interfaces for NU and Rice yarns are summarized in Table 1. The theoretical strength of 30 nm diameter DWCNT bundles in NU yarns was estimated by assuming that the outer shells of the DWCNTs on the outer layer of the bundle fail at 100 GPa, the theoretical strength of a single shell of a CNT[37]. Similarly, the theoretical strength of a MWCNT in Rice yarns was estimated by assuming that the outer shell of the MWCNT fails at 100 GPa.

Table 1: Mechanical properties of fibers and interfaces for NU and Rice yarns.

	Fibers	Fiber diameter (nm)	Fiber length, L_b (μm)	E (GPa)	σ_0 (GPa)	m	σ_{th} (GPa)
NU yarns	DWCNT bundles	10-30	≥ 5	60	2.9	2.7	20.2
Rice yarns	MWCNTs	2-6	5	400	14.8	2.4	42.3
	Interface thickness (nm)		Effective interface shear modulus (MPa)		Interface shear strength (MPa)		
NU yarns	2.5		10		350		
Rice yarns	0.34		100		60		

In order to verify the Monte Carlo modeling algorithm proposed in this study, a coarse-grained molecular dynamics simulation was performed on a small benchmark yarn, and the results were compared with those predicted by the Monte Carlo model on the same system. The benchmark yarn is 25 μm long and 10 nm in diameter, and contains 95 (10,10)-(16,16) DWCNTs in total (see the schematic in Figure 9a). The yarn cross-section is made of 19 tubes in hexagonal close packing, and four randomly distributed breaks determined five tubes in the longitudinal direction (i.e. the average tube length is 5 μm). The bead-spring coarse-grained model developed by

Cranford *et al.* for DWCNTs was used to perform a tensile test on the benchmark yarn [38]. In the coarse-grained model, the total energy of the system is expressed as:

$$E_{system} = E_b + E_\theta + E_{pairs} \quad (17)$$

where E_b , E_θ and E_{pairs} represent the energy stored in chemical bonds due to axial stretching, bending and due to weak interactions, respectively. These energy contributions are represented, respectively, by:

$$E_b(r) = \frac{k_b}{2}(a - a_0)^2 \quad (18)$$

$$E_\theta(\theta) = \frac{k_\theta}{2}(\theta - \theta_0)^2 \quad (19)$$

$$E_{pairs}(d) = 4\varepsilon \left[\left(\frac{\delta}{d} \right)^{12} - \left(\frac{\delta}{d} \right)^6 \right], \quad (20)$$

in which a is the bond length between two connected beads, θ is the bond angle, and d is the distance between two non-bonded beads. Calibrated through full-atomistic simulations, the parameters for (10,10)-(16,16) DWCNTs were determined as: $k_b=2000 \text{ kcal mol}^{-1} \text{ \AA}^{-2}$ is the tensile stiffness of bonds, $a_0=10 \text{ \AA}$ is the equilibrium bond distance, $k_\theta=45000 \text{ kcal mol}^{-1} \text{ rad}^{-2}$ is the bending stiffness related to equilibrium bond angles, $\theta_0=180^\circ$ is the equilibrium bond angle, $\varepsilon=21.60 \text{ kcal mol}^{-1}$ is the Lennard-Jones energy well depth at equilibrium, and $\delta=22.63 \text{ \AA}$ is the Lennard-Jones distance parameter [39]. In order to simulate tube rupture, the original harmonic potential function in Equation (18) was modified as

$$E_b(r) = \begin{cases} \frac{k_b}{2}(a - a_0)^2, & \text{for } a < a_{cut} \\ 0, & \text{for } a \geq a_{cut} \end{cases} \quad (21)$$

where a_{cut} is the cutoff length defining bond rupture. Since the harmonic potential function describes a linear-elastic stress-strain relationship for tubes under tension, the cutoff length can be related to the bond strength σ_f by:

$$a_{cut} = \left(1 + \frac{\sigma_f}{E} \right) a_0, \quad (22)$$

where $E = 400 \text{ GPa}$ is the DWCNT elastic modulus [13].

The coarse-grained model for the benchmark yarn consists of 474,905 beads and 474,791 bonds. Using the algorithm discussed in Section 2.3, a reservoir of 474,791 bond strength values was generated using the Weibull distribution function with the scale and shape factors for the tube strength in Rice yarns listed in Table 1 (see Figure 9b). Accordingly, the Monte Carlo model

contains also 474,791 1-D elements and the same tube configurations as in the coarse-grained model. The strength values from the same reservoir were assigned to the elements.

The coarse-grained simulation was carried out using the molecular dynamics package LAMMPS with a time step of 10 fs [40]. The yarn was first minimized using a conjugated gradient algorithm, and then relaxed to reach equilibrium using the isothermal-isobaric (NPT) ensemble for 5 ns at 300K. Then, the two ends of the yarn were displaced to apply a tensile test with a strain increment of 0.01% until the yarn failed due to tube-tube sliding. After each strain increment, the system was relaxed for 0.25 ns using the canonical (NVT) at 300K. For direct comparison, the same strain increment (0.01%) was used in the Monte Carlo model until the yarn failed. The stress vs. strain curve predicted by the coarse-grained model is shown in Figure 4c. The maximum yarn strength (1.02 GPa) given by the coarse-grained model agrees well with the value predicted by the Monte Carlo model (1.16 GPa). Furthermore, the accumulated tube ruptures as a function of the applied stress were compared in Figure 4d. In the coarse-grained simulation, the first tube rupture occurred when the yarn stress reached 0.82 GPa. The earliest tube rupture was observed in the Monte Carlo simulation at a very similar stress level (0.76 GPa). At peak stress, 113 tube ruptures were observed in the coarse-grained simulation, slightly higher than the 91 observed in the Monte Carlo simulation. This can be explained by the fact that the load transfer between “ineffective” contacts is neglected in the Monte Carlo model. Thus, using the coarse-grained model trained for DWCNTs, we have shown that the new Monte Carlo model developed herein can correctly and efficiently predict yarns’ strength and provide valuable details about the fragmentation of constituent fibers. This justifies our application of the Monte Carlo model to predict the behavior of two realistic CNT yarns synthesized, characterized, and measured in two different groups in the following section.

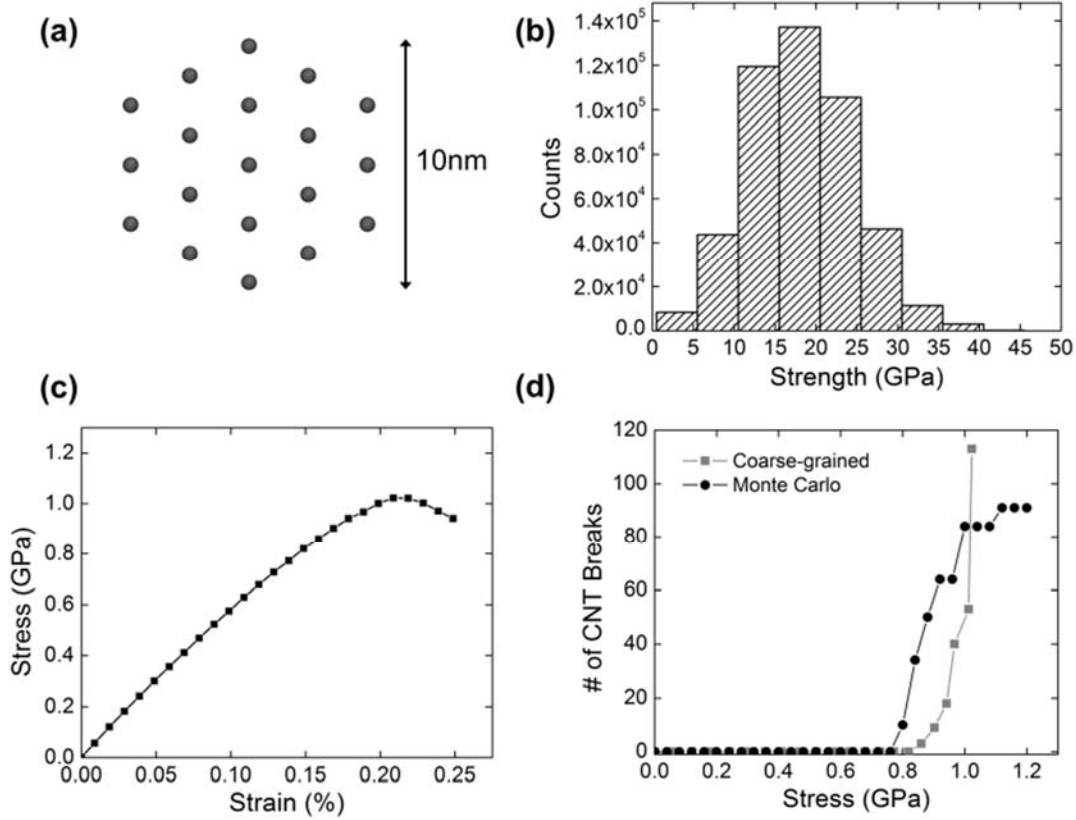


Figure 9: Verification of the Monte Carlo model by Coarse-grained simulations. (a) Front view (top) and side view (bottom) of the benchmark yarn. (b) Histogram of the strength values for tube bonds in coarse-grained model and 1-D elements in Monte Carlo model. (c) Stress vs. strain curve predicted by coarse-grained model. (d) Comparison between numbers of tube breakage predicted by coarse-grained model and Monte Carlo model.

Monte Carlo simulations were performed on both types of yarns listed in Table 1. Each yarn in the simulation was composed of 10 fibers along the yarn radius and 4 fibers along the yarn axis, for a total of 320 fibers. For each system, 100 Monte Carlo simulations were performed, and the average and standard deviation of the yarn strength were calculated. At the beginning of each simulation, the Weibull scale and shape factors listed in Table 1 were used to assign randomly distributed fiber element strengths using the algorithm discussed in Section 2.3. When an external load was applied on the yarn, the resulting stress distribution on fibers was determined using the load-sharing rule discussed in Section 2.4 with the mechanical parameters of the fibers and interfaces listed in Table 1 as inputs. The external load kept increasing until no additional load could be equilibrated, and the maximum external load was recorded as the yarn strength.

X-ray and electron microscopy studies on Rice yarns revealed 5 μm long MWCNTs aligned nearly perfectly along the axial direction, with no appreciable yarn porosity [33]. Therefore, the actual microstructure in Rice yarns is very close to the *idealized* yarn structure assumption presented here. By contrast, NU yarns have much more complicated microstructures that feature DWCNT bundle misalignment and entanglement as well as non-negligible yarn porosity ranging from 50%-80%. In addition, the bundle geometries have noticeable variations. The majority of the bundle diameters are approximately 30 nm, but they can be as small as 10 nm. The distribution of bundle lengths is very difficult to precisely characterize. We speculate a range

from 5 to 60 μm based on SEM characterization of protruding bundles at the fracture surfaces of yarns. Nonetheless, it is very impractical to consider all these variations in the model. To provide useful insights for NU yarns, the model only selectively took into account critical factors. Simulations were performed first with the ideal helical twisted geometry to predict an upper bound of average yarn strength by neglecting complex features such as bundle misalignment and entanglement. As a baseline, 30 nm bundle diameter and 5 μm bundle length were assumed in the model. The model then examined the effects of porosity and bundle size on the NU yarn strength. As shown in Figure 8b, the load transfer between bundles tends to saturate at an overlap length of 1.5 μm ; therefore, the 5 μm bundle length assumption in the baseline simulations was appropriate given that our model does not account for bundle migration. For this reason, simulations performed on 60 μm long bundles did not yield any appreciable difference.

Table 2: Comparison between experimentally measured and model predicted strength for NU yarns and Rice yarns

	Surface twisting angle, α_s	Porosity, p	Experimental yarn strength	Predicted yarn strength
NU yarns	$\sim 15^\circ$	$\sim 60\%$	$0.95 \pm 0.4 \text{ GPa}$	$0.84 \pm 0.04 \text{ GPa}$
Rice yarns	$\sim 0^\circ$	$\sim 0\%$	$1.0 \pm 0.2 \text{ GPa}$	$1.2 \pm 0.07 \text{ GPa}$

Our model predicts the average strength of Rice yarns as $1.2 \pm 0.07 \text{ GPa}$. For the ideally twisted NU yarns consisting of 30 nm diameter and 5 μm long bundles, the predicted yarn strength was $1.45 \pm 0.07 \text{ GPa}$. Shown in Figure 5a are the distributions of predicted yarn strength for NU and Rice yarns, suggesting that for both materials the strength distribution is virtually normal. Even though the predicted strength values for both yarns were similar, the model reveals different dominant failure mechanisms. As shown in Figure 5b, for the ideal NU yarn, the first bundle rupture occurred very early, at a small applied stress of 0.2 GPa, and the rupture rate accelerates gradually until the yarn fails. In the end, a total of approximately 3000 new bundles were generated due to rupture, almost 10 times the original number of bundles. This suggests that in the idealized NU yarns, the bundle strength is the limiting factor in the yarn performance. By contrast, MWCNT rupture in the Rice yarn occurred much later, at a high applied stress of 1.0 GPa (in the Weibull distribution tail for the MWCNT strength), and the total number of ruptured tubes only reached 12 when yarn failure occurred due to tube sliding and pull-out. This suggests that the interface strength is the limit for the Rice yarns' performance.

As discussed previously, the effective shear strength between bundles will be affected by yarn porosity. FIB and SEM characterizations on NU yarns indicated that the porosity ranges from 50%-80% (60% on average). Figure 10c shows that the predicted NU yarn strength drops approximately linearly with yarn porosity up to 80%, due to the previous assumption that the maximum shear strength between fibers decreases by a factor of $(1-p)$. As the porosity increases, the effective interface shear strength weakens because individual bundles have fewer bundle-bundle contacts. Thus, the dominant failure mechanism becomes interface sliding. For example, the final number of bundle ruptures for 60% porous NU yarns is only 382 at an ultimate stress of 0.84 GPa compared with 1494 for the ideal helical NU yarns at an ultimate stress of 1.45 GPa; thus, a more porous yarn results in less effective bundle strengths within the yarns.

Finally, the effect of bundle diameter was examined. As noted by Filleter et al. [12], since the DWCNTs on the outer layer of the bundle carries the load, the effective bundle strength, which is defined by the load divided by the cross-sectional area of all the DWCNTs, is highly dependent on the bundle diameter. When the bundle diameter decreases, the ratio of the number of external to internal tubes increases, and the effective bundle strength will increase. Figure 10d predicts that the average yarn strength could reach 4 GPa if the bundle diameter were reduced to 10 nm.

In summary, our model predictions are compared with experimental values in Table 2. The model prediction for Rice yarns (1.2 ± 0.07 GPa) agrees favorably with the experimental measurement (1.0 ± 0.2 GPa). For NU yarns with 60% porosity, the predicted yarn strength (0.84 ± 0.04 GPa) also agrees well with the experimental measurement (0.95 ± 0.4 GPa). The model predicted standard deviations for both materials that were smaller than the experimental values, especially for NU yarns. This is to be expected for this simplified model in which complexity such as fiber misalignment, entanglement, and waviness were not considered.

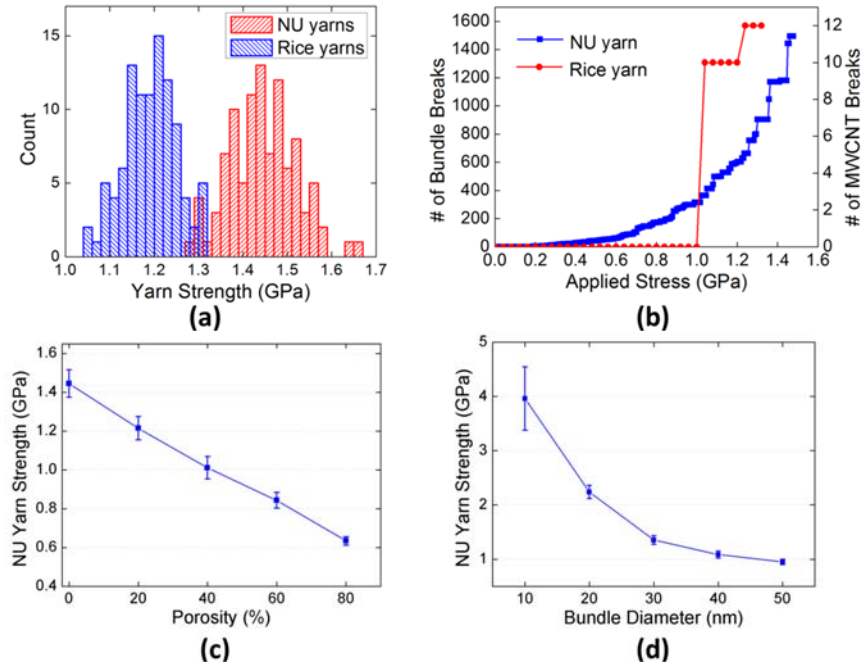


Figure 10: Model Predictions for NU and Rice yarns. (a) Distribution of Monte Carlo model-predicted yarn strengths for ideally twisted NU and Rice yarns. (b) Number of fiber ruptures as a function of the applied axial stress as predicted by the Monte Carlo model. (c) Predicted decrease in yarn strength due to the porosity in NU yarns. (d) Predicted yarn strength as a function of bundle diameter for NU yarns.

Quantifying Adhesion of Chemically Functionalized Carbon Nanotube/Graphite Interfaces

In addition to simulating the global effects that variations in CNT filament properties have in yarns, at a fundamental level, we also explored adhesion between chemically functionalized carbon nanotube/graphite interfaces. Indeed, weak inter-filament van der Waals interactions are potentially a significant roadblock in the development of carbon nanotube (CNT) and graphene-based nanocomposites. Chemical functionalization is envisioned as a means of introducing

stronger intermolecular interactions at nanoscale interfaces which, in turn, could enhance composite strength.

Here we explored the effect of chemical functionalization on the adhesion of nanoscale interfaces between multiwalled carbon nanotubes (MWCNTs) and highly-ordered pyrolytic graphite (HOPG) [41]. We introduced aryl-propionic acid groups (Figure 1) onto these materials to enable hydrogen bonding mechanisms at the interface. We experimentally quantified the adhesive energy, the reversible work of creating the exposed surfaces (i.e., twice the surface energy) as well as the irreversible work of separation during peeling, by peeling MWCNTs from HOPG *in situ* in a scanning electron microscope. We compared these results with our previous peeling study of bare nanoscale graphitic interfaces [42] to explore the possibility of improvements in adhesion associated with chemical functionalization. We also develop atomistic models to explain changes in surface energy (γ) and adhesive energy ($2\gamma + \text{dissipated energy}$) and provide insight into deformation mechanisms at the interfaces between these materials. Our integrated computational-experimental approach provides a means of screening potentially useful functionalizations through computational models and then verifying the adhesion predictions experimentally, enabling the bottom-up design of strong, lightweight composites that effectively leverage the exceptional mechanical properties of carbon nanomaterials.

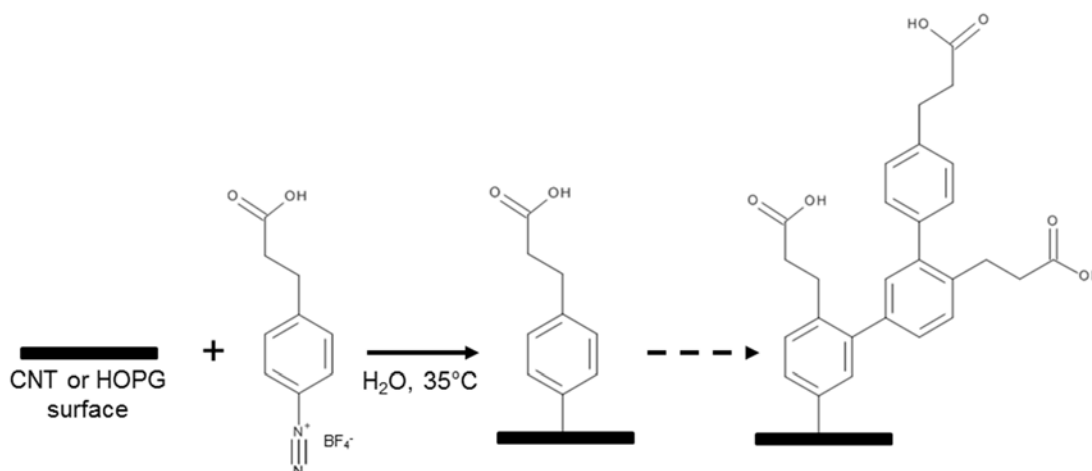


Figure 11: Functionalization of the graphitic surfaces of MWCNTs and HOPG was performed using diazonium chemistry.

Arylpropionic acid functionalization was carried out by the Nguyen group at Northwestern University [41]. Briefly, carbon nanotubes and graphite were functionalized with arylpropionic acid (Figure 11) using diazonium chemistry techniques [43]. AFM scans were conducted to confirm that bare and functionalized surface roughness were minimal (Figure 12) and, thus, expected to have negligible effect on the adhesive energy measurements. Raman spectroscopy (Figure 12b) was also conducted to determine if changes in the “D” peak, corresponding to defect density within the HOPG surfaces, could be observed. The appreciable rise in the D peak of functionalized samples compared to control HOPG and oligomerized samples suggested that covalent bonding of functional groups did take place. However, as discussed later, these results alone cannot determine whether functionalized monomers or oligomers bonded to the surfaces of HOPG, which could have significant implications for the experimental measurements.

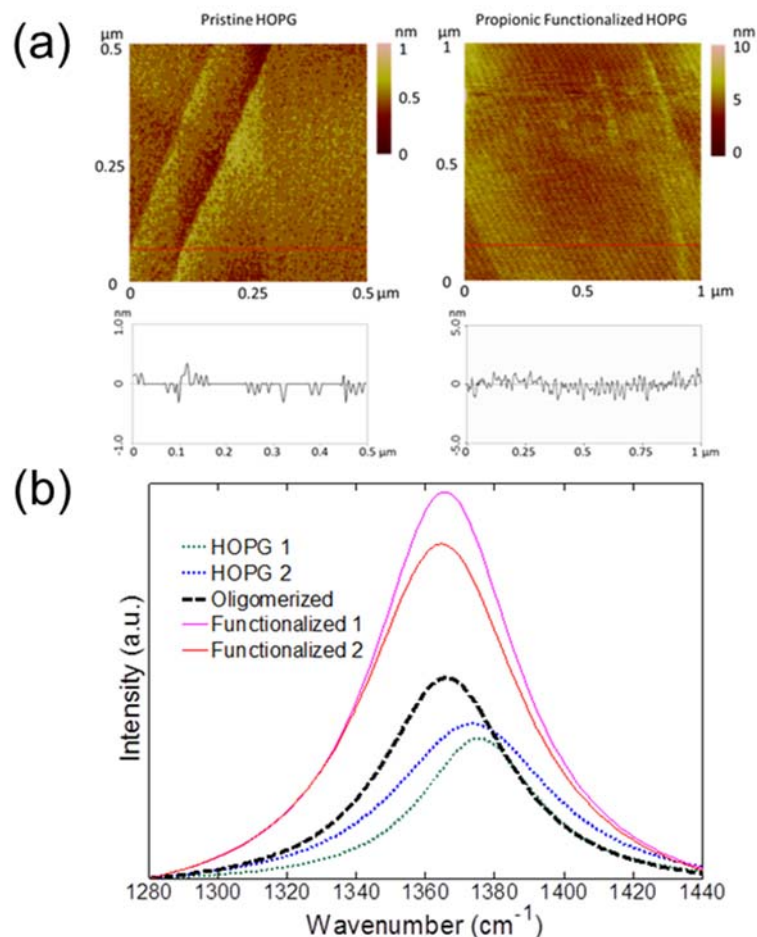


Figure 12: Characterization of MWCNTs and HOPG. (a) Non-contact mode AFM topography scans of pristine and functionalized HOPG. Height profiles of representative line scans are shown below. (b) Lorentzian fits of D peaks for bare, oligomerized (control), and propionic acid functionalized HOPG.

Following these sample preparation and characterization steps, peeling tests were conducted using the same methodology as our previous study on bare MWCNT-graphene and MWCNT-HOPG interfaces [42]. A schematic representation of the experimental setup is shown in Figure 3. Briefly, an AFM cantilever (of known stiffness) extending from a nanomanipulator was brought into contact with a MWCNT *in situ* in an SEM. The $\sim 5 \mu\text{m}$ -long CNT was cut using a focused electron beam and welded to the cantilever *via* amorphous carbon deposition. The tube was then brought into contact with the graphite substrate attached to the SEM stage. Finally, by retracting the stage, the tube detached from the substrate through successive small peels (approximately a hundred nanometers in length). The AFM cantilever deflection and tube profile were recorded at regular intervals to facilitate the evaluation of the applied force and pulling angle at the onset of peeling. A schematic of this testing procedure, as well as an illustration of the scale at which atomistic simulations (conducted by the Schatz group at Northwestern University [41]) are shown in Figure 13.

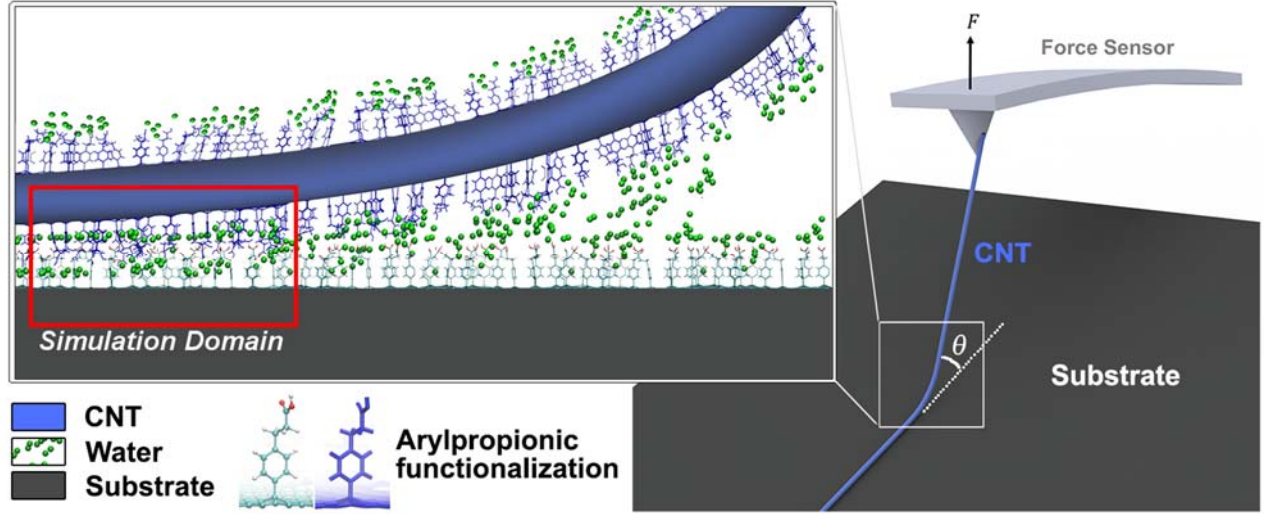


Figure 13: Experimental setup and simulation domain. In the experiments, an AFM cantilever (force sensor) with an attached CNT is brought into contact with an HOPG substrate within an SEM. As the substrate is pulled away, the force F on the CNT and angle θ with respect to the substrate are monitored. In the simulations, graphene bilayers functionalized with propionic groups are used to explore the geometries and energetic associated with peeling.

The adhesive energies were estimated using an analysis developed by Kendall [44]. Kendall's formula, which assumes an energy balance and no dissipation outside the vicinity where the actual separation occurs (i.e., only local dissipation), states

$$F(1 - \cos(\theta)) = R w - \frac{F^2}{2\pi E d t} \quad (23)$$

where F is the applied force, θ is the peeling angle, R is the adhesive energy, w is the effective contact width, E is the elastic modulus of the CNT (taken to be 1 TPa [34, 37]), d is the diameter, and t is the thickness of the outermost wall (which is expected to bear the majority of the load [37]). The term on the left corresponds to work done by the cantilever, while the first and second terms on the right denote the energy required to create new surfaces and the elastic strain energy of the tube, respectively. Rearranging for the parameter of interest, R ,

$$R = \frac{1}{w} \left\{ F(1 - \cos(\theta)) + \frac{F^2}{2\pi E d t} \right\} \quad (24)$$

As noted by Kendall [44], the adhesive energy R measured experimentally includes the work of adhesion as well as local dissipation. If non-local dissipation (e.g., tube or graphite plasticity) is important in a system, Kendall-based estimates of the adhesive energy will be higher than twice the surface energy. In the ideal limit where free surfaces are created without dissipation, the adhesive energy can be equated to the work of adhesion, or twice the surface energy (i.e., 2γ).

To evaluate the adhesive energies of arylpropionic-functionalized interfaces, two CNTs with 1:10 functionalization and two CNTs with 1:30 functionalization were peeled from 1:35 functionalized HOPG substrates. As noted earlier, multiple small peels were induced during a

given test, enabling several data points to be extracted per test. Detailed experimental results, including forces and peeling angles for each peel with functionalized materials, are reported in Table 3.

Table 3: Functionalized Peeling Experimental Results.

<i>Func. Level</i>	<i>Tube #</i>	<i>Peel Angle, θ [°]</i>	<i>Force, F [nN]</i>	<i>Outer Diameter [nm]</i>	<i>Number of Walls</i>	<i>Collapsed Contact Width, w_C [nm]</i>	<i>Flattened Contact Width, w_F [nm]</i>	<i>Collapsed Adhesive Energy, R_C [$J \cdot m^{-2}$]</i>	<i>Flattened Adhesive Energy, R_F [$J \cdot m^{-2}$]</i>
1:10 / 1:35	1	54	46	25	31	14.8	8.0	1.29 ± 0.27	2.37 ± 0.80
1:10 / 1:35	1	52	59	25	31	14.8	8.0	1.56 ± 0.33	2.88 ± 0.96
1:10 / 1:35	2	40	59	26	31	14.9	8.1	0.92 ± 0.18	1.69 ± 0.55
1:10 / 1:35	2	42	94	26	31	14.9	8.1	1.59 ± 0.31	2.94 ± 0.96
1:10 / 1:35	2	42	99	26	31	14.9	8.1	1.71 ± 0.34	3.16 ± 1.03
1:10 / 1:35	2	45	108	26	31	14.9	8.1	2.13 ± 0.42	3.93 ± 1.28
1:10 / 1:35	2	40	114	26	31	14.9	8.1	1.77 ± 0.36	3.28 ± 1.08
1:30 / 1:35	1	54	83	26	31	14.9	8.0	2.31 ± 0.45	4.28 ± 1.39
1:30 / 1:35	1	58	81	26	31	14.9	8.0	2.56 ± 0.49	4.72 ± 1.53
1:30 / 1:35	1	55	96	26	31	14.9	8.0	2.72 ± 0.52	5.03 ± 1.63
1:30 / 1:35	1	54	95	26	31	14.9	8.0	2.63 ± 0.51	4.85 ± 1.57
1:30 / 1:35	2	50	100	27	33	15.1	8.2	2.40 ± 0.46	4.44 ± 1.42
1:30 / 1:35	2	44	141	27	33	15.1	8.2	2.65 ± 0.51	4.94 ± 1.58

It is important to contextualize and standardize the energy values obtained with these functionalized surfaces with respect to i) previously obtained data for bare MWCNT-graphitic interfaces, ii) atomistic simulation predictions, and iii) adhesive energies measured for other classes of materials [45-48]. For comparisons among tests with carbon nanotubes, we focus on comparing adhesive energy results assuming a flattened MWCNT configuration. The term “flattened” is derived from our previous work³⁶ where it was determined that MWCNTs can either be flattened or collapsed on a surface, depending on nanotube diameter and number of walls. This influences the contact width that is utilized in the Kendall analysis, leading to

ambiguity in the adhesive energy values. For completeness, contact widths and adhesive energies are reported using both conformation types in Table 3 (with subscripts ‘C’ and ‘F’ denoting collapsed and flattened, respectively). However, while both conformations are possible, MWCNTs with the diameters and numbers of walls reported in Table 3 are not expected to achieve a collapsed configuration, so adhesive energies assuming a flattened configuration are the most appropriate standard [42]. These results, for functionalized interfaces and bare interfaces studied previously, are shown in Figure 4. (We note that the amount of flattening or other factors, such as graphitic deposits [49], that increase contact area would lead to smaller adhesive energies than are reported.)

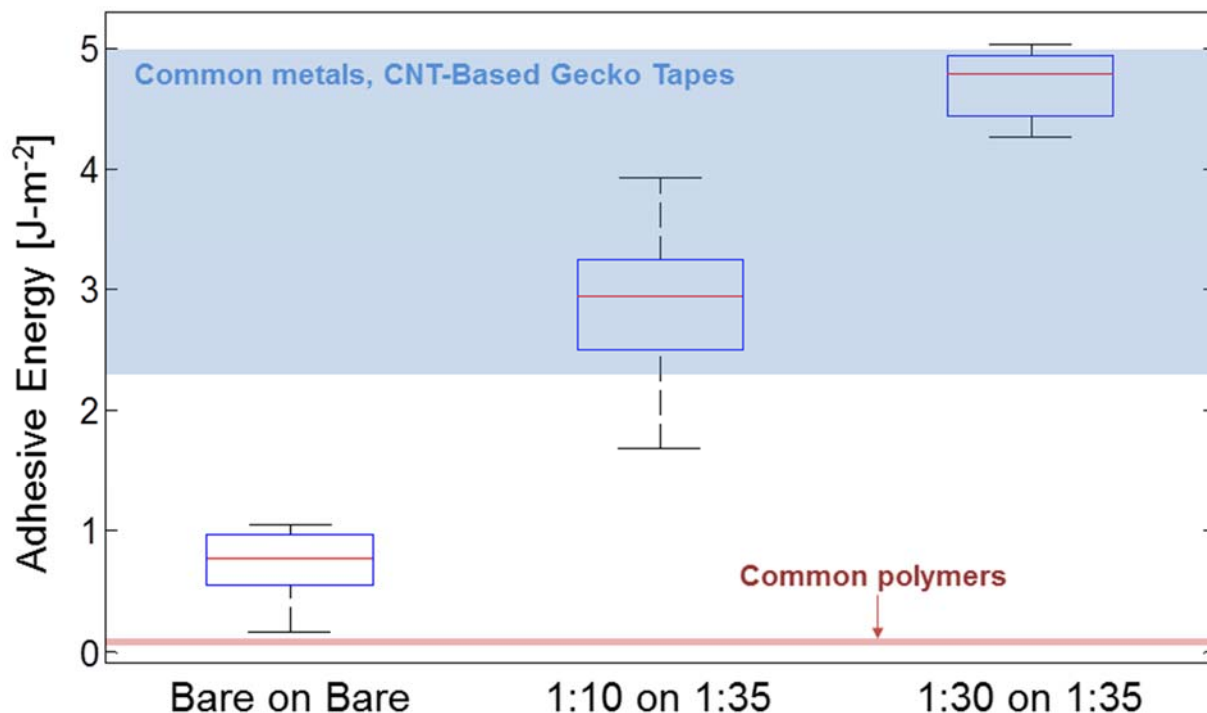


Figure 14: Experimental adhesive energies for bare-bare, 1:10 on 1:35, and 1:30 on 1:35 surfaces. Bare values were taken from [42]. For comparison, adhesive energies reported for common metals CNT-based Gecko tapes (adhered to various substrates) and adhesion energies for common polymers are included [45-48].

The 8 data points reported in [42] for bare graphite and graphene yielded an average adhesive energy (taken as twice the γ values reported) of 0.73 J-m^{-2} with a standard deviation of 0.30 J-m^{-2} . By comparison, the 1:10 on 1:35 tube-HOPG interfaces exhibited an average adhesive energy of 2.89 J-m^{-2} with a standard deviation of 0.71 J-m^{-2} . Finally, the average adhesive energy of the 1:30 on 1:35 interfaces was 4.71 J-m^{-2} with a standard deviation of 0.29 J-m^{-2} . Unpaired t tests between each pair of data sets indicate that there is a statistically significant difference ($p < 0.05$) between each of the mean values.

The role of dissipation in these adhesive energy measurements merits further discussion. In all cases, the energy values measured are small enough and the tubes and graphite are strong enough that we expect no significant non-local dissipation. For bare CNT-graphene/graphite interfaces, the adhesive energy measured was close to twice the surface energy of graphite reported in the

literature, suggesting that energy dissipation is not significant when separating those interfaces [42, 50-52]. However, the adhesive energy measured for arylpropionic-functionalized interfaces cannot be compared with literature values; this is a novel system. Atomistic simulations were performed to predict the surface energy of these interfaces as a function of coverage and, through comparison with experiments, assess the degree to which local dissipation contributes to adhesive energy measurements. In addition, the nature of interfacial interactions predicted *via* simulations can elucidate the mechanisms that govern an interesting experimental finding: intermediate coverages, not high coverages, yield the highest adhesive energies.

Atomistic simulations conducted by the Schatz group at Northwestern studied the adhesion of functionalized interfaces with coverages matching those used in *in situ* SEM experiments. Molecular mechanics (MM) was used for the stepwise compression or opening of interfaces. At each step, the outer layers were fixed after a shift of 0.01 nm [41]. Geometry minimization of the rest of the structure was performed before the next compression or opening step. These stepwise displacements approximate geometry changes and associated energies along reversible paths. To produce accurate descriptions of the interface geometries obtained from the MM calculations, those systems were also equilibrated at 300 K using molecular dynamics (MD) until conservation of energy was established. Two water molecules per functional group were included in the simulations in accordance with XPS measurements and estimated vacuum conditions during *in situ* testing [41]. Representative energy-vs.-distance curves and simulation snapshots are included in Figure 15.

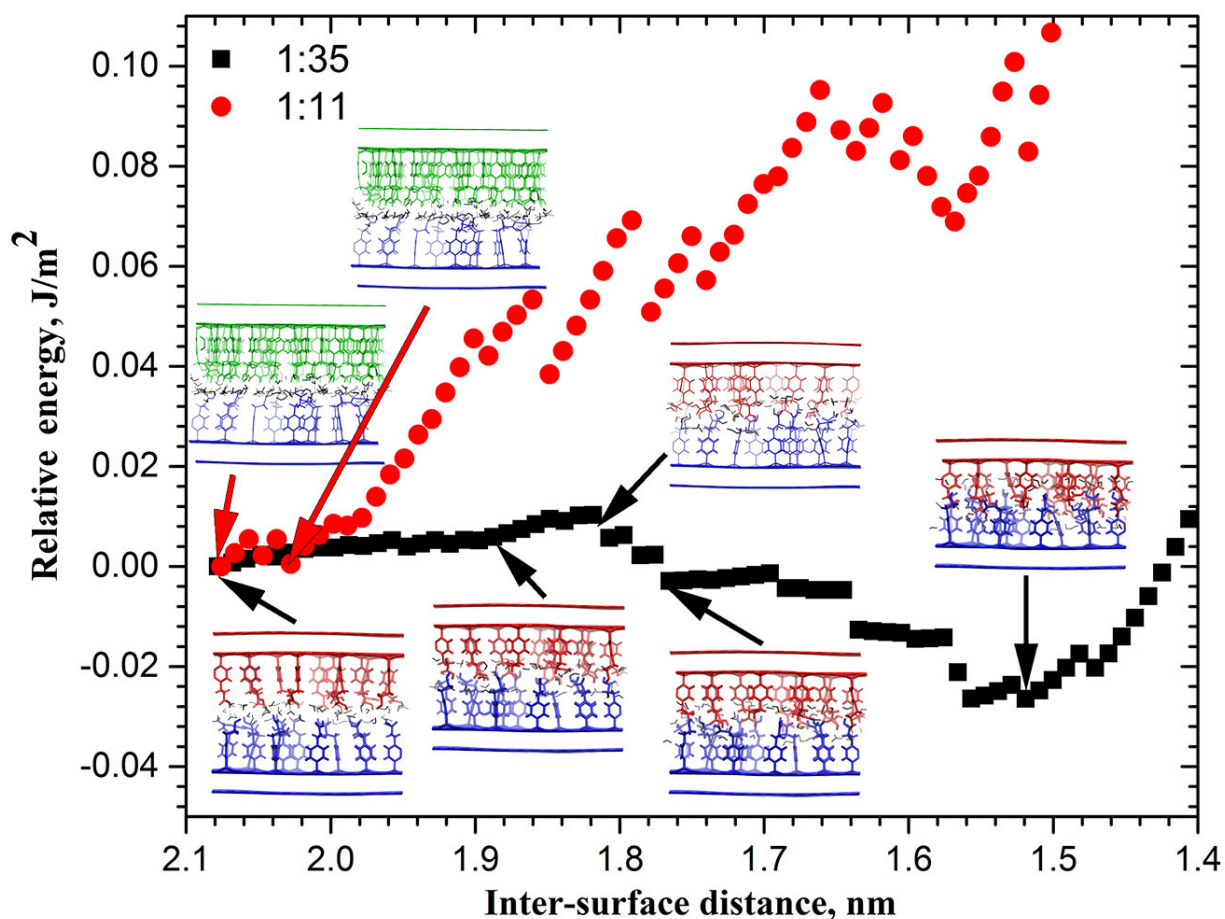


Figure 15: Energy profiles for the stepwise compression of interfaces formed by 1:35 on 1:35 (black squares) and 1:11 on 1:35 (red dots) functionalized surfaces in the presence of water. Insets are illustrations of configurations of interfaces at particular steps.

The simulation results clearly show that, for moderately functionalized surfaces, low energy states can be achieved when functional groups interdiffuse with one another (Figure 15, lower right side). This interdiffusion does not occur when one of the surfaces is highly functionalized. Qualitatively, these results reflect the experimental observations, where significantly larger adhesive energies were measured when both surfaces were moderately functionalized than when one was highly functionalized. Though the experimental measurements and computational predictions are quantitatively different, this correlation among adhesion trends vs. degree of functionalization suggests that functional group interdiffusion is an important mechanism governing the interactions of these interfaces.

Ultimately, the significant difference between the surface energy-based predictions and the adhesive energy measured in experiments indicates that irreversible energy dissipation governs the peeling process. Based on the energy profiles shown in Figure 15, we believe that the primary dissipation mechanism is the rupture of covalent bonds at the junctions between functional groups and the basal planes of CNTs and HOPG and within the propionic functional groups. For instance, the energy profiles computed for 1:35 on 1:35 surfaces exhibit abrupt changes in energy at inter-surface distances of approximately 1.64 and 1.58 nm due to sudden changes of hydrogen bond distributions. Hence, the average normal stresses acting on the surfaces, given by

the derivative of the energy (per unit area) with respect to inter-surface distance, are estimated to be as high as 0.6 GPa to 1.0 GPa. In the simulated 3 nm x 3 nm system (Figure 15, bottom right inset), this corresponds to a force of up to 9 nN acting over ~ 3 inter-surface contact points, or ~ 3 nN per point. This estimate offers an approximate lower bound to the forces that operate at the peeling front in experiments. As the functional groups on the surfaces are likely to be inhomogeneously distributed, localized forces may be even higher in experiments. In addition, the forces estimated from atomistic simulations correspond to those under infinitely slow separation with idealized geometries. As the characteristic experimental peeling time is shorter than the characteristic interdiffusion time, additional forces beyond those estimated from Figure 5 will be required to separate interdiffused surfaces in the experiments. Furthermore, for comparison, the strength of sp^3 carbon bonds has been experimentally measured to be as low as ~ 2.5 nN in some circumstances, which is within range of the approximate lower bound described above [53]. Thus, these high transient normal stresses are expected to cause covalent bond breakage of a substantial number of sp^3 bonds near the joints between functional groups and basal planes and within the propionic groups.

To support this hypothesis, we carried out a first-order estimation of the dissipated energy due to covalent bond breakage by assuming that two sp^3 bonds per pair of functional groups ruptured during peeling. As the dissociation energy of sp^3 bonds is ~ 367 kJ/mol [54], the additional energy per unit area required to separate two surfaces with 1:35 functionalization density is approximately 1.3 J-m^{-2} . This energy value is on the same order of adhesive energy measurements obtained from our experiments for the functionalized interfaces. Further, covalent bond breakage is more likely to arise with interdiffused structures, and hence with the 1:10 on 1:35 measurements. Therefore, it is reasonable to suggest that local covalent bond breakage appears to be the main energy dissipation mechanism leading to the high adhesive energy values measured in the experiments, which greatly exceed the values predicted through surface energy-based atomistic simulations.

In addition to dissipation, quantitative differences between experimental and theoretical results presented here may arise from inhomogeneous surfaces in the experiments. Recent studies suggest that diazonium chemistry leads to covalently bound oligomers on silicon carbide-supported graphene [55] and mostly physisorbed oligomers on graphite [56]. These studies are opposed to other reports that suggest monomers are present on planar surfaces such as HOPG [57-60]. As such, there is not yet a consensus on the way functional groups adhere to graphite, but it appears the propionic groups are present in the form of oligomers. Covalent bonding of propionic monomers is expected to occur on the tubes, as the curvatures of ~ 25 nm diameter tubes are greater than those of the ~ 50 nm diameter nanoparticles studied previously [61]. Compared with the systems of monomers studied in our simulations, oligomers would facilitate additional deformation mechanisms and bonding interactions that contribute to adhesion. In addition, while the aforementioned Raman spectroscopy results suggest that some covalent bonding of functional groups is present on the graphite surfaces, any physisorbed material could also be removed during peeling and, thus, affect energy measurements. Finally, the surfaces are also likely to be fouled by other materials from the atmosphere, such as hydrocarbons, and the tube surfaces are expected to have some amorphous carbon attached [49]. Their presence should also impact the peeling force, as amorphous carbon is expected to have a different functionalization ratio than the graphitic regions.

There are several additional studies that could provide meaningful insights for adhesion of nanoscale interfaces and its implications for nanocomposites design. At the nanoscale, future studies that aim to complement this work should explore interfilament shearing behavior. While enhanced adhesion leads to enhanced shear, it is important to account for multiple modes of interfilament failure, especially in composites such as CNT yarns which have great variation in alignment [62, 63]. The interplay between enhanced adhesion and reduced filament strength (resulting from different concentrations of sp^3 bonds on outer surfaces of MWCNTs due to varying coverages), and the resulting impact on composite performance, could also be explored through nanomechanical experiments [37] and macroscale statistical models [1]. Ultimately, scaling up these interfaces to the macroscopic level and incorporating them into efficient composite systems remain important engineering challenges for the future.

References

1. Wei, X., T. Filleter, and H.D. Espinosa, *Statistical shear lag model—Unraveling the size effect in hierarchical composites*. Acta biomaterialia, 2015. **18**: p. 206-212.
2. Meyers, M.A., J. McKittrick, and P.-Y. Chen, *Structural biological materials: critical mechanics-materials connections*. Science, 2013. **339**(6121): p. 773-779.
3. Meyers, M.A., et al., *Mechanical strength of abalone nacre: role of the soft organic layer*. Journal of the Mechanical behavior of biomedical materials, 2008. **1**(1): p. 76-85.
4. Landis, W., et al., *Mineral and organic matrix interaction in normally calcifying tendon visualized in three dimensions by high-voltage electron microscopic tomography and graphic image reconstruction*. Journal of structural biology, 1993. **110**(1): p. 39-54.
5. Penel, S., et al., *Length preferences and periodicity in β -strands. Antiparallel edge β -sheets are more likely to finish in non-hydrogen bonded rings*. Protein engineering, 2003. **16**(12): p. 957-961.
6. Shao, Y., et al., *Discontinuous crack-bridging model for fracture toughness analysis of nacre*. Journal of the Mechanics and Physics of Solids, 2012. **60**(8): p. 1400-1419.
7. Wei, X., M. Naraghi, and H.D. Espinosa, *Optimal length scales emerging from shear load transfer in natural materials: application to carbon-based nanocomposite design*. ACS nano, 2012. **6**(3): p. 2333-2344.
8. Menig, R., et al., *Quasi-static and dynamic mechanical response of Haliotis rufescens (abalone) shells*. Acta Materialia, 2000. **48**(9): p. 2383-2398.
9. Bazant, Z.P. and J. Planas, *Fracture and size effect in concrete and other quasibrittle materials*. Vol. 16. 1997: CRC press.
10. Bažant, Z., *Size effect on structural strength: a review*. Archive of Applied Mechanics, 1999. **69**(9-10): p. 703-725.
11. Naraghi, M., et al., *A Multiscale Study of High Performance Double-Walled Nanotube– Polymer Fibers*. ACS nano, 2010. **4**(11): p. 6463-6476.
12. Filleter, T., et al., *Ultrahigh Strength and Stiffness in Cross-Linked Hierarchical Carbon Nanotube Bundles*. Advanced Materials, 2011. **23**(25): p. 2855-2860.
13. Naraghi, M., et al., *Atomistic investigation of load transfer between DWNT bundles “Crosslinked” by PMMA oligomers*. Advanced Functional Materials, 2013. **23**(15): p. 1883-1892.
14. Papkov, D., et al., *Extraordinary improvement of the graphitic structure of continuous carbon nanofibers templated with double wall carbon nanotubes*. ACS nano, 2012. **7**(1): p. 126-142.
15. Phoenix, S., M. Ibnabdeljalil, and C.-Y. Hui, *Size effects in the distribution for strength of brittle matrix fibrous composites*. International Journal of Solids and Structures, 1997. **34**(5): p. 545-568.
16. Landis, C.M., I.J. Beyerlein, and R.M. McMeeking, *Micromechanical simulation of the failure of fiber reinforced composites*. Journal of the Mechanics and Physics of Solids, 2000. **48**(3): p. 621-648.
17. Daniels, H., *The statistical theory of the strength of bundles of threads. I*. Proceedings of the Royal Society of London. Series A. Mathematical and Physical Sciences, 1945. **183**(995): p. 405-435.
18. Phoenix, S. and R. Raj, *Overview no. 100 Scalings in fracture probabilities for a brittle matrix fiber composite*. Acta metallurgica et materialia, 1992. **40**(11): p. 2813-2828.
19. Ibnabdeljalil, M. and W. Curtin, *Strength and reliability of fiber-reinforced composites: localized load-sharing and associated size effects*. International Journal of Solids and Structures, 1997. **34**(21): p. 2649-2668.
20. Beese, A.M., et al., *Bio-Inspired Carbon Nanotube–Polymer Composite Yarns with Hydrogen Bond-Mediated Lateral Interactions*. ACS nano, 2013. **7**(4): p. 3434-3446.

21. Pickering, K. and T. Murray, *Weak link scaling analysis of high-strength carbon fibre*. Composites Part A: Applied Science and Manufacturing, 1999. **30**(8): p. 1017-1021.
22. de Andrade Silva, F., N. Chawla, and R.D. de Toledo Filho, *Tensile behavior of high performance natural (sisal) fibers*. Composites Science and Technology, 2008. **68**(15): p. 3438-3443.
23. Okabe, T. and N. Takeda, *Size effect on tensile strength of unidirectional CFRP composites—experiment and simulation*. Composites Science and Technology, 2002. **62**(15): p. 2053-2064.
24. Wei, X., et al., *A new Monte Carlo model for predicting the mechanical properties of fiber yarns*. Journal of the Mechanics and Physics of Solids, 2015. **84**: p. 325-335.
25. Filleter, T. and H. Espinosa, *Multi-scale mechanical improvement produced in carbon nanotube fibers by irradiation cross-linking*. Carbon, 2013. **56**: p. 1-11.
26. Hearle, J.W., P. Grosberg, and S. Backer, *Structural mechanics of fibers, yarns, and fabrics*. 1969.
27. Porwal, P.K., I.J. Beyerlein, and S.L. Phoenix, *Statistical strength of a twisted fiber bundle: an extension of Daniels equal-load-sharing parallel bundle theory*. Journal of Mechanics of Materials and Structures, 2006. **1**(8): p. 1425-1447.
28. Porwal, P.K., I.J. Beyerlein, and S.L. Phoenix, *Statistical strength of twisted fiber bundles with load sharing controlled by frictional length scales*. Journal of Mechanics of materials and Structures, 2007. **4**(2): p. 773-791.
29. Beyerlein, I.J., et al., *Scale and twist effects on the strength of nanostructured yarns and reinforced composites*. Nanotechnology, 2009. **20**(48).
30. Barber, A.H., et al., *On the tensile strength distribution of multiwalled carbon nanotubes*. Applied Physics Letters, 2005. **87**(20): p. 203106.
31. Barber, A., et al., *Stochastic strength of nanotubes: an appraisal of available data*. Composites science and technology, 2005. **65**(15): p. 2380-2384.
32. Klein, C.A., *Characteristic tensile strength and Weibull shape parameter of carbon nanotubes*. Journal of applied physics, 2007. **101**(12): p. 124909.
33. Behabtu, N., et al., *Strong, light, multifunctional fibers of carbon nanotubes with ultrahigh conductivity*. Science, 2013. **339**(6116): p. 182-186.
34. Yu, M.-F., et al., *Strength and breaking mechanism of multiwalled carbon nanotubes under tensile load*. Science, 2000. **287**(5453): p. 637-640.
35. Paci, J.T., et al., *Shear and friction between carbon nanotubes in bundles and yarns*. Nano letters, 2014.
36. Zhang, X. and Q. Li, *Enhancement of friction between carbon nanotubes: an efficient strategy to strengthen fibers*. Acs Nano, 2009. **4**(1): p. 312-316.
37. Peng, B., et al., *Measurements of near-ultimate strength for multiwalled carbon nanotubes and irradiation-induced crosslinking improvements*. Nature nanotechnology, 2008. **3**(10): p. 626-631.
38. Cranford, S.W. and M.J. Buehler, *In silico assembly and nanomechanical characterization of carbon nanotube buckypaper*. Nanotechnology, 2010. **21**(26): p. 265706.
39. Mirzaeifar, R., Z. Qin, and M.J. Buehler, *Mesoscale mechanics of twisting carbon nanotube yarns*. Nanoscale, 2015. **7**(12): p. 5435-5445.
40. Plimpton, S., *Fast parallel algorithms for short-range molecular dynamics*. Journal of computational physics, 1995. **117**(1): p. 1-19.
41. Roenbeck, M.R., et al., *Molecular-Level Engineering of Adhesion in Carbon Nanomaterial Interfaces*. Nano letters, 2015. **15**(7): p. 4504-4516.
42. Roenbeck, M.R., et al., *In Situ Scanning Electron Microscope Peeling To Quantify Surface Energy between Multiwalled Carbon Nanotubes and Graphene*. ACS nano, 2014. **8**(1): p. 124-138.
43. Bahr, J.L. and J.M. Tour, *Highly functionalized carbon nanotubes using in situ generated diazonium compounds*. Chemistry of Materials, 2001. **13**(11): p. 3823-3824.

44. Kendall, K., *Thin-Film Peeling - Elastic Term*. Journal of Physics D-Applied Physics, 1975. **8**(13): p. 1449-1452.
45. Israelachvili, J.N., *Intermolecular and Surface Forces*. 3rd ed. 2011: Elsevier Inc.
46. Drummond, C.J. and D.Y. Chan, *van der Waals interaction, surface free energies, and contact angles: dispersive polymers and liquids*. Langmuir, 1997. **13**(14): p. 3890-3895.
47. Wawra, H., *The surface energy of solid materials as measured by ultrasonic and conventional test methods. Pt. 2*. 1975.
48. Ge, L., et al., *Carbon nanotube-based synthetic gecko tapes*. Proceedings of the National Academy of Sciences, 2007. **104**(26): p. 10792-10795.
49. An, Z., et al., *Inherent carbonaceous impurities on arc-discharge multiwalled carbon nanotubes and their implications for nanoscale interfaces*. Carbon, 2014. **80**: p. 1-11.
50. Zacharia, R., H. Ulbricht, and T. Hertel, *Interlayer cohesive energy of graphite from thermal desorption of polyaromatic hydrocarbons*. Physical Review B, 2004. **69**(15): p. 155406.
51. Benedict, L.X., et al., *Microscopic determination of the interlayer binding energy in graphite*. Chemical Physics Letters, 1998. **286**(5): p. 490-496.
52. Girifalco, L.A. and R.A. Lad, *Energy of Cohesion, Compressibility, and the Potential Energy Functions of the Graphite System*. Journal of Chemical Physics, 1956. **25**(4): p. 693-697.
53. Lebedeva, N.V., et al., *"Fatal Adsorption" of Brushlike Macromolecules: High Sensitivity of CC Bond Cleavage Rates to Substrate Surface Energy*. Journal of the American Chemical Society, 2008. **130**(13): p. 4228-4229.
54. Blanksby, S.J. and G.B. Ellison, *Bond dissociation energies of organic molecules*. Accounts of chemical research, 2003. **36**(4): p. 255-263.
55. Hossain, M.Z., M.A. Walsh, and M.C. Hersam, *Scanning tunneling microscopy, spectroscopy, and nanolithography of epitaxial graphene chemically modified with aryl moieties*. Journal of the American Chemical Society, 2010. **132**(43): p. 15399-15403.
56. Ma, H., et al., *Scanning Tunneling and Atomic Force Microscopy Evidence for Covalent and Noncovalent Interactions between Aryl Films and Highly Ordered Pyrolytic Graphite*. The Journal of Physical Chemistry C, 2014. **118**(11): p. 5820-5826.
57. Koehler, F.M., et al., *Selective Chemical Modification of Graphene Surfaces: Distinction Between Single-and Bilayer Graphene*. Small, 2010. **6**(10): p. 1125-1130.
58. Niyogi, S., et al., *Spectroscopy of covalently functionalized graphene*. Nano letters, 2010. **10**(10): p. 4061-4066.
59. Huang, P., et al., *Graphene covalently binding aryl groups: conductivity increases rather than decreases*. ACS nano, 2011. **5**(10): p. 7945-7949.
60. Fan, X., R. Nouchi, and K. Tanigaki, *Effect of charge puddles and ripples on the chemical reactivity of single layer graphene supported by SiO₂/Si substrate*. The Journal of Physical Chemistry C, 2011. **115**(26): p. 12960-12964.
61. Wu, Q., et al., *Selective surface functionalization at regions of high local curvature in graphene*. Chem. Commun., 2013. **49**(7): p. 677-679.
62. Beese, A.M., et al., *What Limits the Strength of Carbon Nanotube Yarns? Exploring Processing-Structure-Property Relationships*. Submitted to ACS Nano, 2014.
63. Paci, J.T., et al., *Shear and friction between carbon nanotubes in bundles and yarns*. to be appear in Nano Letters, 2014.

The work in the Buehler group focused on atomistic and bottom-up modeling of carbon nanotubes and carbon nanotube based materials. Both reactive and nonreactive full atomistic simulations have been carried out, and **scaled up to larger time- and length-scales** by running coarse-grain simulations. Our study provides theoretical evaluations to use carbon nanotubes combining various polymer systems as building blocks to design and construct continuum structures and materials for multiple functional applications. All activities were closely integrated with experimental efforts in the MURI team. In the scientific accomplishments below we highlight three major activities:

- I) Multiscale Study of Load Transfer Between Functionalized DWNT Bundles toward Understanding of Mesoscale Mechanics of Twisting CNT Yarns.
- II) Nanomechanics of Carbon Fiber: Carbyne in Varied Chemical Environments in Water
- III) Nanomechanics of Ultra-strong Carbyne Network Toward Water Filtering

I. Multiscale Study of Load Transfer Between Functionalized DWNT Bundles toward Understanding of Mesoscale Mechanics of Twisting CNT Yarns.

Published in:

Mirzaeifar R., Qin Z. and Buehler, M. J., Mesoscale mechanics of twisting carbon nanotube yarns. *Nanoscale*, 7, 5435–5445 (2015)

Fabricating continuous macroscopic carbon nanotube (CNT) yarns with mechanical properties close to individual CNTs remains a major challenge. Spinning CNT fibers and ribbons for enhancing the weak interactions between the nanotubes is a simple and efficient method for fabricating high-strength and tough continuous yarns. Here we investigate the mesoscale mechanics of twisting CNT yarns using full atomistic and coarse grained molecular dynamics simulations, considering concurrent mechanisms at multiple length-scales. To investigate the mechanical response of such a complex structure without losing insights into the molecular mechanism, we applied a multiscale strategy. The full atomistic results are used for training a coarse grained model for studying larger systems consisting of several CNTs (Figures 1,2). The mesoscopic model parameters are updated as a function of the twist angle, based on the full atomistic results, in order to incorporate the atomistic scale deformation mechanisms in larger scale simulations. By bridging across two length scales, our model is capable of accurately predicting the mechanical behavior of twisted yarns while the atomistic level deformations in individual nanotubes are integrated into the model by updating the parameters. Our results focused on studying a bundle of close packed nanotubes provide novel mechanistic insights into the spinning of CNTs. Our simulations reveal how twisting a bundle of CNTs improves the shear interaction between the nanotubes up to a certain level due to increasing the interaction surface. Furthermore, twisting the bundle weakens the intertube interactions due to excessive deformation in the cross sections of individual CNTs in the bundle.

Coarse-grained simulation approaches allow the investigation of mechanical properties of larger CNT yarns composed of several nanotubes, which is computationally impractical to be performed by full atomistic models. The coarse grain representation of CNTs is developed based on the full atomistic calculations and by performing a set of standard mechanical tests to describe the nanotube behavior. However, coarse-grained models of CNT treat CNT as a cylinder composed of a series of beads, which simplifies the lateral deformation of the tube in compression, which is essential for studying the twisted CNT yarn as the lateral compression force can alter the contacting shape and area between CNT which can significantly affect the shearing force in the other direction during loading, as what is shown in Figure 1.

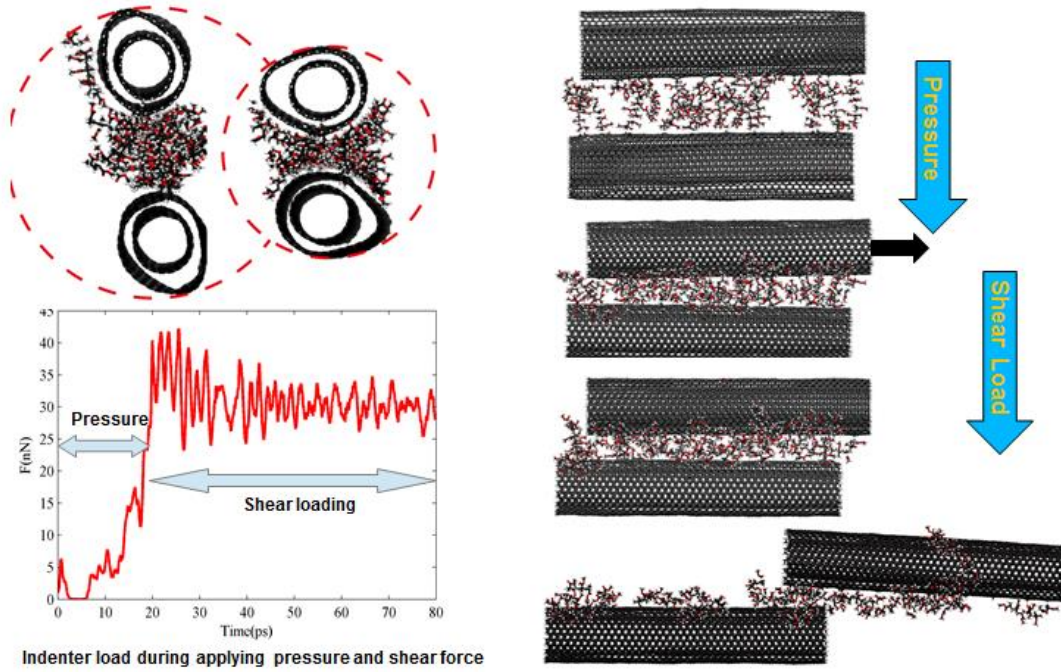


Figure 1. Simulation and snapshots of pressure-dependent shear loading force. It is show that pressure can significantly affect the shearing force. Using full atomic force field, we can quantify the shear force as a function of the compression pressure, which is caused during the twisting of CNT yarns.

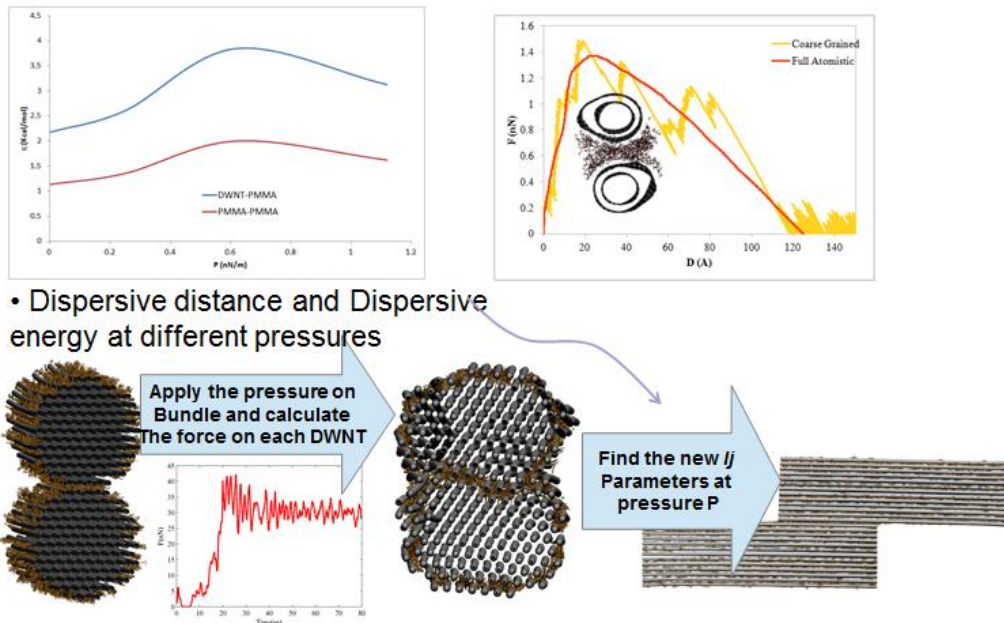


Figure 2. Using full atomic simulation, we investigate the shearing force-displacement curve for each compression pressure on the CNT yarn and then train the mesoscopic model (by tuning the LJ parameters for CNT-PMMA and PMMA-PMMA interactions) to find a good agreement and use the mesoscopic model for studying the large scale yarn assembly and mechanics.

In addition to the full atomistic studies, we have also studied larger systems consisting of several CNTs by implementing a coarse grained (CG) model (Figure 2). In order to incorporate the atomistic scale deformation mechanisms, i.e., the cross section changes in the individual tubes into the coarse grained model, we have introduced a novel strategy for bridging the two length scales by updating the coarse graining parameters based on the full atomistic results. Coarse grained models are powerful tools for studying the mechanical properties of CNT yarns, and these models have been recently used for studying the mechanical behavior and microstructural evolution of CNT continuous fibers under twisting and tension. However, our results show that the mesoscale model should be trained by the atomistic results to bridge the gap between two different length scales. This strategy can be developed for studying various properties of CNTs by the coarse grained models more accurately. In studying large scaled CNT yarns, we have considered two different conditions for investigating the properties of yarns fabricated by directly spinning the as-grown super-aligned CNTs and also the yarns made by twisting CNT films (Figure 3). A recently developed strategy is used in both cases for modeling the randomly entangled nanotubes in the forest or film of CNTs before the spinning.

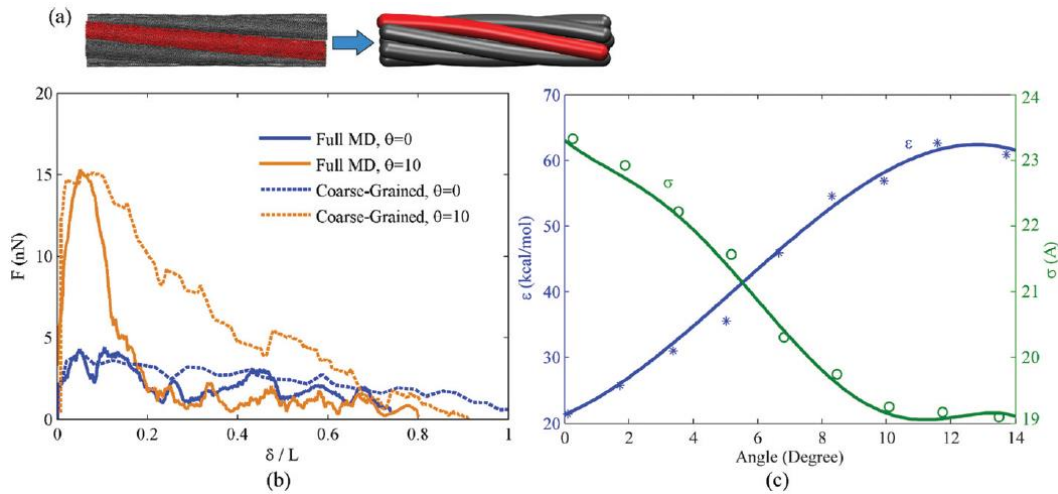


Figure 3. A set of seven close packed DWNTs modeled by the coarse grained model. (b) A sample of matched force–displacement responses for two different twisting angles and (c) the required updated vdW parameters for achieving the best match between the coarse grained and full atomistic models as functions of twisting angles. The cross section distortions shown in Fig. 3 cause an increase in the inter-tube vdW interaction and decrease in the tubes center lines distances (c).

By using full atomic simulations of the pull-out test of twisted CNT and creating a mesoscopic model with its parameters trained according to the atomic simulations, we are about to investigate the large scale mechanical behavior of CNT yarn and discuss the effect of twisting angle on its mechanical behavior. Our results show that twisting the bundle enhances the intertube interactions in a bundle of CNTs up to a certain level by increasing the interaction area (Figure 3). By twisting the tubes more than the optimum angle, the excessive cross section deformations become prominent and weaken the intertube shear strength. A coarse grained model is developed by training the mesoscopic parameters based on the full atomistic model. The obtained coarse grained model bridges two different length scales and incorporates the CNTs deformations at the atomistic level into the larger scale model, which facilitates studying the mechanical behavior of twisted yarns with several CNTs accurately.

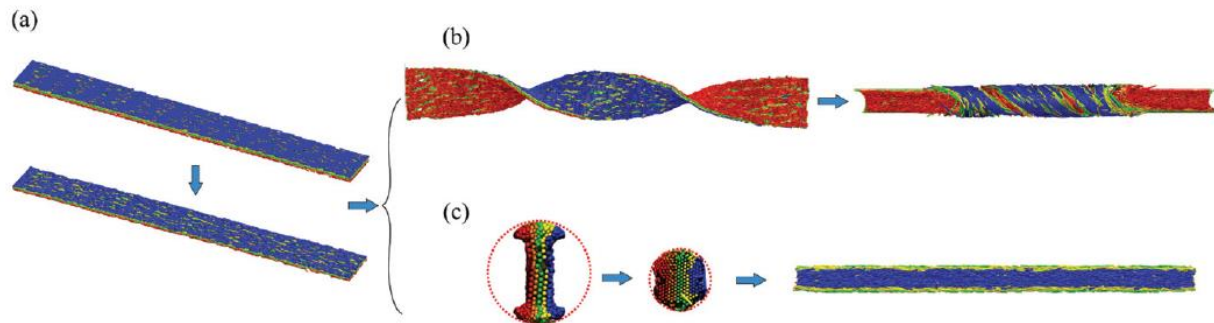


Figure 4. (a) A schematic of the mesoscopic mat composed of five CNT layers with random orientations around the axis. Each layer contains several CNTs with a random length in the range of 5 to 10% of the total length of the mat. The initial system is used for constructing (b) twisted and (c) untwisted yarns. Different colors are used for distinguishing the layers.

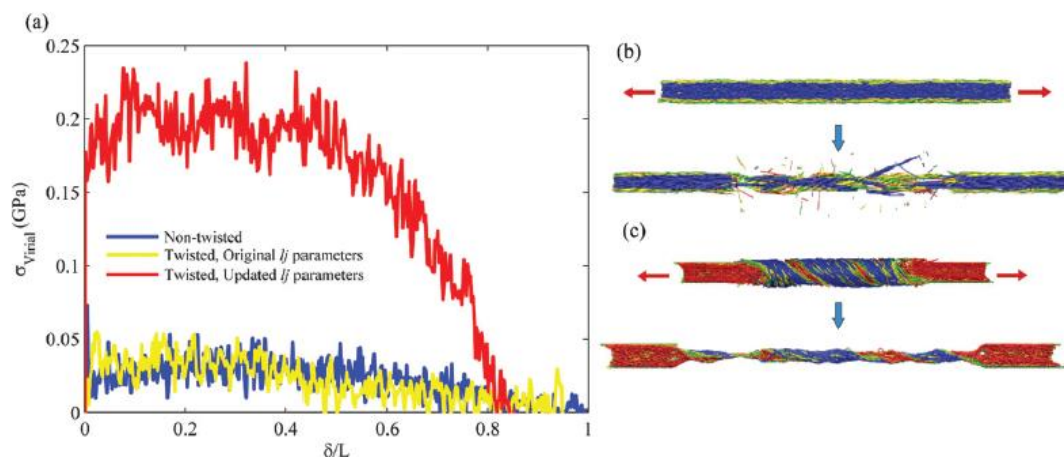


Figure 5. The effect of twisting on the strength of yarns created from spinning and squeezing CNT mats. (a) The stress versus engineering strain for a twisted and untwisted yarn. The stress–strain response predicted by the original coarse grained model is also shown for comparison purposes. (b, c) The deformation of both untwisted and twisted yarns subjected to the axial tension. By using the original vdW parameters the coarse grained model exhibits no significant change in the strength by twisting the yarns but the updated coarse grained model shows the improvement caused by twisting on both the strength and toughness of the yarn consistent with the experimental results (a). The stress–strain responses in all the three cases exhibit a sharp initial slope, which is remarkably high for the twisted yarn. This sharp initial response corresponds to the case that the monotonically increasing force is not sufficient to overcome the vdW interactions between the tubes and the displacements are negligible. The value of force at which sliding begins is larger for the twisted yarns because the vdW interactions are stronger.

II. Nanomechanics of Carbon Fiber: Carbyne in Varied Chemical Environments in Water

Published in:

Mirzaeifar R., Qin Z. and Buehler, M. J., Tensile strength of carbyne chains in varied chemical environments and structural lengths. *Nanotechnology*, 25, article# 371001 (2014)

Carbyne and carbyne-based low-dimensional structures are promising for several applications including ultra-compact circuits and purification devices. Designing any applied carbyne-based structure requires a fundamental understanding of the mechanical strength of carbyne chains with different lengths at different temperatures and operating chemical environment (Figure 6). Here we use molecular dynamics simulations to investigate the strength of carbyne chains with different lengths at different temperatures. A theoretical framework based on statistical mechanics and molecular dynamics results is presented, proving a fast and insightful method for predicting the rupture force and its physical mechanism. The effect of water molecules' interaction is also studied on the mechanical properties and it is shown that both the tensile strength and rupture strain are improved by the water interaction. The results of this work can be used for designing and analyzing the robustness and reliability of various carbyne-based materials and applied devices for various working conditions.

We focus on the dependency of carbyne chains nanomechanical properties, particularly the strength, to the chain length, temperature and also interaction with water molecules. Two different methods are used in this section; molecular dynamics with the first-principles based ReaxFF force field and a theoretical framework based on the extended Bell model. The presented results shed light on the nanomechanical properties of carbyne chains, and can be used for designing network structures for applications that requires specific porosity and strength.

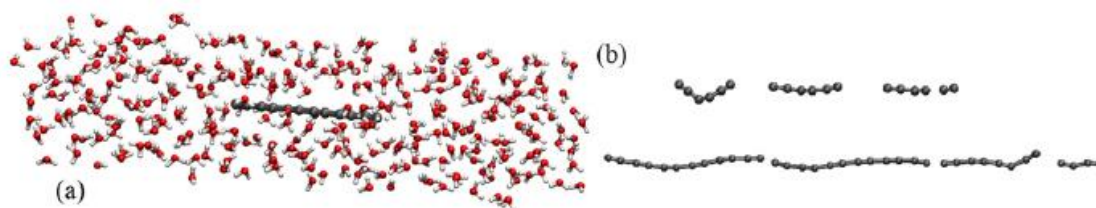


Figure 6 (a) Carbyne chain (of 15 Å in length) inside the water-filled box before equilibration and (b) unfolding and stretching carbyne chains surrounded by water molecules with 7 (upper) and 15 Å (lower) length. Water molecules in (b) are not shown for clarity.

As shown in figure 6, the water molecules slightly affect the response of both carbyne chains. The force-extension of chains in water is associated with several regions with different slopes. Studying the deformation of the chain shows that the deformation mechanism in water consists of unbending the folded chain and extension of the bonds in the chain. The deformation mechanism switches between unbending and stretching due to the varying interaction of the chain with the surrounding water molecules. Both the rupture force and ultimate strain of the chains are slightly improved in water.

Figures 7(a) and (b) compare the force extension curves for 7 and 15 Å pristine carbyne chains with the carbyne chains in acidic and basic solutions. It is observed that the basic environment decreases the chain strength, while the strength in acidic solution is slightly increased. Further analyzing the mechanical response of carbyne chains in the basic solution shows that the force-extension curves has two consequent peaks before the final rupture of the chain.

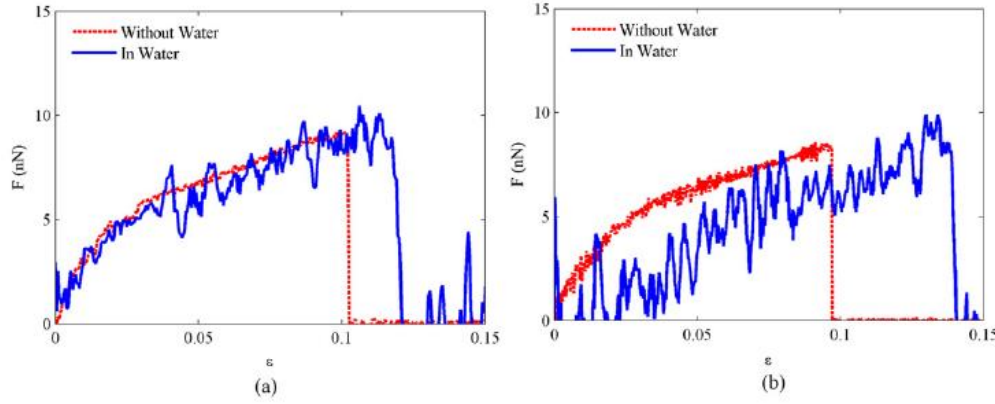


Figure 7. The force extension of carbyne chains with (a) 7 Å and (b) 15 Å length. The force extension curve is compared for the original chains and carbyne chains in water.

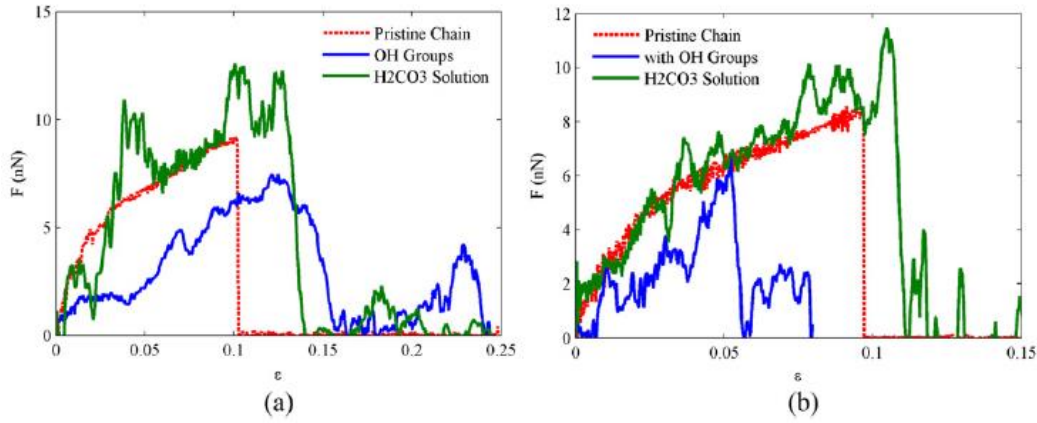


Figure 8. The force extension of carbyne chains with (a) 7 Å and (b) 15 Å length. The force extension curve is compared for the pristine chains and carbyne chains in acidic and basic solutions.

In this work the effect of various parameters, including the chain length, temperature and operating environment, on the mechanical properties of carbyne were studied. Carbyne and carbyne-based structures are supreme candidates for several applications, i.e. water purification, and designing such materials and devices requires a better understanding of carbyne mechanical properties. Molecular dynamics (MD) simulations are performed for calculating the rupture force of carbyne chains with different lengths at different temperatures. In order to facilitate the design procedure, a theoretical framework is presented that is calibrated based on the MD simulations for assessing the rupture force. The effect of water molecules' interaction and the acidic and basic solutions are also studied on the mechanical properties, which presents fundamental knowledge for studying carbyne-based filtration and purification devices.

III. Nanomechanics of Ultra-strong Carbyne Network Toward Water Filtering

Published in:

Qin Z. and Buehler, M. J., Nonlinear Viscous Water at Nanoporous Two-Dimensional Interfaces Resists High-Speed Flow through Cooperativity. *Nano Letters*, 15, 3939–3944, (2015)

Recently emerging ultrathin two-dimensional carbon materials provide potentially game-changing membranes for water filtration. Here we discover a changed water behavior at the nanoscale that is significantly distinct from its bulk state as water flows through two-dimensional carbon allotropes. We find that water exhibits a very high viscosity due to the cooperativity of water molecules that enhances the nonbonded H-bond interactions with the dense lattice of carbon structures, which renders flow significantly more viscous, with a resistance that is inversely proportional to the sixth power of the characteristic length of the nanopores. This is in contrast to a constant value as assumed in conventional knowledge. Our findings reveal how water molecules behave drastically different from their bulk state under extreme nanoconfinement conditions. These insights enable us to incorporate the size analysis of particles in variant untreated water into membrane design and propose the design of more efficient devices with higher filtration throughput and greater mechanical resilience.

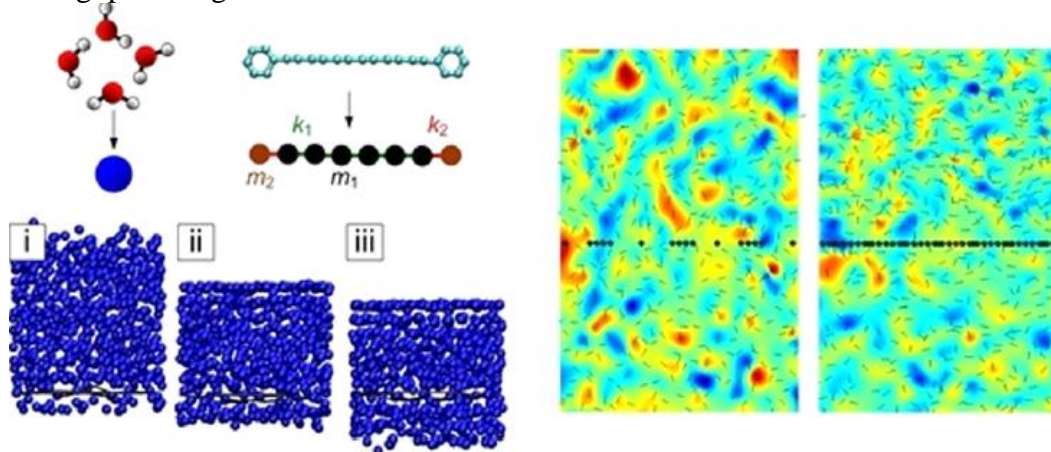


Figure 9. Left: Multiscale modeling of the water–graphyne system model. Schematics of the CG scheme to simplify the system by taking four water molecules as a single bead for water, an aromatic ring of six carbon atoms as a second type of bead, and two carbon atoms bonded by a triple bond as an another type of bead. Beads for carbon atoms are bonded by breakable springs of different stiffness. The simulation snapshots (i, ii, and iii) taken during the filtration, for different movement of the indenter. Right: (b) The velocity distribution of the water beads within the middle slice (of 5 Å thickness, in the y – z plan) of two water–graphyne systems (a porous versus a dense network for the system on left and right side, respectively and both are subjected to the flow rate of $v = 5$ m/s).

Using both full atomic model and coarse-grained model we have compare the different mechanical response of different carbyne network in water flow. We find that the water viscosity is inversely proportional to the sixth power of the characteristic length of nanopores, and its high value is critical for understanding the throughput and mechanical resilience of ultrathin membranes. We expect that a high viscosity may generally exist once transporting through other ultrathin carbon allotropes and carbon nanofiber based membranes, as we find a similar density distribution and molecular structures at the graphene–water interface. Our results provide fundamental guidelines for designing innovative treatment facilities targeting different filtration purposes by removing particles of different sizes; examples are summarized Figure 9.

Optimizing water filtering for lower energy consumption by using lightweight nanomaterials is attracting and challenging, which needs understanding of the physical interaction between water and the filtering material at their interface at nanoscale. Our current study demonstrates that

multiscale modeling, including full atomistic one and CG one, provides the precise and efficient tools to understand such characteristic. Our study shows that the maximum water flow to rupture the membrane is limited by the water nonlinearity and requires properly designs of the boundary confinements for compensation. Thus, far carbon porous materials are the only 2D material known so far that provides the sufficient strength and has the potential to be programmed for different filtering purposes with efficiency. Other filtering materials, having the 2D structure and nanopore-like carbon membrane, can also benefit from our study to improve the design, but the material property needs to be calibrated before using the criterion.

Our fundamental study of the critical conditions of nanoporous membrane rupture under flow provides a guideline for safety design, which can easily be implemented by designing the boundary conditions accordingly. It was raised that incorporating particle size analysis into the design processes can result in innovative treatment facilities. One solution may be designing a hierarchical multilayer system that picks up the qualified membrane type and boundary condition for each layer for different filtering purposes, as shown in Figure 10.

Evolving nanotechnology has shown amazing strength in helping us to reach the limiting performance and capability of many engineering tasks by using low-dimensional nanomaterials. Specifically, by precisely designing the structure and the boundary condition of each layer of nanomembranes and their hierarchical arrangements in the filtration facility, we expect to reduce the energy cost and weight of the equipment, which will be essential for extreme conditions, for example, islands and long-term voyage by sea or in space as well as separation processes in chemical engineering or air filtering.

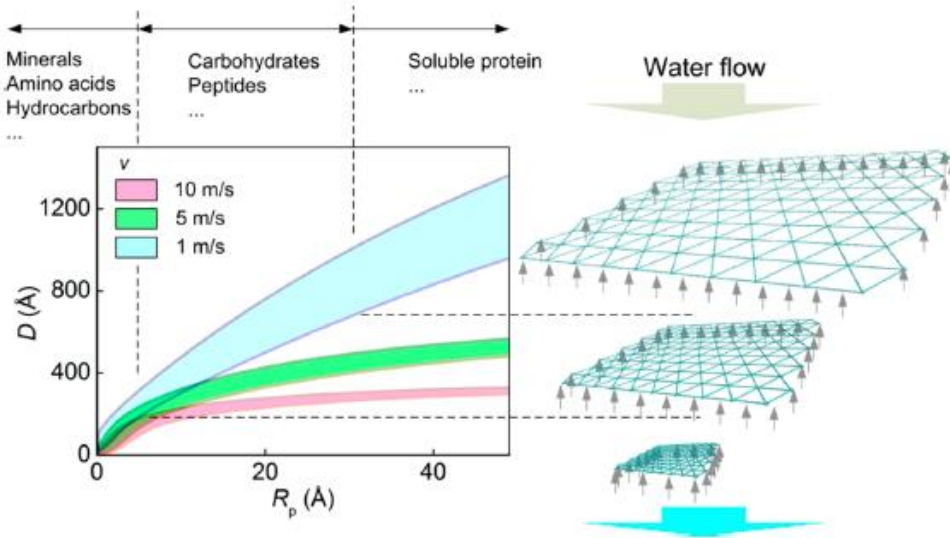


Figure 10. Scaling law for the design of the graphyne membrane system for filtering particles of different characteristic radii. This plot is made according to the equation in paper and each color region gives the critical length of the boundary condition that needs to be satisfied for the specific flow rate. The upper and lower bound of each region is defined by the assumption of rigid lattice and deformable lattice, respectively. Several examples of different characteristic radius (R_p) and snapshots of necessary graphyne structures and boundary conditions are schematically given on the right side for the case of $v = 1$ m/s.